Title

Design Considerations for Earthquake-Resistant Reinforced Concrete Special Moment Frames

Author

Visnjic, Tea

Publication Date

2014

Design Considerations for Earthquake-Resistant Reinforced Concrete Special Moment Frames

By

Tea Višnjić

A dissertation submitted in partial satisfaction of the

requirements for the degree of

Doctor of Philosophy

in

Engineering – Civil and Environmental Engineering

in the

Graduate Division

of the

University of California, Berkeley

Committee in charge:

Professor Marios Panagiotou, Chair
Professor Jack Moehle
Professor Per-Olof Persson

Fall 2014

Design Considerations for Earthquake-Resistant
Reinforced Concrete Special Moment Frames

Abstract

Design Considerations for Earthquake-Resistant
Reinforced Concrete Special Moment Frames

By

Tea Višnjić

Doctor of Philosophy in Engineering - Civil and Environmental Engineering

University of California, Berkeley

Professor Marios Panagiotou, Chair

In recent decades, improvement in construction and design practices and better estimation in seismic demands has led to an increasing number of reinforced concrete special moment resisting frame (SMRF) buildings with height and member sizes exceeding those typically built in the past. While current codes improved greatly over the years, reflecting the development in all areas of structural engineering including design, analytical models, computing capabilities, material technologies and so forth, many design specifications introduced around the prevailing practices from decades ago remain in effect. The aim of this dissertation is to address some potentially problematic areas in current design standards and propose ways to improve them. Specifically, the focal points of the work presented concern with two separate areas in the design of reinforced concrete SMRF buildings.

The first topic is the investigation of the transverse steel spacing requirements in the plastic hinge zones of reinforced concrete SMRF beams. Two large reinforced concrete SMRF beams were built and subjected to earthquake-like damage in the laboratory test with the goal: (a) to demonstrate that the maximum hoop spacing limits specified in the concurrent 2008 ACI 318 Code could produce a beam with performance inferior to the implied expectations at design level ground shaking intensity, and (b) to evaluate the effect of reducing this hoop spacing limit and recommend code changes for the 2011 ACI 318 Code. The experiments included two 30 in. x 48 in. beams with identical size, material properties, and longitudinal reinforcement ratio, but different transverse hoop spacing, which were subjected to reverse cyclic displacement history to simulate the earthquake-induced deformations expected at the design earthquake (DE) hazard level. The first specimen, Beam 1, was designed with the 2008 ACI 318 hoop spacing requirement and exhibited limited ductility before experiencing sudden and significant loss of load bearing capacity at a displacement ductility of 3.4. The second specimen, Beam 2, built with reduced hoop spacing, showed notable improvement in response and was capable of sustaining 90% of its load bearing capacity up to a displacement ductility level of 6.5. Of the two specimens, only Beam 2 sustained the deformation levels compatible with the DE shaking intensity without significant loss of strength. Both beams, however, failed due to longitudinal bar buckling, which pointed to potential vulnerability in the current transverse reinforcement detailing using multiple piece hoops consisting of stirrups with vertical and horizontal crossties

and bracing only alternate longitudinal bars with vertical crossties. Further experimental research in this area is strongly recommended.

The second topic concerns with the global nonlinear response of reinforced concrete SMRFs under strong ground motion, with emphasis placed on seismic shear demand in SMRF columns. Current ACI 318 specifications offer two different approaches in calculating the seismic shear demand, however with some ambiguity and much room for free interpretation that can vastly impact the shear capacity of the column and potentially result in unconservative design. Total of eight numerical models of buildings with perimeter SMRFs of varying configurations were analyzed in two separate studies (four buildings are presented in Chapter 5 and the other four in Chapter 6) under multiple ground acceleration records to find the mean shear envelopes in the columns. Depending on the interpretation of the ACI 318 code, various levels of conservatism in estimating column shears were achieved. A common design approach to estimate seismic column shear from the joint equilibrium with beams having reached the probable moment strengths, while the unbalanced moment is distributed evenly between the columns above and below, was shown to lead to unconservative seismic shear estimate, in some cases resulting in half of the actual demand computed in the nonlinear dynamic analyses. It is demonstrated that the seismic shear demand on columns is better estimated with a method based on amplifying the seismic shear calculated with the elastic code-prescribed modal response spectrum analysis with the system overstrength and dynamic amplification factors.

Посвећено мојој драгој мајци.

Пусть всегда будет солнце,
Пусть всегда будет небо,
Пусть всегда будет мама,
Пусть всегда буду я.

ACKNOWLEDGEMENTS

I would like to thank my advisors, Prof. Marios Panagiotou and Prof. Jack Moehle, for their support and guidance throughout my doctoral studies. I am especially indebted to Prof. Jack Moehle for his encouragement and his endless support and understanding during the most challenging year of my life. It has truly been a privillege to have you as an example of a professor and a mentor.

I am greatful to Prof. Per Persson for serving on my qualifying exam committee and for his efforts in reviewing this dissertation – your lectures were among the most enjoyable ones I have attended at Cal. A special acknowledgmenet and thanks goes to Prof. Stephen Mahin for opening the door to exciting research opportunities for me in China.

To Prof. Božidar Stojadinović – thank you for encouraging me to apply to graduate school at UC Berkeley. It is also fitting at this time to thank the University of California for granting me the Chancellor's Fellowship in my early graduate school pursuits; this generous stipend made coming to this wonderful place possible. I would also like to acknowledge the PEER Tall Buildings Initiative for providing the funding for the portions of the research presented in this dissertation.

Among many invaluable experiences and things I acquired through my years at the SEMM program, by far the best one is the amazing individuals I had the privillege to spend the time with and honor to call you my friends: Marco Broccardo, Vesna Terzic, Panagiotis Gallanis, Ahmet Can Tanyeri, Vladimir Kovacevic, Simon Kwong, Yuan Lu, Katerina Konakli, Catherine Whyte, Vladimir Calugaru, Grigoris Antonellis, Mayssa Dabaghi, Mohammed Ali Mustafa, Jenna Wong, Shamim Pakhzad, Nicola Tondini, Dimitrios Konstantinidis, and so many others.

A special shoutout goes out to my Serbian Berkeley crowd (and those who were just visiting): Milutin Janjic, Lazar Supic, Milos Jorgovanovic, Milos & Marija Drezgic, Miroslav Popovic, Marija Miletic, Jasenka Rakas, Prof. Jasmina Vujic, and Marija Cvijetic among many others. Thank you, my girl Neda Cvijetic, for your always perfectly timed advice and endless talks on academic and life matters.

To my family who engrained their endless love and support in me – my father Nedeljko, my late mother Mirka, and my sister Katarina – I owe everything my littleness has ever accomplished. I am grateful to my grandparents Danica and Spasoje who with their simple and humble peasant life taught me that honor and hard work is the only right way to go through this life. My grandparents Filip and Mirjana – thank you for nourishing my curiosity in science since the time I wore Ciciban shoes.

Mama – you have and always will be my hero, my best friend, my guardian angel. You carried your cross with dignity and conveyed beauty into everything and everyone you touched. You have shown me that love conquers death and you shall live in my heart for as long as it keeps beating. May God grant you the life eternal among His angels and saintly people.

Jonathan, my love, my husband-to-be, you have been my rock, a proof that heroes exist outside the epic tales. I am so lucky to call you mine.

TABLE OF CONTENTS

CHAPTER 1

INTRODUCTION

Reinforced concrete moment frames are among the lateral load resisting systems used in buildings designed to withstand strong ground motion shaking. They are commonly chosen in both residential and commercial construction in the United States, because they provide open view lines and thus more architectural flexibility compared to other structural systems such as braced frames or shear walls, which obstruct the vertical space in the system plane. Reinforced concrete moment frames also tend to have substantial system ductility which makes them desirable in seismic design applications.

Moment frames are composed of beams, columns, and joints, which all engage in resisting the seismic forces by axial, moment, and shear force actions. In a seismic event, an intended nonlinear response of a well-designed moment frame involves a strong column-weak beam mechanism. This mechanism comprises of plastic hinging in the beams along the height of the frame and the columns at the base of the structure, with limited, though ideally no inelastic column deformations in the rest of the stories, except at the column end at the very top of the building.

In the United States, reinforced concrete moment frames are proportioned and detailed in accordance with requirements of ACI 318 (various editions). Those moment frames that are designed to withstand the highest levels of seismic forces are entitled Special Moment Resisting Frames (SMRFs) per ACI 318 and follow the most stringent detailing requirements to ensure sufficient strength and ductility is achieved. In the U.S., the design forces for reinforced concrete SMRFs are typically calculated using the modal response spectrum analysis (MRSA) method with response modification factor $R = 8$ (IBC 2012, ASCE 2010) and with individual modal responses combined using a selected modal combination rule.

Generally speaking, the role of codes is to provide minimum requirements to ensure the life safety of occupants through avoidance of sudden and brittle failures both on system and component level. Some common examples of brittle failures in reinforced concrete members are shear failures of beams, columns, or joints, axial load failures in columns or joints due to concrete crushing, buckling of longitudinal reinforcement bars in beams or columns, rupture of transverse reinforcement, and so forth. Some of these member failures can lead to the formations of story mechanisms in a seismic event, which can lead to structural instabilities and, in the extreme case, collapse. Modern codes (e.g. ACI 318) are aimed at avoiding member failures through capacity design principles, which are based on allowing the structure to yield in ductile modes, while the capacity of the brittle yielding modes is elevated to increase the safety margin.

The design practice in frame buildings aims to reduce the likelihood of localized story mechanisms by detailing frame elements to follow a strong column-weak beam action described earlier. Strong column-weak beam behaviour is enforced by requiring that columns be flexurally stronger than beams at any given joint (except for the joints at the very top of the frame). To this end, according to ACI 318, the sum of the column nominal moment strengths is required to be at least 1.2 times the sum of the beam nominal moment strengths at every beam-column joint.

The strong column-weak beam mechanism implies that the SMRF beams will sustain repeated cycles of large inelastic deformations and thus capacity design is enforced in the beams to ensure ductility on a component level, as well. For this purpose, ACI 318 requires that the shear capacity of the beams exceeds the shear demand occurring at the time when the beam develops plastic hinges in all locations intended to yield in flexure. To provide the beam ductility during inelastic SMRF response, ACI 318 establishes detailing requirements and a limit on a minimum amount of transverse reinforcement that needs to be provided in the beam plastic hinge regions.

Many of the current U.S. code requirements for SMRF buildings were first developed several decades ago and based on the prevailing design practices of that time. Some predate the UBC 1997 code which, in many cases, nearly doubled the seismic forces used in structural design compared to those obtained from the procedures specified in the previous editions (UBC 1994 and earlier). For this reason, in the past, reinforced concrete SMRF members were designed to resist smaller seismic forces and were hence smaller, while the buildings also had fewer stories. However, some portions of the modern day codes that were established at that time remain in effect.

In urban areas of seismically active regions of the United States, and particularly the west coast, modern reinforced concrete moment frame buildings often exceed the heights of those built in the past and can reach up to 30 stories in height. Thus, a question is: can the reinforced concrete SMRF buildings conforming to the modern design codes achieve the projected performance level during the anticipated seismic event? Conversely, are there aspects of the current design standards that need to be improved to ensure a SMRF building can attain the performance expectations implied in the life safety target performance level during the design earthquake?

In the recent decades, 10- to 20- story reinforced concrete frame buildings suffered large earthquake damage worldwide, including those in the 1995 M6.9 Kobe, Japan (Otani, 1999), earthquake, the 1999 M7.6 Chi-Chi, Taiwan (Tsai et al., 2000), and the M6.3 2011 Christchurch, New Zealand, earthquake (Elwood et al., 2012). The earthquake ground motion characteristics in all these cases resulted in significant displacement demands in the period range of the 10- to 20-story buildings. While the affected buildings were designed following the guidelines that are different from the current U.S. codes, the occurrence of damage suggests potential vulnerability of reinforced concrete moment frame systems, and warrants study to better understand the design requirements.

1.1 OBJECTIVES

The main objective of this dissertation is to investigate several specific aspects of current design practice and code requirements as they pertain to reinforced concrete SMRFs and offer enhancements to improve the seismic performance of SMRF buildings under anticipated levels of shaking. In particular, the objectives are the following:

- To investigate the adequacy of transverse reinforcement maximum spacing limits in plastic hinge regions of SMRF beams, as defined in concurrent 2008 ACI 318 code, by testing a large SMRF beam barely satisfying these spacing limits.

- To determine the extent to which reduction in the plastic hinge hoop spacing would improve seismic response of a large SMRF beam.
- To improve understanding of the nonlinear response of reinforced concrete SMRFs under strong ground shaking by numerical investigation of several archetype buildings with the same height and geometry, but slight SMRF design variations.
- To show that beam elongation phenomenon can significantly increase the seismic demand on exterior columns in SMRFs, while demonstrating that post-tensioning in the adjacent reinforced concrete slab does not effectively suppress this elongation, as currently assumed in design.
- To evaluate currently available methods of estimating seismic design forces in columns including axial and shear force by comparing the design estimates to the forces computed in nonlinear dynamic analyses of multiple archetype buildings.
- To develop a method to better estimate the shear force demand in SMRF columns induced by strong ground motion shaking.

1.2 ORGANIZATION OF THE CONTENTS

This dissertation consists of seven chapters, each focusing on one of the objectives presented in the previous section. The background, findings, conclusions, and ideas for future research are addressed separately in each chapter, as they relate to a specific topic. Most important findings and conclusions are summarized in Chapter 7. Where needed, appendices are provided at the end of the dissertation with further information pertaining to the contents of Chapters 2-6.

Chapter 2 presents the laboratory tests of two large SMRF beams. The experiments investigated the plastic hinge transverse steel requirements for SMRF beams in 2008 ACI 318, and served as a basis for 2011 ACI 318 code change.

Chapter 3 discusses the numerical modeling strategies for different response components of reinforced concrete SMRF beams in the context of objectives of this dissertation. That is, the models presented are aimed at providing conservative force demand estimates, rather than correctly simulating failure.

Chapter 4 illustrates the impact of beam elongation on column shear in moment frames, which is commonly neglected in design because of the assumption that the post-tensioned slab which is typically cast uniformly with the beams in the SMRF buildings, suppresses the axial lengthening.

Nonlinear response characteristics of tall SMRF buildings are discussed in Chapter 5, where small design variations are shown to improve the seismic response. This chapter also compares the design column shear and axial forces using current design practices and considers alternative design concept to better estimate these forces.

Chapter 6 focuses on refining the methods for estimating design shear forces in columns of special moment resisting frames to account for system overstrength, higher mode effects, and response variability. The chapter concludes with a recommendation for update in the NIST GCR-8-917-1 SMRF design guidelines pertaining to estimation of design shear in SMRF columns.

Chapter 7 summarizes the most important findings in this dissertation and offers suggestions for future investigation.

CHAPTER 2

EXPERIMENTAL INVESTIGATION OF LARGE REINFORCED CONCRETE SPECIAL MOMENT RESISTING FRAME BEAMS

Recent trends in high-rise construction in seismically active regions of the U.S. are resulting in construction of reinforced concrete special moment resisting frames (SMRFs) having beams that are larger than those that were typical of past practices. For example, it is not uncommon for SMRF beams to reach section depth up to 48 in. The ACI 318-08 Code provisions for these beams could result in hoop spacing as large as 12 in. in the plastic-hinge zone, potentially leading to inferior beam performance during strong ground motion shaking.

With SMRF beam seismic performance being a concern, an experimental study presented in this chapter was undertaken to test the implications of concurrent code hoop spacing limits on beam response. The test included two large, special moment frame beams, one barely satisfying the ACI 318-08 hoop spacing limits and another with closer hoop spacing. These are believed to be the largest flexurally-dominant reinforced concrete beams tested under simulated earthquake loading. The results presented in this chapter provide an important insight into behavior of large reinforced concrete SMRF beams and have served as the basis for building code changes introduced in ACI 318-11.

2.1 SMRF BEAM DESIGN REQUIREMENTS

SMRFs generally conform to the provisions of ACI 318 Code (various editions), which are structured around the strong column-weak beam principle. Under such design, the majority of inelastic flexural deformations are intended to occur in the beams along the height of the building during strong ground shaking and it is expected that the beams would have the ability of sustaining multiple reversing inelastic deformation cycles without significant strength loss. Concrete cracking and yielding of reinforcement in the plastic hinge zones of these beams during the inelastic deformation cycles provide the major source of energy absorption and dissipation in the reinforced concrete special moment frames. Therefore, a stable inelastic flexural behavior of SMRF beams is essential for satisfactory building performance.

ACI 318 requires use of hoops (transverse reinforcement in the form of closed ties) along lengths of SMRF beams where flexural yielding is anticipated. The hoops are intended to confine the core concrete, improve shear resistance, and provide lateral support to longitudinal bars. According to ACI 318, a hoop can be in the form of a closed tie with seismic hooks at both ends or it can be made up of several reinforcement elements each having seismic hooks at both ends (Figure 2.1.1[a] and [b]). Alternatively, a hoop can be made up of a stirrup with seismic hooks at both ends that is closed by a crosstie (Figure 2.1.1[c]).

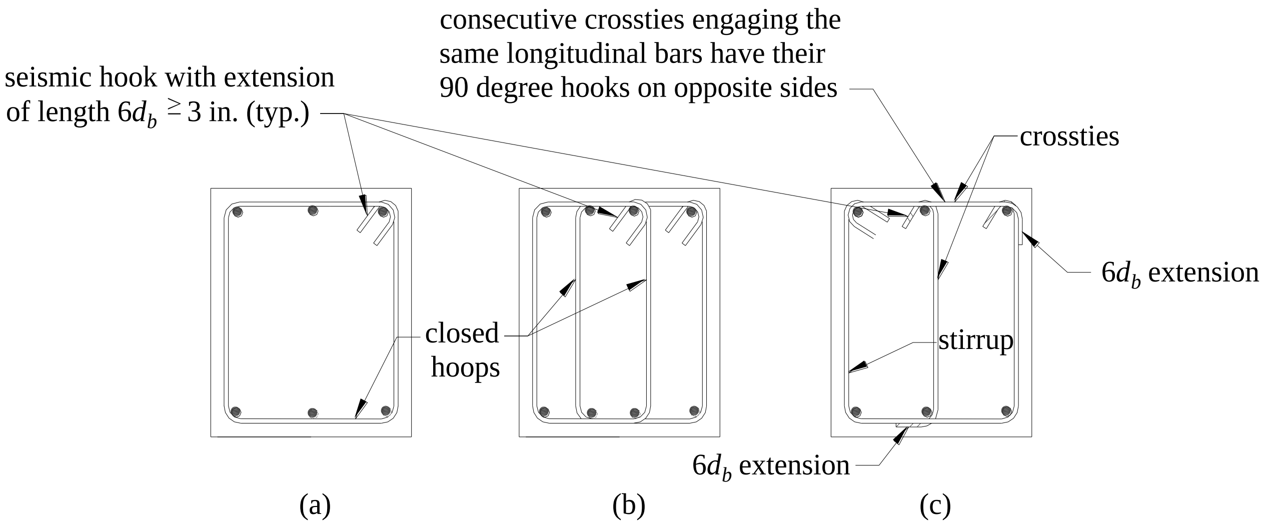

Figure 2.1.1. Typical hoop configurations: (a) single closed hoop; (b) overlapping hoops; and (c) stirrups with crossties (d_b = diameter of a hoop bar).

In consideration of anticipated inelastic flexural response of a SMRF beam, ACI 318 defines the beam design shear force V_u as the shear corresponding to development of beam probable moment strength M_{pr} at both ends of the beam acting in combination with the factored tributary gravity load along its span (Figure 2.1.2). Due to anticipated concrete damage in the plastic hinge regions of the beam, ACI 318 requires that the hoop reinforcement in the plastic hinge be proportioned for shear assuming that there is no contribution from the concrete. Thus, along a length equal to $2h$ from the column face, the design requirement is $\phi V_n \geq V_u$, with $V_n = V_s$, in which h = overall thickness of the beam, ϕ = strength reduction factor ($\phi = 0.75$ for shear), V_n = nominal shear strength, and V_s = shear strength provided by the hoops.

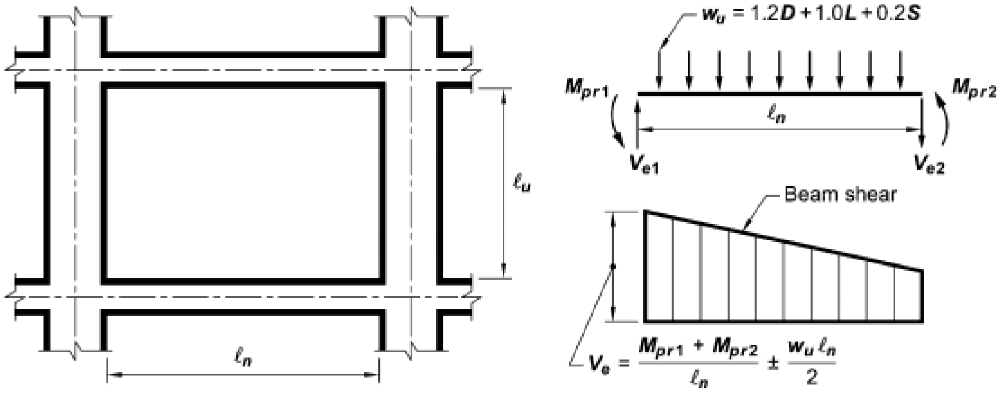

Figure 2.1.2. Design shear for beams according to ACI 318 (source: ACI 318).

To improve lateral support for the longitudinal reinforcement and thereby improve bar buckling resistance, ACI 318 also requires that every corner and alternate longitudinal bar have lateral support provided by the corner of a tie or crosstie, with no unsupported bar located more than 6 in. clear from a laterally supported bar. Furthermore, ACI 318-08 requires that hoop spacing s_h within $2h$ of the beam ends shall not exceed the least of $d/4$, $8d_b$, $24d_{bh}$, and 12 in., where d = distance from the extreme concrete compression fiber to the centroid of the longitudinal tension reinforcement, d_b = longitudinal bar diameter, and d_{bh} = hoop bar diameter. Smaller hoop spacing may be required for shear, as noted previously.

The ACI 318-08 provisions for maximum allowable hoop spacing in SMRF beams were introduced in 1983 based on prevailing practices of that time. Special moment frames of that era typically had multiple bays, were provided along multiple framing lines, and were designed to resist lower seismic design forces, such that SMRF beam depths seldom exceeded around 36 in. Hence, the limit of s_h = 12 in. typically did not control the hoop spacing. When applied to larger SMRF beams in modern construction, however, the hoop spacing can approach or can be limited by s_h = 12 in. This raised a concern that beams with such detailing might not perform well during earthquake-induced inelastic deformations, especially considering possible buckling of beam longitudinal reinforcement.

Numerical simulations of four generic 20-story SMRFs reported in Chapter 5, for buildings located on a hypothetical site in Los Angeles, CA and conforming to ASCE 7-10 and ACI 318-08 provisions indicate that the frames sustained mean story drift ratios of 0.02 during design earthquake (DE) shaking levels and 0.03 during maximum considered earthquake (MCE) shaking levels, along more than 30% of the building height. For the frames investigated in Chapter 5, peak beam chord rotations (drift ratios) were approximately 1.3 times the peak story drift ratios at DE and MCE shaking intensities. This implies that the SMRF beams would have to sustain 0.026 and 0.039 mean chord rotations for the DE and MCE shaking levels, respectively.

2.2 LARGE BEAM EXPERIMENTS REPORTED IN LITERATURE

Few experimental studies have investigated flexure-dominant, cast-in-place reinforced concrete beams (or beam-column subassemblies) with beam thickness h greater than 24 in. under multiple displacement reversals. These are summarized in Table 2.1, along with the relevant beam configuration parameters. In each of these reported tests, the beam cantilevered from a stiff reaction block or column and was loaded by a concentrated force applied transverse to the beam axis with minimal distributed load. These investigations showed that the degree of damage depends primarily on deformation amplitude; amount of longitudinal reinforcement; shear span ratio (defined as the moment M at the beam end divided by the product of the shear force V and the beam height); and quantity, spacing, configuration, and material properties of the transverse reinforcement. Notably, none of the beams had hoop spacing approaching the upper limit of s_h = 12 in. permitted by ACI 318-08.

Predominant failure modes of the reported beams included strength and stiffness degradation due to diagonal cracking and yielding of the transverse reinforcement; longitudinal bar buckling; and bond degradation between longitudinal reinforcement and surrounding concrete within the beam, the anchorage, or both. Table 2.1 lists maximum beam drift ratio amplitude θ_{cap} prior to significant loss of strength and the observed failure mode. Beam drift ratio θ_{cap}, or “chord rotation,” is defined as the displacement at point of load application at the end of the beam cantilever divided by the cantilever length. Significant strength loss is arbitrarily defined as a reduction in resistance exceeding 20% of the maximum resistance.

Table 2.1. Previous tests of large flexure-dominated beams under cyclic loading (Characteristics associated with apparent failure: BF = bond failure; EDC = excessive diagonal cracking; HY = hoop yielding; LRB = longitudinal reinforcement buckling; LRF = longitudinal reinforcement fracture; NF = no failure in beams, i.e. other subassembly components [joints, columns] failed first)

Authors	b_w, mm (in.)	h, mm (in.)	M/Vh	ρ, %	ρ', %	s_h / d_b	Hoop configuration	θ_{cap}	Failure mode
Popov et al. (1972)	483 (19)	737 (29)	2.7	1.58	1.58	2.7	Single closed hoop	0.045	HY/EDC
Blakeley et al. (1975)	457 (18)	889 (35)	3.9	1.10, 1.03	0.70	5.3	Pair of closed hoops	0.050	LRB/ EDC
Birss (1978)	356 (14)	610 (24)	3.6	1.3	1.3	2.5-5.0 (varied s_h within p.h.[1])	Pair of closed hoops	0.036 (Unit B1) 0.032 (Unit B2)	NF
Beckingsale (1980)	356 (14)	610 (24)	3.6	1.10, 0.86	0.58, 0.86	2.7-5.4 (varied s_h within p.h.)	Pair of closed hoops	exceeds 0.040 (units B11 and B12) exceeds 0.027(unit B13)	BF (Units B11 & B12) NF (Unit B13)
Paulay and Scarpas (1981)	356 (14)	610 (24)	3.6	0.9	0.9	5.0	Pair of closed hoops	exceeds 0.038	NF (Units 1 & 3) HY (Unit 2)
Restrepo et al. (1990)	300 (11.8)	700 (27.5)	2.7	0.93	0.95	4.3	Single closed hoop	0.036	BF (Unit 5) EDC (Unit 6)
Warcholik and Priestley (1997),	508 (20)	762 (30)	3.5	1.17	1.17	2.8	Closed hoop with vertical cross tie	exceeds 0.028	NF
Warcholik and Priestley (1998a)	508 (20)	762 (30)	3.5	1.17	1.17	2.8	Closed hoop with vertical cross tie	exceeds 0.039	NF
Warcholik and Priestley (1998b)	508 (20)	762 (30)	3.5	0.83	0.83	2.9	Closed hoop with vertical cross tie (specimen HSJ12-4)	exceeds 0.058	NF
Chang et al. (2008)	483 (19), 559 (22)	914 (36)	3.3	0.60 0.67	0.60. 0.67	1.5	Single closed hoop (beams 3 & 4) vertical cross tie (beam 3)	0.055, 0.071	LRF (Beam 3) NF (Beam 4)

Among the beams reported in literature that were loaded to the point of significant loss of strength, most were capable of sustaining chord rotations in excess of 0.038 without significant loss of resistance. The exception are the specimens reported in Restrepo et al. (1990) which showed stable response up to 0.036 beam chord rotation upon which strength loss was noted due to either bond failure around longitudinal bars within the joint anchorage, accompanied with the crushing of the surrounding concrete cover, or major diagonal cracking and excessive shear deformations. Only one study (Blakeley et al. 1975) reported longitudinal bar buckling as a primary failure mode of the beams tested. Those beams reached θ_{cap} = 0.050.

---

[1] plastic hinge

2.3 EXPERIMENT OVERVIEW

A laboratory test program was undertaken to explore whether a large SMRF beam, barely satisfying the ACI 318-08 hoop spacing limits, would be able to sustain chord rotations consistent with the rotations inferred from the tall building simulations presented in Chapter 5 and also in Visnjic et al. (2012). A second test studied behavior of a beam with nominally identical properties except with closer hoop spacing. The two SMRF beam specimens were constructed at full scale and were tested under reversed-cyclic deformations of progressively increasing amplitude. Two test beams were designed and constructed to test the requirements of ACI 318-08 as well as recommended revisions for ACI 318-11. The beams cantilevered from a common reaction block that was anchored to the laboratory floor (Figure 2.3.1). The beams were tested by imposing upward and downward displacement cycles to simulate the deformation reversals occurring during earthquake loading. Deformations were imposed by hydraulic actuators connected near the beam ends.

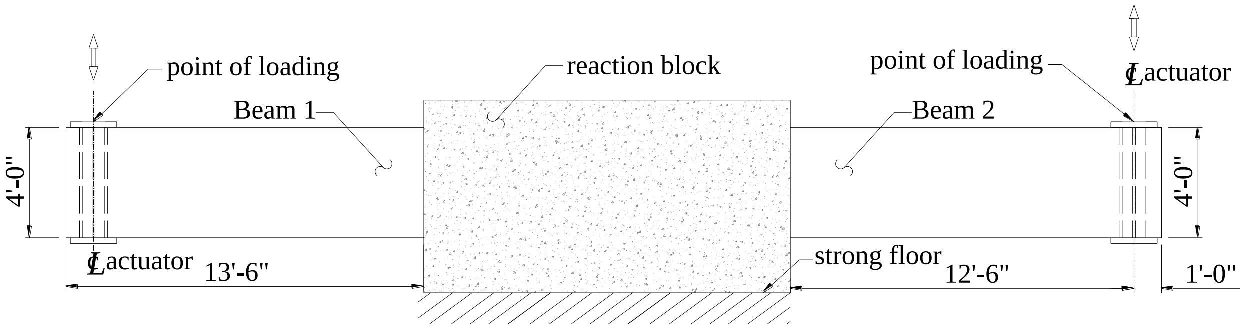

Figure 2.3.1 Test set-up.

2.4 DESIGN OF SPECIMENS

2.4.1 DIMENSIONS AND REINFORCEMENT

The beams were 160 in. long and had rectangular cross section measuring 48 in. deep by 30 in. wide (Figure 2.4.1). The two beams contained nominally identical longitudinal reinforcement consisting of No. 11 ASTM A706 Grade 60 deformed reinforcing bars at both top and the bottom faces, corresponding to longitudinal reinforcement ratio $\rho = A_s/b_w d = 0.0058$ (A_s = area of longitudinal tensile reinforcement, b_w = beam width). Individual hoops of both beams were each made up of three pieces of No. 5 ASTM A706 Grade 60 deformed reinforcing bars: a stirrup with seismic hooks, a crosstie at the top to close the hoop (commonly referred to as cap tie), and an additional vertical crosstie to restrain longitudinal bars along the top and bottom faces. The crossties were alternated end for end along the length of the beams.

Beam 1 (Figure 2.4.2) was designed to satisfy all provisions for SMRF beams according to ACI 318-08 and had hoops spaced at 11 in. The ratio of distributed transverse reinforcement area (vertical legs only) to gross concrete area perpendicular to that reinforcement in Beam 1 was $\rho_t = 0.0028$. In Beam 2 (Figure 2.4.3), the hoop spacing was reduced to 6 in., corresponding to a transverse reinforcement ratio $\rho_t = 0.0051$. The beams also contained No. 4 skin reinforcement to satisfy serviceability requirements of ACI 318-08. That reinforcement extended along the full length of the beam and terminated 6 in. inside the reaction block, as shown in Figure 2.4.1. For both beams, specified strength of concrete was 5 ksi.

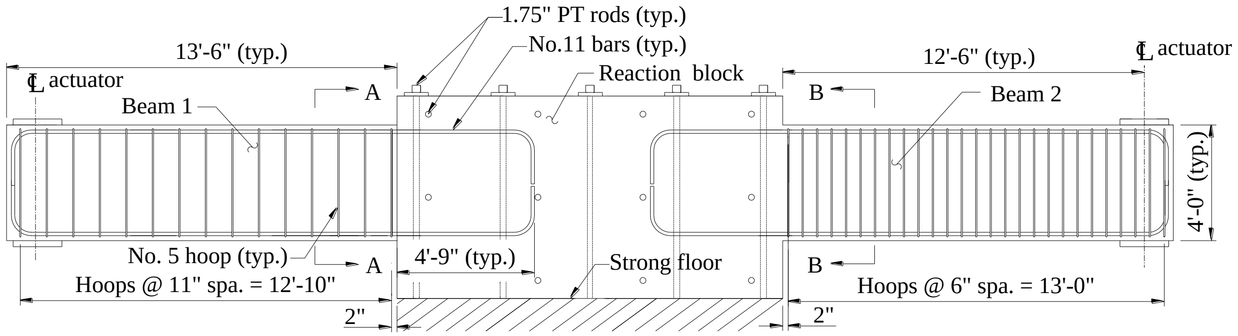

(a) Elevation

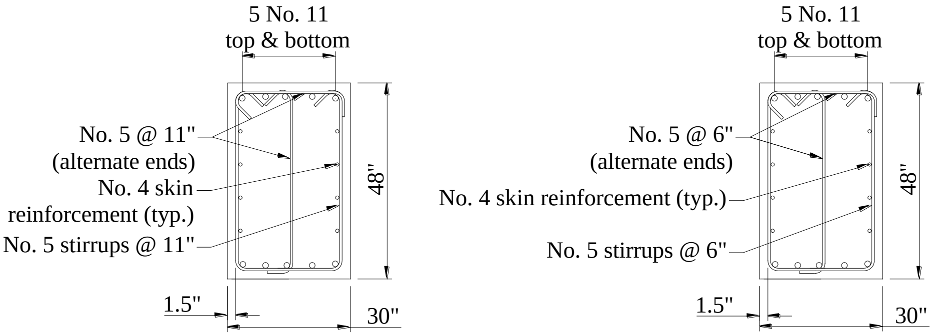

(b) Section A-A (c) Section B-B

Figure 2.4.1. Beam specimens.

Figure 2.4.2. Beam 1 prior to testing.

Figure 2.4.3. Beam 2 prior to testing.

2.4.2 MATERIALS USED IN CONSTRUCTION

2.4.2.1 CONCRETE

Normalweight concrete containing pea gravel (not crushed) as the maximum size aggregate was used in construction of both the beams and the reaction block, with target compressive strength of 5 ksi. A total of 25.6 cubic yards of concrete were required for construction of the two beam specimens and the reaction block. Three batches of concrete were used and 18 standard 6 in. x 12 in. cylinders were cast for material testing. The first batch was mainly cast on the bottom of the reaction block and a portion of the bottom part of both beams. The second batch was cast over the middle portion of the beams and the reaction block, and the third batch topped off the remaining part of the block and the beams. Table 2.2 summarizes the compressive strength results obtained at 28, 60, and 86 days after casting for each of the three concrete batches. The last two tests were conducted on the days the experiments took place for Beams 1 and 2, respectively.

The 28-day strength test included 9 cylinders, three for each batch. Compressive strengths for the three batches ranged from 5.23 to 5.58 ksi, with average of 5.34 ksi. The first beam test took place 60 days after casting the beams and cylinders, at which time two cylinders were tested for each concrete batch. Their corresponding stress-strain relations are plotted in Figure 2.4.4(a). Average compressive strength calculated for the six cylinders was f'_c = 5.8 ksi, and the average strain at maximum compressive strength was calculated to be ε_o = 0.0030. The third batch had the highest average compressive strength of 6.17 ksi which was 10% higher than the lowest measured strength.

Table 2.2. Measured compressive strength of concrete cylinders.

Concrete Age	Batch	Compressive strength of concrete f'_c, MPa (ksi)				
		Specimen 1	Specimen 2	Specimen 3	Average	Batch Average
28 days	1	37.3 (5.41)	35.5 (5.15)	35.7 (5.17)	36.1 (5.24)	(5.34)
	2	36.3 (5.27)	36.2 (5.25)	35.6 (5.17)	36.0 (5.23)	
	3	38.6 (5.60)	39.0 (5.66)	37.7 (5.48)	38.4 (5.58)	
60 days	1	39.2 (5.69)	39.1 (5.68)	-	39.2 (5.69)	40.1 (5.82)
	2	38.3 (5.55)	39.0 (5.66)	-	38.6 (5.61)	
	3	41.9 (6.09)	43.1 (6.26)	-	42.5 (6.17)	
86 days	1	40.7 (5.91)	-	-	40.7 (5.91)	42.3 (6.13)
	2	40.4 (5.87)	-	-	40.4 (5.87)	
	3	45.8 (6.65)	-	-	45.8 (6.65)	

The second beam test took place 86 days after casting and the remaining three cylinders were tested on this day (one for each concrete batch) by which time the average compressive strength of the three batches was f'_{cm} = 6.1 ksi with the average strain at maximum compressive strength at ε_o = 0.0028. The stress-strain curves for these three specimens are plotted in Figure 2.4.4(b). The highest compressive strength (measured again in the third batch) was 6.65 ksi and was 13% higher than the lowest measured compressive strength.

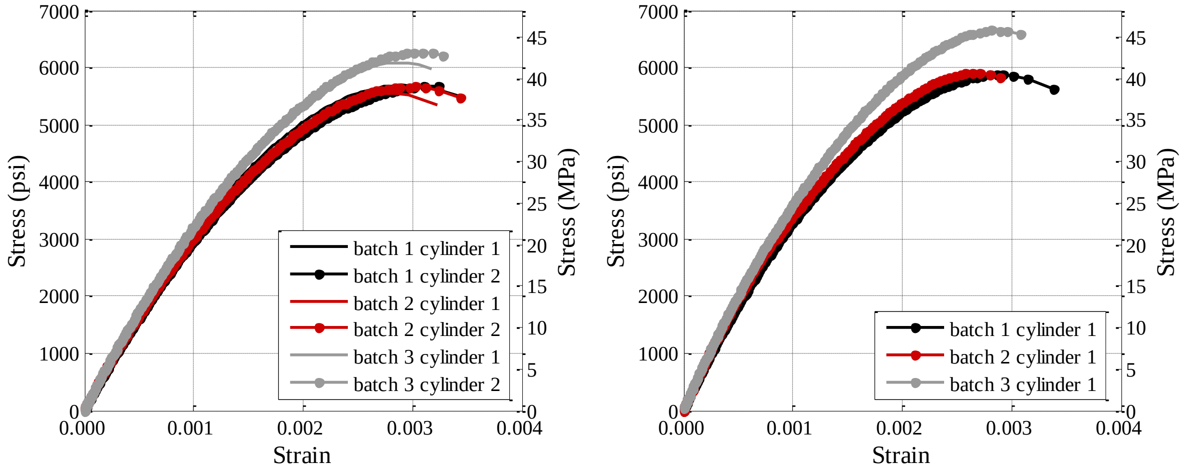

(a) (b)

Figure 2.4.4. Concrete stress-strain curves.

2.4.2.2 STEEL

Type ASTM A706 Grade 60 deformed reinforcing bars were used for both the longitudinal and transverse reinforcement. For each of the No. 11 and No. 5 bar sets, three coupons were tested in tension to obtain the stress-strain relationship of the steel. The curves obtained are shown in Figure 2.4.5. No. 5 reinforcement did not display a yield plateau; rather, the stress-strain curve was characterized by a gradually increasing softening with the strain increase. The point where nonlinear hardening initiated occurred around the stress of f_{ym} = 52 ksi and a strain of ε_y = 0.0020. The average maximum stress of No. 5 bars was f_{um} = 103 ksi. No. 11 longitudinal bars had the mean yield stress of f_{ym} = 73 ksi and a well-defined yield plateau. Average maximum measured stress in the three coupons was f_{um} = 105 ksi with the average corresponding strain of 0.12. Measured yield strain of steel in No. 11 bars was 0.0023 and the E_s = 31,000 ksi.

(a) No. 5 Bars

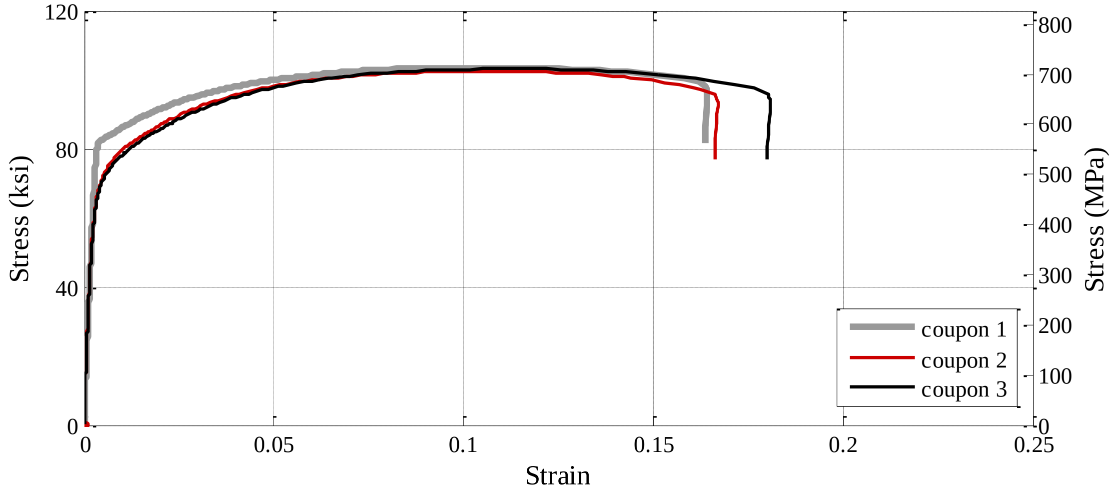

(b) No. 11 Bars

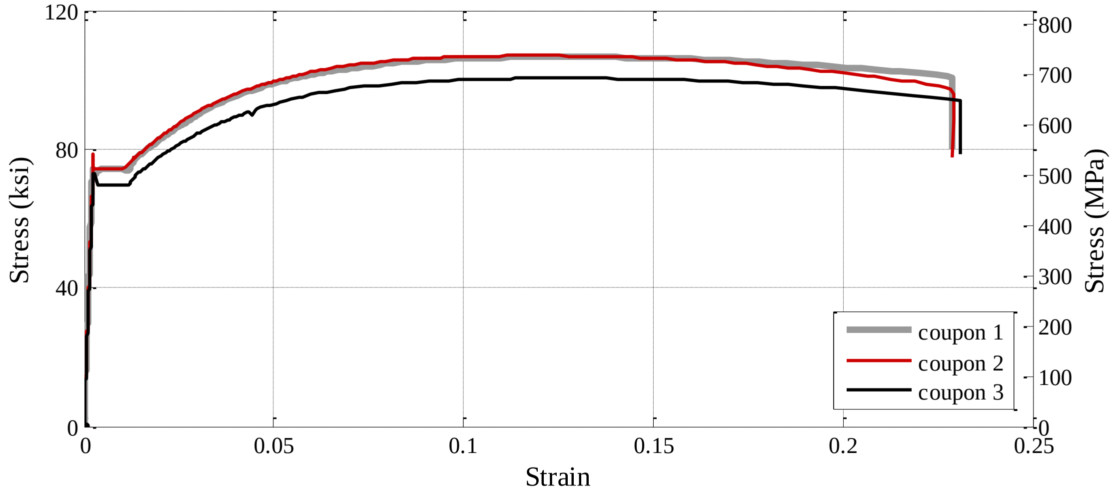

Figure 2.4.5. Monotonic stress-strain curves for steel obtained from tensile coupon tests: (a) hoop reinforcement, and (b) longitudinal reinforcement.

2.4.3 BEAM DESIGN STRENGTH

Probable moment strength M_{pr} of both beams, calculated using specified material properties in accordance with Chapter 21 of ACI 318-08, was M_{pr} = 2110 kip·ft. Skin reinforcement was not included in the strength calculation because it was not fully developed into the reaction block. Consideration of the skin reinforcement, if assumed fully developed into the reaction block, would result in a 9% increase in M_{pr}.

Nominal shear strength was calculated using specified material properties in accordance with ACI 318. Defining nominal shear strength as $V_n = V_c + V_s$, in which $V_c = 2\sqrt{f'_c}b_w d$ (psi) and

$V_s = A_v f_{yt} d/s$, nominal shear strength for Beam 1 is V_n = 420 kips. ACI 318 requires that V_n be calculated assuming V_c = 0 within $2h$ from the column face; therefore, within this length of Beam 1, V_n = 229 kip. In these expressions, V_c = nominal shear strength provided by concrete, V_s = nominal shear strength provided by shear reinforcement, f_c' = specified concrete compressive strength (5000 psi), A_v = transverse reinforcement area (vertical legs only), f_{yt} = nominal yield strength of hoops. For Beam 2, nominal shear strength ignoring the contribution of concrete was V_n = 420 kip, while that with concrete contribution included was V_n = 612 kip.

Assuming the gravity load on the specimens consisting of beam self weight is equal to V_g = 20.3 kips, then the controlling design shear force for both beams is $V_u = M_{pr}/l + V_g$ = 193 kips. For Beam 1, ϕV_n (ϕ = 0.75) is 1.63 times the required V_u. For Beam 2, the factored shear strength ϕV_n is 2.37 times the V_u.

2.5 INSTRUMENTATION

Instrumentation included applied forces, overall displacements, local deformations, and strains. Overall displacement of the beam was measured by a linear variable displacement transducer (LVDT) positioned at the point of load application a distance L = 150 in. from the face of the reaction block, and measuring between the beam bottom face and the laboratory strong floor. To measure local deformations, LVDTs connected between steel rods embedded approximately 1.5 in. into the concrete core at the top, side, and bottom faces of the beams. Two rows of LVDTs were placed along the top face (*TL*, *TR* series, Figure 2.5.1) and bottom face (*BL*, *BR* series, Figure 2.5.2) of each beam. Side LVDTs (Figure 2.5.3) were aligned vertically (*V* series, Figure 2.5.3), diagonally (*S* series, Figure 2.5.3), and horizontally (*H* series, Beam 2 only, see Figure 2.5.3). Strain gauges were attached to longitudinal and transverse reinforcement at selected locations, as shown in Figure 2.5.4 and Figure 2.5.5.

Due to an error in data acquisition system during the Beam 1 test, data from portion of the instruments was permanently lost. These include both the strain gauges and LVDTs located close to the Beam 1 root. Nevertheless, data collected from the remaining instruments was sufficient to capture the behavior of Beam 1. Data recorded in all instruments is included in Appendix A.

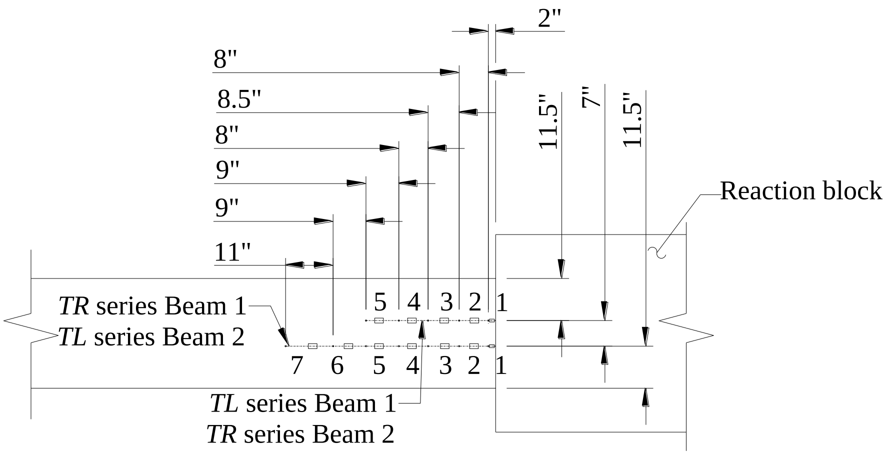

Figure 2.5.1. Layout of displacement transducers: top face of the beams.

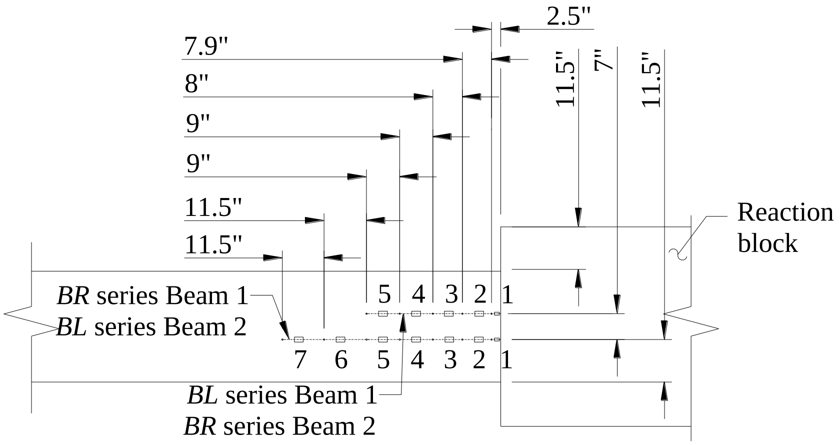

Figure 2.5.2. Layout of displacement transducers: bottom face of the beams.

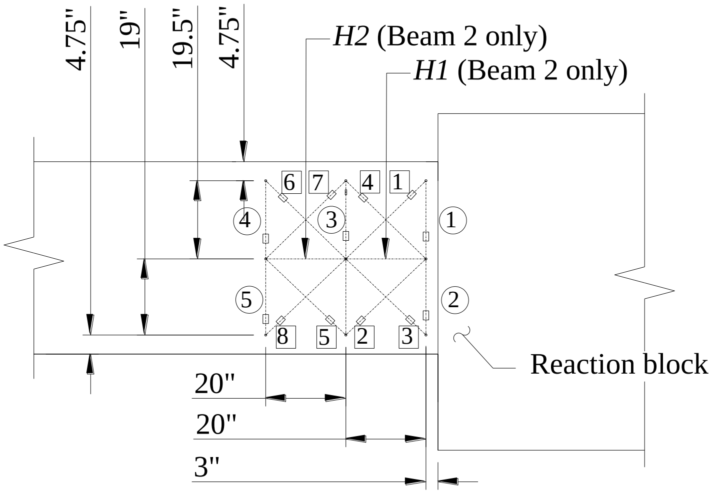

□ = diagonal series (*S*)
○ = vertical series (*V*)

Figure 2.5.3. Layout of displacement transducers: side face of the beams.

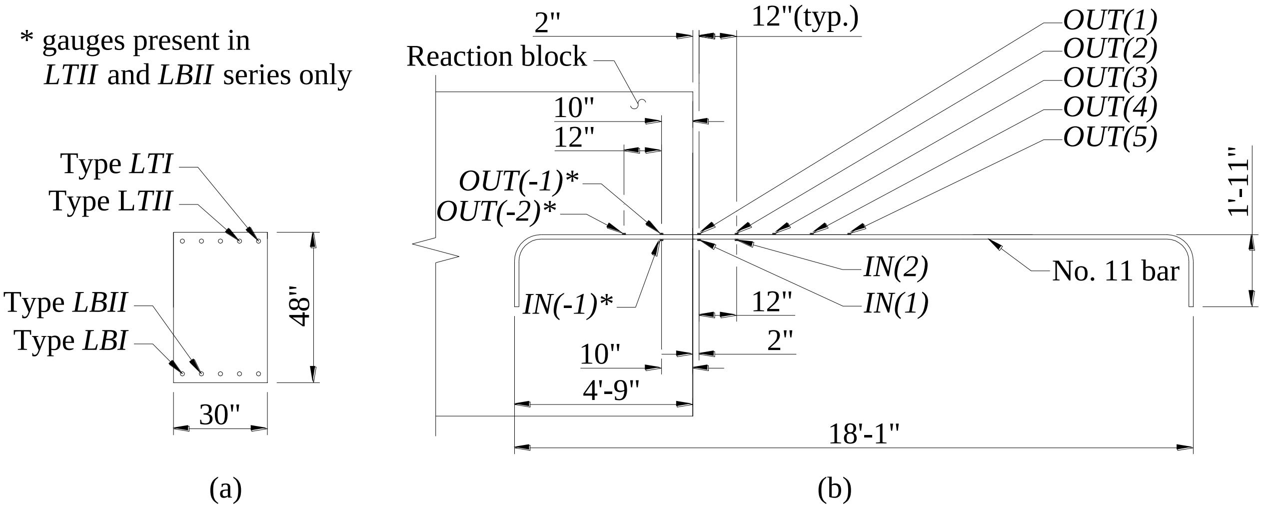

Figure 2.5.4. Layout of longitudinal reinforcement strain gauges: (a) location of instrumented bars; (b) location of strain gauges along a single No. 11 bar.

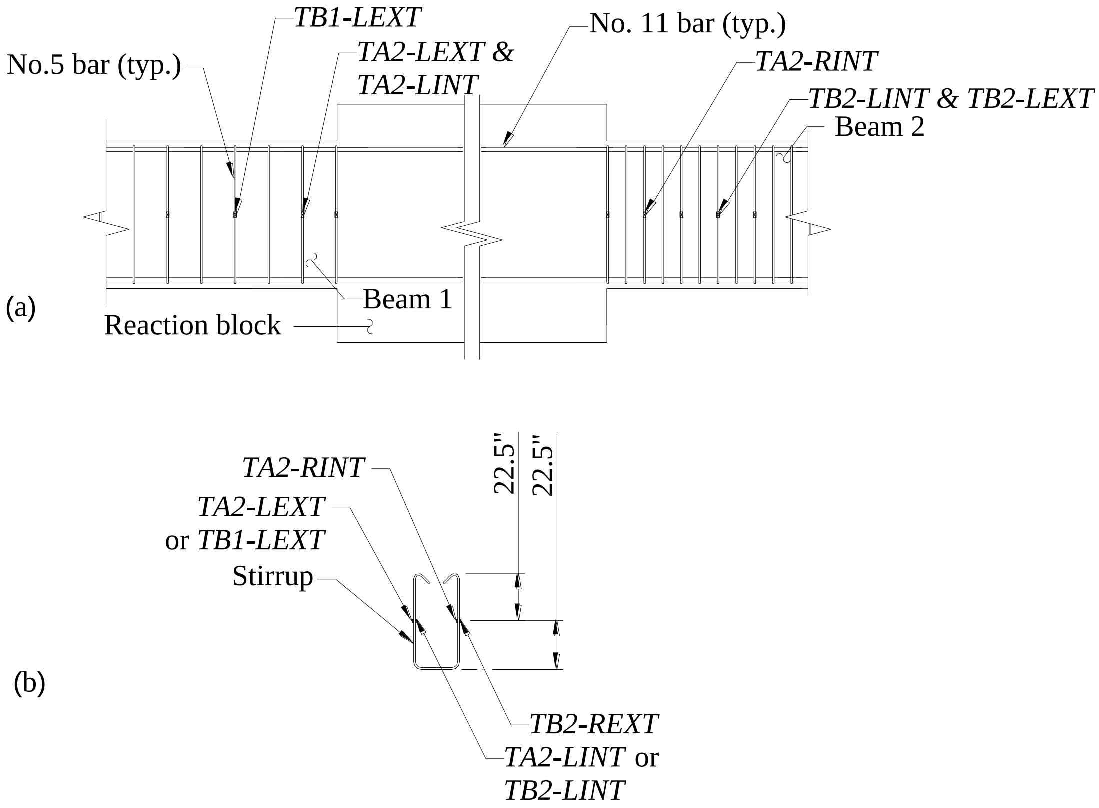

Figure 2.5.5. Layout of transverse reinforcement strain gauges: (a) location of hoops with instrumented stirrups; (b) gauge locations on a stirrup.

2.6 DISPLACEMENT HISTORY

The displacements applied to Beam 1 and Beam 2 are intended to simulate a typical loading history imposed onto a beam acting as a part of a special moment frame during strong ground motion. The displacement history selected was based on the beam rotation histories inferred from numerical simulations of 20-story special moment frames presented in Chapter 5.

Figure 2.6.1 shows the displacement history for the tests. The displacement amplitude Δ corresponds to the displacement at the point of actuator load application. Beam chord rotation θ is defined as Δ/L, where L = distance from the face of the reaction block to the actuator load point. The beam chord rotation is alternatively described in terms of the drift ratio, defined as the beam rotation expressed in percentage.

The displacements shown in Figure 2.6.1 represent the actual displacements applied during the test and hence include the actuator lag, which is the cause of the slight discrepancy in the displacement peak amplitudes (generally less than 2% relative error). The last half cycle to beam chord rotation amplitude of -0.0012 for Beam 1 (occurring around 7000th data point, see Figure 2.6.1) was omitted due to an input error into the actuator control protocol. As can be observed in Figure 2.6.1, the actual displacements applied during the two tests diverged in the final cycles. This was a result of different beam responses described later in this chapter.

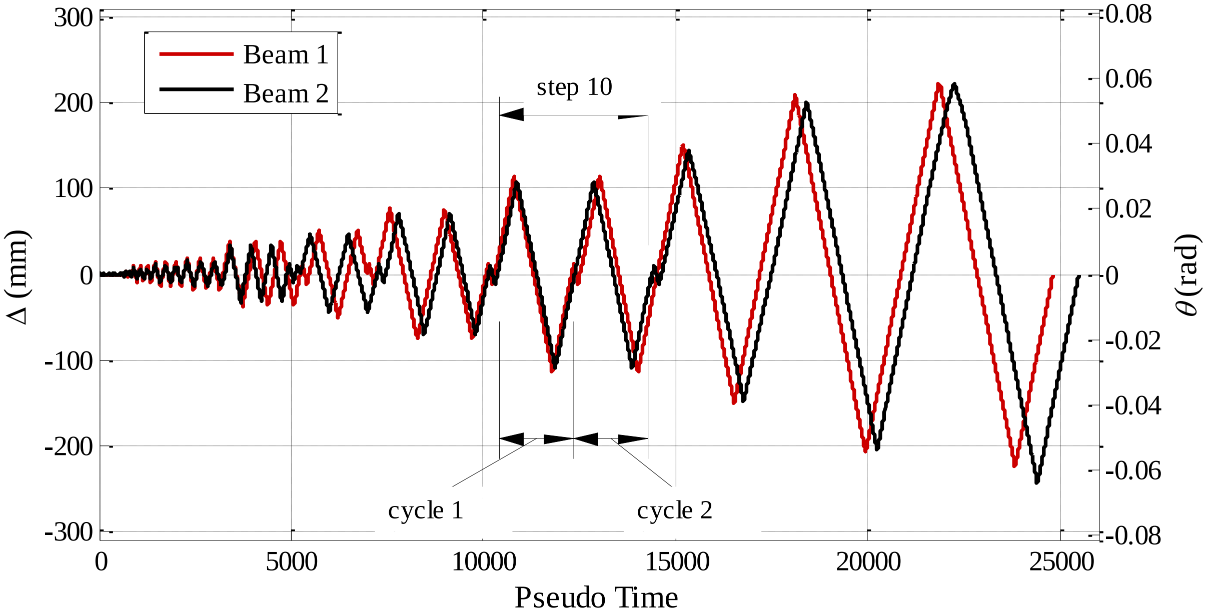

Figure 2.6.1. Displacement history for Beam 1 and Beam 2 (1 in. = 25.4 mm).

Cycles of equal amplitude were grouped into steps. This way, each new step marks a beginning of a series of cycles with displacement amplitudes differing from those reached in the previous step. This is illustrated in Figure 2.6.1. Table 2.3 lists the displacement amplitude for each step of the loading history and the corresponding chord rotation of the beam (θ). In addition, the table lists the approximate peak displacement ductility μ_Δ for each step, defined as Δ / Δ_y. The yield displacement was obtained from the instrumentation data upon completion of the test and it corresponds to the beam tip displacement when the top longitudinal bars yielded in tension (see section 2.8.1). For Beam 1 the yield displacement was $\Delta_y = 1.2$ in, and for Beam 2, $\Delta_y = 0.9$ in.

Table 2.3. Displacement test protocol.

Step	Number of cycles	Displacement Δ (in.)		Chord Rotation $\theta = \Delta / L$		Displacement ductility $\mu_\Delta = \Delta / \Delta_y$	
		Beam 1	Beam 2	Beam 1	Beam 2	Beam 1	Beam 2
1	3	0.1	0.1	0.0007	0.0007	0.1	0.1
2	3	0.3	0.2	0.0018	0.0016	0.2	0.3
3	3	0.4	0.4	0.0028	0.0028	0.4	0.5
4	3	0.6	0.6	0.0038	0.0040	0.5	0.7
5	3	1.2	1.3	0.0081	0.0087	1.0	1.5
6	2[2]	1.8	1.8	0.0120	0.0120	1.5	2.0
7	1	0.5	0.5	0.0033	0.0033	0.4	0.6
8	2	2.7	2.7	0.0180	0.0180	2.3	3.0
9	1	0.5	0.5	0.0033	0.0033	0.4	0.6
10	2	4.1	4.3	0.0270	0.0290	3.4	4.8
11	1	0.5	0.5	0.0033	0.0033	0.4	0.6
12	2	5.5	5.8	0.0360	0.0390	4.5	6.5
13	1	0.5	0.5	0.0033	0.0033	0.4	0.6
14	1	7.6	8.0	0.0510	0.0530	6.4	8.8
15	1	0.5	0.5	0.0033	0.0033	0.4	0.6
16	1	8.3	8.7 (-9.6)	0.0550	0.0580 (-0.0640)	6.9	9.7 (-10.7)

2.6.1 SIGN CONVENTION

Global displacement of the beam is defined as positive downward; beam moment and shear are defined as positive for actions that produce downward displacement. The reported beam moment is the sum of moments at the face of the reaction block due to actuator force and beam self weight, assuming self weight of the beam equal to 20.3 kips. Local deformations and strains are defined as positive for elongation. Deflections due to self weight of the beam are deemed negligible.

2.7 RESPONSE OVERVIEW

Figure 2.7.1 shows the measured relations between beam moment and beam chord rotation for Beam 1. In the early cycles, the beam developed cracks associated with flexure, shear, and dowel action. The response was stable during all cycles after yielding prior to and including the first half cycle to peak chord rotation $\theta = 0.027$. Upon displacement reversal during the second half

---

[2] Last half-cycle omitted for Beam 1.

cycle to $\theta = 0.027$, all of the top longitudinal bars buckled, creating a cave-like fissure running along the longitudinal bars that remained open for all remaining cycles (Figure 2.7.2). During the second cycle with a peak chord rotation of 0.027 the maximum resistance of the beam reduced by 30% of the peak resistance, as can be observed in Figure 2.7.1.

Bottom longitudinal reinforcement buckled during the positive (downward) loading phase of second cycle to 0.027 chord rotation, although the bars were better restrained by the hoops at this location. After buckling of longitudinal bars, increased shear deformations were observed, which were especially apparent during the downward loading phases (see Figure 2.7.3 and also discussions of crack widths and shear deformations to follow). During the subsequent cycles (with peak chord rotations of $\theta = 0.036$ and $\theta = 0.051$), the resistance of Beam 1 reduced to 50% of the peak resistance. At the end of testing, 135-deg. seismic hooks were observed to have opened along the length over which buckling occurred (Figure 2.7.4).

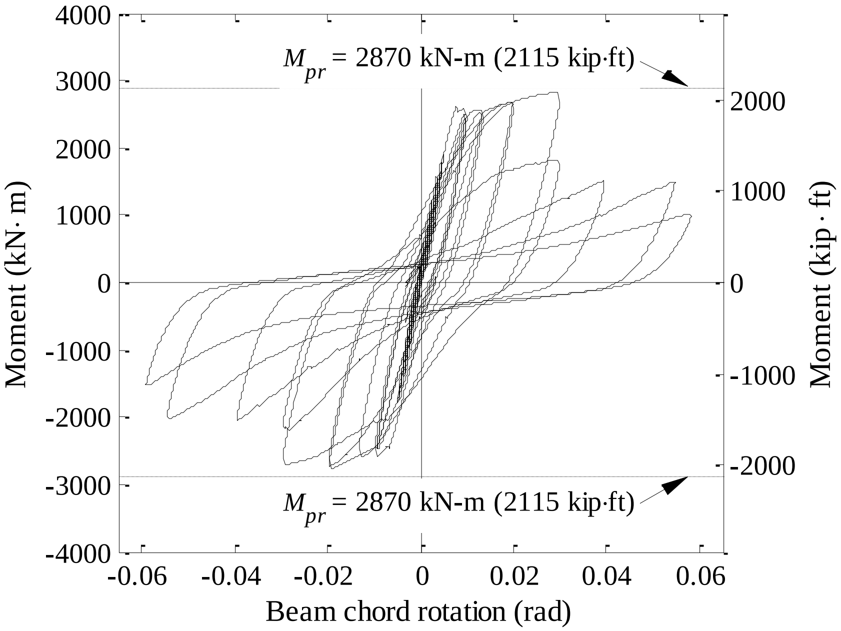

Figure 2.7.1. Relationship between moment and beam rotation for Beam 1.

The measured yield moment and chord rotation for Beam 1 were M_y = 1860 kip·ft and θ_y = 0.008. This value of M_y is 10% higher than the nominal moment strength M_n = 1690 kip·ft calculated with ACI 318 provisions using the nominal steel strength f_y = 60 ksi and specified concrete strength f'_c = 5 ksi. Beam 1 secant stiffness at yield was $0.13E_cI_g$, where E_c is Young's modulus of concrete calculated as $E_c = 57{,}000\sqrt{f'_c}$ psi based on measured cylinder compressive strength for Beam 1, and I_g is second moment of area of the beam gross cross section.

The peak measured moment in Beam 1 was 2100 kip·ft, which is very close to the probable moment strength M_{pr} calculated in accordance with ACI 318 using the specified compressive strength of concrete f'_c = 5 ksi and 1.25 times the nominal yield strength of the longitudinal steel (that is, 1.25 x 60 ksi = 75 ksi). The value of M_{pr} calculated is 2115 kip·ft, which is indicated with dashed lines in Figure 2.7.1. The beam sustained a peak shear force of V = 164 kips, which corresponds to a nominal shear stress of $V/b_w d$ = 121 psi, or $1.6\sqrt{f'_{cm}}$ psi.

Figure 2.7.2. Beam 1 crack patterns and buckling of the top longitudinal bars (first cycle with peak θ = -0.027).

Figure 2.7.3. Buckling of bottom longitudinal bars and large apparent shear deformation in Beam 1 (cycle with peak θ = 0.055).

Figure 2.7.4. Stirrup hook opening at the end of Beam 1 test.

Figure 2.7.5 shows moment versus chord rotation response of Beam 2. The behavior of Beam 2 was similar to that of Beam 1 in the early cycles, including development of cracks associated with flexure, shear, and dowel action (Figure 2.7.6). Beam 2 exhibited stable response prior to the reversal from peak downward displacement during the second cycle with drift amplitude $\theta = 0.029$. At this instance the initiation of buckling in top longitudinal reinforcement was observed. The buckling became excessive and obvious in the measured moment-drift response in the cycle with 0.039 peak chord rotation (Figure 2.7.5 and Figure 2.7.6). The peak resistance of the beam in the subsequent cycle was 10% less than the maximum strength measured during the same direction of loading. Buckling of the bottom longitudinal bars became obvious during a cycle with a peak drift of 0.053 (Figure 2.7.7). During the last loading cycle with chord rotation amplitude of 0.064, one of the top corner bars fractured at an instantaneous beam rotation of 0.007, which resulted in a sudden strength loss in the beam of approximately 38% of the instantaneous resistance prior to bar fracture. The peak resistance for this cycle was 43% lower than for the previous downward cycle, and 48% lower than the peak strength for loading in this direction. Similarly to Beam 1, the 135-deg. seismic hooks were observed to have opened along the length over which buckling occurred in Beam 2 (Figure 2.7.8).

Beam 2 moment resistance at yield was M_y = 1880 kip·ft, which is 11% higher than the calculated nominal moment M_n = 1690 kip·ft. Secant stiffness calculated at this instance (at $\theta_y = 0.006$) corresponded to $0.16EI_g$. The maximum measured moment in Beam 2 was 2320 kip·ft, which is 10% higher than the calculated M_{pr}. Peak shear force measured in Beam 2 was 181 kips, corresponding to a nominal shear stress of V/b_wd = 134 psi or $1.7\sqrt{f'_{cm}}$ psi.

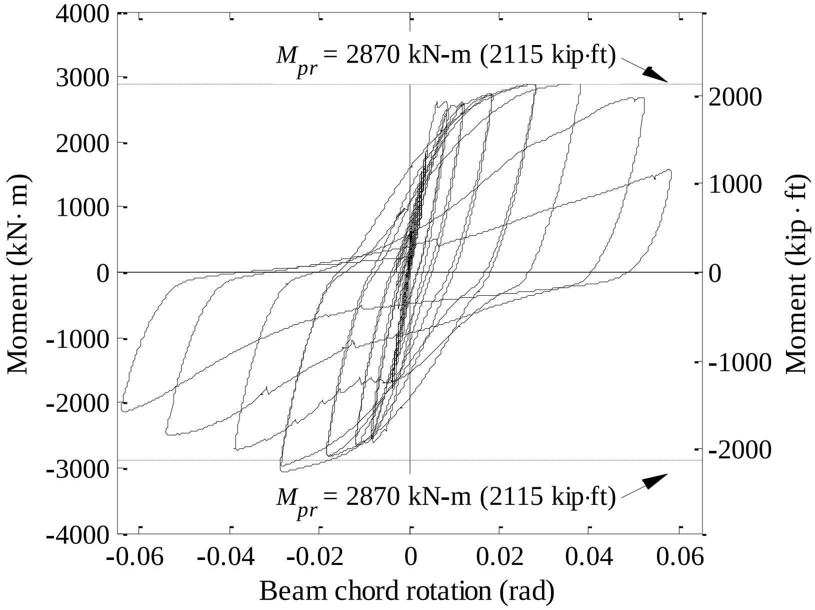

Figure 2.7.5. Relationship between moment and beam rotation for Beam 2.

Figure 2.7.6. Crack patterns and buckling of the top longitudinal bars in Beam 2 (first cycle with peak θ = - 0.039).

Figure 2.7.7. Buckling of bottom longitudinal bars in Beam 2 ($\theta = 0.053$).

Figure 2.7.8. Apparent opening of the cap tie on top face of Beam 2 as observed upon completion of Beam 2 test.

Beams 1 and 2 have similar moment-chord rotation responses until the cycle with peak chord rotation of 0.018, as can be seen in Figure 2.7.9. For both beams, fixed-end rotation associated with slip of the longitudinal reinforcement from the anchorage block comprises roughly 40% of the total beam tip deflection for the cycles prior to longitudinal bar buckling. During the cycle with a peak rotation of 0.027, longitudinal bar buckling resulted in rapid loss of strength in Beam 1; therefore, the maximum rotation capacity of Beam 1 can be taken as $\theta_{cap} = 0.027$. For Beam 2, minor strength degradation occurred during cycles with 0.029 peak drift, with more significant strength loss delayed until the cycles with peak chord rotation of 0.039. Therefore, for Beam 2, the maximum rotation capacity can be taken as $\theta_{cap} = 0.039$.

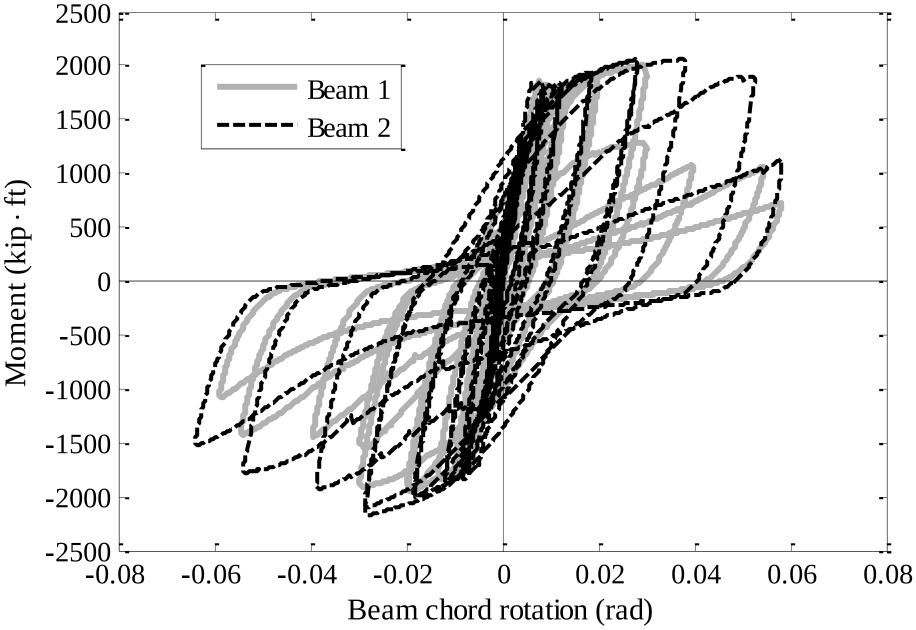

Figure 2.7.9. Comparison of Beam 1 and Beam 2 responses.

2.8 MEASURED LOCAL RESPONSE

Local responses include reinforcement strains, crack widths, and local deformations between fixed points measured by the LVDTs along the top, bottom, and side faces of the beams. Initially, measurements from the LVDTs could be used to estimate average longitudinal strains, defined as the elongation measured by an LVDT divided by its gauge length. After buckling of longitudinal reinforcement initiated, however, distortion of the concrete cover resulted in displacement and rotation of the steel instrumentation rods, such that the resulting measurement no longer represented the average strain correctly. Consequently, deviations from expected longitudinal strains provide a good indication of the onset and extent of buckling. The majority of the strain gauges failed after measuring a strain of about 0.02, such that strains were not recorded during the largest displacement cycles, including those for which buckling was observed.

2.8.1 LONGITUDINAL REINFORCEMENT STRAINS

Figure 2.8.1 shows the evolution of strains in the longitudinal bars through the progression of the cycles for the two beams. Two strain histories are shown for each beam: one from the gauge attached to one top longitudinal No. 11 bar (Figure 2.8.1[a] and [c] for Beam 1 and Beam 2, respectively) and the other from the gauge attached to one bottom No. 11 bar (Figure 2.8.1[b] and [d] for Beam 1 and Beam 2, respectively). The readings shown were measured by the gauges indicated in the respective plot titles, which were attached to the longitudinal bars 2 in. from the reaction block.

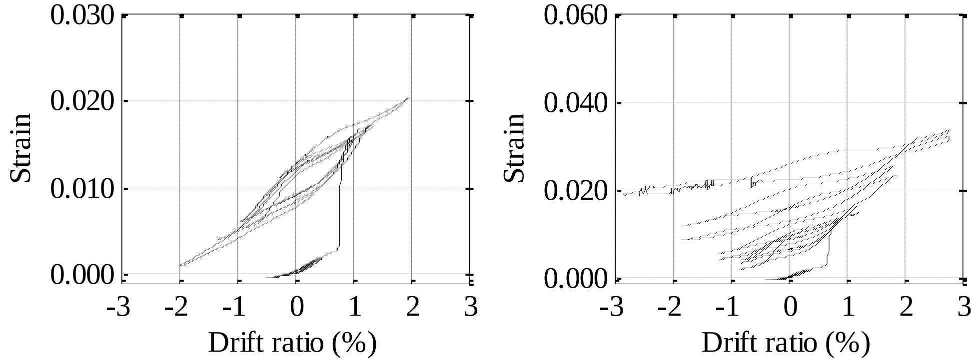
(a) Beam 1 Gauge *LTI OUT(1)*

(c) Beam 2 Gauge *LTI OUT(1)*

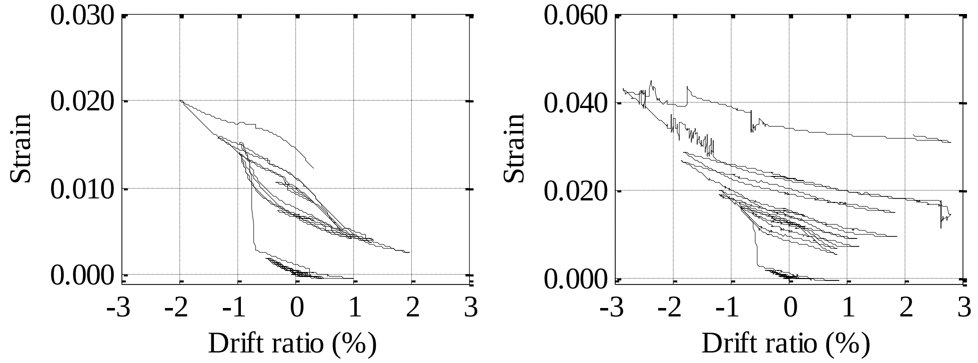
(b) Beam 1 Gauge *LBII IN(1)*

(d) Beam 2 Gauge *LBII OUT(1)*

Figure 2.8.1. Propagation of strain in longitudinal reinforcement at beam root with increasing drifts measured in (a) top and (b) bottom bar of Beam 1 for cycles up to and including the first cycle with $\theta = 0.018$, and (c) top and (d) bottom bar of Beam 2 for cycles up to and including the first cycle with $\theta = 0.029$.

The plots in Figure 2.8.1 indicate minor excursions of the bars into the compressive strain range in the early stages of the test. The top No. 11 bars experience compressive strains during the upward cycles with the rotation amplitudes $|\theta| < 0.005$, while the bottom bars experience compressive strains for the downward cycles with the rotation amplitudes $|\theta| < 0.009$. Thereafter, the reinforcement strain histories indicate that only tensile strains develop with the increasing beam rotation, which is the sort of longitudinal strain history typical of reinforced concrete beams in the absence of axial force. The top and bottom longitudinal bars in Beam 1 yield in tension at chord rotations of 0.008 and -0.007, respectively. For Beam 2, the top and bottom bars yield at 0.006 and -0.005 chord rotation, respectively.

Figure 2.8.2 through Figure 2.8.5 plot the progression of the longitudinal reinforcement strains through the beam displacement cycles. Each curve in these figures represents the instantaneous longitudinal reinforcement strain measured at the moment when the beams reach the displacement amplitude for the corresponding cycle. The x-axes in the figures represent the location of the given strain gauge, measured from the face of the reaction block. Negative distance indicates that the gauge was located along the portion of the longitudinal bar embedded within the reaction block. A solid black vertical line has been added to all figures to indicate the location of the beam interface with the reaction block.

As expected for this type of loading, the highest levels of the longitudinal strain are reached in the close proximity of the beam root. Within the beam, the longitudinal reinforcement strains gradually decrease with the distance from the reaction block for all beam displacement cycles prior to yielding (Figure 2.8.2[a], Figure 2.8.3[a], Figure 2.8.4[a], and Figure 2.8.5[a]). Once yielding has occurred, the highest levels of strains tend to concentrate within the first 26 in. of the reaction block (Figure 2.8.2[b], Figure 2.8.3[b], Figure 2.8.4[b], and Figure 2.8.5[b]), which is approximately the length of the plastic hinge observed in the tests.

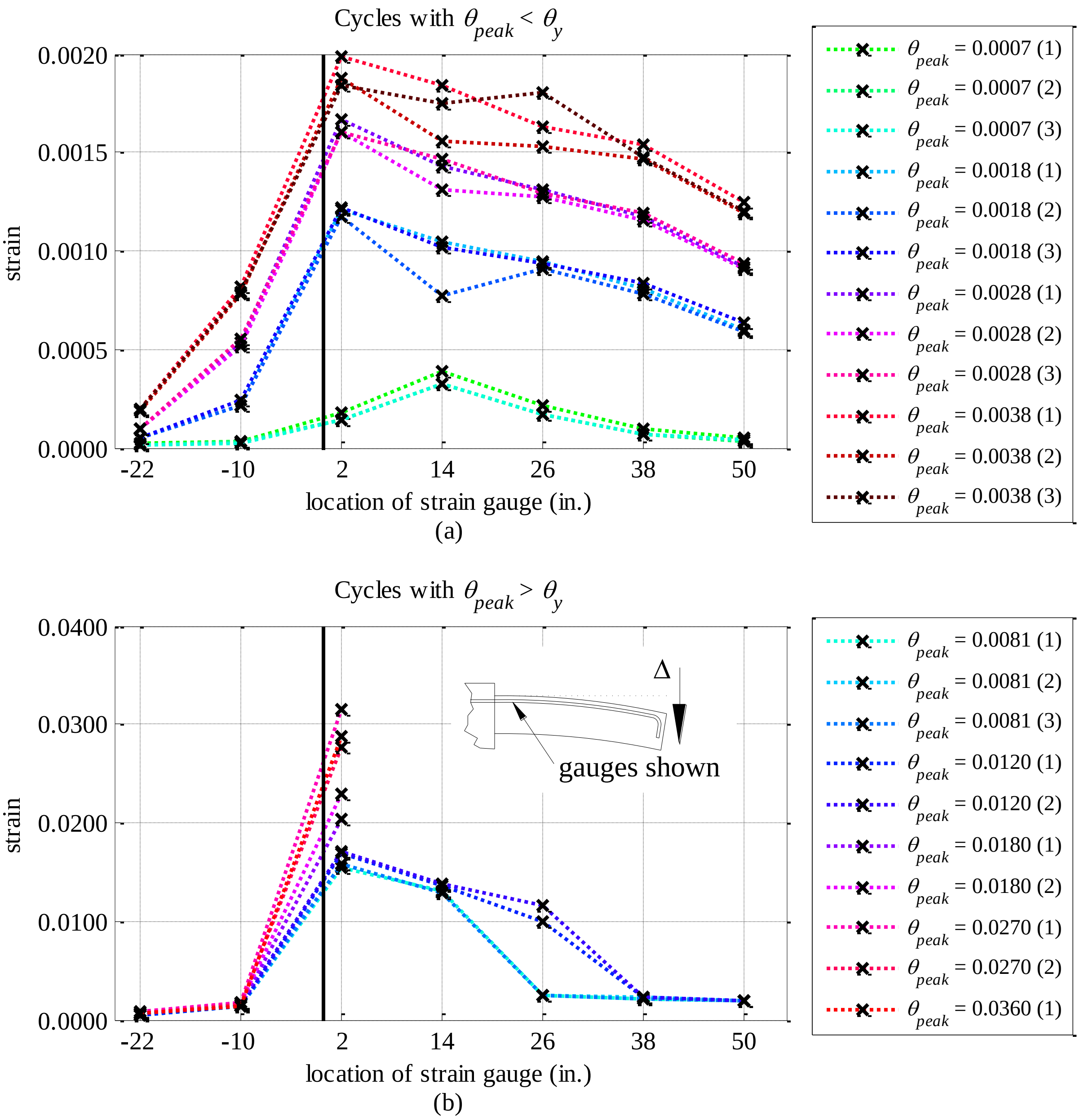

Figure 2.8.2. Strain distribution along the instrumented top longitudinal bars, Beam 1.

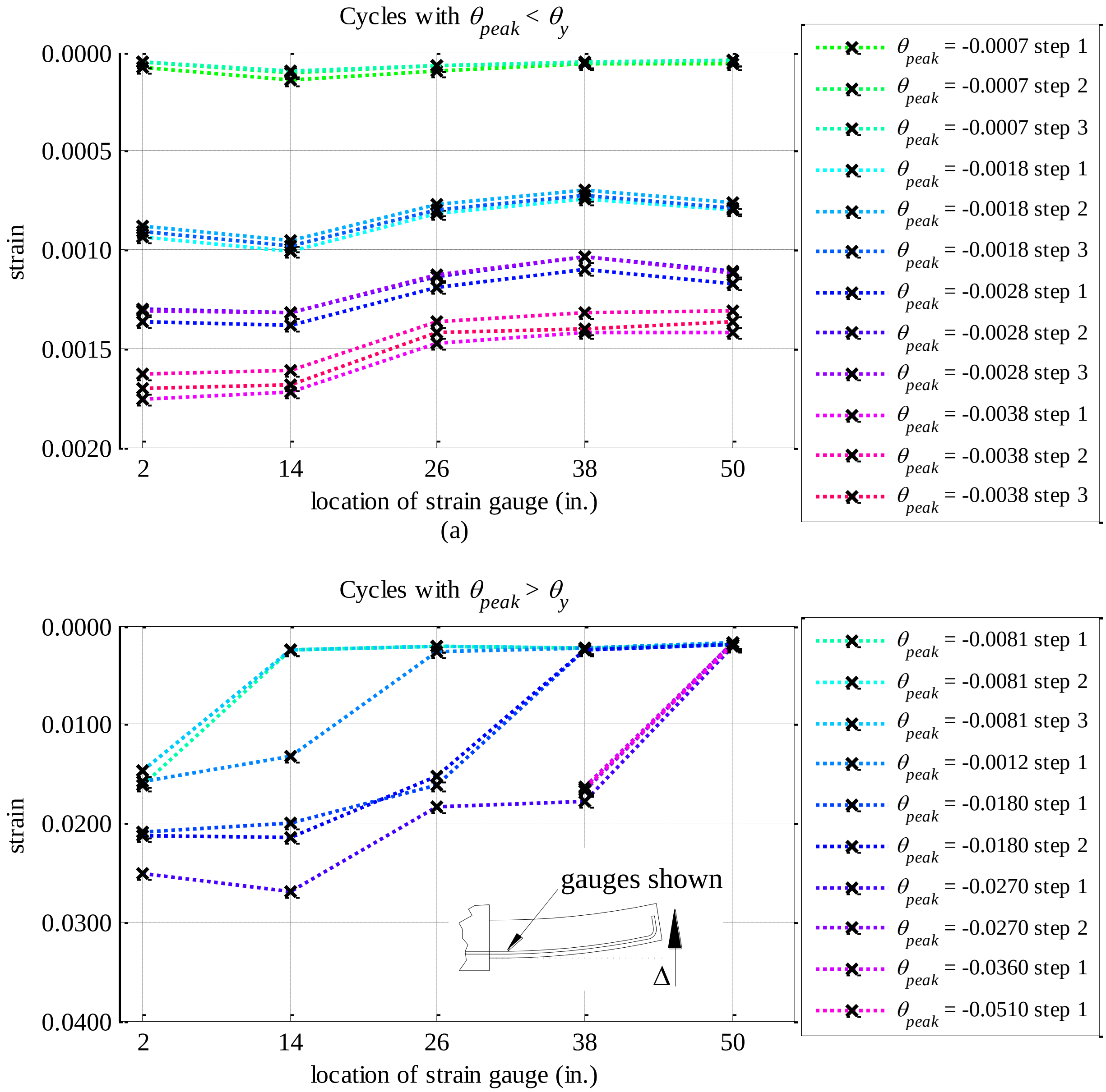

(b)

Figure 2.8.3. Strain distribution along the instrumented bottom longitudinal bars, Beam 1.

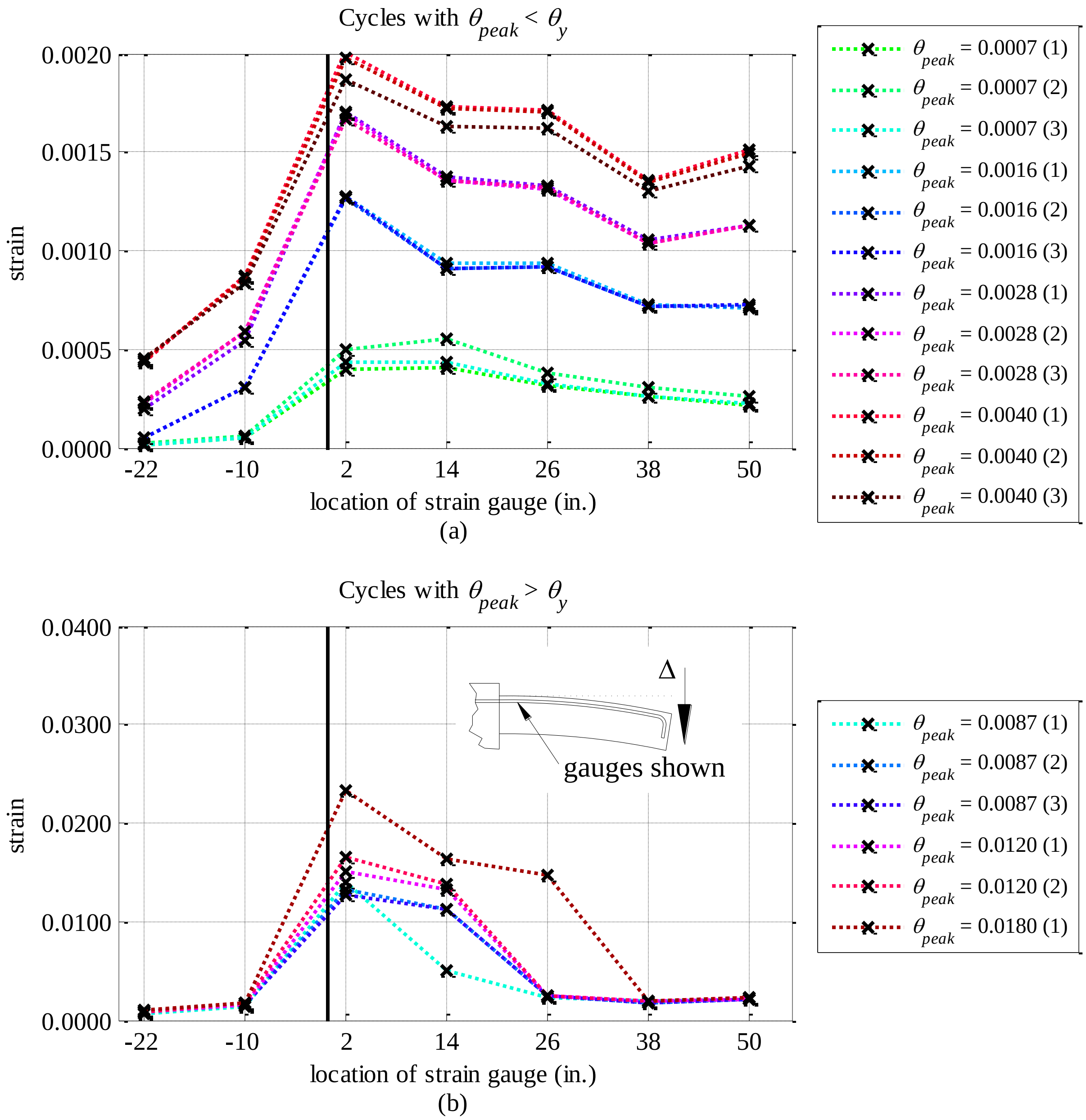

Figure 2.8.4. Strain distribution along the instrumented top longitudinal bars, Beam 2.

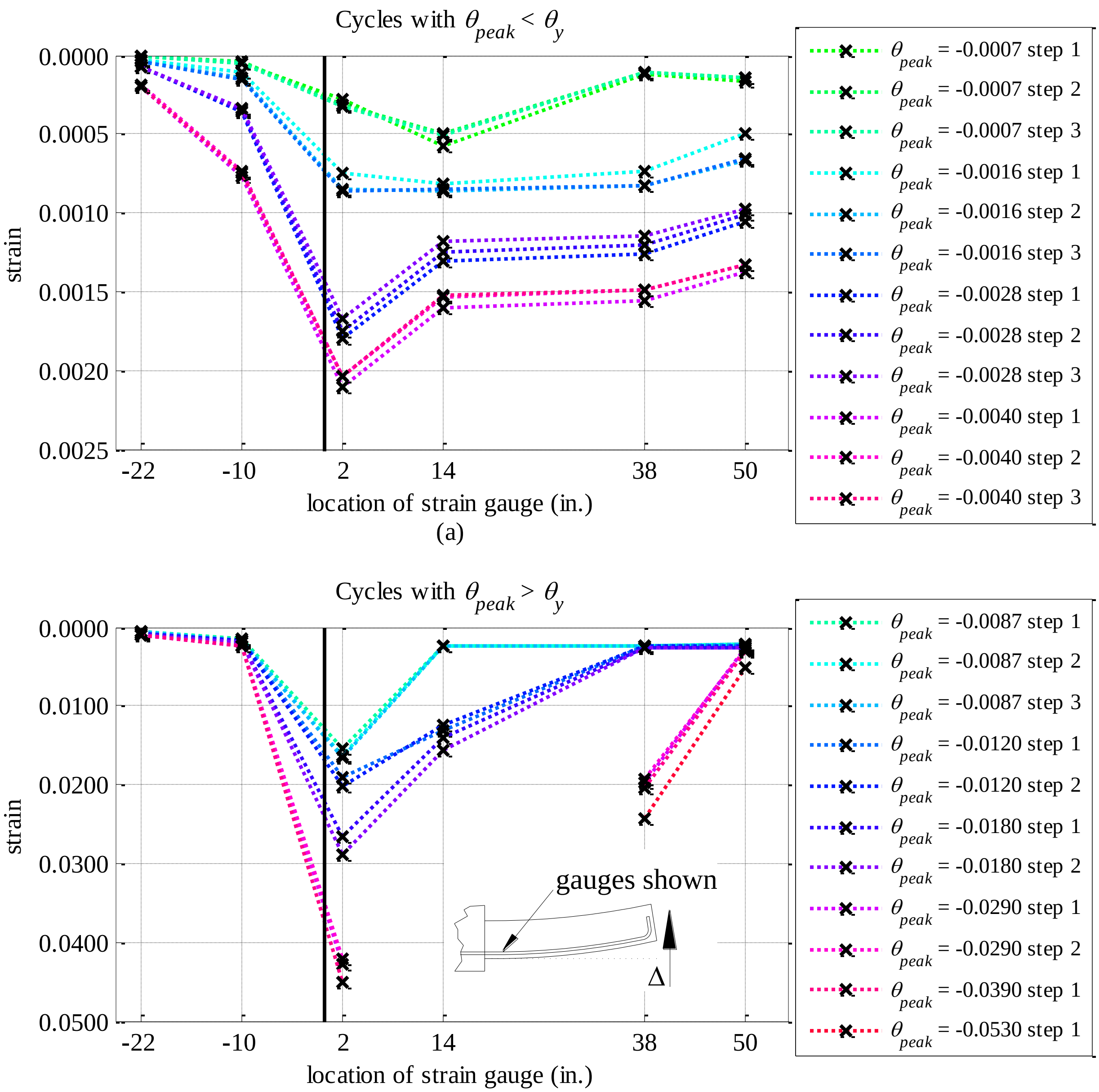

(a)

(b)

Figure 2.8.5. Strain distribution along the instrumented bottom longitudinal bars, Beam 2.

2.8.2 CURVATURE DISTRIBUTION

Figure 2.8.6 through Figure 2.8.9 show the approximate curvature distribution along the beam length at different rotation amplitudes of Beams 1 and 2 for the cycles preceding the longitudinal bar buckling. Curvature φ at a given location is computed using the measurements from pairs of LVDTs (*TR*, *TL*, *BR* and *BL* series), located on opposite sides of the beams, using the following expression:

$$\varphi(x_i)=\frac{1}{R_v}\left(\frac{T_i}{L_i}+\frac{B_i}{L_i}\right) \tag{2.1}$$

where x_i signifies the approximate location of the midspan of each LVDT pair (plotted along the x-axis in Figure 2.8.6 through Figure 2.8.9), T_i and B_i are the measurements from the top and bottom LVDTs, respectively, L_i is the length of instrument i, and R_v is the vertical distance between the top and bottom instruments, approximately 53 in. It should be noted that the buckling of the longitudinal bars affected the measurements of the top and bottom LVDT instruments after 0.012 rotation amplitude cycles in Beam 1, and second cycle to 0.029 rotation amplitude in Beam 2. Thus, in the curvature levels computed for these cycles were do not reflect the actual values, but are nevertheless included in the plots to indicate the changing deformations due to impending longitudinal bar buckling.

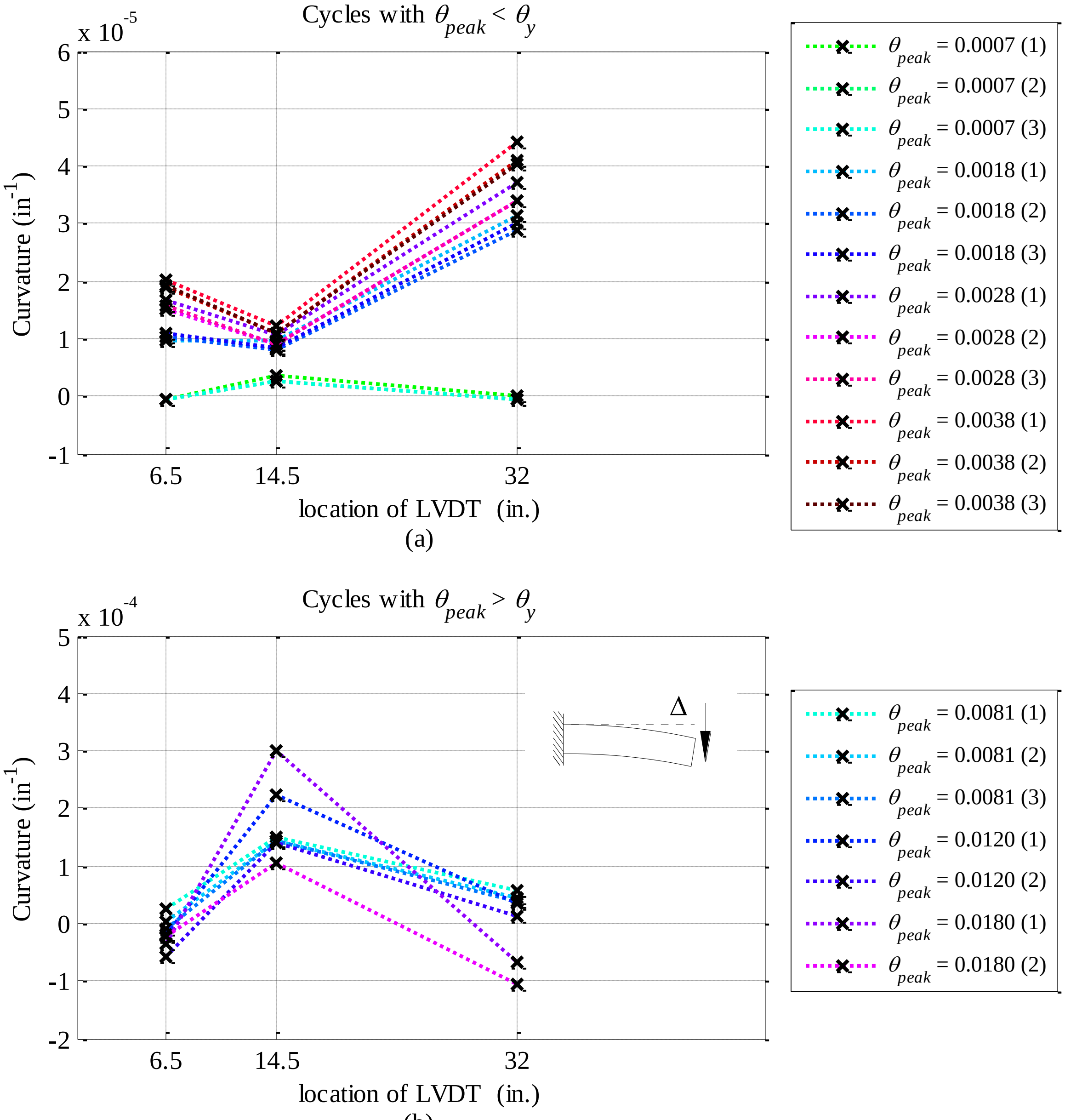

(a)

(b)

Figure 2.8.6. Curvature distribution at the downward displacement peaks in Beam 1.

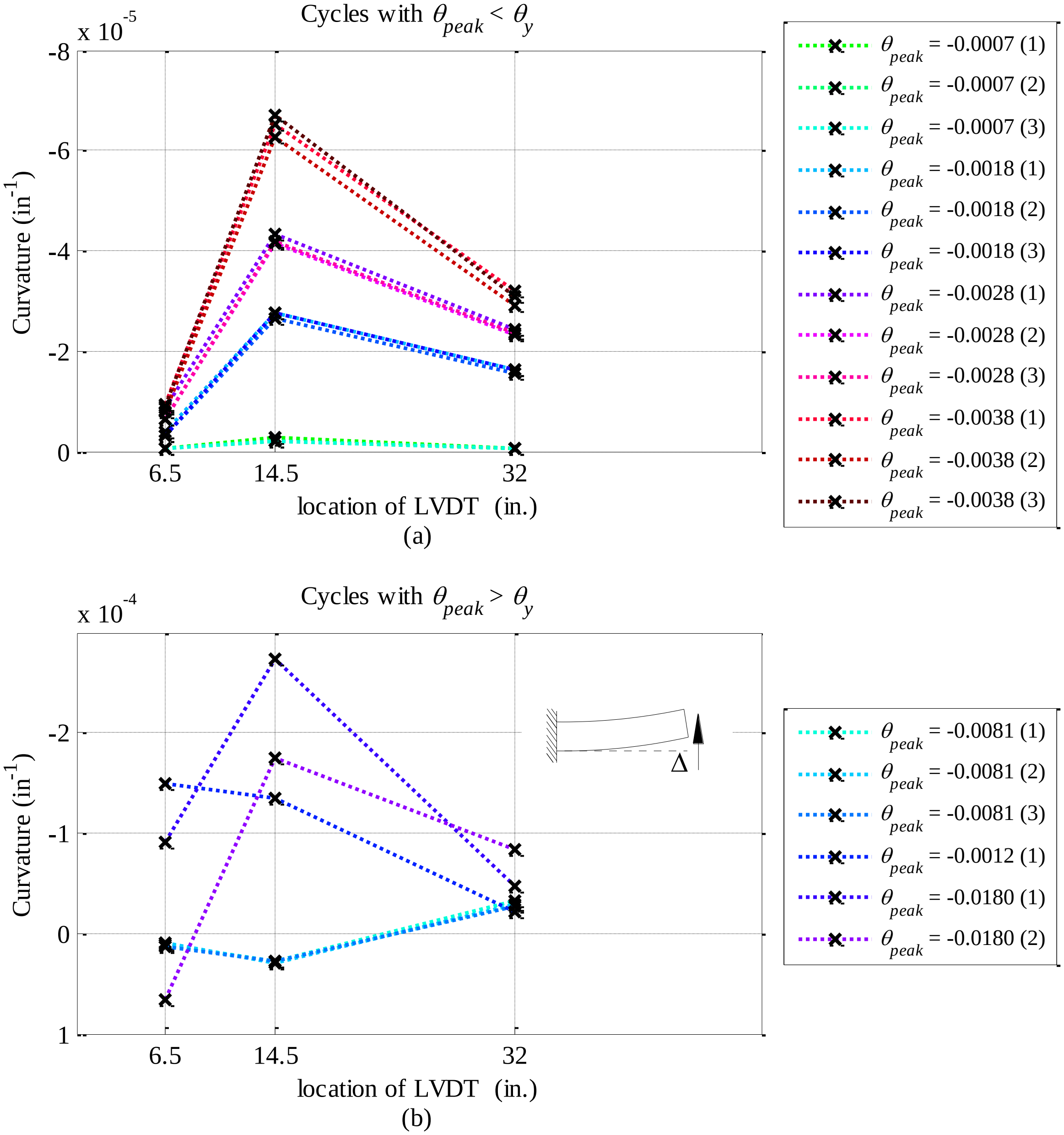

(a)

(b)

Figure 2.8.7. Curvature distribution at the upward displacement peaks in Beam 1.

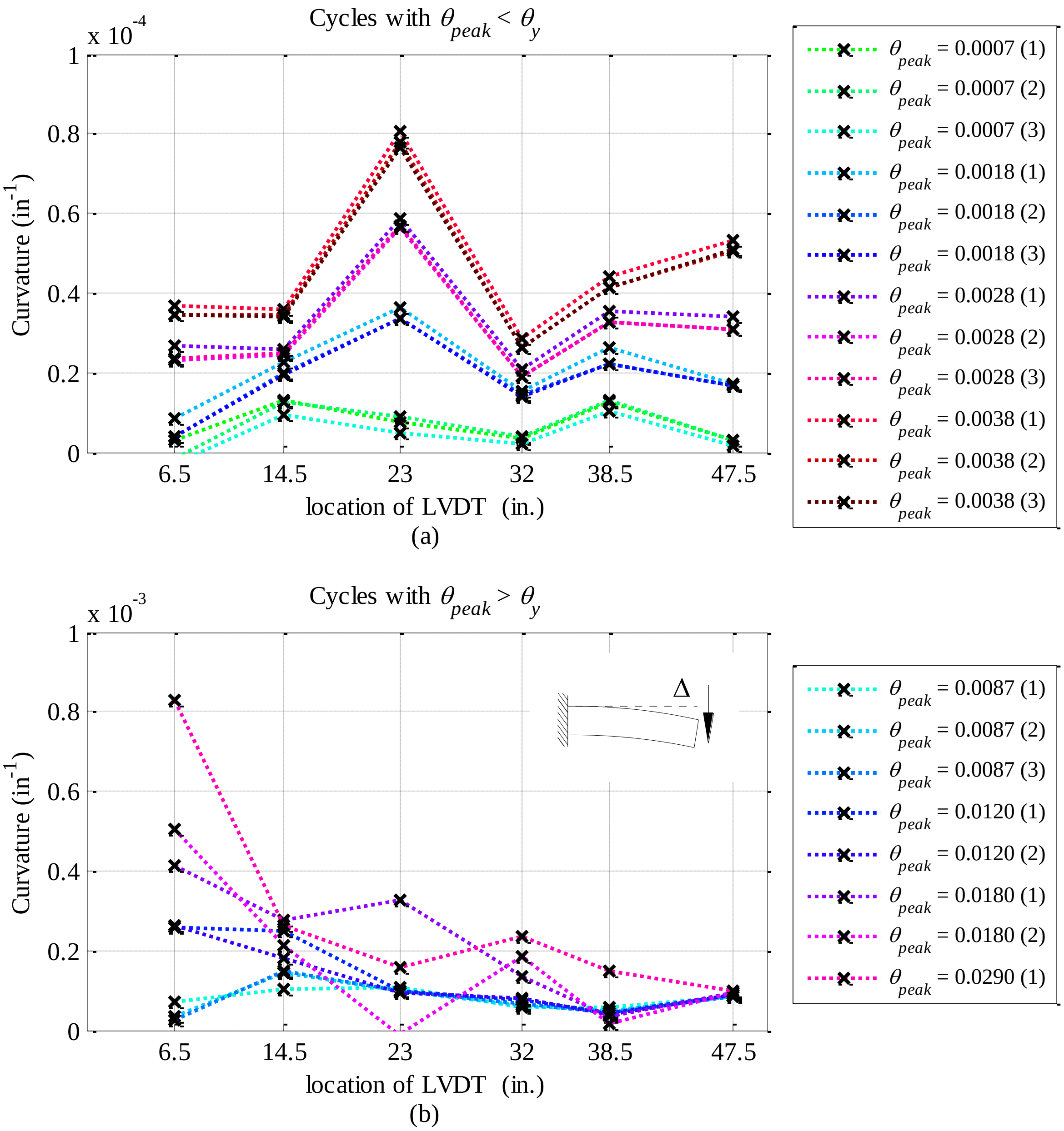

(a)

(b)

Figure 2.8.8. Curvature distribution at the downward displacement peaks in Beam 2.

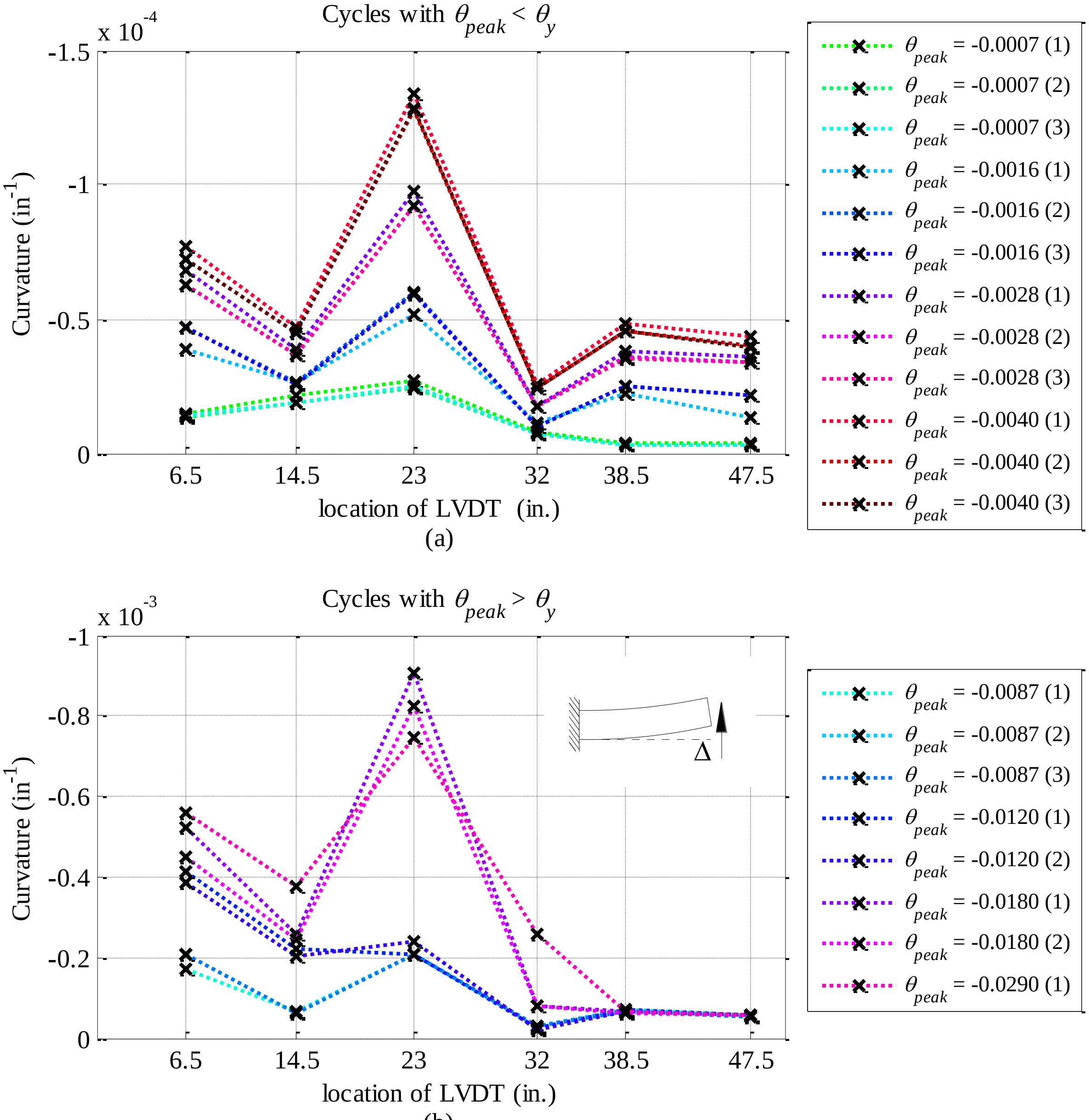

(a)

(b)

Figure 2.8.9. Curvature distribution at the upward displacement peaks in Beam 2.

2.8.3 CRACK WIDTHS

In both beams, vertical cracks associated with flexural action were the first to form, followed by the inclined cracks attributable to shear and horizontal cracks attributable to dowel actions. The propagation of vertical and inclined cracks through the cycles is plotted in Figure 2.8.10(a) and (b), respectively. The points shown in the graph represent the measurements taken at the peak displacement at a *first* cycle of a given step (refer to Figure 2.6.1). For Beam 2, residual crack widths were also recorded at the zero beam displacement upon completion of each step (i.e., completion of each sequence of cycles to equal drift amplitude). These are also are plotted in Figure 2.8.10(a). Residual crack widths increase at an increasing rate beyond the yield displacement (which approximately corresponds to chord rotation of 0.008 and 0.006 for Beams 1 and 2, respectively). Beyond yield displacement, the crack width accumulates during each beam displacement cycles at a given step, due to the beam elongating under inelastic deformations. This is can be observed in Figure 2.8.10(a) by noting that for a given post-yield chord rotation amplitude, the residual width of the crack exceeds the crack width measured at the peak displacement during the first cycle of the step. Accumulation of the crack widths is also visible in the strain history recorded with the horizontal *H1* and *H2* LVDTs attached to the side face of the beam (refer to Appendix A for instrument readings and Section 2.8.7 for more details).

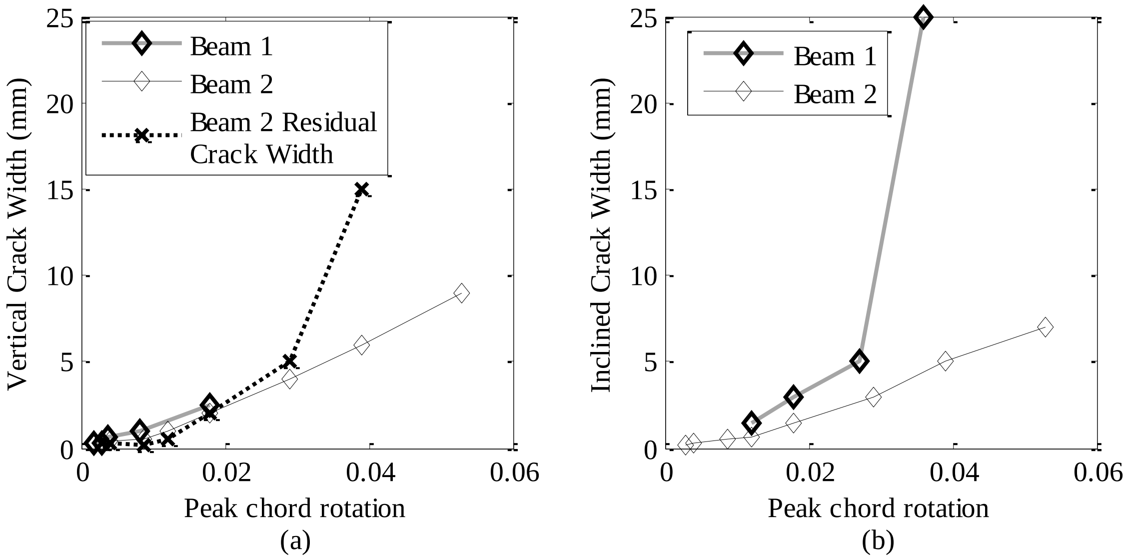

Figure 2.8.10. Crack propagation with drift (1 in. = 25.4 mm).

2.8.4 ONSET OF LONGITUDINAL REINFORCEMENT BUCKLING

The onset and progression of buckling can be identified by the readings of LVDTs attached to the top and bottom faces of the beams. Figure 2.8.11 plots the LVDT readings for peak displacement amplitudes during various displacement cycles for Beams 1 and 2. The LVDT deformations measured have been normalized to the respective gauge lengths. For LVDTs attached to the top face (*TL* series and *TR* series), data are presented for upward displacement peaks, while for LVDTs attached to the bottom face (*BL* series and *BR* series), data are presented for downward displacement peaks. For Beam 1, the data show an "elongation bulge" associated with buckling of the top longitudinal reinforcement, which becomes apparent during the 0.018 rotation amplitude cycles, and is centered around 20 in. from the beam end (Figure 2.8.11[a]).

Along the bottom face (Figure 2.8.11[b]), the data show a similar bulge associated with buckling of the bottom longitudinal reinforcement, which initiated during the cycles with 0.018 peak beam rotation and became more noticeable for the 0.027 drift amplitude cycles, and is centered around 16 in. from the beam end. This is consistent with the observations during the test (see Figure 2.7.2 and Figure 2.7.3). Beam 2 LVDT data, plotted in Figure 2.8.11(c) and (d), also show the "elongation bulge" in both top and bottom faces. In both locations, the bulge was more pronounced during the second load cycle to 0.029 chord rotation amplitude and was centered around 15 in. from the beam support for both top and bottom instruments. This agrees with the test observations shown in Figure 2.7.6 and Figure 2.7.7.

Deformation histories of LVDT instruments which recorded the largest elongation associated with bar buckling (see Figure 2.8.11) are plotted individually in Figure 2.8.12. The measurements are plotted for the cycles with peak drift ratio of $|\theta| < 2.7$ % and $|\theta| < 2.9\%$ for Beam 1 and Beam 2, respectively. For Beam 1, longitudinal bar buckling is evident during the cycles with drift ratio amplitude $\theta = 1.8\%$, especially at the top face of the beam. During these cycles, as the beam moves towards $\theta = -1.8\%$ after having reached peak tensile strain of 0.041 and 0.043 (during 1st and 2nd cycle with $\theta = 1.8\%$, respectively), the tensile strain on the compressive side (top face) of the beam starts to increase, as shown in Figure 2.8.12[a]. Similar behavior can be observed at the bottom face of the beam based on LVDT *BL3* (see Figure 2.8.12[b]).

(a) Beam 1 top face (*TL* series) (c) Beam 2 top face (*TR* series)

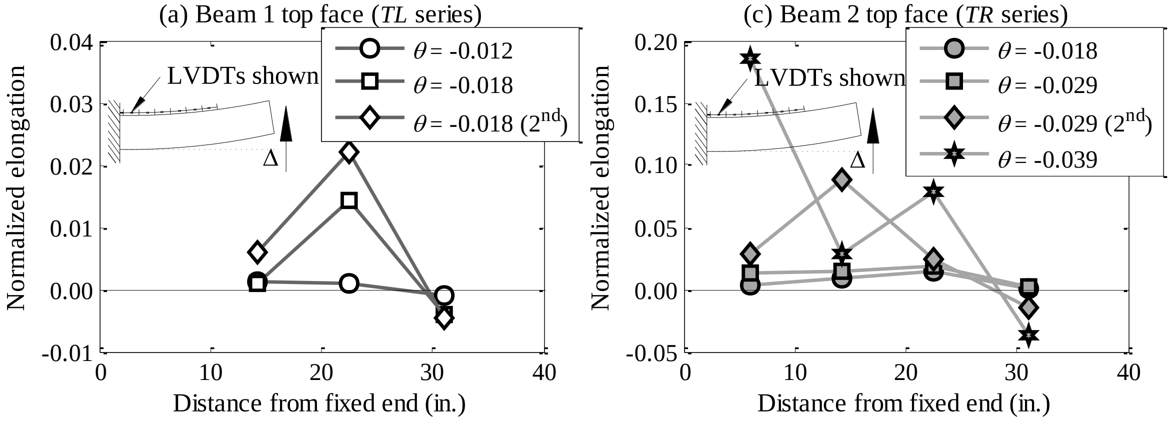

(b) Beam 1 bottom face (*BL* series) (d) Beam 2 bottom face (*BR* series)

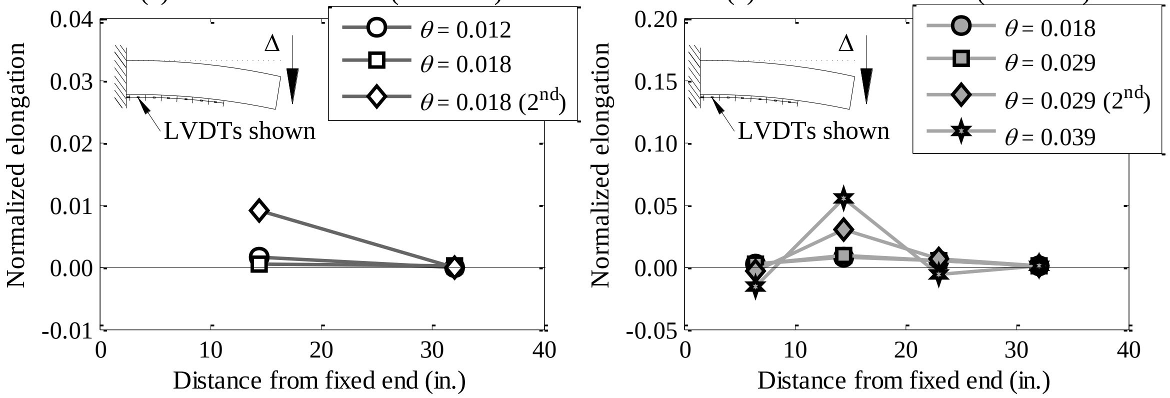

Figure 2.8.11. Profiles of elongation measured between steel instrumentation rods normalized to gauge length: (a) Beam 1 top face; (b) Beam 1 bottom face; (c) Beam 2 top face; and (d) Beam 2 bottom face. Note: Negative elongation corresponds to shortening.

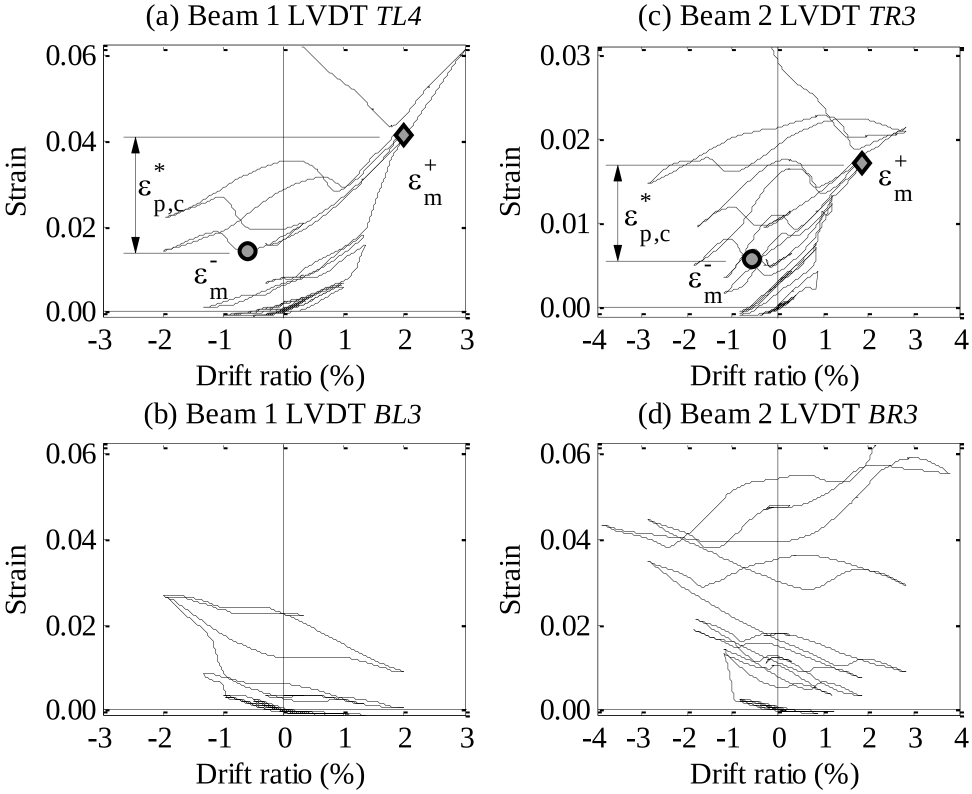

Figure 2.8.12. LVDT strain measurements along the top and bottom faces of the beam vs. beam drift ratio: (a) instrument *TL4* (Beam 1 top face); (b) instrument *BL3* (Beam 1 bottom face); (c) instrument *TR3* (Beam 2 top face); and (d) instrument *BR3* (Beam 2 bottom face).

For Beam 2, LVDT strain measurements indicate buckling during the second cycle with peak drift ratio of θ = 2.9% at both the top and the bottom side of the beam (see Figure 2.8.12[c] and [d]). However, increasingly positive strains as the beam moves upward are noted along the top face even for the cycles with amplitude $|\theta| < 1.9\%$, as indicted by a "bump" in the curve, occurring at approximately 1% instantaneous drift ratio. Note that the LVDT measurements in the locations indicate that for the cycles with drift ratio amplitude $|\theta| > 1.2\%$, only positive strains develop along the top and bottom faces of the beam, indicating that the cracks do not close during compressive loading. This is consistent with the observations made from strain gauge measurements (Figure 2.8.1).

Buckling of longitudinal reinforcement was accompanied by vertical growth of the side face of the beams, as might be expected considering that buckling occurred in the vertical direction. Figure 2.8.13 plots variations of strain as inferred from strain gauges and from vertically oriented LVDTs spanning middle 38.5 in. of the beam side face. Strain gauges show strains approaching or exceeding the "nominal" yield strain of 0.0028 for Beam 1 (refer to earlier discussion on material properties). Strains less than this nominal yield strain occurred for Beam 2. Average strains obtained from LVDT measurements generally exceeded the strain gauge readings, suggesting that the vertical dilation of the beam exceeded the amount that could be accounted for by stirrup strain alone. It is likely that stirrup hook opening at the top of the beams contributed to vertical dilation of the specimens (Figure 2.7.4 and Figure 2.7.8), without having to yield the stirrup.

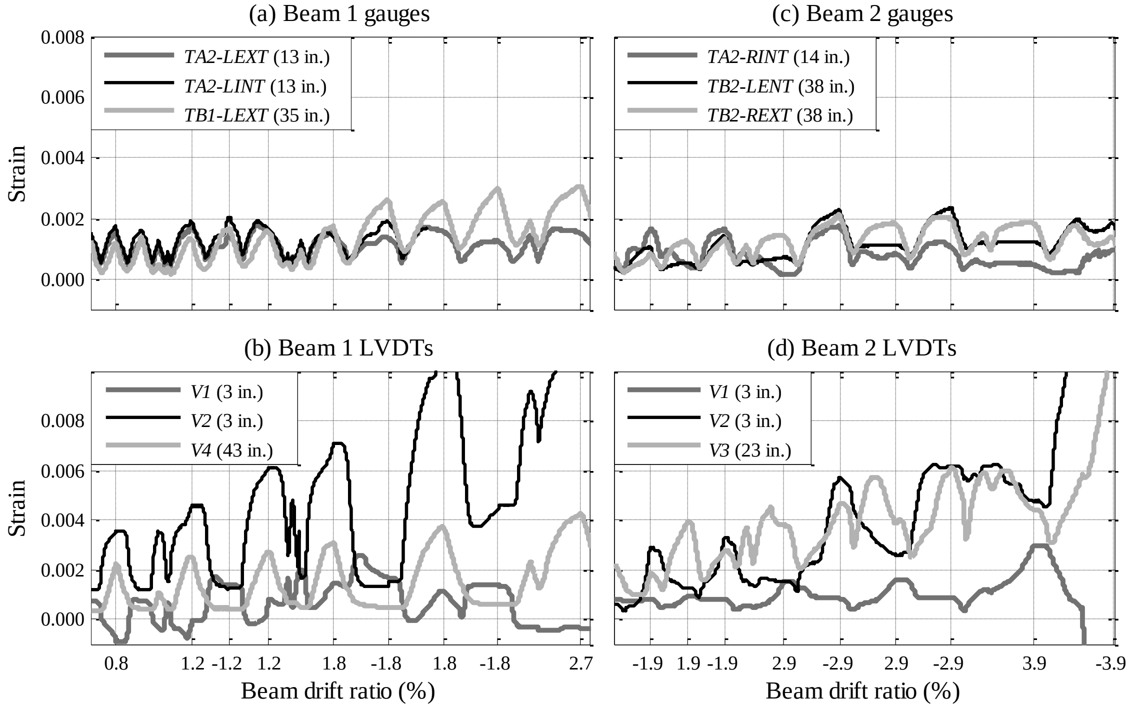

Figure 2.8.13. Deformation history recorded in instruments along the side face of the beams: (a) Beam 1 stirrup strain gauges; (b) Beam 1 vertical LVDTs; (c) Beam 2 stirrup strain gauges; and (d) Beam 2 vertical LVDTs.

2.8.5 FIXED-END ROTATION

For the test specimens, beam longitudinal reinforcement was developed within the reaction block using a standard 90-degree hook that extended 57 in. into the reaction block (Figure 2.4.1). During the test, beam moment results in flexural tension force in either the top or bottom longitudinal reinforcement, which must be developed through bond within the reaction block. Consequently, the tension longitudinal reinforcement is subjected to tensile strains over the development length, which leads to reinforcement elongation and slip between the reinforcement and surrounding concrete. The slip, in turn, results in fixed-end rotation between the beam and the reaction block at their interface. Past tests have shown the fixed-end rotation contributes substantially to the total beam rotation.

Fixed-end rotations were measured by two pairs of LVDTs placed at the beam-reaction block interface – two LVDTs were located at the top face of each beam and two were located at the bottom face. The instruments were positioned to span a very short length of the beam (2.5 in.) so as to minimize flexural and shear deformation components in the measurement. Figure 2.8.14(a) shows the relationship between the fixed-end rotation and the total beam drift ratio for Beam 2 for the cycles prior to longitudinal bar buckling. As can be observed, fixed-end rotation comprises roughly 40% of the total beam tip deflection. A 50% increase in fixed-end rotation is noted for the second cycle of 2.9% drift ratio, which is likely attributable to bond deterioration both within the anchorage and with the beam span along the length of the buckled reinforcement.

Instrumentation problems for Beam 1 precluded measurement of the fixed-end rotation. Measured reinforcement slip in tension (Figure 2.8.14 [b]), however, was similar up to drift ratio 0.7%. At drift ratio 1.8%, slip for Beam 1 was 1.9 times that for Beam 2. It is plausible that impending buckling for Beam 1 had reduced bond along the buckling length of the beam, increasing the fixed-end rotation for that beam in comparison with Beam 2.

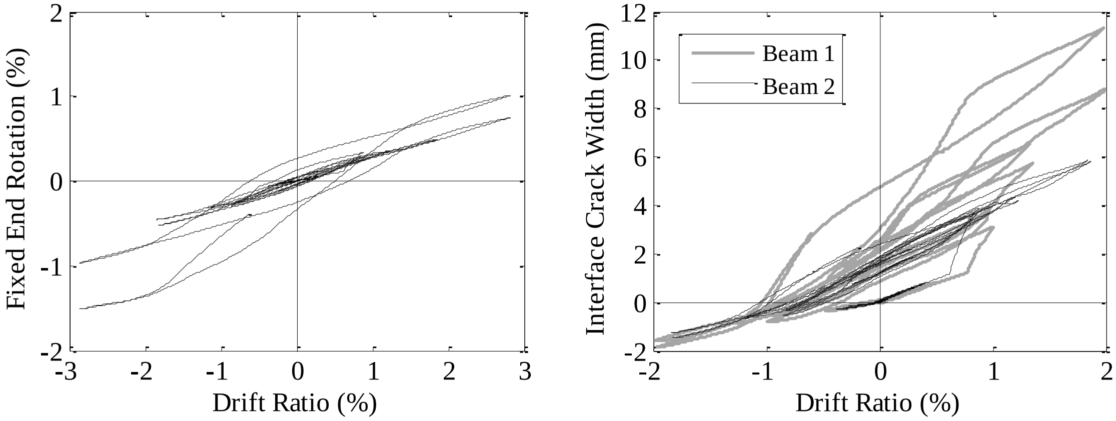

(a) (b)

Figure 2.8.14. (a) Fixed-end rotation vs. drift ratio for Beam 2 and (b) interface crack width measured by TL1 instruments for beams 1 and 2 (1 in. = 25.4 mm).

2.8.6 SHEAR DEFORMATION

Shear deformations in reinforced concrete beams have been traditionally measured using a single pair of diagonal LVDTs arranged in a grid such as the one shown in Figure 2.8.15(a), consisting of series of multiple grid bays, shown in Figure 2.8.15(b). Note that this differs from the instrumentation arrangement in Beams 1 and 2. For clarity, total deformation of any given instrument in Figure 2.8.15 is labeled using the same name as the element itself. Under pure flexure, the bay deforms as shown in Figure 2.8.15(c). Because curvature φ across the bay length l is uniform, this type of bending causes no deformation in diagonal LVDTs (here labeled as *D1* and *D2*). Pure shear deformation (Figure 2.8.15[d]) causes equal and opposite elongation of the diagonal instruments, *D1* and *D2*, while vertical dilation causes the diagonals to expand by equal amounts (Figure 2.8.15[e]). Thus, correcting the *D1* and *D2* measurements for the vertical dilation contribution, the shear deformation within a single grid bay, Δ_{sb}, has historically been computed with the following equation:

$$\Delta_{sb} = \frac{D2 - D1}{2\sin\alpha} \qquad 2.2$$

where α is the angle of the diagonal instruments with respect to the horizontal (labeled in Figure 2.8.15[b]).

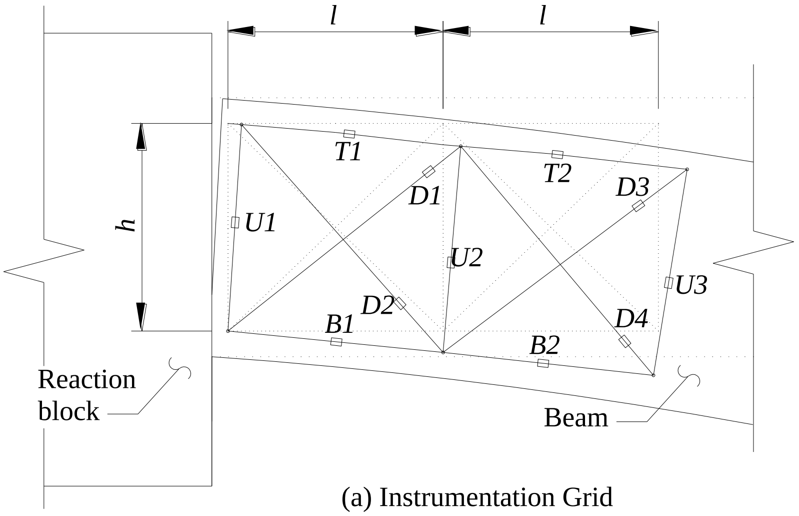

(a) Instrumentation Grid

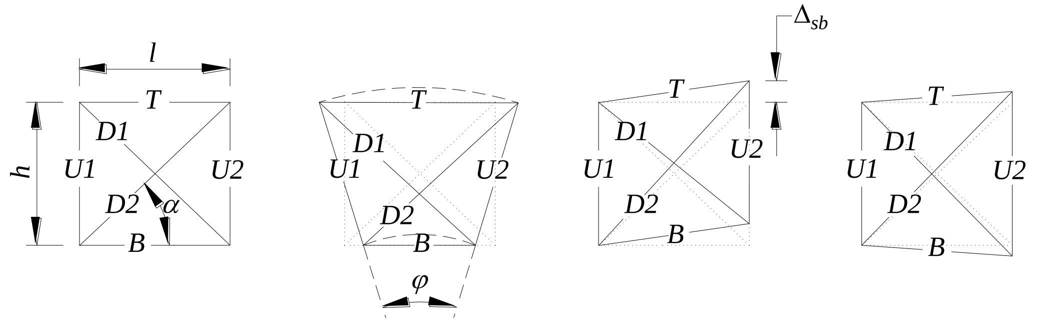

(b) Undeformed Bay (c) Pure Flexure (d) Pure Shear (e) Pure Vertical Dilation

Figure 2.8.15. Typical LVDT grid arrangement.

The assumption in Equation 2.2 is that the curvature is uniform across the instrumentation bay, such that the measurements *D1* and *D2* are not affected by the flexural deformations in the beam. However, upon flexural yielding in reinforced concrete beams, significant curvature gradient may be present across length *l* spanning the plastic hinge zone. This means that portion of the deformations recorded with diagonal instruments *D1* and *D2* are due to flexure, and not shear. In this case, Equation 2.2 leads to overestimation of shear deformations.

Hiraishi (1984) noted this problem (Figure 2.8.16) and offered a modification of Equation 2.2 to correct the shear deformation computation from by using the measurements from the horizontal LVDTs *T* and *B*, positioned as shown in Figure 2.8.15. However, in the absence of top and bottom LVDT instruments spanning the grid bay, as is the case in the instrumentation layout used in Beams 1 and 2, it is not possible to make this correction.

Massone and Wallace (2004) presents the analysis of the data from 4 different laboratory tests of reinforced concrete shear walls having the aspect ratio of 3, which is almost identical to the aspect ratio of Beams 1 and 2, and the axial load of $0.10A_gf'_c$. Using the approach of Hiraishi (1984), Massone and Wallace (2004) estimates 16-31% error in shear deformations computed within the plastic hinge region by using Equation 2.2.

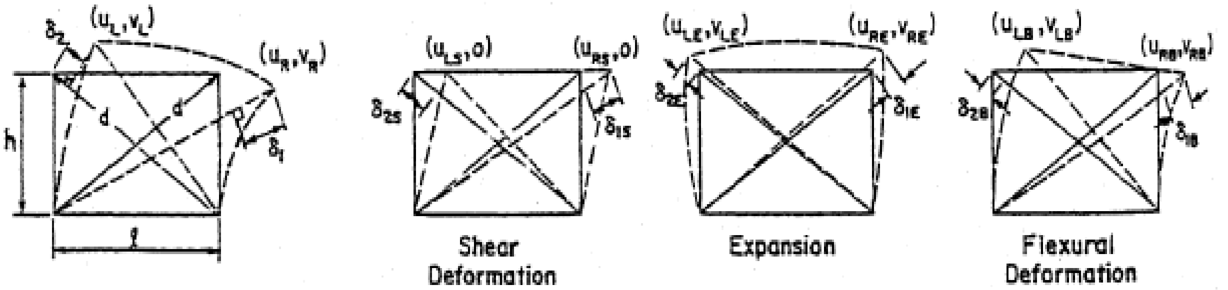

Figure 2.8.16. Deformation components contributing to elongation of diagonal LVDTs in the shear panel (after Hiraishi 1984).

As noted before, the arrangement of LVDTs attached along the side face of Beams 1 and 2 was different from the one shown in Figure 2.8.15. Four smaller grids of length *l* and height *h* were used to calculate the approximate beam shear deformations within the 43-in. instrumented beam length (Figure 2.5.3). These were calculated using the following expression:

$$\Delta_{shear} = \frac{\sqrt{l^2 + h^2}}{2h}[(S4 - S2) + (S6 - S8)] \qquad 2.3$$

Here, Δ_{shear} is the vertical displacement due to shear within the instrumentation block on the side face of the beam, *l* and *h* are the dimensions shown in Figure 2.8.17, and *S2*, *S4*, *S6*, and *S8* are the deformations of the corresponding diagonal LVDTs. Equation 2.3 takes into account the sign of the displacements recorded with the instruments (e.g. for a given positive shear deformation, instrument *S4* shortens, which is recorded as a negative deformation, while *S2* lengthens, which is recorded as a positive deformation). Assuming constant vertical beam dilation along the beam height for the displacement cycles prior to buckling, the portion of the deformation of diagonal *S* instruments due to vertical dilation cancels out in Equation 2.3. Upon buckling, many instruments became permanently displaced, thus their readings are disregarded after this point.

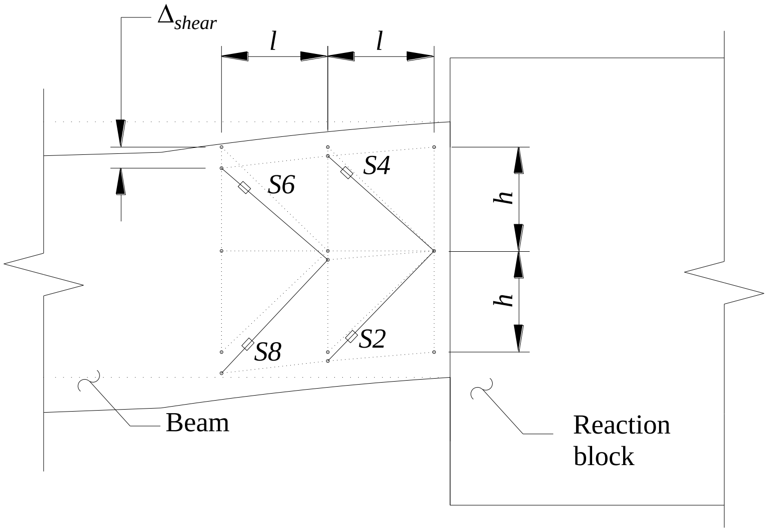

Figure 2.8.17. Computing the shear deformation in Beams 1 and 2 with diagonal LVDTs attached to the side face of the specimens.

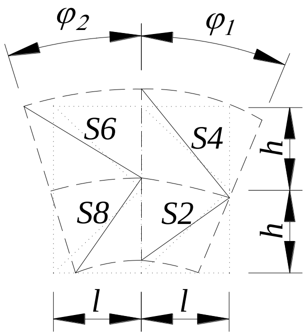

Figure 2.8.18. Instrumentation panel under idealized curvature distribution.

Equation 2.3 is analogous to Equation 2.2 in the sense that it is written under the assumption of uniform curvature distribution along the span of any given diagonal LVDT in Figure 2.8.17. Using the instrumentation grid of Beams 1 and 2, this is illustrated in Figure 2.8.18. Here, the left two panels experience curvature φ_2, while the right two panels experience curvature φ_1. It is expected that the level of error in shear deformations calculated using Equation 2.3 would be similar to those calculated using Equation 2.2 in structures of similar aspect ratio, such as the shear walls studied by Massone and Wallace (2004).

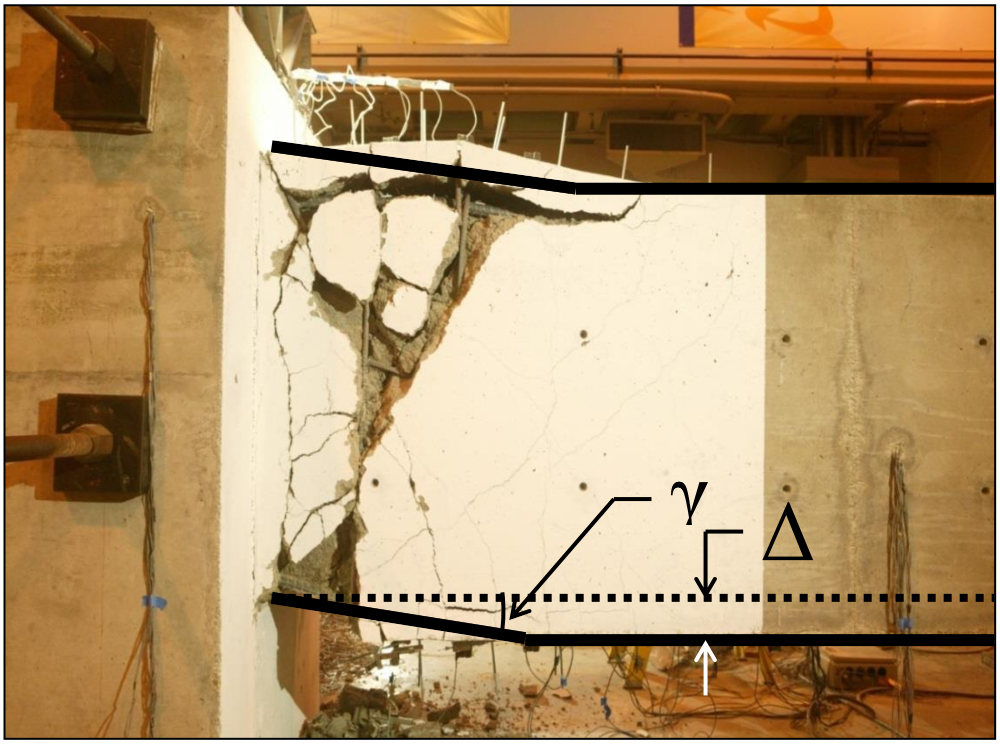

Figure 2.8.19. Shear deformations as observed during Beam 1 test.

Shear damage and deformations in the two specimens were most visible within the region of largest damage, extending to approximately 40 in. from the supports (see Figure 2.8.19). Within this region, movement along inclined cracks was visible in later stages of the tests. Outside this region, only narrow inclined cracks were observed, extending along approximately half the cantilever beam length. The concentration of shear deformations around the plastic hinge regions observed in the tests is typical of reinforced concrete beams responding inelasticaly.

The relationship between the total resisting shear (including that due to self-weight) and the approximate shear deformation within the 43-in. gauge length is shown in Figure 2.8.20. The relationship is plotted only for the cycles prior to longitudinal reinforcement buckling. Although nominal shear strength V_n calculated in accordance with ACI 318 was more than twice the peak resisting shear for Beam 1, deterioration of shear stiffness is notable as the cycles progress. For example, shear displacement measured during the first cycle to rotation 0.018 nearly doubled during the second cycle to the same drift amplitude (Figure 2.8.20). Shear stiffness deterioration is also evident in progressively greater pinching in the moment-drift ratio curves in Figure 2.7.9, although pinching is also partially attributable to longitudinal bar buckling and slip.

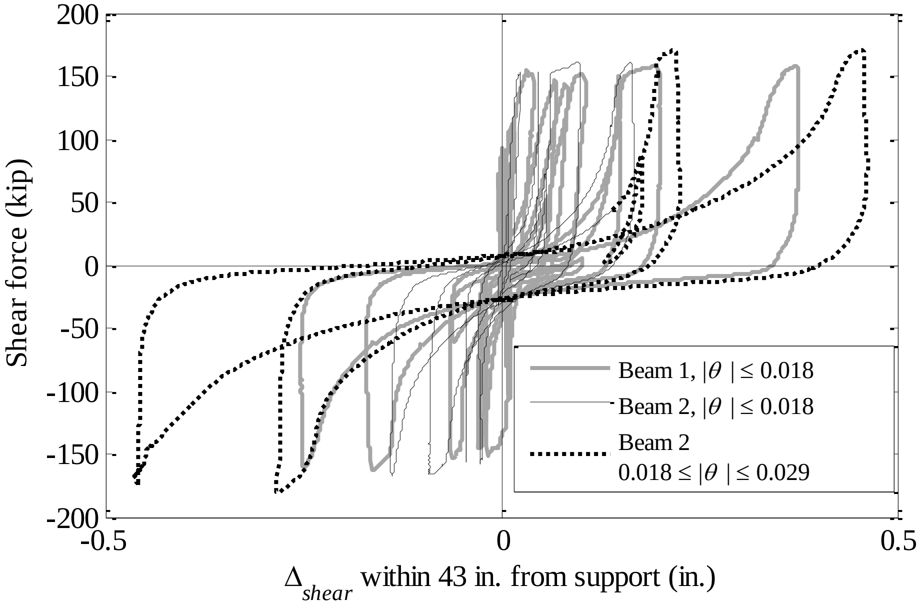

Figure 2.8.20. Estimated shear deformations in beams 1 and 2.

For a given displacement amplitude, Beam 2 exhibited smaller shear deformations than Beam 1 (Figure 2.8.20). For example, during the last cycle with rotation amplitude 0.018, shear deformation in Beam 2 was approximately half the shear deformation of Beam 1. Beam 2 was loaded to less than 30% of the calculated ACI 318 nominal shear strength, yet about 10% of the total beam displacement was attributable to shear deformations for the cycles preceding longitudinal bar buckling.

Figure 2.8.21 shows the relationship between the approximate shear deformations in the test beams and the total beam chord rotation. It is evident that the amount of shear deformations increases in nonlinear fashion as the total beam chord rotation increases, implying that the shear deformations increase with the damage accumulation even in these flexure-dominant beams which have not yielded in shear for the displacement cycles shown.

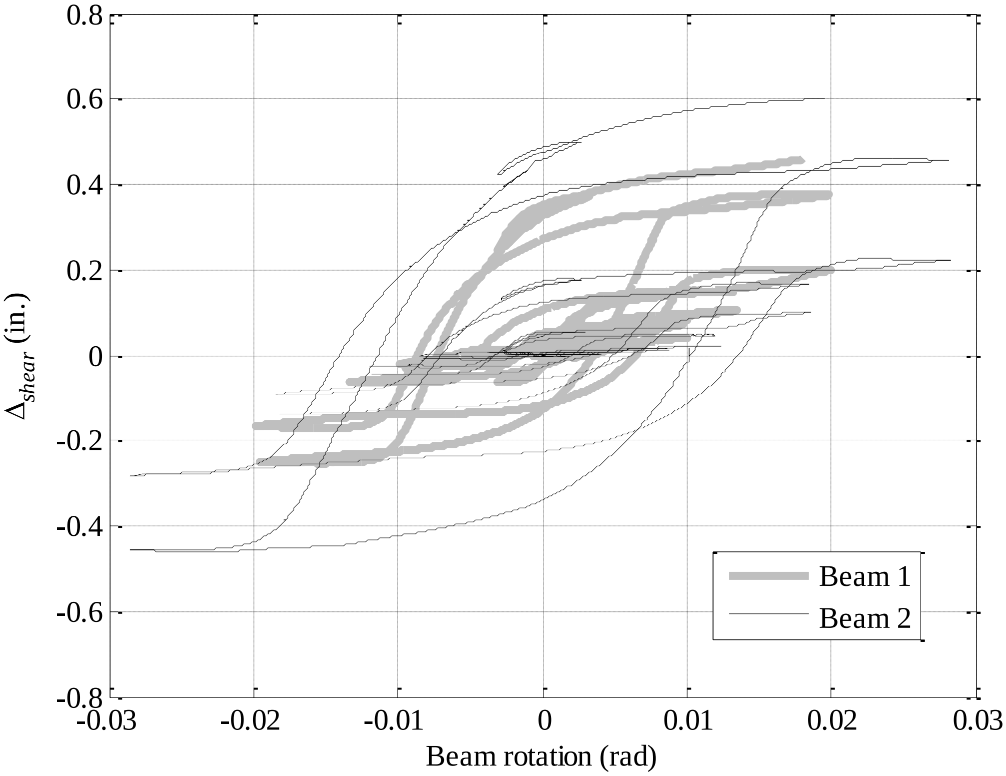

Figure 2.8.21. Relationship between the shear deformations measured within the plastic hinge region and the total beam rotation.

2.8.7 BEAM AXIAL LENGTHENING

In a beam without axial load, reversed cyclic loading has been observed to result in beam elongation (e.g. Fenwick and Fong 1979, Qi and Pantazopoulou 1991). This elongation can be especially important in the lower stories of buildings with column restrained at the ground level, and in buildings with precast floors supported on short seats (Corney et al. 2013). Figure 2.8.22 shows the measured elongation in the plastic hinge region for the two specimens. The curve plotted corresponds to the elongation along the centerline of the beam, computed by averaging the elongations measured along the top and bottom face of the beams. This calculation excluded the contribution of bar slip at the interface with the reaction block. The results indicate that in the early cycles, beam elongation is roughly equal to $\theta \cdot h/4$ (where θ is chord rotation expressed in radians). For the loading cycles with rotation amplitudes greater than 0.02 rad, axial elongation of the beam is closer to $\theta \cdot h/2$.

The deformation measurements in the LVDTs along the top and bottom face of the beams indicate that only tensile strains develop throughout the history (see Appendix A for instrument data). Apparently, cracks that opened under flexural tension never fully closed under flexural compression. This is also evident in the longitudinal bar strain histories plotted in Figure 2.8.1. For loading in the direction that would tend to result in flexural compression, the gauges indicate partial crack closure (due to compression) during the cycles which precede longitudinal bar buckling. Even less crack closure is apparent once longitudinal bar buckling commences.

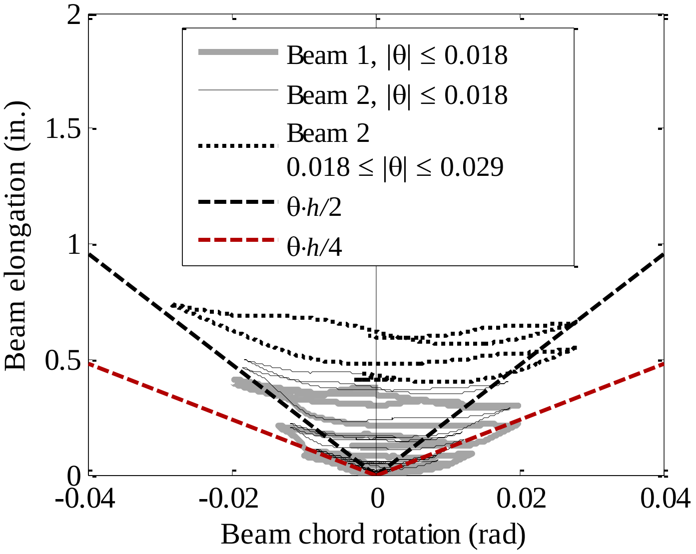

Figure 2.8.22. Elongation of beams 1 and 2 prior to buckling.

2.9 BUCKLING BEHAVIOR OF LONGITUDINAL BARS

Studies on cyclic behavior of reinforcing bars deformed into the inelastic range (Monti and Nuti 1992, Rodriguez et al. 1999) have demonstrated that the ratio of the unsupported bar length L_b to the bar diameter d_b is the primary factor that determines the buckling behavior of bars for a specific axial deformation history. The ratio L_b/d_b is typically considered equivalent to s_h/d_b ratio in reinforced concrete specimens where the transverse reinforcement (spaced at s_h) provides the lateral support of the longitudinal bars. It is of interest to compare the behavior of longitudinal bars in Beams 1 and 2 to what was observed in the latter study, which considered the effects of inelastic cyclic deformation of the steel bars (Rodriguez et al. 1999).

As noted before, the deformation history of No. 11 bars in Beams 1 and 2 is characterized by increasing inelastic tensile strains with no compressive strains for drift ratios larger than 0.9% (Figure 2.8.1). Rodriguez et al. (1999) hypothesized that the onset of buckling, after unloading from the maximum tensile strain ε_m^+ (Figure 2.9.1), under this type of strain history would depend on the strain range $\varepsilon_p^* = \varepsilon_0^+ - \varepsilon_p$, where ε_0^+ is the strain for which the bar experiences compressive stress after unloading from ε_m^+ and ε_p is the strain at buckling initiation (shown in Figure 2.9.1). Rodriguez et al. (1999) defines the variables ε_p^*, ε_m^+, ε_m^-, ε_0^+, and ε_p (all shown in Figure 2.9.1) based on the average bar strain calculated by dividing the total axial deformation by the length of the test coupon. Buckling was said to occur when the gauges located on opposite faces of test coupons indicate 20% difference in strain readings, as a result of the buckling-induced curvature in the bar.

Rodriguez et al. (1999) demonstrated the dependence of onset of bar buckling on parameter ε_p^* by showing a trend in the data obtained from bar tests using loading histories representative of those experienced by the longitudinal bars in beams and columns, as Figure 2.9.1 illustrates. Figure 2.9.1 also shows the values of ε_p^* estimated from the mean curve of Rodriguez et al.

(1999) for s_h/d_b ratios of 7.8 and 4.25, corresponding to Beams 1 and 2, respectively. The values estimated are approximately 0.012 for Beam 1 and 0.06 for Beam 2, as marked in Figure 2.9.1.

The available instrumentation in the beam tests did not permit determination of the strain at initiation of buckling, ε_p, in the same way as was done in Rodriguez et al. (1999). Instead, the strain range $\varepsilon_{p\ ,c}^{*} = \varepsilon_0^{+} - \varepsilon_m^{-}$ was inferred from the average strains recorded by the LVDTs spanning the buckling region before significant bulging was observed. For this purpose, the strain ε_0^{+} at zero stress after unloading from ε_m^{+} was taken as $\varepsilon_0^{+} = \varepsilon_m^{+} - \varepsilon_y$, where $\varepsilon_y = 0.002$ (Figure 2.9.1). The strain ε_m^{-} was taken at the instant when the LVDTs recorded a local minimum tensile strain in the compression side of the beam during unloading (Figure 2.8.12). These points are marked with a solid circle in Figure 2.8.12 (a) and Figure 2.8.12 (c). Diamond markers in the same figure indicate peak tensile strain ε_m^{+} measured prior to reaching ε_m^{-}.

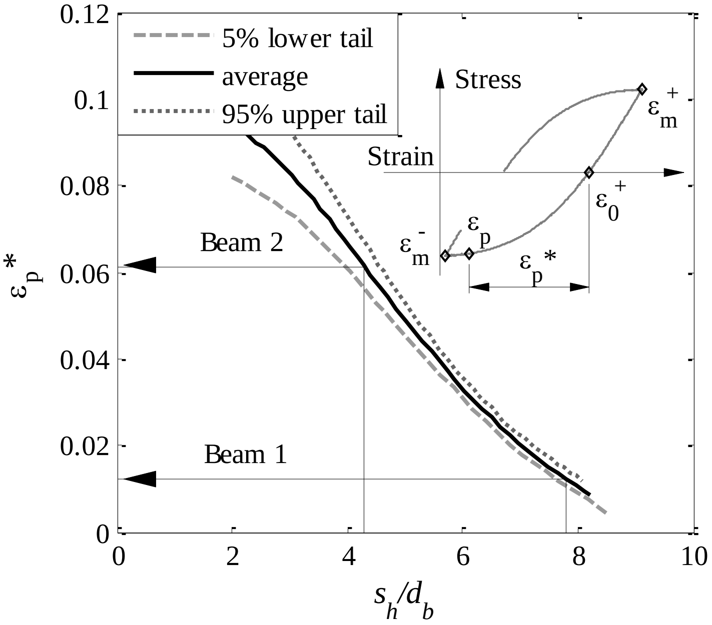

Figure 2.9.1. Strain range ε_p as a function of s_h/d_b (after Rodriguez et al. 1999).

The value of $\varepsilon_{p\ ,c}^{*}$ for top bars in Beam 1 reached 0.027 prior to buckling, compared with $\varepsilon_p^{*} = 0.012$ obtained from the Rodriguez et al. (1999) curves. For Beam 2 top bars, the calculated $\varepsilon_{p\ ,c}^{*}$ was 0.011 compared to $\varepsilon_p^{*} = 0.06$ obtained from Rodriguez et al. (1999) curves. Despite the inherent differences in experiment configurations (bare steel coupons versus bars embedded in concrete) and strain measurement methods between Rodriguez et al. (1999) tests and Beams 1 and 2, the discrepancies in the ε_p^{*} values can provide an insight into buckling behaviour of bars in the beams and help reinforce the observations made during beam tests.

The buckling of top and bottom longitudinal bars in Beam 1 occurred during the cycles with the same drift ratio amplitude and prior to spalling of concrete cover. Though dowel cracks in Beam 1 appeared prior to buckling at both top and the bottom, the presence of concrete cover increases bar resistance to buckling when compared to a bare bar, which supports why $\varepsilon_{p\ ,c}^{*}$ reached in Beam 1 was larger than Rodriguez et al. (1999) estimate. The striking difference in measured vs. predicted $\varepsilon_{p}{}^{*}{}_{,c}$ in Beam 2 bars and also the delayed buckling of the bottom bars may point to insufficient lateral support provided by the hoops. An interesting crack pattern noted along the top face of Beam 2, and shown in Figure 2.9.2, may be the evidence of this. A narrow crack appeared during the upward displacement of the first cycle to -0.019 rotation, coinciding with the location of the No. 11 bar which was not directly supported by a vertical crosstie, and was oriented parallel to the bar. The crack was progressively wider with the increasing upward displacements, until the bars buckled (shown in Figure 2.9.2), which may indicate that the outward excursion of the buckling No. 11 bars was the cause of this crack. It is possible that the buckling initiated in the bars not directly braced by a vertical crosstie (those that are next to the outermost top and bottom bars), which have the unsupported length exceeding the hoop spacing s_h. The outward excursion of these bars likely caused the cap ties to disengage, forcing the neighbouring bars to also buckle. This may explain why the beams reported in Blakeley et al. (1975) with comparable design parameters to those of Beam 2, but with all longitudinal bars braced directly by a vertical crosstie, sustained larger deformations before bar buckling occurred.

Buckling of the bottom bars in Beam 2 became apparent at drift ratio amplitudes 35% larger than those for which the top bars buckled, suggesting that the presence of cap ties may reduce the effectiveness of the hoops in lateral bracing of the bars. Cap ties used in the beams of the present study are likely to be most effective in closing a hoop where a slab is cast at the top of the beam. Where there is no slab, or where the beam is upturned with the slab at the bottom of the beam, the presence of cap ties creates a weakness at the top of the beam. As a result, the 90-degree hook as well as the seismic hook with only $6d_b$ extension in a horizontal crosstie may have led to premature opening of the hoop. The use of longer extensions in the seismic hooks of the stirrups, cross-ties, and cap ties may potentially enhance the resistance against longitudinal bar buckling. Whether the presence of the slab actually would have improved performance, however, was not part of the present study. Further research is needed to investigate effectiveness of this hoop arrangement and also alternative hoop configurations within the plastic hinge regions of reinforced concrete beams.

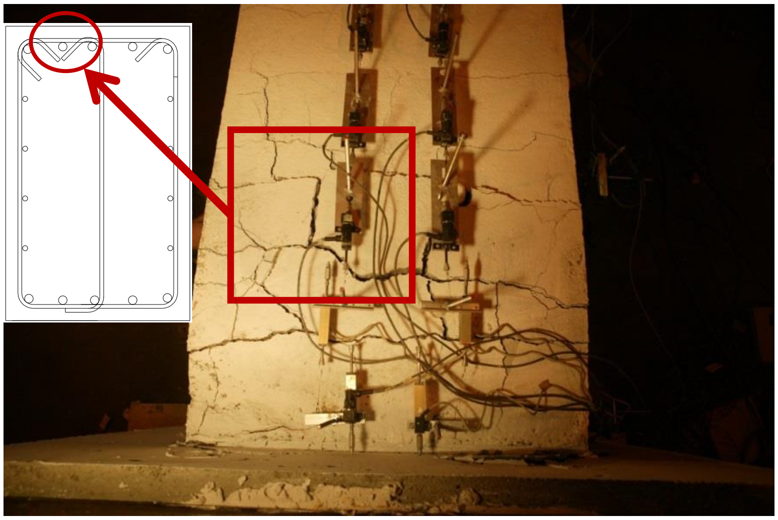

Figure 2.9.2. Possible buckling of bar with no direct lateral restraint by a vertical crosstie.

2.10 PERFORMANCE EVALUATION

Responses of Beams 1 and 2 are evaluated based on ASCE 41 (ASCE 2006) and FEMA 356 (2000), which define several structural performance levels and the corresponding damage states. The state of least damage is at the Immediate Occupancy (IO) performance level where "only very limited structural damage has occurred" (FEMA 356). Minor cracking may be present, but no concrete crushing should occur in primary elements of concrete frames. The most severe damage state is at the Collapse Prevention (CP) performance level, where "the building is on the verge of partial or total collapse" while "significant components of the gravity load-resisting system must continue to carry their gravity load demands".

According to FEMA 356, the damage states for beams are established based on the maximum plastic rotation angle, defined as $\theta_p = \theta_{cap} - \theta_y$. For reinforced concrete beams at CP performance level, $\theta_p = 0.025$ (rad.). Beams 1 and 2 reached $\theta_p = 0.019$ and 0.033, respectively, prior to losing significant amount of vertical load carrying capacity. Thus, only Beam 2 satisfies the CP performance level.

The IO performance level for reinforced concrete beams is defined when $\theta_p < 0.010$, which corresponds to beam rotation of 0.02 and 0.019 for Beams 1 and 2, respectively. At this level of deformation, neither beam exhibited concrete crushing. The residual cracks were only measured for Beam 2, and thus only this beam can be fully evaluated against the IO performance level criteria. The maximum residual crack width of Beam 2 when $\theta_p < 0.010$ was 2 mm (0.08 in.), which can loosely be considered in excess of "minor hairline cracking", if hairline cracking limit is usually considered to be less than a tenth of a millimeter wide. Thus, despite the improved general performance of Beam 2, the current detailing of ACI 318 may need to be further investigated to ensure the performance is consistent with the criteria in ASCE 41.

2.11 RECOMMENDED CODE CHANGES

Beam 1 was designed and detailed in accordance with ACI 318-08. Specifically, the hoop spacing within the intended plastic hinge zone was 11 in. based on the requirement of Section 21.5.3.2 that spacing not exceed the least of $d/4$, $8d_b$ of the smallest longitudinal bars, $24d_b$ of the hoop bars; and 12 in. The beam was able to resist inelastic cyclic deformations up to a chord rotation of 0.027, at which point buckling of longitudinal reinforcement caused major loss of lateral force-resisting capacity. This performance is deemed, in general, to be unsatisfactory for a beam of a special moment frame, because rotations exceeding this rotation capacity generally can be anticipated for shaking at the MCE level.

By decreasing the hoop spacing to 6 in., as was done for Beam 2, longitudinal reinforcement buckling resulting in strength decay was delayed until equivalent beam rotation of 0.039. This performance would generally be considered acceptable for a beam of a special moment frame. Based on these observations, a Code Change Proposal to ACI 318-08 Section was made and implemented into ACI 318-11, limiting the bar hoop spacing to the smallest of $d/4$, $8d_b$ of the smallest longitudinal bars, $24d_b$ of the hoop bars; and 6 in.

2.12 CONCLUSIONS

Based on the results presented in this chapter, the observations and conclusions are the following:

1. Beam 1 flexural stiffness at yield point was $0.13E_cI_g$ while that of Beam 2 was $0.16E_cI_g$. Rigid body displacements associated with slip of reinforcement from the anchorages constituted approximately 40% of the total beam displacement.
2. Beams 1 and 2 developed peak moment strengths equal to $0.99M_{pr}$ and $1.10M_{pr}$, respectively, where M_{pr} is probable moment strength calculated in accordance with ACI 318.
3. Maximum nominal shear stresses for both beams were on the order of $1.7\sqrt{f_c'}$ psi using measured concrete compressive strength. Even though shear forces were less than provided shear strengths, notable shear deformations occurred in the plastic hinge region.
4. In both beams, initiation and progress of damage were dominated by longitudinal reinforcement buckling. For Beam 1, buckling initiated during a cycle with a peak rotation 0.018 and became more extensive during the cycles with 0.027 rotation amplitude. For Beam 2 with reduced hoop spacing, buckling was delayed until the first cycle with rotation amplitude of 0.029 and became more extensive during the cycle with 0.039 peak rotation.
5. Longitudinal bar buckling in both beams initiated at the top of the beam where local concrete strength would be expected to be lowest. It seems more likely, however, that the tendency for earlier buckling at the top of the beam was influenced mainly by the presence of the cap ties that closed the hoops at the top of the beam. The use of longer extensions in the seismic hooks of the stirrups, crossties, and cap ties may enhance the resistance against cap ties disengaging and longitudinal bar buckling. Further research is needed to explore the effect of different hoop configurations within the plastic hinge regions on cyclic response of large beams.
6. Existing models for estimating the onset of longitudinal bar buckling (Rodriguez et al. 1999) have shown to not be good indicators of when the buckling occurs in a beam where the bars are embedded in concrete, and cracking, shear deformations, and curvature gradient are present. These models should thus be used only in qualitative comparison of different design alternatives (for example, variation of transverse hoop spacing) and not as an indicator when the buckling might occur in a reinforced concrete member.
7. Beam 1 with hoop spacing satisfying the requirements of ACI 318-08 did not meet the performance expectations at the deformation levels expected during the design earthquake level of shaking, implicit in that code or explicit in ASCE 41. By reducing the hoop spacing to no greater than 6 in. and $6d_b$ of the longitudinal bars, the performance met the expectations. Maximum permitted hoop spacing within the intended plastic hinge zone was modified in the 2011 ACI 318 edition to the least of $d/4$, $6d_b$ of the smallest longitudinal bars, and 6 in.
8. Significant elongation was present in both Beams 1 and Beam 2 as a result of reverse inelastic displacement loading. This axial lengthening was proportional to $\theta \cdot h/2$ (θ = beam chord rotation, h = beam depth). This is an important aspect of inelastic behavior of

reinforced concrete members and should be taken into account in design and analysis of moment frames.

9. In a large reinforced concrete beam similar to those tested in this study, with equal areas of top and bottom longitudinal reinforcement, flexural tension cracks formed during loading in one direction tend to remain open for loading in the reversed direction. As a result, flexural compression is resisted mainly by the longitudinal reinforcement near the flexural compression face and not by the concrete. Thus, requirements for hoop reinforcement need not be based on considerations of concrete confinement, but instead should be based on considerations of beam shear and longitudinal reinforcement buckling restraint.

CHAPTER 3

NUMERICAL MODELING OF LARGE REINFORCED CONCRETE BEAMS IN SPECIAL MOMENT RESISTING FRAMES

This chapter serves as a foundation to develop and justify a reinforced concrete beam modelling approach implemented in the nonlinear static and dynamic analyses of special moment resisting frames (SMRF) presented in Chapters 4-6. The following sections explore different options for numerical representation of reinforced concrete beam force-deformation response components which are used as a basis for selecting the modeling strategies for frame analysis. Beam response components addressed include: flexural behavior including axial beam lengthening, fixed-end rotations due to longitudinal bar strain penetration into the anchorage and the associated bar slip, and shear deformations. Beam elongation is emphasized in this chapter as a response component that can impact the level of column forces computed in the nonlinear analysis of reinforced concrete moment frame structures.

Although it is reasonable to expect that the degradation of strength would occur in the reinforced concrete members during strong ground shaking (due to longitudinal bar buckling, bond failure, shear failures, etc.), modeling strategies presented in this chapter only consider the beams which respond in ductile manner and without strength degradation. Because the purpose of Chapter 3 is to establish a beam model adequate for nonlinear analyses of SMRFs aimed at estimating peak design forces in frames, not accounting for strength degradation leads to conservative computations of maximum forces and thus the aforementioned assumptions fit the scope of this dissertation. For the same reason, beam shear force-deformation response is only addressed for completeness and is not used as a parameter in selecting the numerical model for large SMRF beams.

3.1 SIGNIFICANCE OF ELONGATION IN REINFORCED CONCRETE BEAMS

The phenomenon of axial lengthening in reinforced concrete beams under lateral cyclic deformations, also referred to as beam growth, has been known for over three decades. It was noted in the laboratory tests around the same time by several research groups - Takiguchi and Ichinose (1977) and Fenwick and Irvine (1977) both observed elongation of beam specimens that was mostly concentrated in the plastic hinge region and reaching up to 1% of the member length. Since then, beam growth was noted in many experiments including both isolated beam tests and also frame subassemblies where elongating beam imposed outward column deflections in the plane of the frame (Fenwick and Fong 1979, Restrepo et al. 1990, Qi and Pantazopoulou, 1991, Fenwick and Megget 1993, Fenwick et al. 1996, Kim et al. 2004, Peng et al. 2006). It was observed that in the frames under sidesway displacements, this kinematic interaction lead to the largest deformation demand on the base exterior column sustaining the largest compression from the overturning moment (Figure 3.1.1).

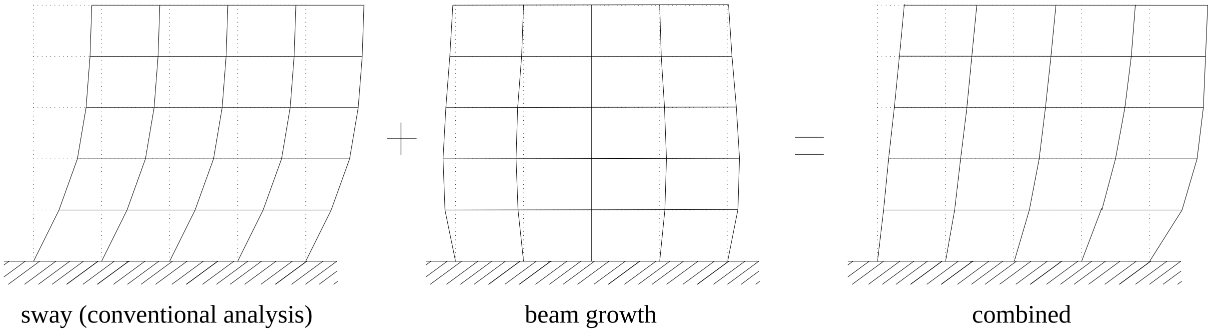

Figure 3.1.1. Effect of beam elongation on frame kinematics (after Kim et al. 2004).

Axial elongation can conceptually be divided into two components. The first occurs when the sidesway frame motion creates a gap opening at the interface between the beam and the column. The gap-opening is inherent to precast concrete frame construction (El-Sheikh et al. 1997, MacRae and Gunasekaran 2006), timber and steel members with rocking beam joints, but also reinforced concrete members due to bar slip at the support. Because the center of beam section rotation (or neutral axis) does not coincide with the section mid-height, the overall distance between the beam ends along the member centerline increases, causing the outward push on the columns supporting the beam, shown in Figure 3.1.2.

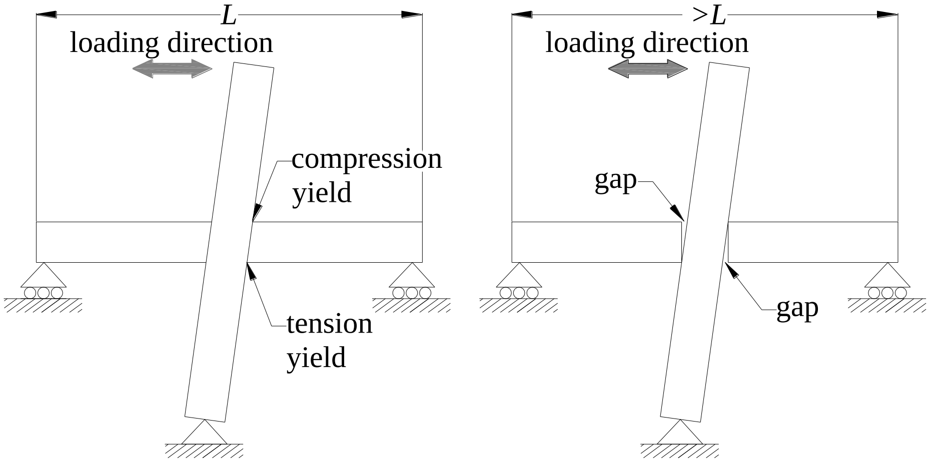

(a) steel (b) reinforced concrete / gap systems

Figure 3.1.2. Gap opening in reinforced concrete/gap systems, as opposed to steel systems (after MacRae and Gunasekaran 2006).

The second component of axial elongation occurs within the member itself, such as the reinforced concrete beam undergoing inelastic flexural deformations, as a result of accumulating residual tensile strains in reinforcing steel. Due to shallow compression zone on a beam section, the compressive strains reached are much smaller compared to the tensile reinforcement strains developed upon yielding. Loading reversal is not sufficient to bring the steel tensile strains to zero, resulting in a gradual buildup of elongation as the beam undergoes deformation cycles (see Figure 2.8.22, Chapter 2). This is evident in the increasingly positive strain histories with almost no excursions into the negative range recorded in the longitudinal steel of Beam 1 and Beam 2 (refer to Chapter 2, Section 2.8.1 and also Appendix A for individual strain gauge histories).

3.2 OVERVIEW OF BEAM DEFORMATION COMPONENT MODELS

The following sections present the major components of the inelastic response of reinforced concrete beam under reverse cyclic loading. In order to develop the models to properly simulate the beam cyclic behavior, response components and the adopted models are described here with the basic assumptions, variables, and computations of key parameters. These are the flexural deformations within the beam as a result of beam curvature, reinforcement slip, fixed-end rotations, and shear deformations. The discussions exclude torsion effects because the nonlinear dynamic analyses in this dissertation are limited to planar 2D frame models.

3.2.1 REINFORCEMENT SLIP BEHAVIOR

A reinforced concrete beam undergoing flexural deformations while anchored into a concrete support (such as a beam-column joint, reinforced concrete wall, or a reaction block) develops resisting moments at the supports that result in flexural tension force in either the top or bottom longitudinal reinforcement. The reinforcement which is anchored into the beam support must be developed through bond within the reaction block that occurs between the steel and the surrounding concrete. Consequently, the tension longitudinal reinforcement is subjected to tensile strains over the development length, which leads to reinforcement elongation and slip between the reinforcement and surrounding concrete. The slip, in turn, results in fixed-end rotation between the beam and the support at their interface.

Different empirical models relating the stress of an anchored bar to bond strength and consequent slip are available in literature (Moehle 2014). Here, we adopt a relationship by Sezen and Setzler (2008) because of its simplicity and relatively good agreement with the test data presented in Chapter 2, as will be shown in the subsequent sections. Figure 3.2.1 shows the diagram of the reinforcement slip model proposed by Sezen and Setzler (2008). The free body diagram on the very left shows a longitudinal bar extruding from the anchorage, the stress f_s developed in the bar of cross sectional area A_s, and the bond stress u_b occurring at the interface of the embedded portion of the bar and the surrounding anchorage concrete. The middle of the three diagrams on the right shows the assumed bar stress distribution within the anchorage.

The bond stress distribution function shown to the left is adopted from Lehman and Moehle (2000) and is stepped in such way that the bond stress equals to $u_b = 12\sqrt{f'c}$ (psi) along the length l_d where bar experiences stresses below the steel yield strength f_y. Along the portion of the bar denoted l_d' where steel stresses exceed f_y, bond stresses are assumed to reduce due to bond deterioration and are set to $u_b' = 6\sqrt{f'c}$ (psi) according to the model. Note that the total length of the bar experiencing nonzero stress $l = l_d + l_d'$ does not equal to the total embedment length of the bar. If the bar development length complies with the minimum code requirements of ACI 318, the $l_d + l_d'$ will typically be less than the embedment length with the assumed bond stress values in Sezen and Setzler 2008. Steel strain is assumed to vary linearly with the stress, upon the yielding is reached, as can be seen in the strain diagram on the very right.

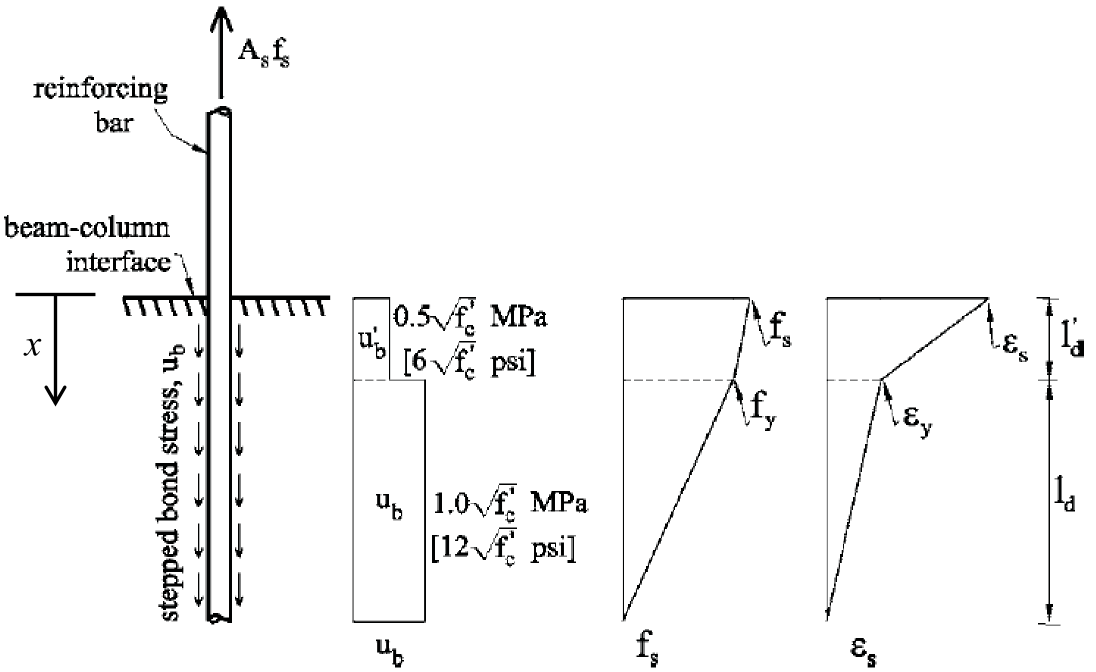

Figure 3.2.1. Reinforcement slip model (after Sezen and Setzler 2008).

Based on a known value of bar stress at the interface $f_s(x=0)$, lengths l_d and l_d' can be computed from the equilibrium of forces acting on the bar of diameter d_b within the embedment and shown on a free body diagram in Figure 3.2.2. This leads to the following expressions:

$$l_d = \begin{cases} \dfrac{f_s(x=0)d_b}{4u_b}, & f_s(x=0) \le f_y \\ \dfrac{f_y d_b}{4u_b}, & f_s(x=0) > f_y \end{cases} \tag{3.1}$$

$$l'_d = \frac{d_b}{4u'_b}(f_s(x=0) - f_y) \tag{3.2}$$

The amount of bar slip S from the anchorage is calculated by integrating the strain along the bar under the stress distribution corresponding to the bond stress step function shown in Figure 3.2.1:

$$S = \int_0^{l'_d} \varepsilon_s dx + \int_{l'_d}^{l_d} \varepsilon_s dx = \frac{\varepsilon_s + \varepsilon_y}{2} l'_d + \frac{\varepsilon_y}{2} l_d \tag{3.3}$$

Which in the case when bar stresses at the interface are below f_y reduces to:

$$S = \int_0^{l_d} \varepsilon_s dx = \frac{\varepsilon_s}{2} l_d \tag{3.4}$$

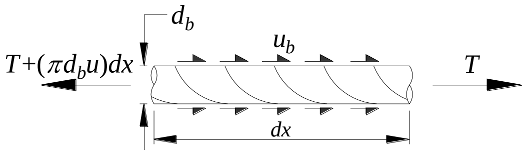

Figure 3.2.2. Free body diagram of a reinforcing bar segment of length *dx* with bond stresses u_b acting across the bar surface.

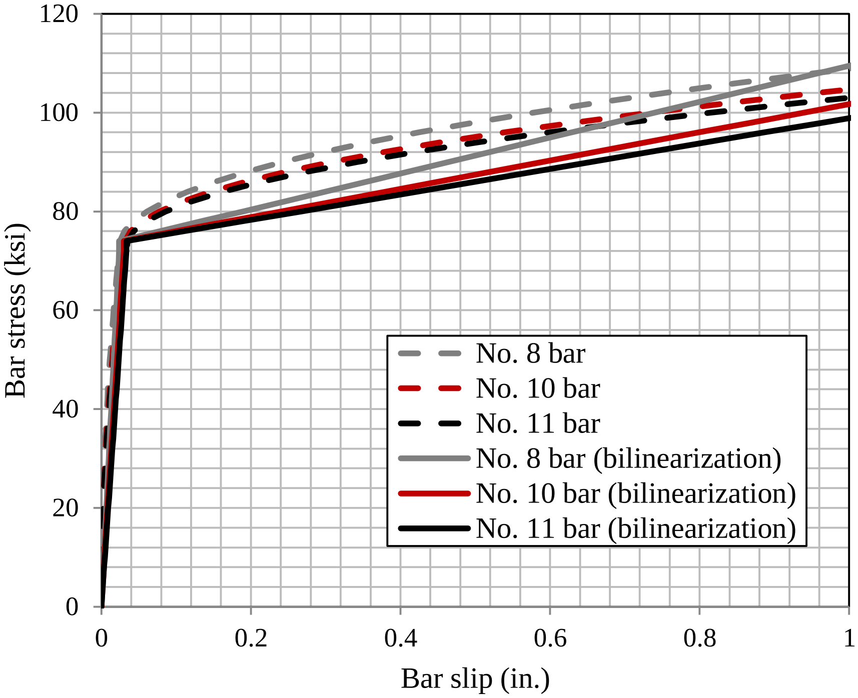

Figure 3.2.3. Bar stress vs. slip relationship based on bond stress distribution adopted from Lehman and Moehle (2000) including the simplified bilinear curves.

Figure 3.2.3 plots the relationship between the bar stress at the interface and the amount of slip from anchorage computed for bars with several different diameters and assuming the bond stress distribution proposed by Lehman and Moehle (2000). The bars were arbitrarily selected to be No. 8, No. 10 and No. 11 size in order to observe the relationship trend. The steel yield stress and concrete compressive strength are selected to approximately correspond to the average values obtained from Beam 2 material tests, presented in Chapter 2. That is, f_y = 73 ksi and f'_c = 6.13 ksi. As can be seen, bars of larger diameter exhibit larger slip for a given bar stress, while the stress-slip relation is not a linear function. Figure 3.2.3 also plots a bilinear approximation of the stress-slip curve that was selected to have an "elastic" initial stiffness equal to the secant stiffness of the corresponding nonlinear curve taken at the yield stress f_y = 73 ksi, and a post-yield hardening ratio of β_{slip} = 0.012. The significance of the post-yield hardening ratio will be discussed in the consequent sections describing the rotational spring for modeling fixed-end deformations. The curves in Figure 3.2.3 generally show good agreement for the range of steel stress lower than the ultimate strength of steel (f_u).

3.2.2 Fixed-End rotations From Bar Slip

Knowing the amount of slip *S*, fixed-end rotations θ_s are calculated based on the diagram shown in Figure 3.2.4, where *c* is compression zone depth and *d* is the distance between the tensile bar and the outmost compression fiber on the opposite side of the beam section:

$$\theta_s = \frac{S}{d-c} \tag{3.5}$$

In traditionally used lumped plasticity beam models that do not employ sections with uniaxial material fiber discretization, flexural deformations concentrated at the beam support due to reinforcement slip from the support (fixed-end deformations) are typically accounted for by adjusting the stiffness of the moment-rotation hysteretic curve if a rotational spring is used, by increasing the elastic flexibility of the beam itself, or by appropriately calibrating the length of the plastic hinge to match the response observed in the physical specimens, such as a beam or a column (e.g. ASCE 41 2006, Berry et al. 2006). Distributed plasticity elements with sections that utilize fiber discretization with uniaxial material properties do not account for the contribution of the slip and as a result can lead to an element having less flexibility than exists in a physical element. Therefore, when using fiber-section based elements with distributed plasticity, such as those presented in this chapter, the fixed-end flexibility due to bar slip needs to be explicitly modeled.

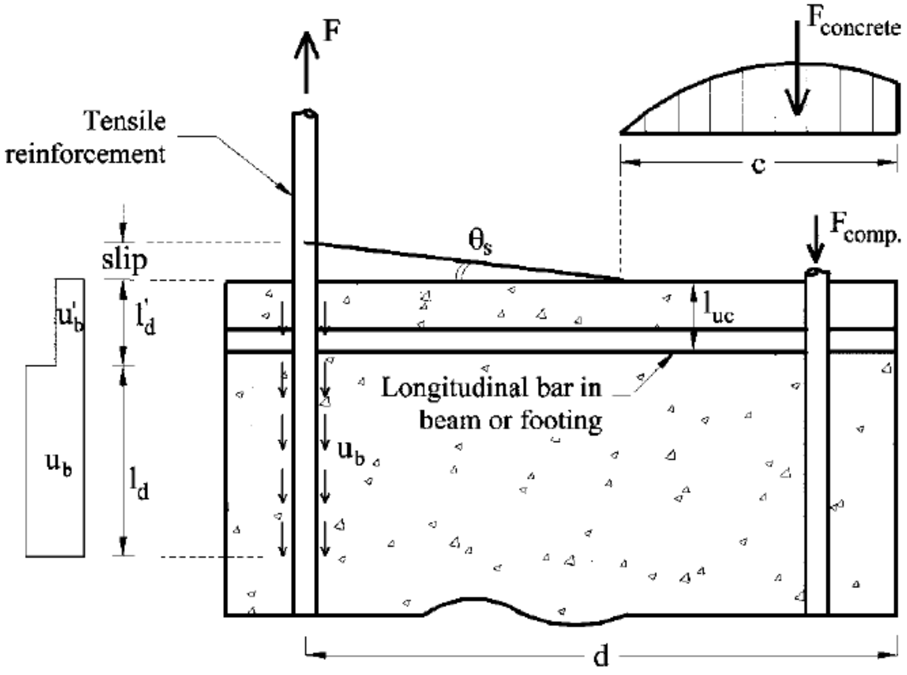

Figure 3.2.4. Calculation of fixed-end rotation after Sezen and Setzler (2008).

The most common way to account for fixed-end rotations is to add a rotational spring between the beam-column element and the support (acting in series with the beam-column element), which would represent the relationship between the beam moment and the fixed-end rotation. The simplest option is the use of linear elastic spring, calibrated to add a desired level of flexibility to the beam-column. Such spring, however, cannot be adjusted to simulate the changing flexibility resulting from the deterioration of the bond after the anchoring steel bars exceed the yield stress.

Another option is using a rotational spring with nonlinear hysteretic rule calibrated to produce the moment-rotation relationship corresponding to the changing bar stress-slip relationship. The simplest way to accomplish this is using a bilinear rotational spring corresponding to the anchored bar stress vs. slip relation idealized in Figure 3.2.3, with the hysteresis parameters (such as elastic stiffness and post-yield hardening slope) computed using the relationship between the bar slip and the fixed end rotation established in Equation 3.5.

The spring elastic branch would correspond to the rotation caused by the bar slip resulting from the bond strength u_b. When the yielding moment is reached in the beam, the spring has a loading stiffness with the post-yield hardening ratio. Thus, the spring has to be calibrated for the appropriate yielding moment in the beam, $M_{y,beam}$. The disadvantage of using the bilinear spring in conjunction with the fiber section elements is that in case the yield moment capacity of the beam-column member increases as the result of an increased axial force during the frame analysis, the "yielding" in the spring at a value $M_{y,spring}$ that was calibrated at a lower axial load and is hence lower will be triggered sooner. This would cause the concentration of excessive plastic rotations within the spring itself, leading to overestimation of the beam flexibility with the underestimation of the computed beam forces as a consequence. A crude way to circumvent this issue is to set the $M_{y,spring}$ to a slightly higher value than the $M_{y,beam}$ projected after some expected level of increase in the axial load in the beam-column element. This approach would lead in underestimation of the post-yield fixed-end rotations occurring in the resisting moment range $M_{y,beam}$ and $M_{y,spring}$.

A more elaborate way to simulate fixed-end rotations that is also compatible with the use of beam-column elements with fiber sections is using the nonlinear spring that also utilizes the uniaxial material fiber discretization. Such spring has the capability to adjust the flexural response based on the changing axial load. Fiber-section spring used in this chapter will be referred to as the "bar slip" element henceforth and is based on the concept proposed in Zhao and Shritharan (2007) and a modification presented in Ghannoum (2007). Bar slip element is represented by an element of zero length with a fiber section discretization identical to the discretization of the sections within the beam elements. In place of steel fibers, this bar slip element uses a material with the hysteretic behavior characterizing the bar stress vs. amount of slip relationship.

For the hysteretic rule of fibers designated to represent the bar stress vs. slip behavior, Zhao and Shritharan (2007) proposed the use of a specific *BondSlip* hysteretic material (OpenSees 2014) in conjunction with concrete fibers (

Figure 3.2.5). The *BondSlip* hysteretic behavior is derived from the empirical data obtained from the bar pull-out tests surveyed in Zhao and Shritharan (2007). Note that the backbone curve shown in the left plot of

Figure 3.2.5 has very similar characteristics with the bar stress vs. slip curves shown in Figure 3.2.3 with a linear elastic loading branch up to a yield point and a gradually softening post-yielding curve. The concrete fibers are modeled as perfectly plastic upon reaching the peak stress in order to accommodate large strains that develop in the zero-length element. The disadvantage of Zhao and Shritharan (2007) model is that it was calibrated for bridge columns and hence it produces moment-rotation relationship that may not be representative of what occurs in the interface section of reinforced concrete beam, which is the focus of this chapter. Moreover, as noted in Ghannoum (2007), this model lacks the ability to adjust the center of fixed-end rotation based on the changing neutral axis depth which occurs in columns of moment frames under varying axial loads.

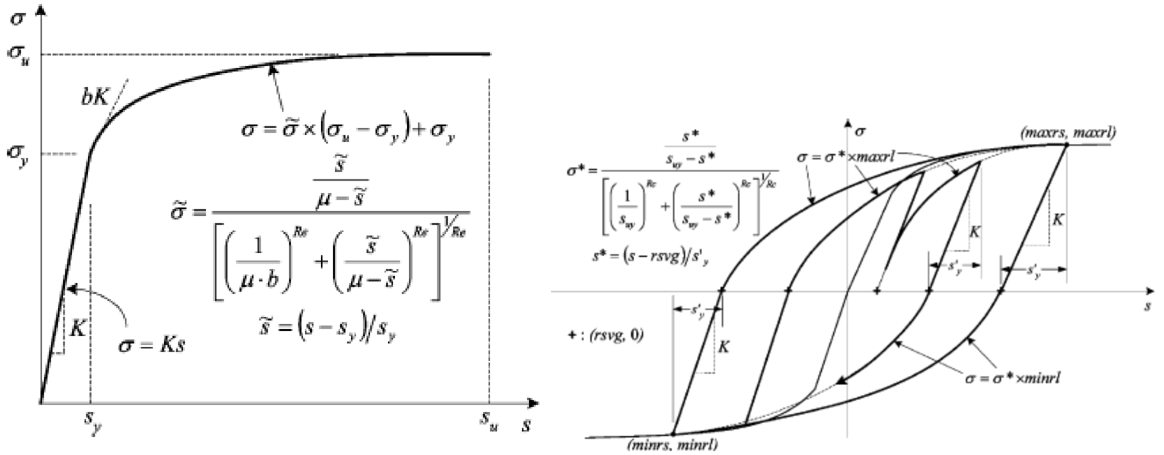

Figure 3.2.5. *Bondslip* hysteretic model proposed by Zhao and Shritharan (2007).

Ghannoum (2007) introduced a modification of fiber-section spring that enforces the fixed-end rotations arising from bar-slip to be centered at the flexural neutral axis of the bar slip element section, such that the amount of slip S computed within the bar stress-slip material fibers produces the fixed-end rotation equal to θ_s in Equation 3.5. This is accomplished by enforcing the strain compatibility between the zero-length fiber section representing flexural spring and the neighboring section of the beam-column element by setting the compression zone depth c in two sections identical.

In order for the neutral axis to remain the same in the bar slip element and the end section of the frame element, the strain profile shown in Figure 3.2.6 is required. Such strain profile is achievable by using the identical fiber discretization and steel and concrete materials in the bar slip and the frame element sections and scaling all of the material strains in the bar slip element by the same factor r_y. This way, for a given set of forces V, N, and M (see Figure 3.2.6) acting on the bar slip element and the distributed plasticity frame element, each of the fibers in the bar slip section has the identical stress as the fiber with the same location in the adjacent frame element, while the deformations are proportionally larger in the bar slip section fibers. Note that this holds true only when the distributed plasticity elements with force based formulation are used.

The bond-slip material is represented by the steel material object that has been adjusted such that the “yield” strain of this modified material represents the amount of bar slip S_y from the anchorage (in units of length) reached when the bar slipping is stressed to f_y. The basis of this concept is no different from the one proposed in Zhao and Shritharan (2007). The elastic stiffness of this material is $E_{slip} = f_y/S_y$. The stress-strain relationship for concrete fibers in the bar slip section are then modified by increasing the material flexibility by a factor $r_y = E_s / E_{slip} = S_y/\varepsilon_y$. Thus, for any given strain in the concrete fiber in the frame element, the concrete fiber with the identical $[y, z]$ coordinates in the bar slip section will have the strain $\varepsilon_c' = (S_y/\varepsilon_y)\varepsilon_c$ (for referenced coordinate system, see Figure 3.4.1 and Figure 3.5.1). For example, the strain at peak compressive stress in a modified concrete fiber within the bar slip element would be $\varepsilon_0' = (S_y/\varepsilon_y)\varepsilon_0$, where ε_0 is the strain at peak stress in concrete material assigned to fibers within the beam column element.

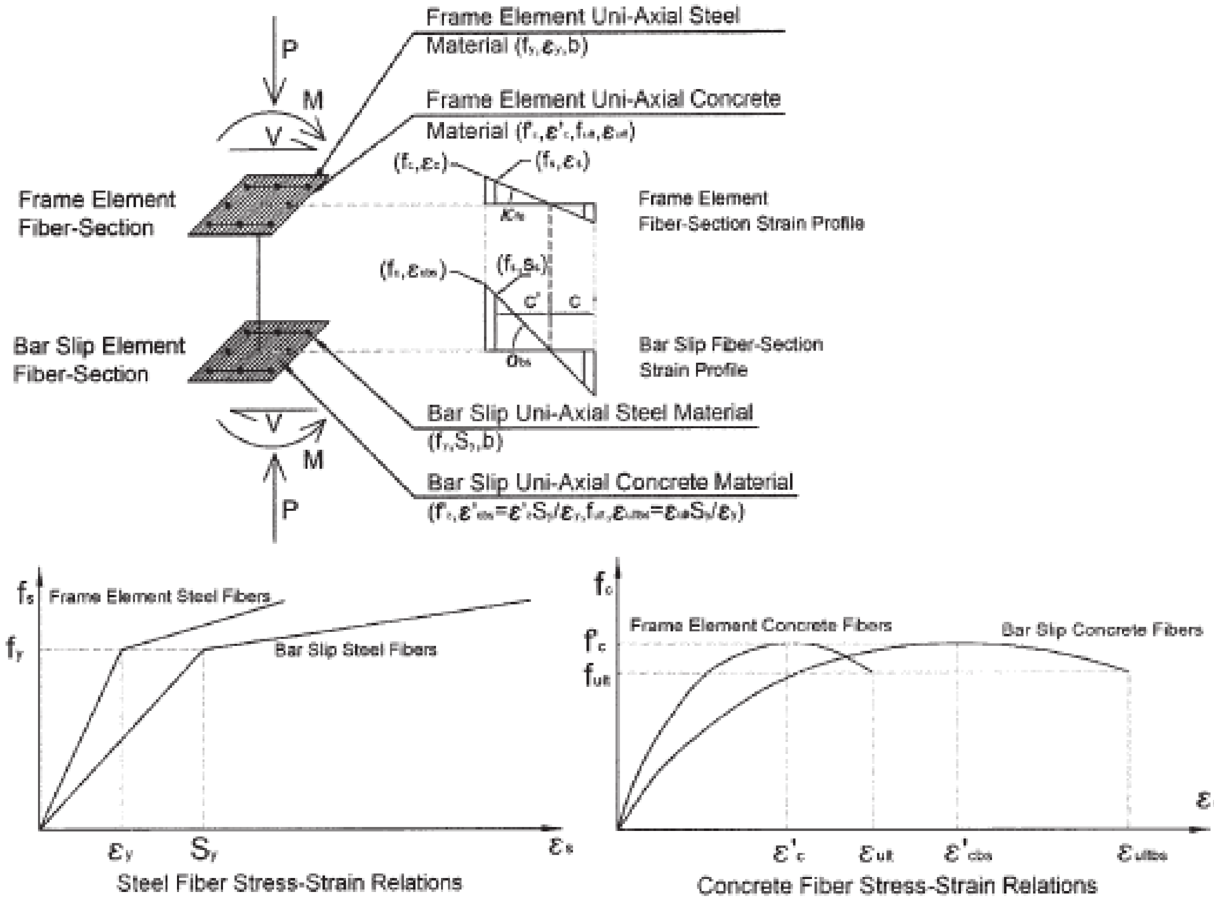

Figure 3.2.6. Bar slip section equilibrium, strain profiles and materials (after Ghannoum 2007).

Similarly, at a given level of loading strains in the steel fiber of a bar slip element will be larger than the strains in the corresponding fiber representing the steel bar in the beam column element by the factor $r_y = S_y/\varepsilon_y$. This way, the bond-slip model represented by material models which exhibit strain hardening such as bilinear, or Giufre Menegotto Pinto (Filippou et al. 1983) model will retain the post-yielding strain hardening ratio of the steel stress-strain curve used for the steel fibers of beam-column element. Section 3.2.1 discussed the bilinear idealization of the bar stress – slip curves derived based on Lehman and Moehle (2000) bond stress distribution model, where it was demonstrated that the hardening stiffness ratio of β_{slip} = 0.012 proved to have reasonable agreement with the “exact” bar stress-slip relationship computed. The steel material itself is typically calibrated to have a post-yield strain hardening ratio of β_{steel} = 0.01-0.02, making the bar slip modeling strategy proposed by Ghannoum (2007) well suited for use where load bearing capacity loss of concrete elements is not of interest. The model implicitly simulates the degrading concrete bond strength within the anchorage compatible with Lehman and Moehle (2000) model.

The method presented in Ghannoum (2007) is attractive in modeling reinforced concrete members with varying axial loads because no calibration of spring stiffness is required once the stress-strain relationship of bond-slip material is established. That is, the center of rotation within the flexural spring adapts to the current state of stress (or strain profile) within the fiber section. The consequence of this "automatization" is that the axial strain at the geometric centroid of the zero-length fiber section is equal to the width of the gap opening at the interface of beam-column support, shown in Figure 3.1.2(b). Thus, the method presented in Ghannoum (2007) makes an ideal candidate in simulating beam elongation that arises due to interface gap opening in reinforced concrete frame nonlinear analysis.

3.2.3 SHEAR DEFORMATIONS

Experimental findings presented in Chapter 2 indicate that shear deformations can have a notable contribution to total beam deformations in the beam displacement cycles after flexural yielding. As the beam is loaded cyclically, the shear deformations increase even though the shear force remains practically constant (see Figure 2.8.20, Chapter 2). This is supported by the evidence presented by others (e.g. Fenwick and Fong 1979, Beyer et al. 2011) indicating that a flexure-dominant reinforced concrete member can exhibit significant shear deformation upon flexural yielding, despite having a large margin between the shear strength capacity and the demand. These shear deformations tend to concentrate in the plastic hinge area, where damage is induced by flexural yielding, as shown in a sketch in Figure 3.2.7 and also in Figure 2.8.19 from Beam 1 experiment (Chapter 2).

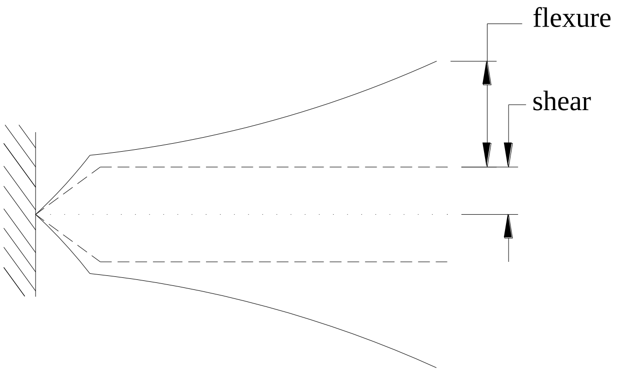

Figure 3.2.7. Concentration of shear deformation in a beam plastic hinge region occurring upon flexural yielding and the resulting damage concentration in plastic hinge (after Fenwick and Fong, 1979).

A general backbone curve relating the shear forces V and deformations γ (in radians) is shown in Figure 3.2.8. The elastic relationship between the shear forces and deformations based on the elastic shear modulus of concrete, G, and a either a gross area of the concrete section A_g or some percentage of the gross area ($A_0 = 0.8A_g$ after Priestley et al. 1994, Sezen and Moehle 2004, $A_0 = 5/6A_g$ after Ghannoum 2007) is:

$$V = (GA_0)\gamma \tag{3.6}$$

where:

$G = \dfrac{E_c}{2(1+\upsilon)}$,

υ = Poisson's ratio of concrete, and

E_c = Young's modulus of concrete.

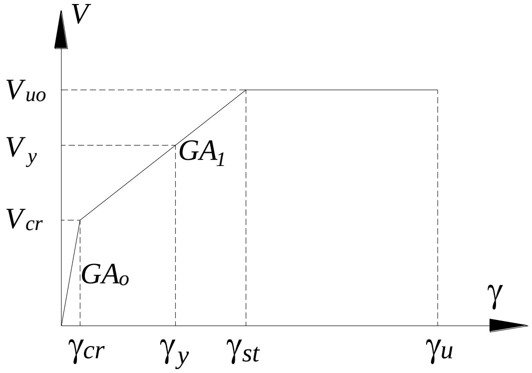

Figure 3.2.8. Backbone curve for shear force-deformation relationship of a beam model proposed by Mergos and Kappos (2012).

Prior to formation of diagonal cracks in the beam, the shear deformations can be assumed constant along the beam length, such that:

$$V = (GA_0)\gamma = (\frac{GA_0}{L_b})\Delta_v = K_{vo}\Delta_v \tag{3.7}$$

Here, L_b is the length of the beam and Δ_v signifies the beam tip displacement resulting from the shear deformations. The limiting shear level for this linear elastic relationship is the cracking shear V_{cr}. Using the tension strength of concrete as the limiting principal stress at the onset of diagonal cracking in a reinforced concrete member with no axial load, Sezen and Moehle (2004) suggest using $6\sqrt{f_c'}$ (psi) for a limiting shear stress at cracking and a cross-sectional area of $A_0 = 0.8A_g$. such that:

$$V_{cr} = \frac{6\sqrt{f'_c}}{a/d}0.8A_g \tag{3.8}$$

After the cracks form, the shear stiffness of the beam reduces. Based on the truss analogy presented in Park and Paulay (1975), the post-cracking shear stiffness, denoted in Figure 3.2.8 as GA_1, is computed as:

$$GA_1 = \frac{\delta V}{\delta \gamma} = \frac{E_s b_w (d-d')\rho_w \sin^4\theta_t \cot^2\theta_t}{\sin^4\theta_t + \eta\rho_w} \qquad 3.9$$

where:

E_s = Young's modulus of reinforcing steel,
b_w = beam width,
d-d' = distance between the centerline of the top and bottom longitudinal reinforcement,
ρ_w = volumetric ratio of transverse reinforcement,
η = modular ratio (E_s / E_c), and
θ_t = angle of the compressive struts in the beam truss model (usually assumed as 45°).

The shear stiffness established in Equation 3.9 reduces upon flexural yielding, which in Figure 3.2.8 is denoted with V_y and γ_y. This is evident in the increasing shear deformations despite the almost constant shear force applied visible in the shear force-deformation relationship plotted in Figure 2.8.20 in Chapter 2 for Beams 1 and 2. Note that V_y and γ_y in Figure 3.2.8 signify the resisting shear and the corresponding shear deformation that occur at the instance when the beam experiences flexural yielding, and not the shear corresponding to the yielding of the transverse reinforcement.

Different studies proposed various approaches to establishing the force-deformation relationships for post-cracking shear stiffness beyond the point of flexural yielding (e.g. Ozcebe and Saatcioglu 1989, Petrangeli et al. 1999, Sezen and Moehle 2004, Marini and Spacone 2006). Mergos and Kappos (2012) adopted a multi-linear shear force-deformation relationship compatible with the phenomenological beam-column model that simulates the spread of flexural and shear inelasticity by adjusting the plastic hinge lengths with appropriate factors that depend on the moment diagram distribution. The sketch of the backbone curve used to establish the proposed model is shown in Figure 3.2.8. Mergos and Kappos (2012) propose a modification of the GA_1 slope from the point of flexural yielding occurring at point (γ_y, V_y) in Figure 3.2.8 until the loading reaches the point V_{uo} based on the flexural displacement ductility demand in a beam. That is, the reduced stiffness GA_{eff} (corresponding to the branch connecting [γ_y, V_y] and [γ_{st}, V_{uo}] in Figure 3.2.8) reduces with increased beam chord rotation. Finally, as the beam reaches the point (γ_{st}, V_{uo}) defined at the instance that the beam reaches the shear force causing the transverse steel yielding, the shear resisting mechanism is assumed perfectly plastic.

Although the numerical beam modeling strategies explored in this chapter differ from those presented in Mergos and Kappos (2012), the backbone curve shown in Figure 3.2.8 is used as a concept for exploration in the subsequent sections due to its simplicity.

3.3 OVERVIEW OF BEAM MODEL CALIBRATION AND LOADING HISTORY

The basis for numerical modeling strategies explored in this chapter is the response of Beam 2 specimen discussed in Chapter 2. Hence, the geometry, reinforcement configuration, material properties, and loading history are selected to match those of the specimen itself (see Chapter 2).

All computations are performed on OpenSees software framework (McKenna et al. 2007) using the readily-available element and material objects. The focus on this portion of the study is to adequately estimate the beam response for all cycles for which no strength deterioration occurs. This serves the ultimate goal of computing the peak element forces in nonlinear analyses of frames (Chapters 4-6), and thus, the beam response upon initialization of strength deterioration such as that observed upon the longitudinal bar buckling in Beam 2 is not a concern for the present study.

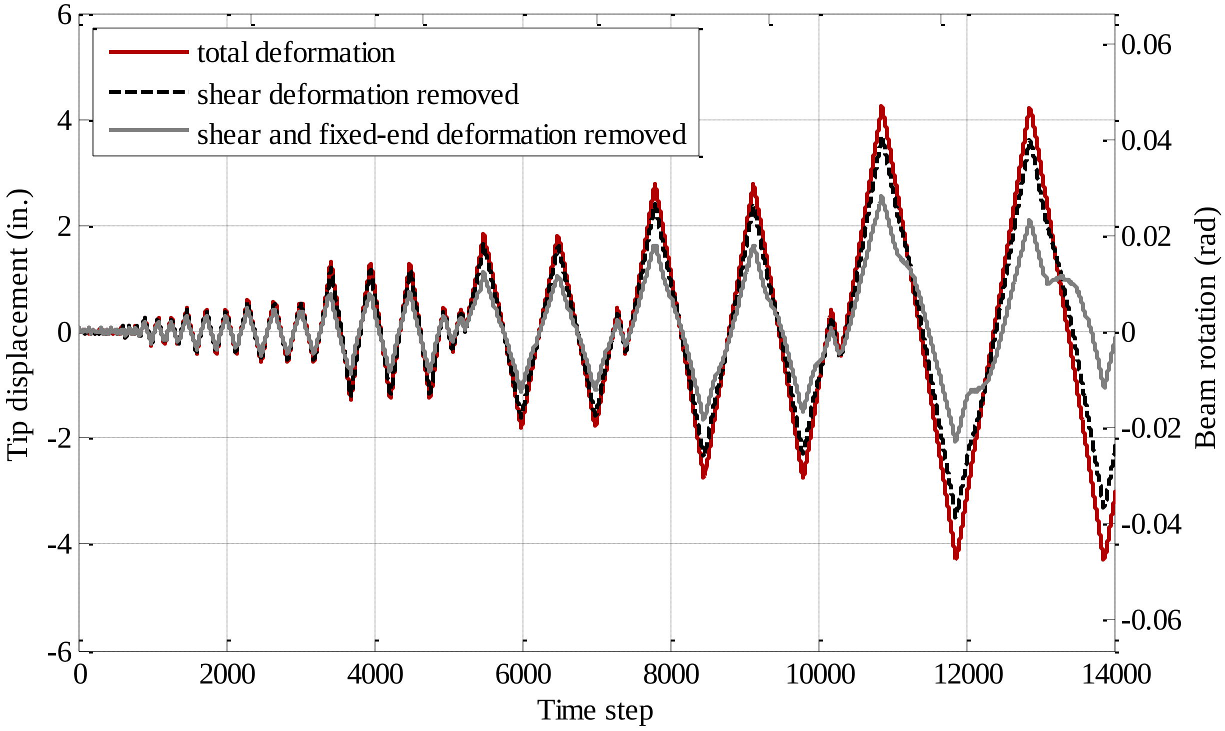

Figure 3.3.1. Deformation components of Beam 2 used in the model calibration.

The displacement history logged during the cyclic loading of Beam 2 is used to calibrate the numerical models of the test specimen in the sections to follow. In addition, where flexural and shear response components are represented by separate elements (i.e. flexural and axial springs used for fixed-end and shear deformation representation), loading history was adjusted to only include the response components that are being calibrated. For example, if only distributed plasticity elements are calibrated with neither shear deformation nor the fixed-end deformation component modeled, the loading history of Beam 2 is adjusted to exclude the shear and fixed-end deformations measured during the laboratory test.

Figure 3.3.1 plots the displacement histories used in subsequent sections. Alongside the Beam 2 displacement history, Figure 3.3.1 shows the displacement history without the shear and the shear and fixed-end deformation contribution. These loading protocols were obtained by subtracting the measured shear deformations (Section 2.8.6 in Chapter 2), and both the shear and the fixed-end rotation (attributable to bar slip and presented in Section 2.8.5 of Chapter 2) contributions, respectively.

3.4 FIBER SECTION DISCRETIZATION AND CALIBRATION OF UNIAXIAL MATERIALS

This section describes the numerical representation of Beam 2 cross section used to develop the appropriate numerical models in Chapter 3 including the distributed plasticity models, the fixed-end rotation springs, and the moment-curvature analysis used to calibrate the lumped plasticity model. The numerical model of Beam 2 section is shown in Figure 3.4.1. It is discretized into 32 layers stacked along the *y*-axis, i.e. perpendicular to the principal axis of bending (the local *z*-axis, shown in Figure 3.4.1) representing the concrete material. The longitudinal steel is represented by the individual fibers with the locations coinciding with the location of the reinforcement bars. No. 4 skin reinforcement present in the Beam 2 test specimen is not included in the model, because it was not fully developed into the anchorage and hence unable to develop full strength of the bar. Constitutive properties of materials represent those obtained from the laboratory material tests, and are described next.

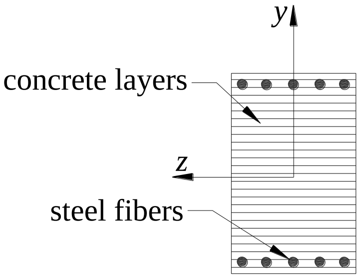

Figure 3.4.1. Fiber section discretization.

3.4.1 STEEL

Two different material models were considered for representing the steel material: *ReinforcingSteel* (Kunath et al. 2009) based on Chang and Mander (1994) hysteretic curve and *Steel02* based on Giufre-Menegotto-Pinto (Filippou et al. 1983) curve. *ReinforcingSteel* was selected because of its capability of simulating the yielding plateau and subsequent strain hardening which leads to a better agreement with the experimentally recorded steel hysteretic behavior. *Steel02* is less computationally complex compared to the *ReinforcingSteel* and thus has a greater appealing for use in nonlinear dynamic analyses of larger structural models where numerical stability and computation time may be a concern.

Table 3.1 lists the properties used for the two steel models in OpenSees. The properties were selected in order to match the cyclic stress-strain curve obtained experimentally for the coupon made from the No. 11 longitudinal bar from the same batch as those used in Beam 2. The bar strain history was selected to approximately mimic the strain history experienced by No. 11 bars in Beam 2, that is, the tensile strains were increasingly larger and no compressive strains were applied onto the bar. This curve, plotted in grey in Figure 3.4.2(a) and Figure 3.4.2(b), is superimposed with the corresponding stress-strain relationship computed with *ReinforcingSteel* and *Steel02*, respectively, for the same loading history. As can be seen, the *ReinforcingSteel* follows a post-yield changing stiffness with great accuracy, while *Steel02* displays constant strain hardening. Therefore, *Steel02* was calibrated in such way to result in the monotonic stress-strain curve that reaches the ultimate stress f_{su} = 105 ksi at the strain ε_{su} = 0.087. With the presence of isotropic hardening, however, the actual stresses computed during cyclic strain history will be slightly higher than this.

Table 3.1. Input parameters for steel materials in OpenSees.

Uniaxial material input parameter	Description	*ReinforcingSteel*	*Steel02*
f_y	Yield stress (ksi)	73 ksi	73 ksi
E_s	Young's modulus (ksi)	31000	31000
f_u	Ultimate stress (ksi)	105	-
β_{steel}	Strain hardening ratio	-	0.012
E_{sh}	Tangent stiffness at initial strain hardening	1100	-
ε_{sh}	Strain at initiation of strain hardening	0.006	-
ε_{su}	Strain at ultimate stress	0.18	-
Ro, cR1, cR2	Parameters for controlling transition from elastic to plastic branches	-	16, 0.925, 0.15
a1, a2, a3, a4	Parameters for controlling isotropic hardening	-	0.01, 1, 0.01, 1

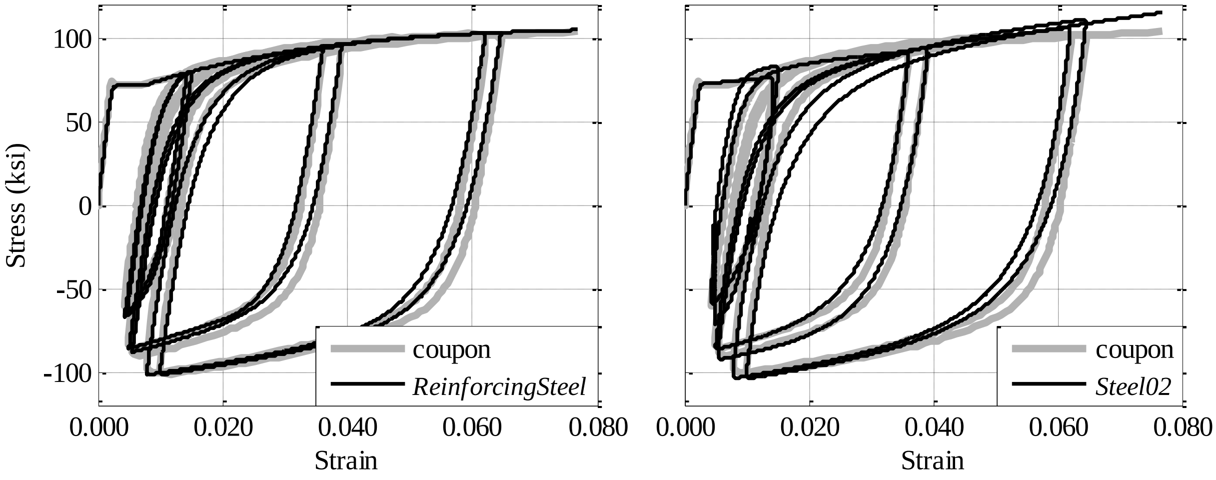

(a) (b)

Figure 3.4.2. Comparison of hysteretic stress-strain relationship for steel models: (a) *ReinforcingSteel* and (b) *Steel02*.

3.4.2 CONCRETE

Concrete03 material based on Kent-Park model (Figure 3.4.3) is selected to represent concrete material layers indicated in Figure 3.4.1. This model features degradation in unloading and reloading stiffness and tensile strength with nonlinear tension softening. The stress-strain relationship defined for the concrete material fibers is based on the unconfined concrete properties. Peak concrete stress f'_c and the corresponding strain ε_0 were selected to fit the monotonic stress-strain curve obtained from the compressive cylinder tests. In general, small variations in compressive concrete strength in tension-controlled beam-column sections exhibit little impact on the section flexural response, because the concrete does not reach the limiting strain when the tension steel yields during flexural deformations. Because Beam 2 contained mostly concrete from the 2nd batch (Section 2.4.2, Chapter 2), the curves obtained from Cylinder

1 test from Batch 2 was selected to define the stress-strain relationship for the numerical model. Thus, f'_c = 5.87 ksi and ε_0 = 0.0029. In lieu of Cylinder 1 properties, average compressive cylinder strength with the corresponding strain could have been used leading to comparable section behavior. Note that adjustment factor for concrete cylinder strength reduction, typically set at 0.85f'_c, was not used.

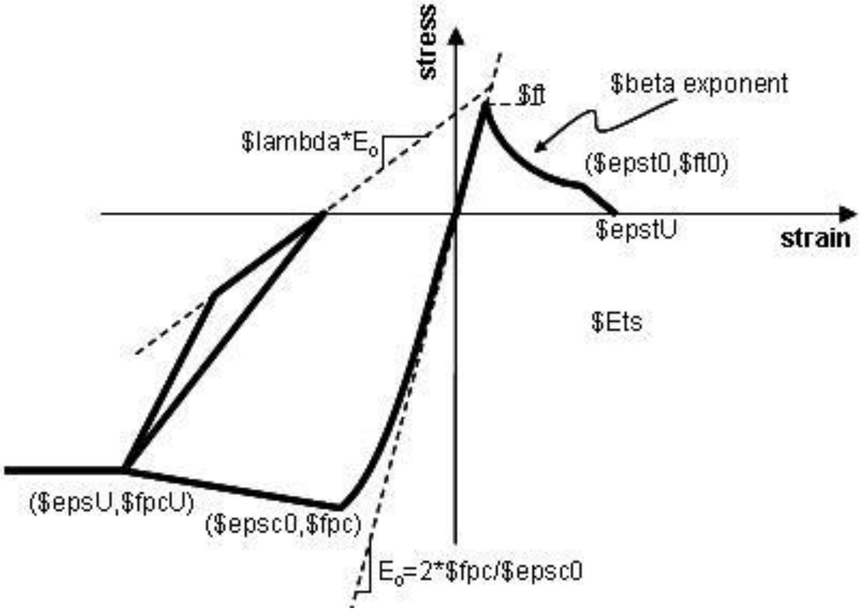

Figure 3.4.3. *Concrete03* model based on Kent-Park stress-strain curve and the corresponding input parameters.

Figure 3.4.4 shows the numerical model for concrete plotted together with the backbone stress-strain curve obtained from the cylinder test. The cylinder tests were terminated when the concrete resistance decreased by about 5% upon reaching the peak strength (see Figure 2.4.4, Chapter 2) and the path of the stress-strain curve and the strain at zero strength upon softening is not available from the tests. Thus, the compressive portion of the curve was set to unload to zero residual strength at ultimate strain of $\varepsilon_u = 2\varepsilon_0 \approx 0.0060$, which is typically assumed for the spalling strain of unconfined concrete (Moehle 2014).

When the beam section yielding mechanism is not controlled by concrete crushing, that is – the beam section does not exhibit post-yield softening due to concrete crushing, this unloading path is not crucial to capturing correct global response. Concrete strains exceed those at the peak strength and causing the softening of the beam section can lead to numerical localization which produces a model with global response sensitive to element discretization (number and location of integration points along the element, and integration length).

Scott and Fenves (2006) offer several approaches to retain modeling objectivity. One includes the material regularization technique whereby the concrete fiber material stress-strain curve is modified based on the numerical length of the plastic hinge in order to satisfy the constant fracture energy released in concrete crushing over the integration length. Alternatively, a concrete constitutive model obtained in cylinder tests is recommended for use in conjunction with a plastic hinge length observed in the laboratory – which corresponds to a damage localization length over which the crushing of concrete occurs in the physical specimen. The present study employs the latter approach. Numerical localization is not a concern in Chapter 3, because beam section does not exhibit softening response, however this becomes a concern in Chapter 4 where implications of suppressing beam elongation are explored.

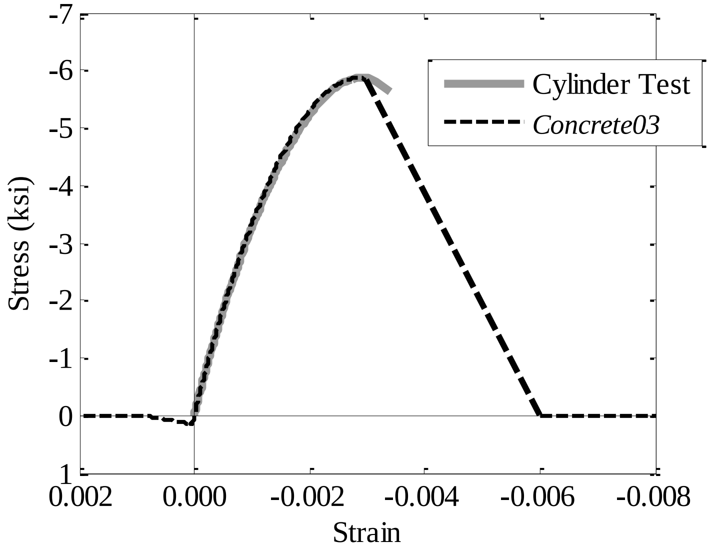

Figure 3.4.4. Unconfined concrete stress-strain relationship.

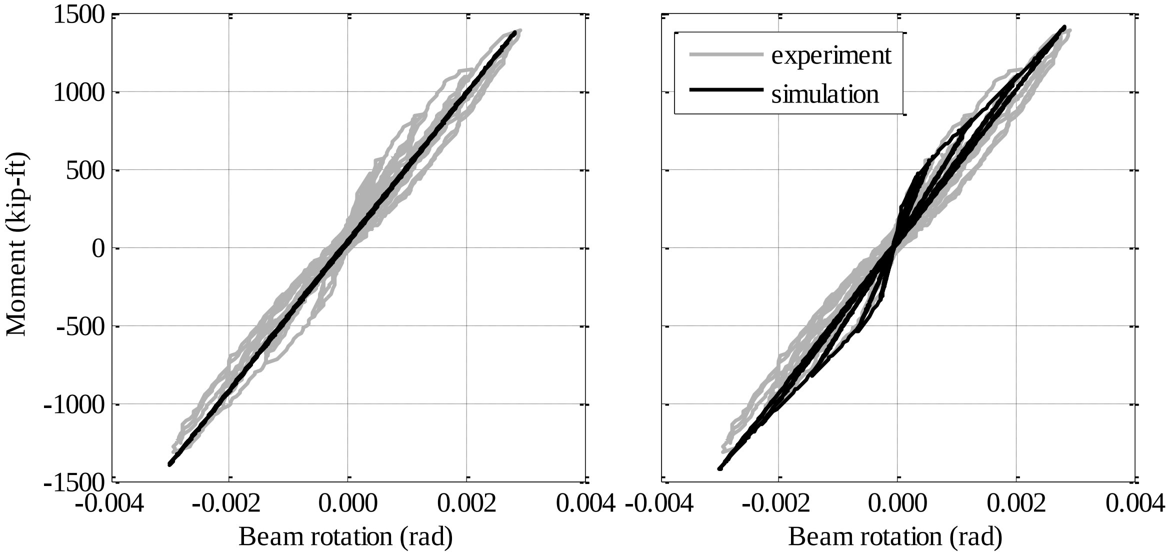

(a)

(b)

Figure 3.4.5. Initial cycles of Beam 2 moment-rotation response and corresponding numerical simulation using *ReinforcingSteel* and *Concrete03* with: (a) no concrete tensile strength, (b) concrete tensile strength $f_t = 2\sqrt{f_c'}$ (f'_c in psi).

Tensile strength of concrete, f_t, was not experimentally obtained for the tests presented in Chapter 2. For the purpose of numerical modeling, the value of f_t was selected such that the moment-rotation curve obtained numerically from the distributed plasticity model described in Section 3.5 closely follows the measured pre-cracking stiffness of Beam 2. To this end, an assembly containing distributed plasticity elements described in Section 3.5 using *ReinforcingSteel* material for steel fibers was subjected to flexural deformation history measured from the experiment and described in Section 3.3.

The comparison of the flexural component of force-drift ratio curve computed with numerical model with that measured in the experiment is shown in Figure 3.4.5. Note that shear and fixed-end deformations are removed from the loading history applied to the model which contains only the distributed plasticity elements. As can be seen from the plot in Figure 3.4.5(a), if concrete model is assigned $f_t = 0$, the stiffness of the initial deformation cycles is underestimated leading to a beam response equivalent to having an initial stiffness of a cracked section. The computed response is improved by selecting a concrete tensile strength of $f_t = 2\sqrt{f'_c}$,obtained by trial and error, as observed in Figure 3.4.5(b). The computed moment-rotation curve in Figure 3.4.5(b) closely follows both the moment-rotation recorded from the experiment for both the loading and unloading paths and the contour of the hysteresis. Table 3.2 lists the input parameters for *Concrete03* material in OpenSees.

Table 3.2. Input parameters for *Concrete03* material.

Uniaxial material input parameter	Description	Value
$fc1U	Compressive strength	-5,873 psi
$eps1U	Strain at compressive strength	-0.003
$fc2U	Ultimate stress	0 psi
$eps2U	Strain at ultimate stress	-0.006
$lambda	Parameter controlling unloading slope	0.2
$ft	Tensile strength	153 psi
$epst0	See Figure 3.4.3	0.0009
$ft0	See Figure 3.4.3	0 psi
$beta	See Figure 3.4.3	1.0
$epstu	See Figure 3.4.3	0.20

3.5 DISTRIBUTED PLASTICITY BEAM-COLUMN ELEMENTS

Lumped plasticity models based on phenomenological moment-curvature or moment-rotation hysteretic rules have been traditionally employed for modeling of reinforced concrete beams in nonlinear analysis of special moment resisting frames. Such models have a decoupled flexural and axial force-deformation behavior and thus lack the capability of simulating the axial elongation of the beam which accumulates during inelastic flexural deformations. This section presents a distributed plasticity fiber-section model that, with relatively good accuracy, simulates the evolution of axial elongation while correctly representing the cyclic force-deformation response of the reinforced concrete beam with post-yield hardening section behavior.

Figure 3.5.1 shows the general schematic of the numerical representation of Beam 2 (Chapter 2). This mathematical model is a combination of both phenomenological components and finite element components that utilize constitutive relationships of steel and concrete materials. Two Euler-Bernoulli beam-column elements with fiber section discretization represent the cantilevered beam specimen (Elements 1 and 2) and simulate flexural and axial deformations occurring within the beam itself. Fixed-end rotation, which occurs as a result of longitudinal reinforcement slip from the beam support, is represented by a zero-length rotational spring (bar slip Element 3). For completeness, the shear component of the total beam deformation is represented by a zero-length shear spring (Element 4) placed in parallel with the rotational spring.

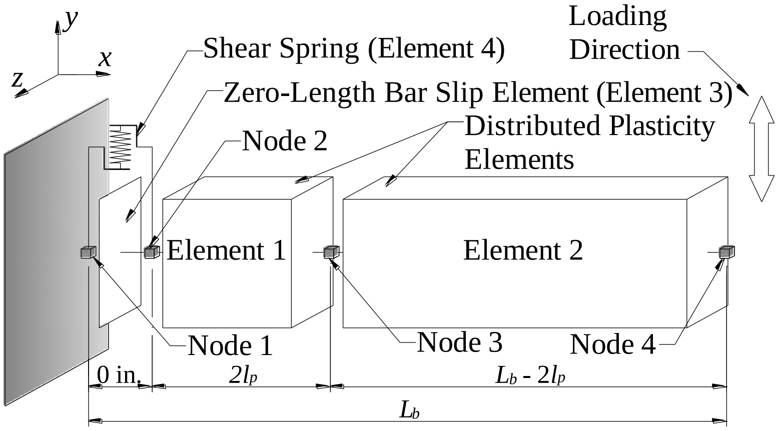

Figure 3.5.1. Numerical model schematic.

Two distributed plasticity beam-column elements with force-based formulation (Taucer et al. 1991) placed in series represent the beam itself: Element 1, which is 48 in. long, and Element 2, which measures 102 in. Each element contains two numerical integration points. Such subdivision of the cantilever beam was chosen in order to control the tributary length of the first integration point where the largest flexural and axial deformations are concentrated, as opposed to assigning the integration lengths based on those computed with the default element integration scheme (i.e. using the Gauss Lobatto quadrature rule).

The tributary length of first integration point in Element 1 is set to be equal to the approximate beam plastic hinge length l_p which was selected to provide a good estimate of the global moment-rotation response of the cantilever beam. Plastic hinge length of $l_p = h/2 = 24$ in. (h = beam height) was found to lead to satisfactory estimate of this relationship for Beam 2 with the model presented. In lieu of using two separate elements (1 and 2), comparable results can be obtained via single element with multiple integration points, where the first integration point has the tributary length close to l_p. The latter approach reduces the global degrees of freedom and the number of equations solved in analysis and is used in modeling beams the frame structures in Chapters 4, 5, and 6.

3.5.1 Comparison of Global Flexural Beam Response Computed with Distributed Plasticity Elements with Experimental Results

Numerical beam discretization using distributed plasticity Elements 1 and 2 described previously was evaluated by comparing the cyclic force-deformation curves computed with those obtained from the test of Beam 2. A force-deformation curve recorded for the test specimen had been adjusted to exclude the portion of deformations attributable to fixed-end rotations and shear deformation, as explained in Chapter 2 and plotted in Figure 3.3.1. This enabled isolating the flexural deformations arising from the curvature section deformations within the beam itself in order to compare them to the deformations computed by the numerical model consisting of Elements 1 and 2.

The flexural displacement history (plotted in solid grey line in Figure 3.3.1) is applied to beam model consisting of Element 1 and 2 at Node 4 (see Figure 3.5.1), while Node 2 is held fixed. With Node 2 held fixed, only Elements 1 and 2 are allowed to deform. The resulting moment-rotation curve is shown in Figure 3.5.2. The corresponding curve obtained from the test data of Beam 2 experiment is also plotted. Figure 3.5.2(a) shows the moment-flexural deformation relationship computed for the distributed plasticity model using the using *ReifnorcingSteel*, while Figure 3.5.2(b) plots the same relationship computed using the *Steel02* uniaxial material model.

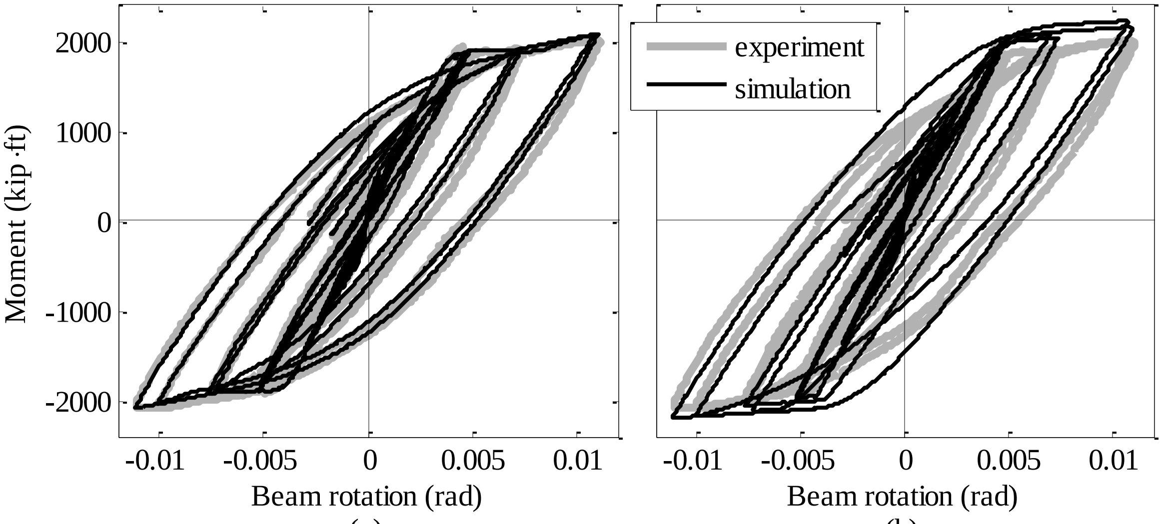

(a) (b)

Figure 3.5.2. Moment-chord rotation curves for flexural components of Beam 2 deformation and Elements 1 and 2 using (a) *ReinforcingSteel* and (b) *Steel02*.

Figure 3.5.2(a) shows that Model 1 consisting of distributed plasticity elements with fiber section computes with high accuracy the initial stiffness, yield point, post-yield hardening and unloading and reloading curve for the beam when *ReinforcingSteel* material is used. Slightly less accurate but satisfactory results are obtained using *Steel02* material, as shown in Figure 3.5.2(b).

3.6 ROTATIONAL SPRING FOR FIXED-END DEFORMATIONS

This section explores three different approaches in modeling the fixed-end rotations in reinforced concrete beam. These are: nonlinear fiber section rotational spring, nonlinear rotational spring with bilinear hysteretic material, and linear elastic rotational spring. Flexibility induced by fixed-end rotations is accounted for by a bar slip Element 3 shown in Figure 3.5.1. First, each bar slip element is calibrated with moment vs. fixed-end rotation curve obtained from the Beam 2 test, followed by the comparison of the global moment-beam chord rotation response of Beam 2 with the response computed by adding the bar slip element (Element 3) to the distributed plasticity Elements 1 and 2, which were calibrated in the previous section.

3.6.1 FIBER SECTION ROTATIONAL SPRING (BAR SLIP ELEMENT)

The theory behind the bar slip modeling approach based on the fiber section was discussed in Section 3.2.2. The method presented in Ghannoum (2007) and adopted here was tested in conjunction with both steel material models used: namely the *ReinforcingSteel* and *Steel02*. First, the experimental stress-slip relationship is derived for Beam 2 specimen to use as a benchmark in calibrating the uniaxial material used to represent the bar-slip behavior in the bar slip element (Element 3). Then, the computed moment-rotation hysteresis of the bar slip element is compared with the corresponding experimental results obtained by plotting the Beam 2 resisting moment versus the fixed-end rotations. Lastly, global moment-rotation of Beam 2 (corrected to exclude the shear deformations) is compared with the moment-rotation hysteresis using Elements 1-3.

3.6.1.1 DERIVING THE EXPERIMENTAL STRESS-SLIP RELATION

To calibrate the uniaxial bar stress-slip material, a corresponding experimental bar stress-slip curve needs to be established first. In traditional bar pullout experiments (e.g. Jirsa and Marques 1972, Viwathanatepa et al. 1979, Eligehausen et al. 1982) where tension or compression force is applied onto a single bar embedded in concrete, the bar stresses can be directly obtained by dividing the measured pullout force applied on a bar by the bar cross sectional area. The amount of slip is obtained from the instrument positioned in such way to directly measure the amount of bar slip at the interface. In Beam 2 test, such measurements were not possible. However, the instrumentation data along with the appropriately calibrated theoretical stress-strain relationship model of the steel material can be used to infer the approximate bar stress-slip curves in the test specimen.

Measurements from the LVDT instruments positioned at the root of the beam at the top and bottom faces are used to obtain the amount of bar slip. The underlying assumption here is that the slip is approximately equal to the interface crack width which roughly corresponds to the data recorded by the LVDTs, due to the close proximity of the longitudinal No. 11 bars and the LVDT instruments. Using the strain histories recorded in the strain gauges positioned on the No. 11 bars close to the beam root, bar stress histories are computed via mathematical relationship from a uniaxial material model that is calibrated to match the behavior of the No. 11 steel coupons. Here, bar stresses are computed using the steel stress-strain model by Kunath et al. (2009) calibrated as explained in Section 3.4.1 and shown in Figure 3.4.2(a).

Figure 3.6.1 shows the strain history recorded in the *LTI-OUT(1)* and *LTI-IN(1)* gauges installed on a top and bottom side, respectively, of the top longitudinal No.11 bar of Beam 2 and located 2 in. from the support (refer to Chapter 2, Section 2.5 for detailed instrumentation layout). The strain histories are very similar at first and then diverge due to a differential in bar curvature once the buckling starts, evident around the 9000th loading point in the figure. Thus, the average strain is used to compute the stresses in the top bars. Figure 3.6.2 shows the strain gauge measurements obtained from *LBII-IN(1)* and *LBII-OUT(1)* gauges installed on a top and bottom side, respectively, of the bottom longitudinal No.11 bar of Beam 2 and located 2 in. from the support (detailed instrumentation plan is shown in Figure 2.5.4, Chapter 2). As can be seen, gauge *LBII-IN(1)* becomes damaged immediately after yielding (around the 3600th loading point), but otherwise shows consistent readings with gauge *LBII-OUT(1)*. Thus, the strain history measured by the latter instrument is used to compute the approximate bar stresses. The stress-strain curves computed in the No. 11 top and bottom bars based on the strain gauge data and using the Kunath et al. (2009) model are plotted in Figure 3.6.3. These are plotted for the cycles preceding the bar buckling, which includes the first cycle with the beam rotation amplitude $|\theta| = 0.029$.

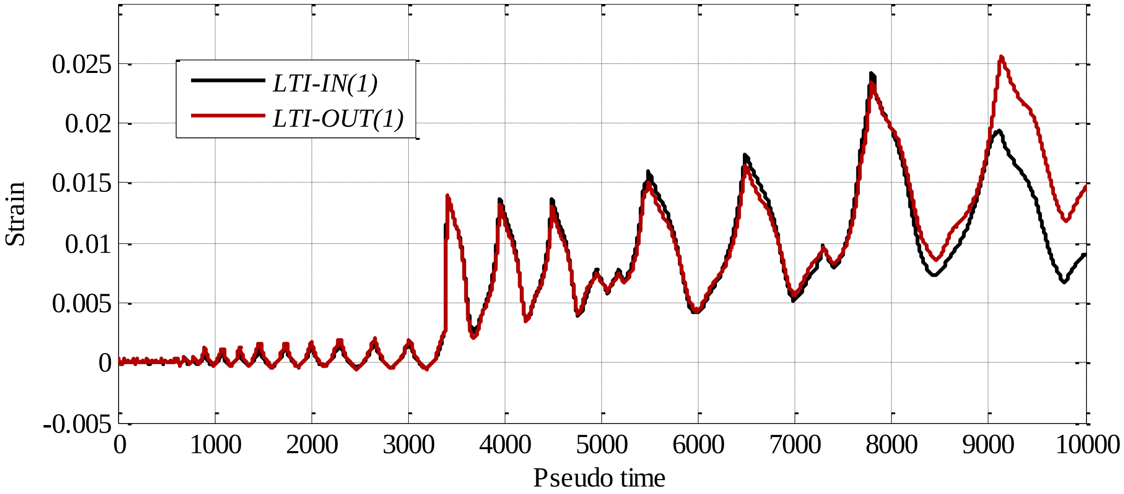

Figure 3.6.1. Strain measured in strain gauges located at the top No. 11 bar in Beam 2.

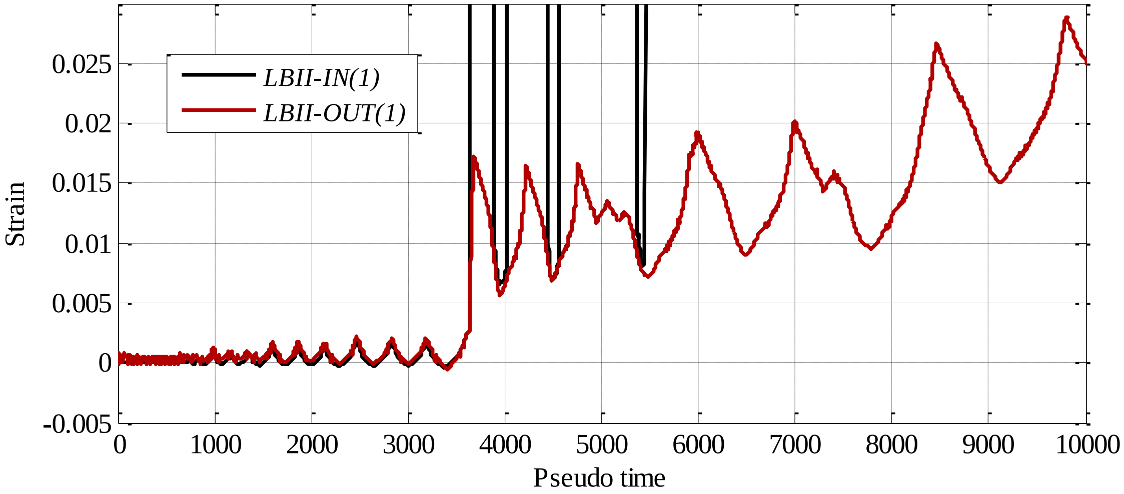

Figure 3.6.2. Strain measured in strain gauges located at the bottom No. 11 bar in Beam 2.

Figure 3.6.4 shows the readings of the LVDT instruments placed on the top (*TL1* and *TR1*) and bottom (*BL1* and *BR1*) faces of Beam 2, respectively. Each pair of instruments (top and bottom) were placed approximately 11.5 in. from either side edge of the beam, along the beam width (refer to Figure 2.5.1 and Figure 2.5.2 in Chapter 2). The readings of top instruments *TL1* and *TR1* are almost identical over the first 13000 data points, corresponding to the deformation cycles prior to longitudinal bar buckling (refer to Chapter 2 for Beam 2 response discussion). After this point in loading history, the readings slightly diverge, with instrument *TR1* showing smaller readings and indicating possible instrument distortion when compared with the *TL1* data. Thus, the measurements obtained from instrument *TL1* were selected to represent the interface crack width, corresponding approximately to the amount of bar slip at the interface of the beam with the reaction block.

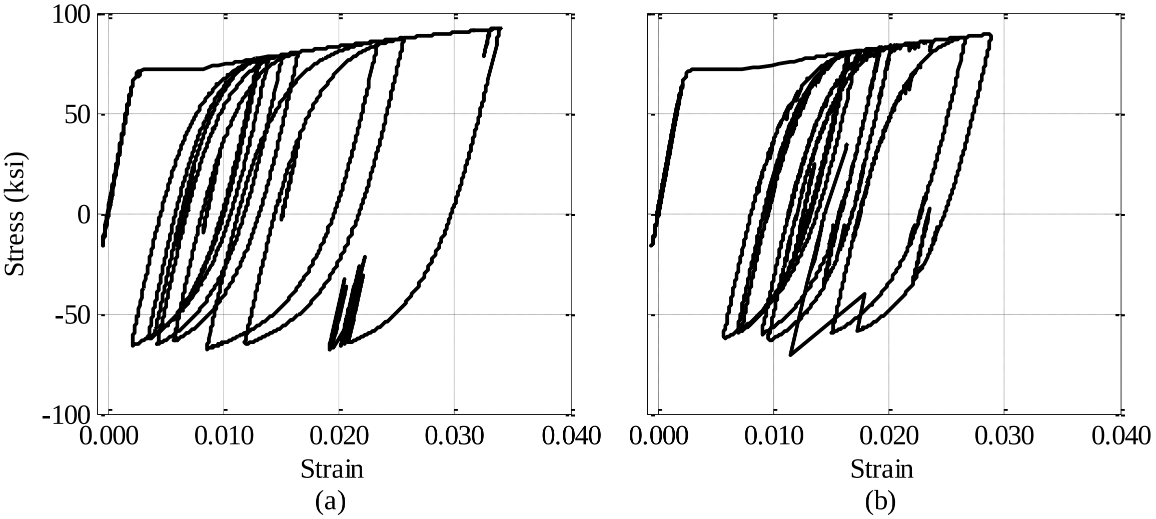

Figure 3.6.3. Bar stresses at the interface of the beam support as computed by Kunath et al. (2009) model based on the strain gauge readings from Beam 2 experiment. Stresses in: (a) top No. 11 bars, and (b) bottom No. 11 bars.

The bottom LVDT pair shows very different readings over the entire loading history. The *BL1* instrument measured deformations which differed from the *BR1* readings by approximately 40-50% throughout the loading history shown in Figure 3.6.4. While for the downward direction of beam loading, instrument *BL1* was showing larger absolute deformations (larger compressive strains), during the upward direction of beam loading, the trend reversed, with *BL1* showing smaller extensions compared to *BR1*. Because the instruments were carefully calibrated prior to beginning of the test, and the initial readings do start from zero, this discrepancy could possibly be attributed to an instrument rotation from the neutral position during the test. Because the bond strength within the concrete reaction block is expected to be approximately uniform along the height of the reaction block due to post-tensioning (see Figure 2.4.1[a]), and the variation in longitudinal bar strains at the beam support showed very similar trends both in the top and the bottom bars, it is plausible that the levels of bar slip would be comparable at the top and the bottom. Thus, the data from *BR1* are selected from the bottom pair, because the absolute values of deformations recorded are consistent with the corresponding values at the opposite cycles for the top instruments.

The strain histories recorded in top instruments are plotted as a function of the bar slip which was taken to be equal to the reading from *BR1* and *TR1* instrument. The corresponding relationships are shown in Figure 3.6.5. The trends are very similar between the top and bottom bars. In both cases, there is an almost linear relationship between the amount of slip and the bar stress prior to yielding, whereas the backbone contour softens upon yielding. The curves unload at the slope similar to the "elastic" slope, but tend to soften and display pinching as the cycles progress, indicating the deterioration in the bond and also the reverse slip of the bar (into the block).

The measured slip at yield point (steel yield stress $f_{y,m}$ = 73 ksi) in both cases is approximately equal to $S_{y,m}$ = 0.038 in. and 0.04 in. for top and bottom bars, respectively. This agrees relatively well with the S_y = 0.033 calculated with Equation 3.4 and Lehman and Moehle (2000) bond stress distribution model using the measured material properties (the avg. cylinder strength f'_c = 6,130 psi, steel E_s = 31,000 ksi, and d_b = 1.41 in.). At the instance when the bars reach the stress of 90 ksi, the approximate slip measured is 0.26 in. and 0.27 in., in the top and bottom bars, respectively, which is within 25% of the 0.34 in. estimated by the Equation 3.4.

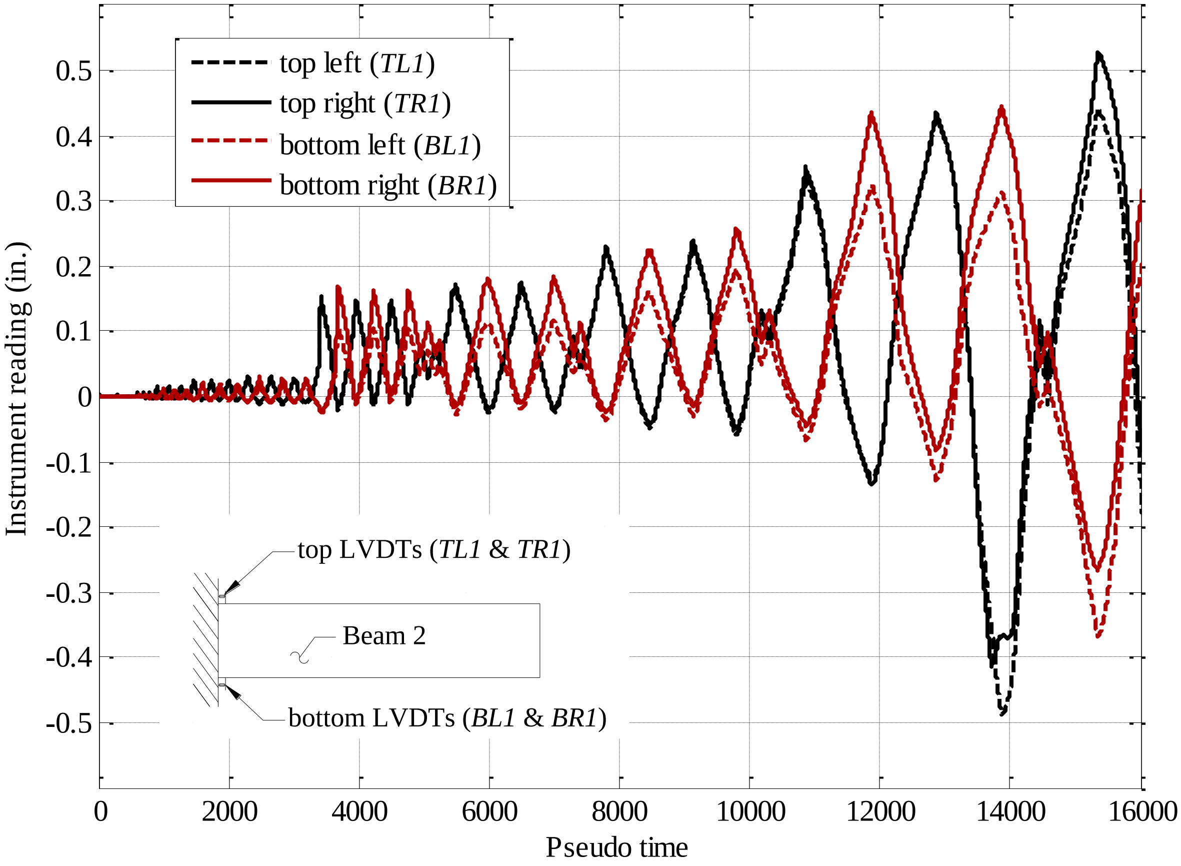

Figure 3.6.4. LVDT readings from instruments spanning first 2 inches of beam from reaction block at the top and the bottom faces.

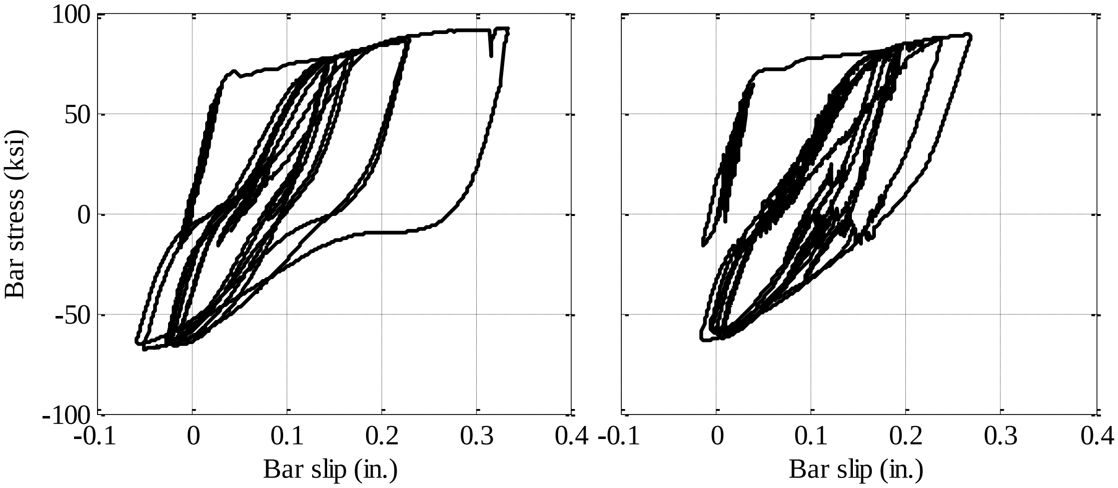

(a) (b)

Figure 3.6.5. Bar stress vs. slip for Beam 2 as computed for: (a) top bar (including first cycle with 0.029 peak rotation) and (b) bottom bar (including cycles prior to 0.029 amplitude cycle).

3.6.1.2 CALIBRATION OF STRESS-SLIP MATERIAL MODEL

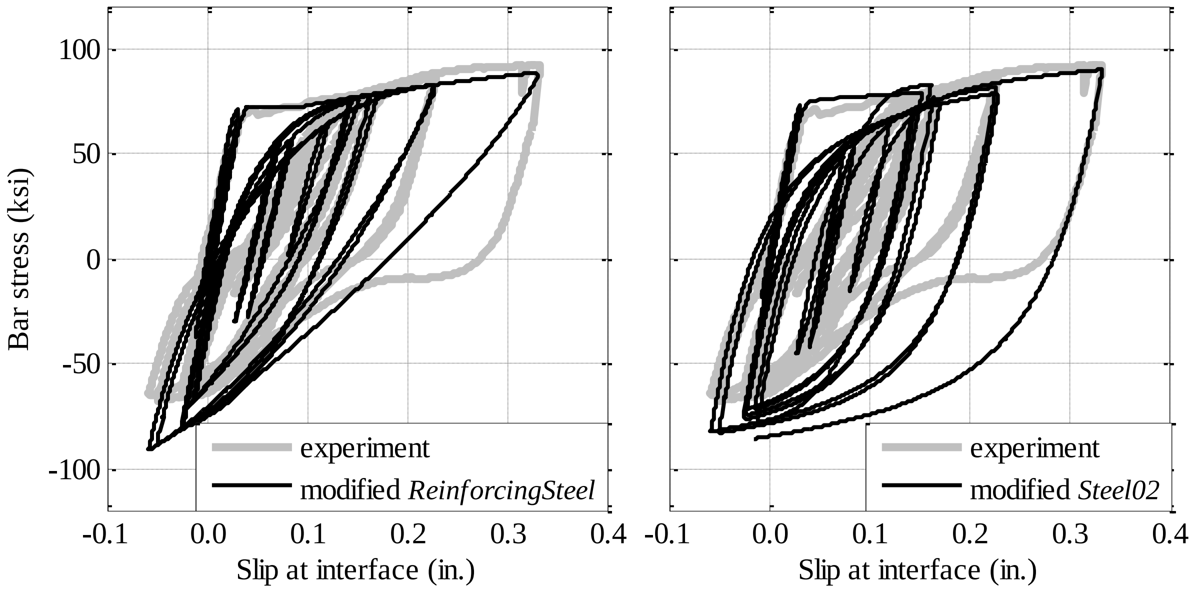

(a) (b)

Figure 3.6.6. Comparison of experimentally obtained bar stress vs. slip behavior with that simulated by using: (a) *ReinforcingSteel* based on Kunath et al. (2008) curve, and (b) *Steel02* based on Giufre-Menegotto-Pinto curve.

The stress-strain uniaxial material curves calibrated for steel fibers of Element 1 and 2 using the two different steel stress-strain relationship models, namely *ReinforcingSteel* and *Steel02*, are modified as explained in Section 3.2.2 to represent the bar stress vs. slip behavior. This mandated calculating the amount of bar slip at the instance when the longitudinal bars in tension reach the yield stress f_y. According to Equation 3.4 and using Lehman and Moehle (2000) bond stress distribution assumption, the slip at yield for No. 11 bars is S_y = 0.033. Thus, all of the parameters of *ReinforcingSteel* and *Steel02* were multiplied by the factor $r_y = E_s / E_{slip} = S_y / \varepsilon_y$ = 14.34.

A single steel fiber element was subjected to a deformation history equal to the bar slip measured experimentally and shown in Figure 3.6.4. Readings from *TL1* instrument were used as a benchmark for the experimental data because more points were recorded by *TL1* in comparison with the other three LVDTs before the data became incoherent (see data readings in Appendix A). Figure 3.6.6(a) shows the numerically simulated stress-slip hysteresis superimposed with the experimentally obtained hysteretic curve from Figure 3.6.5(a). The backbone curve of the numerical model agrees well with the experimental data, with initial stiffness, the yielding point, and the post-yield hardening ratio being closely together. However, as the *ReinforcingSteel* material model is only intended to simulate hysteretic behavior inherent to steel material, the pinching that occurs when reloading from zero stress in the cycles after the yielding is not simulated. Nevertheless, for any given point level of bar stress, the amount of slip computed is very close to the amount of slip measured in the experiment. Similar trends can be observed for *Steel02* model, plotted in Figure 3.6.6(b). In comparison with the *ReinforcingSteel*, *Steel02* with softened material properties exhibits rounder hysteretic loops, however, the model is still found to be appropriate for simulating the bar stress-slip response. The concrete stress-strain curves are adjusted as described in Section 3.2.2.

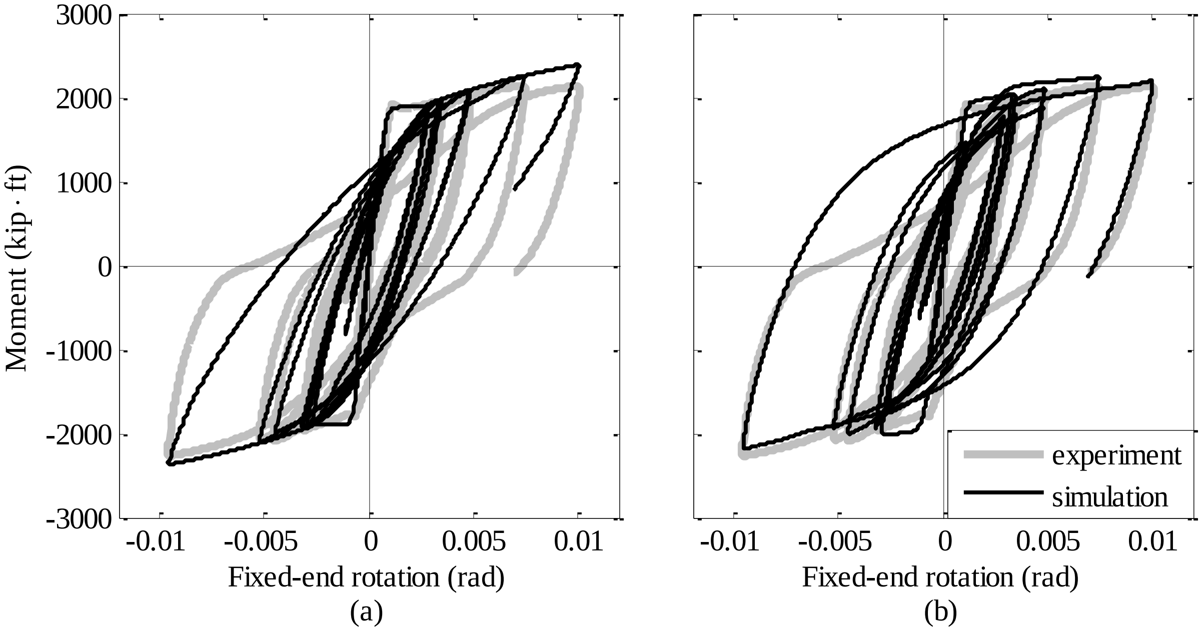

Figure 3.6.7. Comparison of Beam 2 moment vs. fixed-end rotation curves obtained experimentaly and numerically using fiber section zero-length element and: (a) *ReinforcingSteel*, and (b) *Steel02*. Note: cycles plotted include the first cycle when bar buckling caused a decrease in the moment resistance, with 0.029 rotation amplitude.

3.6.1.3 MOMENT-ROTATION RESPONSE OF FLEXURAL SPRING

Bar slip element (Element 3, Figure 3.5.1) representing the fixed-end rotation spring and using the materials described in Sections 3.4.1 and 3.4.2 is evaluated against the experimental data. The fixed-end rotation history obtained from the LVDT instruments located at the root of the beam (as explained in Chapter 2 and plotted in Figure 2.8.14[a]) is applied to a bar slip element alone and the resisting moment is logged.

Moment-rotation hysteresis obtained from bar slip Element 3 using the two steel uniaxial materials are plotted in Figure 3.6.7 and compared to an experimentally obtained moment-fixed-end rotation behavior of Beam 2. An experimental moment-rotation relationship is obtained by plotting a resisting moment of Beam 2 versus the fixed-end rotations calculated using the LVDT instruments (see Section 2.8.5, Chapter 2). The moment plotted on the *y*-axis corresponds to the moment resisted by the beam at the support, corrected for the beam self-weight, as explained in Chapter 2. Figure 3.6.7(a) indicates good agreement between the experimental hysteretic loop and the numerical simulation using *ReinforcingSteel* uniaxial material in the zero-length element fiber section. Similarly good results are obtained using *Steel02* in the zero-length fiber section, as shown in Figure 3.6.7(b).

3.6.1.4 GLOBAL BEAM RESPONSE INCLUDING FLEXURAL AND FIXED-END DEFORMATIONS

In this section, we examine the response of the beam model consisting of Elements 1, 2, and 3, while Element 4 is set to have infinite stiffness. That is, no shear deformations are allowed to occur. The goal is to examine the interaction between the zero-length spring representing the flexibility due to bar slip and the element representing the beam itself. Numerical model of Beam 2 consisting of elements 1-3 is subjected to a monotonically increasing displacement at the tip and also the cyclic displacement history from the Beam 2 experiment, adjusted to exclude the deformations attributable to shear (plotted in black dashed line in Figure 3.3.1).

The monotonically increasing loading history is applied at Node 4 (Figure 3.5.1), and the depth of the compression zone measured from the uppermost fiber is monitored at the integration point located in Element 1 at the very root of the beam and within the bar slip Element 3 simulating the fixed-end rotation behavior. The compression zone depth computed using *ReinforcingSteel* and *Steel02* is plotted as a function of the beam tip displacement and is plotted in Figure 3.6.8. As can be observed in both cases, the curves are identical for the zero-length section element, proving the section strain compatibility is enforced for all the beam deformation levels. Similarly, curves in Figure 3.6.9 show the strain compatibility is realized during most of the cyclical loading, with the curves only diverging at few computation points, which can be attributable to numerical error.

Figure 3.6.10 shows the relationship between the beam moment and the total chord rotation (excluding the shear deformations) and the fixed-end rotation as a function of total beam chord rotation obtained from the cyclic displacement loading for the beam model using the two different steel uniaxial materials. As before, the curves have been superimposed with the experimental results. The top two graphs show the analytical results obtained from the numerical model using *ReinforcingSteel*, while the bottom two show the results obtained using *Steel02*. The plots include all cycles prior to those where loss of strength was noted due to bar buckling. As can be seen from Figure 3.6.10(a) and (c), both beam models result in hysteretic curves that agree with the experimental data remarkably well for the cycles shown. Figure 3.6.10(b) and (d) indicate that the zero-length element simulates the fixed-end flexibility reasonably well.

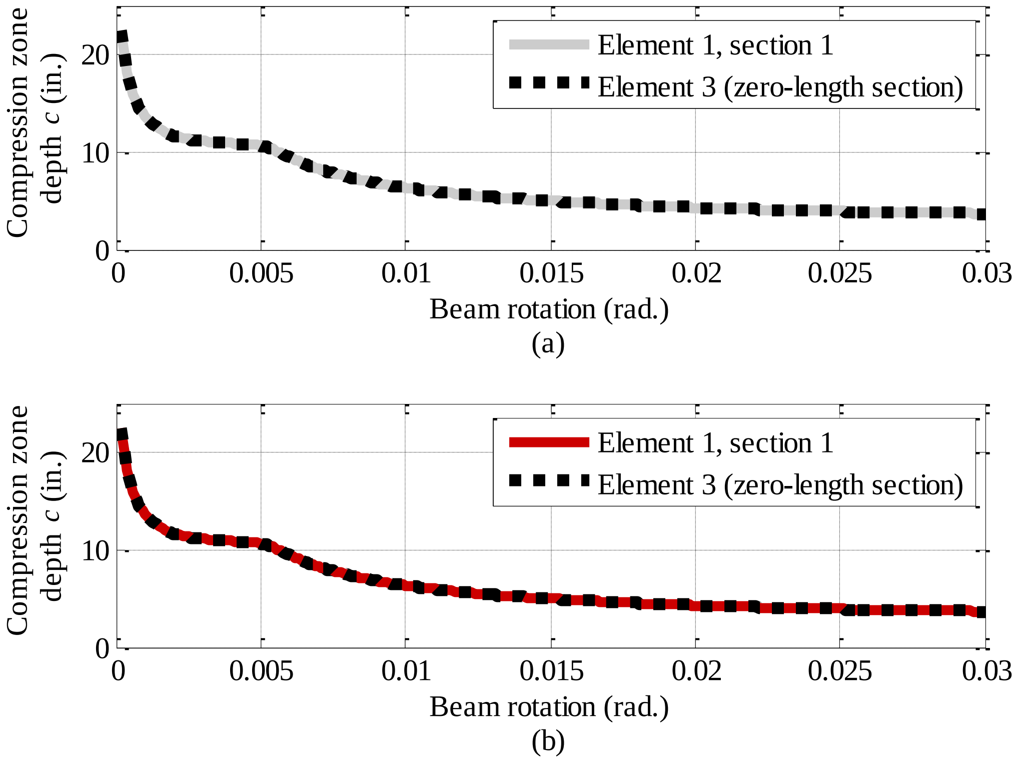

Figure 3.6.8. Monotonic pushover curves and variation of neutral axis depth within the zero-length element section and the adjacent section of beam-column Element 1, as computed using: (a) *ReinforcingSteel* and (b) *Steel02*.

Figure 3.6.11 plots the elongation computed with the numerical model using Elements 1-3 to that measured in the experiment of Beam 2. The total beam elongation (Figure 3.6.11[a]) is divided into the portion of the elongation computed within the Elements 1 and 2 (corresponding to the elongation of the beam itself, and plotted in Figure 3.6.11[b]) and the elongation within the bar-slip element corresponding to the gap opening (interface crack) width recorded at the beam interface with the reaction block (Figure 3.6.11 [c]). The gap opening measured in the laboratory was computed as the average reading of *LT1* and *LB1* instruments (shown in a picture inset in Figure 3.6.4), respectively. In each plot, the curves computed using *ReinforcingSteel* and *Steel02* are in good agreement with the experimental data obtained from Beam 2 test.

Agreement in the overall elongation vs. drift evolution plotted in Figure 3.6.11 indicates that the modeling strategies based on distributed plasticity elements which utilize fiber sections with appropriate hysteretic materials are an adequate tool to use in modeling reinforced concrete beams when analyzing structures that may be impacted by the beam elongation. Chapter 4 explores this further.

The pitfall of modeling bar slip element using fiber section as described is that it may lead to erroneous computation results when the beam-column elements are loaded with axial forces prior to experiencing flexural deformations. An example of such case is numerically applying post-tensioning to the beams, or applying gravity loads to columns prior to laterally applied loads such as a pushover force pattern or ground acceleration. The reason is that the rotational spring fiber section has an axial flexibility that is a function of uniaxial material fiber properties and thus cannot be decoupled from the flexural flexibility.

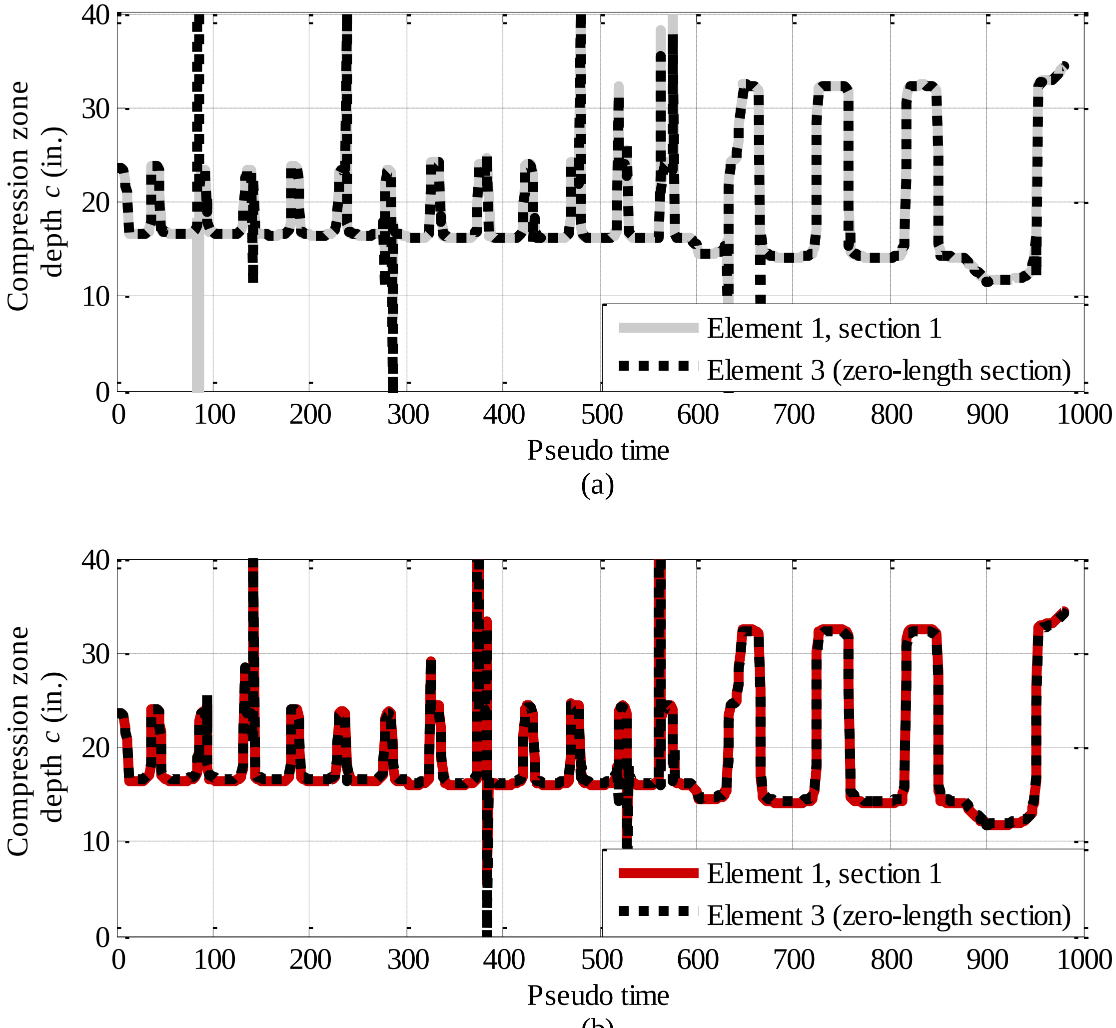

(a)

(b)

Figure 3.6.9. Variation of compression zone depth for Element 1, section 1, and Element 3 as measured from the top edge of the section using: (a) *ReinforcingSteel* and (b) *Steel02* materials.

As noted before, the material stress-strain curves in the bar slip element section are adjusted by a factor r_y and are thus an order of magnitude more flexible that the fibers in the beam-column elements (in this case $r_y = 14.34$). This implies that under a constant axial load, a bar slip element section deforms axially 14.34 times more than the beam-column section. Thus, the node between the bar slip element and the beam-column element moves past the beam-column support, leading to a deformed beam length greater than would be computed otherwise. The direct consequence of computing such length is that the beam would experience smaller axial forces than may exist in actuality. In bar slip sections at the bottom of columns of comparable cross section in regular frames, the effect of this phenomenon can be ignored, because all of the columns support nodes shift by approximately same length. In beams, and where post-tensioning slabs are to be included in the analysis, it is important to avoid this problem.

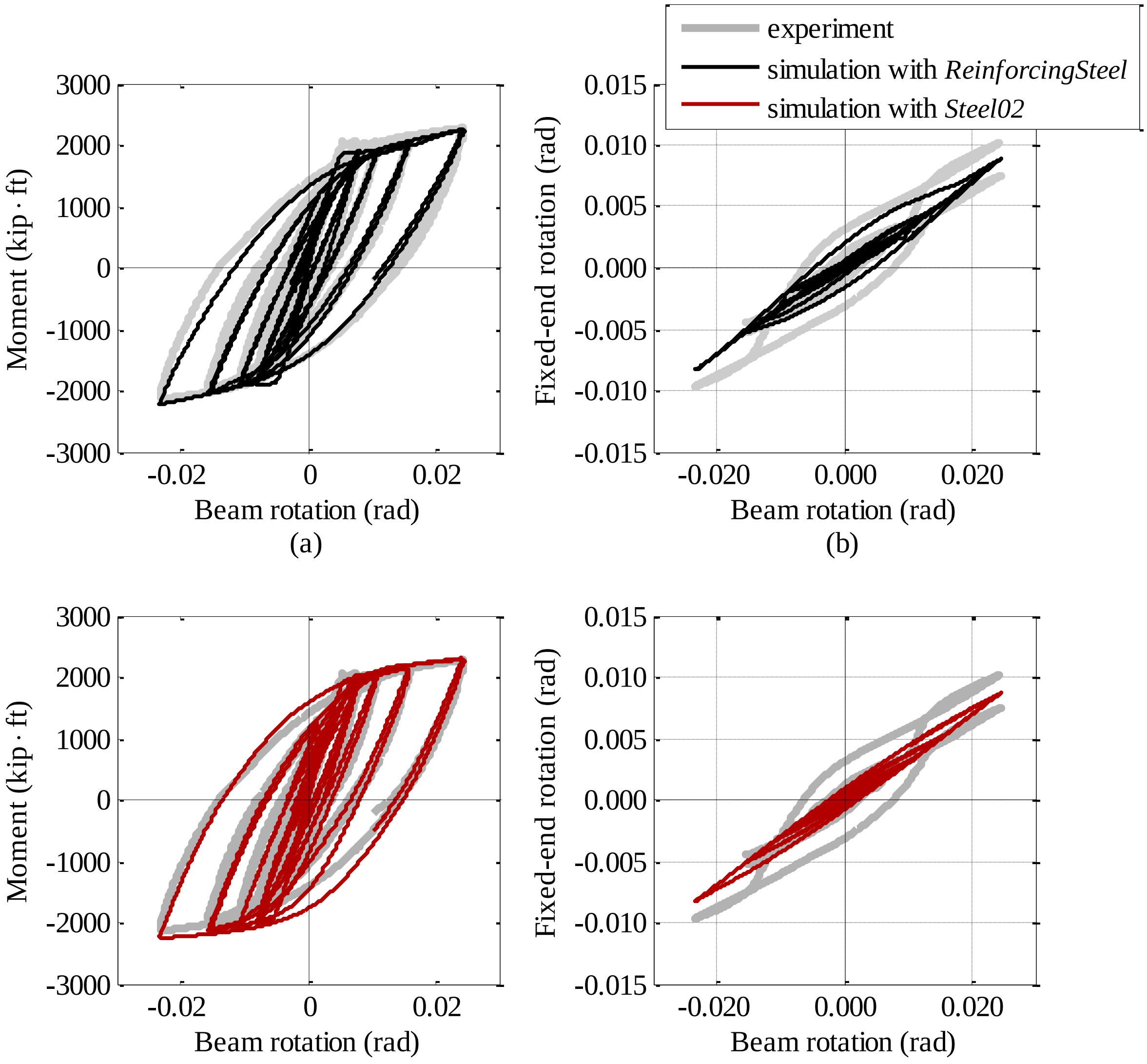

(a) (b)

(c) (d)

Figure 3.6.10. Comparison of experimental and numerical results of cyclic test: (a) moment-rotation curve for Beam 2 using *ReinforcingSteel*, (b) fixed-end rotation vs. total beam rotation for Beam 2 using *ReinforcingSteel*, (c) moment-rotation curves using *Steel02*, and (d) fixed-end rotation vs. total beam rotation using *Steel02*.

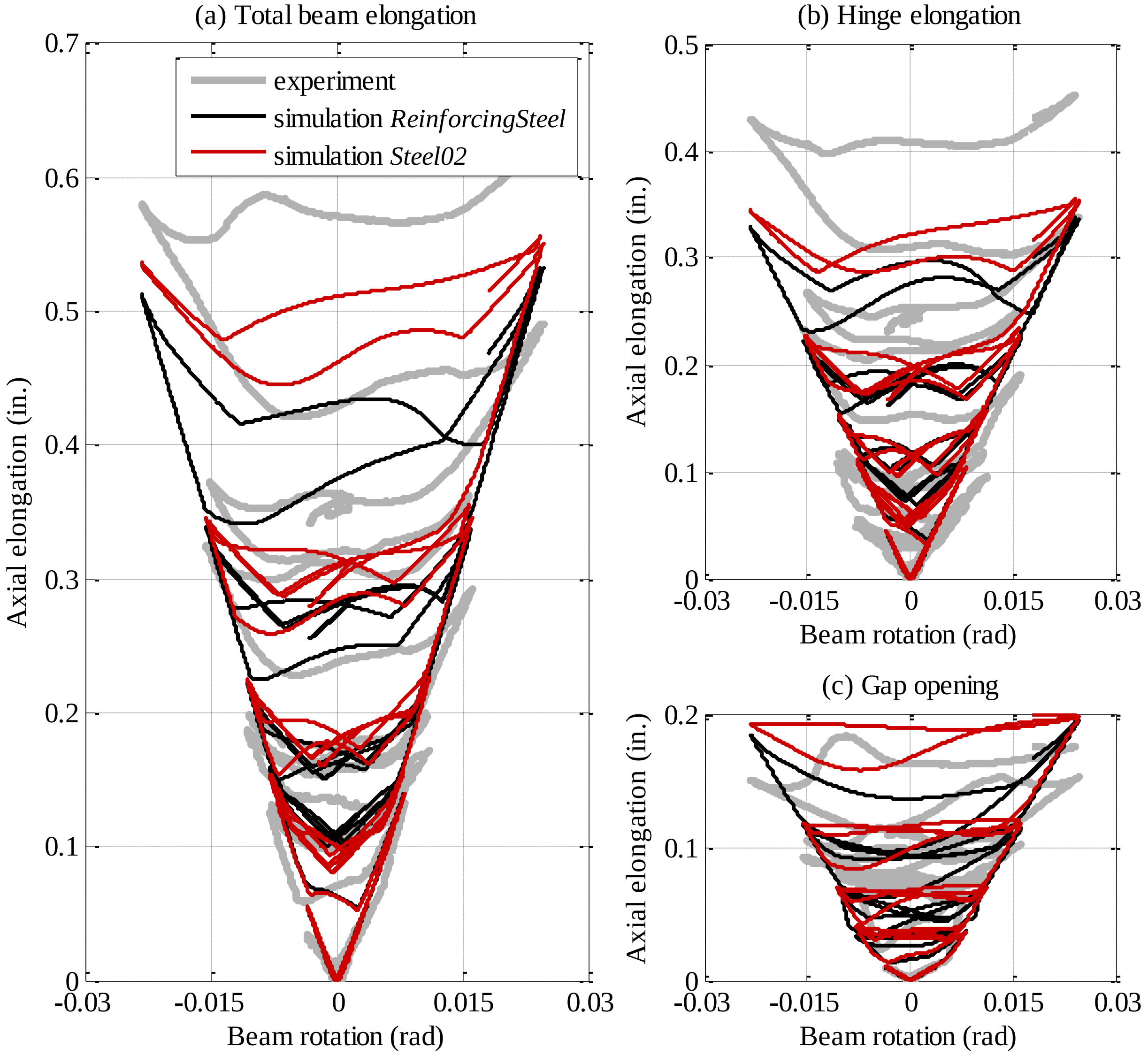

Figure 3.6.11. Comparison of experimental and numerically computed elongation of Beam 2: (a) lengthening of the beam itself, (b) gap opening at the beam interface with the support, and (c) total beam elongation.

3.6.2 BILINEAR AND LINEAR ELASTIC ROTATIONAL SPRINGS

Where post-tensioning axial loads in beam-column elements are non-zero, as described in previous section, fixed-end rotation deformations can be accounted for by a rotational spring with a decoupled flexural and axial behavior as described next. The distributed plasticity beam-column elements are thus the only elements to simulate the beam elongation (i.e. gap opening at the beam interface with the support is not explicitly modeled). Here, we use the same Elements 1 and 2 described before with uniaxial material *Steel02*. In lieu of a bar slip section in Element 3, a rotational spring with a unit area and both bilinear hysteretic and linear elastic moment-rotation relationship is used.

The bilinear spring is modeled with *Hysteretic* material in OpenSees (Figure 3.6.12). The backbone curve is defined with the bilinear relationship between the beam moment and the appropriate fixed-end rotation. Thus, only two points are necessary to define the moment-rotation relationship: the yield moment M_y and the ultimate moment M_u with the corresponding fixed end rotations θ_{sy} and θ_{su}. The two moment capacities are computed from moment-curvature section analysis presented in Section 3.8 and the fixed-end rotations for the two levels of load were obtained using Equation 3.5 and the appropriate amounts of bar slip S_y and S_u computed assuming Lehman and Moehle (2000) bond stress distribution (refer to Section 3.2.1).

Hysteretic material requires an input of ultimate force-deformation capacity (labeled as [$e3p, $s3p] and [$e3n, $s3]). The values for ultimate moment capacity were set to be very large to avoid localization of inelastic deformation within the rotational spring in case that the beam moment capacity increases during nonlinear analysis, as a result of possible axial load increase. Therefore, [θ_{su}, M_u] pair was used to determine the post-yield hardening slope β_h = 0.0127, which was then utilized to set the rotation corresponding to the very large moment capacity. The input parameters for the *Hysteretic* material are listed in Table 3.3. Note that additional parameters controlling the pinching of the hysteresis and damage accumulation are set to zero. Parameter $beta, which controls the softening of the unloading stiffness is also set to zero.

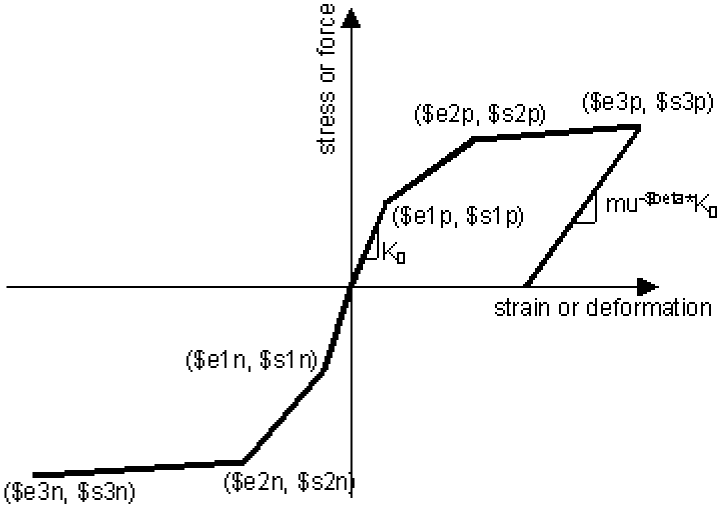

Figure 3.6.12. Hysteretic material (OpenSees 2014).

Table 3.3. Input parameters for *Hysteretic* material.

Input Parameter	Description	Value
$e1p, $e1n	Rotation at positive and negative yield moment (radians) θ_{sy}	0.0008, -0.0008
$s1p, $s1n	Positive/Negative yield moment (kip·in)	(23,500), (-23,500)
$e2p, $e2n	Rotation at ultimate moment capacity θ_{su}	0.0267, -0.0267
$s2p, $s2n	Positive and negative ultimate moment capacity	(32,800), (-32,800)

Linear elastic spring was modeled by an *Elastic* material in OpenSees. The only input needed for this material is the stiffness, which was computed as the slope from a line connecting the origin to the [θ_{sy}, M_y] point. Essentially the linear elastic spring exhibits the moment-rotation behavior identical to the elastic branch of the bilinear rotational spring shown in Figure 3.6.12.

3.6.2.1 COMPARISON OF RESPONSE

Beam model consisting of Elements 1-3, where Element 3 is represented by either bilinear hysteretic spring or linear elastic spring is subjected to the loading history from Figure 3.3.1 that does not include shear deformation component. The resulting moment vs. fixed-end rotation behavior of the Element 3 is plotted along with the experimental curve from Beam 2 test and is shown in Figure 3.6.13. Clearly, the linear elastic spring only captures the initial rotation pre-yielding, whereas the bilinear spring simulates the fixed-end rotations due to bar slip quite well.

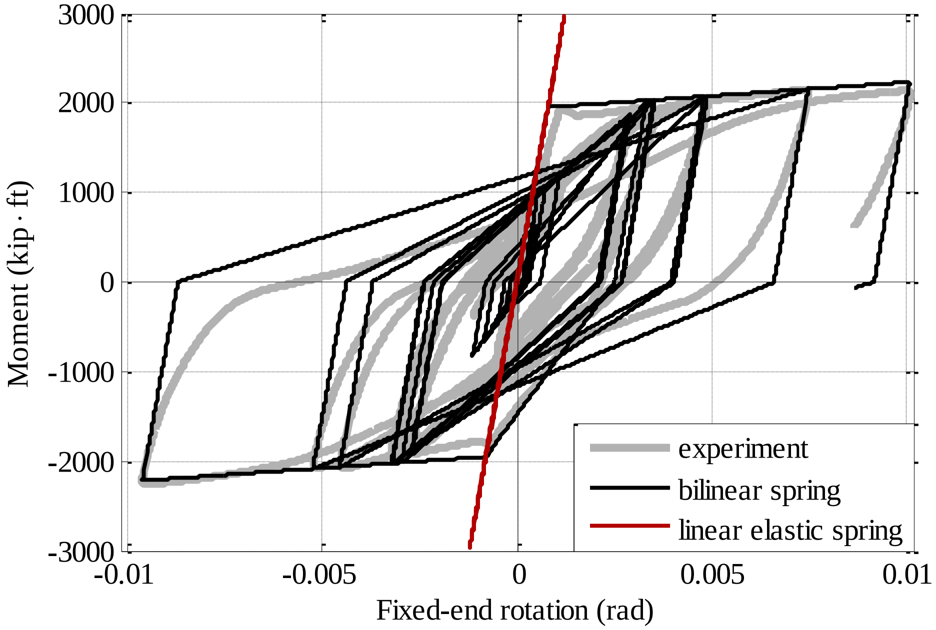

Figure 3.6.13. Comparison of experimentally computed moment vs. fixed-end rotation relationship with numerically computed using bilinear rotation spring and linear elastic spring in Element 3.

The fixed-end rotation computed with the two different springs are plotted as a function of total beam chord rotation in Figure 3.6.14. Clearly, the bilinear spring faithfully estimates the fixed-end rotation levels due to bar slip after yielding, while the linear elastic spring lacks this capability. However, the global moment-rotation response is very similar between the two models, as can be seen in Figure 3.6.15. As expected, the beam model which contains linear elastic spring results in roughly 6% higher peak moment computed in post-yield deformation cycles, compared to the one computed when bilinear spring is used. However, if beam elongation is a concern, the use of linear elastic spring produces better estimation of beam elongation, while approximately capturing the added flexibility from bar slip, as can be seen in Figure 3.6.16. This is expected, because elongation is roughly proportional to the amount of chord rotation and the more rotation comes from the fiber based elements, the more elongation is computed.

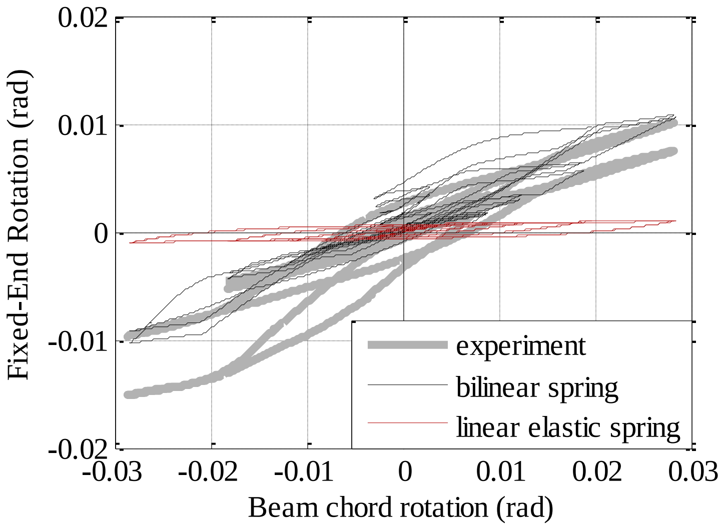

Figure 3.6.14. Fixed-end rotation as a function of total beam rotation.

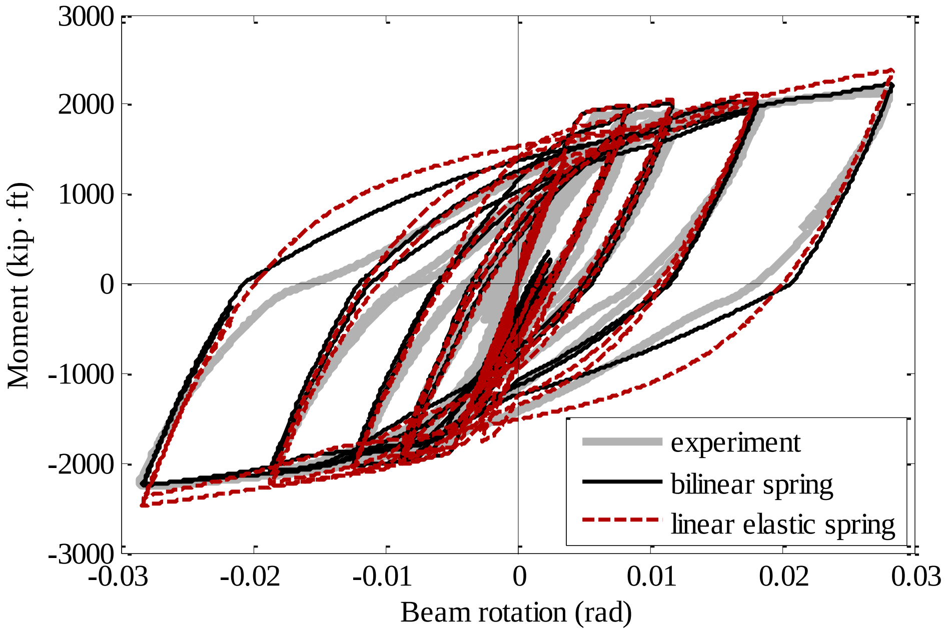

Figure 3.6.15. Comparison of moment-rotation response for the numerical models.

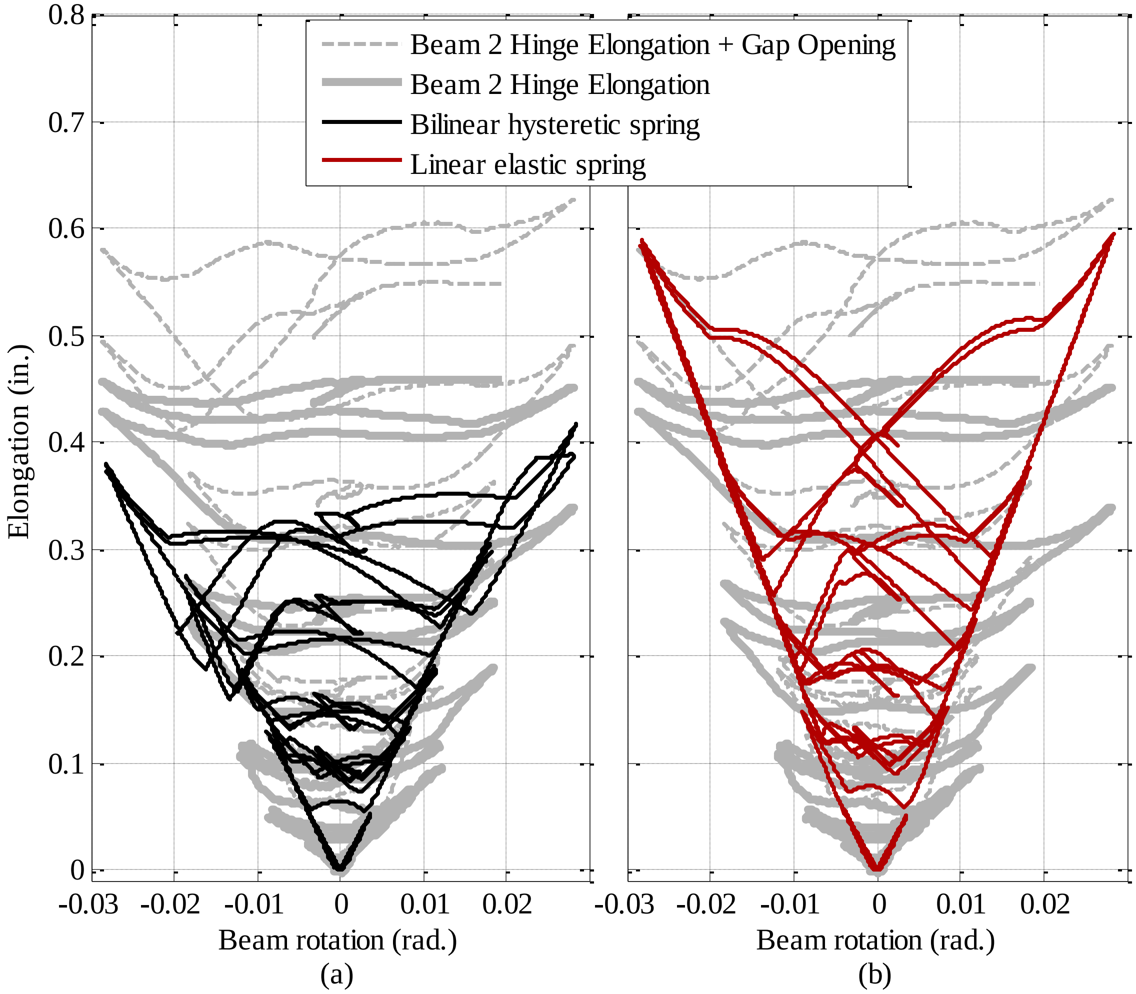

Figure 3.6.16. Beam elongation computed with numerical model using: (a) bilinear spring and (b) linear elastic spring.

3.7 SHEAR SPRING

The global moment-rotation behavior of the fiber-section based beam model developed in the preceding sections is adjusted in this section to include a shear spring to account for the shear deformations during cyclic loading. This is accomplished by using a shear spring labeled as *Element 4* in Figure 3.5.1 which acts in parallel with the bond-slip *Element 3* developed in Section 3.6.1. Thus, the relationship modeled is that of shear force vs. beam displacement along the local *y*-axis due to shear deformations (denoted here as Δ_v and expressed in units of length), as opposed to shear deformations defined as an angular distortion (γ, expressed in units of radians) from the centerline of the undeformed beam.

Shear force-deformation relationship is represented with *Pinching4* material in OpenSees, with the points defining the hysteretic shape shown in Figure 3.7.1. As previously noted, the ordinate of the graph shown represents the shear force V (kips), while the abscissa represents the shear deformations Δ_v (in.). The initial slope in the V-Δ_v relationship is set to correspond to the elastic shear stiffness defined in Equation 3.7, where the elastic stiffness of the shear spring is

K_{v0} = 85,690 kip/in. The K_{v0} was calculated as explained in Section 3.2.3 using L_b = 150 in., υ = 0.18 as the concrete Poisson's ratio, E_c = 4,463 ksi as the concrete Young's modulus based on the average compressive cylinder strength f'_c = 6.13 ksi for Beam 2 on the day of the testing, and the shear modulus of elasticity of G = 8,926 ksi. Thus, the elastic shear deformations occurring prior to formation of diagonal cracks are integrated over the entire length of the beam.

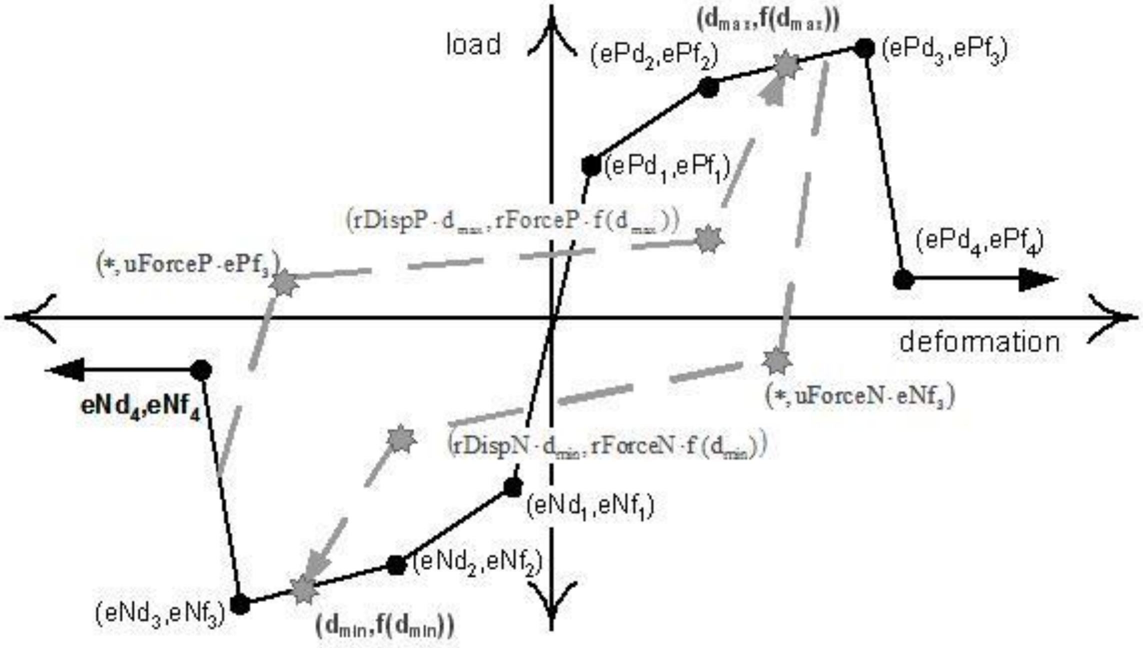

Figure 3.7.1. *Pinching4* uniaxial material parameters (OpenSees, 2014).

The cracking shear V_{cr} for Beam 2 calculated with Equation 3.8 is 173 kips. However, Beam 2 test results indicate that the diagonal cracks formed even before the specimen reached this value of shear force. From Table A.2 (Appendix A), it is evident that the diagonal cracks occurred during the first cycle to peak chord rotation of θ = 0.0028, which corresponds to the peak resisting shear of 109 kips including beam self-weight. Thus, the empirically observed V_{cr} = 109 kips was used instead of that obtained from Equation 3.8. The corresponding shear deformation computed with elastic shear stiffness is Δ_{cr} = 0.0011 in, which is equivalent of having uniform shear deformation along the length of the beam of γ_{cr} = 8.5x10^{-6} rad.

The post-cracking slope of the backbone curve is determined using the stiffness $\delta V/\delta\gamma = GA_1$ calculated with Equation 3.9. Using Beam 2 design parameters (E_s = 31500 ksi, b_w = 48 in., d-d' = 42.34 in., ρ_w = 0.0057, η = 0.1424, and θ_t = 45°), Equation 3.9 results in GA_1 = 141,922 kip/in. As discussed in Section 3.2.3, the stiffness of the shear mechanism in the beam reduces upon the beam reaching flexural yielding point. Thus the shear stiffness GA_1 is assumed to be valid up to V_y which denotes the shear resisted at the instance that M_y is reached at the root of the beam. The yielding moment of Beam 2 was computed by the moment-curvature analysis and verified experimentally as approximately M_y = 23,500 kip·in., which for the moment distribution resulting from the point load at the end of the cantilever and assumed uniformly distributed beam weight w_{self} = 1.45 kip/ft leads to:

$$V_y = \frac{M_y}{L_b} - \frac{w_{self} L_{total}}{2} = 146.9\text{kip} \qquad 3.10$$

Note that L_{total} = 162 in. is the total length of the Beam 2 specimen, as opposed to the L_b = distance of the actuator force point of application from the beam support which is the same as the length of the numerical model presented in Figure 3.5.1. Using GA_1, the change in the shear deformation $\delta\gamma = \delta V/GA_1 = (V_y\text{-}V_{cr})/GA_1 = 0.000267$. If it is assumed that this post-cracking stiffness is roughly uniform throughout the beam length, the beam tip displacement at V_y due to shear would be $(\gamma_{cr} + \delta\gamma)L_b = 0.041$ in. However, this assumption leads to computation of excessive shear deformations, because the shear deformations would tend to decrease from the beam support to the beam tip due to less flexural cracking present and smaller shear-flexure interaction. A better agreement with experimental results is obtained by assuming that the post-cracking shear deformations occur within a limited region at the root of the beam. The length of this region was arbitrarily set equal to h_b = 48 in. which lead to computed shear deformations more consistent with the experimental data. Therefore, $\Delta_{v,y} = \Delta_{cr} + \delta\gamma H_b = 0.014$ in, and the second branch of backbone curve has the slope K_{v1} = 2985 kip/in.

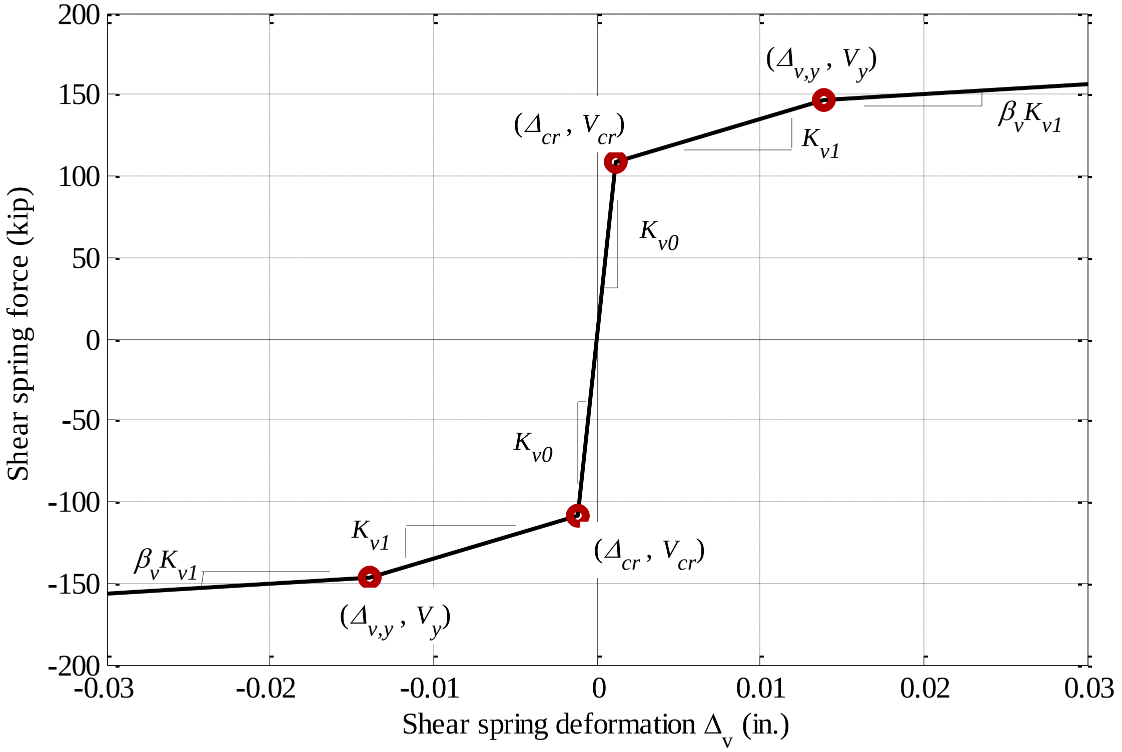

Figure 3.7.2. Force-deformation backbone curve for shear spring (Element 4).

In lieu of the varying post-yielding stiffness of the shear mechanism as a function of flexural deformation ductility proposed by Mergos and Kappos (2012), a constant stiffness with the slope of $\beta_v GA_1$ was used because of its simplicity and also the fact that the shear spring is modeled separately from the flexural beam-column elements and not compatible with the numerical modeling methods of the said study. The factor β_v = 0.05 was empirically selected to give an acceptable agreement with the test data. A positive $\beta_v GA_1$ slope ensures that no localizations occur during the computations. The backbone curve of the force-deformation relationship for shear spring represented by Element 4 is illustrated in Figure 3.7.2. The shear-deformation curve is assumed to not reach the plastic branch described in Section 3.2.3, because shear yielding did not occur for Beam 2 and is of no interest to a present study. The rest of the parameters of the *Pinching4* material were selected to produce the pinching of the moment-chord rotation curve consistent with what is observed in the Beam 2 test results.

A numerical model consisting of Elements 1-4 is subjected to the same displacement protocol as the Beam 2. The displacement history in this case corresponds to the total displacement of the beam tip, because all of the considered beam deformation components have been calibrated and accounted for. Elements 1-3 utilize *ReinforcingSteel* to represent steel fibers, as described in Sections 3.4.1 and 3.4.2. Figure 3.7.3 shows the shear force vs. tip displacement due to shear hysteretic relationship obtained experimentally and computed using the hysteretic shear spring with *Pinching4* material with parameters identified in Table 3.4. The data include cycles up to 0.029 beam rotation when major buckling occurred in the longitudinal bars, after which the shear deformations recorded with the instrumentation were incoherent. The plot indicates relatively good agreement between the experimental data and the computed deformations.

Figure 3.7.4(a) plots the equivalent beam rotations caused by the shear deformation (defined as Δ_v/L_b) versus the total beam chord rotation. The curves are shown for experimental data and the computed curves. As can be seen, the correlation between the two variables is effectively simulated with the hysteretic shear spring using *Pinching4* material calibrated as discussed.

Table 3.4. Input parameters for *Pinching4* material (all units in kips and inches).

Uniaxial material input parameter	Description	Value
$ePf1, $ePd1	See Figure 3.7.1	109, 0.0012
$ePf2, $ePd2		146, 0.0139
$ePf3, $ePd3		363, 1.504
$ePf4, $ePd4		363, 100
$eNf1, $eNd1		-109, -0.0012
$eNf2, $eNd2		-146, -0.0139
$eNf3, $eNd3		-363, -1.504
$eNf4, $eNd4		-363,-100
$rDispN, $rForceN, $uForceN		-0.1, 0.1, 0
$rDispP, $rForceP, $uForceP		-0.1, 0.1, 0
$gK1, $gK2, $gK3, $gK4, $gKLim		0.01, 0.01, 1, 1, 0.9
$gD1, $gD2, $gD3, $gD4, $gDLim		0, 0, 0, 0, 0.5
$gF1, $gF2, $gF3, $gF4, $gFLim		1.0, 0, 1.0, 1.0, 0.9
$gE		10
$dmgType		"energy"

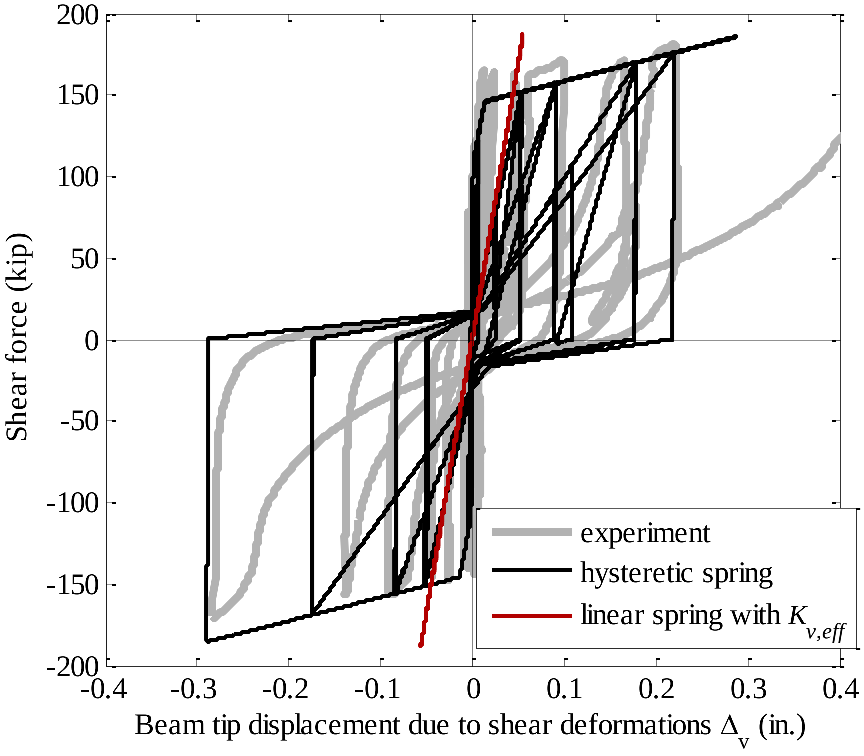

Figure 3.7.3. Comparison of shear force-deformation hysteresis computed with the test results of Beam 2.

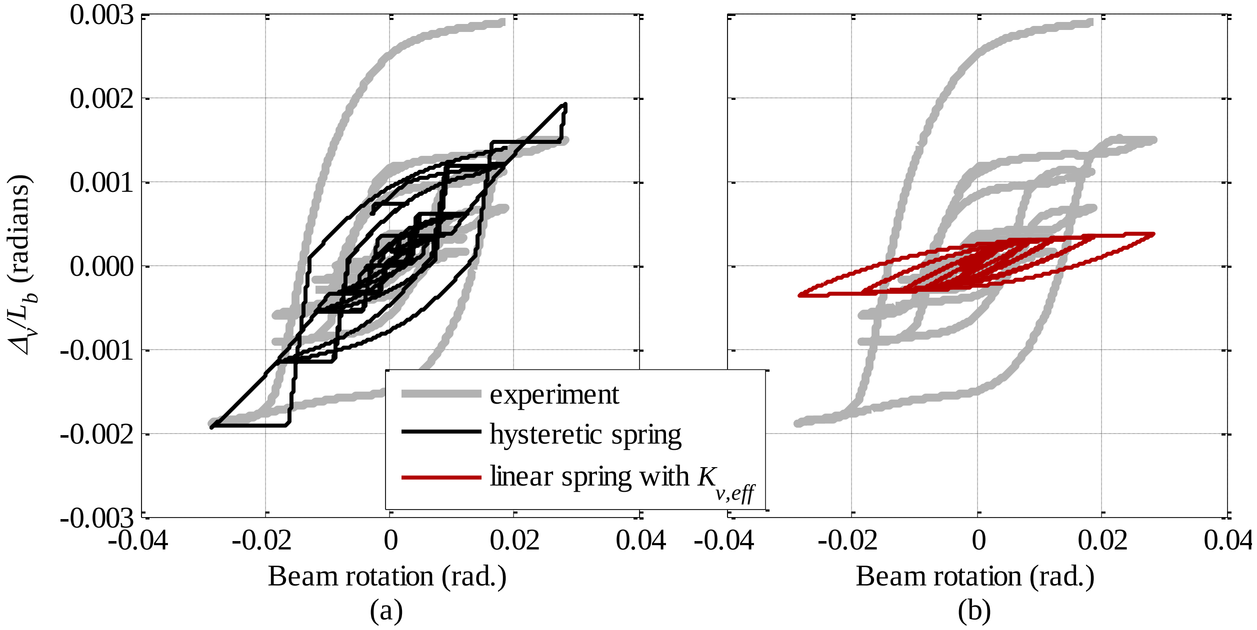

Figure 3.7.4. Comparison of tip displacement attributable to shear as a function of total beam rotation obtained experimentally and numerically using shear spring with: (a) hysteretic behavior defined with *Pinching4* material, and (b) linear elastic stiffness $K_{v,eff}$.

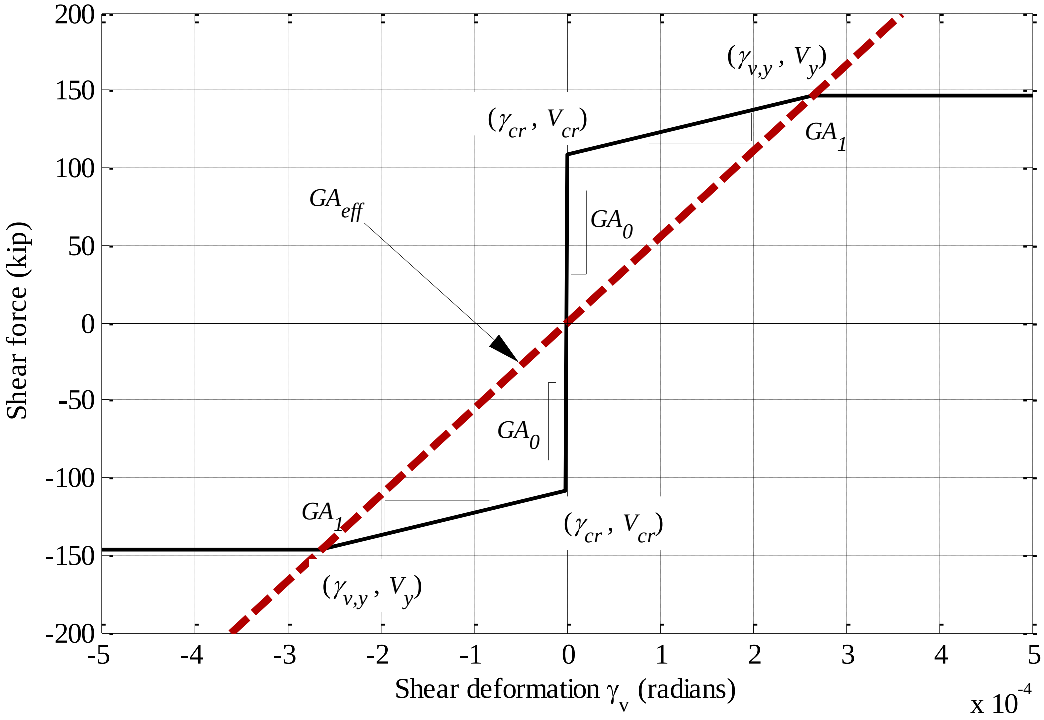

Figure 3.7.5. Linear elastic shear force-deformation relationship based on the effective shear stiffness defined as the secant stiffness to flexural yield point.

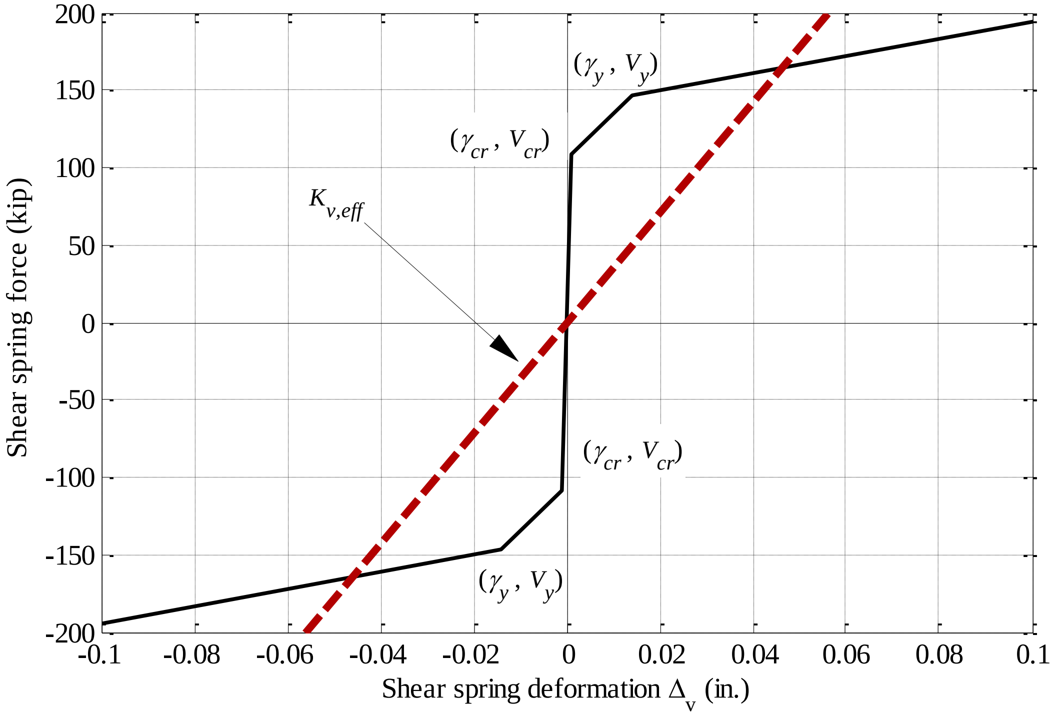

Figure 3.7.6. Linear elastic shear spring force-deformation relationship based on equivalent shear stiffness of the beam.

A simpler alternative of accounting for the shear deformations using a linear elastic spring is explored. Analogous to computing effective flexural stiffness at yield in beam moment-deflection computations, an effective shear stiffness GA_{eff} is used with an assumption that the beam element has the same effective shear stiffness along the length (i.e. shear deformations are uniform and no concentration of deformation occurs in any particular region) equivalent to the secant stiffness from the (0,0) point to (V_y,γ_y) (Figure 3.7.5). With V_y and γ_y as defined previously, this leads to GA_{eff} = 533,212 kip/rad. The resulting $K_{v,eff}$ used for the elastic shear spring is obtained by using $K_{v,eff} = (GA_{eff}/L_b)$ = 3555 kip/in. The linear elastic shear spring behavior is also plotted in Figure 3.7.3. The relationship between total beam rotation and the equivalent beam rotations caused by the shear deformation (Δ_v/L_b) is shown in Figure 3.7.4(b). Simulated and experimental responses agree for the initial beam deformation cycles, after which the shear deformations are underestimated by the linear elastic spring model.

3.7.1.1 COMPARISON OF GLOBAL BEAM RESPONSE

Figure 3.7.7 shows the moment-rotation relationship for the numerical model and the test specimen, including all cycles up to 0.029 beam chord rotation. The numerical model shows good agreement with the physical response to lateral deformation cycles for both nonlinear spring and the equivalent linear elastic spring. Utilization of nonlinear spring as described earlier introduced slight pinching of the moment-rotation curve (Figure 3.7.7[a]), while this phenomenon is not present in the response computed with linear shear spring (Figure 3.7.7[b]).

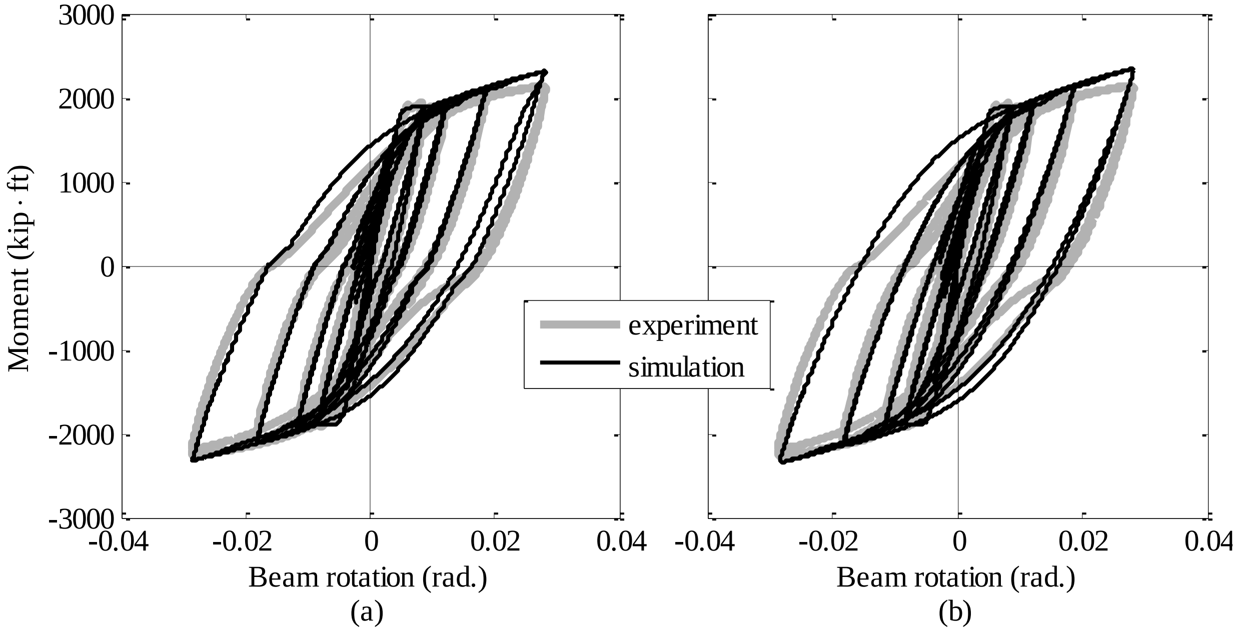

(a)

(b)

Figure 3.7.7. Comparison of experimentally obtained moment-rotation curves for Beam 2 with numerical computations obtained using distributed plasticity elements and shear spring based on: (a) hysteretic material *Pinching4* and (b) equivalent linear elastic spring stiffness.

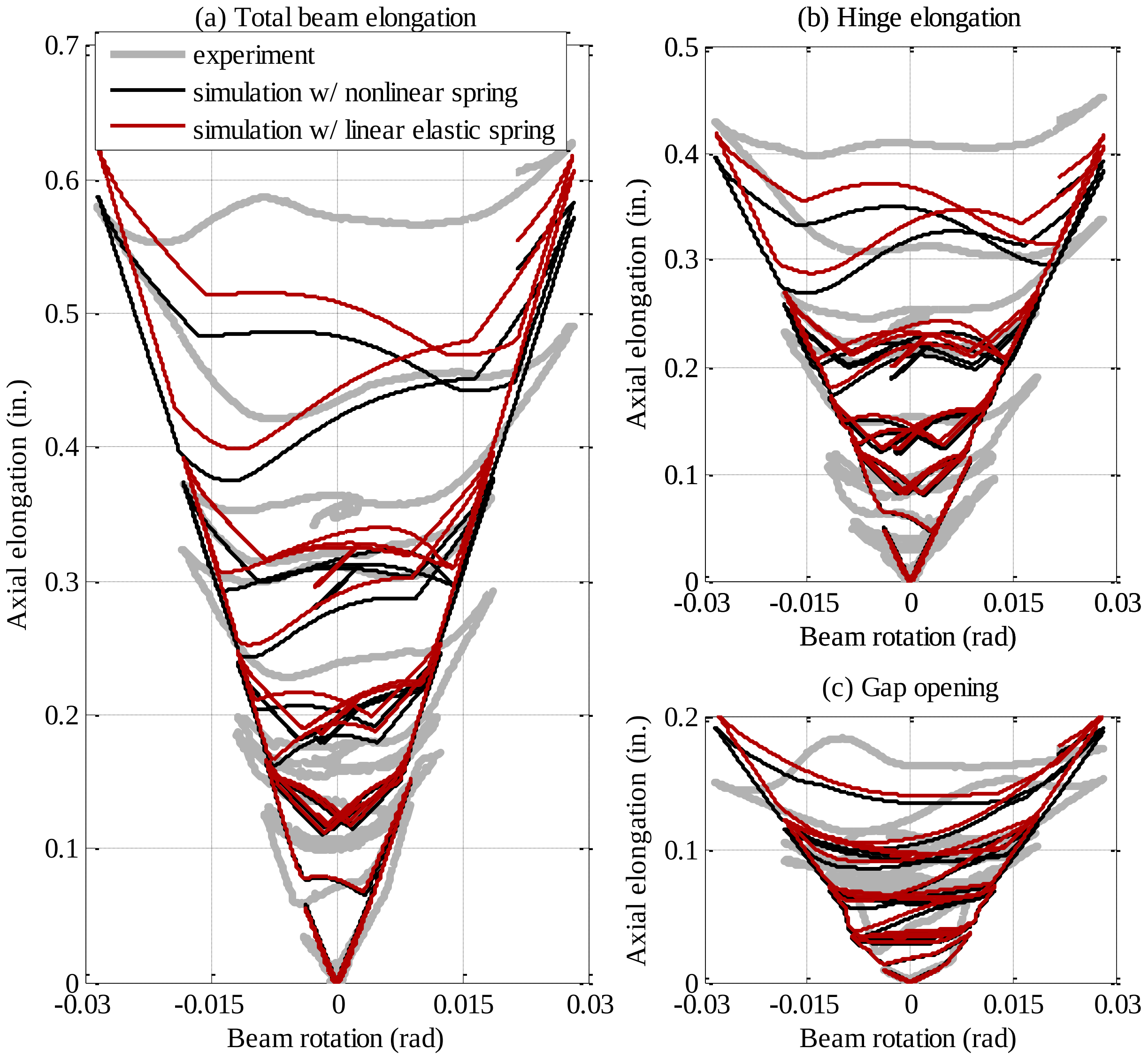

Figure 3.7.8. Beam elongation computed with distributed plasticity element models with shear spring.

Figure 3.7.8 compares the beam elongation computed with the numerical model of Beam 2 shown in Figure 3.5.1 using distributed plasticity elements and bar slip element with fiber section discretization with *ReinforcingSteel* and the nonlinear and linear elastic shear springs for Element 4. It can be seen that a beam model with nonlinear shear spring results in computing slightly smaller beam elongation compared that computed using the linear elastic spring. This is expected, because as the nonlinear spring becomes more flexible upon flexural yielding, the shear deformations have larger contribution to total tip displacement. This leads to smaller contribution of flexural deformations and proportional to these, smaller elongation. Nevertheless, both models (linear elastic shear spring and nonlinear shear spring) are consistent with the elongation levels recorded in the Beam 2 during the test.

Figure 3.7.9 shows the moment-rotation curves computed with the beam model using linear elastic shear spring and rigid shear spring (model including Elements 1-3 only). As before, the distributed plasticity elements and the corresponding fiber-based bar slip element utilize *ReinforcingSteel* material. The beam is subjected to loading history corresponding to the total deformation of Beam 2 (including all deformation components). The figures indicate practically identical moment-rotation curves are computed without utilizing any shear flexibility. This holds true in the present case because limited shear stiffness deterioration was noted in the portion of the test prior to buckling. Because ultimately, a numerical model is sought that would be utilized in nonlinear analyses of Chapters 4 through 6 to determine peak forces in the frames, shear strength degradation is conservatively assumed to not occur at any point during the loading history. Therefore, in absence of a more robust nonlinear shear model to be used with fiber-based models of reinforced concrete beams with flexure-dominant response, either a linear elastic shear spring based on equivalent beam shear stiffness or a rigid shear spring (that is, no shear behavior modeled) may be used in modeling of beams in frame structures of Chapters 4 through 6. The latter option is used to reduce efforts in calibration of shear spring properties.

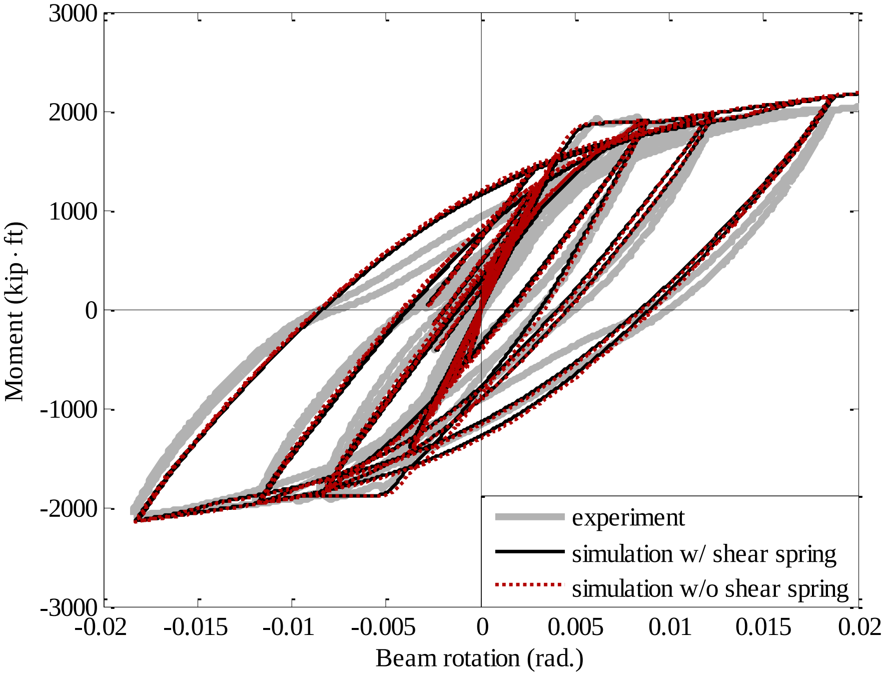

Figure 3.7.9. Effect of modeling shear spring on moment-rotation curves.

3.8 LUMPED PLASTICITY BEAM ELEMENT

The lumped plasticity model is based on the most common approach in modeling reinforced concrete beams and assuming that the inelastic deformations are confined to a finite length of the beam l_p concentrated at the beam support. This assumption is valid when the moment distribution along the beam is such that the maximum moment occurs at the end of the beam, as in a cantilever beam or a beam supported at both ends experiencing anti-symmetric bending (typical of beams in a frame with gravity loads sufficiently low to avoid the occurrence of irreversible hinges).

The plastic hinge model requires a definition of moment-curvature relationship of a beam section. To this end, a numerical model of representing a cross-section of Beam 2 and discretized as shown in Figure 3.4.1 using *Concrete03* and *ReinforcingSteel* materials calibrated as described in Sections 3.4.1 and 3.4.2 is subjected to monotonically increasing curvature. The resulting curve is plotted in Figure 3.8.1, together with a bilinear idealization used to develop the lumped-plasticity model. The idealization was done by establishing the elastic portion of the M_z-ϕ to represent the secant stiffness of the section. The yield point of the section is set at $M_{z,y}$ = 23,500 kip·in and ϕ_y = 0.000075 in^{-1}. The post-yielding portion of the curve was done by establishing a straight line from the yield point to the moment strength reached when the steel bar in tension reaches ε_u = 0.12 strain, which was arbitrarily selected to be a maximum usable strain. This instance corresponds to ϕ_u = 0.002866 in^{-1}, and $M_{z,u}$ = 32,800 kip·in, as shown in Figure 3.8.1.

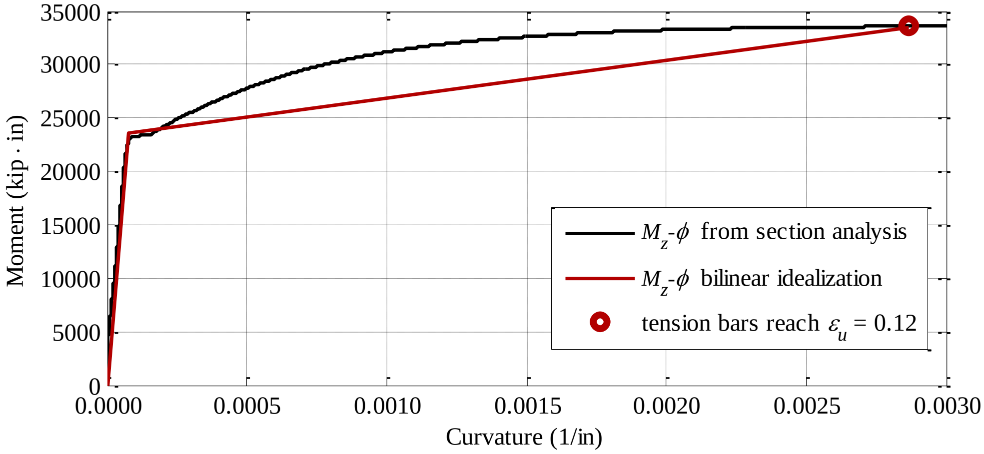

Figure 3.8.1. Moment-curvature relation computed for Beam 2 section with fiber discretization section model and corresponding bilinear idealization.

Under concentrated load acting at the tip of a cantilever beam with bilinear hardening section response such as the one shown in Figure 3.8.2(a), the moment and curvature distribution will approximately correspond to those shown in Figure 3.8.2(b) and (c), respectively. Thus, the beam tip deflection due to the yield and the ultimate moments can be expressed as:

$$\Delta_{f,y} = \frac{1}{3}\phi_y L_b^2 \quad \text{for } M(x{=}0) = M_y \tag{3. 11}$$

$$\Delta_{f,u} = \frac{1}{3}\phi_y (L_b - l_p)^2 + \frac{1}{2}\phi_y l_p{}^2 + \frac{1}{2}(\phi_u - \phi_y)(L_b - \frac{1}{3}l_p)l_p \quad \text{for } M(x{=}0) = M_u \tag{3. 12}$$

Where the length of the plastic hinge zone depends on the level of moment resisted at the root of the beam:

$$l_p = L_b(1 - \frac{M_y}{M_u}) \tag{3. 13}$$

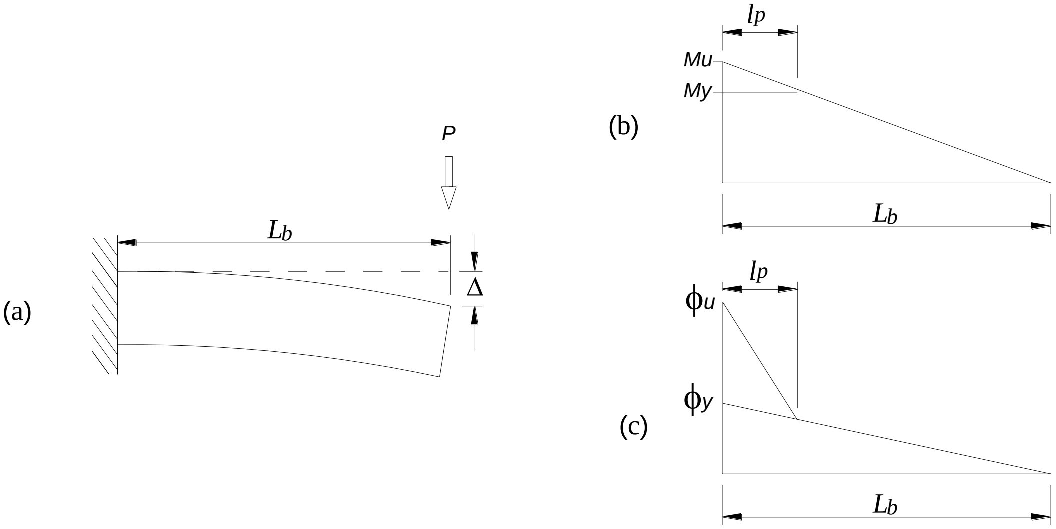

Figure 3.8.2. Curvature distribution in a cantilever beam with bilinear hardening moment-curvature section behavior under concentrated point load at the tip.

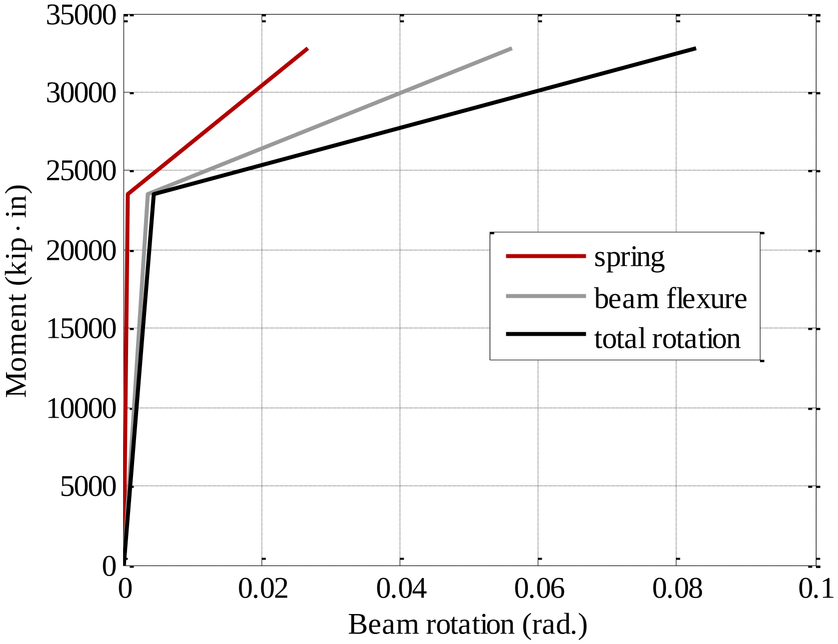

Figure 3.8.3. Moment-rotation envelope for bilinear beam force-displacement behavior.

Using these equations, the beam tip deflections at yield and at ultimate moment based on the curvature deformations within the beam are computed as $\Delta_{f,y}$ = 0.5625 in. and $\Delta_{f,u}$ = 8.42 in, which in terms of rotation can be expressed as $\theta_{f,y} = \Delta_{f,y}/L_b$ = 0.0038 (rad) and $\theta_{f,u} = \Delta_{f,u}/L_b$ = 0.0561 (rad) , respectively. The previous computations do not account for the fixed-end rotation from bar slip from the anchorage. These were calculated in Section 3.6.2 and were $\theta_{s,y}$ = 0.0008 and $\theta_{s,u}$ = 0.0267 for the bar stress at the yield and ultimate, respectively. Thus, by adding the chord rotation from curvature deformations and the fixed-end contribution, the total beam rotation at the instance of resisting the yield and ultimate moments at the support is $\theta_y = 0.0046$ and $\theta_u = 0.0828$, respectively. The bilinear moment-rotation relationship is plotted in Figure 3.8.3.

Figure 3.8.4 shows a lumped-plasticity model of a beam consisting of a plastic spring located at the beam support and an elastic portion of the beam of a length L_b = 150 in., which is equivalent to the distance between the load application point and the Beam 2 support in the test. The plastic spring is modeled as rigid for any moment less than the yielding moment. The elastic portion of the beam is set to have a flexural stiffness equal to $0.207E_cI_g$,(E_c = 4,463 ksi, I_g = 276,480 in^4). The factor $\alpha = 0.207$ was calculated by setting $\theta_y = M_{z,y}L_b/3\alpha E_cI_g$ which is the elastic beam chord rotation of an Euler-Bernouli beam deforming under a point load at the beam tip. Therefore, the flexural stiffness of the beam responding elastically ($M_{max} < M_{z,y}$ = 23,500 kip·in) is the slope of the moment-rotation relationship M-θ:

$$k_{el} = \frac{M_{z,y}}{\theta_y} = 5{,}108{,}695 \frac{\text{kip} \cdot \text{in}}{\text{rad}} \qquad 3.14$$

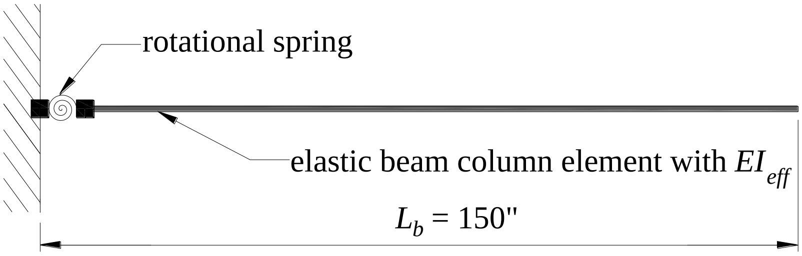

Figure 3.8.4. Representation of a cantilever beam with elastic element and plastic spring.

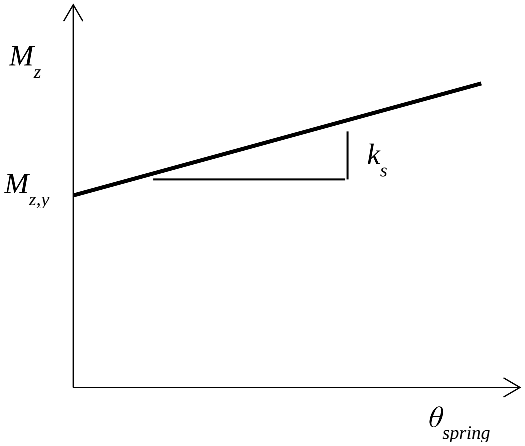

Figure 3.8.5. Rigid-hardening moment-rotation behavior of a spring element with stiffness k_s.

The plastic spring is represented by a rigid-hardening behavior depicted in Figure 3.8.5. The spring resists bending moments lower than $M_{z,y}$ = 23500 kip·in with no deformation. Once the moment in a spring exceeds the yielding moment, the rotation in a spring increases linearly with the moment at a rate k_s, which is the spring flexural stiffness. The coefficient k_s was calibrated to match the theoretically obtained hardening slope for Beam 2 shown in Figure 3.8.6. The post-yield slope of the moment-rotation curve of Beam 2 is approximately $k_h = 0.023k_{el}$ = 118,926 kip·in/rad. Since the beam and the spring act in series, the relationship between the stiffness of the rotational spring, the elastic element, and total beam stiffness is:

$$\frac{1}{k_{bm}} = \frac{1}{k_{el}} + \frac{1}{k_s} \qquad 3.\ 15$$

For the elastic portion of the loading, the second term on the right of the equation approaches zero since $k_s = \infty$ for $M_{z,y}$, and therefore the beam total stiffness is equal to the stiffness of the elastic element. For the post-yield portion of loading, the stiffness of the spring that would result in overall beam stiffness with hardening ration $k_{bm} = k_h$ is the following:

$$k_s = \frac{k_{el}k_h}{k_{el} - k_h} \qquad 3.\ 16$$

And thus, the stiffness of the rotational spring is set to k_s =121,760 kip·in/rad.

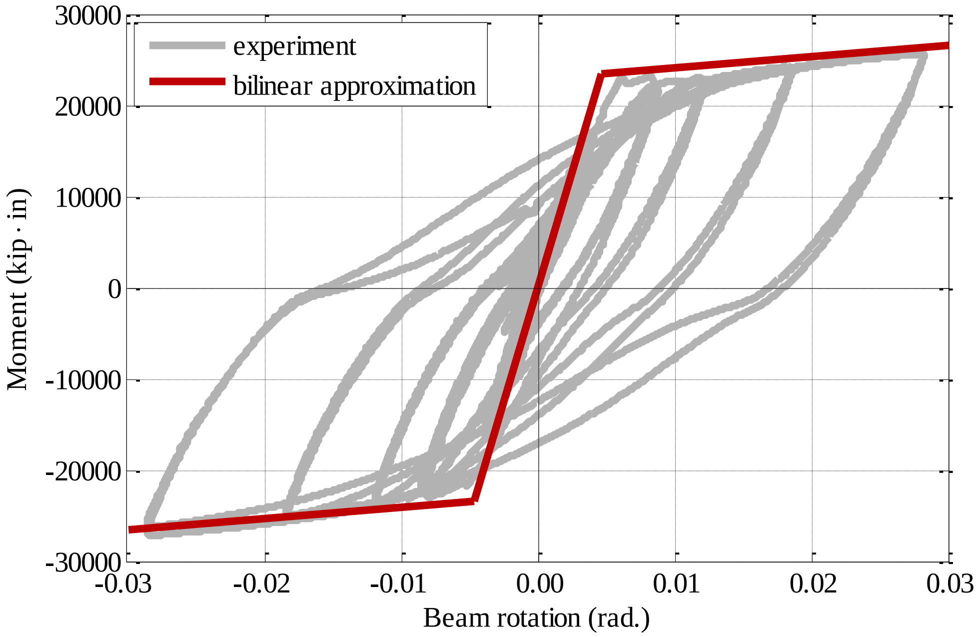

Figure 3.8.6. Bilinear approximation of the backbone curve of moment-rotation hysteresis for Beam 2.

Lumped plasticity beam model from Figure 3.8.4 is subjected to Beam 2 loading history which includes all deformation components. The moment-rotation hysteresis occurring in rotational spring is shown in Figure 3.8.7, while Figure 3.8.8 plots the numerical moment-rotation curves for the entire lumped plasticity beam model superimposed with the corresponding experimental curve for Beam 2. The initial stiffness and the yield moment is slightly overestimated by the lumped plasticity model, however the two curves show good agreement in the overall response.

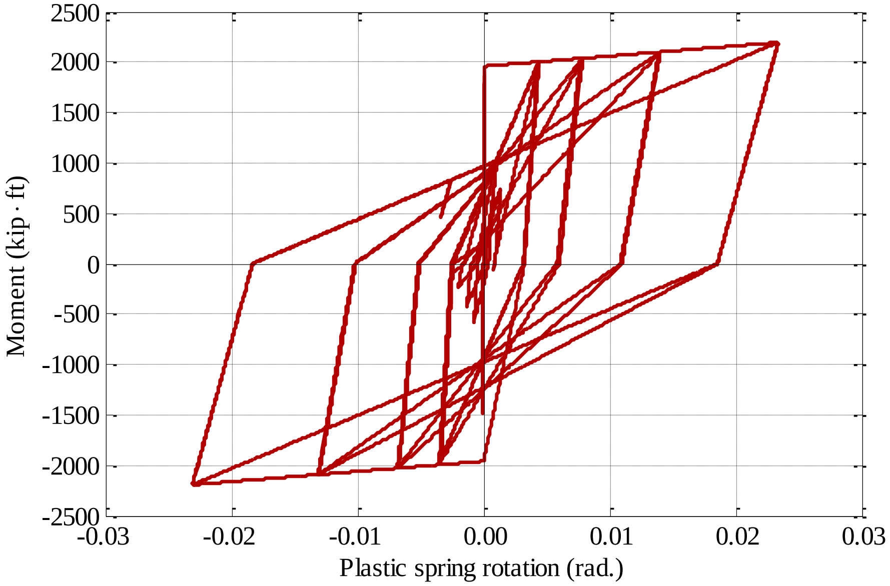

Figure 3.8.7. Bi-linear rotational spring hysteresis.

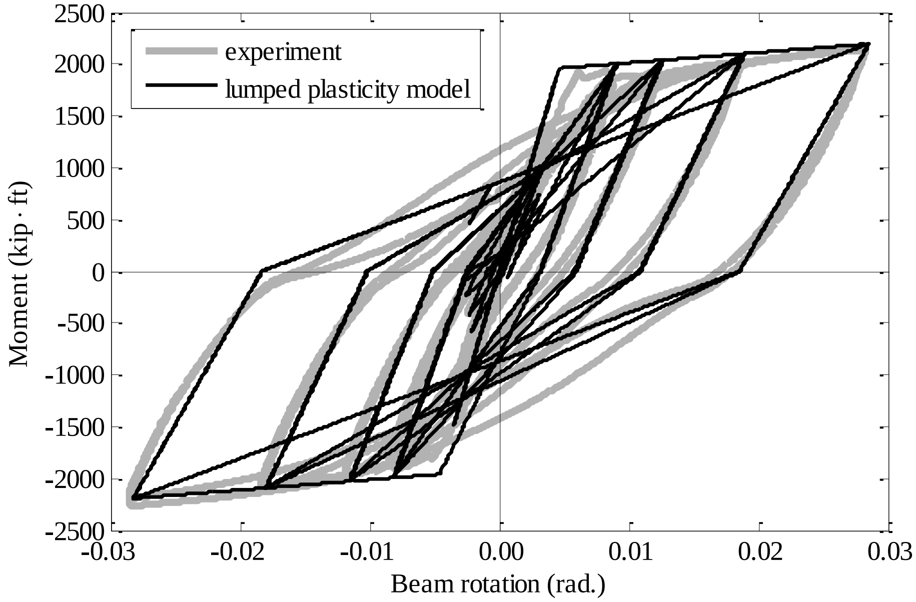

Figure 3.8.8. Lumped plasticity model moment-rotation hysteresis vs. experimental results.

CHAPTER 4

IMPACT OF BEAM ELONGATION ON SEISMIC RESPONSE OF REINFORCED CONCRETE SPECIAL MOMENT FRAMES

Elongation of reinforced concrete beams undergoing flexural deformation cycles has been known to increase force and deformation demands on columns in frames deforming under lateral loads. The kinematic interaction between the elongating beam and column under frame sidesway displacements leads to the largest deformation demand on the base exterior column sustaining the largest compression from the overturning moment. The beam elongation phenomenon gained much attention particularly in New Zealand where post-earthquake damage in frame buildings pointed to vulnerability of precast floor systems to collapse due to loss of support as the beams dilated axially.

Over the last few decades, much effort has been invested in estimating the amount of beam elongation (Fenwick and Megget 1993, Restrepo 1993, Matthews 2004, Lau et al. 2003, Lee and Watanabe 2003) and developing analytical tools to accurately simulate this mechanism in beams acting as a part of the frame system (Kabeyasawa et al. 2000, Lau et al. 2003, Peng et al. 2013). It was found that beam growth imposes additional shear forces onto exterior columns under compression, altering the shear force distribution from the one assumed in the absence of axial beam deformations (Fenwick et al. 1996, Kabeyasawa et al. 2000, Kim et al. 2004, Visnjic et al. 2012).

Current US design practice assumes that post-tensioning in the slabs cast monolithically with the beams restrains the axial beam growth and the phenomenon is not considered in the analysis and design of moment frames. This chapter demonstrates that restraining beam from elongating lowers the beam ductility and that the beam would elongate under typical levels of prestress in concrete slabs under seismic loads. Thus, beam elongation should be accounted for in the analysis and design of special moment resisting frames to ensure satisfactory global behavior under strong ground motion.

This chapter includes two short studies: the first one investigates the effects of the post-tensioned (PT) slab on beam elongation; the second one is a parametric study of multiple one-story frames with varying geometry and beam sizes to note the variation of impact of beam elongation on different frame configurations.

4.1 EFFECT OF PT SLAB ON BEAM ELONGATION

Special moment resisting frames in perimeter configuration, such as the one shown in Figure 4.1.1, are commonly selected for buildings having 20 or more stories in height. The SMRFs are placed along the two principal directions of the building and are assumed to solely resist the lateral load. The gravity framing is provided with sufficient ductility to accommodate earthquake-induced lateral deformations while fully sustaining the gravity loads from the tributary floor areas. In such systems, concrete slabs are typically cast monolithically with SMRF and gravity framing beams and are generally post-tensioned to reduce out-of-plane slab deflections which allows for larger spacing between gravity columns and also smaller slab thickness necessary to provide acceptable levels of deflection for serviceability requirements. Unbonded tendons are placed in the principal directions of a concrete slab either at approximately even spacing in one direction and clustered in several locations along the other principal direction, as shown in Figure 4.1.1.

If the PT slab is idealized as having point loads acting at the tendon anchorage points (Figure 4.1.1), then based on Saint-Venant's principle, uniform axial compression can be assumed to act across the slab away from the edges. The ACI 318 (ACI 2014) requires the post-tensioning to provide minimum 125 psi prestress on the slab (excluding the area of beams cast monolithically), but the values of prestress in common design practices often reach up to 400 psi. Under such configuration, it is assumed that the slab acts as a diaphragm in transmitting in-plane seismic forces to the outer SMRFs and because of its high axial stiffness in the direction of loading, the gravity and seismic framing is assumed to have little or no relative movement in this direction (the diaphragm however may or may not be assumed rigid in the horizontal direction perpendicular to the lateral load line of action).

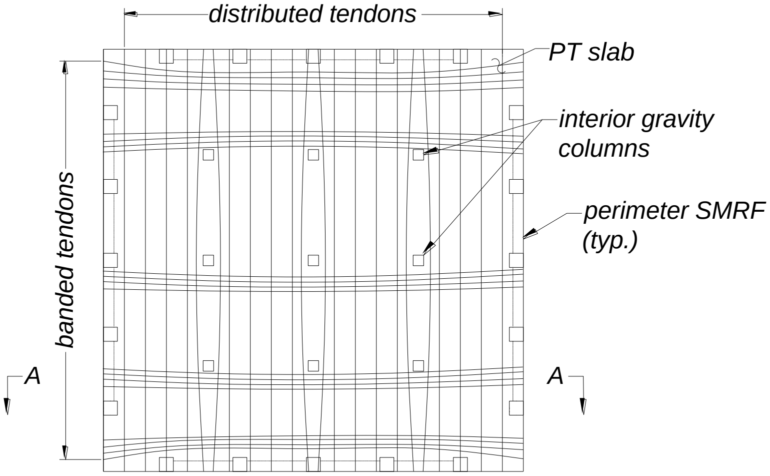

Figure 4.1.1. Floor plan of typical perimeter SMRF building with post-tensioned slab (Section *A*-*A* shown in Figure 4.1.6).

When analyzing SMRF buildings with post-tensioned (PT) slabs, the horizontal diaphragm is modeled either explicitly by invoking the appropriate geometric constraint or implicitly by modeling beams and/or slab with rotational hinges and a de-coupled axial spring with high elastic stiffness. Thus, the implied notion of common design practice is that axial slab rigidity in the presence of PT slab would suppress the beam growth – at least to a level where the beam growth itself would not impose additional column shears or deformations. Laboratory tests of beam-slab subassemblies, however, have indicated that reinforced concrete slab without prestressing does not provide restraint against beam axial elongation (Restrepo 1993). On other hand, the compressive stress added by post-tensioning in the slab is assumed to provide sufficient resistance to the beam axial elongation, but no experimental study has confirmed the extent of this restraint from post-tensioned slabs of common SMRF frame arrangements used in the United States.

The present numerical investigation is aimed at two goals. First, a short numerical exercise is used to show that allowing for beam to elongate is imperative to beam ductile response. The second is to demonstrate the effect of slab post-tensioning on beam elongation under for the lower and upper bound of prestress levels typically used in SMRF construction. Both topics are addressed using the same archetype beam models as described next.

4.1.1 BEAM SECTION CONFIGURATIONS

Three different beam-slab configurations shown in Figure 4.1.2 are considered. The first is the Plain Beam (Figure 4.1.2 [a]) and represents a SMRF beam cast with no slab. This configuration served as the basis for numerical model development in Chapter 3 and is used here to demonstrate the implications of suppressing the beam elongation (described in Section 4.1.2). The dimensions, reinforcement layout, and material properties were selected to match the Beam 2 in Chapter 2 which was used to validate the numerical model. This beam cross section was 30 in. x 48 in. and contained five No. 11 longitudinal bars both at the top and the bottom, resulting in longitudinal reinforcement ratio $\rho = \rho' = 0.59\%$. Measured yield strength of steel was $f_y = 73$ ksi and concrete compressive strength was $f'_c = 6.1$ ksi. The beam was tested in cantilever configuration with actuator force applied 150 in. from beam support, resulting in the shear span ratio 3.1.

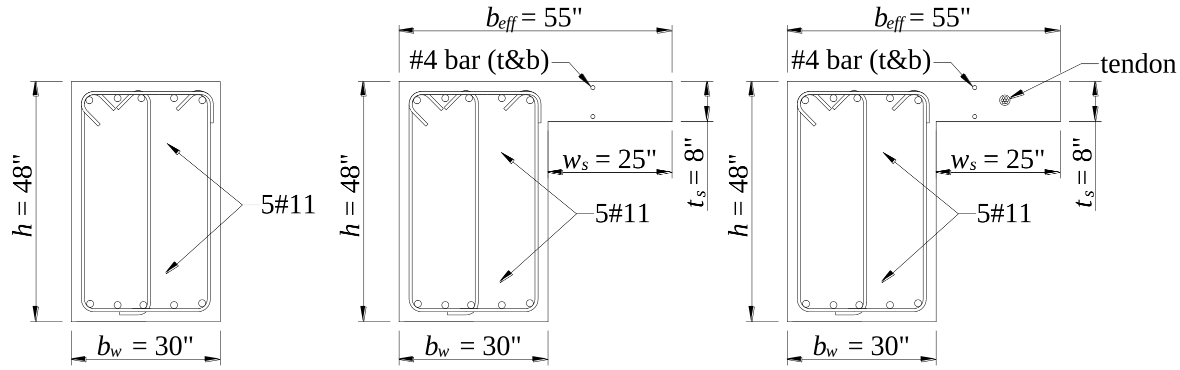

(a) Plain Beam (b) Beam w/ RC slab (c) Beam w/ PT slab

Figure 4.1.2. Three beam configurations considered.

Portion of the slab cast monolithically with the beam acts as a beam flange and increases the beam flexural stiffness and strength. Two additional SMRF beam configurations are used to investigate the effects of slab and also post-tensioning on the elongation of the beam and the results are presented in Section 4.1.3. The two configurations are shown in Figures 2(b) and (c) and comprise of the beam identical to Plain Beam (Figure 2[a]), but considering the portion of the monolithically cast reinforced concrete slab without and with post-tensioning, respectively. As the two limiting values, this study considers effects of slab post-tensioned to provide 125 ksi and 400 ksi slab prestress.

When the slab is cast only on one side of the beam, such as in the perimeter SMRF beams, the slab overhang acting as a flange is approximated by the ACI 318 as the minimum of $6t_s$ (t_s = slab thickness), one half the clear distance to next web, or one-twelfth the span length of the beam. In all cases where slab is considered (Figure 2[b] and [c]), the size of the slab considered as the effective flange width is computed in accordance with the ACI 318-14, which results in the 25 in. overhang and 55 in. overall effective beam flange width. ACI 318 states that this does not apply to prestressed concrete slabs, however, it is deemed reasonable in this study to estimate the effective flange width of the beam using the same expression.

4.1.2 IMPLICATIONS OF AXIAL DEFORMATION RESTRAINT ON CYCLIC RESPONSE

The purpose of this section is to demonstrate that allowing for beam to elongate is imperative to beam ductile response. A numerical model of Plain Beam (Figure 4.1.2[a]) used for this exercise is shown in Figure 4.1.3. The beam model consists of two distributed plasticity elements (Elements 1 and 2) restrained from axial deformation by a pin support at Node 3, as shown in the schematics in Figure 4.1.3. All three degrees of freedom at Node 1 are also fixed. The zero-length element representing the bar slip is not included in this portion of the study in order to avoid numerical deformation localization, as will become clear shortly. The length of Element 1 is 48 in., while the length of Element 2 is 102 in. Each of the two elements contains 2 numerical integration points. Thus, the first integration point of Element 1, which represents the plastic hinge region of length l_p, has a tributary length of $l_p = h_b/2 = 24$ in. Both elements have corotational formulation.

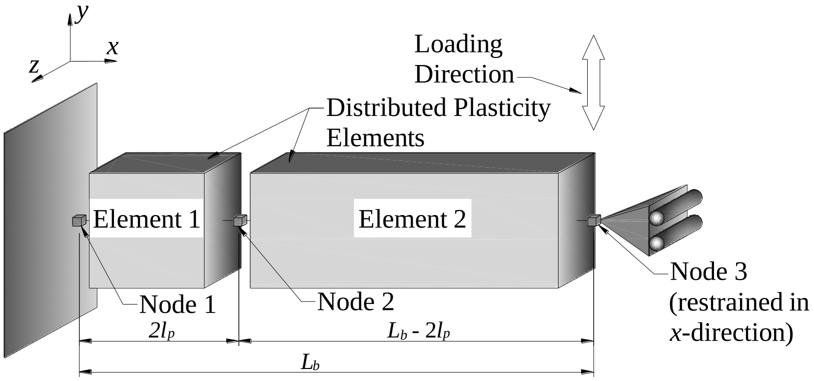

Figure 4.1.3. Numerical model of beam restrained from elongating.

Figure 4.1.4(a) and (b) plot the beam rotation versus the axial force and moment, respectively, resisted by the beam undergoing deformation cycles of increasing amplitude while being prevented from elongating along the neutral chord position. The cyclic displacement history discussed in Chapter 2 and shown in Figure 2.6.1 is applied to Node 3. For comparison, Figure 4.1.4 [b] shows also the moment-rotation response for the Plain Beam if it is allowed to dilate axially. While the longitudinal tension reinforcement in the unrestrained beam yields around the beam rotation of 0.003, the restrained beam does not reach the "yield" point until the approximate rotation of 0.008 (Figure 4.1.4[b]). For the cycles corresponding to beam rotation amplitude less than approximately 0.008 the resisting axial force and moment in the restrained beam are increasing with the increasing drift. The increase in the flexural resistance occurs as a result of the increase in axial force within the beam, which acts as a tension-controlled member up to the point where axial load causes the concrete to crush before the yielding of tension steel occurs.

Upon reaching the chord rotation of 0.008, concrete fibers within the plastic hinge begin to soften and the beam begins to lose the axial and flexural resistance. This means that the beam is not responding as a tension-controlled member. Rather, brittle failure with concrete crushing as the yielding mechanism occurs at relatively small rotation levels implying low, if any, ductility in the beam (Figure 4.1.4[b]). Looking at the Figure 4.1.4[b], may lead one to think that the restrained beam cyclic response would follow that of the unrestrained beam once the crushing occurs at 0.008 rotation, as the two response curves converge for rotation amplitudes exceeding 0.01. However, this would likely not be true, because in the physical specimen, the loss of concrete core would lead to longitudinal bar buckling, or shear sliding along the plane where concrete was crushed, or another failure mode, which was not considered in this numerical model. Thus, the response curve of restrained beam shown in Figure 4.1.4[b] is only to be used for conceptual understanding of how the beam behavior may be affected by the axial restraint.

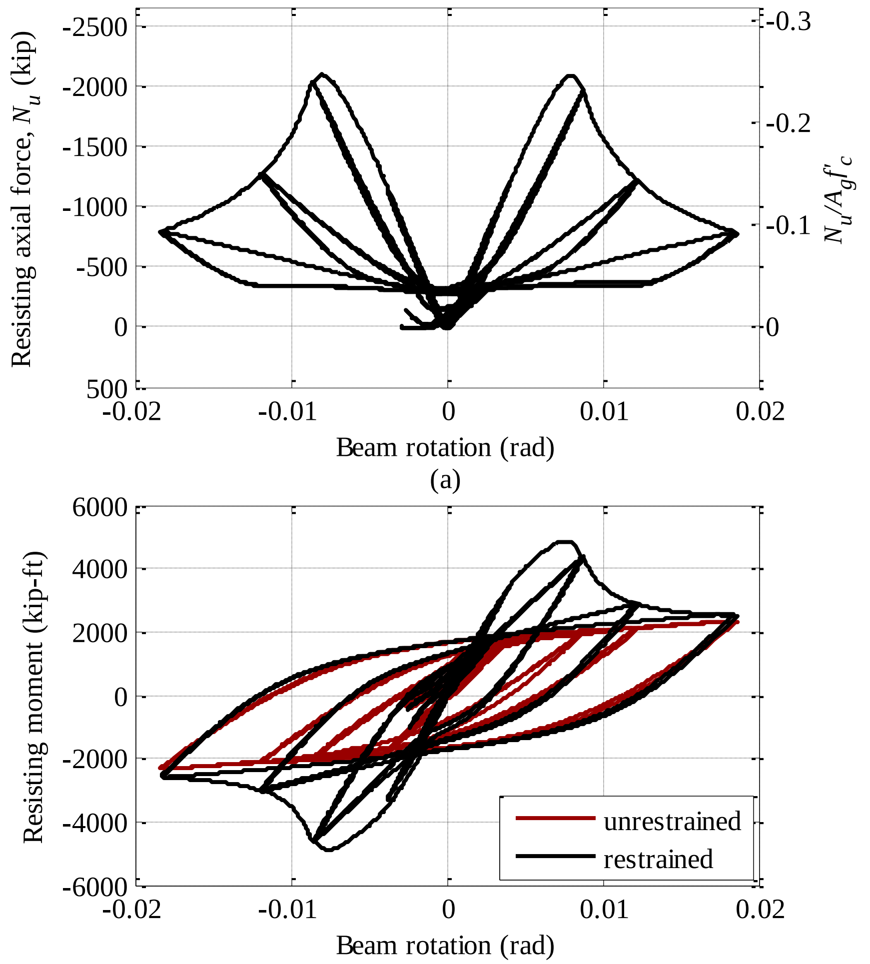

(a)

(b)

Figure 4.1.4. (a) Axial force and (b) moment resisted by a beam during lateral deformation cycles with suppressed axial deformation.

This numerical exercise underlines two important points. Restraining the beam from elongating during nonlinear cyclic response would lead to brittle failure that is controlled by the concrete crushing, rather than the steel yielding. Consequently, the ductile response of the beam is inherently accompanied by the axial dilation and thus this phenomenon will be present in any reinforced concrete SMRF deforming nonlinearly under seismic forces.

In most frame tests reported in literature, where the columns are under relatively low axial load and have smaller sections, the axial stiffness of the elongating beam is higher than the flexural stiffness of the columns and the beam pushes the columns out. In tall RC SMRFs column sizes often reach or exceed 48 in. depth and carry large compressive load both due to gravity and lateral load-induced overturning moment. Thus the columns of tall SMRFs are notably stiffer and may largely restrain the beams from axial elongation, impacting the SMRF beam ductility. This, however, is dependent on the concrete confinement level within the beam and the relative strengths of beams and columns, so conclusions cannot be made based only on numerical simulations. Laboratory tests are needed to examine the performance of beams and columns under kinematic interaction in tall SMRFs.

4.1.3 BEAM RESPONSE TO CYCLIC LOADING IN THE PRESENCE OF PT SLAB

This section focuses on investigating the extent to which the PT slab cast uniformly with the beam affects the beam elongation. This is done by comparing the cyclic response of several variations of two section configurations shown in Figure 4.1.2: a) beam with cast-in-place slab, which provides a baseline response for comparison (shown in Figure 4.1.2[b]), b) the same beam with added post-tensioning of f_{pc} = 125 psi on the slab (shown in Figure 4.1.2[c]), and c) the same beam with increased post-tensioning of f_{pc} = 400 psi (also shown in Figure 4.1.2[c]). The schematics of a numerical model used in this investigation in shown in Figure 4.1.5.

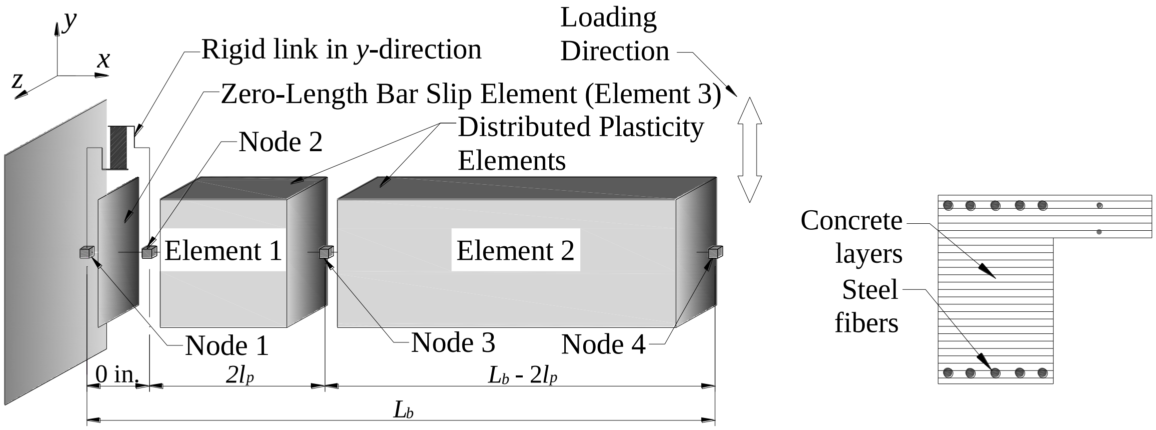

Figure 4.1.5. Numerical model schematic.

Numerical model of the cross section has the same characteristics described in Section 3.4 (Chapter 3), using *ReinforcingSteel* and *Concrete03*. The PT tendon depicted in Figure 4.1.2(c) is not explicitly modeled; rather, an axial force producing the stress σ_{avg} is imposed on the beam and is held constant during all cycles of deformation. The stress σ_{avg} is related to the slab prestress, f_{pc}, as $\sigma_{avg} = f_{pc}(A_{slab}/A_{total})$ where A_{slab} and A_{total} signify the cross-sectional area of the slab only, and slab including the beams, respectively, as shown in Figure 4.1.6.

Section *A*-*A*

Figure 4.1.6. Definition of the slab area and the total cross section area of slab and beams. See Figure 4.1.1. for reference on the floor plan.

The beams with three different cross section variations are first subjected to a monotonically increasing tip displacement and the response is logged in plots shown in Figure 4.1.7. As a reference, the plot in the figure shows also the monotonic moment-rotation curve for a Plain Beam (Figure 4.1.2[a]). The presence of reinforced concrete slab only slightly alters the beam strength, as can be seen in Figure 4.1.7. The additional post-tensioning stress causes the beam initial stiffness to increase, and also results in larger flexural yield strength of the beam. For the beam and slab configuration at hand (see Figure 4.1.2[b] and [c]), the post-tensioning stress of 125 psi increases the yield moment by a factor of 1.15, while the post-tensioning stress of 400 psi increases it by a factor of 1.5.

There is an important implication in this observation. SMRF reinforced concrete beams are designed for shear based on capacity design principles which assume that the beam has reached its moment strength at both ends, and thus the ultimate shear $V_u = V_{pr}$ is computed as:

$$V_{pr} = \frac{M_{pr,1} + M_{pr,2}}{l_n} \pm \frac{w_u l_n}{2} \qquad 4.1$$

Where $M_{pr,1}$ and $M_{pr,2}$ are the probable moment strengths at either end of the beam, l_n is the beam clear span, and w_u is the distributed gravity load calculated using the appropriate load combination. Based on the observations made in Figure 4.1.7, for a range of post-tensioning levels, the M_{pr} of the beams considered in this study increases by a factor ranging between 1.15-1.5. Thus, the design shear in the beams is also going to increase in the presence of post-tensioned slab. To avoid potential shear failures in SMRF beams, it is important to consider the M_{pr} levels developed in the beams after the post-tensioning is applied.

Next, the three beams are subjected to a cyclic loading history plotted in Figure 2.6.1 in Chapter 2 and the axial elongation versus the beam rotation is plotted in Figure 4.1.8. Presence of reinforced concrete slab results in an elongation that is slightly higher in one loading direction, as a result of asymmetry in reinforcement and also the concrete about the neutral axis (note that the beam elongation in the nonlinear range is expected to be asymmetric because material fibers will exceed elastic strains first in one direction despite the symmetric reinforcement configuration). Overall the beam elongation is only slightly affected by the presence of reinforced concrete slab with no post-tensioning.

The addition of 125 psi prestress decreases the level of beam elongation at a neutral position (zero rotation) to 0.6 of the elongation in the same beam with no PT slab present. However the elongations are reduced only by 10% at the maximum beam rotation (Figure 4.1.8). Further increase of post-tensioning to 400 psi results in reduction of beam elongation at a neutral position to 0.18 of the elongation when no post-tensioning is present. This increased post-tensioning leads to only 25% reduction in beam elongations occurring at the extreme beam deflections (Figure 4.1.8).

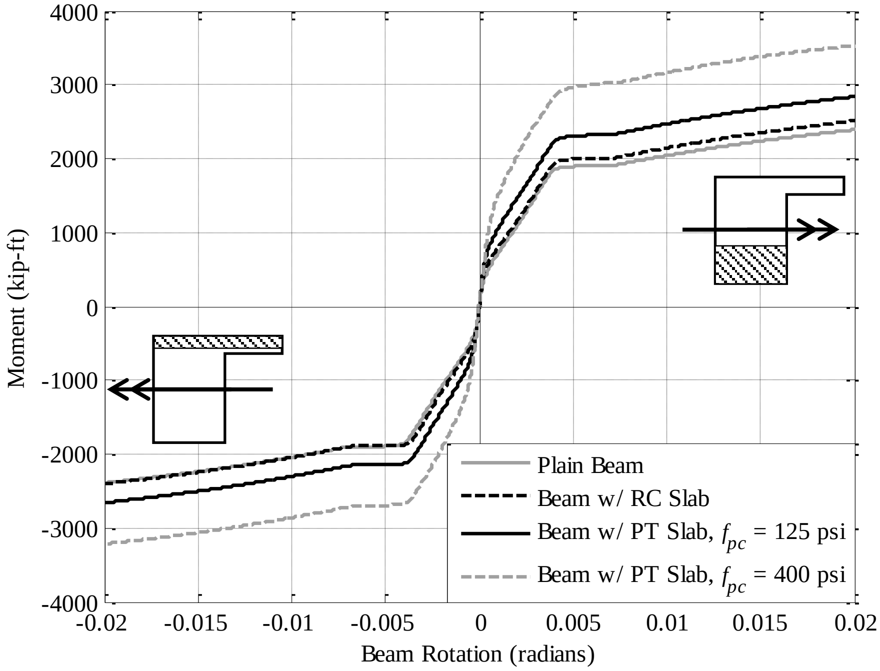

Figure 4.1.7. Moment-rotation response variation with presence of slab and post-tensioning.

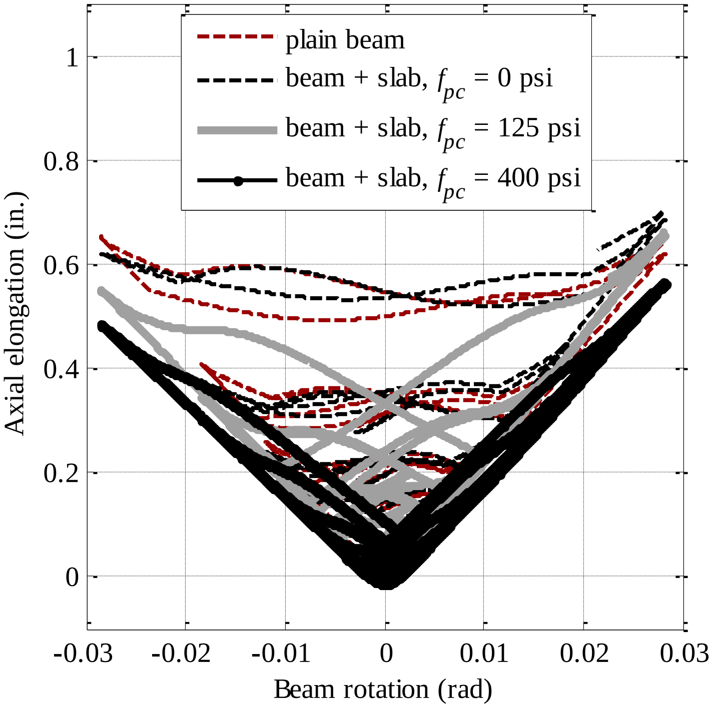

Figure 4.1.8. Axial elongation variation with presence of PT slab.

The trends observed are consistent to those obtained experimentally for RC beams with constant nonzero axial force applied (Issa et al. 1997, Matti et al. 1998, Cooper et al. 2005). Thus, it is clear that the common range of axial compression in beam provided by the post-tensioned slab does not suppress the beam growth, contrary to the common assumptions in the current U.S. design practice.

4.2 IMPACT OF BEAM ELONGATION IN MULTI-BAY FRAMES

Previous studies (Kabeyasawa et al. 2000) found that the additional shear force in the exterior columns imposed by the elongating beam is affected by the number of bays and beam depth. To examine the effect of beam elongation on column shear distribution in multi-bay reinforced concrete frames in the context of US state of practice, a series of single story RC frame numerical models are subjected to pushover analyses. One of the archetype frames was also subjected to post-tensioning force in order to examine the extent to which a presence of a PT slab would alter the shear distribution in the columns impacted by a beam elongation.

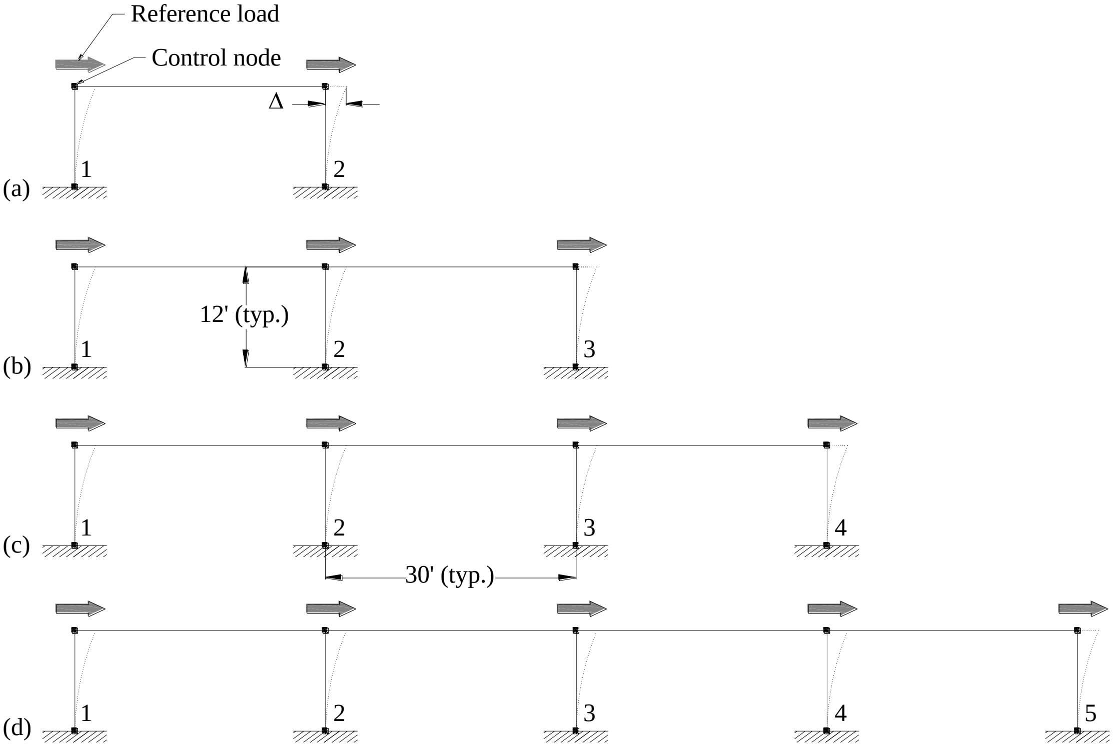

Figure 4.2.1. Frame geometry of single-story multi-bay model frames.

The archetype structures selected for this short parametric study consist of 1-, 2-, 3-, and 4-bay single story frames, depicted in Figure 4.2.1. All frames measure 12 ft (144 in.) in height (H_{frame}) and have bays that have length of L_{bay} = 30 ft The dimensions of the beams and columns are selected to represent those encountered in taller SMRF buildings, rather than those typically selected in single-story structures. All beams are identical in cross-section size and strength and have been assigned the properties of Beam 2 studied in Chapter 2. That is, the beam cross section measures 30 in. x 48 in. and has the same amount of longitudinal reinforcement (ρ_l = 0.0058), with all the material properties matching those in Beam 2. Because the bay length is twice as long as the cantilever Beam 2 discussed in Chapter 2, the beams in single-story archetype frames also have the same shear span ratio of 3.1. The columns of all four frames have square cross sections which measure 48 in. x 48 in. The concrete properties in columns were also selected to match the average concrete strength of Beam 2 (Chapter 2).

4.2.1 KINEMATIC RELATIONS FOR HORIZONTAL BEAM ELEMENTS IN FRAMES UNDER SMALL DISPLACEMENT LINEARIZATION

To aid the discussion presented in this chapter and also in Chapters 5 and 6, basic kinematic relations between the beam deformations and the global displacements of a planar frame structure are defined here. Figure 4.2.2 shows a single story one-bay frame displacing in a simple sidesway motion. The nodes are shown as black squares and the undeformed structure is shown with a dotted line. The tangent lines to the deformed beam shape at each node are also drawn with a dotted line. Terms U_1-U_6 represent the global degrees of freedom (DOFs) at the nodes with no restrained motion; those corresponding to the nodes at the base of the structure are omitted from the diagram for clarity. The arrows corresponding to DOFs point in the positive direction for each degree of freedom.

Beam deformations are defined as follows: v_ε is the axial deformation, v_i and v_j are the beam chord rotations at ends *i* and *j*, respectively. Chord rotations are defined as the angle between the element chord (defined as the line segment connecting the structural nodes in the *deformed* state). The chord rotations v_i and v_j as depicted in Figure 4.2.2 show the elastic deformations of the beam, but they refer to total beam chord rotation which also contains a plastic hinge rotation upon beam yielding. The v_i and v_j correspond to rotations $\theta = \Delta/L_{beam}$ in a cantilever beam laboratory setup, such as the one in Beam 1 and Beam 2 discussed in Chapters 2 and 3.

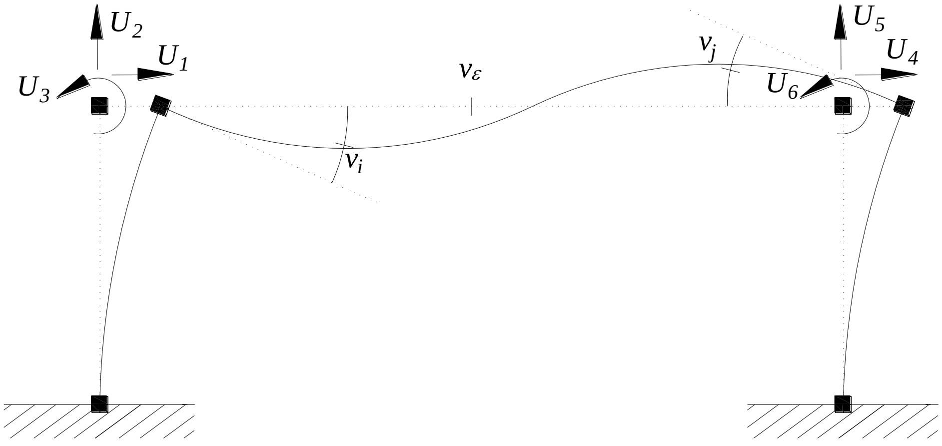

Figure 4.2.2. Kinematics of a beam in a two dimensional frame.

Under the small displacement assumption, the basic kinematic relations for a beam in a structure in Figure 4.2.2 are the following:

$$v_\varepsilon = U_4 - U_1 \tag{4.2}$$

$$v_i = U_3 - \frac{U_5 - U_2}{L_{bay}} \tag{4.3}$$

$$v_j = U_6 - \frac{U_5 - U_2}{L_{bay}} \tag{4.4}$$

When joint rigidity is taken into account by including the rigid offsets of length l_r in the beam at both ends, as shown in Figure 4.2.3, the compatibility equations for beam chord rotations under small displacements approximation become:

$$v_i = U_3 - \frac{U_5 - U_2}{L_{beam}} + \frac{l_r}{L_{beam}}(U_3 + U_6) \tag{4.5}$$

$$v_j = U_6 - \frac{U_5 - U_2}{L_{beam}} + \frac{l_r}{L_{beam}}(U_3 + U_6) \tag{4.6}$$

where $L_{beam} = L_{bay} - 2l_r$. Here it is assumed that the rigid offsets at both ends have equal lengths, which is the case in all frames considered in this dissertation.

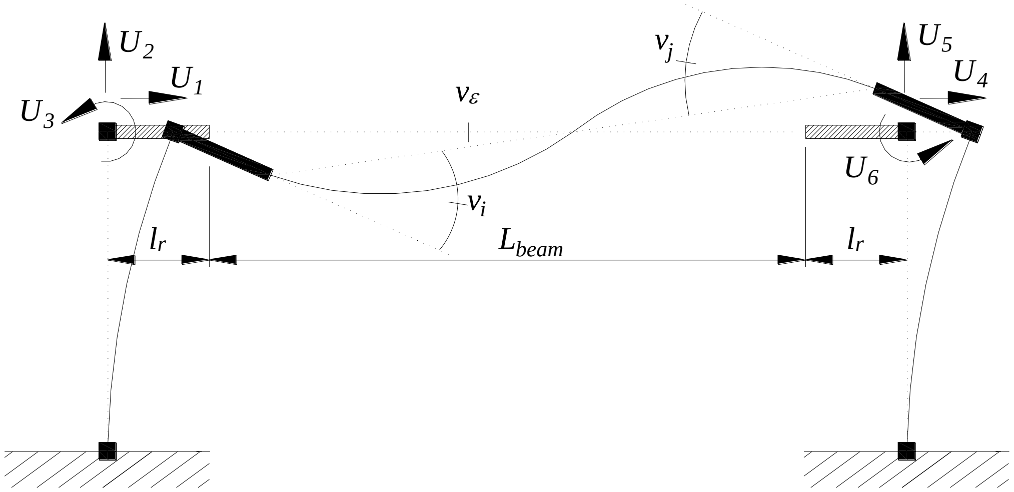

Figure 4.2.3. Kinematics of a beam in two-dimensional frame with the presence of rigid offsets.

4.2.2 NUMERICAL MODELS

All analyses are performed on OpenSees. The schematics of the numerical models employed for this parametric study are shown in Figure 4.2.4. The first model, shown in Figure 4.2.4(a), serves as a basis for frame behavior with no beam elongation impact. It is used only to compare the single story frame behavior of a one-bay frame, as discussed in Section 4.2.3. The second model, shown in Figure 4.2.4(b), is used for all other analyses, where beam elongation is taken into account.

In both frame model types shown in Figure 4.2.4, columns are represented with elastic elements to isolate the effect of kinematic interaction of beam and columns. That is, the flexural stiffness of the exterior columns will not be affected by the difference in axial load, and thus the columns will resist the same shear if displaced by the same amount at the top joint (in both translation and rotation). The flexural section stiffness of the elastic elements representing the columns is $E_cI_{eff} = 0.5E_cI_g$, which is the value typically assigned in elastic analysis of reinforced concrete columns. Modulus of elasticity of concrete E_c is arbitrarily selected to match that measured in Beam 2 in Chapter 2. Neither frame model considers the joint rigidity, i.e. the beams do not have rigid offsets at either end.

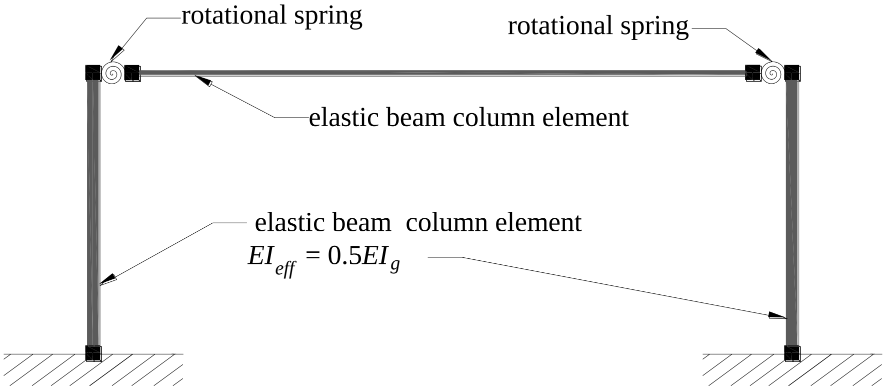

(a)

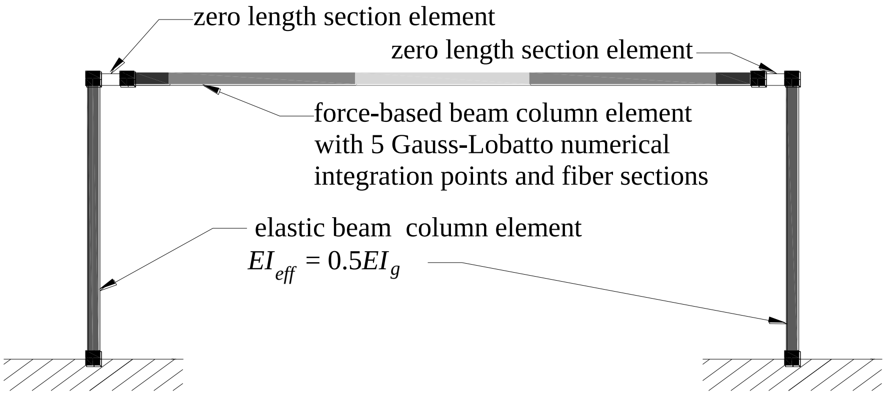

(b)

Figure 4.2.4. Schematic of a numerical model: (a) "control" frame with no beam elongation simulated and (b) frame with simulated beam elongation (each tributary length of the beam element integration point is hatched with a different color).

In the first frame model (Figure 4.2.4[a]), beam is represented with an elastic Euler-Bernoulli element in series with the nonlinear rotational springs at beam ends. Both the elastic frame element and the nonlinear springs were calibrated in Chapter 3 to adequately simulate the nonlinear response of the reinforced concrete beam with the design parameters selected in this study. For details on calibration of this beam model, refer to Section 3.8 in Chapter 3.

In the second frame model (Figure 4.2.4[b]), beams are represented with force-based beam-column element using fiber sections. The element is discretized with 5 Gauss Lobatto integration points along the element length, such that the end points have tributary length of $0.05L_{beam}$. For the given beam dimensions, this corresponds to $0.31h_b$ (h_b = beam height) as is generally in the range of the plastic hinge lengths observed in physical specimens. The fiber section discretization is described in Section 3.4 and depicted in Figure 3.4.1. Present model considers steel model based on Giufre-Menegotto-Pinto formulation, which is discussed in Section 3.4.1. Concrete is modeled with *Concrete03* with stress-strain relationship assumed as perfectly plastic once peak compressive stress is reached in order to avoid numerical localization problems, discussed in Section 3.4.2 in Chapter 3. The effects of reinforcement slip from the columns are considered using the zero-length section element with fiber discretization, as described in Section 3.6 in Chapter 3.

Archetype frames are subjected to a monotonically increasing lateral load using displacement control algorithm to a maximum story drift ratio measured at the horizontal DOF in the leftmost column (labeled as Column 1 in Figure 4.2.1), where the displacement is monitored during the analysis. Reference load is assigned to all horizontal DOFs, as shown in Figure 4.2.1 and gravity load is not assigned to any of the frames.

4.2.3 BEAM ELONGATION IMPACT IN A SINGLE-BAY ARCHETYPE FRAME

This portion of the investigation considers a single-bay frame response to monotonic pushover with and without consideration of beam axial lengthening. The frame models shown in Figure 4.2.4 are analyzed under increasing lateral displacement up to 0.04 story drift ratio, defined as the displacement U_1 (see Figure 4.2.2) normalized by the height of the frame, H_{frame} = 144 in.

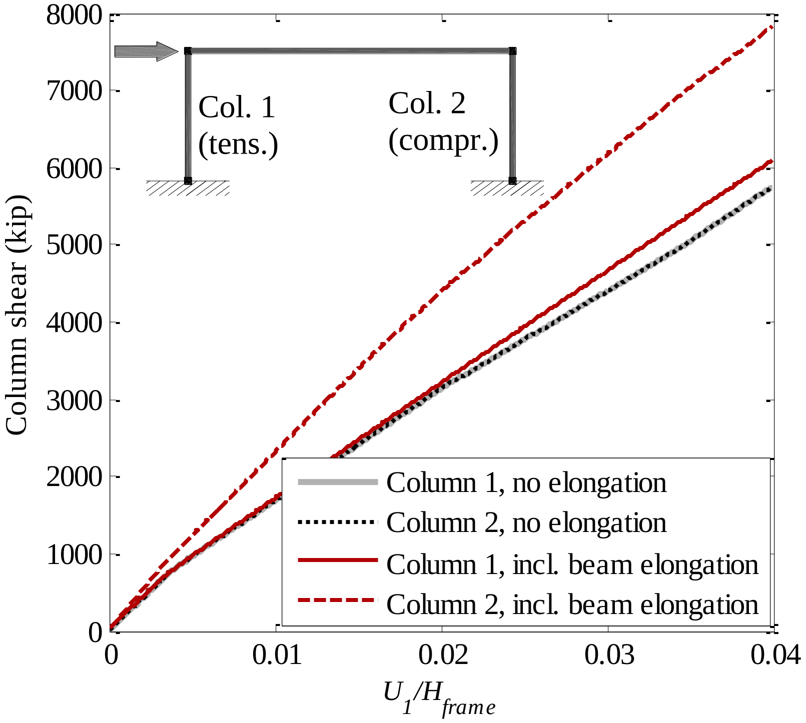

Figure 4.2.5. Comparison of column shear developed in single-story frames with and without considering the kinematic interaction of elongating beam with the columns.

Figure 4.2.5 plots the shear force in the columns of the single-story frame as a function of a horizontal story displacement. The column shear is identical in both Columns 1 and 2 when beam elongation is not considered. When beam elongation is modeled, the shear in the column on the compression side of the frame (Column 2), $V_{col,2}$, increases compared to the column shear $V_{col,1}$ on the tension side of the frame (Column 1). The difference in shear force between the two columns also increases with the lateral drift. It should be noted that the total resisting shear in a single story frame ($V_{frame} = V_{col,1} + V_{col,2}$) is higher in the frame with a distributed plasticity beam model, which is due to differences in beam stiffness computed with different numerical models, and not the function of beam elongation.

To analyze the beam elongation impact on frame structures, results from the pushover analysis of a single story frame considering beam elongation are studied further. Figure 4.2.6 plots the joint displacements as a function of lateral drift measured at a joint at the Column 1 on the left of the frame (DOF labeled as U_1 in Figure 4.2.2). The horizontal translations of DOFs U_1 and U_2 are plotted in Figure 4.2.6(a), while the rotations at DOFs U_3 and U_6 are shown in Figure 4.2.6(b). As evident in these plots, the beam lengthening causes the lateral translations to increase at the joint on top of Column 2. Column 2 is thus further displaced to the right, causing larger rotations at the top (DOF U_6), than those experienced by Column 1 at the top (DOF U_3).

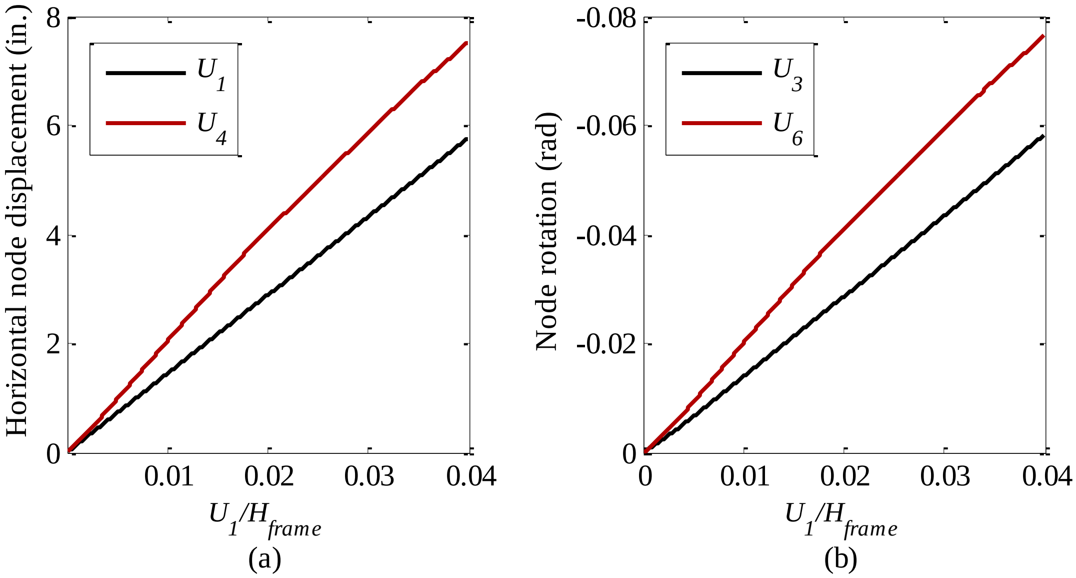

(a) (b)

Figure 4.2.6. Difference in node displacements at columns 1 and 2: (a) horizontal translational DOFs and (b) rotational DOFs.

The relative difference in the joint rotations at the two columns leads to different levels of beam chord rotations at ends *i* and *j*, as shown in Figure 4.2.7. Thus, the beam does not bend in anti-symmetric fashion anymore, and the difference between the chord rotations at beam ends increases with the increasing lateral drift. As a reference, in addition to total beam chord rotation at either end, Figure 4.2.7 also plots the portion of beam rotation attributable to longitudinal reinforcement slip from the joint.

Figure 4.2.8 plots the total elongation of the beam on either side of the counter-flexure point as a function of the total beam chord rotation. To verify that the elongation levels computed with the numerical model of the single-story frame are representative of the levels that may be expected in a physical structure, Figure 4.2.8 also plots the beam elongation - chord rotation curve obtained from Beam 2 laboratory test (Figure 2.8.22, Chapter 2). The curves agree well for the rotations shown.

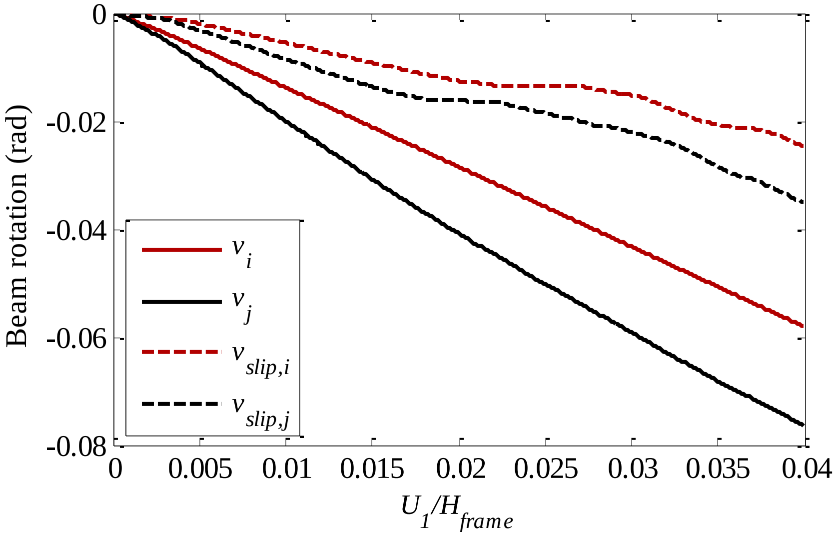

Figure 4.2.7. Difference in beam chord rotations at ends *i* and *j*.

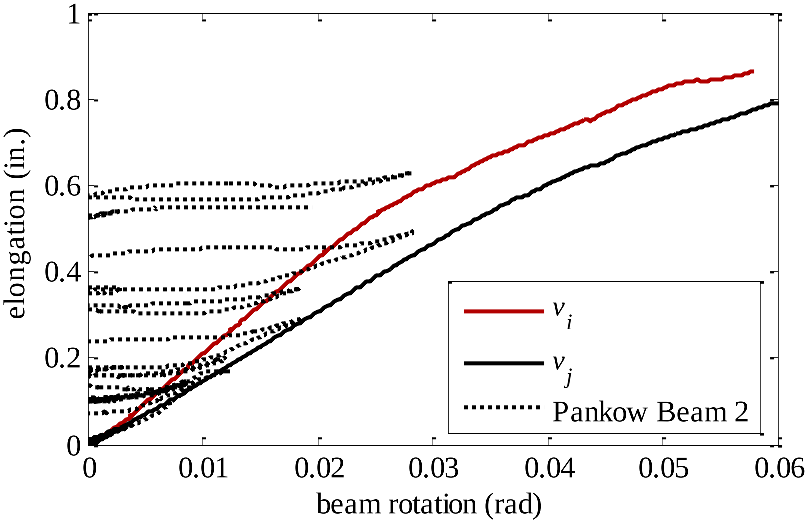

Figure 4.2.8. Beam elongation as a function of chord rotations at ends *i* and *j*.

Another direct cause of beam elongation is the increase in beam axial force. This is shown in Figure 4.2.9, which plots the beam axial force N_u normalized with $A_g f'_c$ as a function of lateral drift U_1/H_{frame}. ACI 318 defines beam-column elements as those with axial compression exceeding $0.1A_g f'_c$ and SMRF beams are generally not considered as beam-columns. However, with beam elongation in place, it is possible that the beam acts as a beam-column during the seismic event, depending on the flexural stiffness of columns relative to axial stiffness of the SMRF beams. A direct consequence of this is the increased moment strength of beams, which in turn, causes larger beam shears transferred to columns, and thus increased axial forces on columns. Because SMRF beams are designed as tension-controlled members per ACI 318, the increase in axial load results in increased moment capacity. This is illustrated in Figure 4.2.10, which plots the beam moment resistance as a function of beam rotations v_i and v_j. The same plot also shows a beam moment-rotation computed when no axial load is present, and also for a reference, when a constant axial load of -0.07$A_g f'_c$ is imposed on a beam (negative sign indicates compression). The moment overstrength increases with increasing beam rotations, which are in proportion to increasing lateral drifts, and thus, the beam axial lengthening. At the beam rotation 0.04, the beam moment capacity is about 1.2 times the strength when no beam elongation is considered in the model.

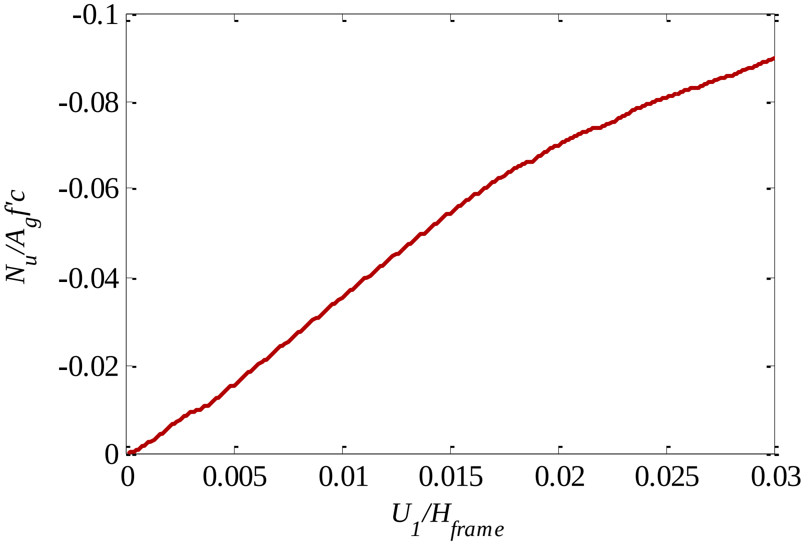

Figure 4.2.9. Increase in axial force in beam as a result of elongation.

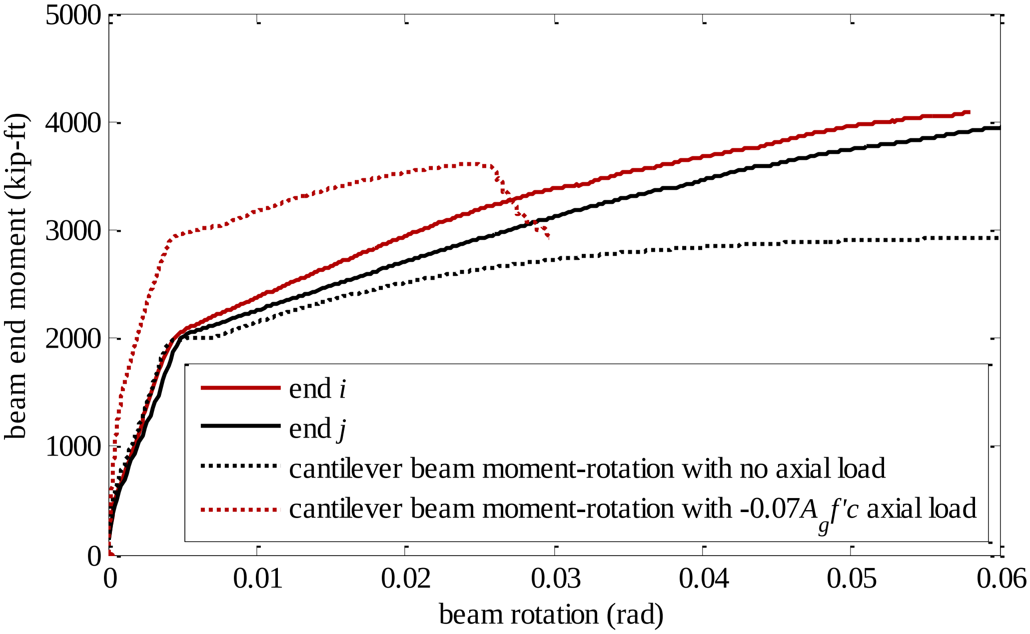

Figure 4.2.10. Increase in beam moment overstrength as a result of elongation.

4.2.4 COLUMN SHEAR IN MULTI-BAY FRAMES

This section illustrates the way that the axial beam lengthening affects the distribution of the shear forces in columns. Numerical models of frames with 1, 2, 3, and 4 bays (Figure 4.2.1) are investigated under a monotonically increasing lateral loads. As before, the control DOF for lateral displacements is the horizontal translation at the leftmost column (labeled with number 1 in each of the frames depicted in Figure 4.2.1). All frames are represented with the numerical model described in Figure 4.2.4(b), which utilizes fiber sections in beams with the material properties as described before.

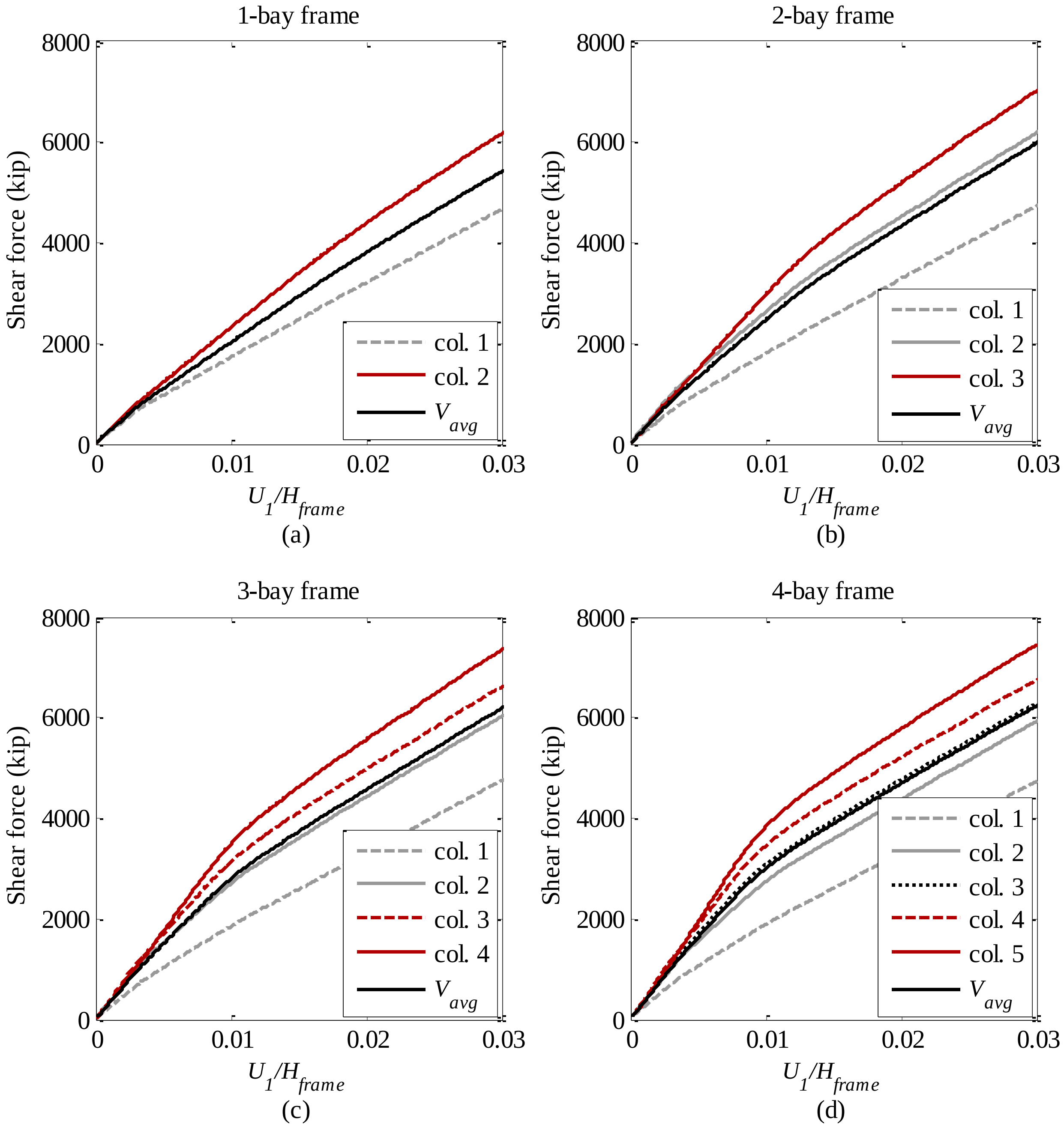

(a) (b) (c) (d)

Figure 4.2.11. Column shear forces during pushover analysis in frames with: (a) one bay, (b) two bays, (c) three bays, and (d) four bays.

When no beam elongation is present, the interior columns in a planar moment frame structure with bays of equal lengths carry approximately the same shear, and each of the exterior columns carries roughly a half of the shear of the interior columns. Figure 4.2.11 shows the column shear forces versus the story drift computed during the pushover analysis of the frames. Each plot also shows the average column shear V_{avg}, which is defined as the total base shear divided by the number of columns and serves as a reference curve to illustrate the variation in shear force among the columns.

The curves plotted in Figure 4.2.11(a) are identical to those in Figure 4.2.5 corresponding to frame with axial beam lengthening. The curve V_{avg} in the case of a one-bay frame corresponds to a column shear if there were no beam elongation present. In all frames, it is evident that beam elongation alters the distribution of the column shear from what would be expected if no elongation was considered. Beam lengthening counteracts the lateral displacements on the tension side of the frame and causes the exterior columns on that side to have smaller shear forces that would be expected otherwise. The opposite holds true for the exterior columns on the compressive side, as discussed before. Beam elongation also impacts the interior columns, as can be seen in the varying shear between the interior columns in Figure 4.2.11(c) and (d).

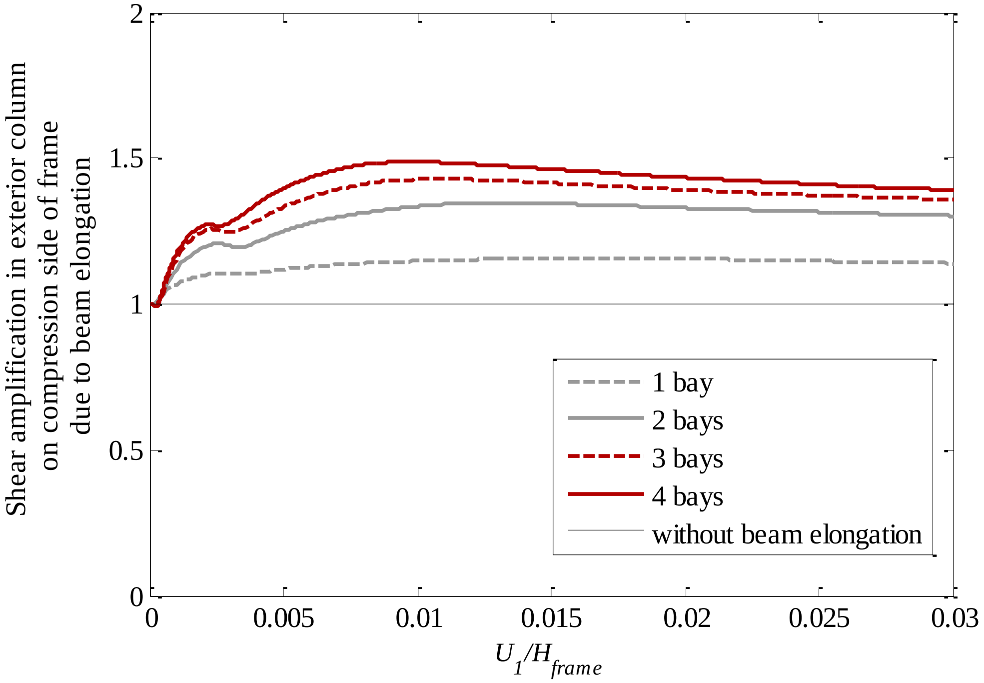

Figure 4.2.12. Impact of number of bays on the exterior column shear amplification due to kinematic interaction between the elongating beam and the column.

Figure 4.2.12 plots the amplification of exterior column shear under compression, as a function of lateral drift and number of bays. The *y*-axis represents the exterior column shear developed when beam elongation is present, versus the exterior column shear of the same frame undergoing the same motion, but with no beam elongation considered. Clearly, the shear amplification increases with number of bays, as also noted by others (Kabeyasawa et al. 2000). In 3- and 4-bay frames, which are typically employed in SMRF construction, the exterior column shear can be amplified by a factor of 1.4 and 1.5 due to the presence of beam elongation only.

Interior columns located directly next to the exterior columns under compression are also impacted, but less severely (Figure 4.2.13).

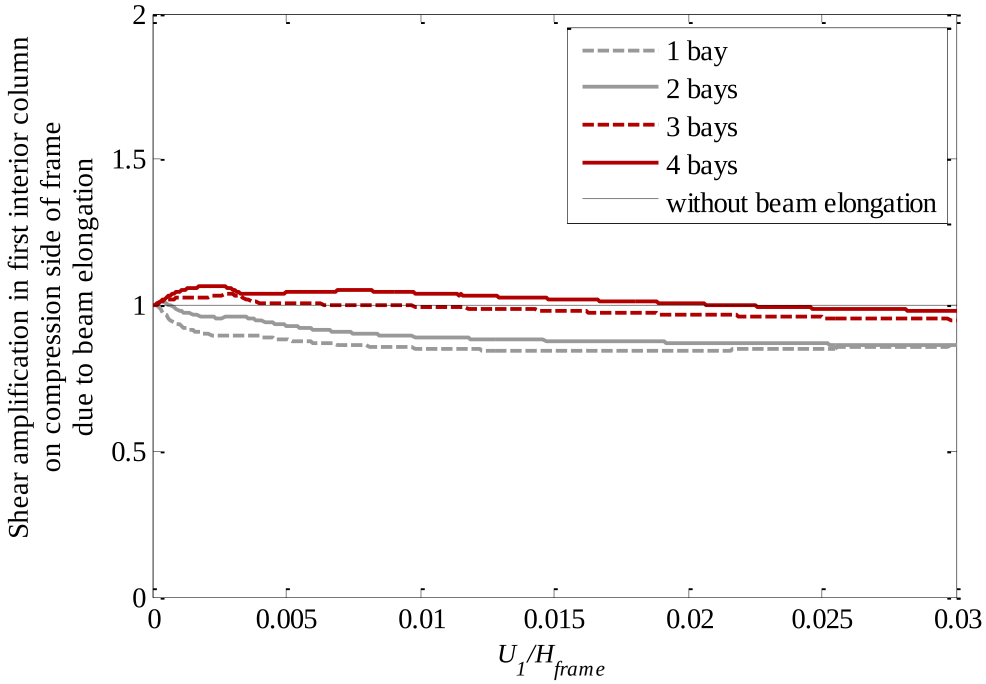

Figure 4.2.13. Impact of number of bays on the first interior column shear amplification (on compressive side of the frame) due to kinematic interaction between the elongating beam and the column.

Lastly, to demonstrate the effect of post-tensioned slab cast uniformly with the SMRF beams, a single story 4-bay frame from Figure 4.2.1(d) is subjected to axial compression acting in line with the beam, which produces f_{pc} = 400psi on the beam cross section. As noted in Section 4.1, this level of prestress can be considered to be on a higher end in SMRF design. As before, the frame is pushed to 0.03 drift and the column shear forces are logged and plotted in Figure 4.2.14(b) next to the forces computed with no prestress in Figure 4.2.14(a) (corresponding to those shown in Figure 4.2.11[d]). The post-tensioning acts to reduce the shear in the exterior columns under compression, however, the reduction in total shear amplification in exterior columns is reduced by less than 10% for this level of post-tensioning, as demonstrated in Figure 4.2.15. It should be noted that the reason that the curve corresponding to frame with PT in Figure 4.2.15 begins at a nonzero drift is that due to post-tensioning, the top of Column 5 (Figure 4.2.1[d]) is initially displaced to the left, and the column shear force acts in the opposite direction from the lateral load applied in the pushover analysis. The point where the curve begins indicates the point where the column is returned to the neutral position during the pushover analysis.

The findings presented in this section indicate that neglecting the beam elongation phenomenon leads to underestimation of column force and deformation demands and beam elongation should be considered in numerical modeling in order to more accurately compute global response of SMRFs. It is recommended to use fiber-based model where nonlinear analyses are conducted to determine force and deformation demands in the frames. In addition, it has been demonstrated, that the beam elongation has similar level of impact on column shear regardless of whether the floor slabs have been post-tensioned or not.

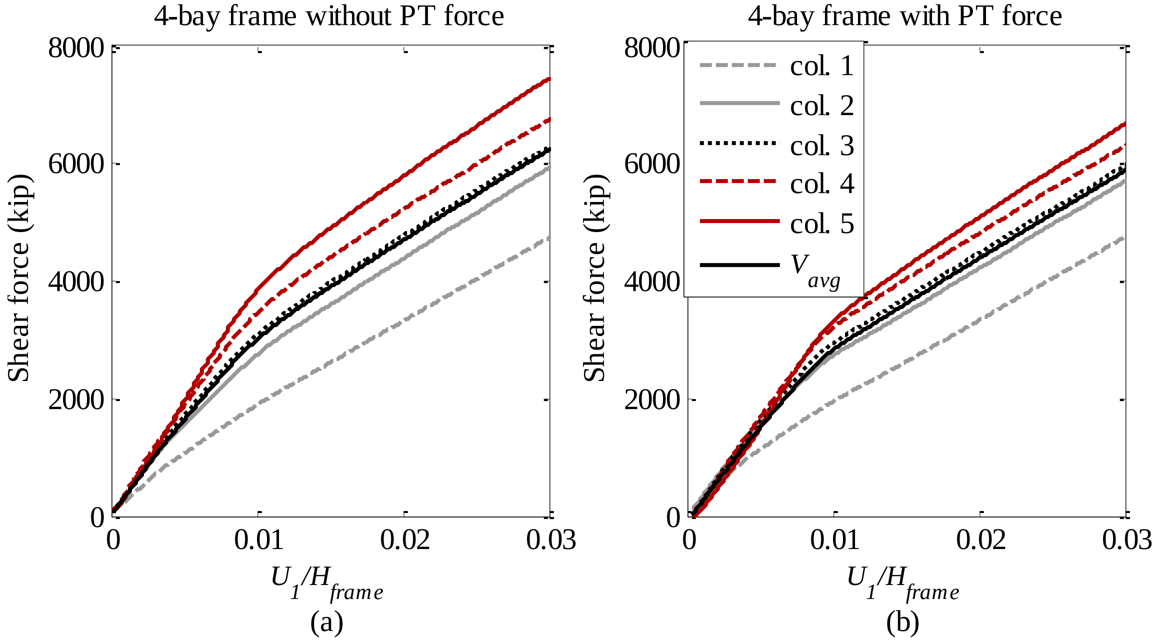

(a)

(b)

Figure 4.2.14. Effect of post-tensioning on shear distribution in columns of RC frame impacted by beam elongation.

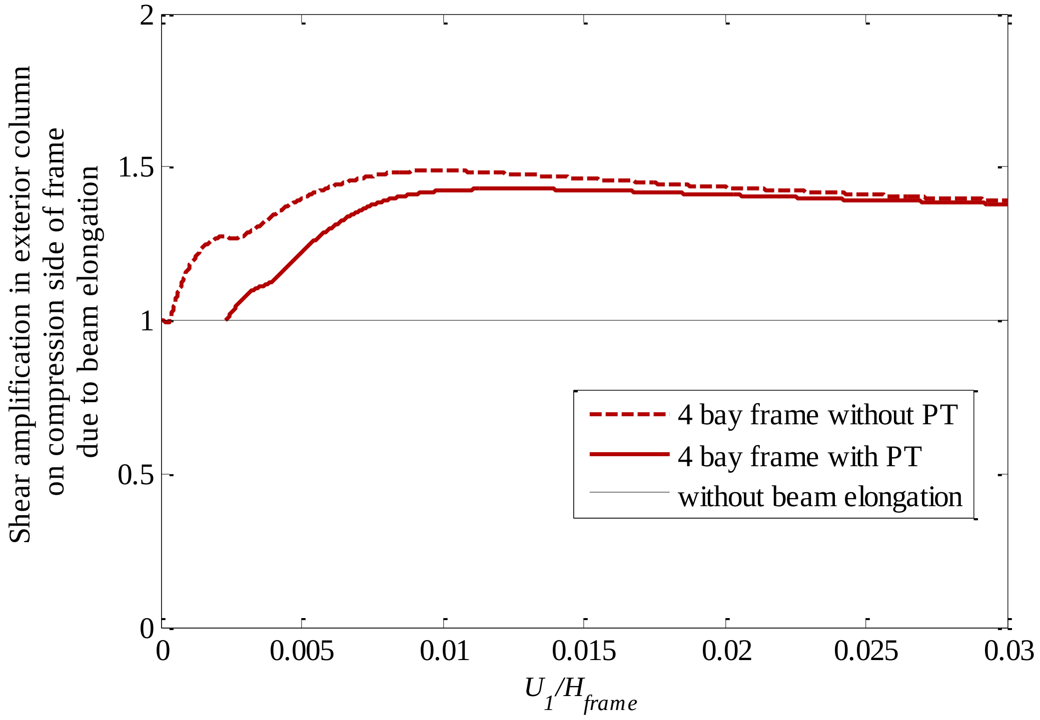

Figure 4.2.15. Impact of post-tensioning on the exterior column shear amplification due to kinematic interaction between the elongating beam and the column.

4.3 CONCLUSIONS

The present chapter illustrates simple techniques for simulating axial elongation of a reinforced concrete beam – a deformation component usually overlooked in the current analysis and design practice in the United States. Modeling approach that is based on the use of distributed plasticity elements with fiber section discretization containing path-dependent hysteresis materials was shown to provide acceptable level of elongation estimate under cyclic beam loading. Short numerical exercise demonstrated that suppressing the axial elongation of a beam may lead a brittle beam response. In addition, it was demonstrated that under all practical levels of post-tensioning in the slabs cast uniformly with the perimeter SMRF beams, the elongation was only slightly reduced by the slab post-tensioning, and thus the post-tensioned slabs would not prevent the beam elongation from impacting the column shear.

A parametric numerical exercise consisting of single-story frames with varying number of bays showed that exterior column shear induced by beam elongation increases with the increasing number of bays. For the frames studied in this chapter, under sidesway frame deformation, beam elongation lead to column shear 50% higher than the column shear computed if beam elongation was disregarded. Further experimental investigation is necessary to better understand the implications of beam growth phenomenon on seismic performance of tall buildings with common SMRF-slab configurations.

CHAPTER 5

SEISMIC RESPONSE OF 20-STORY TALL REINFORCED CONCRETE BUILDINGS WITH SPECIAL MOMENT RESISTING FRAMES

Construction of buildings exceeding 160 ft in height, referred herein as "tall," is increasing in earthquake-prone regions of the United States and worldwide (Emporis 2012). Reinforced concrete (RC) special moment resisting frames (SMRFs) are commonly selected as the seismic force-resisting system in such buildings. Considerable damage of 10- to 20-story reinforced concrete frame buildings in past earthquakes has been reported, including the 1995 M6.9 Kobe, Japan earthquake (Otani 1999), the 1999 M7.6 Chi-Chi, Taiwan earthquake (Tsai et al. 2000), and the M6.3 2011 Christchurch, New Zealand, earthquake (Elwood et al. 2012). The occurrence of damage suggests potential vulnerability of these systems, and warrants study to better understand design requirements.

Several groups have described performance expectations, analysis requirements, and proportioning and detailing requirements tailored to tall buildings (SEAONC 2007, Moehle et al. 2008, Willford et al. 2008, TBI 2010, Moehle et al. 2011, LATBSDC 2011). In the U.S., design forces for reinforced concrete SMRFs typically are calculated using the modal response spectrum analysis (MRSA) method with response modification factor $R = 8$ (ASCE 2010) and with individual modal responses combined using either the square root of the sum of squares (SRSS) or the complete quadratic combination (CQC) modal combination rules. The RC SMRF itself is subsequently proportioned and detailed in accordance with requirements of ACI 318 (ACI 2011). Typical design practice in frame buildings aims to reduce the likelihood of localized story mechanisms by detailing frame elements to follow a strong column-weak beam philosophy. In ACI 318, the sum of column nominal moment strengths is required to be equal to at least 1.2 times the sum of beam nominal moment strengths at every beam-column joint, except the roof where column axial forces are small and consequences of column yielding are minor. Recognizing that this approach cannot preclude inelastic flexure in columns, ACI 318 requires confinement reinforcement in columns above and below every beam-column joint.

Kuntz and Browning (2003) showed that inelastic deformations may occur in the columns above the base level of multi-story frames designed to satisfy the strong-column weak-beam requirement of ACI 318. The occurrence of column yielding above the base in SMRFs satisfying U.S. design requirements is in accord with more recent findings by Haselton et al. (2011) noting also that the predominant collapse mechanism was a partial collapse engaging only several floors and including column yielding above the base.

Several other studies of dynamic response of multi-story frame buildings have been reported. Pettinga and Priestley (2005) investigated analytically the response of reinforced concrete frame buildings up to 20 stories tall, designed with a displacement-based design method. This study noted the significant contribution of higher modes to the forces and story drifts along the building height, and proposed approaches to calculate design shear forces and bending moments accounting for higher-mode effects. Barbosa (2011) reported a study of a 13-story wall-frame system with SMRFs design to resist all of the seismic forces in one direction, noting that system shear demands were higher than those obtained from the equivalent lateral force procedure as described in ASCE 7. Moehle et al. (2011) studied numerically a 42-story dual system consisting of a reinforced concrete core wall and perimeter SMRFs designed to resist 25% of the total lateral seismic force as required by prescriptive code criteria in the U.S. The study found column axial forces well in excess of values indicated by the design analysis, but none of the force or deformation demands exceeded available capacities.

Numerical studies investigating the response of steel moment frames around 20 stories tall (Hall et al. 1995, Hall 1998, Alavi and Krawinkler 2004, Krishnan 2007, Muto and Krishnan 2011) have indicated that strong pulse-type near-fault excitations cause significant inelastic deformation demands in frame elements that may exceed available capacities. Thus, it is important to consider appropriate ground motion characteristics when studying performance potential of a seismic force-resisting system. Thus far, the number of numerical studies of the inelastic response of tall RC frames subjected to near-fault ground motions is limited (Liao et al. 2001, Akkar et al. 2005).

This chapter investigates the seismic response of four 20-story tall RC SMRFs designed in accordance with ASCE 7 and ACI 318 code provisions and subjected to strong earthquake excitation. Analytical models of the buildings are developed for nonlinear dynamic analysis. These are subjected to a set of ground motions scaled to two different smoothed design response spectra representing the design earthquake (DE) and the maximum considered earthquake (MCE) hazard levels. The results of analyses are quantified in terms of global response (story drifts, story shears, etc.) and local response (column shears, axial loads, longitudinal reinforcement strain). The forces computed in the nonlinear dynamic analysis are then compared to the forces calculated using MRSA described in ASCE 7. In addition, two methods for estimating design column shears described in ACI 318 are evaluated.

5.1 BUILDING DESCRIPTION

The four buildings considered in this study have the same plan and elevation view (Figure 5.1.1). They have two reinforced concrete special moment resisting frames (SMRFs) as the seismic force resisting system in each of the two principal directions of the buildings. Each SMRF is located at the perimeter and has four bays (each 21 ft long) and 20 stories (each 12 ft tall). Total building height is H = 144 ft. In this study, reference will be made to various column lines in the SMRFs. Column lines A and E (1 and 5) are designated “exterior columns,” column lines B and D (2 and 4) are designated “interior columns,” and column line C (3) is designated the “middle column” (see Figure 5.1.1).

Two frame types are considered. Type A has column size and longitudinal reinforcement ratio that decrease along height, while Type B has uniform column size and reinforcement ratio over building height. The beams are identical in both frame types, with smaller beams in levels 11-20 than in levels 1-10. One Type A building is considered, designated A20-1. Three Type B buildings are considered, designated B20-1, B20-2, and B20-3. Table 5.1 lists beam and column dimensions as well as the longitudinal and transverse steel ratios of the studied buildings. In building A20-1, column dimensions are constant from levels 1-10, with reduced dimensions in levels 11-20. Column longitudinal reinforcement is curtailed at levels 6, 11, and 16, as listed in Table 5.1. In building B20-1, column size and longitudinal reinforcement in every story are the same as those used in the first story of building A20-1. Buildings B20-2 and B20-3 are identical to B20-1 except the size and longitudinal steel ratio are different for the exterior columns (see Table 5.1).

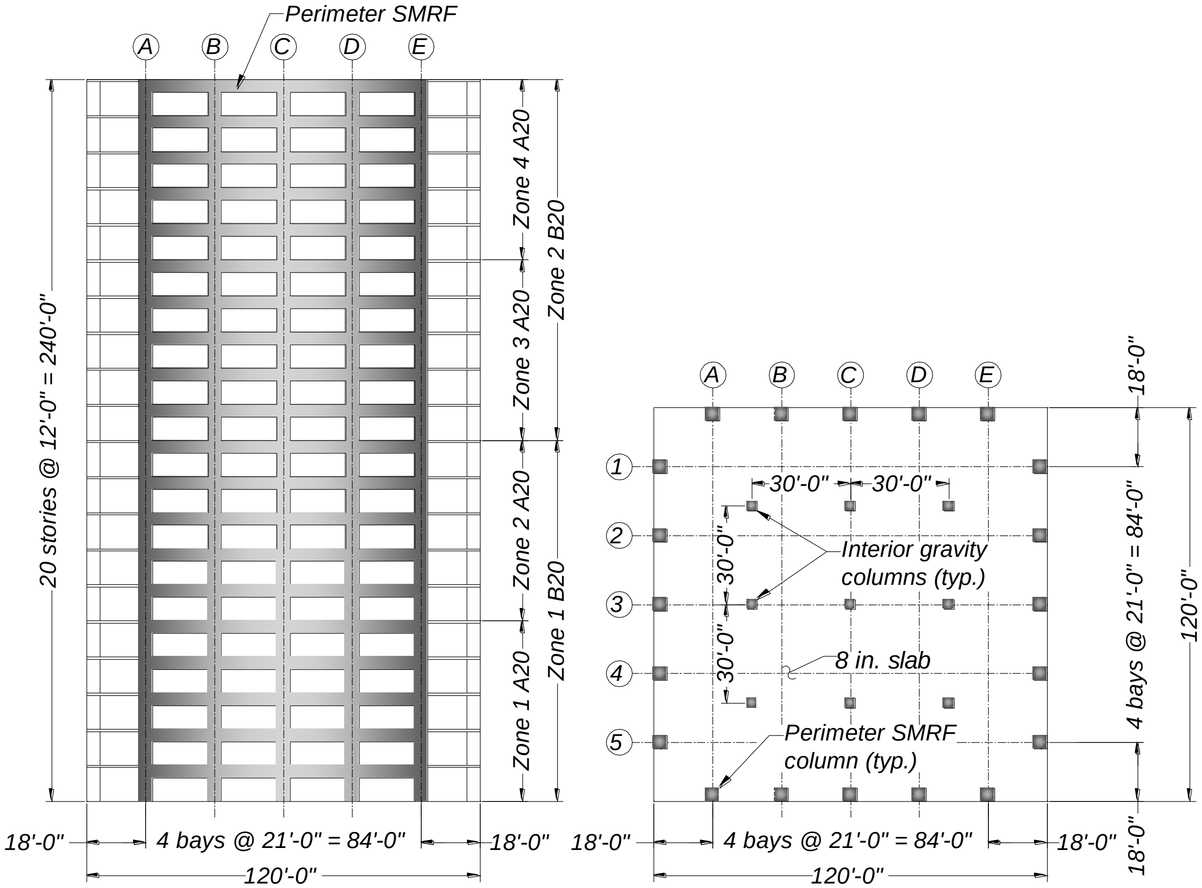

Figure 5.1.1. (Left) Elevation and (Right) floor plan of buildings considered.

5.2 SEISMIC HAZARD AND GROUND MOTION SELECTION

The studied buildings are considered to be at a site in Los Angeles, California, with soil type D (ASCE, 2010). The site seismic hazard and corresponding smooth design spectra were determined in accordance with ASCE 7 at both DE and MCE levels. A set of fourteen ground motions was selected and linearly scaled such that the mean spectrum approximately matches the smooth design spectra over the period range of interest. The ground motion set consisted of fault-normal components of near-fault pulse-type ground motions affected by directivity effects. Individual ground motion information and scale factors are listed in Table 5.2.

Table 5.1. Frame element sizes and steel ratios (b = width, h = height, ρ_l = longitudinal reinforcement ratio, ρ_t = transverse reinforcement ratio). Note: * = ρ_t in first-story column only.

		A20-1				B20-1		B20-2		B20-3	
	zone	1	2	3	4	1	2	1	2	1	2
	stories	1-5	6-10	11-15	16-20	1-10	11-20	1-10	11-20	1-10	11-20
beam	b (in.)	24	24	24	24	24	24	24	24	24	24
	h (in.)	42	42	36	36	42	36	42	36	42	36
	ρ_l (%)	2.2	2.2	1.8	1.8	2.2	1.8	2.2	1.8	2.2	1.8
	ρ_t (%)	1.0	1.0	0.9	0.9	1.0	0.9	1.0	0.9	1.0	0.9
exterior column	b (in.)	48	48	42	42	48	48	60	60	72	72
	h (in.)	48	48	42	42	48	48	60	60	72	72
	ρ_l (%)	2.8	1.1	1.1	1.0	2.8	2.8	2.0	2.0	1.7	1.7
	ρ_t (%)	2.1* 1.2	1.2	1.2	1.2	2.1* 1.2	1.2	1.9* 1.2	1.2	1.9 * 1.2	1.2
interior/ middle column	b (in.)	48	48	42	42	48	48	48	48	48	48
	h (in.)	48	48	42	42	48	48	48	48	48	48
	ρ_l (%)	1.5	1.0	1.1	1.0	1.5	1.5	1.5	1.5	1.5	1.5
	ρ_t (%)	1.9* 1.6	1.6	1.6	1.6	1.9* 1.6	1.6	1.9* 1.6	1.6	1.9* 1.6	1.6

Table 5.2. Near-fault pulse-type ground motions and their scale factors.

					Scale Factor	
No.	M_w	Year	Event	Station	DBE	MCE
1	6.5	1979	Imperial Valley	El Centro Differential Array	1.35	2.02
2	6.7	1987	Superstition Hills	Parachute Test Site	0.59	0.89
3	6.9	1989	Loma Prieta	LGPC	1.67	2.50
4	7.3	1992	Landers	Lucerne	1.29	1.93
5	6.7	1994	Northridge	Newhall – Fire Station	1.67	2.50
6	6.7	1994	Northridge	Sylmar Olive View Med FF	0.71	1.06
7	6.7	1994	Northridge	Jensen Filter Plant	0.46	0.70
8	6.7	1994	Northridge	Rinaldi Receiving Sta	1.02	1.53
9	6.7	1994	Northridge	Sylmar Converter Station	0.77	1.16
10	7.6	1999	Chi-Chi, Taiwan	TCU065	0.50	0.75
11	7.6	1999	Chi-Chi, Taiwan	TCU067	1.35	2.03
12	7.6	1999	Chi-Chi, Taiwan	TCU071	1.67	2.50
13	7.6	1999	Chi-Chi, Taiwan	TCU074	0.75	1.12
14	7.6	1999	Chi-Chi, Taiwan	TCU102	0.78	1.17

Figure 5.2.1(a) and (d) show the mean pseudo-acceleration and displacement spectra of the scaled ground motions together with the corresponding DE and MCE design spectra. The mean scale factors were 0.88 and 1.32 for the DE and MCE levels, respectively. The rest of Figure 5.2.1 shows the individual scaled pseudo-acceleration and displacement spectra and their mean for the DE and MCE levels. The plots also identify the first two modal periods of building A20-1, T_1 and T_2, computed using uncracked section properties with the numerical model described in Section 5.4 (These periods are representative of all four buildings, as explained in Section 5.5). Very good agreement between the design spectra and the mean response spectra is observed for

periods between 0.5 and 4.0 s for both sets of ground motion. Conditional mean response spectra (Baker 2011) were not pursued because response of these tall buildings is strongly affected by multiple modes and practical techniques using conditional mean spectra are not available for such cases.

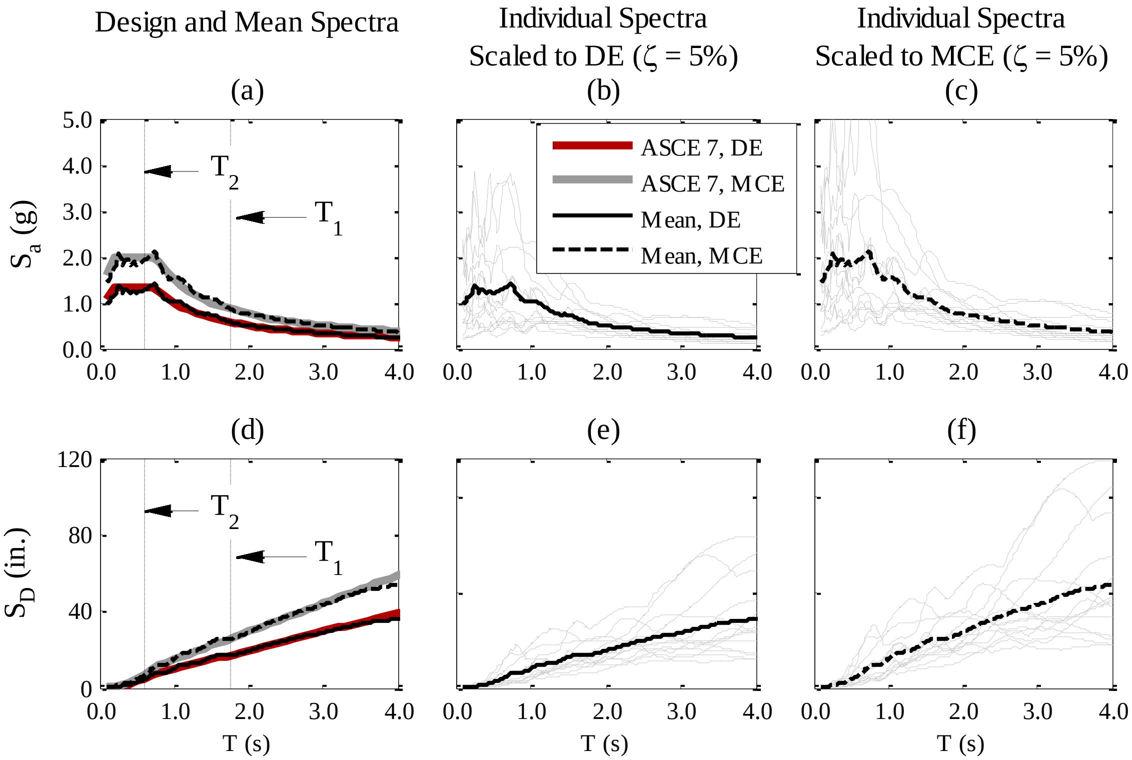

Figure 5.2.1. Design and linear pseudo-acceleration and displacement response spectra of ground motions scaled to DE and MCE design seismic hazard levels (ζ = damping ratio).

5.3 DESIGN OF THE BUILDINGS

The buildings were designed based on ACI 318-11 and ASCE 7-10 provisions. Dead load was 172 psf including self-weight of the structure and permanent non-structural components. The service floor live load was 60 psf. Total seismic weight, W_{total}, including 25% of the live load, is listed for each building in Table 5.3. Nominal concrete compressive strength, f'_c, was 7.5 ksi, and nominal steel yield strength, f_y, was 60 ksi. For the remainder of this paper the design and analysis of one of the two SMRFs is considered and discussed for each of the buildings. The seismic weight of each of the two SMRFs is W=W_{total}/2.

Table 5.3. Total seismic weight (per frame) of archetype buildings.

Building	A20-1	B20-1	B20-2	B20-3
Seismic weight per frame, *W* (kip)	26140	26780	27070	27430

Design forces were determined using the code-prescribed MRSA procedure using SRSS modal combination rule with a response modification factor $R = 8$. The first five modes were included in the elastic analysis, which accounted for more than 90% of the modal mass. The effective flexural rigidities used for columns and beams were $0.5E_cI_g$ and $0.35E_cI_g$, respectively (Moehle et al. 2008), where I_g = gross section moment of inertia and E_c = elastic modulus of concrete = 4932 ksi. The design base shear force of each SMRF (V_b) for all four buildings was controlled by minimum base shear requirements of ASCE 7, resulting in a base shear coefficient $V_b / W = 5.36\%$. The following load combinations, numbered consistent with ASCE-7, were considered in the design:

1. $1.4D$,
2. $1.2D + 1.6L$,
5. $(1.2 + 0.2S_{DS})D + 0.5L \pm 1.0E$, and
7. $(0.9 - 0.2S_{DS})D \pm 1.0E$,

where D = dead load, L = live load, S_{DS} = design spectral response acceleration parameter at short periods (ASCE 7), and E = earthquake load.

Beam design shear forces were calculated considering development of probable moment strength, M_{pr}, at both ends of the beam plus the uniformly distributed gravity load. Transverse reinforcement in beams comprised No. 5 hoop and a cross tie (with 5/8 in. diameter), spaced at s = 4 in. in the lower ten stories and s = 4.25 in. in the upper ten stories. Longitudinal and transverse steel ratios (ρ_l and ρ_t) of the beams were identical among the four buildings and are listed in Table 5.1. Note that because shear behavior of frame elements is not modeled in these archetype buildings, the amount of transverse reinforcement is only used to establish the constitutive relationship for confined concrete core (where applicable) and also to provide a reader with a reference point on the amount of reinforcement typically required in buildings of this size.

Longitudinal reinforcement in columns was reduced in building A20-1 every five stories but was constant in the other three buildings (see Table 5.1). The exterior columns were in the transition region between compression- and tension-controlled section at the base, according to ACI 318, with 0.3% strain in extreme tensile reinforcement at nominal flexural strength M_n. Interior and middle columns were in the tension-controlled region. For all three B20 buildings the column longitudinal steel ratio was selected to be uniform along the height. Base exterior columns of B20-1 and B20-2 were in the transition region between tension- and compression-controlled sections (0.3% and 0.49% strain in extreme tensile reinforcement at M_n, respectively), while for B20-3 building, the exterior column at the base had a tension-controlled section (0.7% strain in extreme tensile reinforcement at M_n). Interior and middle columns were in the tension controlled region for all three B20 buildings.

Column transverse reinforcement of the buildings is categorized within three zones: bottom story, second story and stories three to twenty (Table 5.1). The provided transverse reinforcement satisfied the shear and confinement requirements of ACI 318. Shear requirements based on Method B2 described in Section 5.6 controlled the column design at the bottom story for all four buildings. In all cases, for load combination 7, the factored axial compressive force was less than $A_gf'_c/20$, and therefore the nominal shear strength was calculated considering only the contribution of transverse reinforcement (V_s) and ignoring that of concrete (V_c).

In all four buildings, column transverse reinforcement comprised a No. 5 hoop and multiple No. 5 crossties in each transverse direction, spaced vertically at 4 in. along column height. The transverse reinforcement in the two orthogonal directions of the columns was equal and uniform along the column height, resulting in a volumetric transverse steel ratio $\rho_s = 2\rho_t$. In all buildings, joint shear strength and the strong column-weak beam requirements of ACI 318 were satisfied.

5.4 NUMERICAL MODEL

The 2-dimensional nonlinear response history analysis (NRHA) described below was performed using the Open System for Earthquake Engineering Simulation software platform (McKenna et al. 2007, OpenSees 2012). The model consisted of a single SMRF with lumped mass and vertical load applied at the joints. Force-based Euler-Bernoulli nonlinear fiber-section frame elements with P-Δ geometric transformation were used for all beams and columns, with five and four integration points along beam, and column elements, respectively. This modeling approach includes axial force - bending moment interaction; interaction between shear force and bending moment and/or axial force was not considered. Beam-column joints were modeled with rigid end zones in both columns and the beams.

Based on the Gauss-Lobatto integration used for the nonlinear frame elements, the integration weights of the end integration points are $0.05L_b$ and $0.08L_c$, for the total of five and four integration points used, respectively. Here, L_b and L_c signify the clear length of the beams and the columns, respectively. Thus, the strain levels reported in this study represent the average strain values computed within the $0.05L_b$ and $0.08L_c$ from either end of a given element. In beams, for example, the strains discussed in the results represent the average values over the 9-10 in. from the end node of each beam, which is about $h/4$ where h is the beam depth. For the given deformation level, strain values in a physical specimen are expected to be higher.

Gravity framing was assumed to provide sufficient strength and stiffness to resist P-Δ effects under tributary gravity load, but, consistent with the approach of Haselton et al. (2008), the gravity framing was assumed to not provide lateral resistance. Gravity loading on frames in the numerical model included all of the dead load and 25% of the live load, in accordance with ASCE 7. Foundation flexibility was not considered. Initial stiffness Rayleigh damping with 2% damping ratio in modes 1 and 3 was used. Slab effects were not considered in the numerical model.

The numerical models accounted for strain penetration of beam longitudinal reinforcement into joints and column longitudinal reinforcement into the foundation. This was modeled using fiber-based zero-length section elements as described in Section 3.6.1, Chapter 3. The Menegoto Pinto material model, *Steel02* (OpenSees 2012), was used to model reinforcing steel and also the bar stress-slip relationship in the zero-length section elements. The strain hardening ratio for both materials was defined as $\beta_{steel} = 0.012$. The *Steel02* material constituitive model accounted for material overstrength and thus, the numerical model was specified to have $f_y = 69$ksi. Bar buckling and fracture was not considered in the model. Concrete was modeled using the *Concrete03* material model (OpenSees 2012) with the confined concrete strength f'_{cc} and the corresponding strain ε_{cc} calculated based on Mander et al (1988). At strain levels exceeding concrete strain ε_{cc} at f'_{cc}, the concrete stress-strain relationship was modeled as perfectly plastic.

5.5 Vibration Properties and Strength

The buildings have similar modal characteristics with a first modal period T_1 between 1.51 and 1.60 s and a ratio of first to second mode period T_1 / T_2 of about 2.9. The effective modal mass of the first mode normalized with the total mass M_1 / M ranged between 0.73 and 0.75 while the corresponding range for the second mode is 0.13 to 0.15. These modal properties are summarized in Table 5.4.

Figure 5.5.1 shows the force-displacement curves up to 4% roof drift ratio obtained from a monotonic nonlinear static (pushover) analysis using the first-mode lateral force distribution of each of the four buildings. The force-displacement relationships are similar in the effectively linear range, with a system base shear of approximately 0.073W at 0.4% roof drift ratio. The relations diverge beyond this due to different column flexural strengths. At 2% roof drift ratio, the base shear is between 1.7 and 1.9 times the design base shear of 0.054W, the increase due to design factors and section overstrength of the frame members. Figure 5.5.1 also identifies instances when the tensile strain in longitudinal steel of base-level exterior columns on the uplift side first reaches 0.01, 0.02, and 0.03.

Table 5.4. Characteristics of the first three modes of the buildings considered.

Mode q	A20-1			B20-1			B20-2			B20-3		
	T (s)	M_q / M	H_q / H	T (s)	M_q / M	H_q / H	T(s)	M_q / M	H_q / H	T(s)	M_q / M	H_q / H
1	1.75	0.73	0.69	1.76	0.74	0.69	1.71	0.75	0.69	1.67	0.75	0.69
2	0.61	0.15	0.04	0.61	0.14	0.02	0.58	0.14	0.02	0.57	0.13	0.01
3	0.33	0.04	0.10	0.32	0.04	0.10	0.32	0.04	0.11	0.31	0.04	0.12

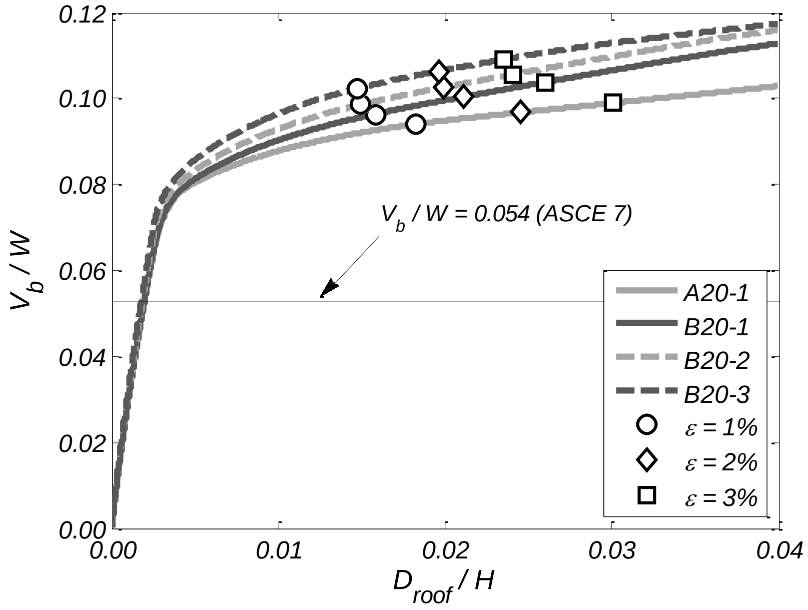

Figure 5.5.1. Force-displacement curve for the buildings from first-mode pushover analysis.

5.6 RESULTS FROM NONLINEAR RESPONSE HISTORY ANALYSIS

Representative response quantities obtained from the NRHA are summarized in Tables 5.5 and 5.6, which lists the computed mean and standard deviation for the peak responses calculated from the 14 ground motions. Response quantities presented in Table 5.5 include: roof drift ratio, defined as D / H, where D is roof displacement relative to base and H height from base to roof; system base shear V_b normalized by W; maximum story drift ratios θ along the building height; shear force at the base of the exterior columns normalized with $A_g\sqrt{f'_c}$; and peak compressive and tensile forces of exterior columns normalized by f'_cA_g. Table 5.6 includes: beam longitudinal reinforcement tensile strain; compressive strains in confined concrete at the base of the exterior columns; and column longitudinal reinforcement tensile strains in levels 1, 6, 11, and 16, which is where the column size and/or amount of longitudinal reinforcement was reduced in building A20-1.

For the remainder of this chapter, discussions regarding material strains refer to those computed in the most extreme tensile reinforcement steel fibers and the most extreme confined concrete core fibers. As mentioned before, the strain values reported represent the average strain occurring over a tributary length of a numerical integration point, and are likely to be lower than those occurring in a physical specimen at the same deformation levels. For this reason, the material strains computed are intended to serve as qualitative indicators of differences in seismic response among different buildings, as will be discussed in the following sections. Expressions involving $\sqrt{f'_c}$ are written for f'_c in units of psi. Shear force responses have been processed using a low-pass filter with 10 Hz cut-off frequency to eliminate numerically induced spurious high-frequency spikes that occur due to sudden changes in the tangent modulus for the material models used (Wiebe and Christopoulos 2010).

Tale 5.5. Summary of mean (standard deviation) values of selected response quantities for the four buildings subjected to the 14 ground motions.

Response Quantity	A20-1		B20-1		B20-2		B20-3	
	DE	MCE	DE	MCE	DE	MCE	DE	MCE
Roof drift ratio, D / H (%)	1.2 (0.6)	1.8 (0.8)	1.2 (0.6)	1.8 (0.8)	1.2 (0.6)	1.8 (0.8)	1.3 (0.7)	1.9 (0.9)
Maximum story drift ratio along building height, θ (%)	2.2 (1.2)	3.1 (1.8)	1.9 (1.1)	2.9 (1.6)	1.9 (1.1)	2.8 (1.5)	1.9 (1.0)	2.7 (1.4)
System base shear, V / W	0.12 (0.02)	0.14 (0.02)	0.12 (0.02)	0.14 (0.02)	0.13 (0.02)	0.14 (0.02)	0.14 (0.02)	0.15 (0.02)
Exterior column base shear, $V_{ext} / A_g\sqrt{f'c}$	6.26 (1.25)	7.48 (1.67)	6.28 (1.24)	7.54 (1.70)	4.92 (0.90)	5.82 (1.21)	3.99 (0.73)	4.65 (0.89)
Interior column base shear, $V_{int} / A_g\sqrt{f'c}$	4.04 (0.53)	4.53 (0.73)	4.08 (0.52)	4.56 (0.73)	3.70 (0.43)	4.05 (0.55)	3.53 (0.38)	3.85 (0.49)
Ext. col. base tensile force, T / f'_cA_g	0.14 (0.03)	0.15 (0.02)	0.14 (0.03)	0.15 (0.02)	0.08 (0.02)	0.09 (0.01)	0.05 (0.01)	0.06 (0.01)
Ext. col. base compressive force, C / f'_cA_g	0.31 (0.02)	0.32 (0.02)	0.31 (0.02)	0.32 (0.02)	0.22 (0.02)	0.23 (0.02)	0.17 (0.01)	0.17 (0.02)

Table 5.6. Summary of mean (standard deviation) values of material strains for the four buildings subjected to the 14 ground motions.

Response Quantity			A20-1		B20-1		B20-2		B20-3	
			DE	MCE	DE	MCE	DE	MCE	DE	MCE
Maximum beam reinforcement tensile strain along building height (%)			6.8 (3.3)	7.9 (3.3)	6.9 (3.2)	7.9 (3.3)	6.2 (3.1)	7.5 (3.4)	6.0 (3.0)	7.5 (3.4)
Concrete compressive strain, exterior column base (%)			1.0 (1.0)	2.3 (2.0)	1.0 (0.9)	2.2 (1.9)	0.5 (0.4)	1.0 (0.8)	0.2 (0.1)	0.3 (0.2)
Column reinforcement tensile strain (%)	Exterior	1st floor	2.3 (2.6)	5.3 (4.9)	2.2 (2.50)	5.2 (4.80)	2.2 (2.4)	4.8 (4.4)	2.0 (2.3)	4.1 (3.7)
		6th floor	0.5 (0.5)	1.7 (1.9)	0.1 (0.05)	0.3 (0.33)	0.1 (0.04)	0.2 (0.2)	0.1 (0.04)	0.1 (0.06)
		11th floor	0.6 (0.4)	1.2 (0.8)	0.1 (0.03)	0.1 (0.04)	0.1 (0.02)	0.1 (0.02)	0.1 (0.03)	0.1 (0.03)
		16th floor	0.3 (0.2)	0.7 (0.6)	0.1 (0.06)	0.2 (0.13)	0.1 (0.09)	0.2 (0.2)	0.1 (0.08)	0.2 (0.2)
	Interior	1st floor	2.7 (2.9)	5.9 (5.2)	2.7 (2.80)	5.9 (5.10)	2.4 (2.5)	5.4 (4.8)	2.3 (2.4)	4.9 (4.2)
		6th floor	0.4 (0.5)	1.6 (1.8)	0.2 (0.20)	0.7 (0.85)	0.2 (0.2)	0.6 (0.8)	0.2 (0.2)	0.5 (0.6)
		11th floor	0.8 (0.5)	1.5 (1.0)	0.2 (0.05)	0.2 (0.06)	0.2 (0.06)	0.2 (0.09)	0.2 (0.07)	0.3 (0.1)
		16th floor	0.6 (0.4)	1.2 (0.8)	0.2 (0.10)	0.4 (0.30)	0.3 (0.2)	0.5 (0.5)	0.3 (0.2)	0.6 (0.6)
	Middle	1st floor	2.1 (2.3)	4.8 (4.3)	2.0 (2.20)	4.7 (4.30)	1.9 (2.0)	4.3 (4.0)	1.8 (1.9)	3.9 (3.6)
		6th floor	0.4 (0.5)	1.4 (1.7)	0.2 (0.20)	0.6 (0.80)	0.2 (0.2)	0.6 (0.7)	0.2 (0.2)	0.5 (0.6)
		11th floor	0.8 (0.5)	1.5 (0.9)	0.2 (0.04)	0.2 (0.06)	0.2 (0.06)	0.2 (0.07)	0.2 (0.06)	0.3 (0.1)
		16th floor	0.5 (0.3)	1.0 (0.6)	0.2 (0.11)	0.4 (0.27)	0.3 (0.2)	0.5 (0.5)	0.3 (0.2)	0.6 (0.6)

5.6.1 RESPONSE OF BUILDING A20-1

The response of building A20-1 is discussed first. Figure 5.6.1 presents mean envelopes of relative displacements, story drift ratios, story moments, and story shear forces. The envelopes of all response quantities have similar shapes for the DE and MCE response levels. The computed mean roof drift ratios are 1.2% for the DE and 1.6% for the MCE hazard levels (Table 5.5). As shown in Figure 5.6.1(a), the mean displacement envelopes have a maximum value at the roof of the building. The story drifts build up mainly in the bottom two stories, which is associated with significant inelastic deformations of the columns and beams in this region (Figure 5.6.1[b]). The mean story drift envelope has similar values between 0.2H and 0.7H at both DE and MCE levels, with local peaks at 0.3H and 0.6H. The largest value of the mean story drift is 2.0 and 3.1%, at DE and MCE levels, respectively.

The mean base shear for the DE motions is 0.13W, increasing to 0.15W for the MCE shaking level (Figure 5.6.1[c]). The mean base shear at DE is 49% higher than the base shear computed from the nonlinear static pushover analysis using the first-mode lateral force profile at 1.2% roof drift ratio (the mean roof drift ratio for the DE motions), also plotted in Figure 5.6.1(c). This difference resulted from higher-mode contributions to the system base shear response. Only 6% increase is noted in the mean computed story moments going from DE to MCE hazard level (Figure 5.6.1[d]). The story moment profile from the first-mode monotonic pushover analysis, also plotted, agrees very well with the mean story moment envelopes indicating negligible higher mode contribution to the system moment.

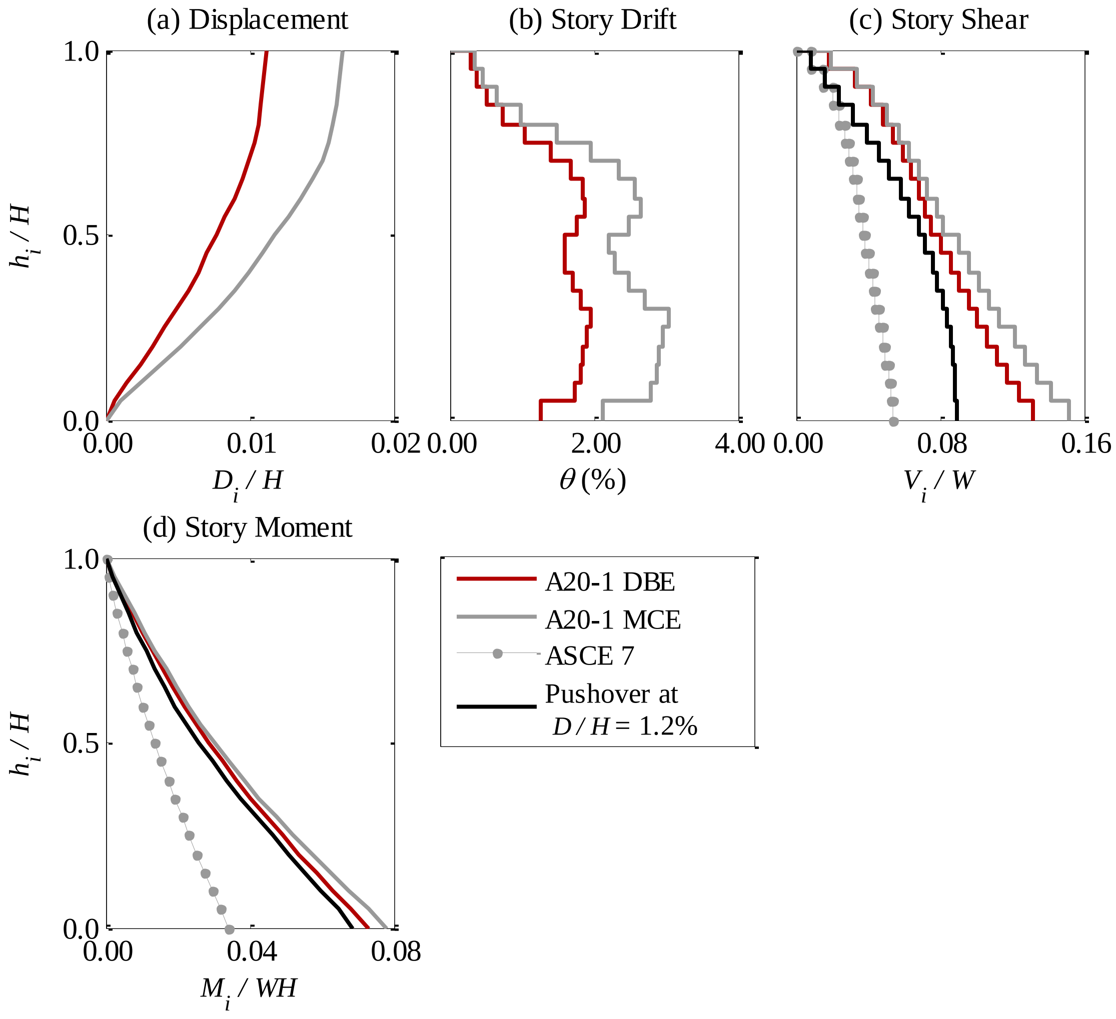

Figure 5.6.1. System mean response envelopes for building A20-1: (a) Relative displacement ratios; (b) Story drift ratios; (c) Story shear force; (d) Story moment.

Peak inelastic tensile strains in column longitudinal reinforcement occur at the base of the building for both shaking intensities, as shown in Table 5.6 and Figure 5.6.2(a) through (c). The mean tensile strain in the first-story exterior columns is 2.1% for the DE shaking. The mean tensile strain at MCE is 4.1%, which is roughly four times the strain obtained from the pushover analysis at drift ratio equal to the mean MCE drift ratio of 1.6% (shown in Figure 5.5.1), indicating different deformation patterns arising from these two different methods of analysis, as has been reported before (ATC 2005). The static pushover analysis does not appear to be an accurate tool for estimating the expected deformation demands in the columns at the base of the building.

Inelastic deformations occurred in columns above the bottom story in different locations along the height of the buildings (Figure 5.6.2 [a]-[c]). Over the building height, the interior and middle columns develop roughly 30% larger reinforcement tensile strains than the exterior column. At the DE, the mean reinforcement tensile strains above the base in the exterior columns are less than 0.9%, while at the MCE level they reach up to 2.2%. The largest mean strain above the bottom two stories of the columns occurs in the locations of column size reduction or longitudinal column reinforcement curtailment.

Significant longitudinal reinforcement tensile strains developed in the beams for both the DE and MCE shaking levels, as can be observed in Figure 5.6.2 (d). The strain envelopes at both seismic hazard levels had similar shapes, roughly following the pattern of peak story drifts (Figure 5.6.1[b]), with nearly uniform strain levels in the bottom 70% of the building height. The mean tensile strain envelopes of the beams reached a peak value at 0.3*H* (Figure 5.6.2 [d]) and were 3.4 and 5.3% at the DE and MCE levels, respectively.

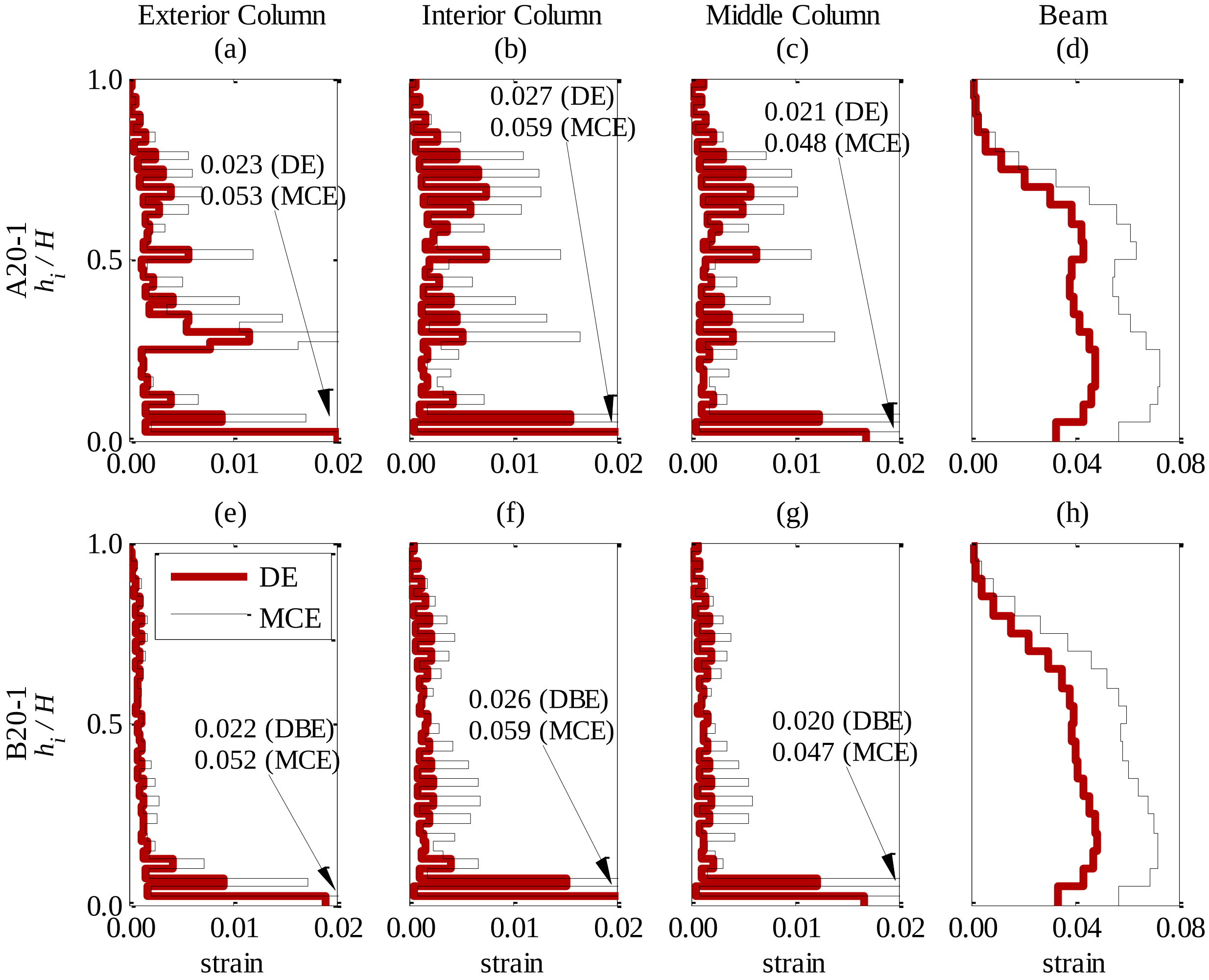

Figure 5.6.2. Longitudinal reinforcement mean tensile strain envelopes in frame members of buildings A20-1 and B20-1.

The exterior columns of A20-1 at the base developed mean concrete compressive strains equal to 1.0 and 2.0% at DE and MCE hazard levels, respectively (Table 5.6). Relatively large strains at the base of the exterior columns were the result of large inelastic deformations and significant axial compressive forces. For the total volumetric transverse steel ratio in the plastic hinge region, ρ_s = 0.04, the maximum concrete compressive strain according to Scott et al. (1982) was calculated as ε_{cu} = 5.4%. Note that the calculated confined concrete strain capacity does not consider simultaneous shear, axial force, and inelastic lateral deformations, which may reduce the strain capacity of the confined concrete in columns when acting concurrently over several cycles. In stories 3 to 20 the mean concrete compressive strains in all columns are less than 0.3% for both the DE and MCE levels.

Figure 5.6.3 shows the envelope of the computed axial load ratios P/f'_cA_g for the exterior columns and for the beams, plotted along height. The computed mean compressive axial force in the exterior columns is $0.33f'_cA_g$ at DE and increased by less than 4% to ($0.34f'_cA_g$) at the MCE hazard level. The exterior column mean tensile axial force is $0.15f'_cA_g$ and $0.17f'_cA_g$ at the DE and MCE, respectively. These magnitudes of forces exceeded the design axial forces calculated by the code-specified modal response spectrum analysis (MRSA), primarily because the code procedures do not account for the design overstrength which arises mostly from the as-designed flexural strength of beams. Section hardening of the beams along the height of the building with increasing lateral displacements is the second cause of increased axial force demands computed with NRHA. The mean DE (MCE) level compressive axial force computed with the NRHA for a first-story exterior column was 1.39 (1.42) times the design value estimated with MRSA and load combination 5 [$(1.2 + 0.2S_{DS})D + 1.0E + 0.5L$]. The mean tensile forces computed at the base of the exterior columns in NRHA for DE and MCE were, respectively, 2.0 and 2.2 times the demand calculated by MRSA and load combination 7 [$(0.9 - 0.2S_{DS})D + 1.0E$].

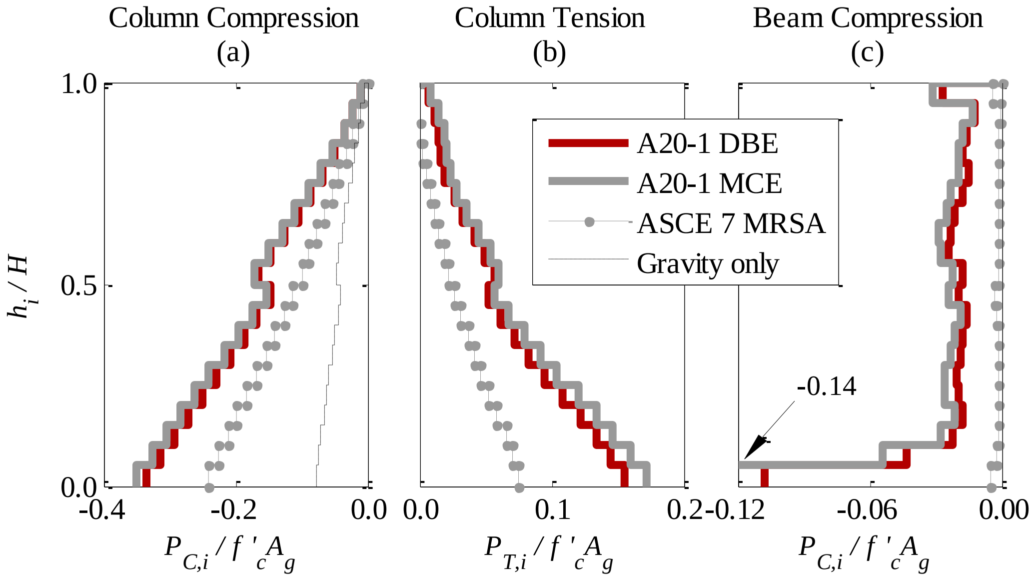

Figure 5.6.3. Exterior column axial forces and beam axial compression forces for building A20-1.

Based on the pushover analysis at 0.5% roof drift ratio (the drift for which major nonlinearity in the system force-displacement relation initiates for the studied buildings), the tension and compression forces at the base of the exterior columns were roughly 1.6, and 1.3 times the design forces computed with MRSA and load combinations 7 and 5, respectively (Figure 5.6.3 [a] and [b]). At 1.6% roof drift ratio (the mean roof drift ratio at MCE level) the corresponding tension and compression forces were about 2.1 and 1.4 times the design values, respectively.

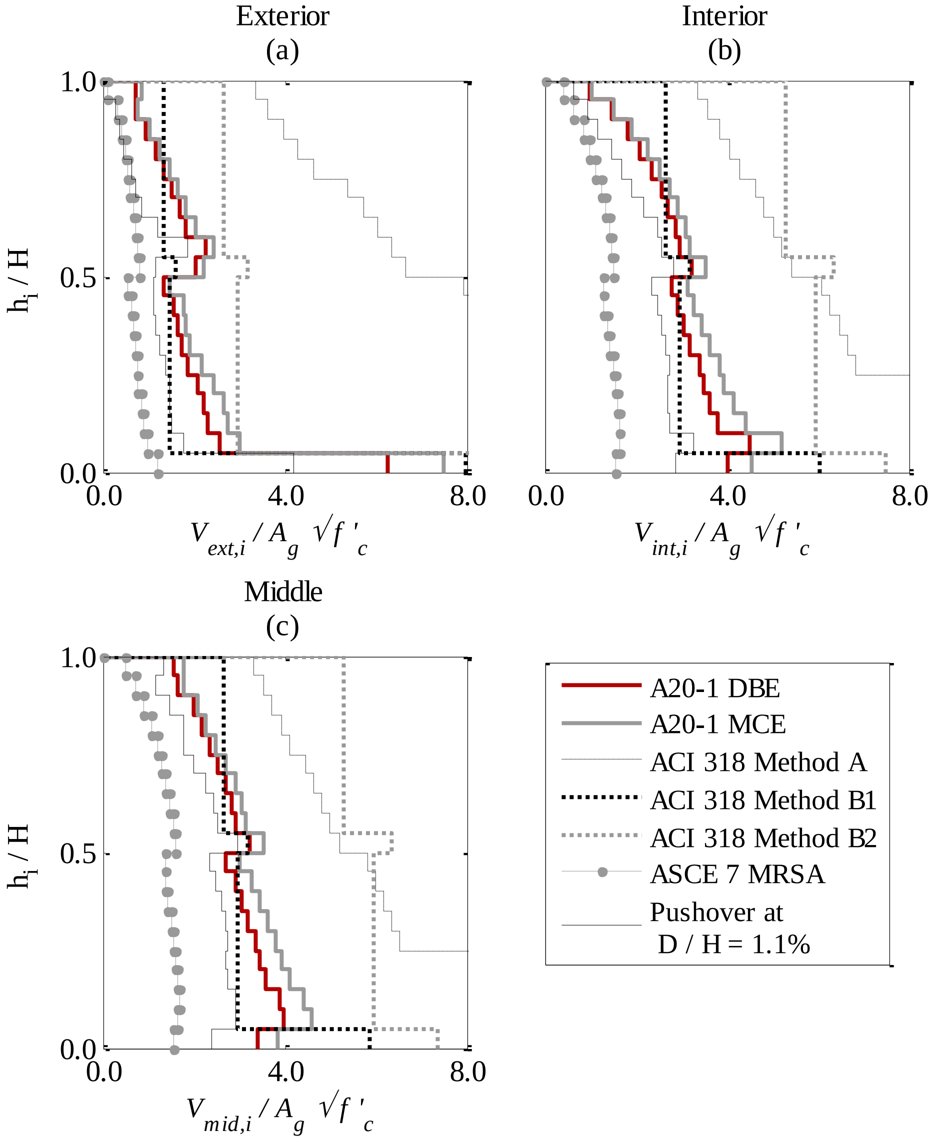

Figure 5.6.4. Column shear envelopes for building A20-1.

Lastly, individual column shear envelopes normalized by $A_g\sqrt{f'_c}$ are plotted in Figure 5.6.4, along with the design forces calculated by different methods for the exterior, interior, and middle columns, respectively. The column shear calculated using NRHA typically is more than twice the value computed using MRSA. Note that while the mean shear force in the third-story interior column is 64% larger than the corresponding exterior column shear, the relation switched in the first story, where the exterior column experiences 54% larger shear than the interior column at the DE hazard level. The larger first-story exterior column shears are a result of kinematic interaction between the beams and the columns. Inelastic flexural deformations of the beam result in beam elongation that forces the exterior columns outward leading to increased shear force and rotations mainly of the exterior column, as demonstrated in Chapter 4 and also noted by others (e.g. Fenwick and Fong 1979, Restrepo et al. 1990, Qi and Pantazopoulou 1991, Fenwick and Megget 1993, Kim et al. 2004, Peng et al. 2006). The increasing axial compression in exterior bay beams toward the bottom of the building (Figure 5.6.3[c]) indicates that beam elongation mostly impacts the columns in the first story and, to a lesser extent, the second story for the building studied. In exterior columns, the mean shear is $6.26A_g\sqrt{f'_c}$ for the DE and $7.48A_g\sqrt{f'_c}$ for the MCE ground motions. The magnitude of the calculated forces, and the shear stresses associated with them, suggests that beam growth can be an important component of the shear forces that develop in the columns in the first few stories, a factor that may should be considered in design.

The NRHA-computed column shears are compared with the design shears computed by two methods specified in ACI 318. Method A considers the shear V_i developed in the column at the time when both of its ends reach the maximum probable moment strength, $M_{pr,c}$, associated with the range of factored axial loads, P_u, calculated from load combinations 5 and 7 (ASCE 7). Specifically, this shear is $V_i = 2M_{pr,c,i} / l_{u,i}$ where l_u is the column clear height. Method B considers column shear corresponding to development of beam probable moment strengths, $M_{pr,b}$, at the joints but the resisting moments in column above and below are indeterminate and it is up to a designer to decide the moment distribution pattern. It is not uncommon in practice to assume the resisting moment $\sum M_{pr,b}$ at a given joint to be divided evenly between the column above and below the joint, which would roughly correspond to the point of contraflexure being located at the story mid-height. This approach, termed here B1, yields a design shear at floor $i > 1$ equal to $V_i = (\sum M_{pr,b,i} + \sum M_{pr,b,i-1}) / 2l_{u,i}$. For clarity, the contribution of beam shear at the face of the column to joint moment equilibrium was ignored in this expression, but it is included in the shears presented in Figure 7. In the first story, column design shear is obtained by replacing the $\sum M_{pr,b,i-1}$ values by the column $M_{pr,c}$ at level i-1, that is, at the base of the building.

An alternative approach, B2, is essentially an upper-bound of Method B. It conservatively assumes that column at level i resists all the probable moments from beams framing into floors above and below the column, that is, $V_i = (\sum M_{pr,b,i} + \sum M_{pr,b,i-1}) / l_{u,i}$. This approach doubles the values of shear forces found by approach B1, except at the bottom story. This is because both methods consider the development of $M_{pr,c}$ at the base of the column, which is typically much larger than $M_{pr,b}$ of the beams and thus controls the value of V_1. For example, in building A20-1 the $M_{pr,c}$ of first-story columns under design P_u leading to the largest probable moment strength is 3-5 times the $M_{pr,b}$ in the bottom story beams.

Method A significantly overestimated the shear force demands compared with those computed using NRHA for all columns along the height (Figure 5.6.4). Shear forces calculated by this method at the base of the columns were approximately twice the mean shear forces computed by the NRHA for the MCE hazard level. Method B1 underestimated the shear forces in all columns along most of the bottom two-thirds of the building height. The exception was at the bottom story where Method B1 resulted in shear forces 1.08, 1.35, and 1.55 times the mean shears computed by the NRHA for the MCE level in the exterior, interior, and middle columns, respectively. Method B2 overestimated the shear forces in columns everywhere, except at the second story exterior column where it slightly underestimates the mean MCE level response.

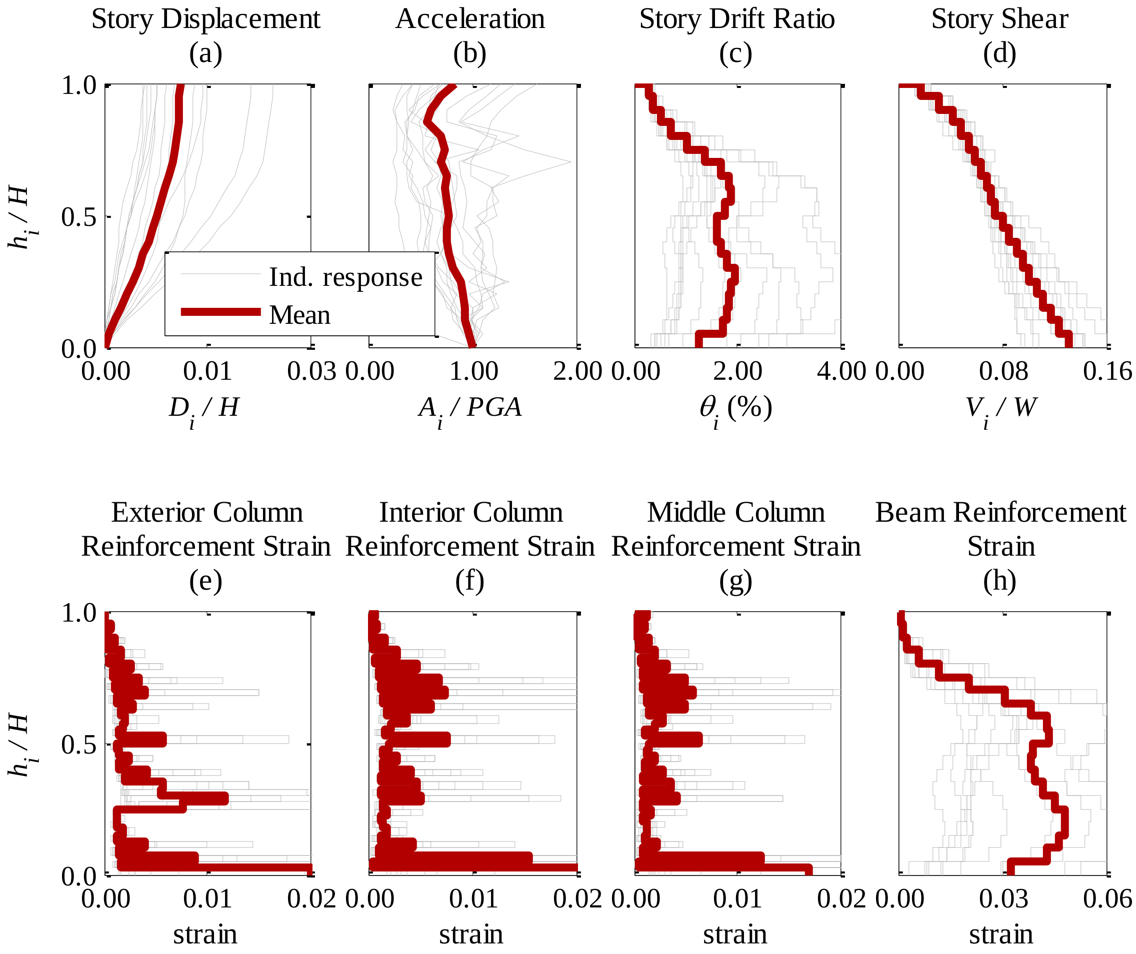

Figure 5.6.5. Scatter in the system response parameter envelopes for building A20-1 and near fault pulse-type ground motion set scaled to DE.

The shears in the exterior columns near the base of the building are of particular interest because of the boost in shear resulting from beam axial growth. In the first story, the shear by Method A is 1.96 times the mean value from NRHA for MCE motions. Methods B1 and B2 produce shears that are 1.08 and 1.18 times, respectively, mean shears from NRHA at the same hazard level. The applicable code in New Zealand, NZS3101 (SNZ 2006) considers the effect of beam growth on exterior columns by requiring that a method equivalent to Method A be used for shear design in regions affected by beam growth. For the second-story exterior columns of the present study, which is also affected by the beam growth, the mean shear is roughly the same as the value estimated by Method B2 at MCE shaking level.

Figure 5.6.5 and Figure 5.6.6 show the individual response envelopes for building A20-1 under 14 near-fault pulse-type ground motions scaled to DE and MCE hazard levels, respectively. Higher scatter is observed in story displacements, accelerations and story drifts. Less scatter is observed in the shear forces and even less in the bending moments (which are not shown).

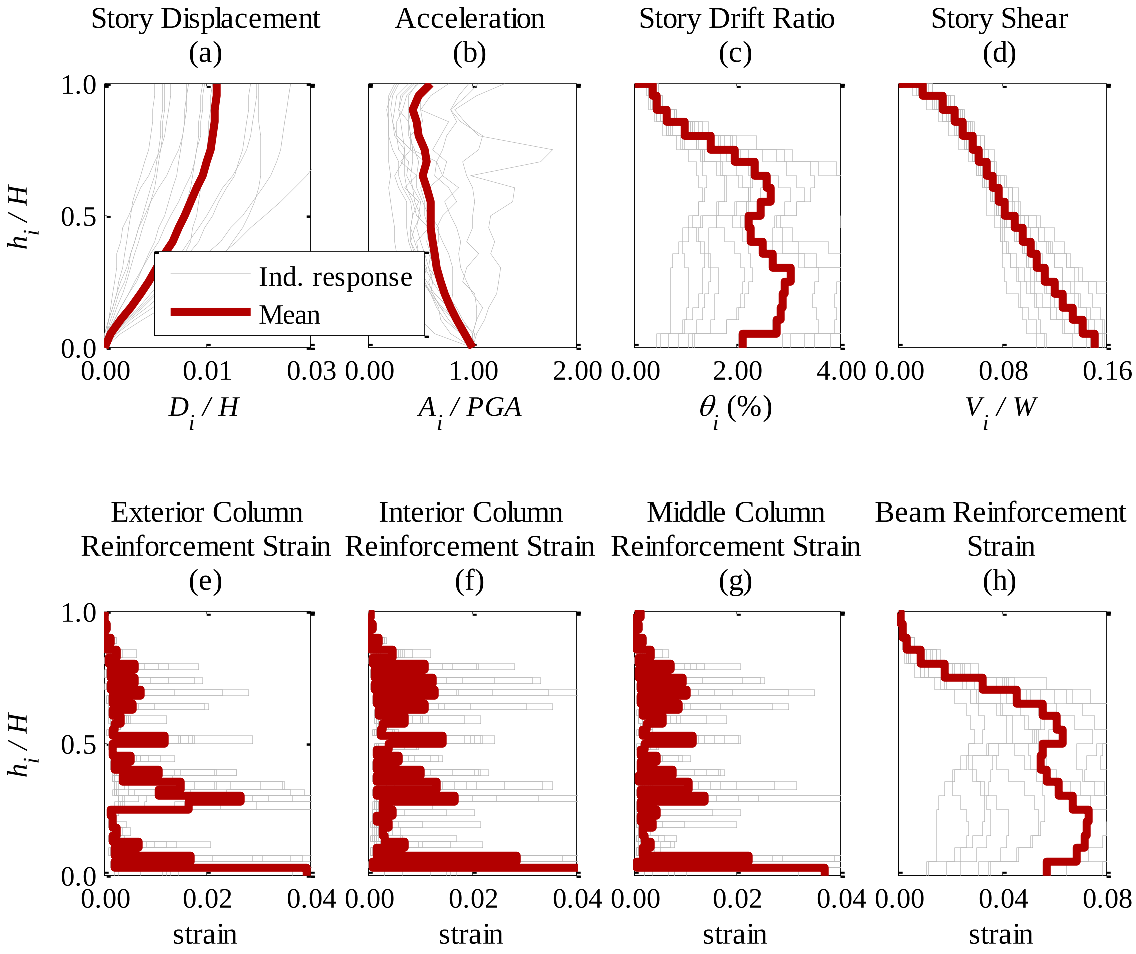

Figure 5.6.6. Scatter in the system response parameter envelopes for building A20-1 and near fault pulse-type ground motion set scaled to MCE.

5.6.2 RESPONSE OF TYPE B BUILDINGS

We now turn our attention to the response of Type B buildings. The main global response envelopes are plotted in Figure 5.6.7. The analyses of building B20-1 under DE and MCE level motions showed global responses very similar to those of building A20-1. The mean and peak roof drift ratios, base shear forces, axial forces at the base of the exterior columns, and beam tensile strains were practically the same as those of A20-1 (Table 5.5 and Figure 5.6.7). However, contrary to behavior of building A20-1, the reinforcement tensile strain values at levels 6, 11, 16 of B20-1 for DE level were below yielding, as can be seen in Figure 5.6.2(e)-(g) and Table 5.6.

At the MCE levels, the mean tensile strain in these floors reached up to 0.7% for B20-1, while for A20-1 the strains at the same locations reached 2.2%. Reinforcement tensile strains in the exterior column were less than 0.2% in all of these locations (see Table 5.6 and Figure 5.6.2). The difference in strain distribution between the two buildings is evident by comparing the plots in Figure 5.6.2, which plot the mean longitudinal reinforcement strains in columns and beams of buildings A20-1 and B20-1. The concentration of large reinforcement tensile strains at levels 6, 11, and 16 in columns of building A20-1 is attributable to the reduction of column size and longitudinal reinforcement curtailment in that building. On other hand, building B20-1 had no curtailment in column size or amount of longitudinal reinforcement over height and hence no associated concentrations of large strain.

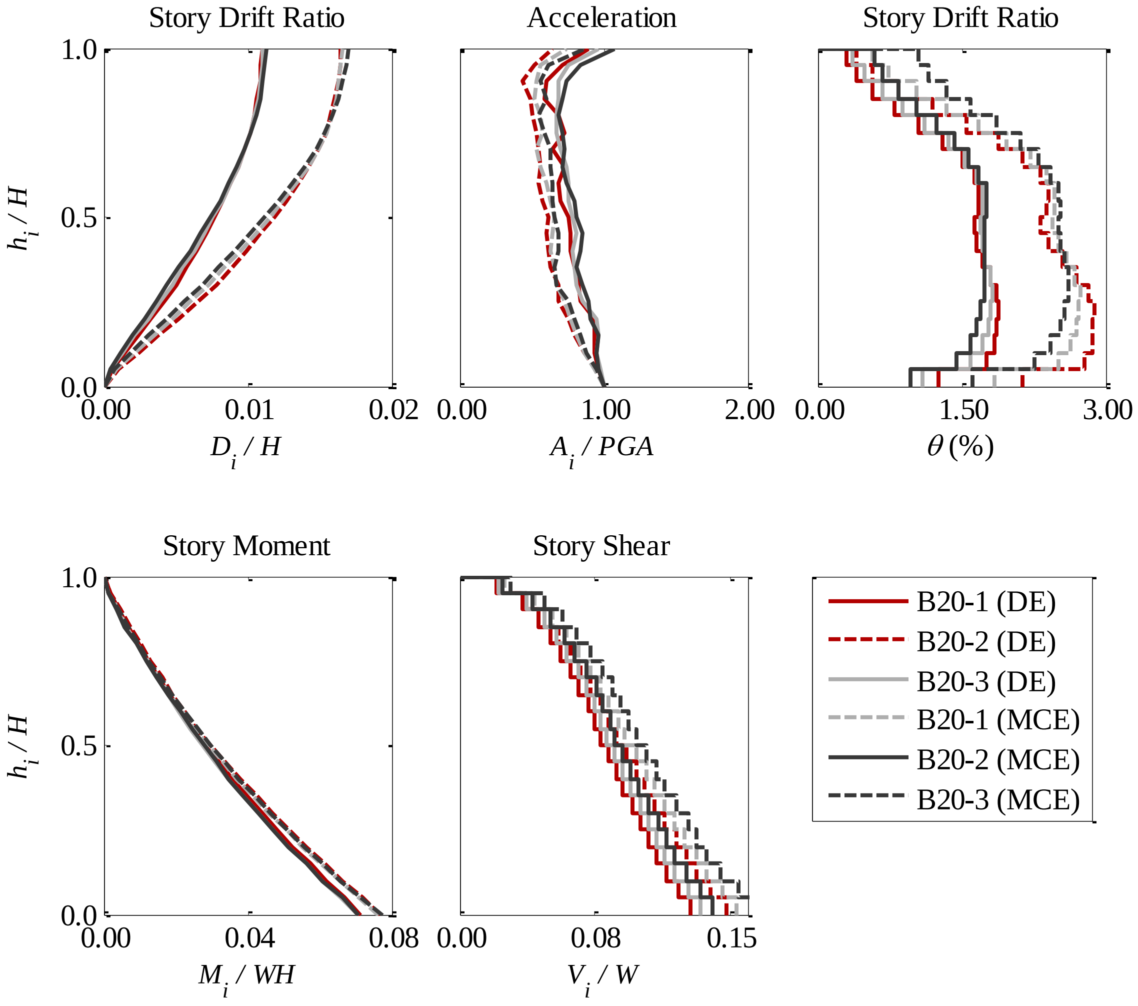

Figure 5.6.7. Comparison of mean response envelopes for B20 buildings under near-fault pulse-type ground motion set, and two levels of ground motion intensity.

Buildings B20-2 and B20-3 had small differences in mean displacement and shear force envelopes compared with building B20-1, as can be seen in Figure 5.6.7. Mean system base moment at DE varied only slightly for the three B20 buildings. As shown in Table 5.5, there was a less than 10% difference in mean roof drift ratio, system base shear, and maximum along the height story drifts. Figure 5.6.7(c) shows the reduction in story drift ratios in the lower half of the buildings, as the exterior column size increased from B20-1 to B20-2 to B20-3.

While the mean displacement envelopes were very similar among the three B20 buildings, significant reduction in column compressive strain was accomplished with the increase of exterior column cross section size. Mean compressive strains in concrete at the base of the exterior column for B20-1, -2, and -3 buildings were 1.0, 0.5, and 0.2% at the DE level (Table 5.6). At the MCE level, the mean compressive strains in concrete at this location were 1.9, 1.0, and 0.4%, for the three buildings. The difference in the reinforcement tensile strains along the building height above the base for the three B20 buildings was negligible (Table 5.6). With the exception of the bottom story, mean tensile strains were either well below or slightly above the yielding levels for both ground motion intensities.

Due to the increased exterior column size, the axial load ratio was reduced in the exterior columns for buildings B20-2 and B20-3 (Table 5.5) compared with that in B20-1, even though the actual exterior column axial force increased compared with that in B20-1 (by 9 and 17% for B20-2 and B20-3 at DE, respectively). For B20-2, the compressive axial load ratio at the base was 30% lower than that of B20-1, whereas in building B20-3, it was 51% lower. Reduction of axial load ratios resulted in decreased concrete compressive strain at the exterior column base, which could correspond to smaller post-earthquake damage.

Exterior column shear stress was also reduced by using larger exterior columns. In the first-story exterior column of buildings B20-1, B20-2, and B20-3 the mean shear force normalized with $A_g\sqrt{f'_c}$ at DE (MCE) levels were 0.52(0.62), 0.41 (0.48) and 0.33 (0.39), respectively (Table 5.5). Shear forces in middle and interior columns of all buildings were well under those computed by Method B2 of ACI 318, as shown in Figure 5.6.8. Method B2 provided a conservative design shear estimate in exterior columns of buildings A20-1 and B20-1, except in the second story. As the column size increased in B20-2 and B20-3, however, the method increasingly underestimated the shear demand in the exterior columns. For building B20-2, the DE-level exterior column shear exceeded the design shear between stories 2-6 and 11-15, while for B20-3, the shear demand was higher than the design estimate along most of the building height, except in the stories 1, 7-10 and at in the upper two floors. Method A significantly overestimated design shear forces in all buildings with the overestimation increasing with increase of column size.

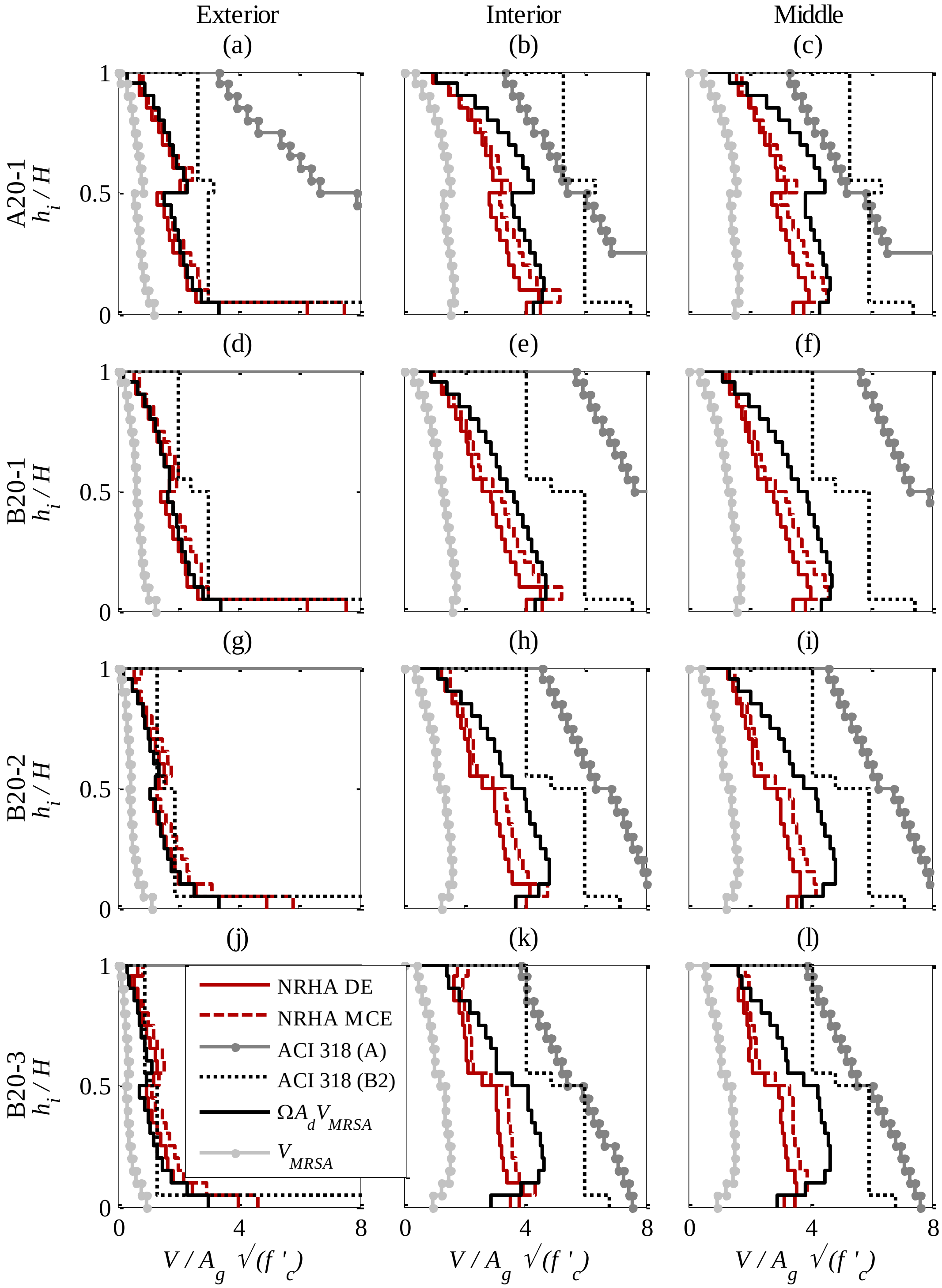

Figure 5.6.8. Comparison of column mean shear force response envelopes with proposed design method and ACI 318 design shear force envelopes.

5.7 MODIFICATIONS FOR ESTIMATION OF COLUMN DESIGN FORCES

The ASCE 7 and ACI 318 code procedures significantly underestimated axial forces in columns of the studied buildings. Furthermore, depending on the method used, ACI 318 procedures either significantly underestimated or overestimated the column shear forces. In this section we present alternative approaches intended to better estimate design column axial forces, design system shear forces, and design column shear forces.

Axial forces in exterior columns of SMRFs subjected to earthquake excitation arise from the shear forces transferred from the beams framing into the column as well as the gravity loads of the column itself and, if vertical ground motion component is present, the corresponding inertia forces. Ignoring the latter, the design tension and compression forces in the exterior columns can be computed using Equations 5.1 and 5.2, which combine axial forces from gravity loads and probable moment strength in beams.

$$P_{U,T,i} = \gamma_T \sum_{j=i}^{N} V_{pr,\,j} - P_{g,\,i} \qquad 5.1$$

$$P_{U,C,i} = \gamma_C \sum_{j=i}^{N} V_{pr,\,j} + P_{g,\,i} \qquad 5.2$$

In these equations, gravity load $P_{g,}$ is the sum of all tributary gravity loads above the level in question computed from the load combination used in NRHA (1.0D+0.25L). V_{pr} is the shear corresponding to development of probable moment strengths M_{pr} in beams framing above the level in question, calculated assuming zero gravity loads. Factors γ_T and γ_C are the average percentage of the probable shear force developed by all the beams above this level i. This approach for estimating the axial forces in exterior columns is similar to the one outlined in New Zealand concrete design code NZS3101 (SNZ 2006). In NZS3101, however, these factors are calculated for each individual story; here, one single value was pursued.

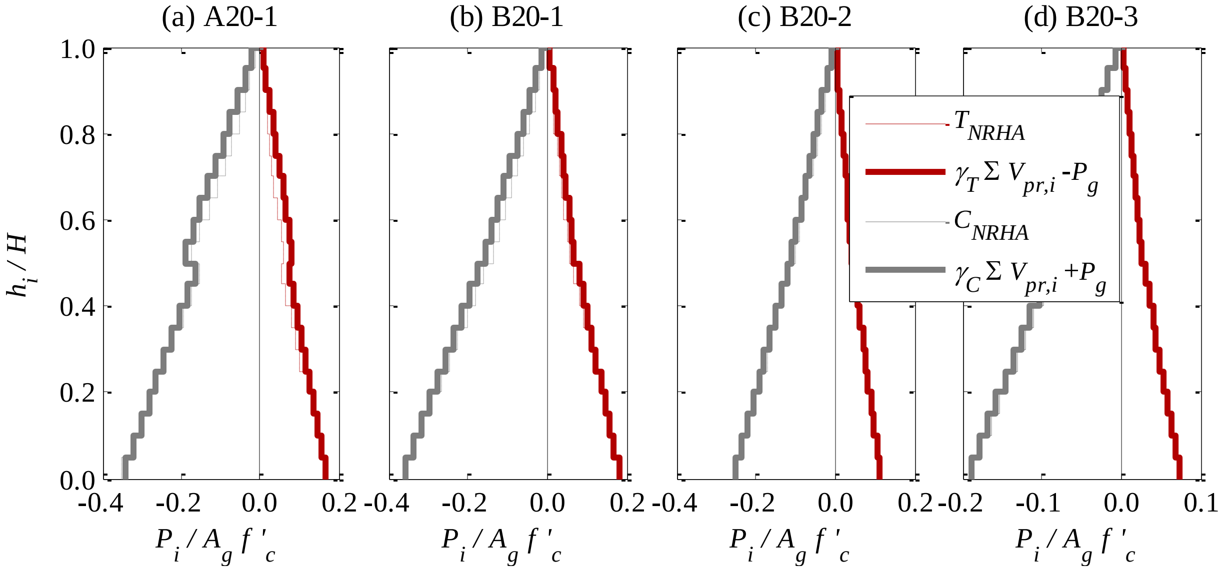

Figure 5.7.1. Comparison of exterior column mean axial force envelopes and axial forces by the proposed design method. All results for MCE level.

Factors γ_T and γ_C were calibrated so that Equations 5.1 and 5.2 produce exterior column axial force equal to the mean axial force calculated using NRHA procedures. The values of γ_T ranged between 0.73 and 0.76, while the values of γ_C varied between 0.78-0.80 for the mean axial force at the DE level, as can be seen in Table 5.7. The values are close to, but higher than the 0.7 value recommended by the NZS3101 at the base of the buildings. At the mean MCE level, the γ_T factors increased to 0.77-0.80, while the γ_C increased to 0.80-0.86 (Table 5.7).

Figure 5.7.1 plots the exterior column axial force envelopes calculated for the NRHA for the MCE hazard level and also by the design method considered previously. Very good agreement is observed at mean response with uniform γ factors calibrated based on the first story axial load. A designer may conservatively use an upper bound value $\gamma_T = \gamma_C = 0.86$.

For system shear forces a modification of the elastic modal response spectrum analysis is proposed using Equation 5.3. This approach is based on amplifying the shear forces, V_{MRSA}, calculated using the code procedure, by the system overstrength factor Ω, which considers the design and section hardening overstrength, and factor A_D, which accounts for higher-mode effects.

$$V_u = A_D \Omega V_{MRSA} \qquad 5.3$$

In Equation 5.3, V_{MRSA} is the shear calculated by the elastic MRSA procedure of ASCE 7. The factor Ω is calculated using Equation 5.4 as the ratio of the system moment capacity at the base of the building, $M_{b,\Omega}$, to the corresponding system moment at the base, $M_{b,u}$, computed from the MRSA.

$$\Omega = \frac{M_{b,\Omega}}{M_{b,u}} = \frac{\sum M_{pr,c,g} + \kappa\left(P_{T,\Omega} + P_{C,\Omega}\right) B/2}{M_{b,u}} \qquad 5.4$$

$M_{b,\Omega}$ corresponds to a level of response equal or larger than that corresponding to the DE seismic hazard level. $M_{b,\Omega}$ is calculated as the sum of the probable flexural strength of the columns at the base of the building and the moment due to axial forces in the columns. The $\sum M_{pr,c,g}$ is the sum of probable moment strengths of columns at the base when subjected to axial load equal to gravity load used for the NRHA, that is $1.0D + 0.25L$. The latter term is calculated based on the axial forces $P_{T,\Omega}$ and $P_{C,\Omega}$ of the exterior columns at the base and is amplified with the factor κ to account for the relative contribution of the interior column axial forces to the base moment. Axial forces $P_{T,\Omega}$ and $P_{C,\Omega}$ are calculated using Equations 5.1 and 5.2 with the difference of setting γ_T and γ_C factors equal to unity. In Equation 5.4, B represents the distance between the centerlines of two exterior columns. Dynamic amplification factor A_D was calculated for each building by dividing the base shear computed from the NRHA by the base shear computed by MRSA multiplied by the system overstrength factor from Equation 5.4.

Design factors A_D, κ, and Ω computed for the individual buildings studied are listed in Table 5.7. The computed mean value of A_D ranged from 1.0-1.12 for DE, and from 1.18-1.29 for MCE shaking level. Values of factor A_D computed at the peak values of the DE and MCE levels were similar to the dynamic magnification factor ω=1.3 used in NZS3101 for individual column shear force estimation. An upper bound value is recommended for use when estimating V_u during the design process, that is $A_D = 1.3$. Factor κ was calculated equal to 1.1 for the frames considered in this chapter.

Using the factors computed, design envelopes were generated for the system shear of the four buildings. These are presented alongside the corresponding NRHA-computed response envelopes at DE and MCE shaking intensities in Figure 5.7.2 for all four buildings. The system shear envelopes computed by the method presented bounded the NRHA-calculated system shear forces at all levels for building A20-1 and across all stories, except for the top two stories of building B20-1 and in the second and third stories of B20-2 and B20-3.

Table 5.7. Design factors at mean response.

		A20-1	B20-1	B20-2	B20-3
κ		1.1	1.08	1.05	1.02
Ω		2.35	2.29	2.39	2.35
γ_T	DBE	0.73	0.74	0.75	0.76
	MCE	0.77	0.79	0.79	0.80
γ_C	DBE	0.78	0.78	0.79	0.80
	MCE	0.81	0.80	0.83	0.86
A_D	DBE	1.05	1.05	1.08	1.12
	MCE	1.20	1.21	1.24	1.28

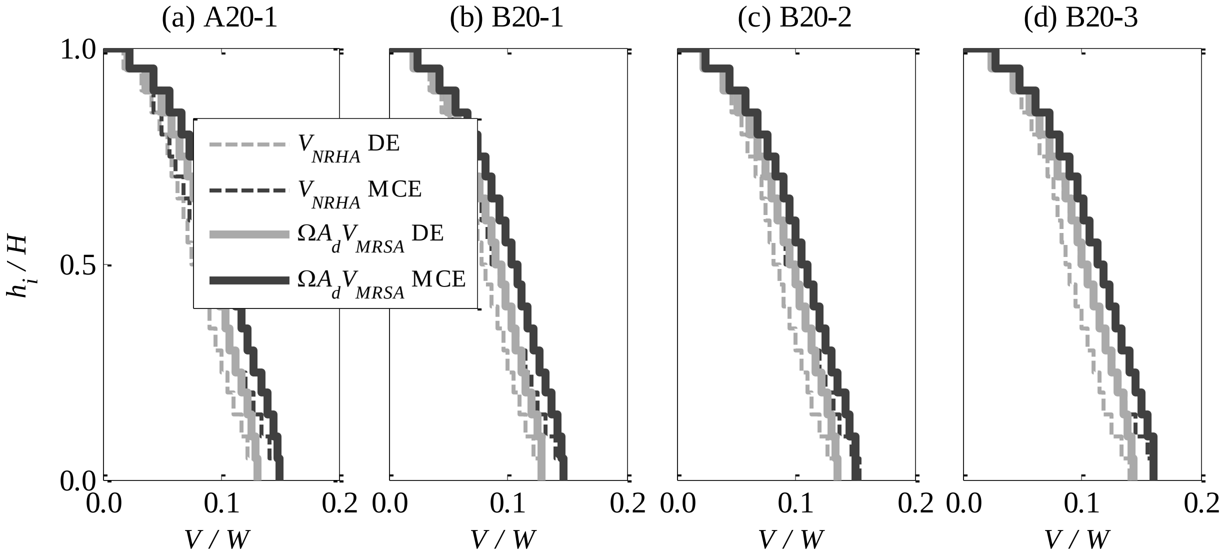

Figure 5.7.2. System shear force response envelopes for Type B buildings.

While the estimated design system shear is not directly used as a design parameter, it can be an important tool in estimating the individual column shears. A correct distribution of story shear provides the estimate of the individual column shears. The applicability of the proposed method to estimating individual column shears was explored by applying the amplification factors Ω and A_D to MRSA-estimated column shear envelopes and comparing the obtained quantities to the NRHA shear demands. Findings are summarized in Figure 5.6.8.

For all four buildings, the method provided conservative estimate of interior and middle column design shears in most of the stories. The NRHA-calculated shears slightly exceed those estimated by the proposed method in the upper and lower two stories of some buildings (Figure 5.6.8). In all cases, the method gave closer estimate to design shear than Method B2 of ACI 318. It is recommended that the column design shear estimated by the proposed method at a given story i not be taken less than the design shears in stories above, that is stories $j > i$. For the buildings considered this resulted in conservative estimation of design shear forces of all interior and middle columns. Alternatively Method B2 provides a much more conservative estimate for design shears in interior and middle columns.

In the exterior column the proposed Equation 5.3 provided a conservative estimate at the DE level in building A20-1 everywhere except the top story and the bottom two stories which were significantly affected by beam elongation effects. The MCE-level shears slightly exceeded those estimated by the method proposed except the base story where the underestimation was significant. In Type B buildings, the method increasingly underestimated the column shear as the size of the exterior column increased. Here, shear demands were on average 1.1-1.5 times the design shears estimated by the method for DE hazard level. The largest underestimation was observed in the bottom two stories and especially in the first that was mostly affected by beam elongation effects. Further refinement of proposed shear calculation method is needed to find a more suitable way for estimating design shear forces in exterior columns. This is further explored in Chapter 6.

5.8 CONCLUSIONS

This chapter numerically investigated seismic response of four 20-story reinforced concrete special moment resisting frames numerically simulated on OpenSees platform. The buildings were designed according to ASCE 7-10 and ACI 318-11 code provisions. Building A20-1 (Type A) had columns with dimensions and longitudinal steel ratio reduced at levels 6, 11, and 16. The other three buildings, labeled as Type B, had uniform column size and reinforcement ratio along the height. Building B20-1 had columns with size and longitudinal reinforcement identical to that used at the base of building A20-1. Buildings B20-2 and B20-3 differed from B20-1 only in the size and longitudinal reinforcement of exterior columns. The buildings were subjected to a set of ground motions scaled to both the DE and the MCE design spectra of ASCE 7, for a site located in Los Angeles, California. Based on the results presented in the preceding sections, the following conclusions are drawn:

1. All of the studied buildings developed significant inelastic deformations in the columns at the base of the building and in 70% of the beams along the building height for both DE and MCE hazard levels.
2. Increasing the size of exterior columns significantly reduces compressive strains in confined concrete and, to a lesser extent, reinforcement tensile strains developed in the up-sized columns, possibly leading to less post-earthquake damage. The mean compressive strains computed at DE (MCE) shaking levels at the base of the exterior columns of the four buildings were 1.0(2.0), 1.0(1.9), 0.5(1.0), and 0.2(0.4)% for buildings A20-1, B20-1, B20-2, and B20-3, respectively. The size increase of the exterior columns also resulted in a decrease of story drift at the first story.
3. Building A20-1, for which columns had progressively smaller cross-sections and amount of longitudinal reinforcement with height, developed moderate inelastic deformations in the columns around the levels where the size and reinforcement reduced. At these locations the reinforcement tensile strains ranged between 0.2-0.9% at the DE and 0.5-2.2% at the MCE shaking level. The same locations of building B20-1 developed negligible inelastic deformations.

4. Equivalent elastic modal response spectrum analysis (MRSA) of ASCE 7 significantly underestimates axial forces in the exterior columns because it does not consider the design as well as the section overstrength of frame elements. For the DE hazard level, the mean axial tensile forces in exterior columns were roughly 2 times the values computed by MRSA while mean axial compressive forces in exterior columns were roughly 1.4 times values calculated by MRSA. A simple method of calculating the exterior column axial forces based on beam flexural overstrength led to a very good design force estimate.
5. The mean story shears were between 2.2 and 2.8 times the design base shear computed with MRSA of ASCE 7. This discrepancy is attributable to design and section overstrength in addition to the effect of higher modes on dynamic response. Amplifying the design system shear forces with an overstrength factor (calculated based on the probable flexural strength of the beams and the columns at the bottom story) and a dynamic amplification factor between 1.05 and 1.28 resulted in very good estimations of the seismic system shear forces demand. Extrapolation of the proposed method to interior and middle columns provided satisfactory estimates of design shears, but further refinement is needed to adequately estimate the exterior column design shears.
6. Kinematic interaction between beams and columns at the bottom two stories due to beam elongation resulted in significant increase of the first-story exterior column shear. Mean values of first-story exterior column shears were between 1.12-1.65 times those in the first-story interior columns. This effect should be considered in the design of the columns.
7. ACI 318 procedures for determining column design shear resulted in widely different design values. The shear corresponding to development of column probable moment strengths at column ends (referred to as Method A herein) grossly overestimated the design shear forces. The shear corresponding to development of beam probable moment strengths at beam ends resulted in different column design shears depending on the interpretation of the Code requirement. If the column above and below each joint was assumed to resist half of the resulting moment (referred to as Method B1 herein), then the design shears were significantly underestimated in several stories. If the column was assumed to resist the entire moment within the story being analyzed for shear (referred to as Method B2 herein), then the design shears were overestimated in most stories. Method B2 resulted in underestimation of design shear forces in exterior columns, along many stories above the base story, in buildings B20-2 and B20-3 at both the DE and the MCE level of shaking. This method underestimated the design shear forces in exterior columns at the first story only of buildings A20-1 and A20-2 at MCE level of shaking.

CHAPTER 6

SEISMIC SHEAR DEMAND ON COLUMNS OF SPECIAL MOMENT FRAMES

As was seen in Chapter 5, current methods for approximating design column shear in special moment frames do not always result in a conservative estimate of ultimate shear forces that columns need to sustain. Overloading of a column in shear is likely to reduce the flexural deformation capacity, and in extreme cases may cause shear failure, which may in turn lead to localized damage and failure of the structural system. Therefore, conservative methods for estimating shear should be implemented in design.

The aim of this chapter is to develop a method of estimating earthquake-induced ultimate shear forces in columns of tall reinforced concrete special moment resisting frames. The method is developed through an investigation of four archetype frame buildings via series of two dimensional nonlinear dynamic analyses. The four buildings range in height and in number of bays per frame. The designs conform to requirements of ASCE 7-10 and ACI 318-14. All four buildings have perimeter SMRF configuration, which is typical of design practices in the seismically active regions of the United States. Note that the four archetype buildings presented in this chapter are different from the buildings investigated in Chapter 5.

6.1 STATE OF PRACTICE DESIGN METHODS FOR SMRF COLUMN SHEAR

Columns in special moment frames are detailed according to the provisions of ACI 318 (ACI 2014). In general, shear in reinforced concrete columns is resisted by the concrete itself (which is considered to provide shear capacity V_c) and the transverse steel reinforcement (which is considered to provide shear capacity V_s). The usual practice is to sum the two nominal strength contributions, resulting in the following design requirement:

$$V_u < \phi(V_c + V_s) \tag{6.1}$$

where V_u is the ultimate shear demand used in design and ϕ is the strength reduction factor for shear. In ACI 318, ϕ for shear is set to 0.75.

According to ACI 318, the portion of the shear strength carried by the transverse reinforcement is:

$$V_s = \frac{A_v f_{yt} d}{s} \tag{6.2}$$

where:

s = shear reinforcement spacing,

A_v = area of shear reinforcement within spacing s,

f_{yt} = nominal strength of transverse reinforcement steel, and

d = distance from extreme compression fiber to centroid of tensile reinforcement.

The portion of the shear strength carried by concrete in members subjected to axial compression (such as the columns) is defined in ACI 318 as:

$$V_c = 2(1+\frac{N_u}{2000A_g})\lambda\sqrt{f'_c}b_w d \qquad 6.3$$

Here:

N_u = factored axial force (in units of pounds, lb) normal to cross section occurring simultaneously with V_u; taken as positive for compression,

A_g = gross area of a concrete section,

λ = correction factor for light weight concrete,

f'_c = nominal strength of reinforced concrete (in units of psi), and

b_w = section width of a member.

When the reinforced concrete member is subjected to significant axial tension, V_c can be assumed to be zero. ACI 318 also offers the following expression, where N_u takes on a negative sign in tension:

$$V_c = 2(1+\frac{N_u}{500A_g})\lambda\sqrt{f'_c}b_w d \qquad 6.4$$

In columns of special moment frames, ACI 318 requires that all shear be resisted with transverse steel within the region of length l_o from each column joint face (and on both sides of any section likely to form a plastic hinge), when both: a) the earthquake-induced shear force represents one-half or more of the maximum required shear strength within l_o, and b) the axial compressive force P_u, including earthquake effects, is less than $A_g f'_c/20$. The region l_o is defined as the maximum of: a) the depth of the member at the joint face or at the section where flexural yielding is likely to occur, b) 1/6 of the clear span of the member, and c) 18 in.

Avoiding shear failure in reinforced concrete members is accomplished through capacity-design principles. Flexural yielding regions in beams and columns are first identified, and then these regions are designed for moments and axial forces computed in appropriate code-based procedures. Subsequently, the design shear is computed using equilibrium and with the assumption that the members develop probable moment strengths in these flexural yielding regions. Currently, two different publications used in the U.S. design practice address the methods of estimating the ultimate design column shear V_u in reinforced concrete moment frames: the ACI 318 code (ACI 2014) and the NIST GCR 8-917-1 (Moehle et al. 2008) document. The procedures of finding V_u defined in these two documents are described in the following two sections.

6.1.1 V_u ACCORDING TO ACI 318-14

The design shear for SMRF columns, according to ACI 318-14, shall in no case be less than the factored shear determined from the analysis of the structure (such as the modal response spectrum analysis or the equivalent lateral force procedures in ASCE 7). In addition, the seismic shear force V_e used in the design shall not be less than the shear determined from consideration of the maximum moments that can be developed at each end of the column adjacent to the joint faces. The column moments at the joint faces can be taken equal to the maximum probable moment strengths, $M_{pr,c}$, at each end of the column associated with the range of factored axial loads acting on the column. ACI 318-14 implicitly recognizes that this latter approach could result in a large overestimation of column shears and the reinforcement required would potentially be unfeasible to construct. Hence, the maximum column shear that needs to be considered in the design is defined as the column shear at the instance when the beams framing into the joint above and below reach their respective probable moment strengths, $M_{pr,b}$. However, the ACI 318 does not specify what the moment distribution pattern in columns should be and it is up to a designer to decide the resisting moments in the column above and below (Figure 6.1.1). As seen in Chapter 5, this can lead to very different results, some resulting in large underestimation of design shear.

It is not uncommon in practice to assume the resisting moment $\sum M_{pr,b}$ at a given joint to be divided evenly between the column above and below the joint, which would roughly correspond to the point of contraflexure of the columns being located at the story mid-height. This approach, termed here B1, yields a design shear at floor $i > 1$ equal to $V_i = (\sum M_{pr,b,i} + \sum M_{pr,b,i-1}) / 2l_{u,i}$. For clarity, the contribution of beam shear at the face of the column to joint moment equilibrium was ignored in this expression, but it is included in the shear forces presented later in this chapter. In the first story, column design shear is obtained by replacing the $\sum M_{pr,b,i-1}$ values by the column $M_{pr,c}$ at level i-1, that is, at the base of the building.

An alternative approach, B2, is essentially an upper-bound of Method B1. It conservatively assumes that column at level i resists all of the probable moments from beams framing into floors above and below the column, that is, $V_i = (\sum M_{pr,b,i} + \sum M_{pr,b,i-1}) / l_{u,i}$. This approach doubles the values of shear forces found by approach B1, except at the bottom story. This is because both methods consider the development of $M_{pr,c}$ at the base of the column, which is typically much larger than $M_{pr,b}$ of the beams and thus controls the value of shear in the first story. For example, in building A20-1, $M_{pr,c}$ of the first-story columns under the design value of P_u leading to the largest probable moment strength is 3 to 5 times $M_{pr,b}$ in the first-story beams.

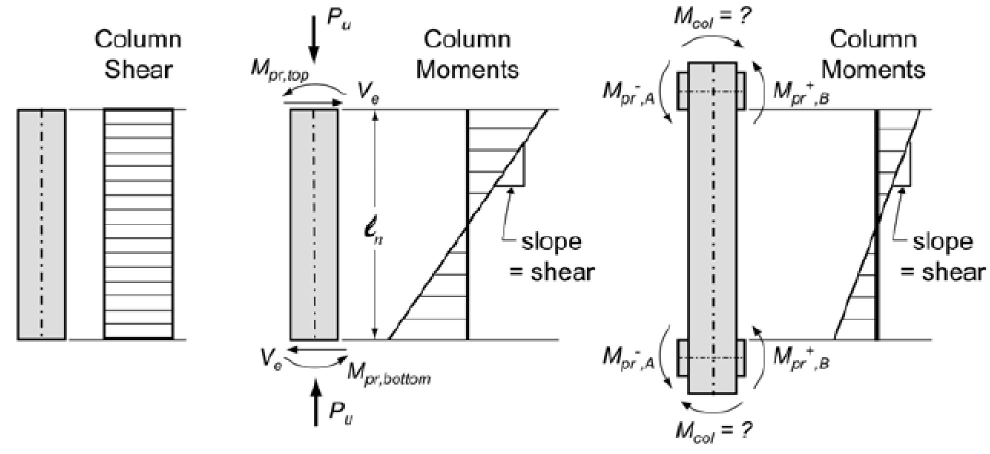

(a) From analysis (b) Column hinging (c) Beam hinging

Figure 6.1.1. Options for calculating design shear in column members, according to ACI 318 (source: NIST GCR 8-917-1).

6.1.2 V_u ACCORDING TO NIST GCR 8-917-1

In 2008, National Earthquake Hazard Reduction Program (NEHRP) released a NIST GCR 8-917-1 document titled "Seismic design of reinforced concrete special moment frames: a guide for practicing engineers" (Moehle et al. 2008) intended to serve as a guide to practicing structural engineers in applying the ACI 318 requirements in reinforced concrete SMRF design. Particularly, the guide follows the 2008 edition of ACI 318 and addresses main SMRF design aspects such as flexural and shear design of beams and columns, joint design, and anchorage requirements. For the remainder of this chapter, the NIST GCR 8-917-1 document will be interchangeably referred to as the "NIST Design Guide".

ACI 318-14 introduced notable changes in the design of transverse steel for confinement requirements in plastic hinge regions of columns. Nevertheless, the shear requirements remain the same as they were in the 2008 and 2011 code editions, and therefore the NIST Design Guide remains current in this aspect. The column shear design method recommended in that document is therefore included in the subsequent discussions.

NIST Design Guide dissuades calculating the column design shear based on the beam-yielding mechanism and distributing the unbalanced moments at a joint to columns in proportion to their flexural rigidities (this loosely corresponds to ACI 318 method B1 defined previously). The guide recommends using ACI 318 method A whenever feasible. NIST Design Guide recognizes, however, that the latter may lead to column section that is difficult to construct; hence, it recommends computing the column design shear based on the shear from lateral analysis but amplified to account for the beam flexural overstrength.

Individual column shear computed by an MRSA or similar procedure following the recommendations of the ASCE 7 or similar code serves as a baseline value, here denoted as V_{MRSA}. This is also the minimum design shear required by the ACI 318. The V_{MRSA} is amplified by a factor corresponding to an average flexural overstrength of all beams framing into the column, Φ_m = average($M_{pr,b,i,j}/M_{u,i,j}$), where $M_{pr,b,i,j}$ = probable moment strength of beam i (where more than one beam frames into the column at a given floor) of story j and $M_{u,i,j}$ = design moment for that same beam.

6.2 DESCRIPTION OF ARCHETYPE FRAMES

In order to investigate the effect of height on column shear distribution, the four SMRF buildings investigated consist of both 10- and 20-story buildings. Both 3- and 4-bay frame configurations are considered for each building height to note the effect of different frame configuration on building response. To be consistent with Chapter 5, all buildings are named starting with a letter A, which indicates that the columns of these buildings have gradual reduction in cross section size and amount of longitudinal reinforcement along the height (unlike building type B in Chapter 5, which had uniform size and reinforcement for all stories).

Table 6.1. Building parameters.

	10 story	20 story
3 x 28-ft bays	A10-3	A20-3
4 x 21-ft bays	A10-4	A20-4

The buildings are systematically labeled with a suffix "# of stories - # of bays" to ease the discussion. For example, A10-3 represents a building having 10 stories height and 3 bays in the special moment resisting frame, while A20-4 represents a 20-story building having 4 bays in the SMRF. Story height in all buildings is 12 ft, while the bay length varies, as shown in Table 6.1.

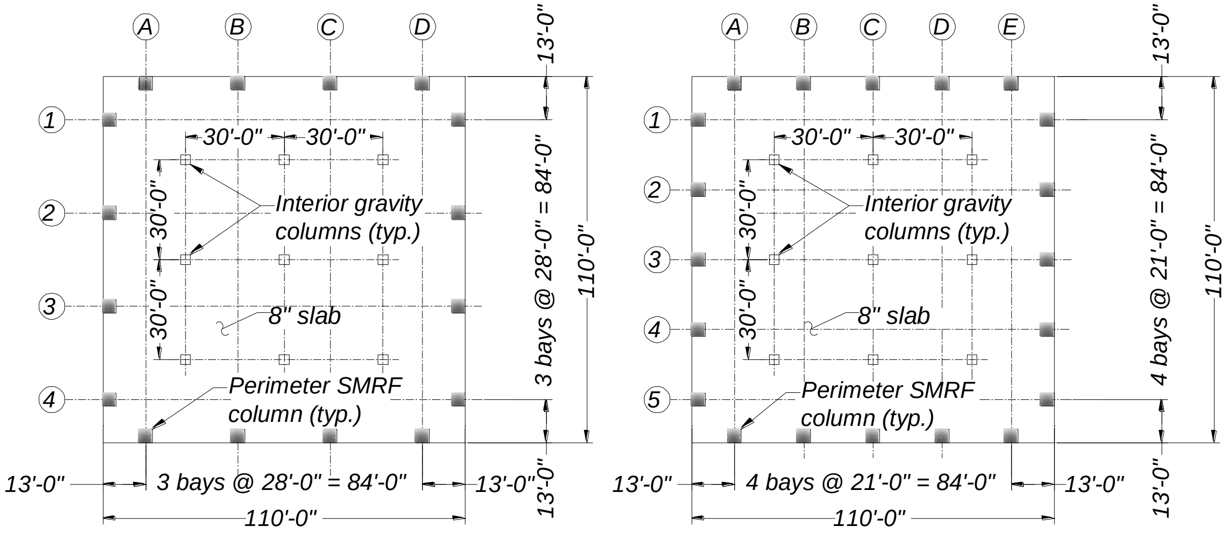

(a) (b)

Figure 6.2.1. Floor plan of the archetype buildings: (a) 3-bay SMRF configuration and (b) 4-bay SMRF configuration.

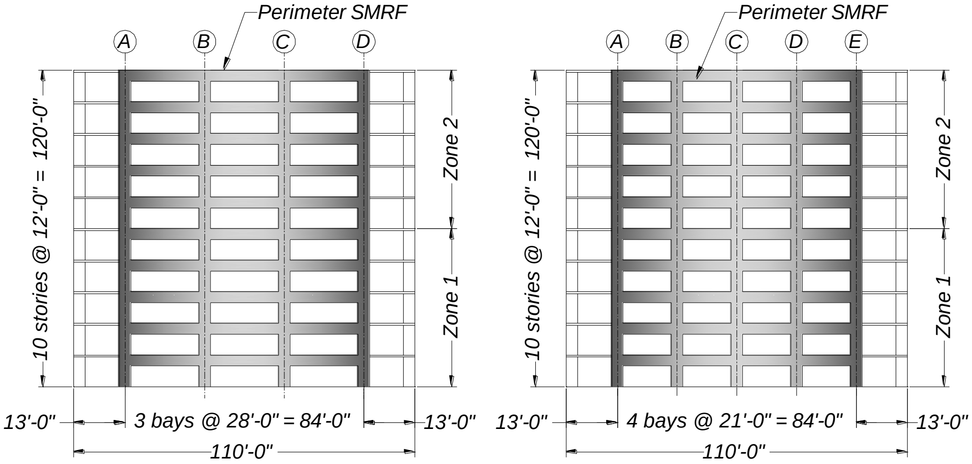

(a) (b)

Figure 6.2.2. Elevation of 10-story archetype buildings: (a) A10-3 and (b) A10-4.

All buildings have identical floor plan (110 ft x 110 ft) and feature two special moment resisting frames in each orthogonal direction, with interior gravity framing, as shown in Figure 6.2.1. The center-to-center distance of 84 ft between the two end columns is identical in all frames. Figure 6.2.2 shows the elevation view of the 10-story buildings, while Figure 6.2.3 shows the elevation view of the 20-story buildings. For simplicity, cross-sectional area of gravity columns is identical in all four buildings. This configuration allows the two buildings of the same height to have approximately the same natural frequencies, seismic masses, and strengths. In the 3-bay frames, the exterior columns are those identified in column lines A, D, 1, and 4 (Figure

6.2.1[a]), while the remaining columns are referred to as interior columns. In the 4-bay frames, the exterior columns are those positioned along column lines A, E, 1, and 5 (Figure 6.2.1[b]). Term "middle column" in further discussion refers to the columns located on lines C and 3, and the remaining columns are referred to as "interior".

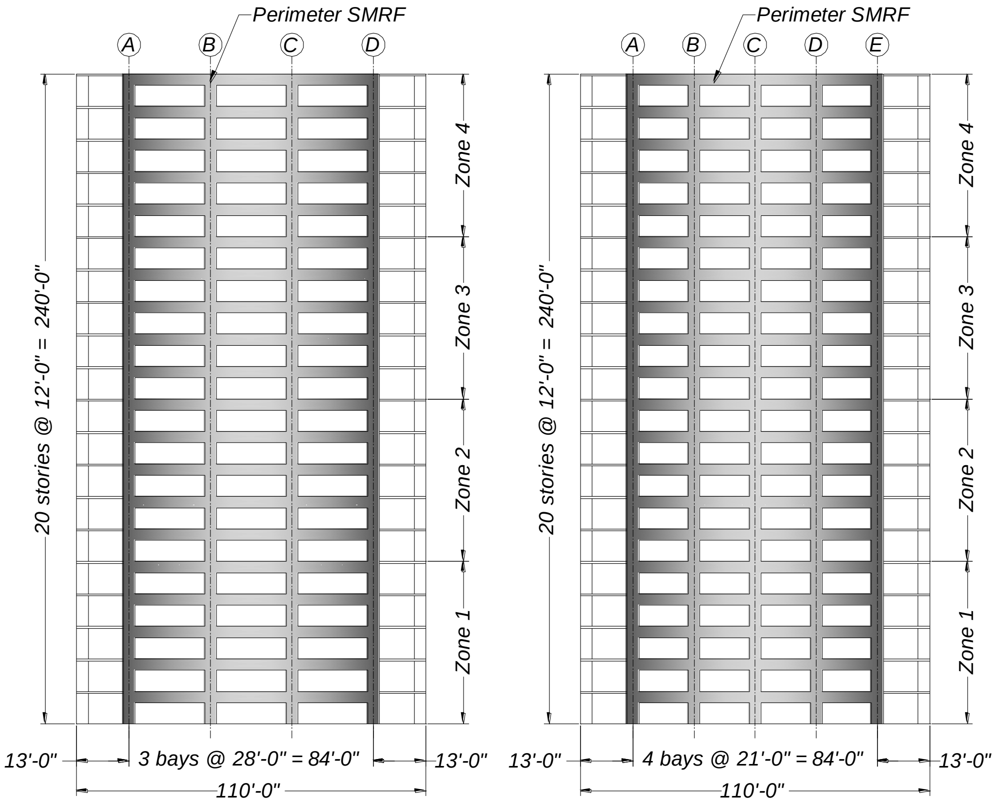

(a) (b)

Figure 6.2.3. Elevation of 20-story archetype buildings: (a) A20-3 and (b) A20-4.

In all of the buildings, the beams are of uniform size and longitudinal reinforcement ratio along all of the height. The sizes of beams are listed in Table 6.2. In all of the buildings, column strength is reduced along the height either by reduction of size, amount of longitudinal reinforcement, or both. In the 10-story buildings, the size of the columns is uniform along the height; however, the longitudinal reinforcement ratio is reduced at the 6th floor. In the 20-story buildings, the amount longitudinal reinforcement is reduced every 5 stories, and the column size is also reduced at the 11th floor. The stories of a given building that contain identical column cross section and longitudinal reinforcement are lumped into zones, as illustrated in Figure 6.2.2 and Figure 6.2.3. The size and longitudinal reinforcement ratio of columns are also indicated in Table 6.2. Interior and middle columns of buildings with 4-bay frames are identical in cross section, thus, Table 6.2 only includes specifications for interior columns. Due to design constraints, longitudinal reinforcement reduction in interior columns of A20-3 and A20-4 and exterior columns of A20-4 at the 16th story would have resulted in less than 15% reinforcement ratio reduction. Thus, the amount of longitudinal reinforcement was kept constant in zones 3 and 4 of these columns.

Table 6.2. Frame element sizes and steel ratios (b = width, h = height, ρ_l = longitudinal reinforcement ratio. Note: for beams $\rho_l = A_s/bd$, for columns $\rho_l = A_s/bh$, with A_s = area of longitudinal reinforcement on one face of the beam, and for columns $\rho_l = A_s/bh$, with A_s = total area of longitudinal reinforcement in the cross section).

Building	Zone	beam			exterior column			interior column		
		b (in.)	h (in.)	ρ_l	b (in.)	h (in.)	ρ_l	b (in.)	h (in.)	ρ_l
A10-3	1	24	36	0.0078	36	36	0.0171	36	36	0.0171
	2				36	36	0.0110	36	36	0.0110
A10-4	1	24	32	0.0071	32	32	0.0154	32	32	0.0185
	2				32	32	0.0117	32	32	0.0154
A20-3	1	28	46	0.0064	48	48	0.0151	48	48	0.0123
	2				48	48	0.0110	48	48	0.0110
	3				44	44	0.0114	44	44	0.0147
	4				44	44	0.0100	44	44	0.0147
A20-4	1	24	38	0.0092	42	42	0.0202	42	42	0.0159
	2				42	42	0.0125	42	42	0.0125
	3				36	36	0.0122	36	36	0.0216
	4				36	36	0.0122	36	36	0.0216

6.3 SEISMIC HAZARD

The four archetype buildings are located on a hypothetical site in the financial district of downtown San Francisco, California (Figure 6.3.1). The selected location is on stiff soil, which categorizes as site class D, according to the ASCE 7 classification. For a design earthquake (DE) level and 5% damping, ordinates of pseudo-acceleration spectrum at a short- and 1s- period are $S_{DS} = 1.0g$ and $S_{D1} = 0.6g$, respectively (g = gravity constant). At maximum considered earthquake hazard, the corresponding spectral ordinates are $S_{MS} = 1.5g$ and $S_{M1} = 0.9g$. Figure 6.3.2 shows the ASCE 7 design spectrum at DE level. The MCE level design spectra are obtained by multiplying the DE spectral ordinates by 1.5.

Figure 6.3.1. Hypothetical location of archetype buildings from United States Geological Survey report (marked with a bull's-eye).

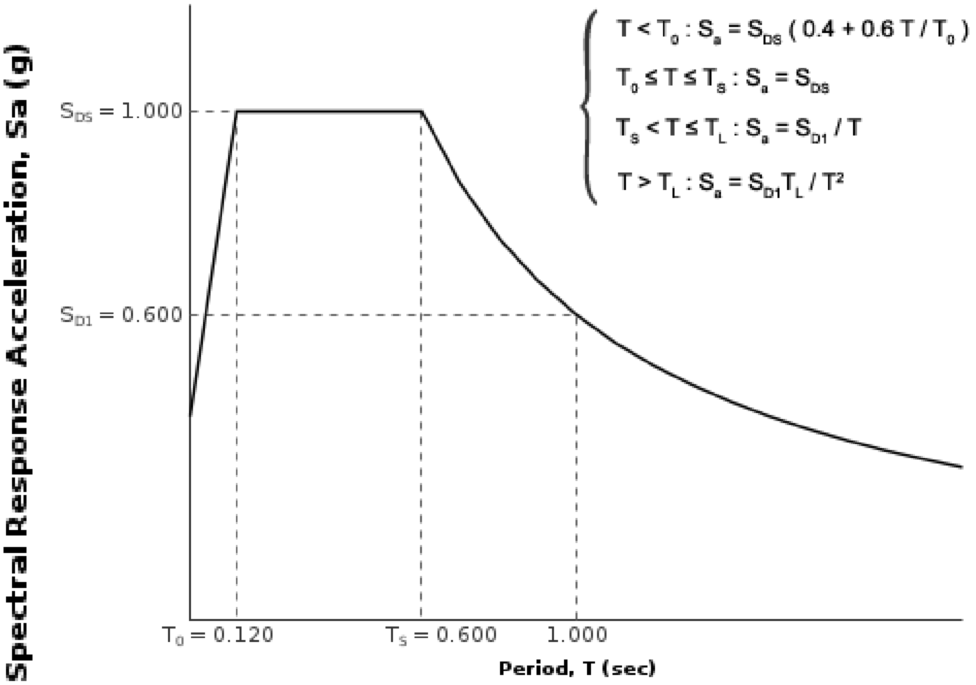

Figure 6.3.2. Pseudo-acceleration design spectrum for DE hazard level and 5% damping at the hypothetical building site in San Francisco, CA (source: USGS).

6.4 DESIGN OF BUILDINGS

The four archetype buildings conform to ACI 318-14 and ASCE 7-10 provisions. According to ASCE 7 classification, each building belongs to risk (occupancy) category II with seismic importance factor $I_e = 1.0$. All four buildings classify under seismic design category D, according ASCE 7. Gravity loads include the self-weight of structure and permanent non-structural components and contents. The design floor live load is 60 psf. Total seismic weight of the four buildings, W_t, includes 100% of dead load and 25% of the live load. Because each principal building direction has two special moment frames, the seismic weight per frame is $W = W_t/2$. Table 6.3 lists the seismic weights (per frame) of the four buildings.

Table 6.3. Total seismic weight (per frame) of archetype buildings.

Building	A10-3	A10-4	A20-3	A20-4
Seismic weight per frame, W (kip)	10,400	10,700	23,635	22,065

The nominal concrete compressive strength used in design of SMRF members, f'_c, is 6.0 ksi, and the nominal steel yield strength, f_y, is 60 ksi. The following load combinations, numbered consistent with ASCE 7, were considered in the design:

1. $1.4D$,
2. $1.2D + 1.6L$,
5. $(1.2 + 0.2\,S_{DS})D + 0.5L \pm 1.0E$, and
7. $(0.9 - 0.2S_{DS})D \pm 1.0E$,

where:

D = dead load,
L = live load,
S_{DS} = design spectral response acceleration parameter at short periods (ASCE 7), and
E = earthquake load.

Design forces were determined using the code-prescribed MRSA procedure using square root of sum of squares (SRSS) modal combination rule with a response modification factor R = 8. The first five modes were included in the elastic analysis of 10-story buildings, which accounted for more than 97% of the modal mass. The first ten modes were included in the elastic analysis of 20-story buildings, which accounted for more than 98% of the modal mass. The effective flexural rigidities for columns and beams used in the elastic MRSA analysis were $0.5E_cI_g$ and $0.35E_cI_g$, respectively (Moehle et al., 2008), where I_g = gross section moment of inertia and E_c = elastic modulus of concrete = 4596 ksi. The design base shear force from code (V_b) for all four buildings was controlled by minimum base shear requirements of ASCE 7, resulting in the base shear magnification factors (defined as $0.85V_{min}/V_{b,E}$, where V_{min} = minimum base shear determined as per ASCE 7 and $V_{b,E}$ = base shear computed from elastic MRSA analysis using the response modification factor R = 8) and design base shear coefficients (V_b /W) listed in Table 6.4.

All four buildings satisfy the story drift limit set forth in ASCE 7 for the DE seismic hazard level. Peak story drifts are calculated during the MRSA from story displacements at design earthquake forces and appropriate deflection amplification factor (defined as C_d = 5.5 for RC frame buildings) to account for the nonlinear response. More specifically, peak (inelastic) story drifts for the archetype buildings are $0.014h_{sx}$ (A10-3), $0.013h_{sx}$ (A10-4), $0.010h_{sx}$ (A20-3) and $0.011h_{sx}$ (A20-4) and are well under the $0.02h_{sx}$ limit (h_{sx} = story height).

Table 6.4. Base shear magnification factor for minimum base shear requirement (ASCE 7) and resulting design base shear coefficient.

Building	A10-3	A10-4	A20-3	A20-4
Base shear magnification factor, $0.85(V_{min}/V_b)$	1.55	1.47	1.86	2.00
Design base shear coefficient, V_b /W	0.038	0.036	0.032	0.033

Table 6.2 lists the longitudinal steel ratios (ρ_l) of the beams. Beam design shear forces were calculated considering development of probable moment strength, $M_{pr,b}$, at both ends of the beam and the uniformly distributed gravity load acting simultaneously. In all cases, the beam end moments due to factored gravity load contributed to less than 15% of the ultimate design moment M_u. Transverse reinforcement in beam plastic hinge regions (within $2h$ of member ends) was controlled by shear requirements, with s/d_b ranging between 3.5 – 4.9 for the four buildings (s = hoop spacing, d_b = longitudinal reinforcing bar diameter). Transverse reinforcement in these regions comprised of No. 5 hoop and a cross tie (5/8 in. diameter), placed at spacing s_h ranging between 5 in. and 6 in., depending on the building.

Table 6.2 also lists the longitudinal steel ratios of the columns. Amount of longitudinal reinforcement in columns was reduced every five stories in most buildings. The exception is building A20-4 and also interior columns of building A20-3, where the column longitudinal reinforcement was kept constant along floors 11-20. In most locations, the minimum amount of longitudinal reinforcement required ρ_l was controlled by the load combination 7 ($[0.9 - 0.2S_{DS}]D$

± 1.0E). In the upper stories (Zones 3 and 4 – see Table 6.2), the design was controlled by either the strong column-weak beam requirement (mostly as a consequence of keeping the beam flexural capacity uniform throughout the building height) or the minimum allowed longitudinal steel ratio $\rho_l = 0.01$ set forth in ACI 318. In all buildings, joint shear strength and the strong column-weak beam requirements of ACI 318 were satisfied.

Amount of transverse reinforcement (referred to in terms of volumetric ratio $\rho_t = A_t/sb$) was selected based on criteria for confinement requirements of ACI 318-14 and also design shear. Because the very aim of this chapter is to develop the method of estimating column design shear, the latter check was somewhat ambiguous and obsolete at this point, but was included as a check and a general indicator of which criterion might control the design of column transverse reinforcement in plastic hinge regions, if the more conservative Method A of ACI 318 was followed. It is important to keep in mind that the transverse reinforcement is only indirectly considered in numerical modeling by the way in which it affects the theoretical stress-strain relationship for the confined core concrete model. The transverse reinforcement volumetric ratios are listed in the appropriate tables of Appendix B.

6.5 NUMERICAL MODELS

Numerical modeling of the four archetype buildings studied in this chapter was similar to that conducted for the buildings in Chapter 5, with few changes. As before, a two-dimensional mathematical model consisting of a single SMRF with lumped mass and vertical load applied at the joints was implemented on the OpenSees platform. Both beams and columns were represented by the force-based Euler-Bernoulli nonlinear fiber-section frame elements with P-Δ geometric transformation. This modeling approach includes axial force – bending moment interaction and allows the beam elongation effects to be represented adequately, as was shown in Chapter 3.

The nonlinear beam-column elements were discretized in such way that the tributary length of numerical integration points at element ends (where plastic hinges form) was approximately 0.25-0.5h, where h represents the height of reinforced concrete element cross section. In all building models, beams were discretized into 5 numerical integration points, while the columns were discretized into 4 integration points. Beam-column joints were modeled with rigid frame elements connecting between the centerline of columns to the ends of beams, as shown in Figure 6.5.1. The length of a rigid frame element on either side of the joint is equivalent to half of the dimension of the column in that direction (h/2), so that the total rigid zone has the same width as the column width in the plane of the frame. Rigid end zones with a length of a beam depth were also included in the columns (Figure 6.5.1). Slab effects were not considered in the numerical model. Damping matrix was defined based on initial stiffness Rayleigh damping with 2% damping ratio in modes 1 and 3.

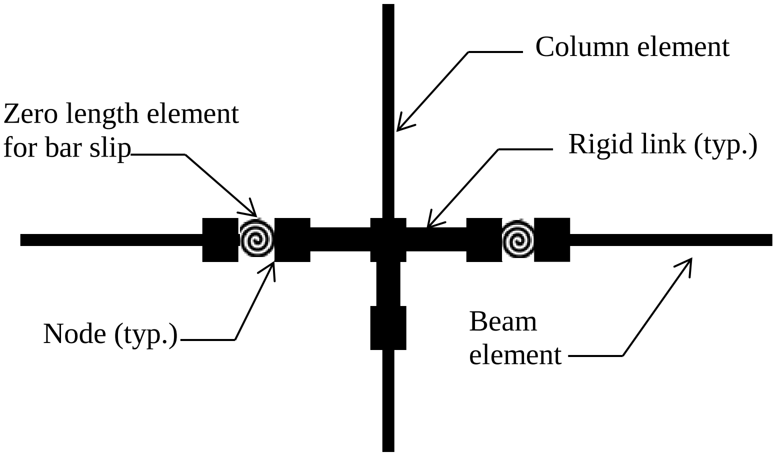

Figure 6.5.1. Schematic of numerical model at the joint.

The numerical models accounted for strain penetration of beam longitudinal reinforcement into joints and column longitudinal reinforcement into the foundation, based on a model developed in Chapter 3. The Giuffre-Menegoto-Pinto material model, *Steel02* (OpenSees 2014), with a post-yield hardening ratio of β_{steel} = 0.012 was used to represent the reinforcing steel material fibers. The numerical steel model includes the material overstrength, which for A706 Grade 60 steel used in seismic design implies that the actual yield strength of the steel is approximately 69 ksi (Bournonville et al. 2004). As explained in detail in Chapter 3, Section 3.6.1, the relationship between the bar stress and amount of slip from anchorage was represented also with a *Steel02* model object with identical post-yield hardening ratio as the steel material in the adjoining element (β_{steel} = 0.012), but with initial stiffness adjusted to produce S_y (amount of slip at yield computed per Section 3.2.1, Chapter 3) at the time that the steel bar reaches f_y. Concrete was modeled using the *Concrete03* material model (OpenSees 2014) which uses Kent-Park relationship. The confined concrete strength was based on Mander et al. (1988). At strain levels exceeding concrete strain ε_{cc} at f'_{cc}, the concrete stress-strain relationship was modeled with a descending branch, to a point where zero residual strength was reached, which was set to occur at the compressive strain of ε_{cu} = 0.05.

Because the aim of this chapter is to compute the levels of shear in columns that would need to be accommodated during nonlinear response, it was assumed that shear yielding does not occur, and hence no shear springs, such as those discussed in Section 3.7 in Chapter 3, were included in the structural models. This way, the shear forces are not bounded by some hypothetical capacity, but were rather allowed to reach any level necessary to balance the moments developing in the beams and columns during the dynamic response of the buildings.

6.6 VIBRATION CHARACTERISTICS AND SYSTEM STRENGTH

Modal properties of the first three translational modes of the planar models, based on uncracked section properties, are listed in Table 6.5. The buildings of same height have very similar modal properties, with 10-story buildings having fundamental period T_1 = 1.4 to 1.47, and 20-story buildings having T_1 = 2.12 to 2.24. For all four buildings, the ratio of first to second mode period T_1/T_2 is approximately 3.1, while the ratio of the first to third mode period T_1/T_3 ranges between 5.4-5.7. The effective modal mass of the first mode normalized with the total mass M_1/M is around 0.68 for all four buildings, while the corresponding range for the second mode is 0.10 for 10-story and 0.13 for the 20-story buildings. The effective modal heights (H_q) of equivalent single degree of freedom systems are also listed for the first three modes and these values are shown as a fraction of a total building height H.

Table 6.5. Characteristics of the first three modes of the archetype buildings.

Building	Mode q	T (s)	M_q / M	H_q / H
A10-3	1	1.47	0.810	0.687
	2	0.47	0.103	0.123
	3	0.27	0.037	0.143
A10-4	1	1.40	0.814	0.686
	2	0.45	0.105	0.126
	3	0.26	0.036	0.135
A20-3	1	2.12	0.767	0.679
	2	0.68	0.130	0.036
	3	0.37	0.037	0.101
A20-4	1	2.24	0.760	0.681
	2	0.73	0.136	0.012
	3	0.40	0.037	0.095

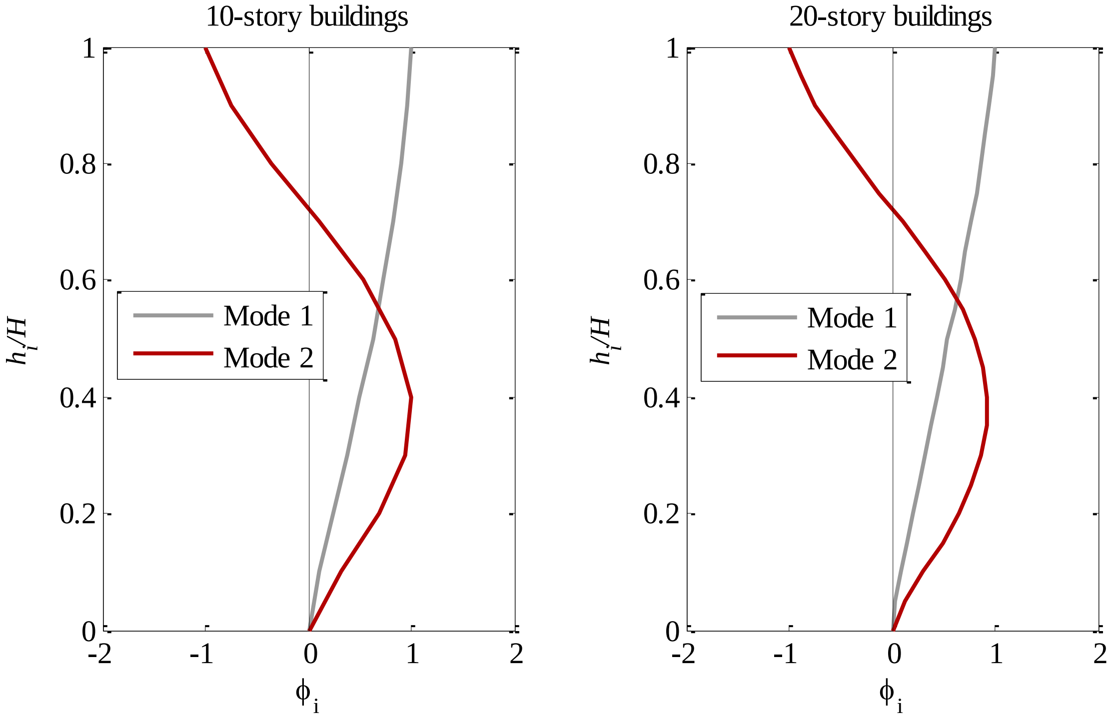

(a) (b)

Figure 6.6.1. Spatial distribution of lateral story displacements of 10- and 20- story buildings corresponding to the first two modes of vibration.

Pushover analysis of the four buildings was done for the 1st and 2nd mode. The corresponding deflected shape in the first two modes of the 10- and 20- story buildings was almost identical; it is plotted in Figure 6.6.1. Figure 6.6.2 through Figure 6.6.5 show the base shear versus the roof displacement D_{roof} (normalized by the total height, H) for the four buildings subjected to increasing story displacements with a spatial distribution along the height of the building proportional to the first and second mode force vectors. The figures also show the design base shear computed with the elastic modal response spectrum analysis using strength reduction factor R = 8 and the appropriate minimum base shear amplification factor discussed in Section 6.4.

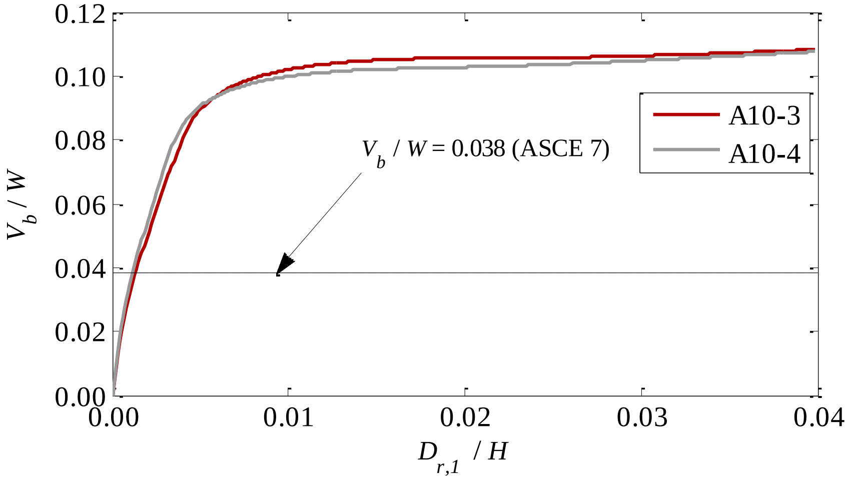

Figure 6.6.2. First mode pushover curve for buildings A10-3 and A10-4.

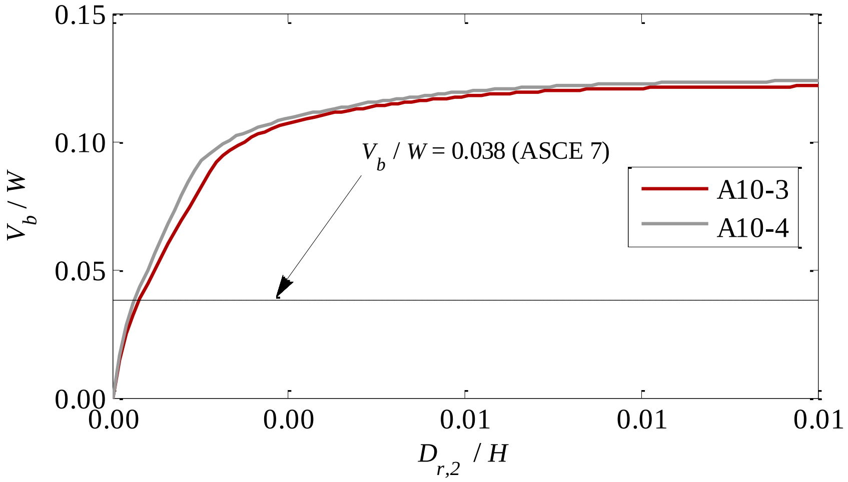

Figure 6.6.3. Second mode pushover curve for buildings A10-3 and A10-4.

As can be seen in Figure 6.6.2 and Figure 6.6.3, the 10-story buildings have almost identical nonlinear force-deformation characteristic, with building A10-3, which has only three bays in the SMRF, having slightly more flexibility than building A10-4. The roof drift at yield for first-mode pushover is roughly $D_{r,1,y}$ = 6" (0.004H) for both A10-3 and A10-4, with the base shear at system yield at approximately 0.08W for both frames. In the second-mode pushover, system yield occurs at approximately roof displacements of $D_{r,2,y}$ = 2.1" (0.0014H) and 1.7"(0.0012H) for the A10-3 and A10-4, respectively. Base shear at system yield in the second mode is approximately 0.093*W* and 0.088*W* for A10-3 and A10-4, respectively.

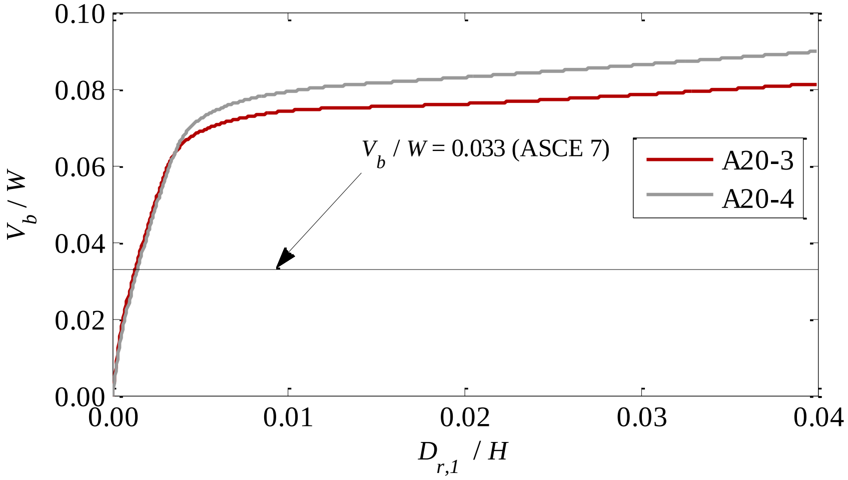

Figure 6.6.4. First mode pushover curve for buildings A20-3 and A20-4.

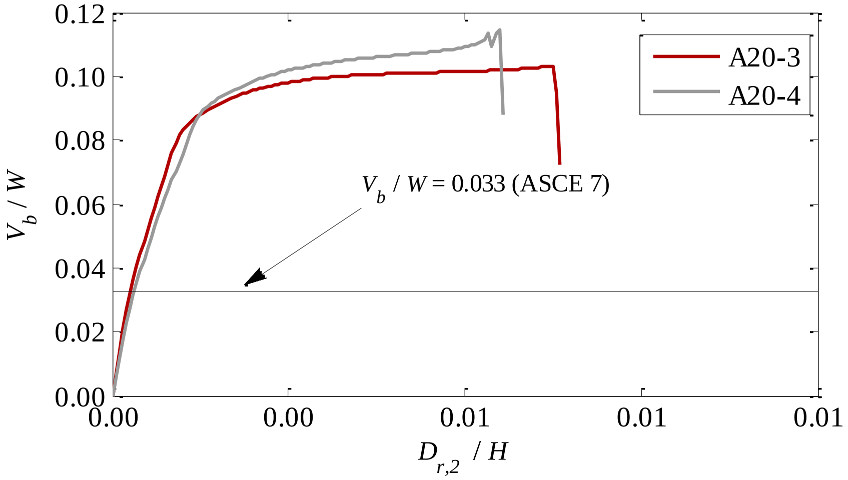

Figure 6.6.5. Second mode pushover curve for buildings A20-3 and A20-4.

Pushover curves for 20-story buildings, shown in Figure 6.6.4 and Figure 6.6.5, indicate that while the three- and the four-bay SMRF buildings have almost identical stiffness at a given roof displacement, building A20-3 is slightly weaker. Roof displacement at yield for A20-3 first-mode pushover is about $D_{r,1,y}$ = 9" (0.003*H*) and the base shear at this instance is 0.06*W*. For building A20-4, first-mode pushover the roof displacement occurs at about $D_{r,1,y}$ = 11" (0.0038*H*) at which time the base shear is approximately 0.066*W*. For the second mode pushover analysis, the roof displacements at yield are $D_{r,2,y}$ = 2.6" (0.0009*H*) and 3.4" (0.0012*H*), with base shear 0.079*W* and 0.088*W* for buildings A20-3 and A20-4, respectively.

It is interesting to note the differences in the base-shear strength of the buildings between the first mode- and second mode-proportional lateral force distribution. For all four archetype buildings, the base shear at system yield for the lateral force distribution proportional to the second mode is actually higher than the base shear occurring at system yield when the buildings are subjected to first mode- proportional lateral forces. In the case of A10-3 and A10-4, the ratio of the base shear "strength" at yield in the second versus first mode is 1.16 and 1.10, respectively. For A20-3 and A20-4 buildings, this ratio is around 1.3. This is easily observed in the *x*-axis values of story shear distributions plotted in Figure 6.6.6 and Figure 6.6.7. Each figure shows a story shear distribution at a given roof displacement for first and second mode lateral force vector. The roof displacements are expressed as a factor of yield displacement for a given mode *n*, labeled as $D_{r,n,y}$.

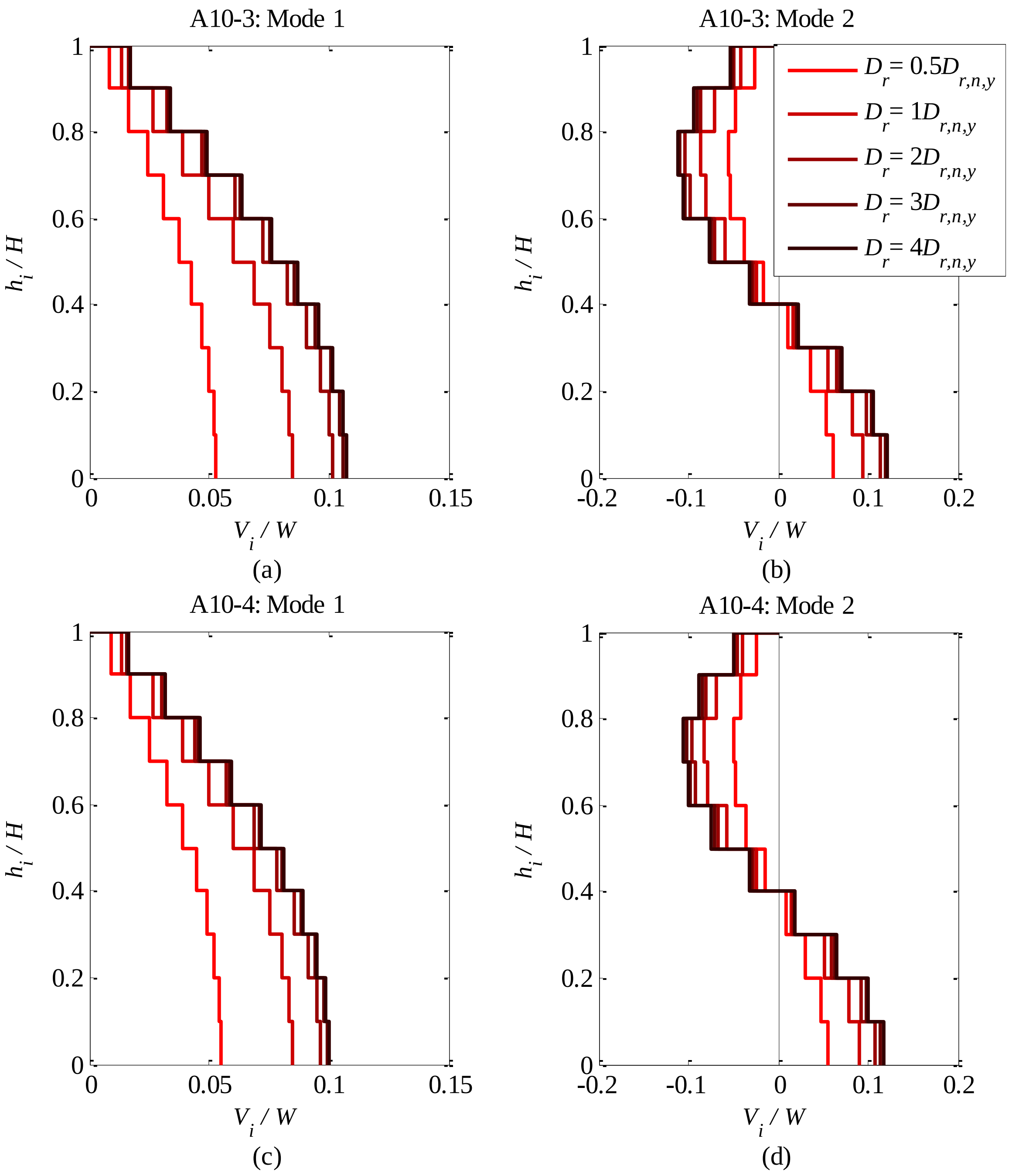

Figure 6.6.6. Story shear profiles for mode 1 and 2, buildings A10-3 and A10-4 and various roof drift ratios.

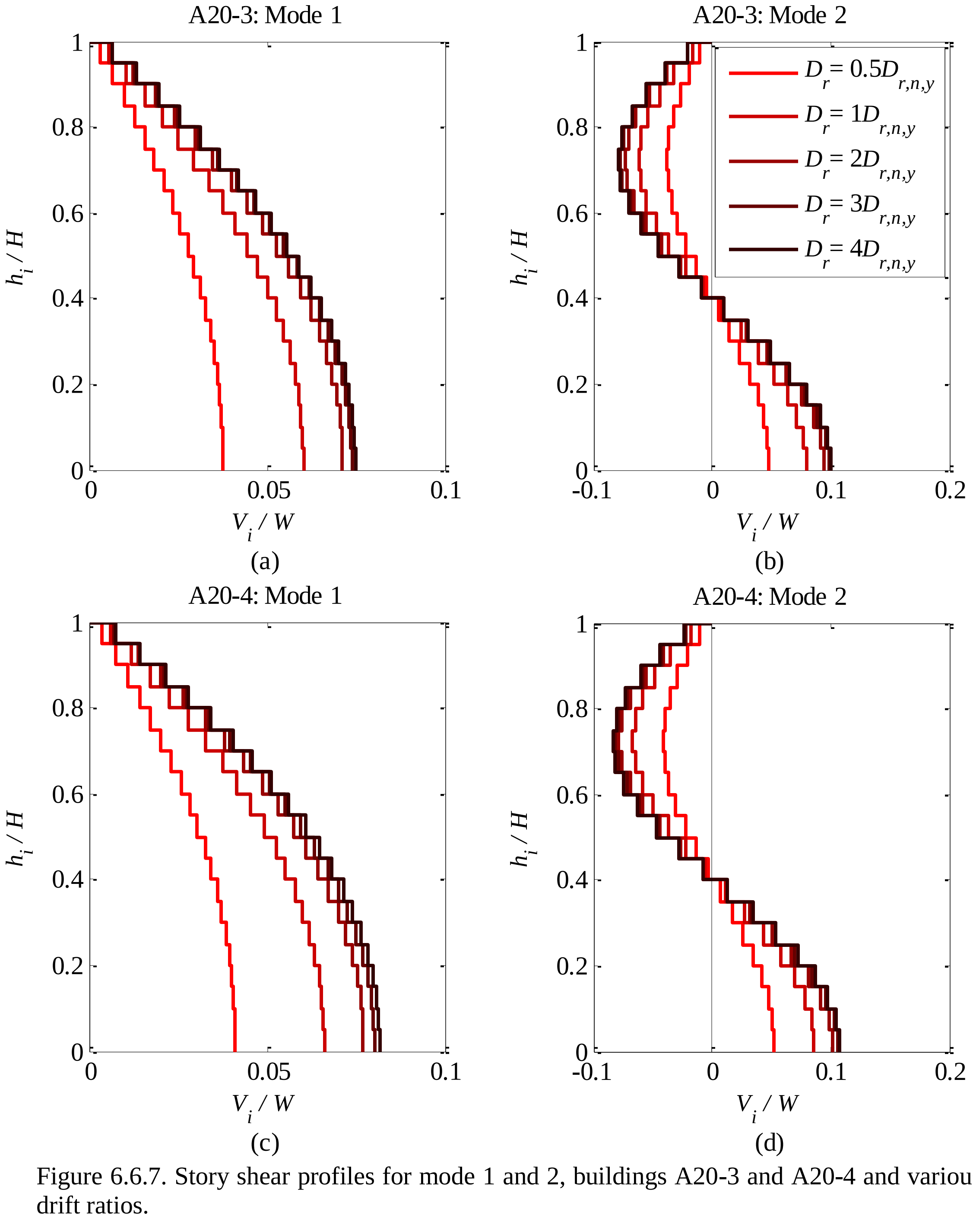

Figure 6.6.7. Story shear profiles for mode 1 and 2, buildings A20-3 and A20-4 and various roof drift ratios.

6.7 GROUND MOTION SELECTION

The analyses presented in this chapter are investigated at two shaking intensities: design earthquake (DE) and maximum considered earthquake (MCE) intensity. Ground motions were selected using the PEER Ground Motion Database selection tool (PEER 2014) to match the 5% damping ratio smoothed design spectrum of ASCE 7. Because of differences in vibration periods between the 10- and the 20-story buildings, the ground motions were different for the two building heights, and are selected independently and grouped into two separate bins: Bin 1, used for 10-story building nonlinear dynamic analyses, and Bin 2, used for 20-story building nonlinear dynamic analyses.

Each bin contains thirty different ground motions, each of which includes both fault-normal and fault-parallel ground acceleration components. Thus, at each hazard level, each building is subjected to total of 60 analysis runs – 30 fault-normal and 30 fault-parallel ground motions. All of the motions selected occurred in events on strike-slip fault types and some ground motions include distinct velocity pulses due to directivity effects. The acceleration records were linearly scaled so that the geometric mean of all FN and FP components approximately matches the smoothed design spectrum prescribed by ASCE 7 for a given site, between the specified periods of interest. For 10-story buildings, the period range was between T_2 and $1.5T_1$ (T_1, T_2 = first and second mode of vibration periods, respectively). Although factors for linear GM scaling even in the range of 3.5-12 have been shown to also provide acceptable average estimates of the response (Watson-Lamprey and Abrahamson 2005), the bounding scaling factors for the analyses in this chapter were defined to be well below these values at [0.3, 2.2] at DE and [0.45, 3.3] at MCE.

6.7.1 BIN 1: GROUND MOTIONS FOR 10-STORY BUILDINGS

Bin 1 ground motions and respective scale factors are listed in Appendix C. Figure 6.7.1 shows the mean response spectra for both FN and FP components, and their geometric mean. Figure 6.7.2 shows the scatter in the scaled ground motion spectra along with the 50th, 84th and 98th percentile spectrum for both pseudo-acceleration and displacement response spectra and 5% damping ratio.

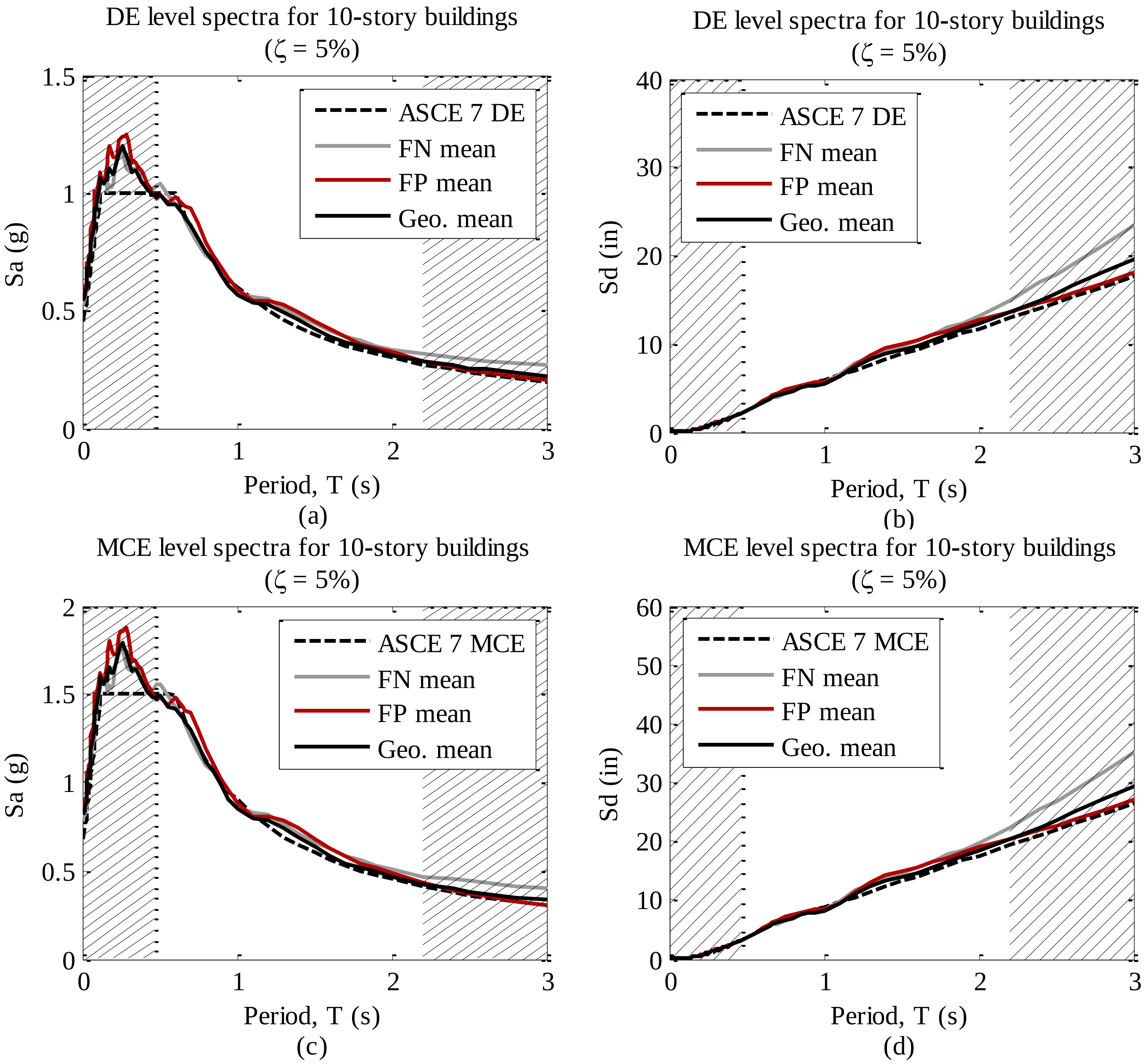

Figure 6.7.1. Pseudo-acceleration and displacement design spectra and smoothed mean spectra for 30 ground motions at DE and MCE shaking intensities. Unhatched area represents range of periods of interest.

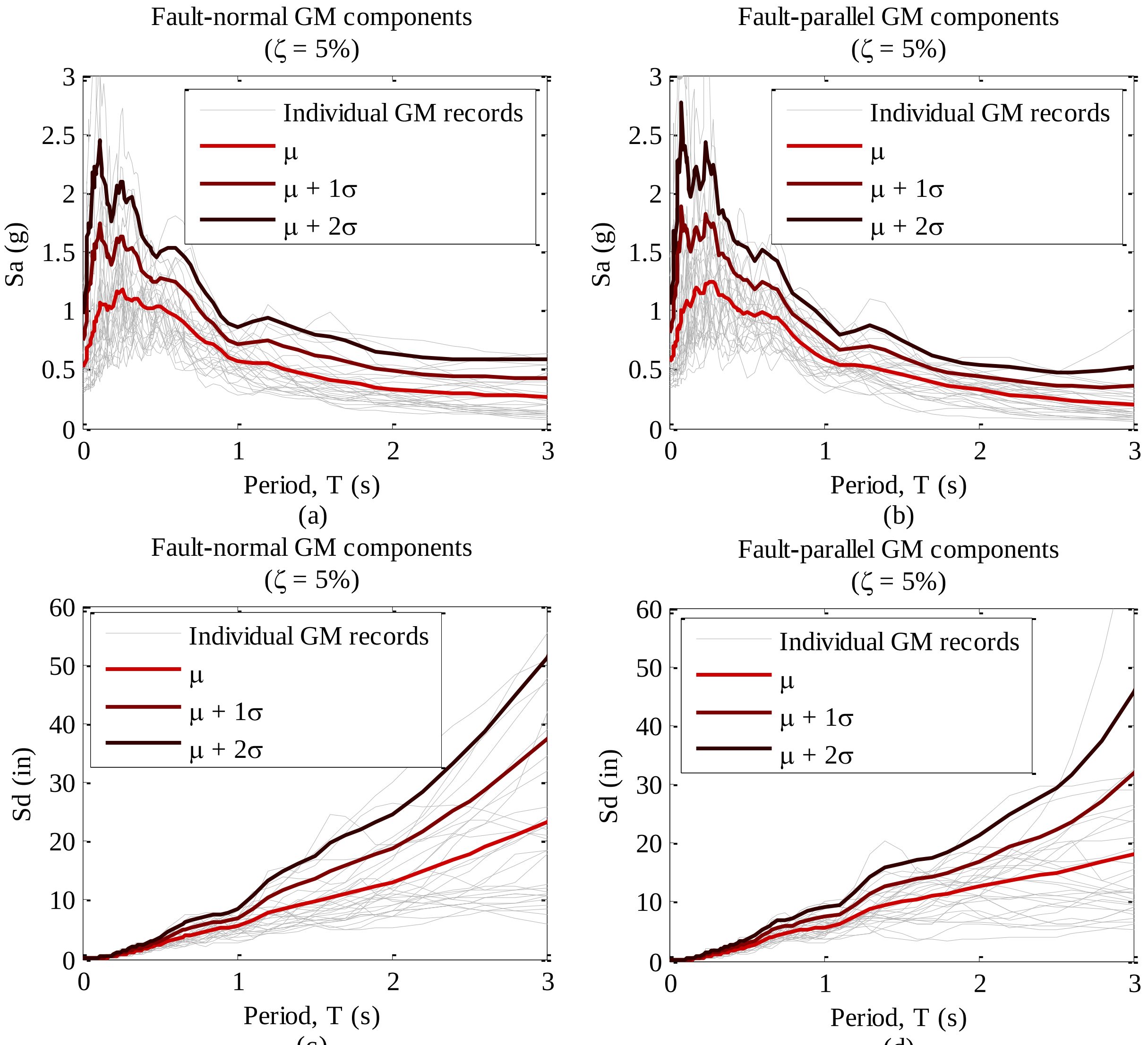

(a) (b) (c) (d)

Figure 6.7.2. Scatter in Bin 1 ground motion spectra at DE level: (a) pseudo-acceleration spectra for FN components, (b) pseudo-acceleration spectra for FP components, (c) displacement spectra for FN components, and (d) displacement spectra for FP components.

6.7.2 BIN 2: GROUND MOTIONS FOR 20-STORY BUILDINGS

Bin 2 ground motions and respective scale factors are listed in Appendix C. Figure 6.7.3 shows the mean response spectra for both FN and FP components, and their geometric mean. Figure 6.7.4 shows the scatter in the scaled ground motion spectra along with the 50th, 84th and 98th percentile spectrum for both pseudo-acceleration and displacement response spectra and 5% damping ratio.

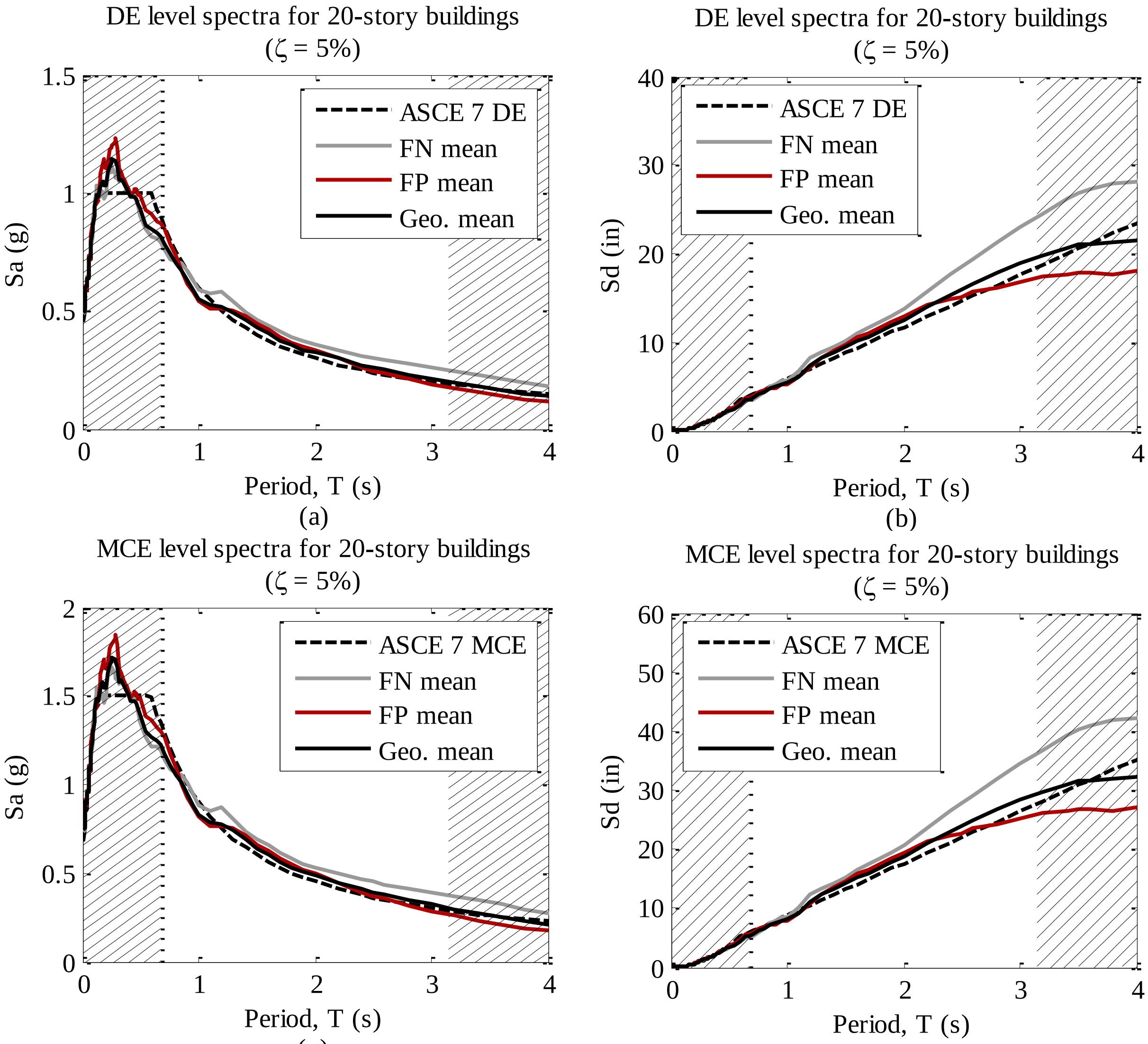

(a) (b) (c) (d)

Figure 6.7.3. Pseudo-acceleration and displacement design spectra and smoothed mean spectra for 30 ground motions at DE and MCE shaking intensities. Unhatched area represents range of periods of interest.

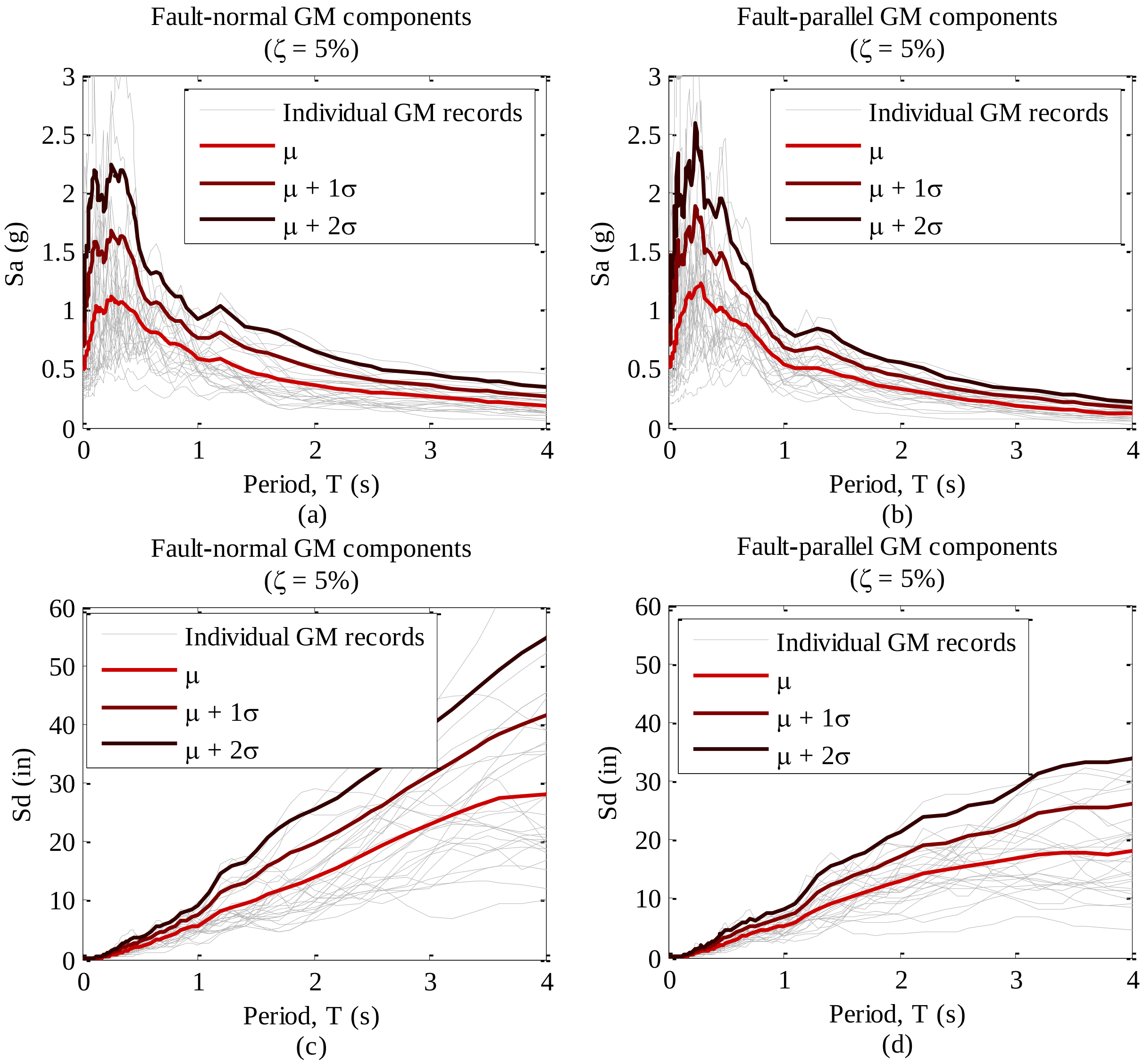

Figure 6.7.4. Scatter of Bin 2 ground motion spectra at DE level: (a) pseudo-acceleration spectra for FN components, (b) pseudo-acceleration spectra for FP components, (c) displacement spectra for FN components, and (d) displacement spectra for FP components.

6.8 BUILDING RESPONSE FROM NONLINEAR DYNAMIC ANALYSES

General response characteristics discussed in this section include: story displacements, story drift ratios, absolute floor accelerations, story shears, story moments, and individual column shears. For each ground motion analysis run, absolute maxima of these response quantities are logged and plotted as a function of the height of the building. The response envelopes are separated into fault normal (FN) and fault parallel (FP) bins, and statistical characteristics such as the mean and standard deviation are calculated for each group. In the discussion that follows, reference is made to various statistical measures of these response quantities, such as the mean of the response quantity. Unless otherwise noted, a reported response quantity refers to the maximum of the absolute value of the response quantity as logged during an individual ground motion analysis.

Story displacements U are normalized by the total height of the building H and represent the peak story displacements relative to the ground. Story drift ratios, θ, are defined as the difference between the horizontal displacements of the two consecutive stories, normalized by the individual story height h_i. Floor accelerations A represent the absolute floor accelerations and are plotted as normalized with respect to the peak ground acceleration of the corresponding input ground motion. Story shear V represents the total shear on a single SMRF and is normalized by the seismic weight W carried by a single SMRF (in the configuration of the SMRFs presented in this chapter, W represents half of the building seismic weight W_t). Lastly, the story moment M represents the total overturning moment acting on a single frame and normalized by W and height H, defined previously.

6.8.1 GENERAL RESPONSE CHARACTERISTICS: DISPLACEMENTS

Figure 6.8.1 and Figure 6.8.2 show mean response envelopes for the 30 ground motions responding under design earthquake and maximum considered earthquake shaking intensities. The plots also include the story displacement profiles calculated from the ASCE 7 procedure by magnifying the story displacement under design seismic forces by a factor $C_d = 5.5$. Global response quantities are almost identical for the two buildings having the same height; mean roof drift ratios for building A10-3 are 0.0165 (FN) and 0.011 (FP), while those of building A10-4 are 0.017 (FN) and 0.012 (FP). Buildings A20-3 and A20-4, respectively, reached the mean roof drift ratios of 0.010 under FN and 0.007 under FP ground motion components and DE level of shaking. The MCE level responses were roughly 1.5 times those for DE level, as can be seen in Figure 6.8.1 and Figure 6.8.2. In all four buildings, the shape of the peak story displacement envelopes indicates that most of the displacement builds up in the lower two thirds of the height of the buildings, with the top stories having almost uniform peak displacements. This is also evident from the story drift ratio envelopes (Figure 6.8.1[b] and [d] and Figure 6.8.2[b] and [d]) which confirm that the story drift ratios are largest in the bottom half of the building.

Peak story drift ratio θ was computed around $0.3H$ for all four buildings. In the 10-story buildings, θ was almost uniform in the bottom third of the building, with the ratio of the peak θ to the θ at the base level (first story) equal to 1.08 and 1.18 for FN and FP response components, respectively. On other hand, the distribution of story drift ratios in the 20-story building peaks out at roughly 0.25-0.3H, but tapers off toward the base of the building, with the ratio of the peak story drift to the story drift at the base level equal to 1.55 and 1.70 for the FN and FP response components, respectively. Interestingly, both 10-story buildings exhibited much larger story drift ratios in comparison with the 20-story buildings. Peak story drift ratios in the 10 story buildings were approximately 2.1 (FP) and 3.25 (FN). This is approximately 1.6 times the peak story drift ratios computed in the 20-story buildings at DE level of shaking, which were 1.25 (FP) and 2.10 (FN).

It is interesting to compare the trends in the story drift distribution to those observed for 20-story buildings analyzed in Chapter 5, where story drift ratio envelopes exhibited two distinct peaks – one occurring around $0.25H$, and the other around $0.6H$ of the building. The reduction in beam strength (and stiffness) in the upper building stories, leads to accumulation of larger story drift ratios at these levels. Conversely, uniform strength and stiffness of beams along the frame height produces smaller relative story drift ratios in the upper half of the building, regardless whether the column curtailment is present or not.

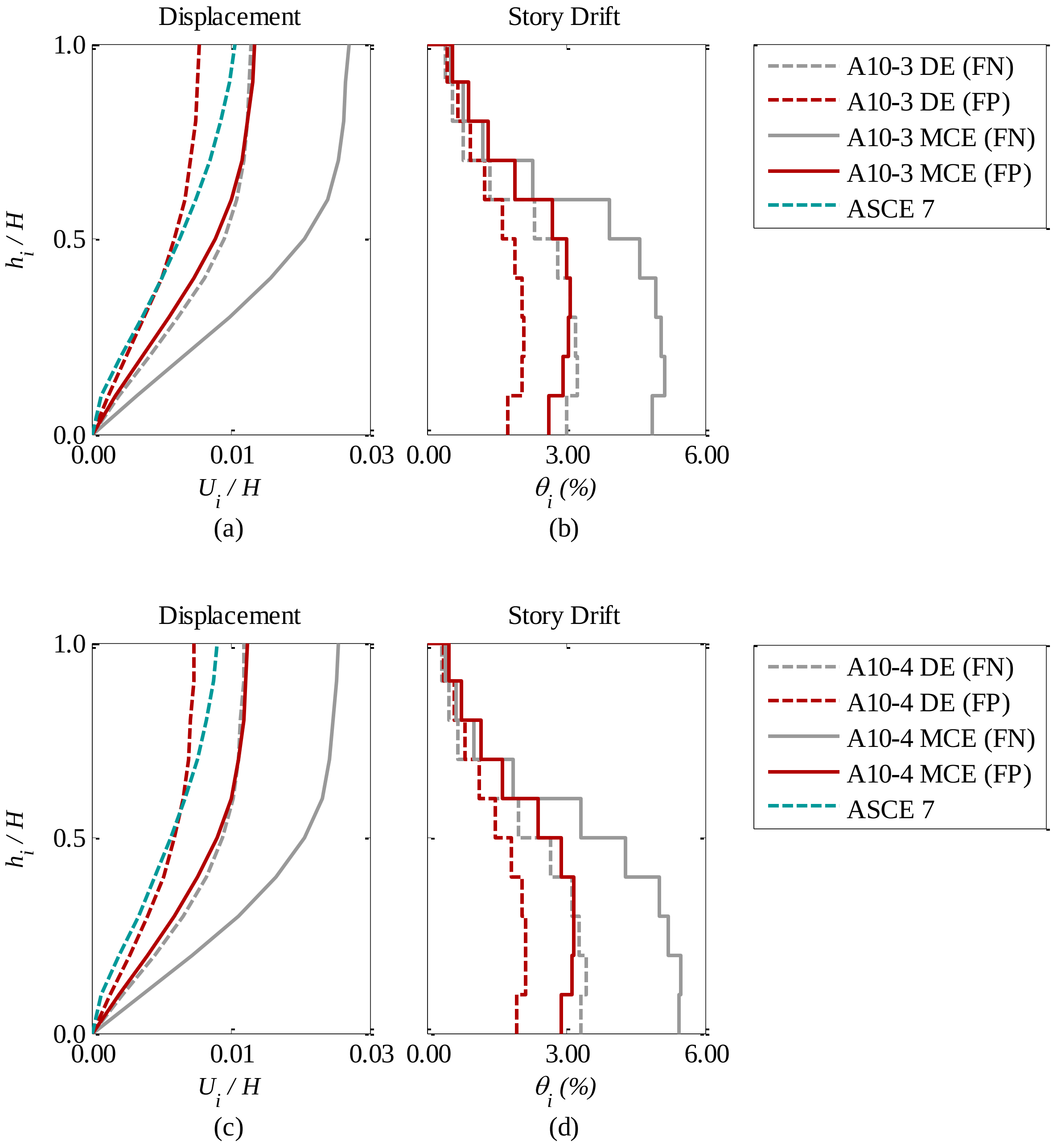

Figure 6.8.1. Response envelope plots for buildings A10-3 [(a) and (b)] and A10-4 [(c) and (d)].

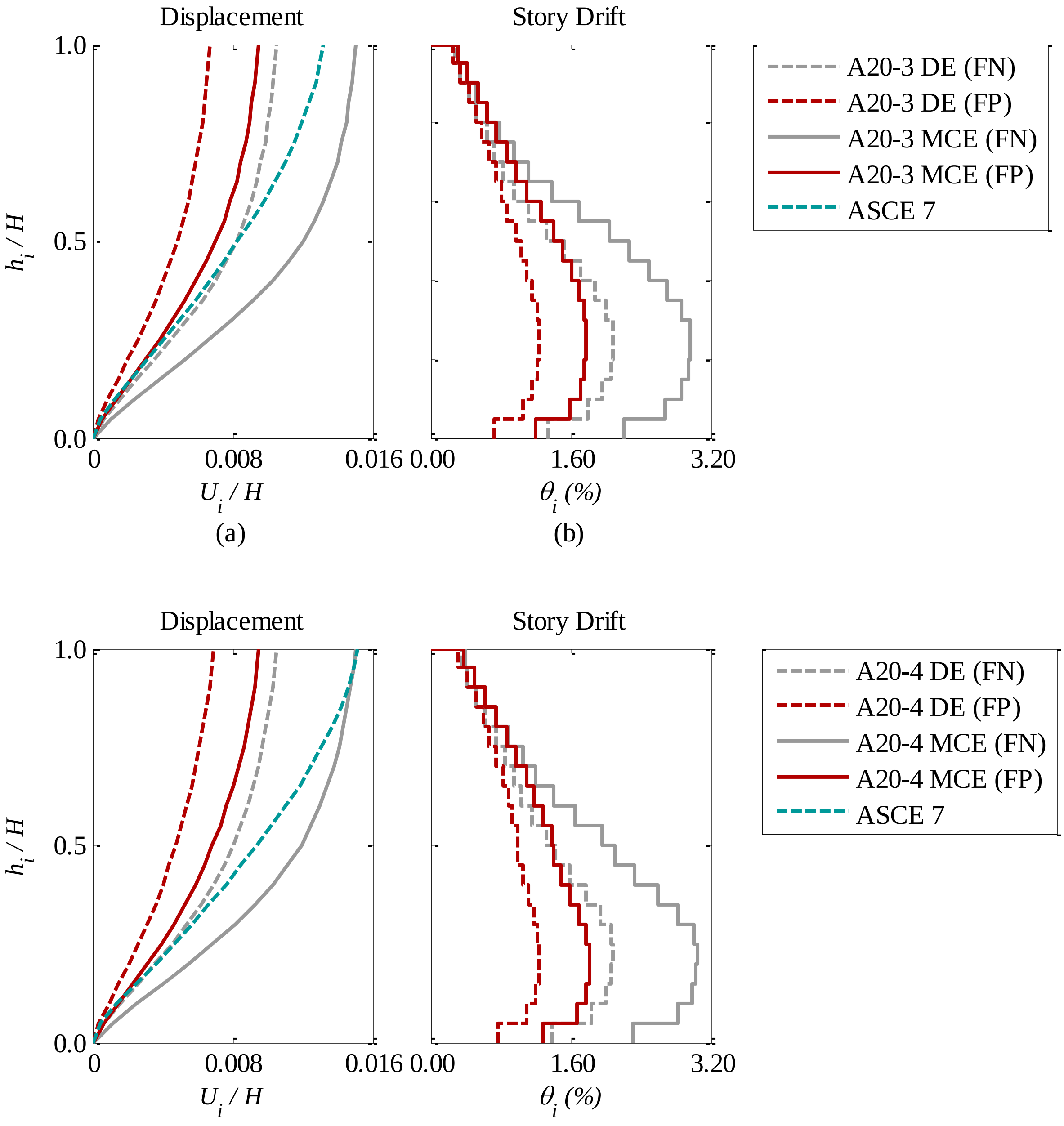

(a) (b)

(c) (d)

Figure 6.8.2. Response envelope plots for buildings A20-3 [(a) and (b)] and A20-4 [(c) and (d)].

The displacement related responses U and θ plotted in Figure 6.8.1 and Figure 6.8.2 point to significant difference between the responses to fault-normal and fault-parallel ground motion components. The roof drift ratio at a DE level response to FN ground motions for all buildings is approximately 1.5 times that in FP response. Because the GM bins include ground motions affected by the fault rupture directivity, some difference in displacement demand is expected due to the fact that fault-normal components of near-field motions tend to place larger displacement demands on the building in comparison with the fault-parallel components.

Figure 6.8.3 and Figure 6.8.4 show the scatter observed in the story drift ratio distribution for 10- and 20-story buildings, respectively. As can be seen, in 10-story buildings, limited variation in peak story drift ratio exists in the top 0.3*H* of the building height, while the stories in the bottom 0.7*H* exhibit large scatter in the peak story drift ratios, with two fault-normal ground motion components causing θ amplitudes in exceedance of 8%. The story drift ratios in the fault-parallel direction were generally under 6% for the A10-3 and A10-4 building. The two 20-story buildings also show the largest θ scatter in the bottom half of the stories. However, the scatter present in top floors is larger than what was observed in the top floors of the 10-story buildings.

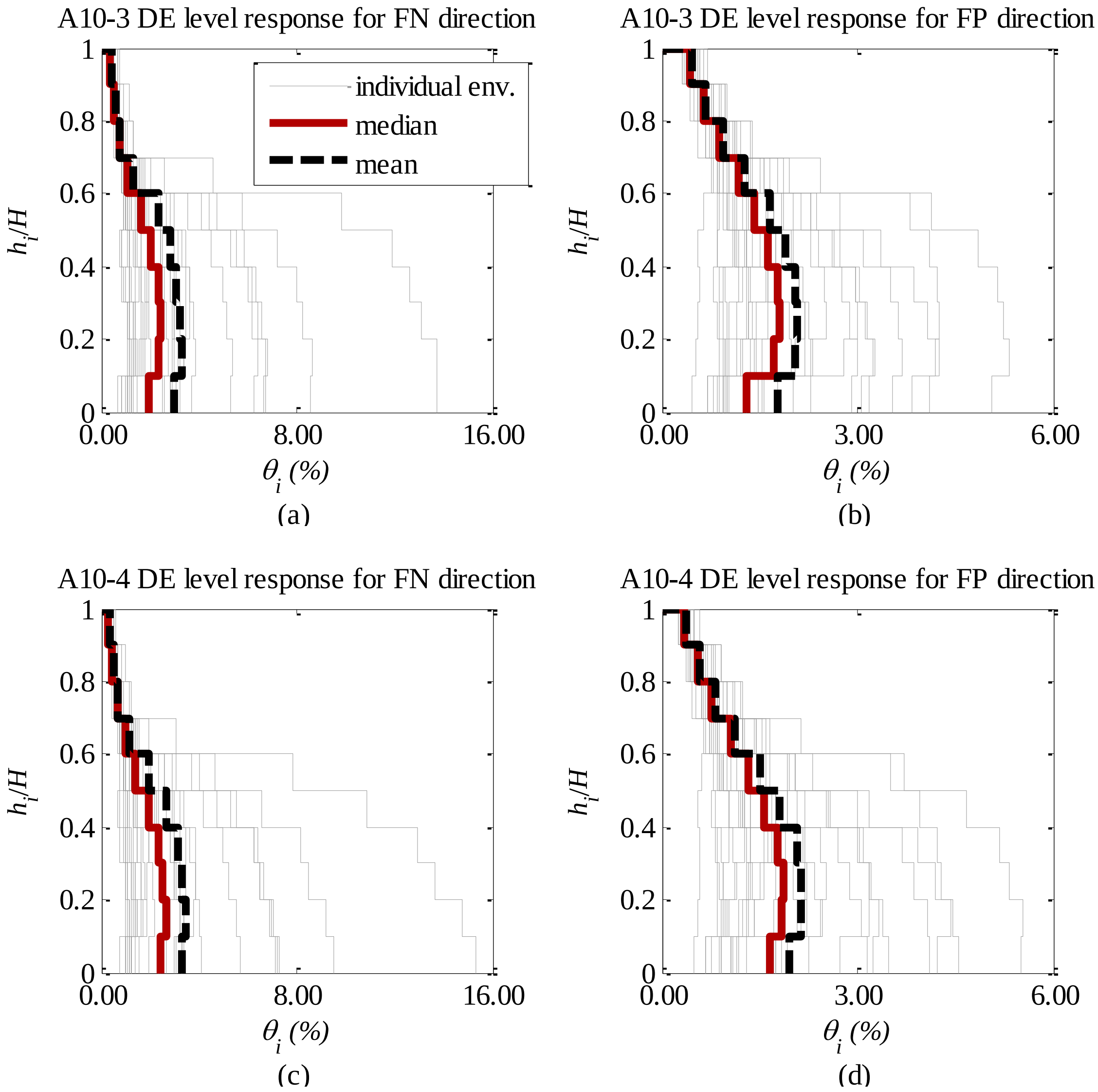

(a) (b)

(c) (d)

Figure 6.8.3. Scatter in story drift ratio for 10-story buildings at Design Earthquake hazard level: (a) A10-3 response in fault normal direction, (b) A10-3 response in fault parallel direction, (c) A10-4 response in fault normal direction, (d) A10-4 response in fault parallel direction.

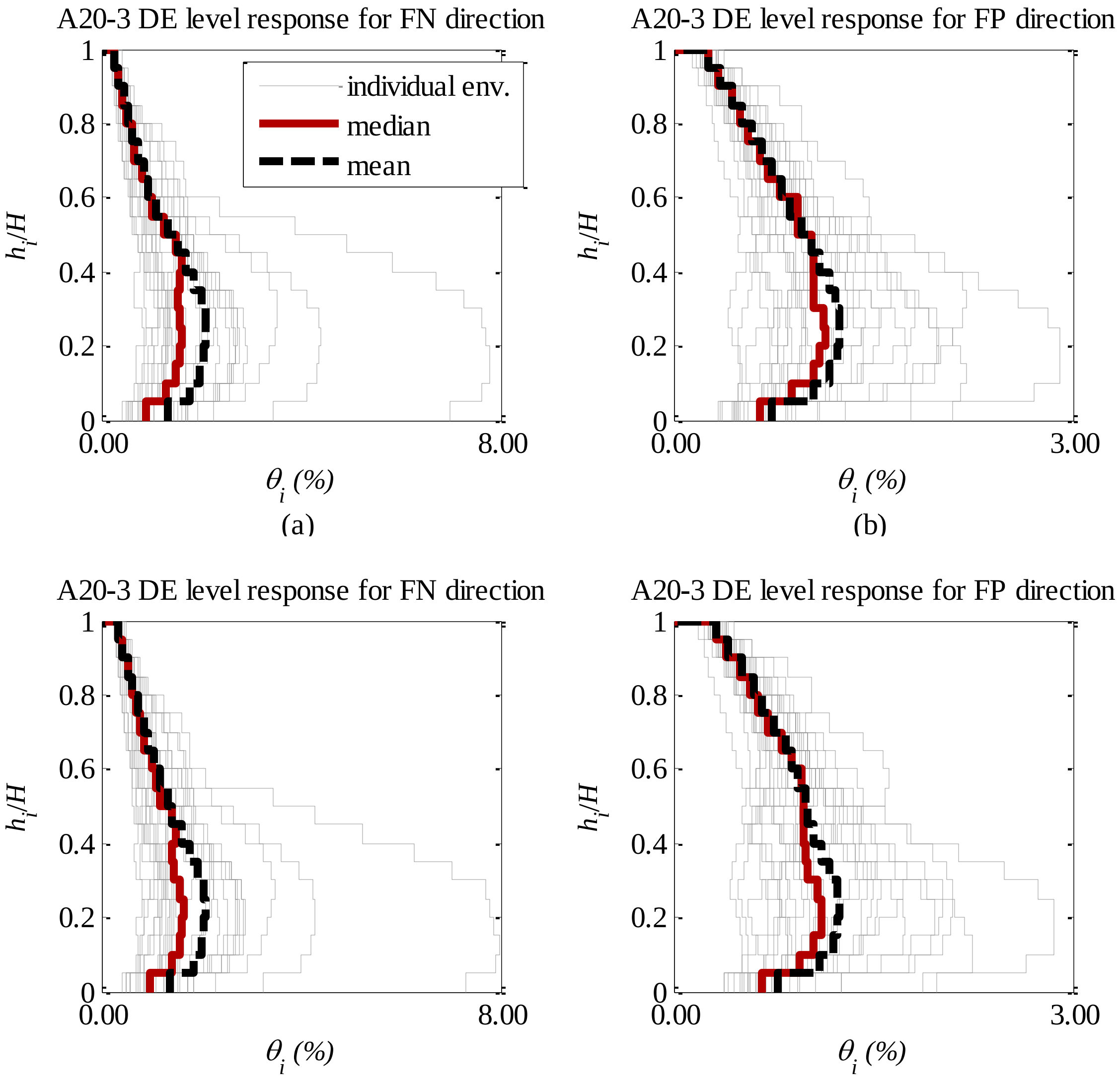

(a) (b) (c) (d)

Figure 6.8.4. Scatter in story drift ratio for 20-story buildings at Design Earthquake hazard level: (a) A20-3 response in fault normal direction, (b) A20-3 response in fault parallel direction, (c) A20-4 response in fault normal direction, (d) A20-4 response in fault parallel direction.

Most of the fault-normal components of the ground motions caused peak story drift ratio less than 4% (with the exception of one ground motion where both A20-3 and A20-4 reached $\theta \approx 8\%$ at or below $0.2H$), which is less than a half of the story drift demands in the 10-story buildings. In the fault-parallel direction, 20-story buildings sustained $\theta < 3\%$ for all ground motions. For the ground motions causing the largest story drift ratio amplitudes, the maximum story drifts occur at the base floor and decrease along the height in 10-story buildings. This is not the case in the 20-story buildings, where the largest θ amplitudes tend to concentrate around $0.2H$ of the building.

6.8.2 GENERAL RESPONSE CHARACTERISTICS: FORCES

Mean response envelopes for floor accelerations, system (story) shears, and system (story) moments for the four buildings subjected to the DE and MCE level earthquake ground motions are plotted in Figure 6.8.5 for 10-story buildings and Figure 6.8.6 for 20-story buildings. In general, the differences between the DE and MCE level responses are significantly smaller than those observed in the displacement responses (story displacements and story drift ratios).

Floor accelerations reduce in an almost linear fashion along the height, starting from 1PGA mean value at the base and a fraction of this value at $0.9H$, where there is a sudden increase in the floor accelerations at the top floor (Figure 6.8.5 and Figure 6.8.6). MCE-level floor acceleration envelopes are almost identical in shape with the DE level envelopes. However, the mean floor accelerations reduce by roughly 20% at this stronger level of shaking, compared to those occurring at the DE hazard level.

The buildings of equal heights developed similar level of system shears and moments. At DE level of shaking, the respective mean base shears for buildings A10-3 and A10-4 were $0.127W$ and $0.118W$ in FN direction, and $0.123W$ and $0.113W$ in FP direction. The respective mean base shears for buildings A20-3 and A20-4 at DE shaking were $0.095W$ and $0.099W$ in FN direction, and $0.092W$ and $0.096W$ in FP direction. While the base shears in FN direction were generally larger, system forces computed in upper half of the buildings for the FP direction exceed those in FN direction. In the case of 10-story buildings, the mean story shear at 8th floor during the FP response exceeds that in FN direction by roughly 10%. At MCE level, mean base shear envelopes were approximately 10% higher for all buildings and in both directions.

System shear envelope plots in Figure 6.8.5 and Figure 6.8.6 include the shear profiles computed with: i) first-mode static pushover analysis (see Section 6.6) at a mean roof drift ratio corresponding to the mean envelope for FN direction at DE level, ii) a code-based MRSA analysis using strength reduction factor R = 8 with the appropriate base shear amplification factors as described in Section 6.4, and iii) an MRSA envelope amplified by a factor Φ_v, such that the shear at the base is equal to that computed with the NRHA at a DE level of shaking. The base shear from NRHA used in scaling of the MRSA envelopes is the geometric mean of the mean base shears computed in the two orthogonal orientations with respect to the direction of the fault generating the ground motion. The story moment envelope plots in Figure 6.8.5 and Figure 6.8.6 only include the distribution from the first-mode static pushover analysis at the roof displacement equivalent to the mean roof drift in the FN direction.

A small difference in NRHA- computed mean story moment envelopes and the story moment distribution from the first-mode static pushover analysis indicates that the mean story moment is only slightly affected by the higher mode contribution for the frame buildings analyzed, which is most evident in the upper half-height of the buildings. In contrast, large deviation in the corresponding shear envelopes from the first-mode proportional distribution can be observed for all buildings, suggesting larger presence of higher mode response components (Figure 6.8.5[b] and [e] and Figure 6.8.6[b] and [e]). For example, the base overturning moment due to first-mode static pushover is only 3 to 4% higher than the geometric mean of the DE-level base overturning moment for 10- and 20-story buildings, respectively. On other hand, the base shear due to first-mode static pushover is 15 to 16% lower than the geometric mean at the DE-level response for 10- and 20-story buildings, respectively.

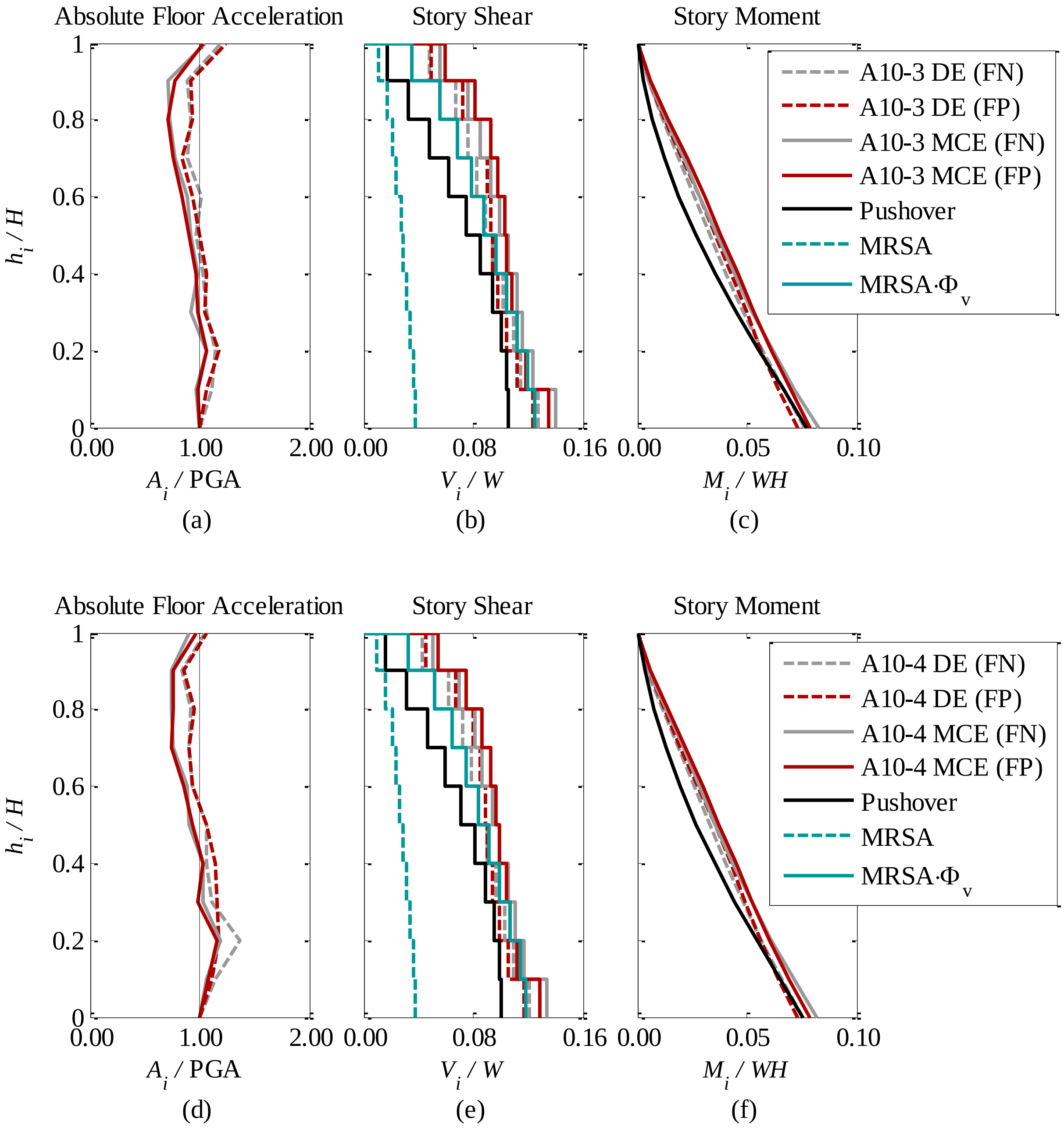

Figure 6.8.5. Floor acceleration, story shear, and story moment envelopes for buildings A10-3 and A10-4. (DE = design earthquake level response envelopes; MCE = maximum considered earthquake response envelopes; Pushover = response envelopes under first-mode pushover analysis at the roof displacement corresponding to the mean roof displacement from nonlinear response history analysis; MRSA = response envelopes obtained from elastic modal response spectrum analysis corresponding to design earthquake level forces; Φ_v = amplification factor applied to MRSA shear envelope to match the mean base shear from nonlinear response history analysis at design earthquake hazard level)

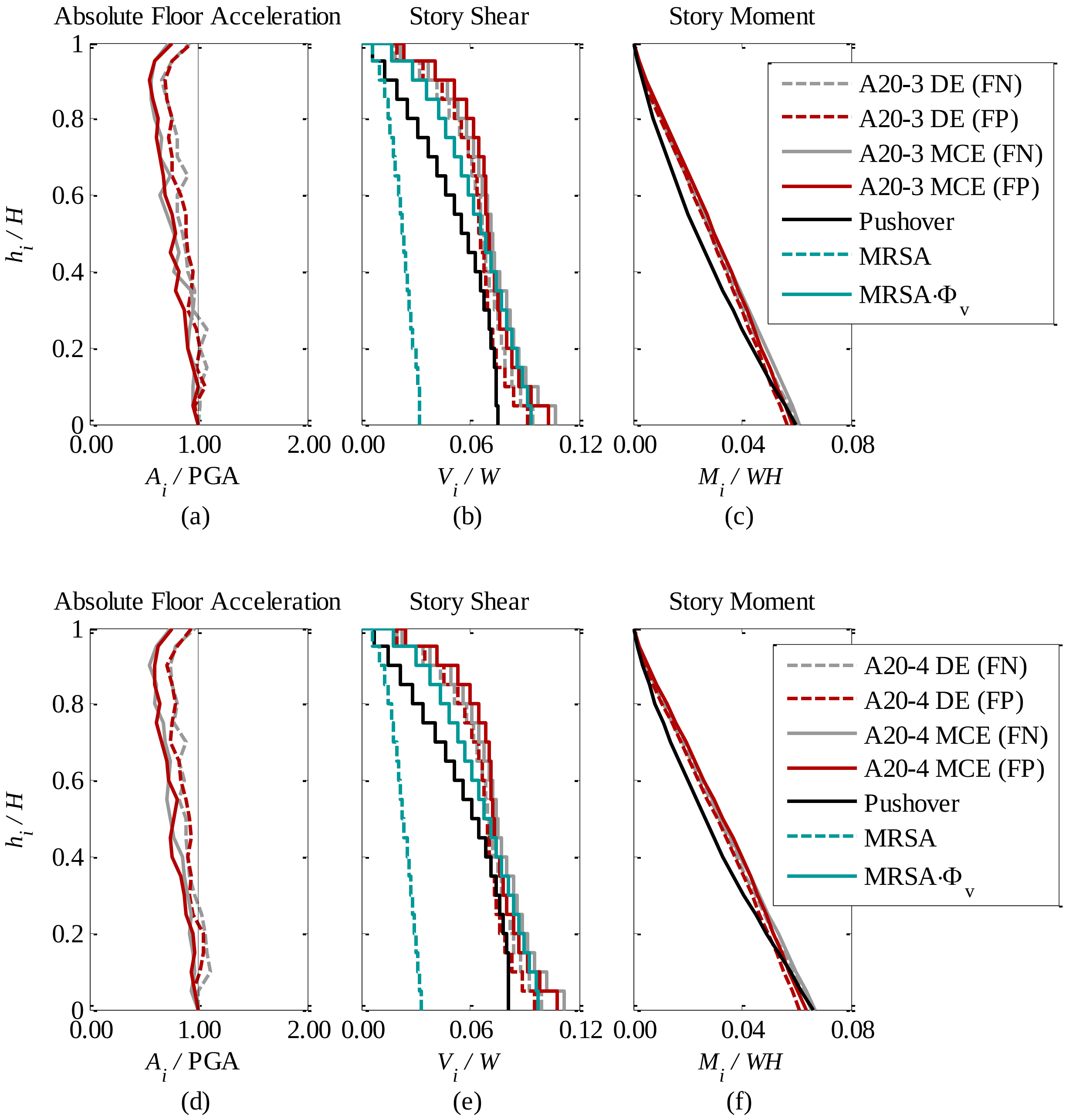

(a) (b) (c)

(d) (e) (f)

Figure 6.8.6. Floor acceleration, story shear, and story moment envelopes for buildings A20-3 and A20-4. (DE = design earthquake level response envelopes; MCE = maximum considered earthquake response envelopes; Pushover = response envelopes under first-mode pushover analysis at the roof displacement corresponding to the mean roof displacement from nonlinear response history analysis; MRSA = response envelopes obtained from elastic modal response spectrum analysis corresponding to design earthquake level forces; Φ_v = amplification factor applied to MRSA shear envelope to match the mean base shear from nonlinear response history analysis at design earthquake hazard level)

Story shear computed with elastic MRSA procedure was amplified to match the mean story shear envelope at the base. This was accomplished by multiplying all story shears by a factor Φ_v, as labeled in the plots of story shear envelopes (Figure 6.8.5 and Figure 6.8.6). Because MRSA accounts for the contribution of the higher modes, the amplified MRSA story shear envelope shapes (Figure 6.8.5[b] and [e] and Figure 6.8.6[b] and [e]) resemble more closely the mean story shear envelopes than the first-mode pushover envelope discussed earlier (Figure 6.6.6 and Figure 6.6.7). However, the story shears computed from the NRHA are not proportional to the MRSA story shears, which is particularly evident in the upper half of the stories in all buildings. For example, at the DE hazard level, the NRHA- mean shears in the 10-story buildings occurring at 0.8*H* are roughly 1.1 times the amplified MRSA shears, while at the top floor they are 1.3 times the shears from amplified MRSA. In the 20-story buildings at 0.85*H*, the DE-level mean story shears are 1.2 times the amplified MRSA, and at the top floor they are 1.1 times the amplified MRSA shears.

The deviations in the mean story shear envelopes from the MRSA-developed story shear envelopes follow a trend. The latter is identified by observing the individual story shear amplification factors plotted as functions of the building height in Figure 6.8.7. The story shear amplification factor is defined as the ratio of the mean story shear for a given set of ground motions at a given level of shaking intensity (V_i) to the story shear computed with the MRSA code-procedure ($V_{u,MRSA}$). Plots in Figure 6.8.7 show the variation of the story shear amplification factors along the height for both fault-normal and fault-parallel orientations of ground motion sets and at both DE and MCE ground shaking intensity levels. As a reference point, each plot also shows the Φ_v factor representing the amount of story shear amplification reached at DE level at the base considering the geometric mean of the FN and FP direction, as defined earlier.

Amplification factors follow very similar distribution for all four buildings, as can be seen in the individual plots of Figure 6.8.7. They vary between approximately 2.6 and 5.5 depending on the floor level and the building height. In the lower 0.5*H* to 0.6*H* of each building, the shear amplification factors fluctuate between 2.5 and 3.5 about the central value set to the base shear amplification factor defined previously. In the upper 0.4*H*, shear amplification factors diverge from Φ_v and reach the values up to $1.5\Phi_v$ to $1.8\Phi_v$ in the top stories. In 10-story buildings, the highest shear amplification occurs in the very top floor as is between $V_i / V_{u,MRSA} = 4.2$ and 5.5, while in the 20-story buildings, the highest shear amplification occurs slightly below the top story and is somewhat lower in value (between 3.3 and 4.2) compared to that in the shorter buildings.

For all four buildings responding at a given shaking intensity, the fault-parallel ground motion components produce higher story shear amplification in the upper stories, as noted before, while the trends reverse in the lower stories. In all cases, shear amplification factors increase with the shaking intensity. This difference in the amplification can be quantified in terms of a ratio between the mean story shear at MCE and DE level of shaking, which is plotted in Figure 6.8.8 for all four buildings. In all cases, the additional amplification factor due to stronger shaking intensity increases in the top 0.25*H* to 0.30*H* of the building height. In the 10-story buildings, the ratio of MCE to DE level story shears roughly equals 1.1 along the bottom 0.80*H* of the buildings and increases to about 1.2 in the top floors (see Figure 6.8.8[a] and [b]). Similar trends are observed in the 20-story buildings (see Figure 6.8.8[c] and [d]).

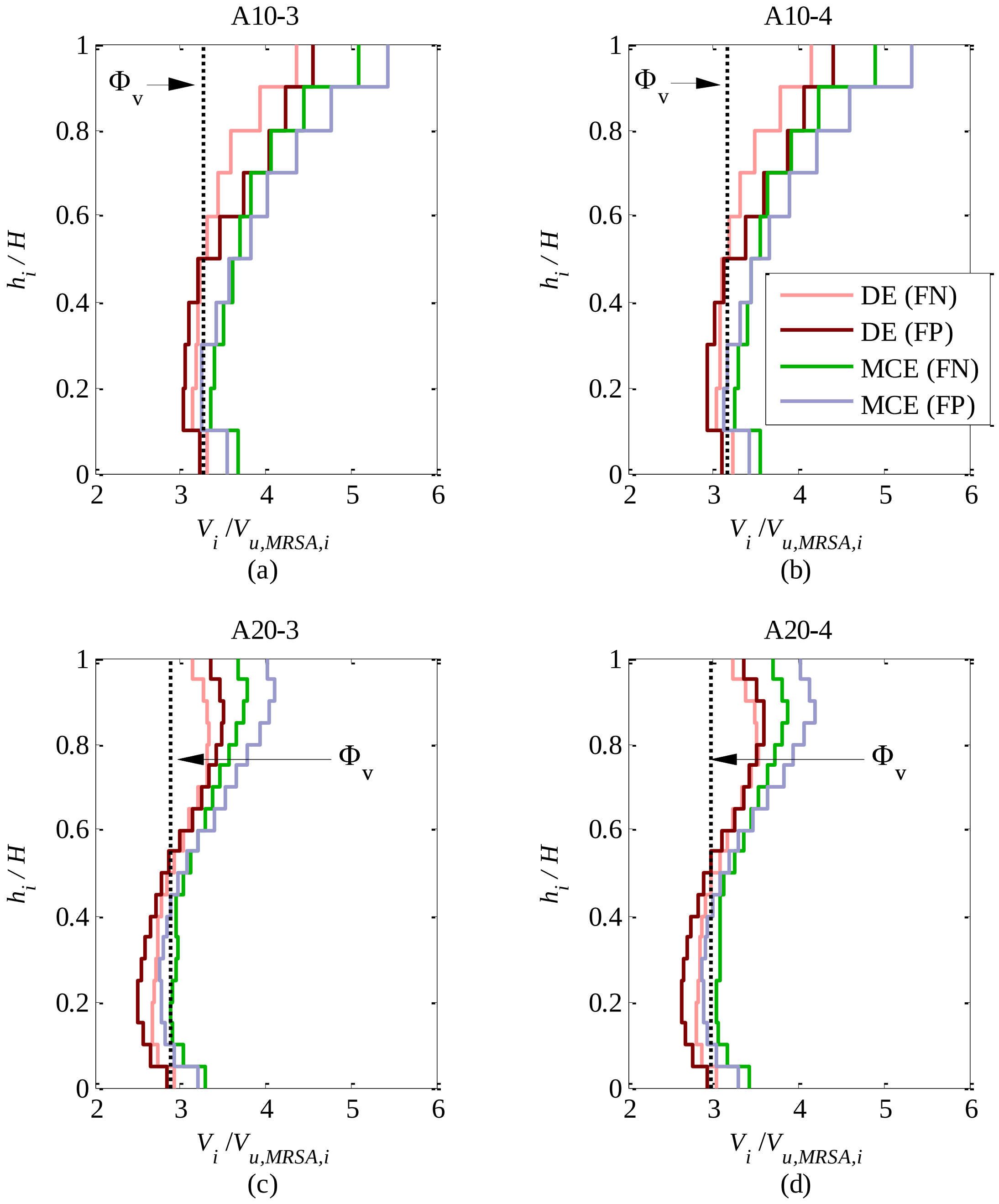

Figure 6.8.7. Ratio of the mean story shears to the corresponding story shears computed with MRSA analysis for buildings: (a) A10-3, (b) A10-4, (c) A20-3, and (d) A20-4.

The deviation of the mean response story shear envelopes from the MRSA shear envelope shown in Figure 6.8.7 suggests the following: in a building responding in nonlinear range, individual modes and hence their relative contributions to the total response are different from the relative response contributions of the elastic modes calculated by the standard elastic MRSA and using a single strength reduction factor (*R*) applied to all the elastic modes used in a combination rule. This effect is further amplified by the increased shaking intensity, as noted in

Figure 6.8.8. This is important to account for when estimating shear forces to be used in the design of the SMRFs.

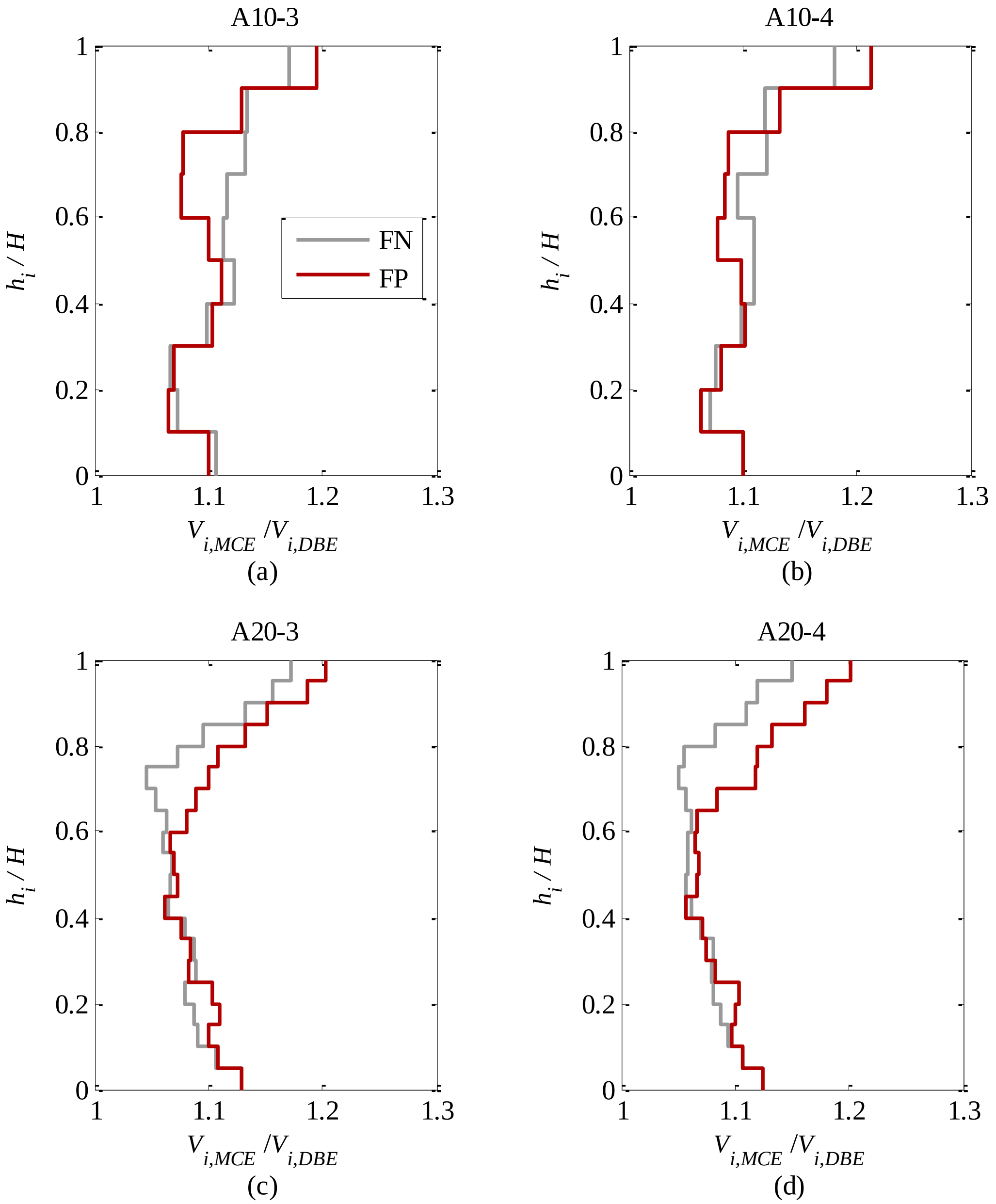

(a) (b) (c) (d)

Figure 6.8.8. Ratio of the mean story shears at MCE to the mean story shears at DE for buildings: (a) A10-3, (b) A10-4, (c) A20-3, and (d) A20-4.

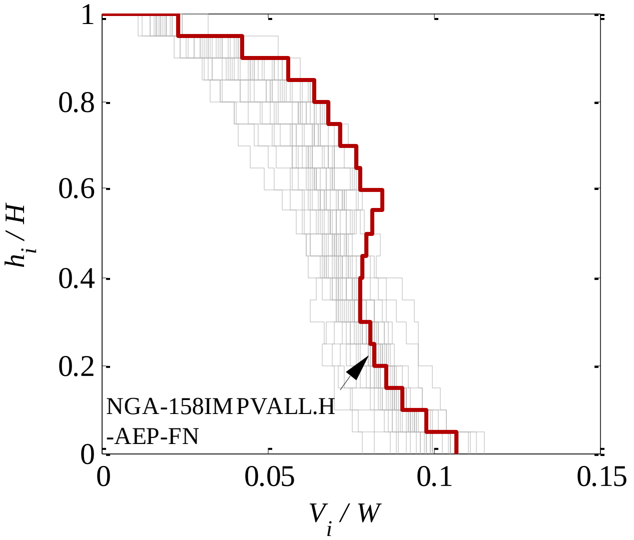

Figure 6.8.9. Story shear envelopes for A20-4 building under FN components of ground motion. Response to NGA158IMPVALL.H-AEP causing the largest story shear at 0.5*H* and 0.8*H* is highlighted in red.

It is informative to take a closer look at the dynamic response of a single building during a single nonlinear response history analysis. As an example, response of building A20-4 to fault-normal component of NGA158IMPVALL.H-AEP ground motion scaled with factor 2.2 (scaled to DE hazard level) is examined. The selected ground motion caused the largest shear at 0.5*H* and 0.8*H* out of all 30 ground motion analyses for this building in the FN direction. This can be seen in Figure 6.8.9, which highlights the story shear envelope corresponding to the selected ground motion plotted together with all the peak story shear envelopes computed for FN components at DE level of shaking.

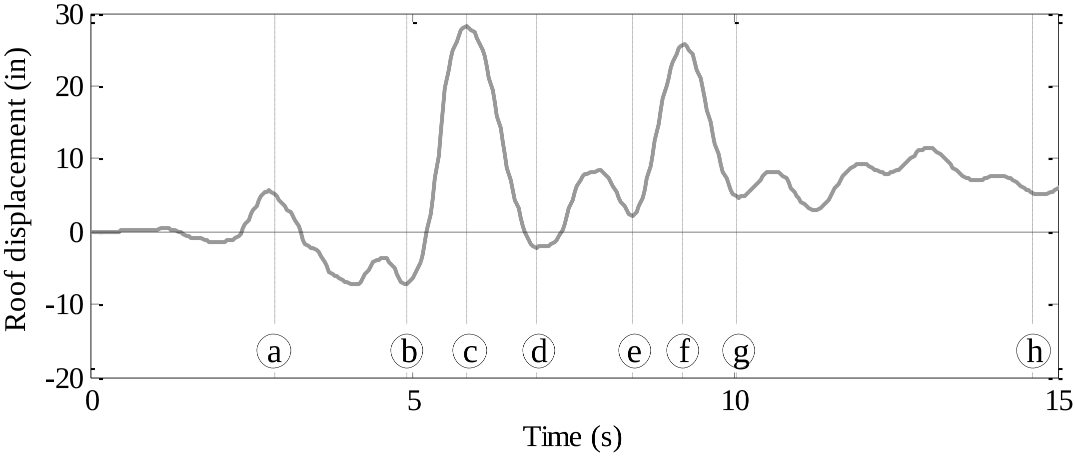

Figure 6.8.10. Roof displacement history for A20-4 building under FN component of NGA158IMPVALL.H-AEP scaled with factor 2.2.

The roof drift ratio history computed during the NGA158IMPVALL.H-AEP ground motion is plotted in Figure 6.8.10. Figure 6.8.11 shows the story shear profiles at specific instances identified in Figure 6.8.10. As evident in Figure 6.8.11 plots, large presence of higher modes contribution is evident in all instances, with none of the pictured shear distributions resembling the first-mode proportional shear distribution shown in Figure 6.6.7(c). Story shear distributions at instances labeled with a, f, g, and h are loosely proportional to the second-mode story shear distribution, suggested by the similarity in the force diagram shape to that in Figure 6.6.7(d). For reference, the instantaneous story displacement profiles at the six instances are also shown in Figure 6.8.12.

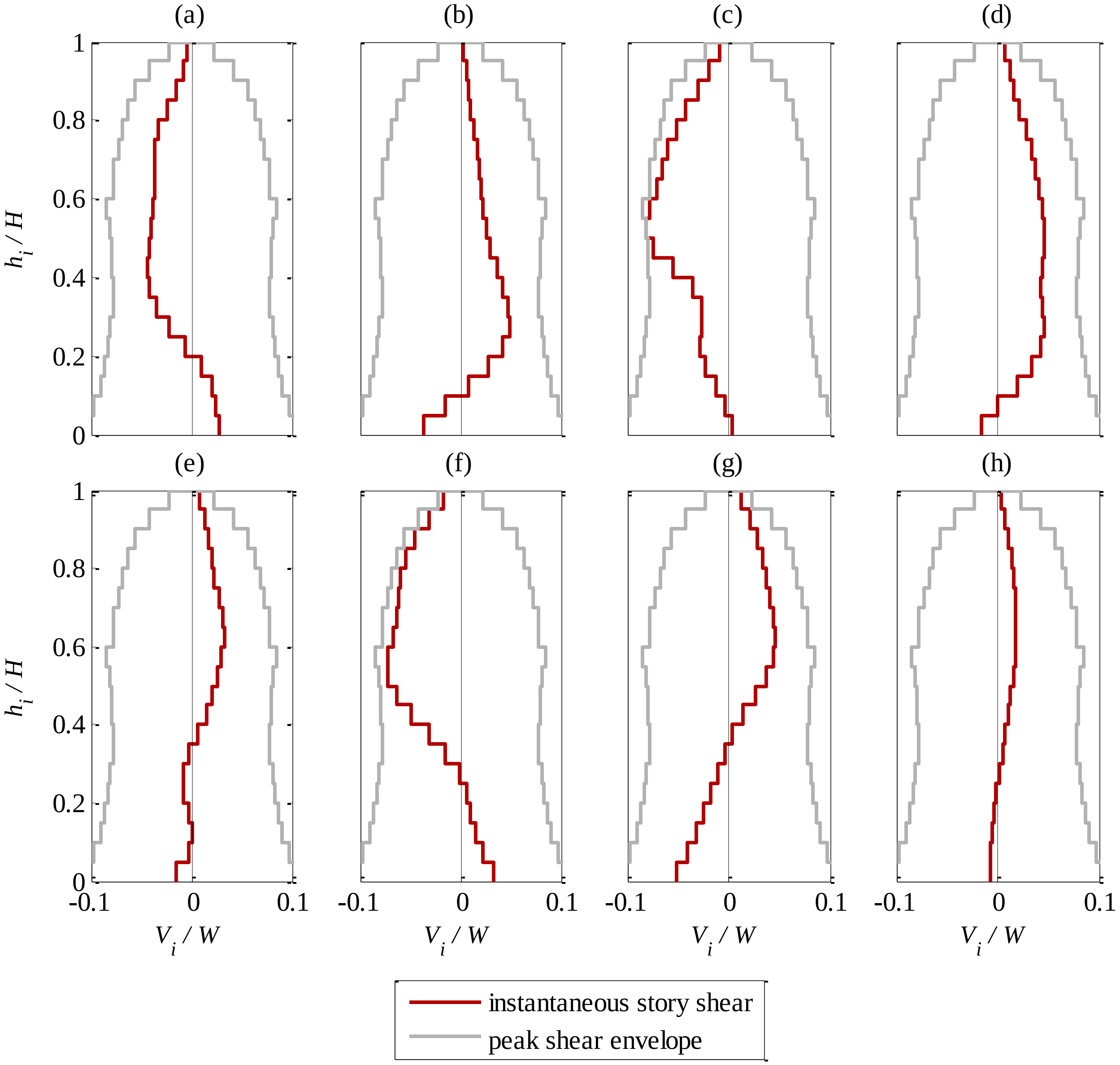

Figure 6.8.11. Instantaneous story shear distribution for A20-4 building under FN component of NGA158IMPVALL.H-AEP scaled with factor 2.2.

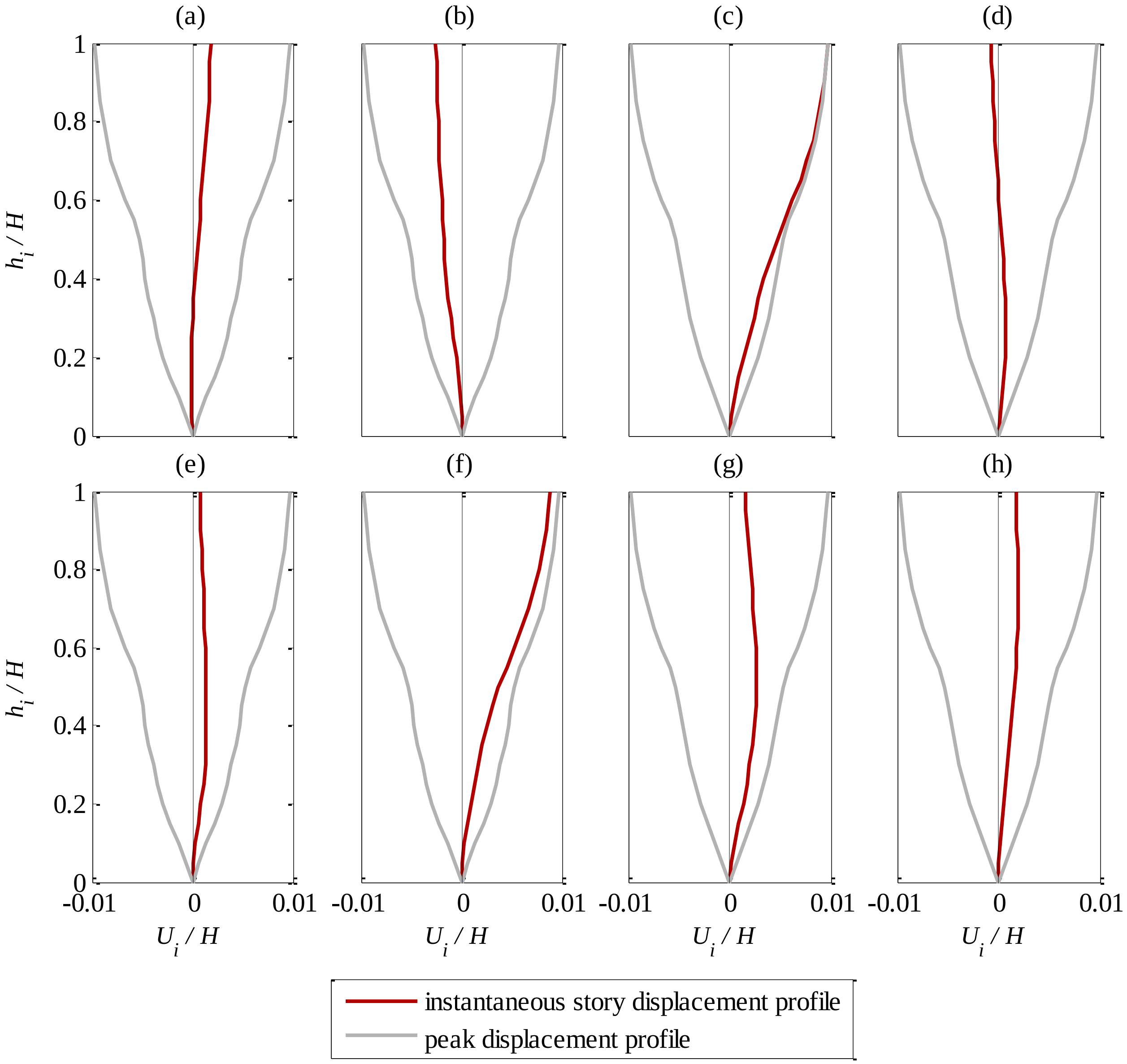

Figure 6.8.12. Instantaneous story displacement distribution for A20-4 building under FN component of NGA158IMPVALL.H-AEP scaled with factor 2.2.

Returning to shear response envelopes, let us look into the scatter in the results. Figure 6.8.13 through Figure 6.8.16 show the individual peak story shear envelopes computed in all four buildings for all ground motions at a given level and orientation with respect to the fault. Less scatter is present in shear envelopes compared to story displacements and drifts discussed in Section 6.8.1. Generally, force-related response quantities are largely bound by the system strength, as the buildings respond well in the nonlinear range at the two levels of shaking investigated. Thus smaller scatter is expected. Both mean and median curves are plotted to illustrate that the two curves are almost identical, contrary to what was observed in story displacements and story drifts. The shear envelopes also follow normal distribution. Figure

6.8.13 through Figure 6.8.16 also show the story shear envelopes representing 84.1, 97.72, and 99.86 percentile (mean + 1 standard deviation, mean + 2 standard deviations, and mean + 3 standard deviations, respectively) and also a maximum shear envelope bounding the story shear amplitudes for the 30 ground motions selected. There is generally greater dispersion in the shears higher up in the buildings, compared to the shears in the lower stories of the buildings, which is most evident in the fault normal direction of all buildings, shown in plots (a) and (c) in Figure 6.8.13 through Figure 6.8.16.

A closer examination of coefficients of variation (c_v) in story shear along the height of the buildings reveals an interesting trend. Figure 6.8.17 and Figure 6.8.18 plot the coefficients of variation (defined as a standard deviation divided by the mean of the distribution) for the 10-story and 20-story buildings, respectively, responding at two different shaking intensities and two different ground motion component directions considered. The c_v in the bottom $0.60H$ of all buildings is approximately 0.10 or less, while in the top $0.40H$ it increases to up to 0.30 in the FN direction and up to 0.20 in the FP direction. Thus, more scatter is present in the upper floors, which are more affected by the higher mode response, as noted before. The scatter seems to have little correlation with the shaking intensity at DE and MCE levels, likely because the column forces are bounded by the building capacity at these levels of inelastic nonlinear response.

The magnitudes of coefficients of variation indicate that, for the ground motions studied, an amplification factor of 1.1 to 1.3 can result in 34% increase of a safety margin against shear failures (from 50th to 84th percentile, or from mean to mean + one standard deviation), compared to simply using the mean shear envelopes as the basis of estimating seismic shear demands. In the lower stories, where shear forces are the largest, an amplification of 1.2 (approximately corresponding to mean + two standard deviations), can result in an increased safety margin against 98% of the ground motions selected in this study. This idea will be revisited in the next section, where a method of estimating design shear for SMRF columns will be developed.

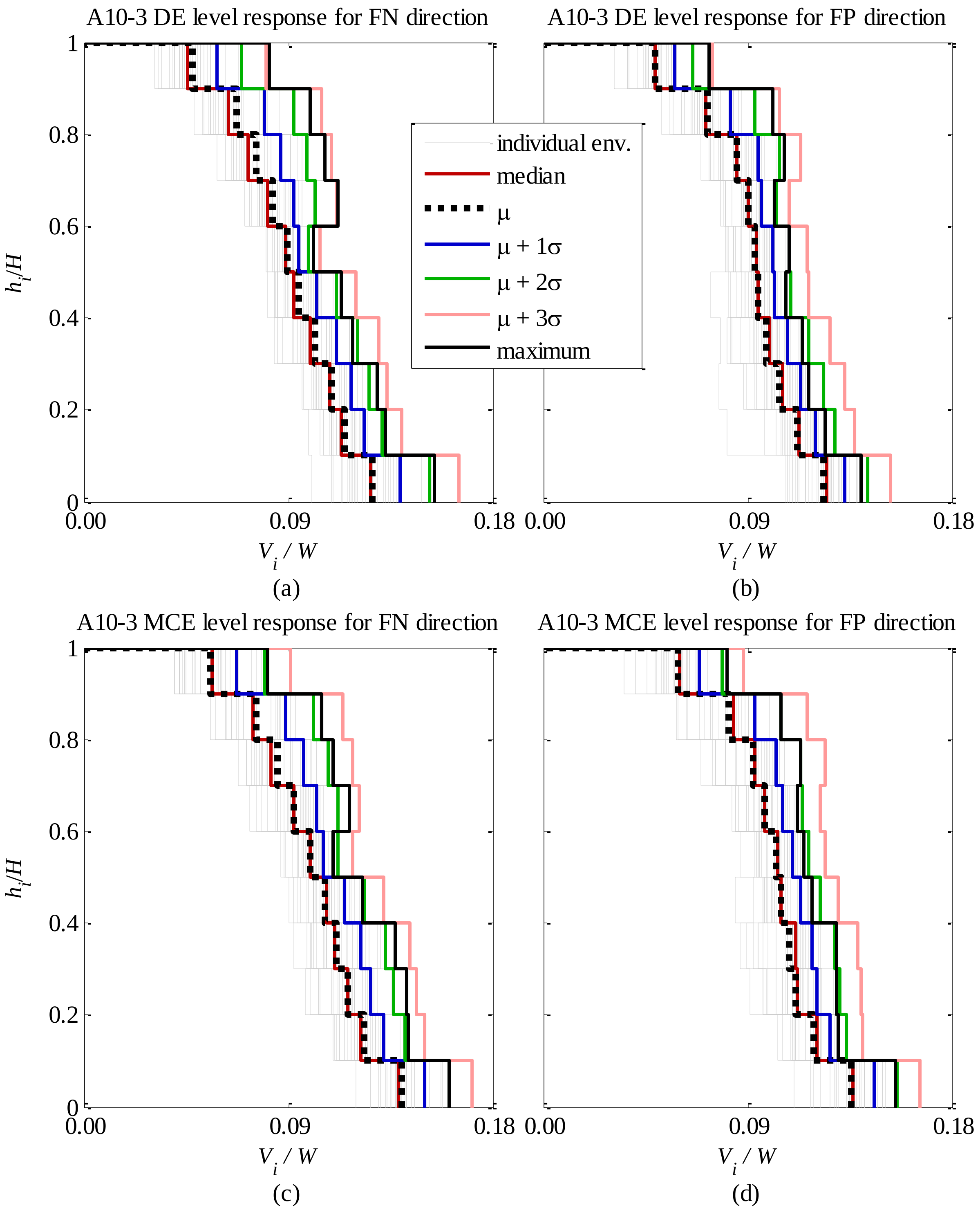

(a) (b)

(c) (d)

Figure 6.8.13. Story shear scatter for A10-3 building: (a) FN direction, DE level, (b) FP direction, DE level, (c) FN direction, MCE level, (d) FP direction, MCE level.

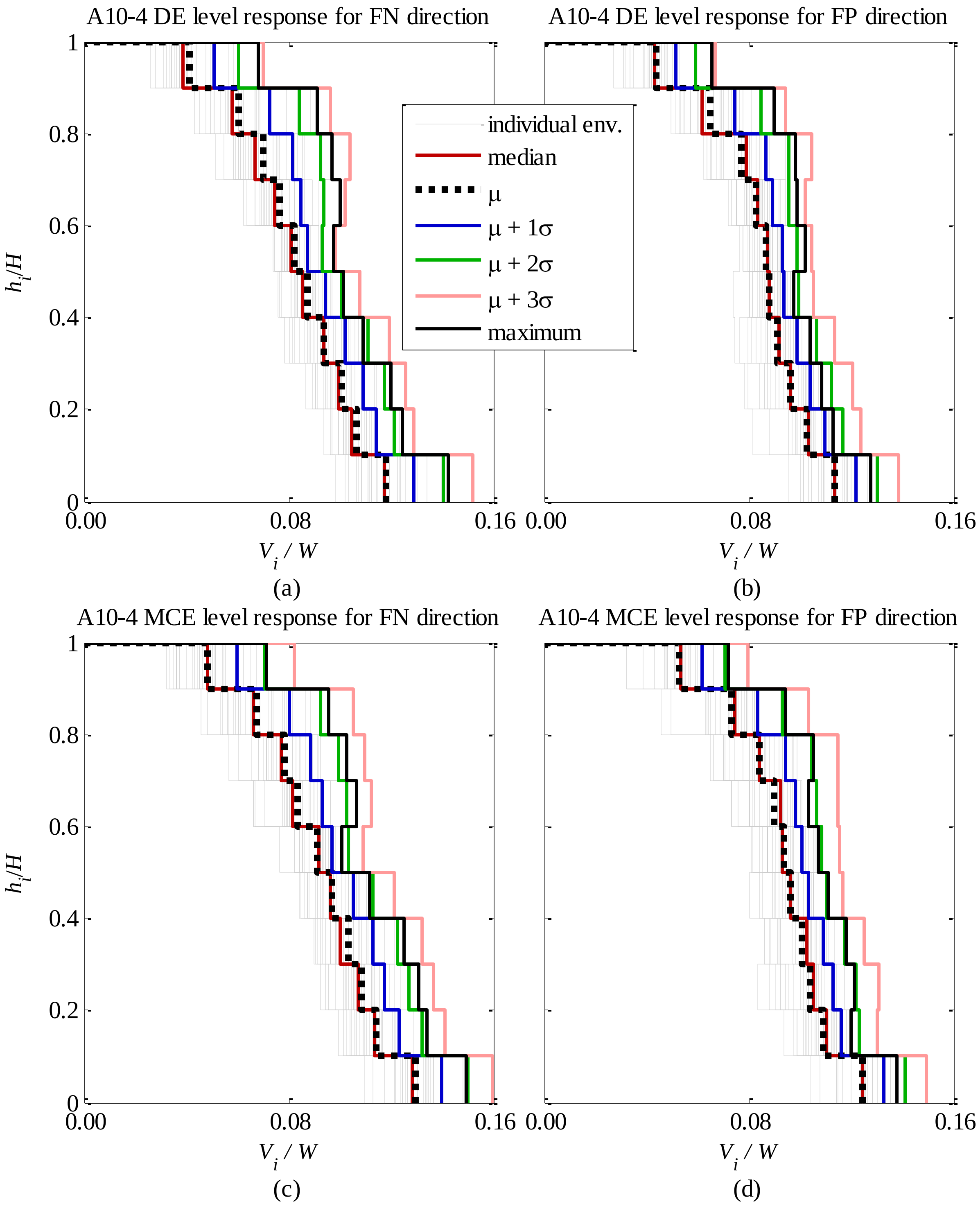

Figure 6.8.14. Story shear scatter for A10-4 building: (a) FN direction, DE level, (b) FP direction, DE level, (c) FN direction, MCE level, (d) FP direction, MCE level.

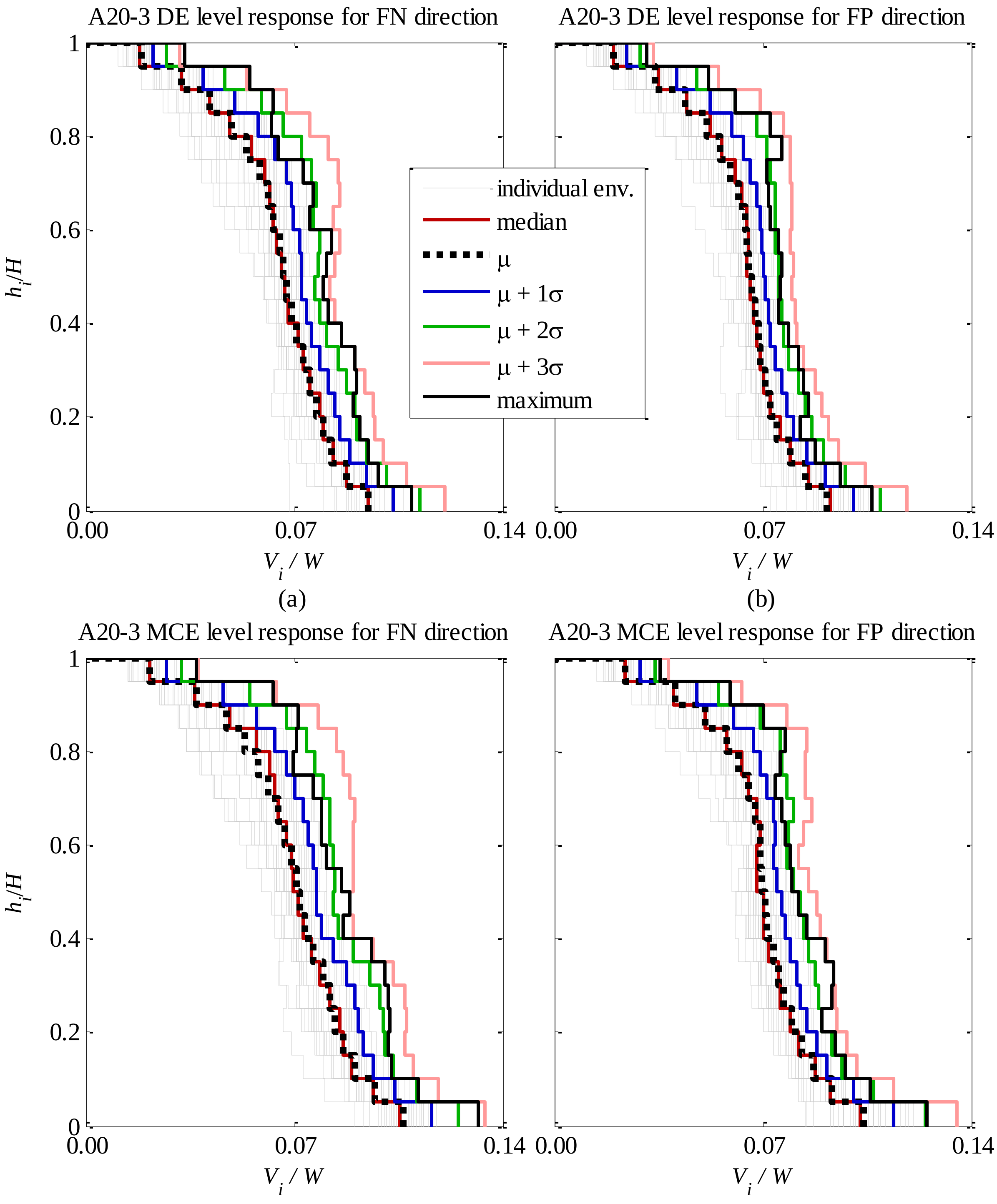

(a) (b)

(c) (d)

Figure 6.8.15. Story shear scatter for A20-3 building: (a) FN direction, DE level, (b) FP direction, DE level, (c) FN direction, MCE level, (d) FP direction, MCE level.

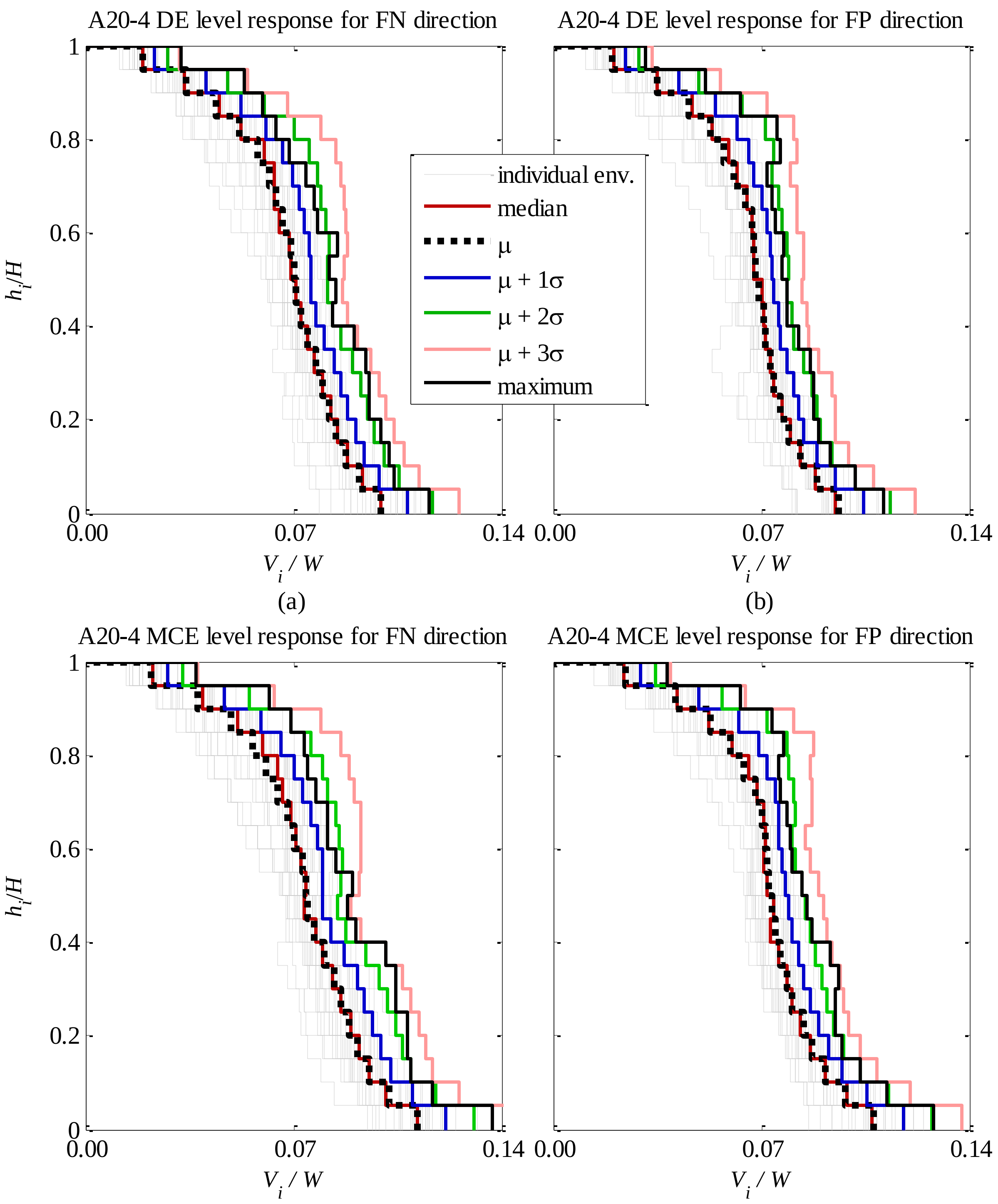

(a) (b) (c) (d)

Figure 6.8.16. Story shear scatter for A20-4 building: (a) FN direction, DE level, (b) FP direction, DE level, (c) FN direction, MCE level, (d) FP direction, MCE level.

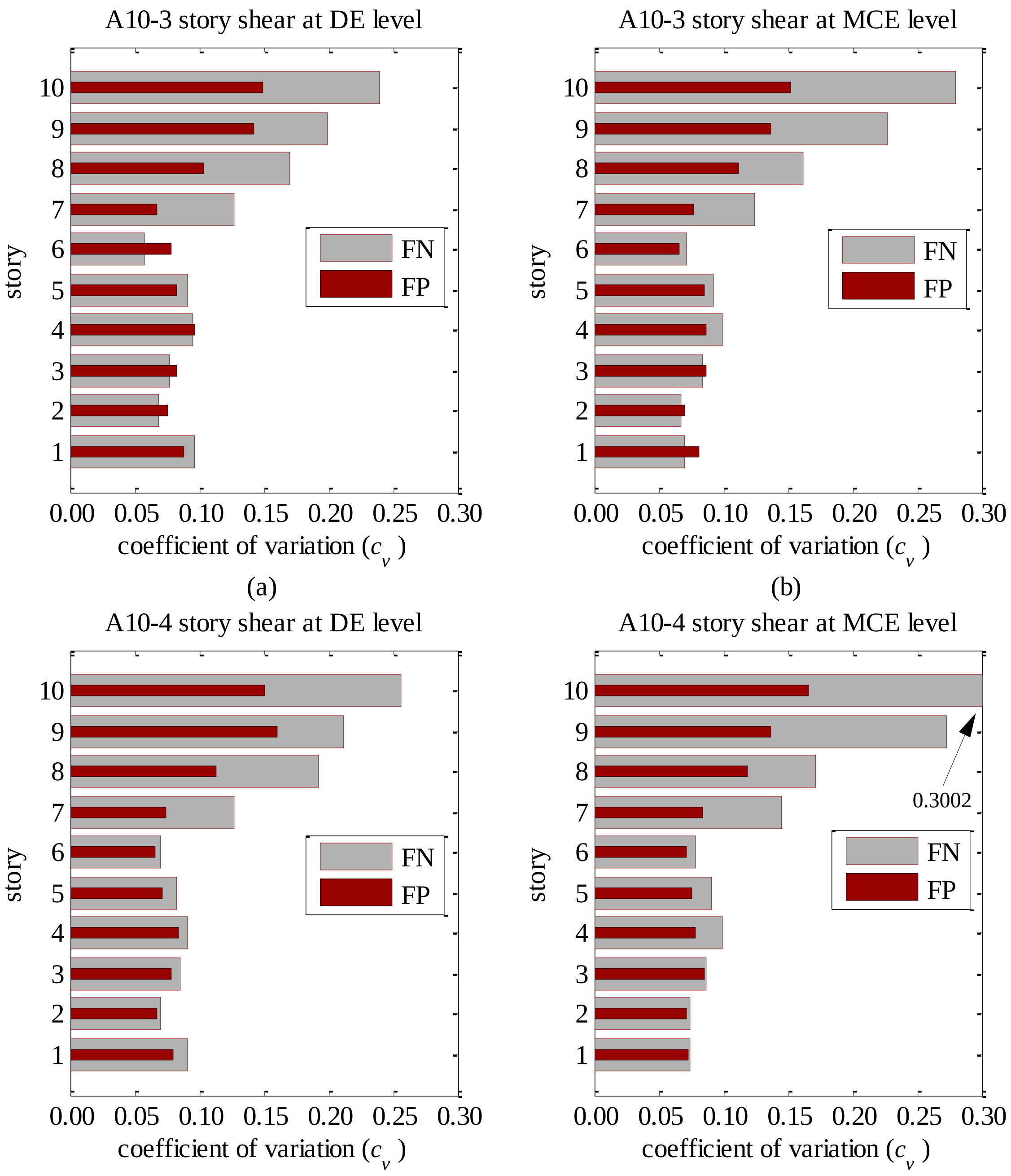

(a) (b)

(c) (d)

Figure 6.8.17. Coefficient of variation in story shear as a function of building height for 10-story buildings.

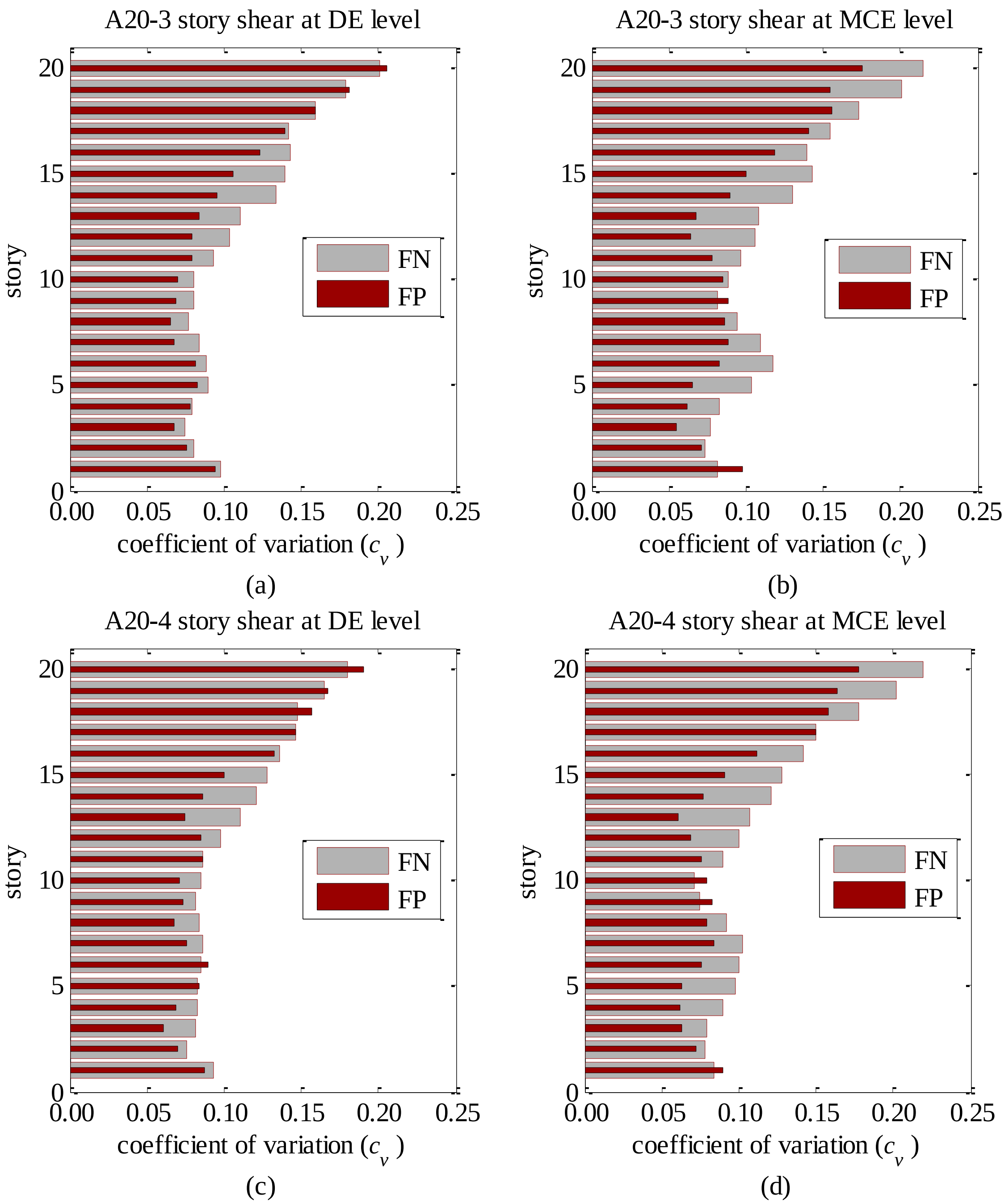

Figure 6.8.18. Coefficient of variation in story shear as a function of building height for 20-story buildings.

6.8.3 COLUMN SHEAR RESPONSE ENVELOPES

Figure 6.8.19 through Figure 6.8.22 plot the column shear envelopes for the archetype buildings under DE and MCE hazard levels. Each plot shows the envelopes corresponding to: i) peak column shear envelope for each ground motion run (both FN and FP components), ii) mean envelopes from NRHA for both FN and FP components, iii) the corresponding design level shear calculated by the MRSA analysis of ASCE 7-10 code, using the appropriate strength reduction factor (R) and minimum base shear amplification factor (discussed in Section 6.4), iv) design shear envelopes from ACI 318 corresponding to methods A, B1 and B2 as described in Section 6.1.1, and v) the design column shear envelope corresponding to NIST GCR 8-917-1 design guidelines (described in Section 6.1.2). All quantities shown are normalized with the gross area of the column multiplied by $\sqrt{f'_c}$. As can be seen in Figure 6.8.19 through Figure 6.8.22, method B2 in some cases results in higher design shear than method A. This happens in the upper stories, where columns become smaller and have less flexural capacity than in the lower stories, while the beams are designed with the same cross section as those in the lower stories. Note that the strong column – weak beam condition spelled out in ACI 318 is still satisfied in these locations. It is understood that method A will control the design in this case, as it is bounded by the column flexural capacity.

The shear distributions along the height of the building follow the same trends as was observed with the story shear. Peak shear reached in the exterior columns is approximately 0.6 times that in the interior columns, in all cases. In all buildings, the kinematic interaction between the elongating beam and the exterior column of the first floor has a notable effect on the column shear at the base. For example, in the A10-4 building, the amplification of mean exterior column shear at the base is 1.5 and 1.4 times the amplification of shear in the remaining column locations, based on amplifying the MRSA shear envelope for the nonlinear response history analyses for FN and FP ground motion direction.

The impact of beam elongation can be seen in the instantaneous column shear distribution along the column height during a nonlinear dynamic response. Figure 6.8.23(a) shows the instantaneous column shear distribution at t = 5.45 s during dynamic response to FN component of ground motion NGA_158IMPVALL.H-AEP scaled to 2.20. The illustration corresponds to the instance when the exterior column on the right in the sketch (colored with blue) reached maximum shear forces, during peak first-story displacements. Accompanying this plot are the displacement history of the first story (Figure 6.8.23[b]) and also the roof displacement history (Figure 6.8.23[c]).

Based on the results presented in Figure 6.8.19 through Figure 6.8.22, it is evident that some of the referenced design methods underestimate the ultimate shear forces developed in the columns under the ground motions compatible with the Design Earthquake seismic hazard level. The exception is the ACI 318 method A, which corresponds to the columns hinging at both ends and is the upper bound for the design shear. This method overestimates the column shears in all cases. ACI 318 method A seems to provide the best shear estimate in the interior columns of 10-story buildings, and in the buildings studied, seems to provide more conservative ultimate shear estimate where larger number of bays are present in a SMRF. This is, however opposite of the trends seen in the 20-story buildings, where the shear is overestimated by about the same amount in both 3-bay and 4-bay configuration (see Figure 6.8.20 and Figure 6.8.22). In interior columns of 20-story buildings, ACI 318 method A tends to overestimate design shear by a factor of 4 or more. This overestimation is further augmented in exterior columns, because the latter tend to carry roughly a half of the shear of the interior columns, while having larger probable moment capacity as a result of higher axial loads (under the assumption that the exterior and interior columns have approximately equal capacities and the exterior columns are in tension-controlled region under the axial loads experienced).

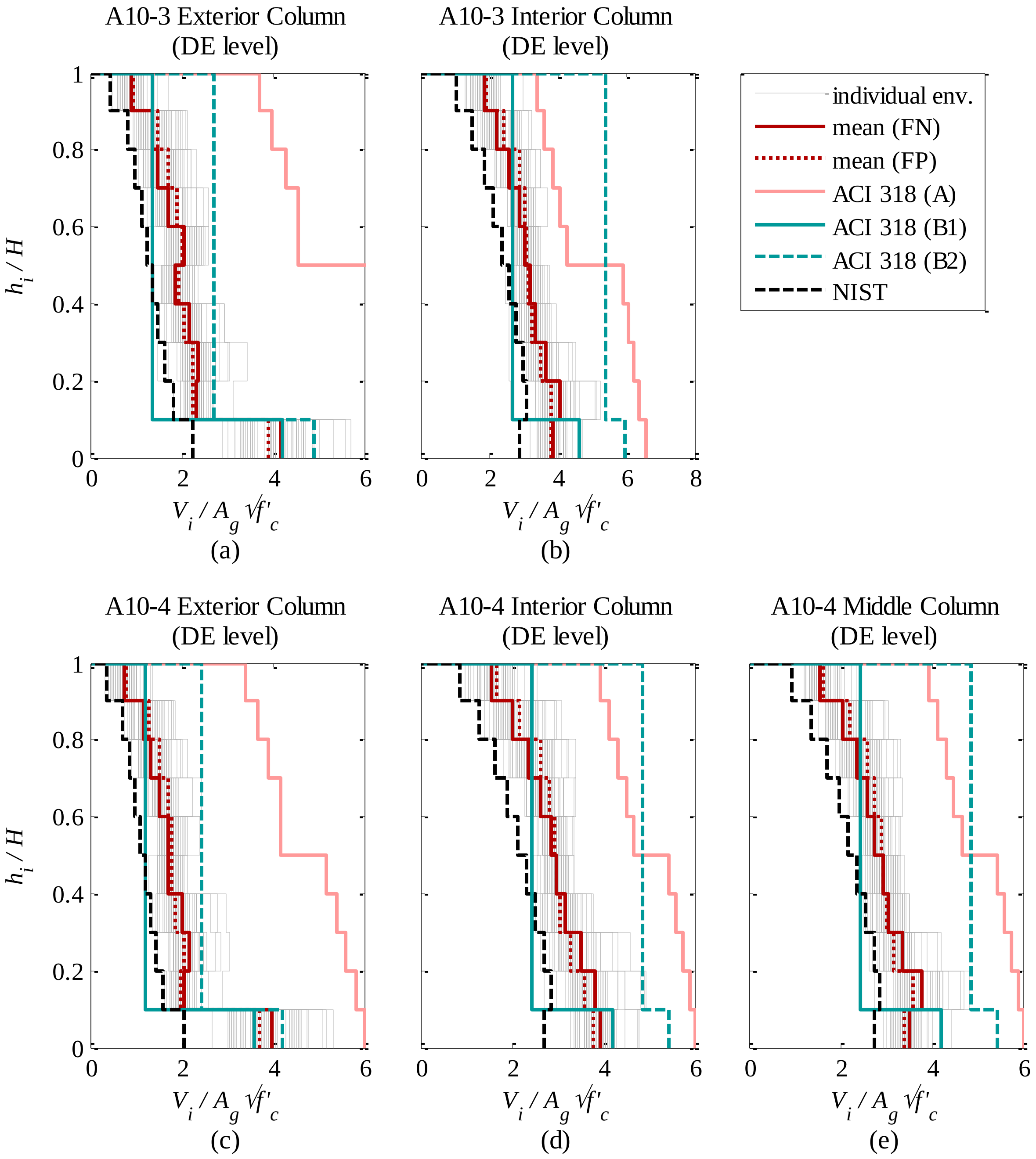

(a) (b) (c) (d) (e)

Figure 6.8.19. Shear response envelope plots for 10-story buildings under Design Earthquake hazard level.

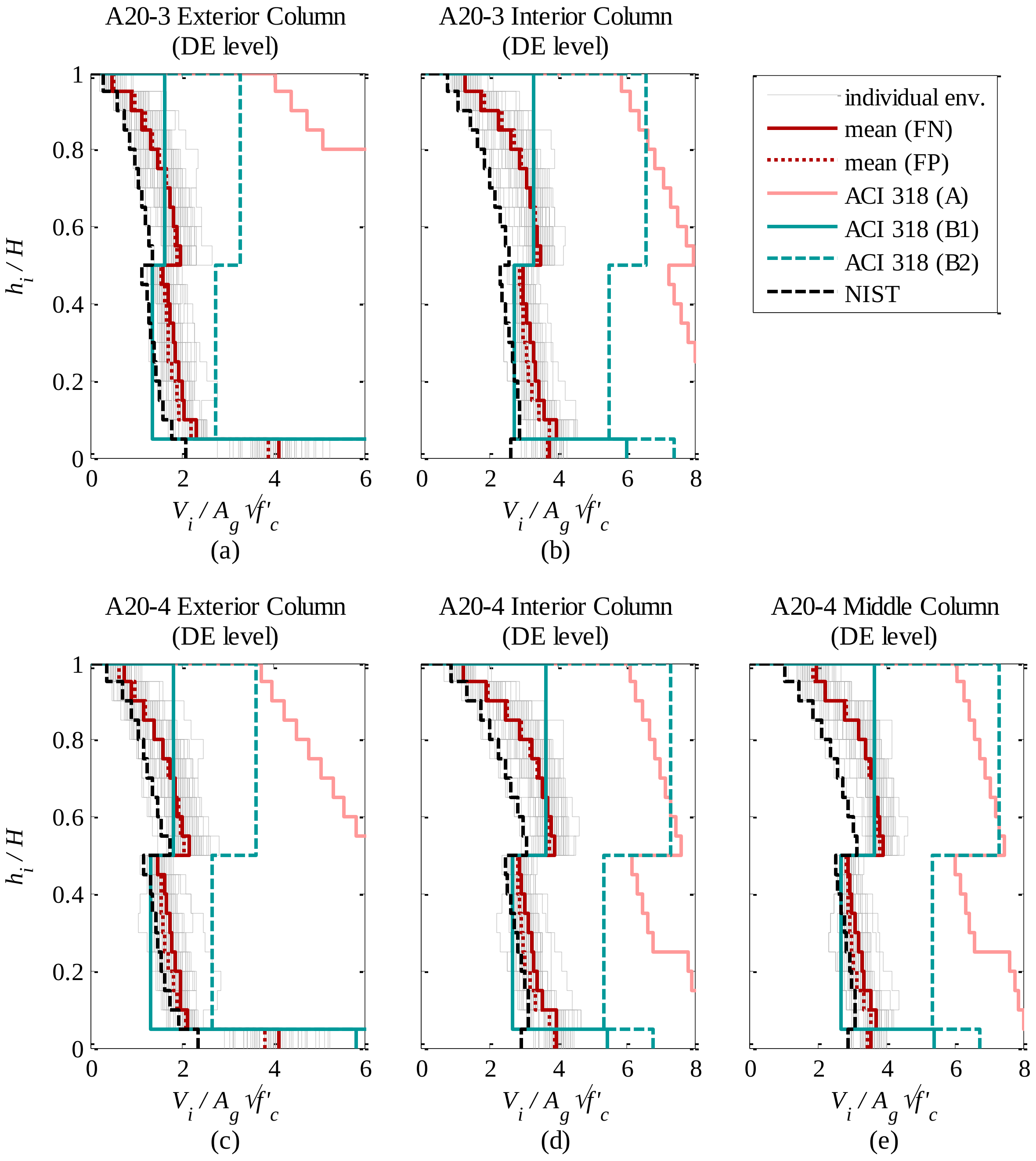

(a) (b)

(c) (d) (e)

Figure 6.8.20. Shear response envelope plots for 20-story buildings under Design Earthquake hazard level.

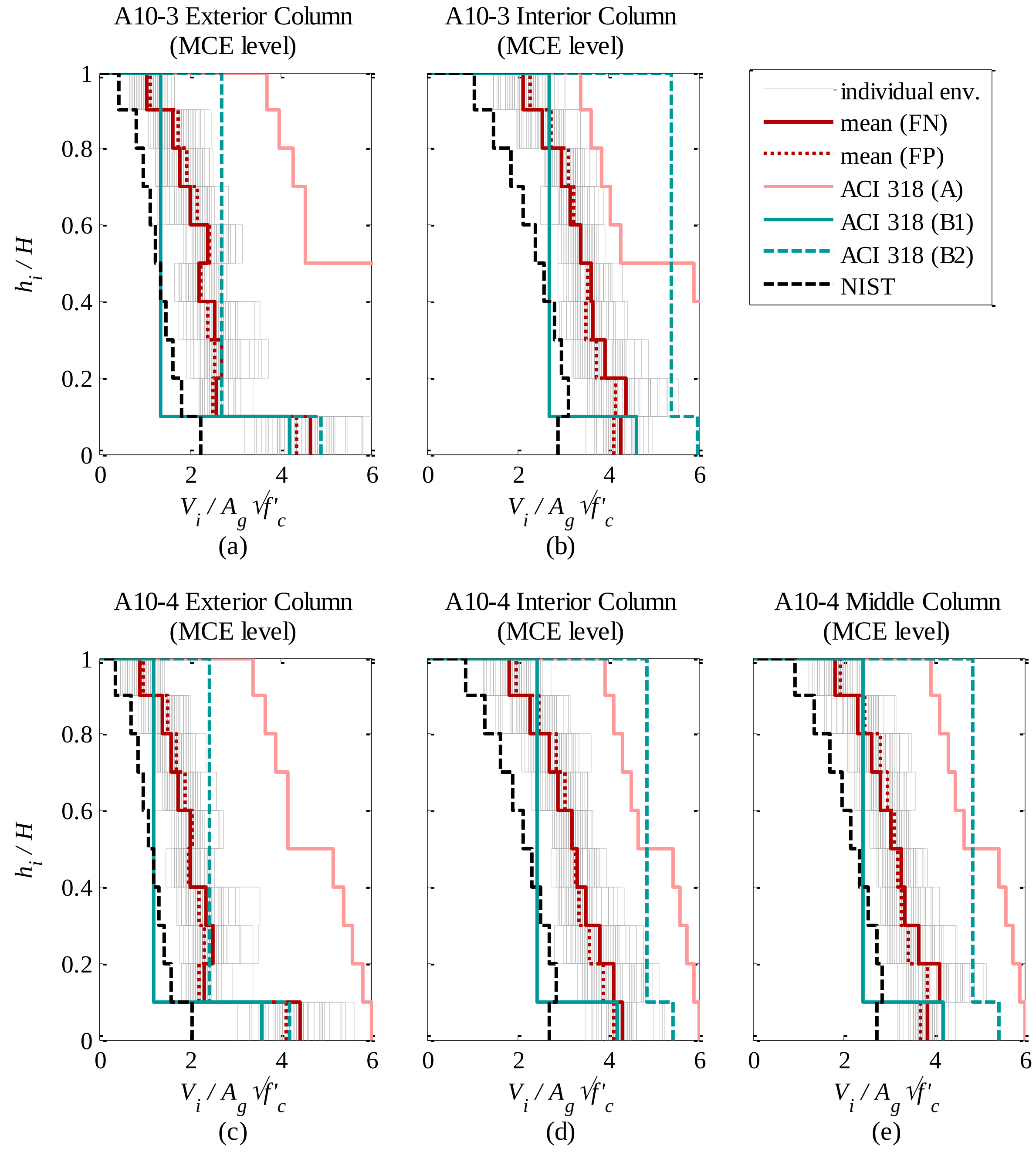

(a) (b) (c) (d) (e)

Figure 6.8.21. Shear response envelope plots for 10-story buildings under Maximum Considered Earthquake hazard level.

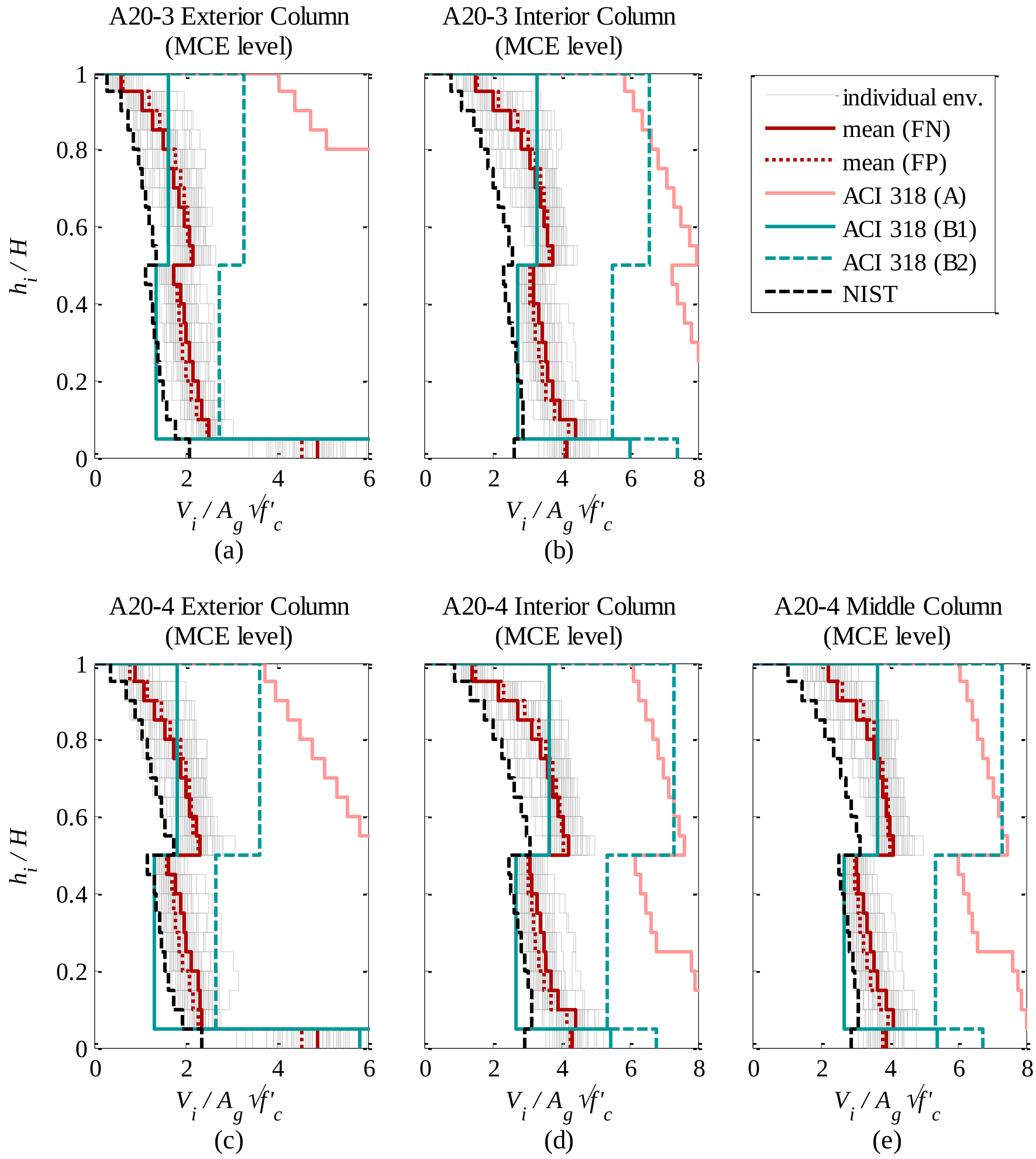
A20-3 Exterior Column (MCE level)

A20-3 Interior Column (MCE level)

A20-4 Exterior Column (MCE level)

A20-4 Interior Column (MCE level)

A20-4 Middle Column (MCE level)

(a) (b) (c) (d) (e)

Figure 6.8.22. Shear response envelope plots for 20-story buildings under Maximum Considered Earthquake hazard level.

Commonly used ACI 318 method B1 underestimates the ultimate column shear along at least 70% of the building height in all four archetype buildings. Thus, this method should be avoided in design, as suggested before by others (Moehle et al. 2008).

ACI 318 method B2 provides more conservatism in all columns and all buildings. However, for the four archetype buildings where beam flexural capacity was kept uniform along the height, this method can also result in overestimating the design shear by more than a factor of 3 in the upper half of the height in each building. This is especially evident in the interior columns of 20-story buildings (see Figure 6.8.20 for DE level response and Figure 6.8.22 for MCE level response). This overestimation would likely reduce in the buildings where the flexural strength of the SMRF beams is reduced along the building height; however, further investigation is necessary to draw a more definite conclusion regarding this method.

Method suggested by NIST GCR 8-917-1 and labeled simply as NIST in Figure 6.8.19 through Figure 6.8.22 underestimated the mean column shear in all cases by at least 25%. However, because this design method was based on MRSA, it resulted in an ultimate shear envelope that most closely follows the mean column shear envelopes from NRHA.

ACI 318 Method A was the only design method which consistently provided a safety margin against the increased shear in the base exterior column. Thus, this method is recommended to use in the base stories of exterior columns, impacted by the beam elongation. In all other location, Method A is deemed overly conservative.

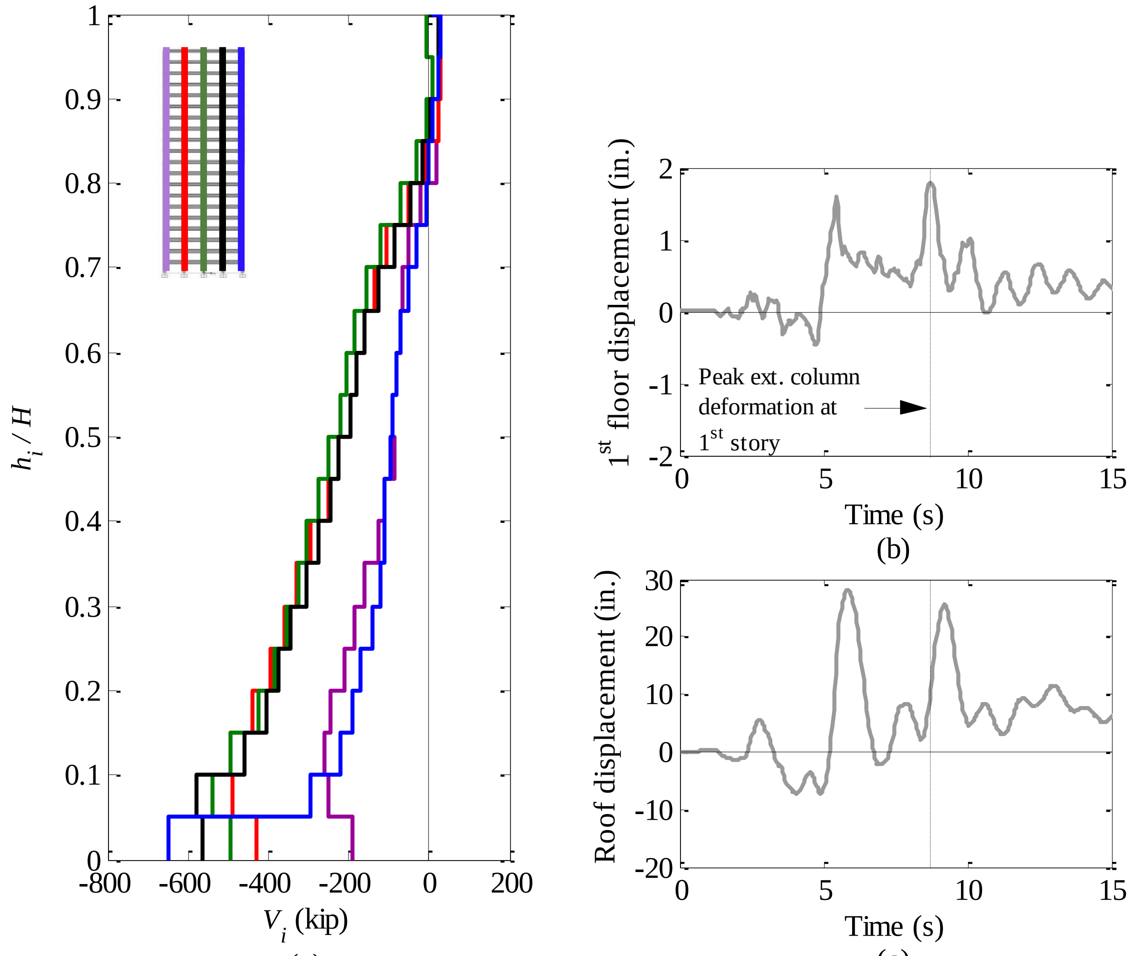

(a) (b) (c)

Figure 6.8.23. Instantaneous column shear distribution in building A20-4 under FN component of ground motion record NGA_158IMPVALL.H-AEP scaled to 2.20.

6.9 ESTIMATING SYSTEM (STORY) SHEAR

The focus of this section is to develop a method to estimate, within some acceptable level, the story shear distribution and amplitude during nonlinear response of the four SMRF buildings studied. The objective is to identify the key factors affecting this engineering parameter. Although story shear is not directly used in design of reinforced concrete special moment frames, it is anticipated that the same general principles affecting this global response quantity will also govern the column shear demand. Conveniently, a conceptually sound estimation of the story shear will serve as a basis for developing a procedure for establishing the level of shear forces to be used for column design.

As the mean response envelopes in this chapter (and also in Chapter 5) indicate, the level of base shear in SMRFs during nonlinear dynamic response is mostly affected by the system capacity, or base moment overstrength. This is also evident in the pushover curves where the base shear at system yield is multiple times higher than the design base shear. Thus, this quantity needs to be an integral part of a design procedure developed. In addition, system shear contains a considerable amount of higher mode contribution that seems to have an increased presence in the upper stories, as was shown in Figure 6.8.7, and increases with the amplification of the ground motion intensity, as was noted in Figure 6.8.8. Hence, the design story shear estimation method needs to also consider the shear amplification due to higher modes. Lastly, as shear yielding in RC columns can significantly reduce the ductility, the design method developed also needs to account for statistical dispersion of shear forces during nonlinear dynamic response of buildings (Figure 6.8.13 – Figure 6.8.16) to increase the safety margin against column shear yielding and the resulting performance implications. These individual elements affecting the system shear are addressed separately in the next three sections.

6.9.1 SYSTEM BASE OVERSTRENGTH AMPLIFICATION FACTOR: Ω

The system base overstrength factor Ω is defined as the ratio between the approximate system base overturning moment capacity $M_{b,\Omega}$ and the system base overturning moment demand $M_{b,u}$ computed with the MRSA procedure using the appropriate strength reduction factor R and minimum base shear amplification factor. For regular buildings studied in this chapter, it is computed with the following expression:

$$\Omega = \frac{M_{b,\Omega}}{M_{b,u}} = \frac{\sum_{j=1}^{NCol} M_{pr,c,j} + \left(P_{T,\Omega} + P_{C,\Omega}\right) L_F / 2}{M_{b,u}} \qquad 6.5$$

where $M_{pr,c,j}$ are the probable moment capacities of the columns at the base under the gravity loading considered to act during a seismic event, that is 1.0D + 0.25L, $NCol$ is the total number of columns in a SMRF at the base, $P_{T,\Omega}$ and $P_{C,\Omega}$ are axial forces in exterior columns on tensile and compressive side of the SMRF at the base, and L_F is the center-to-center distance between the external SMRF columns (or frame width). $P_{T,\Omega}$ and $P_{C,\Omega}$ are calculated with the following expression:

$$P_{T,\Omega} = \sum_{i=1}^{N} V_{pr,i} - \sum_{i=1}^{N} P_{g,i} \qquad 6.6$$

$$P_{C,\Omega} = \sum_{i=1}^{N} V_{pr,i} + \sum_{i=1}^{N} P_{g,i} \qquad 6.7$$

In Equations 6.6 and 6.7, $V_{pr,i}$ is the shear corresponding to development of probable moment strengths $M_{pr,i}$ in beams framing into an exterior column at level *i*, calculated assuming zero gravity loads. $P_{g,i}$ represents the axial force due to gravity load at level *i* acting on the tributary area of the exterior column. It should be noted that in the Equations 6.6 and 6.7, both V_{pr} and P_g have positive values. The direction of the axial force action when summing the moments about the base is taken into account in Equations 6.6 and 6.7. For the four archetype buildings with uniform frame bay widths, the sum of the $P_{g.i}$ terms in Equations 6.6 and 6.7 cancel out when plugged into Equation 6.5. However, if the two exterior bays of the frame are of different lengths, this will not be the case.

Using the Equations 6.5 through 6.7, system base overstrength amplification factor Ω was calculated for each of the four archetype buildings. These are listed in Table 6.5, alongside the flexural overstrength factors as determined per the NIST Design Guide, which was described in Section 6.1.2. It is clear that considering the building system overstrength provides a larger factor than considering only the total overstrength of the beams framing into a single column. Thus, amplifying the MRSA-based design forces with a system overstrength factor Ω, rather than the factor Φ_m as defined in NIST Design Guide, will lead to more conservatism.

Alternatively, the definition of the flexural overstrength factor Φ_m as defined in NIST Design Guide can be adjusted to provide equal level of conservatism as the system overstrength factor in Equation 6.5. This can be done by considering the flexural overstrength of all plastic hinges assumed to form in the storng column-weak beam mechanism, i.e., the beams at each joint support and the columns at the base of the frame. An adjusted overstrength factor Φ_m^* is proposed, as follows:

$$\Phi_m{*} = \frac{\sum_{k=1}^{NCol} M_{pr,c,k} + \sum_{k=1}^{NBm} (M_{pr,b,i} + M_{pr,b,j})}{\sum_{k=1}^{NCol} M_{E,c} + \sum_{k=1}^{NBm} (M_{E,b,i} + M_{E,b,j})} \qquad 6.8$$

The numerator in Equation 6.8 represents the sum of the probable moment strengths of all plastic hinge regions; that is, the probable moment strengths of each column at the base floor only, and probable moment strengths of each beam at each end. As before, *NCol* denotes the number of columns and is equal to the number of SMRF bays plus one, while $M_{pr,c,k}$ signifies probable moment capacity of column *k* at the base only. Term *NBm* in Equation 6.8 represents the total number of beam clear spans in a SMRF. For example, in a 4-bay, 10-story moment frame, $NBm = 4 \cdot 10 = 40$. $M_{pr,b,i}$ and $M_{pr,b,j}$ denote the beam moment capacities at each end of the clear span *k*.

The denominator in Equation 6.8 is the sum of the moment demands on all plastic hinge regions assumed to act in the strong column-weak beam mechanism, due to *earthquake loading only*. That is, terms $M_{E,c}$, $M_{E,b,i}$, and $M_{E,b,j}$ are the seismic moment demands calculated using code-based analysis (MRSA) and the appropriate strength reduction and minimum base shear factors, as defined in Section 6.4. They should not include the contribution of gravity moments coming from the load combinations 5 and 7 (Section 6.4). Including the gravity moments in the denominator reduces the overstrength factor calculated, the extent of which depends on the relative magnitudes of gravity and seismic moments acting on the beams.

Table 6.5 lists the factors Φ_m^* calculated per Equation 6.8. As can be seen, the Φ_m^* adjusted factors are almost identical to the overstrength factor Ω calculated with Equation 6.5. Thus, either Equation 6.5 or 6.8 can be used to estimate the flexural overstrength of the system.

Table 6.5. Overstrength factors calculated with different methods.

	A10-3	A10-4	A20-3	A20-4
Ω	2.82	2.67	2.43	2.74
Φ_m (NIST)	2.58/2.62	2.45/2.5/2.54	2.23/2.20	2.62/2.55/2.48
Φ_m^* (NIST adjusted)	2.81	2.72	2.45	2.80

6.9.2 HIGHER MODES AMPLIFICATION FACTORS: A_D AND Ψ_V

The idea of accounting for higher modes nonlinearity in response has been explored before through modal pushover analysis (Chopra and Goel 2002, Chopra et al 2004) and also by using different strength reduction factors in different modes (Eibl and Keintzel 1990, Calugaru and Panagiotou 2011). Priestley (2003) explored a so-called "modified modal response spectrum analysis" in conjunction with the direct displacement based design proposed using a strength reduction factor proportional to the displacement ductility demand on a substitute system for each mode for both structural walls and frames. The study showed that while this method resulted in a more accurate estimate of system shears in reinforced concrete walls, it did not produce satisfactory results in reinforced concrete frames.

For completeness, the idea of modifying the MRSA in a similar manner to estimate the story shears is explored briefly in this chapter using only two buildings: A10-4 and A20-4. Because the objective is to find a simple method to be used in conjunction with the current US code prescriptions, rather than investigating ductility demands of substitute structures in each mode, here an MRSA analysis has been modified such that first mode is divided by $R = 8$ (code value) and higher modes are reduced by a smaller R factor. Two different cases are explored: one using $R = 4$ in higher modes and the other using $R = 5$ on higher modes.

Figure 6.9.1 shows the story shear envelopes computed with the NRHA corresponding to the mean, mean $+1\sigma$ and mean $+ 2\sigma$ for buildings A10-3 (Figure 6.9.1[a] and [b]) and A20-4 (Figure 6.9.1[c] and [d]). The plots in Figure 6.9.1 also include the story shear envelopes obtained by amplifying the story shear from the code-based MRSA using $R = 8$ and appropriate minimum base shear amplification factor required by the code and discussed in Section 6.4 with the system overstrength factor Ω. The modified MRSA story shear envelopes calculated using each $R = 4$ and $R = 5$ on all modes except the first mode (for which $R = 8$ was applied), also shown in the plots in Figure 6.9.1, have been amplified with both the minimum base shear amplification factor *MF* and the system overstrength factor Ω.

In all cases, the story shear envelopes obtained through modified MRSA with the system overstrength factor Ω are more representative in shape of those computed in the NRHA. In the 20-story building, this modified response spectrum analysis using $R = 8$ in the first mode and $R = 4$ in the remaining modes considered (modes 2 through 10) leads to a conservative estimate of story shears along all floors for 25 of the ground motions in the FN direction (Figure 6.9.1[c]) and 29 ground motions in the FP direction (Figure 6.9.1[d]). The modified MRSA using $R = 5$ in modes 2 through 10 conservatively estimates the mean story shear envelopes for the 20-story buildings in both the FN and FP directions.

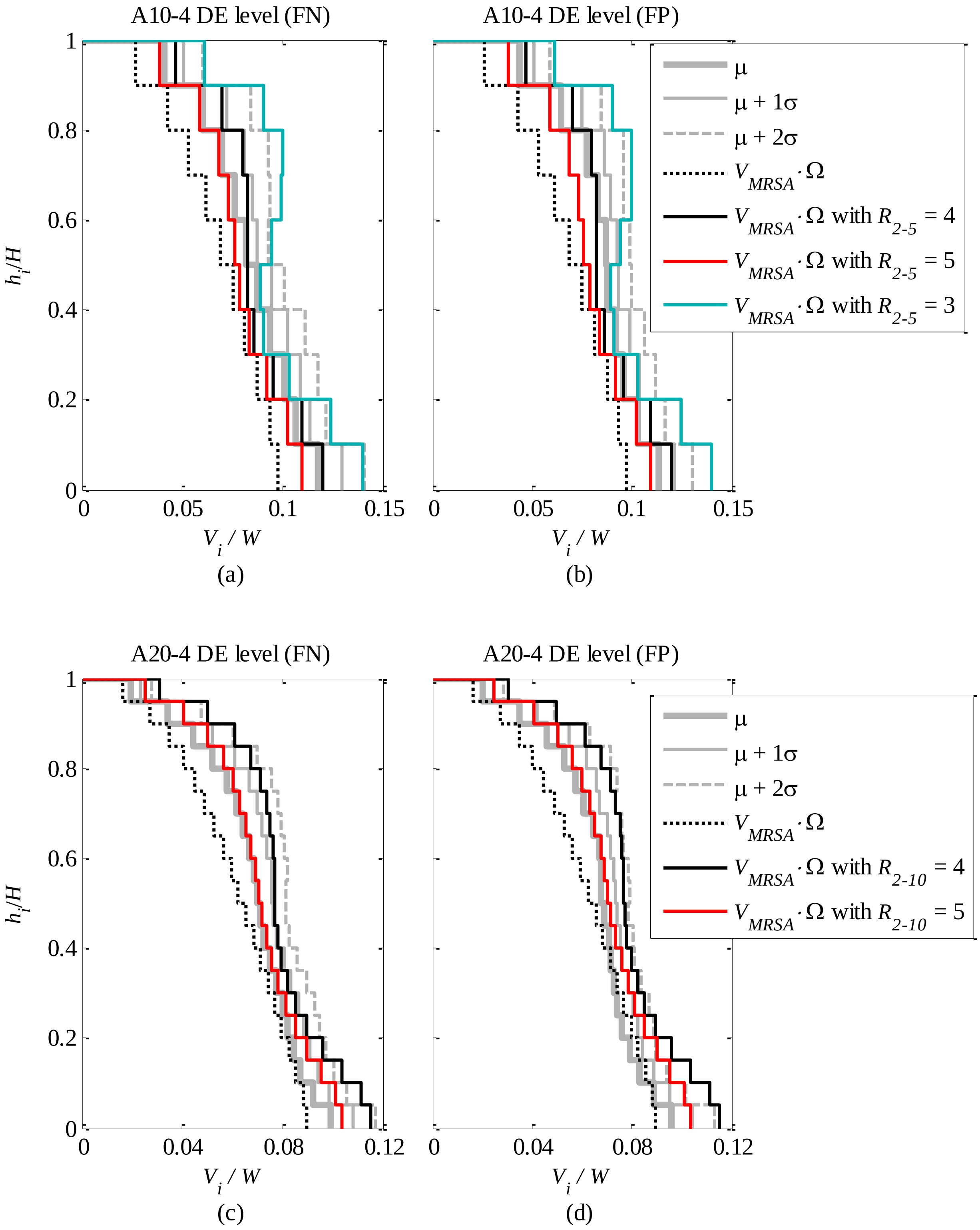

(a) (b) (c) (d)

Figure 6.9.1. Using modal response spectrum analysis from code with different strength reduction factors in higher modes.

In the 10-story building, the modified MRSA leads to slightly less satisfactory estimate of story shears. While leading to a more accurate shape of the shear envelopes than code-based MRSA, both cases of modified MRSA underestimate the mean shear response, with larger strength reduction factor *R* leading to less conservative estimate. Using an even lower strength reduction factor in higher modes ($R = 3$) for A10-4 building was done for numerical exercise and the resulting story shear envelope is plotted in Figure 6.9.1(a) and (b). Clearly, the use of even lower strength reduction factor in higher modes resulted in computation of larger story shear along all floors of the building, but the shape of the story shear distribution begins to deviate from the mean NRHA envelopes largely. As a result, this method does not have the same story shear estimation conservatism along all floors, but tends to overestimate the story shear at the base and in the upper levels, while having disproportionally smaller overestimation margin around mid-height.

While different modified MRSA analyses may lead to better estimates of story shear forces, when adjusted properly, this may not be the most practical approach for design. Most commercial structural design software does not have a built-in option of modifying the modal response spectrum analysis to introduce the variable strength reduction factors. A design engineer wanting to implement any such modifications would face a time-consuming and cumbersome task involving manual post-processing. Thus, the principle of modifying the MRSA procedure is not pursued further in this study, and a simple solution to account for nonlinearity in the higher mode response contribution is sought next.

Higher mode response contribution affects mostly the base shear and the shears in the upper levels of the frame buildings, as was seen in Section 6.8.2, where the shape of the mean story shear envelopes from NRHA indicated increased deviations from the story shear envelopes computed with the MRSA (Figure 6.8.7) at the top and at the bottom of the buildings. Table 6.6 shows the base shear amplification factors Φ_v at each level of shaking for all of the archetype buildings studied in both Chapter 5 and Chapter 6. Factors Φ_v correspond to the ratio between the geometric mean of the peak base shears computed for FP and FN directions at a given hazard level, to the base shear $V_{b,u}$ from MRSA. The table also shows the ratio of the total base shear amplification Φ_v and the system overstrength amplification factor Ω. As can be seen, the additional amplification of base shear due to higher modes fluctuates between 1.09 and 1.19 at DE level, and 1.22 and 1.34 at the MCE level.

Table 6.6. Higher modes base shear amplification factor.

	A10-3	A10-4	A20-3	A20-4	A20-1	B20-1	B20-2	B20-3
Ω	2.82	2.67	2.43	2.74	2.15*	2.13*	2.29*	2.31*
$\Phi_{V,\ DE}$	3.27	3.17	2.88	2.98	2.43	2.41	2.59	2.63
$\Phi_{V,\ MCE}$	3.61	3.48	3.25	3.35	2.78	2.77	2.98	3.03
$\Phi_{V,\ DE}/\Omega$	1.16	1.19	1.18	1.09	1.13	1.13	1.13	1.14
$\Phi_{V,\ MCE}/\Omega$	1.28	1.30	1.34	1.22	1.31	1.30	1.30	1.31

* These overstrength factors were modified from those in Equation 5.4 in Chapter 5 to exclude the contribution of interior columns (in Equation 5.4 labeled as κ). They were calculated using Equation 6.5.

As a basis value for story shear amplification to account for higher mode effects, base dynamic amplification factor A_D is introduced, that in conjunction with the Ω scales the MRSA-computed design base shear to base shear that would correspond to the mean envelope from the

NRHA for a given seismic hazard. This factor is recommended to be 1.2 for the DE level and 1.35 for the MCE level. It is, thus, expected, that a mean design base shear at a given shaking intensity equals to:

$$V_{u,b} = \mathrm{A}_D \Omega V_{MRSA,b} \qquad 6.9$$

As the trends observed in Figure 6.8.7 indicate, the amplification of story shears becomes much larger than what would be accounted for with the uniform amplification factor $\mathrm{A_D}$. Thus, a higher mode amplification shape factor Ψ_v is introduced, which would lead to the following expression for a story shear at a level *i*:

$$V_{u,i} = \mathrm{A}_D \Psi_V \Omega V_{MRSA,i} \qquad 6.10$$

Figure 6.9.2 plots the ratio of the mean story shear to the mean base shear from the NRHA, as a function of the story height, for the four archetype buildings introduced in this chapter, at both DE and MCE shaking levels. The figure suggests that a simplified, piecewise linear variation of Ψ_v with the height of the building follows the trends observed in the NRHA reasonably well. Thus, the shape factor is taken as unity in the bottom half of the building, implying that story shear higher mode amplification for the stories located between ground and 0.5*H* is equal to the base shear higher mode amplification, $\mathrm{A_D}$. For the stories between 0.5*H*-1.0*H*, the higher modes amplification factor is assumed to linearly increase with height until it reaches the maximum value at the top $\Psi_\mathrm{v,N}$. For the buildings and the ground motions studied, this maximum value is taken as 1.4 for the DE level, and 1.6 for MCE level.

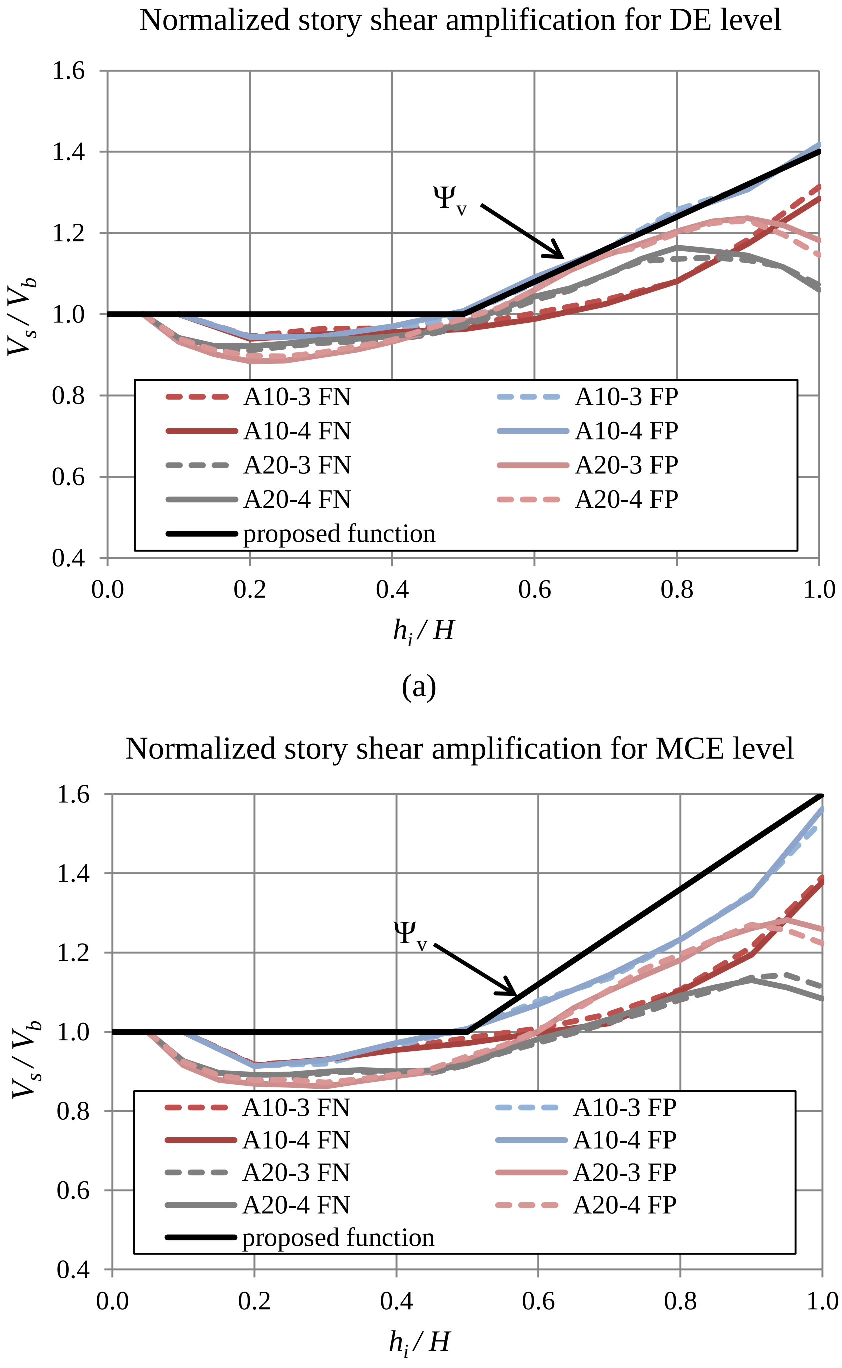

(a)

(b)

Figure 6.9.2. Higher mode amplification factor shape function for (a) DE and (b) MCE levels.

6.9.3 PERCENTILE MODIFICATION FACTOR: χ

The statistical dispersion of shear forces computed is accounted for with a percentile modification factor χ, which is introduced in order to increase the conservatism in estimating the design story shear against larger percentile of the ground motions at a given seismic hazard level. The percentile modification (adjustment) factor χ is related to the mean design value μ (in this case the story shear) and the corresponding coefficient of variation c_v as follows:

$$\chi^{(m)} = \mu(1 + m \cdot c_v) \qquad 6.11$$

The term (*m*), appearing both in the superscript on the left hand side and as a multiplication coefficient on the right hand side expression of Equation 6.11, signifies the number of standard deviations considered above the mean design value. For example, $\chi^{(1)}$ represents the percentile modification factor used when one standard deviation above mean is set as the upper limit on the design quantity, corresponding to the 84th percentile.

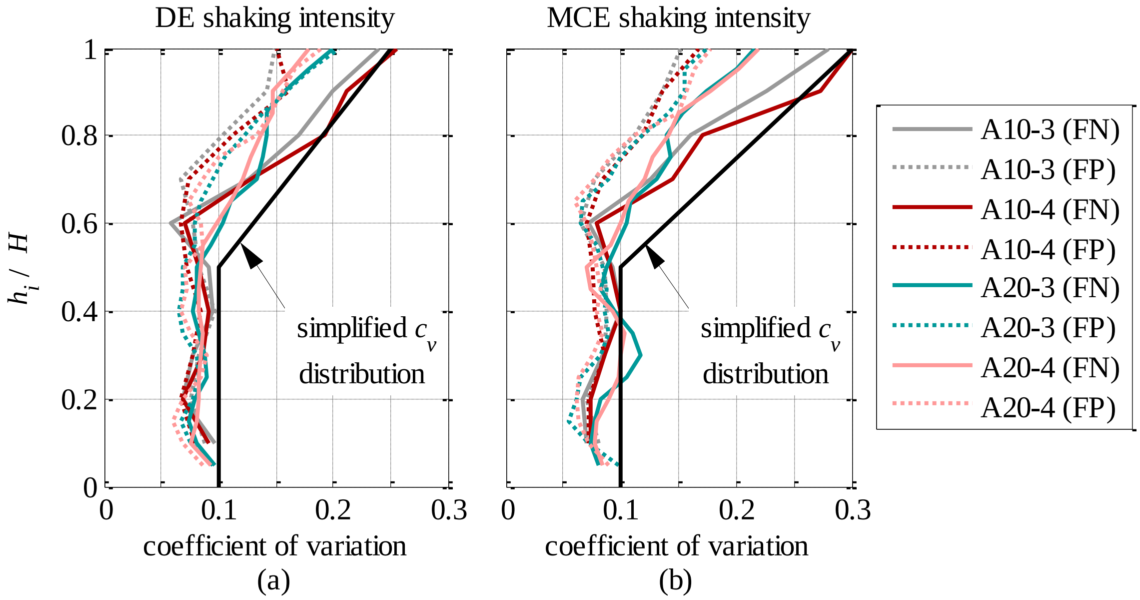

(a)

(b)

Figure 6.9.3. Simplified coefficient of variation distribution for design shear amplification at (a) DE and (b) MCE shaking intensities.

As was seen in Figure 6.8.17 and Figure 6.8.18, the coefficient of variation c_v in story shear is almost uniform in the lower 0.6*H* of the building height for all archetype buildings, tending to a peak value of $c_v = 0.10$. The c_v increases in an almost linear fashion to a maximum at the very top level, which varies between 0.20-0.30, dependent on the building and orientation of GM component with respect to fault. For simplicity, it is proposed to use $c_v = 0.10$ in the bottom 0.5*H* of the buildings, and linearly interpolate between $c_v = 0.10$ and $c_{v,max}$ for the stories between 0.5*H*-1.0*H*, as illustrated in Figure 6.9.3. The selected value of $c_{v,max}$ is 0.25 at the DE level and 0.30 at the MCE level of shaking, which envelopes the actual coefficients of variation computed in the NRHA reasonably well.

Adopting a piecewise linear function to represent the variation in the c_v along the height of the building, the percentile modification factor also follows a piecewise linear function, as shown in Figure 6.9.4. The plots in this figure represent the $\chi^{(1)}$, $\chi^{(2)}$, and $\chi^{(3)}$, for the DE and MCE levels of shaking, and show the values of those percentile modification factors for a given building as a function of the story height. The shears at the bottom half of the stories need to be amplified with the constant factor χ_B, while the shears in the upper half of the stories are amplified by different factors, depending of the height of the story with respect to the base level. Maximum value of percentile modification factor is at the roof and is denoted as χ_N.

Because shear yielding in columns is undesirable, it is recommended that the design shear envelopes represent at least 90% confidence interval, or mean + 1.29 standard deviations based on the results from the NRHA. For this study, two standard deviations (98th percentile) are used; however, the design shears can be adjusted at the discretion of a design engineer.

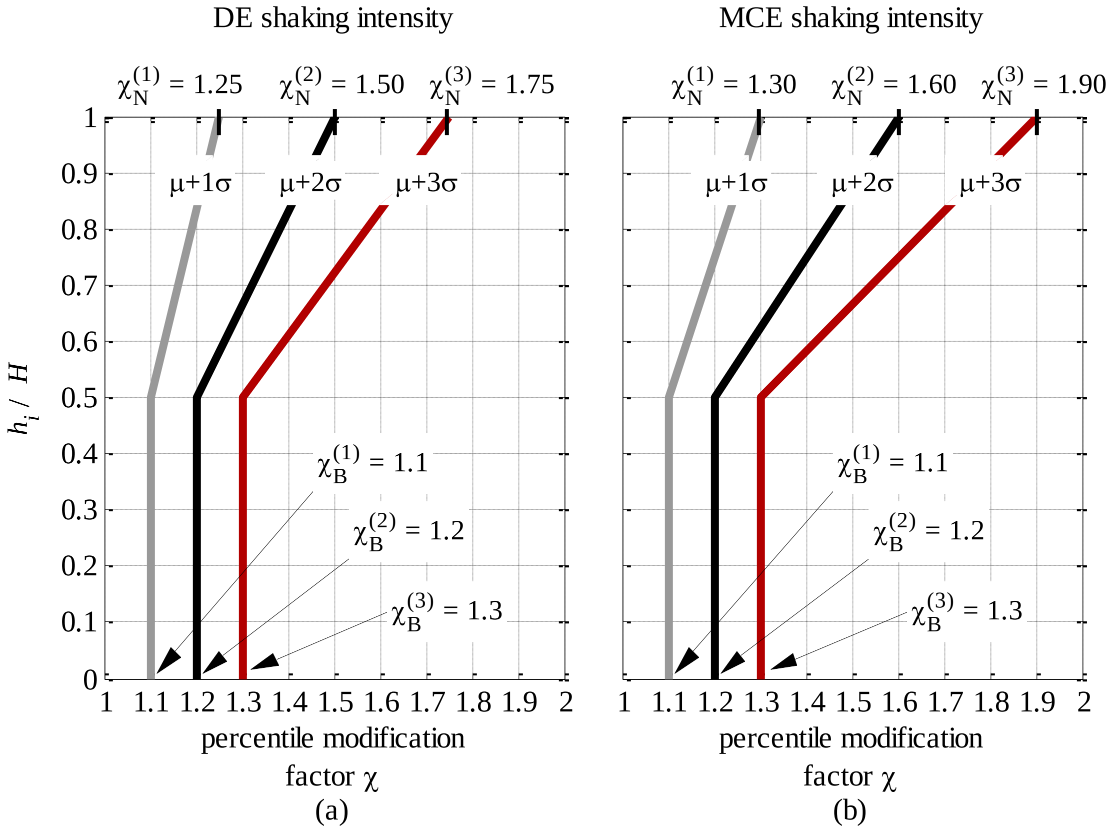

(a) (b)

Figure 6.9.4. Percentile modification factor for (a) DE and (b) MCE hazard levels.

6.9.4 TOTAL STORY SHEAR AMPLIFICATION FACTOR: ω_V

For the ease of implementation, all of the shear amplification factors introduced in Sections 6.9.1-6.9.3 are combined into a single story shear amplification factor, denoted here as ω_v. That is, at any given story level, the total story shear amplification factor ω_v is a product of: system overstrength factor, Ω, dynamic amplification due to higher modes, $A_D\Psi_v$, and percentile adjustment factor, χ. Written in form of an equation:

$$\omega_v = \omega_{v,B}\ , \quad \text{for } h_i/H < 0.5$$
$$\omega_v = \omega_{v,B} + (\omega_{v,N} - \omega_{v,B})(2h_i/H - 1), \quad \text{for } h_i/H \geq 0.5 \qquad 6.\,12$$

The terms in Equation 6.12 are:

$$\omega_{v,B} = \Omega\, A_D\, \Psi_{vB}\, \chi_B = \Omega\, A_D\, \chi_B$$
$$\omega_{v,N} = \Omega\, A_D \Psi_{v,N}\, \chi_N \qquad 6.\,13$$

This concept of using ω_v is illustrated in Figure 6.9.5. Applying the design system shear amplification factor to system shear at DE level for the A20-4 building and 84th percentile is illustrated in Figure 6.9.6. The design story shear envelopes for the four archetype buildings with 98th percentile at DE level of shaking are shown in Figure 6.9.7.

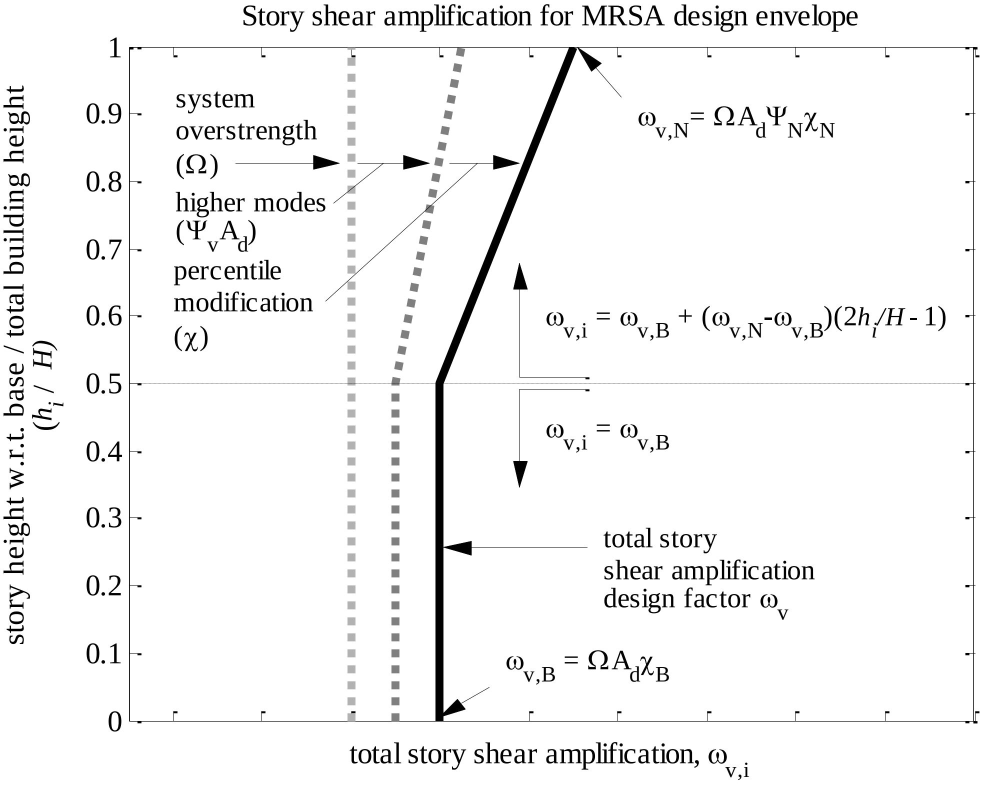

Figure 6.9.5. Proposed story shear amplification factors.

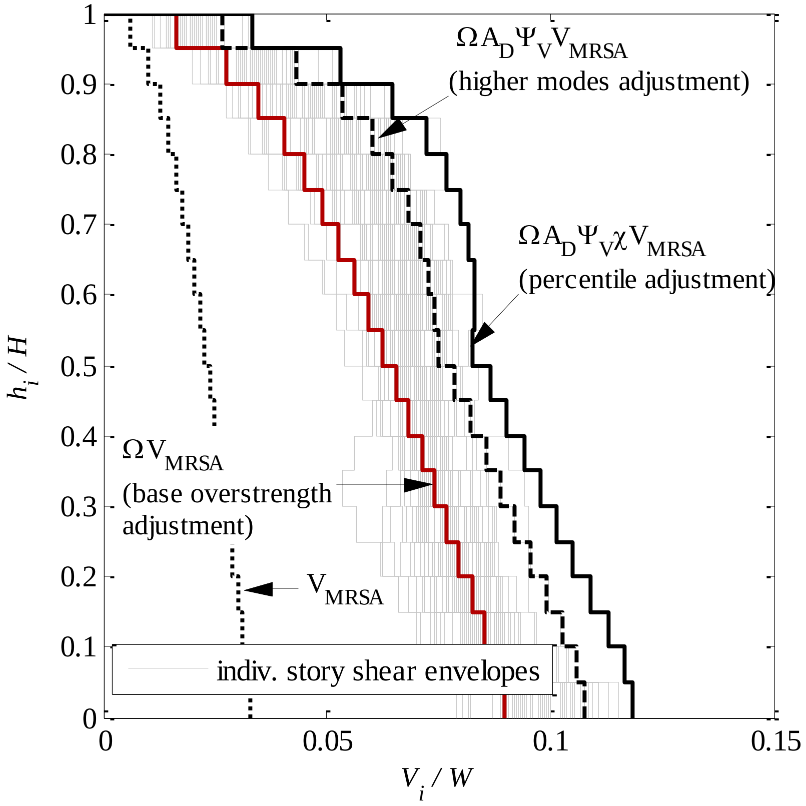

Figure 6.9.6. Shear amplification illustrated on A20-4 building at DE hazard level and 84th percentile ($\mu + 1\sigma$). The plot includes both FN and FP peak shear envelopes, plotted in light grey.

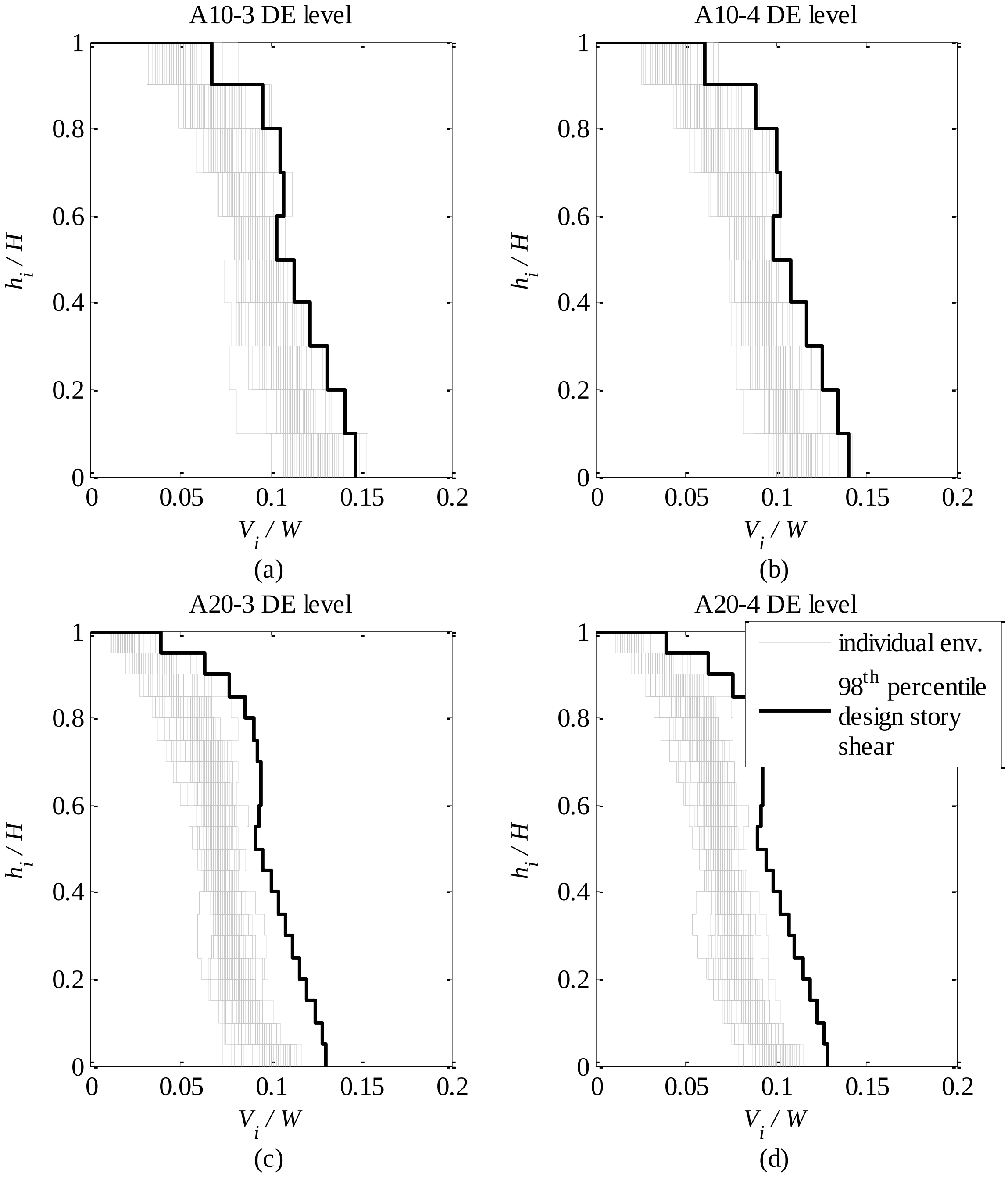

Figure 6.9.7. Design story shear envelopes for 98th percentile and DE level of shaking.

6.10 ESTIMATING ULTIMATE COLUMN SHEAR (V_u)

In previous section, a simplified method was developed for estimating a design story shear by using the code-prescribed MRSA procedure as a basis and multiplying it with the proposed amplification factors. The ultimate goal is to estimate the individual column design shear envelope.

In Chapter 5 it was noted that mean column shears are not necessarily in proportion with those obtained from MRSA. The MRSA analysis is essentially an elastic analysis with results dependent on the user-specified cracked section properties, among other factors. Because it is based on elastic elements with decoupled flexural and axial section behavior, the MRSA does not account for the effects of axial load-moment interaction in concrete columns. Column stiffness increases with the increased axial load. With increased stiffness, the shear forces developed in the exterior columns will be larger in proportion to the interior columns, than what they are comparatively if constant flexural stiffness is assumed at all times (such is the case in the elastic modeling, or lumped plasticity modeling without explicit representation of steel and concrete fibers in cross section). Thus, applying the same amplification factors used for system shear envelope to column shears, would lead to underestimation of exterior column shears (refer to Figure 5.6.8 in Chapter 5).

Let us examine the ratio of mean exterior column shear to mean interior column shear envelopes computed from NRHA analysis and compare them to the ratio of the exterior to interior column shear from simple MRSA analysis. These ratios are plotted in Figure 6.10.1 and Figure 6.10.2 for the four archetype buildings at DE and MCE hazard levels, respectively. For reference, all plots show a vertical line representing 1:2 exterior column shear to interior column shear ratio (or simply, a ratio of 0.5), assumed in a familiar approximate portal frame analysis. As we can see in all plots, the ratio of exterior to interior column shear exceeds that computed in the MRSA. Increased level of shaking (MCE level) increases this difference (Figure 6.10.2).

The ratio between the exterior and interior column shears will depend on relative stiffness of beams, columns and also joints, but an acceptable level of generalization can be made. Figure 6.10.3 plots the ratio of exterior shear magnification to interior shear magnification, labeled as κ_v and defined as $\kappa_v = \Phi_{v,ext}/\Phi_{v,int}$, where $\Phi_{v,ext}$ and $\Phi_{v,int}$ represent the ratio of the mean column shear computed in the NRHA to a column shear from MRSA procedure in exterior and interior columns, respectively. As can be seen in the two plots, the values of κ_v exceed unity along most of the height in all four buildings and for both levels of seismic hazard. At DE shaking level, the nonlinear shear magnification κ_v tends to an average value of 1.1, while at MCE level, κ_v increases to about 1.2. For all practical purposes, an exterior shear magnification factor $\kappa_v = 1.2$ is recommended in design.

Note that in the base floor, κ_v reaches amplitudes 30 to 60% higher than the value in the second floor columns, indicating the impact of the elongating 1st story SMRF beam on the exterior column shear. The trends indicate this impact to worsen with more intense shaking, directly owing to the larger amount of beam rotation and hence elongation and larger spectral displacement demands. Because the increase in column shear is a kinematic effect, it should be treated separately in design. The New Zealand code, NZS3101 (SNZ, 2006) considers the effect of beam growth on exterior columns by requiring that columns in regions affected by beam growth be designed for the shear demand occurring when the plastic hinges form at both ends of the column, which is analogous to Method A of ACI 318 (see Section 6.1.1).

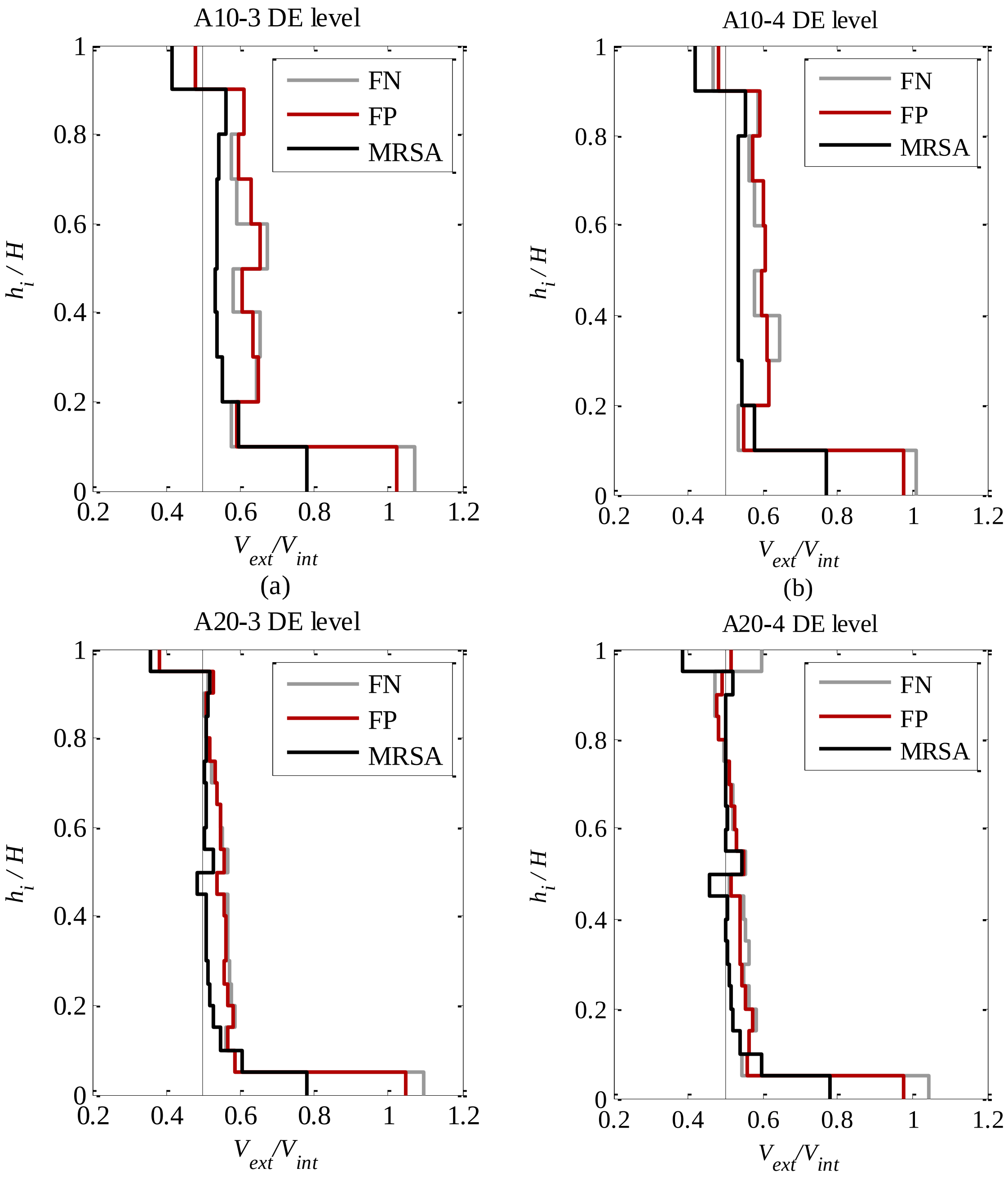

(a)

(b)

(c)

(d)

Figure 6.10.1. Ratio of mean exterior column shears to mean interior column shears at DE level of shaking.

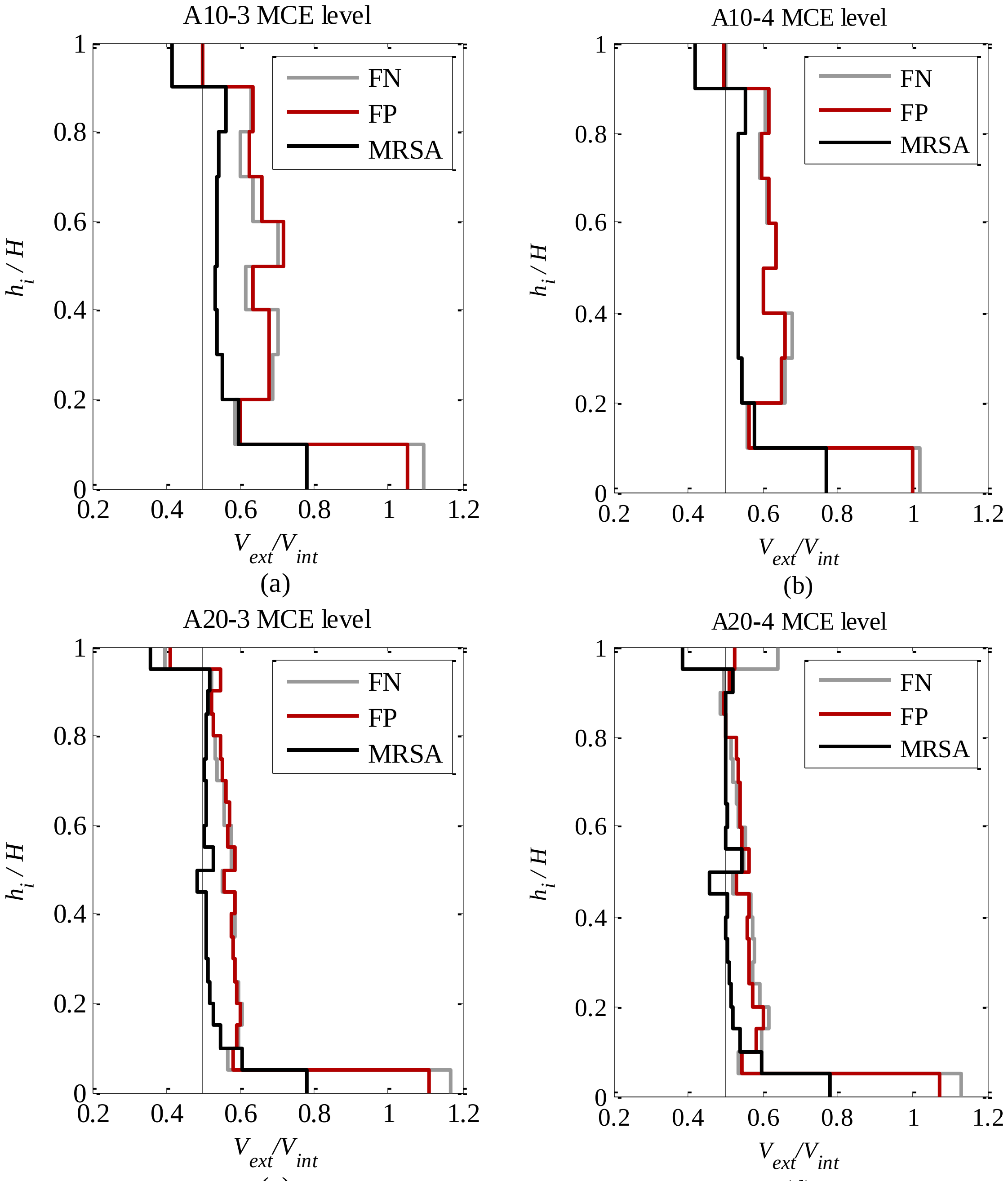

(a) (b) (c) (d)

Figure 6.10.2. Ratio of mean exterior column shears to mean interior column shears at MCE level of shaking.

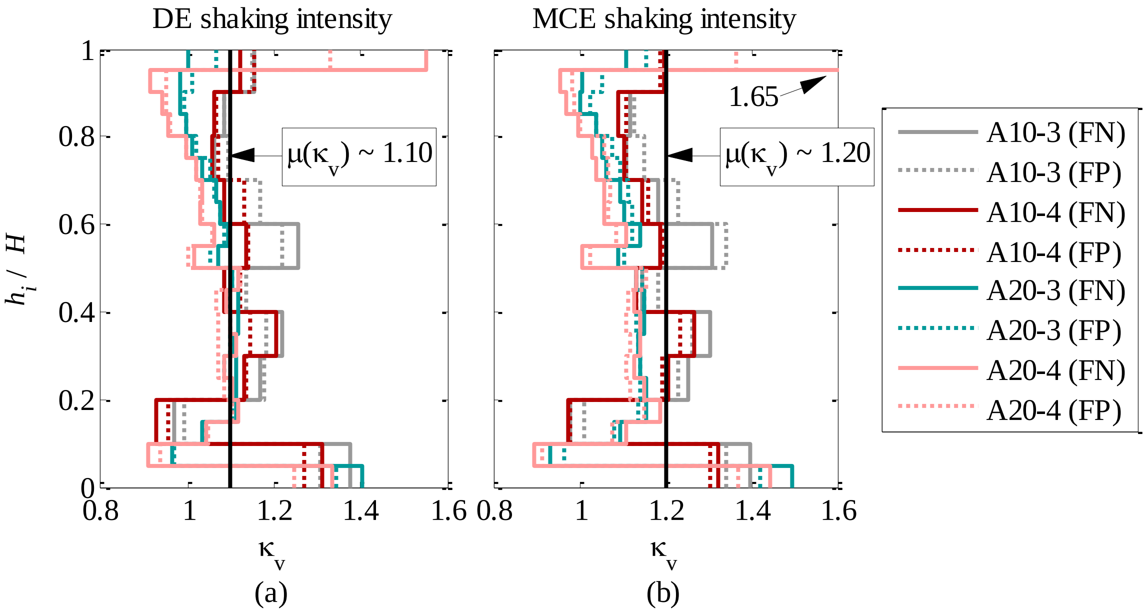

Figure 6.10.3. Exterior column nonlinear response shear magnification at: (a) DE and (b) MCE hazard level.

6.10.1 SUMMARY OF PROPOSED COLUMN SHEAR DESIGN PROCEDURE

This section provides a summary of a procedure for implementing the proposed method of estimating design column shear in reinforced concrete special moment frames. Estimating design column shear follows the following steps:

1. Building geometry and loads have been determined and MRSA has been conducted. Beams have been completely detailed for flexure and shear (i.e. the final amount and arrangement of longitudinal and transverse reinforcement has been selected). All columns have been proportioned and detailed for axial force and moment (i.e., the amount and arrangement of longitudinal column reinforcement has been selected and finalized). The MRSA-based column shears $V_{uMRSA.i}$ have been computed.

2. Calculate probable moment strength of each SMRF column at the base, assuming the axial load acting on a column cross section corresponds to gravity load expected to be present in the frame during a seismic event, that is, 1.0D + 0.25L.

3. Determine P_T and P_C on exterior columns, assuming all beams framing into a given column have developed plastic hinges at both ends. For simplicity, assume that gravity loads on beams do not contribute to the beam shear at the end. In short, at a given story i, each beam applies a vertical force $V_{pr,i} = \Sigma M_{pr,b,i}/l_{b,i}$ onto a column ($l_{b,i}$ = clear span of the beam). Here $\Sigma M_{pr,b,i}$ signifies the sum of the probable moment strengths acting at each end of a beam at story i.

4. Find Ω using the Equation 6.5.

5. Select amplification factor $A_D = 1.25$, and select $\Psi_{v,N} = 1.4$ or 1.6 based on DE or MCE level shaking intensity, respectively.

6. Select the percentile bracket and find corresponding percentile modification factor at the base (χ_B) and at the top floor (χ_N) using Equation 6.10 and assuming constant $c_v = 0.10$ in the lower half of the building, and $c_v = 0.25$ and 0.30 at DE and MCE hazard level, respectively.

7. Determine $\omega_{v,b}$ and $\omega_{v,N}$ values and use the equation in Figure 6.9.5 to find the *story shear* amplification factor at each story.

8. *Interior columns*: Multiply the individual column shears, $V_{uMRSA.i}$, computed with the code-based MRSA procedure with the corresponding shear amplification factor $\omega_{v,i}$ found in previous step. This is the column design shear, $V_{u,i} = (\omega_{v,i})V_{uMRSA.i}$.

Exterior columns: Multiply the individual column shears, $V_{uMRSA.i}$, computed with the code-based MRSA procedure with both: (a) the corresponding shear amplification factor $\omega_{v,i}$ and (b) exterior column magnification factor $\kappa_v = 1.2$. That is, the column design shear is $V_{u,i} = (\kappa_v)(\omega_{v,i})V_{uMRSA.i}$.

Note that in lieu of steps 2 through 4, a designer may follow the recommendations of NIST GCR 8-917-1 and proceed with steps 5 through 8, as specified. The methods give comparable results, as will be demonstrated in the following section. However, it is recommended that Φ computed as specified in NIST GCR 8-917-1 be replaced with the adjusted Φ_m* factor, as defined in Equation 6.8. The Φ_m* factor in Equation 6.8, is based on a system overstrength and does not consider the contribution of gravity moments in the overstrength calculation, contrary to what is implied in the NIST GCR 8-917-1 guidelines.

6.10.2 COMPARISON OF DESIGN SHEAR ENVELOPES DEVELOPED USING PROPOSED METHODS

Using the design procedure proposed, the design column shear envelops were computed for the four archetype buildings at design level earthquake shaking intensity and 98th percentile. These have been plotted in Figure 6.10.4 and Figure 6.10.5 along with individual peak column shear envelopes for all analysis runs, and corresponding mean shears calculated from NRHA for both FN and FP ground motion component orientations. For reference, design shear envelopes developed with methods ACI 318 B1 and B2 and NIST GCR 8-917-1 are also plotted. In addition, the figure shows the design shear envelope calculated with NIST GCR 8-917-1, which has been adjusted with higher mode amplification factor and percentile modification factor as recommended in the previous section.

As can be seen in all plots, the proposed method provides conservative estimate of ultimate column shear in most cases. Modified NIST GCR 8-917-1 procedure shows comparable level of conservatism. At the base of exterior columns, both of these methods lead to unconservative estimate of the shear because they do not account for the impact of beam elongation at the base. Thus, it is recommended to design base story columns assuming column hinging at both ends, that is, ACI 318 Method A is recommended.

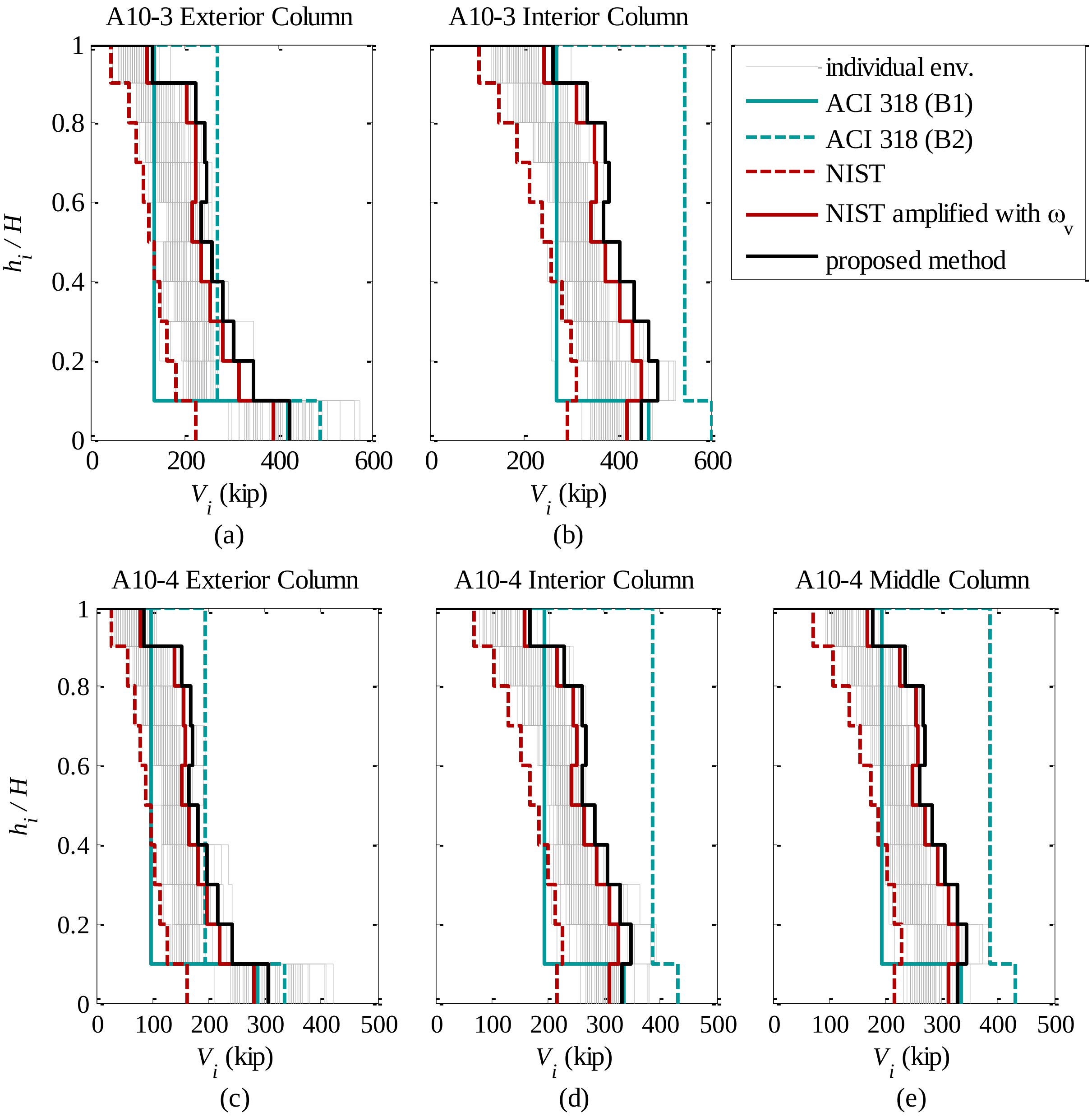

Figure 6.10.4. Comparison of column design shear envelopes for 10-story buildings.

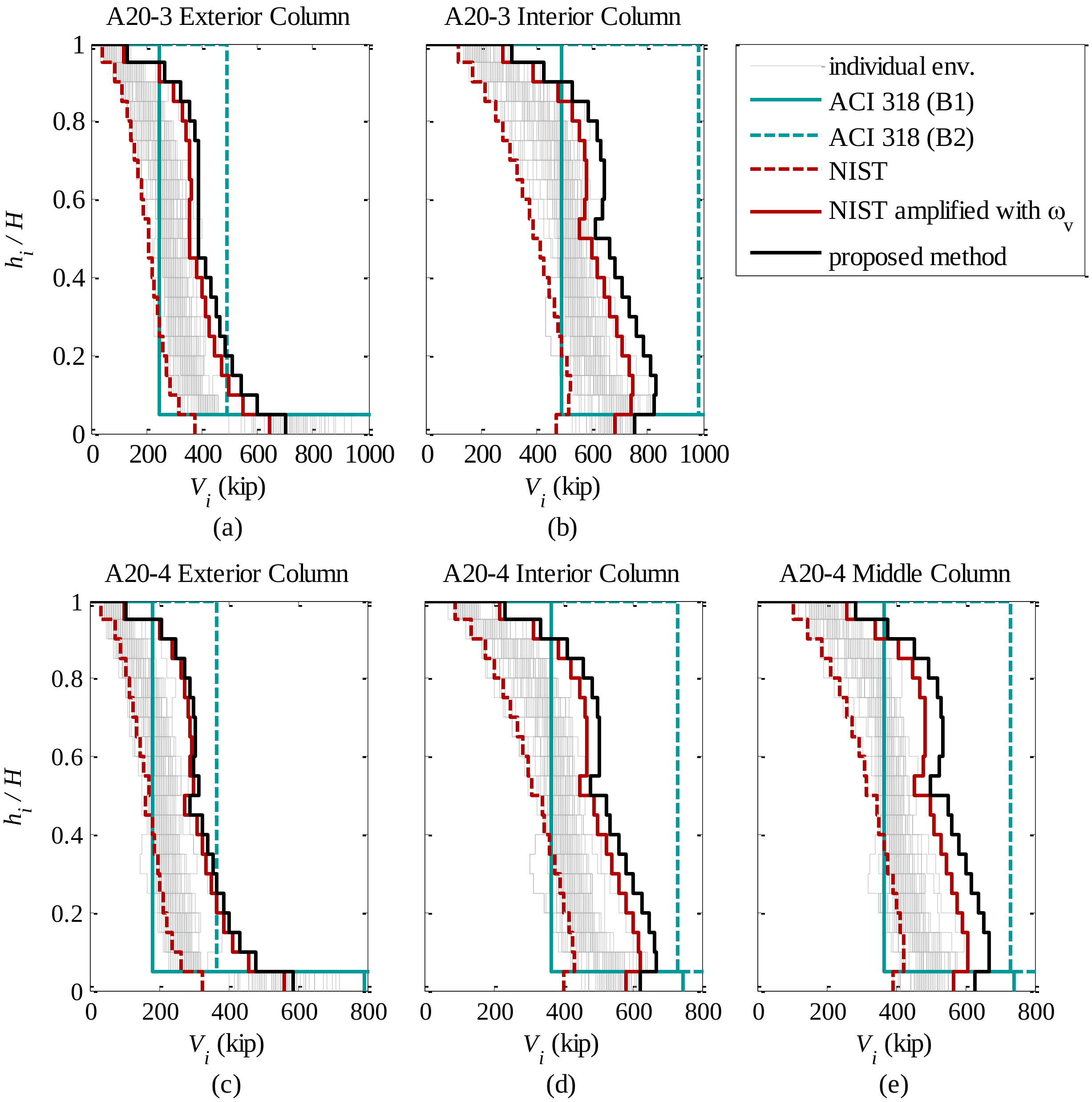

Figure 6.10.5. Comparison of column design shear envelopes for 20-story buildings.

6.11 CONSIDERATIONS FOR FURTHER INVESTIGATION

Once the ultimate column shear V_u has been estimated, the design engineer needs to determine which amount of the shear to design the transverse reinforcement for (V_s), as explained in Section 6.1.1. The highest level of shear in a column determined from the code-based procedure most likely occurs in conjunction with the highest column axial load. The amount of axial load assumed to act simultaneously with V_u impacts the amount of shear capacity ascribed to concrete alone V_c, as indicated in Section 6.1.1.

Figure 6.11.1 and Figure 6.11.2 show the time variation of axial force versus shear in an exterior column during a single response history analysis to FN components of ground motion records NGA_879LANDERS.LCN and NGA_1116KOBE.SHI. In all plots, the y-axis represents the axial force as a function of time, normalized by $A_g f'_c/20$, which is the minimum amount of compression required to be able to account for concrete shear capacity V_c in computing the total shear capacity of a column, V_n. Consistent with the ACI 318 sign convention, positive N(t) corresponds to compression, while negative corresponds to tension. Thus, for design purposes, at any instant that N(t) < 1, V_c should be taken as zero and therefore the entire shear demand needs to be accommodated by the transverse reinforcement. As can be seen in Figure 6.11.1 and Figure 6.11.2, the largest shear demand V_u does not necessarily coincide with the N(t) > $A_g f'_c/20$. Further investigation is necessary in this area.

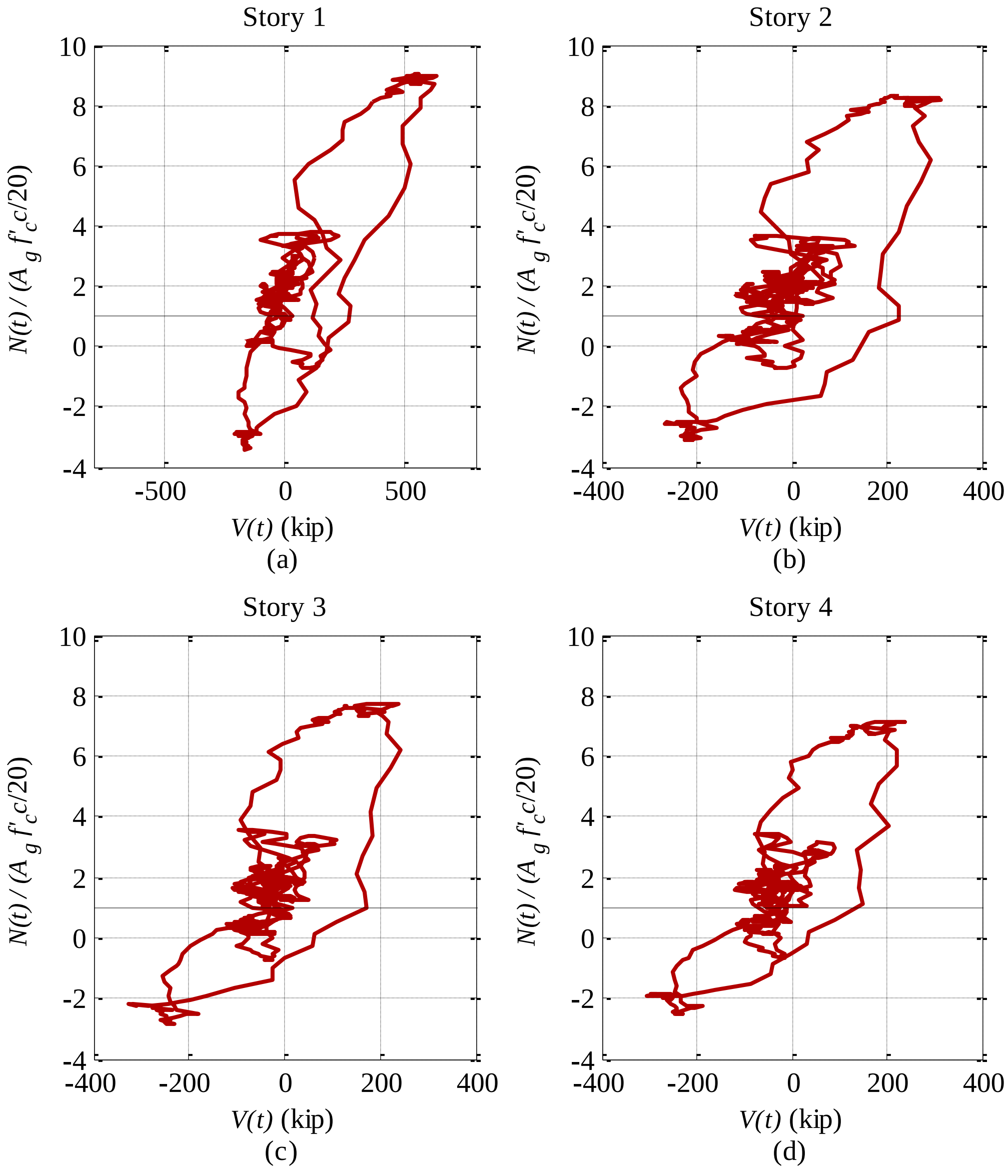

Figure 6.11.1. History of exterior column shear versus axial load during response to FN component of ground motion NGA_879LANDERS.LCN.

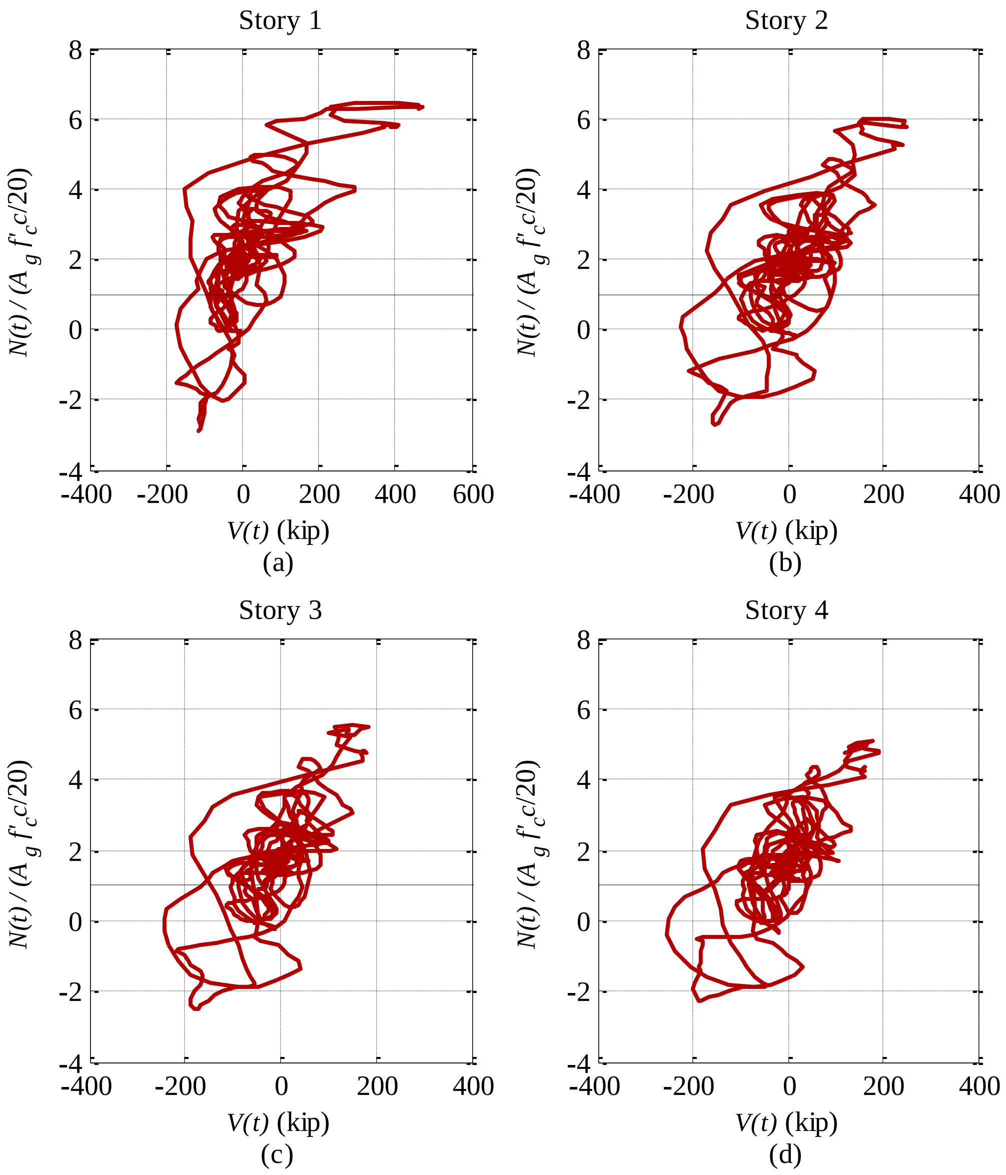

Figure 6.11.2. History of exterior column shear versus axial load during response to FN component of ground motion NGA_1116KOBE.SHI.

6.12 CONCLUSIONS

Four archetype buildings have been designed and analyzed under 30 different ground motions, with each motion represented by acceleration record corresponding to both fault-normal and fault-parallel directions, to determine the seismic demand on SMRFs in terms of both system shear and individual column shears. Based on the results presented in this chapter, the following is concluded:

1. Significant difference in story displacements and drifts is present between the fault-normal and fault-parallel directions of ground motions. While the spectral ordinates of FN- ground motion mean spectra are generally 20% higher than those of FP- components for the period range of interest, the mean story displacements and drifts are generally 50% higher in the FN- direction.
2. FP- ground motion components generally produced higher story and column shears in the upper half of the building height for 20-story archetype buildings compared to the FN- ground motion components.
3. For the ground motions selected, story displacements and drifts exhibited large scatter, while the story and column shears had less scatter and followed a normal distribution.
4. Mean story shears followed similar distribution as the shears computed with the code-based linear elastic MRSA analysis for all four buildings. While the story shears in the bottom half of all buildings were roughly 3 times larger than the corresponding MRSA-based story shears, those in the upper half of the buildings had larger amplification which increased with the building height.
5. Individual column shears exhibited similar level of amplification of MRSA-based values as the story shears. The amplification factors, however, were slightly higher (10-20%) in the exterior columns, likely owing to the increased flexural column stiffness under axial force-moment interaction during the dynamic response.
6. Current verbiage in ACI 318 code as it pertains to estimation of seismic shear on SMRF columns leaves much space for individual interpretation with varying levels of (un)conservatism, depending on the choices made by a design engineer.
7. Method of calculating design column shear presented in NIST GCR 8-917-1 document based on amplification of MRSA-based column shears with an average beam plastic hinge flexural overstrength factor resulted in unconservative estimate of mean column shears for all four buildings. The shear estimate is largely improved if the overstrength factor accounts for column plastic hinge flexural capacity and only considers the momet demands from seismic loads.
8. Amplifying the MRSA- story shears with the proposed system base overstrength factor Ω and a dynamic amplification factor $A_D\Psi_v$ represented by a piecewise-linear function of story height w.r.t. ground, provided good estimate of the mean *story shears* computed with the nonlinear response history analysis in all four buildings. Further amplification of the story shears by a percentile modification factor $\chi^{(m)}$ (which varies between 1.1-1.9 depending on the hazard level) could result in the story shear estimate conservatism against a larger number of ground motion responses.
9. Amplifying the MRSA- based individual column shears with Ω, $A_D\Psi_v$, $\chi^{(m)}$, and an exterior column shear amplification factor $\kappa_v = 1.1\text{-}1.2$ where applicable, resulted in the conservative estimate of individual seismic column shears in all cases.

CHAPTER 7

SUMMARY, CONCLUSIONS, AND RECOMMENDATIONS FOR FUTURE INVESTIGATION

The work presented in this dissertation identified two areas of the ACI 318 Code provisions that could lead to a design of reinforced concrete special moment resisting frames (SMRFs) with performance lower than expected. Namely, the areas of code in need of improvement are the transverse reinforcement maximum spacing limit as applied to the plastic hinge regions of SMRF beams and the existing methods of calculating the seismic shear demand on columns of special moment resisting frames. Supported by the numerical and experimental investigations of the behavior of modern reinforced concrete special moment resisting frames and their components, this dissertation presents recommendation for enhancement of these two areas of ACI 318 provisions.

The problem of maximum hoop spacing limit was examined via testing of two full-scale SMRF beam specimens in the laboratory. The specimen design, test setup, results, and relevant discussion can be found in Chapter 2. Two beams, nominally identical in size, material properties, and amount of longitudinal reinforcement, but differing only in the hoop spacing, were subjected to reverse cyclic loading to characterize the response and compare the performance. As described in Chapter 2, in addition to the differences in the global force-deformation relationship, notable differences in local response were observed, providing the insight into cyclic behavior of SMRF beams representative in size of those constructed in tall buildings. Based on the data obtained in the experimental study reported in Chapter 2, numerical model of large SMRF beams was established for use in all numerical simulations for the remainder of the dissertation. This model (based on distributed plasticity elements with fiber sections) adequately simulated the beam elongation effect, which together with its implications on column shear, are presented in Chapter 4.

The issue of estimating seismic shear demand on SMRF columns was introduced in Chapter 5 as a part of a broader topic focused on identifying the global (numerically computed) response characteristics of four 20-story archetype SMRF buildings and the response sensitivity to design alterations such as changing the exterior column size and column curtailment. The column seismic shear demand was investigated more systematically in Chapter 6 by means of numerical analysis of two 10-story and two 20-story archetype buildings designed for a different hypothetical site and thus different seismic hazard level than the buildings studied in Chapter 5. Two different suites of 30 ground motions characterized both by fault-normal and fault-parallel acceleration records were used in the analysis, with mean response spectra compatible with the code-based design spectra for the period range suited for the natural vibration properties of the buildings.

7.1 KEY FINDINGS

Concerning the issue of the hoop spacing code requirement in the plastic hinge regions of SMRF beams, the experimental study presented in Chapter 2 highlighted the following:

1. The hoop spacing requirements of the 2008 edition of ACI 318 Code investigated were found to lead to SMRF beam cyclic response inferior to the expected level of performance at the deformation levels consistent with the design seismic hazard (event with 10% probability of occurrence in 50 years).
2. Reducing the hoop spacing has led to an improved performance of the second SMRF beam tested, with the beam reaching the displacement ductility 1.9 times the displacement ductility exhibited by the beam specimen with the larger hoop spacing. Subsequently, a more stringent hoop spacing limit requirement was implemented in the 2011 ACI 318 Code.
3. Reduced spacing in the second beam, although resulting in more displacement capacity with sustained strength, did not prevent the occurrence of longitudinal bar buckling in the plastic hinge region, which was the controlling failure mode in both beam specimens. In general, buckling of the longitudinal reinforcement is considered a non-ductile failure mode and it is undesirable for the reinforced concrete members to exhibit bar buckling.
4. The damaged state of the beams observed upon buckling of the longitudinal bars pointed to the top crossties disengaging from the longitudinal bars and seismic hooks opening at the top of the beams.
5. The evidence of cracks forming on top of the longitudinal bars not directly supported by a vertical crosstie around the time that the instrumentation began registering local deformations associated with bar buckling may be a sign that the buckling initiated in these bars and not the adjacent bars that were directly braced by a vertical crosstie.

The studies of characteristics of reinforced concrete SMRFs nonlinear response both experimental (Chapter 2) and numerical nature (Chapters 3 through 5) resulted in the following findings:

1. Column size and reinforcement area curtailment along the height in multistory SMRF buildings lead to concentrations of inelastic deformations during seismic response in the floors where the curtailment is made. Keeping the columns uniform in size along the height of the building reduces the inelastic deformations above the base floor.
2. Increasing the size of exterior columns, while keeping the rest of the columns and beams unchanged, lead to smaller compressive strains in the column concrete core in 20-story tall buildings. Conversely, increasing the exterior column size also led to lower axial loads in columns, which can increase a safety margin against column failure in compression.
3. RC beams tend to elongate roughly in proportion with the level of lateral deformation (or chord rotation), consistent with the findings of previous research (e.g. Fenwick and Megget 1993, Kabeyasawa et al. 2000). The amount of axial elongation within the plastic

hinge is approximately equal to $\theta \cdot h/4$ to $\theta \cdot h/2$, where θ indicates chord rotation in radians and h is the beam section height.

4. The elongation of the beam was found to be adequately numerically simulated using distributed plasticity beam column element with a fiber section discretization which employs hysteretic material models.
5. Consistent with findings of others (e.g. Fenwick et al. 1996, Kim and MacRae 2004), this elongation was found to largely impact the deformation and force demands of columns in RC frames. In single story frames deforming in sidesway mode, the column lateral deformation demand was increased by up to 50% as a result of the kinematic interaction with the axially expanding beam. Among other factors, the level of beam elongation impact was found to be dependent on the number of bays in a frame, consistent with experimental findings of Kabeyasawa et al. 2000.
6. Lengthening of RC beams during inelastic deformation cycles is presently not considered in the design of SMRFs in the US practice, owing to a common conviction that the post-tensioned slabs, typically cast uniformly with the SMRF beams, act as a restraint against the beam growth. Short numerical exercises showed that the slab post-tensioning stresses only marginally reduce the axial beam deformations, and that the column shear is still increased notably as a consequence of beam growth. In a single-story four-bay frame, the beam elongation increased the exterior column shear by a factor of 1.5 when no PT slab was present, while the addition of the PT slab stressed to 400psi compression reduced this factor by less than 10%.

Lastly, the investigation of seismic shear demand of columns via series of nonlinear response history analyses of eight different archetype buildings designed for different levels of seismic hazard resulted in the following observations and findings:

1. ACI 318 recommendations for calculating seismic shear demand on SMRF columns reflect the uncertainty on how to calculate the seismic shear demand that would lead to acceptable design conservatism while ensuring feasibility of column construction. The current code verbiage sets loosely defined guidelines and leaves much room for free interpretation.
2. Depending on how the ACI 318 Code seismic column shear clause is construed, dispersed levels of conservatism in seismic shear estimate are observed, ranging from overly conservative to plain unsafe. In addition, different interpretations of the code lead to inconsistent conservatism in the seismic shear estimates along the building height for the eight archetype buildings studied in this dissertation.
3. The alternative method of estimating seismic shear in SMRF columns presented in NIST GCR 8-917-1 results in the most consistent estimate of column shears with those observed in the nonlinear response history analyses presented in Chapters 5 and 6. The method is based on amplifying column seismic shears obtained from the elastic code-based procedure by a flexural overstrength factor calculated considering the plastic hinge moment strength-to-demand ratio of the SMRF beams framing into a column considered. However, although the distributions of peak shears calculated with the NIST Design Guidelines follow more closely the NRHA envelopes compared to any of the ACI 318

methods, the NIST GCR 8-917-1 method as-is underestimated the DE hazard level column shear in the archetype buildings by at least 25%.

4. The results from NIST GCR 8-917-1 column shear estimation can be improved both of the following are implemented: i) a factor reflecting the system flexural overstrength is used in lieu of the factor calculated considering only the ratio of the beam plastic hinge moment capacity to moment demand, and ii) in calculating this system overstrength factor, the moment demand from linear analysis only considers the seismic demand and excludes the contribution from other loads (e.g. gravity). The second point was shown to impact the results greatly in SMRF buildings where the gravity moment demands on the beams comprise a significant portion of ultimate design moment calculated from the applicable load combinations. For the four archetype buildings, the impact was the largest in shorter buildings where gravity moments exceeded 1/10 of the seismic moment demand on the beams.
5. A proposed method of estimating design column shear that considers system flexural overstrength in combination with a dynamic amplification factor, defined with a piecewise linear function of the story height, was shown to provide the closest estimate of the seismic column shear of all methods considered in this dissertation. A simplification can be made by adopting a single value for dynamic shear amplification along the height of the building – however, this reduces the amount of conservatism in the upper stories of the SMRF buildings.
6. Adopting a separate shear amplification factor to account for uncertainty in the response can increase a safety margin against the shear yielding in SMRF columns. For the buildings and the ground motions considered, a factor as low as 1.1 can increase a safety margin against column shear yielding in the base stories by 34% at DE level of shaking.

7.2 IMPLICATIONS, LIMITATIONS, AND FUTURE RESEARCH

The following sections discuss the main implications of the findings presented in Chapters 2-6. Relevant figures to support the discourse are repeated in this section for convenience.

7.2.1 HOOP SPACING REQUIREMENTS FOR LARGE SMRF BEAMS

Based on the experimental findings on large SMRF beams presented in Chapter 2, recommendation was made to reduce the maximum hoop spacing limit set forth in 2008 ACI 318, which was adopted in 2011 ACI 318 edition. The relevant materials have been originally published in a PEER report (Panagiotou et al. 2013) which is freely accessible online.

While the reduced hoop spacing resulted in increased SMRF beam ductility, the condition of the hoops upon the completion of the laboratory tests raised concern that the present multi-piece configuration of the hoops (shown in Figure 7.2.1[c]) may not effectively brace the longitudinal bars against the outward buckling, as potentially suggested by the crack formation coinciding with the bars not directly supported by a vertical crosstie (shown in Figure 7.2.2) around the time the buckling initiated. Furthermore, the opening of the seismic hooks visible upon the completion of the tests (see Figure 7.2.3) may suggest that seismic hook longer than $6d_b$ (d_b = nominal diameter of a crosstie) may be needed to prevent the crosstie from disengaging upon the formation of plastic hinge region in a SMRF beam. Further experimental research is recommended in this area.

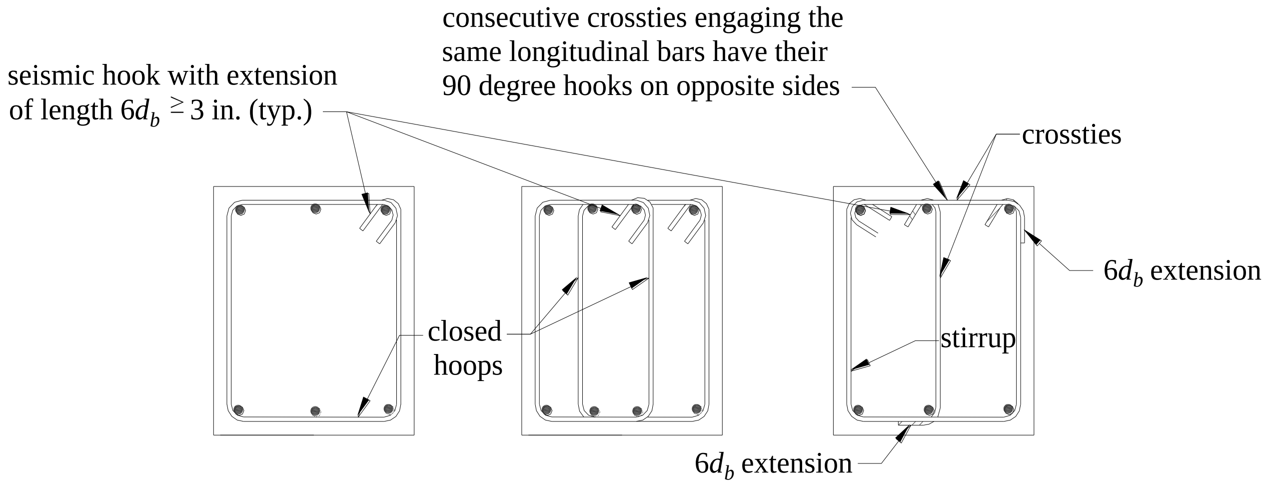

(a) (b) (c)

Figure 7.2.1. Typical hoop configurations: (a) single closed hoop; (b) overlapping hoops; and (c) stirrups with crossties.

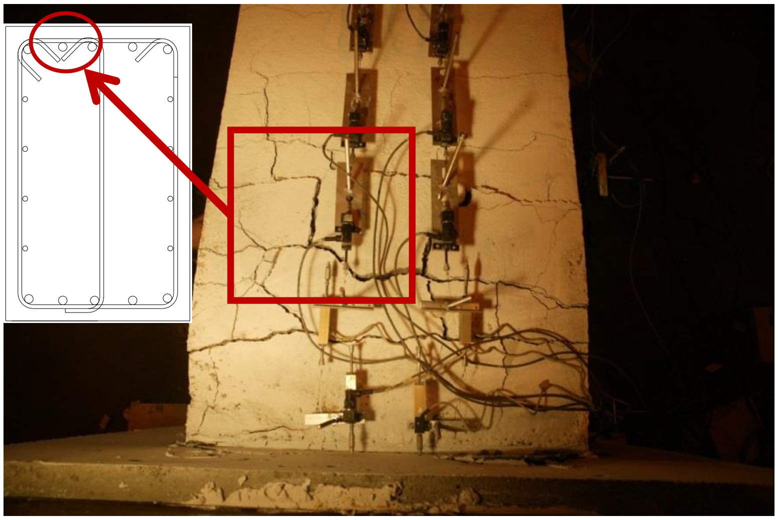

Figure 7.2.2. Possible buckling of bar with no direct lateral restraint by a vertical crosstie.

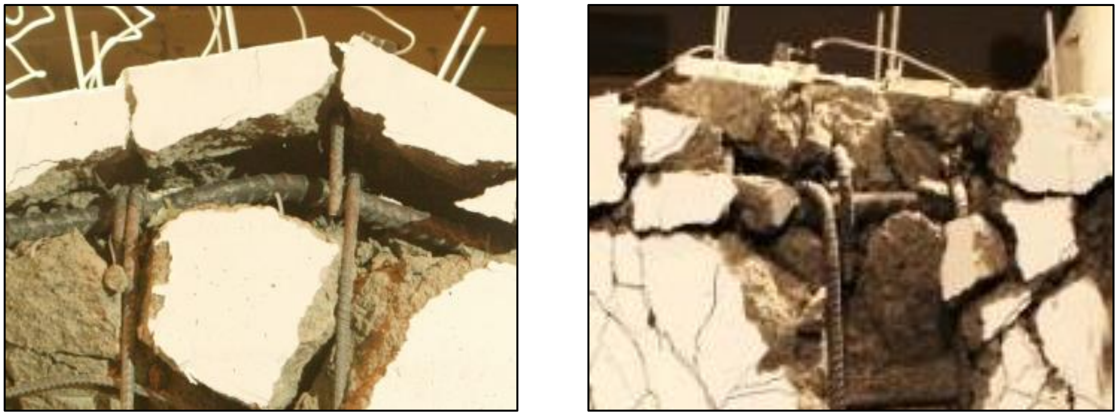

(a) (b)

Figure 7.2.3. Apparent opening of the cap ties observed on top face of the specimens upon completion of tests: (a) Beam 1 and (b) Beam 2.

7.2.2 SEISMIC SHEAR DEMAND ON COLUMNS OF SMRF BUILDINGS

The results of numerical studies of SMRF buildings presented in Chapters 4-6 lead to several important design implications. First, when conducting nonlinear response history analyses as a part of the design check to evaluate the seismic forces in SMRF buildings (i.e. when collapse is not the focus of investigation), a designing engineer is encouraged to use distributed plasticity elements with fiber section discretization for modeling the SMRF beams in order to obtain more realistic seismic demands on SMRF columns, and particularly the exterior columns resulting from beam elongation phenomenon. The engineer is referred to Chapter 3 for details on the modeling strategies in large beams.

Second, estimating seismic shear demands in columns of SMRF buildings using the ACI 318 procedure which involves the assumption of plastic hinging mechanism occurring in the beams, rather than the columns, does not represent either the spatial distribution or the level of the shear forces that the columns may be experiencing during the design earthquake event. As was shown in Chapters 5 and 6, peak column shear envelopes computed in nonlinear response history analyses are best estimated with the methods based on magnifying the shears from the elastic code-prescribed modal response spectrum analysis. Thus, if a design engineer chooses to follow the ACI 318 column design shear estimation methods, he/she is encouraged to, at the very least, check these design shear values against those calculated with the method proposed in Chapter 6 and summarized in Figure 7.2.4 for convenience. The base system overstrength factor Ω proposed in Chapter 6 can be replaced by the NIST GCR 8-917-1 modified overstrength factor Φ_m*, to include the column moment overstrength and exclude the contribution of the non-seismic loads to moment demands, as explained in detail in Section 6.9.1.

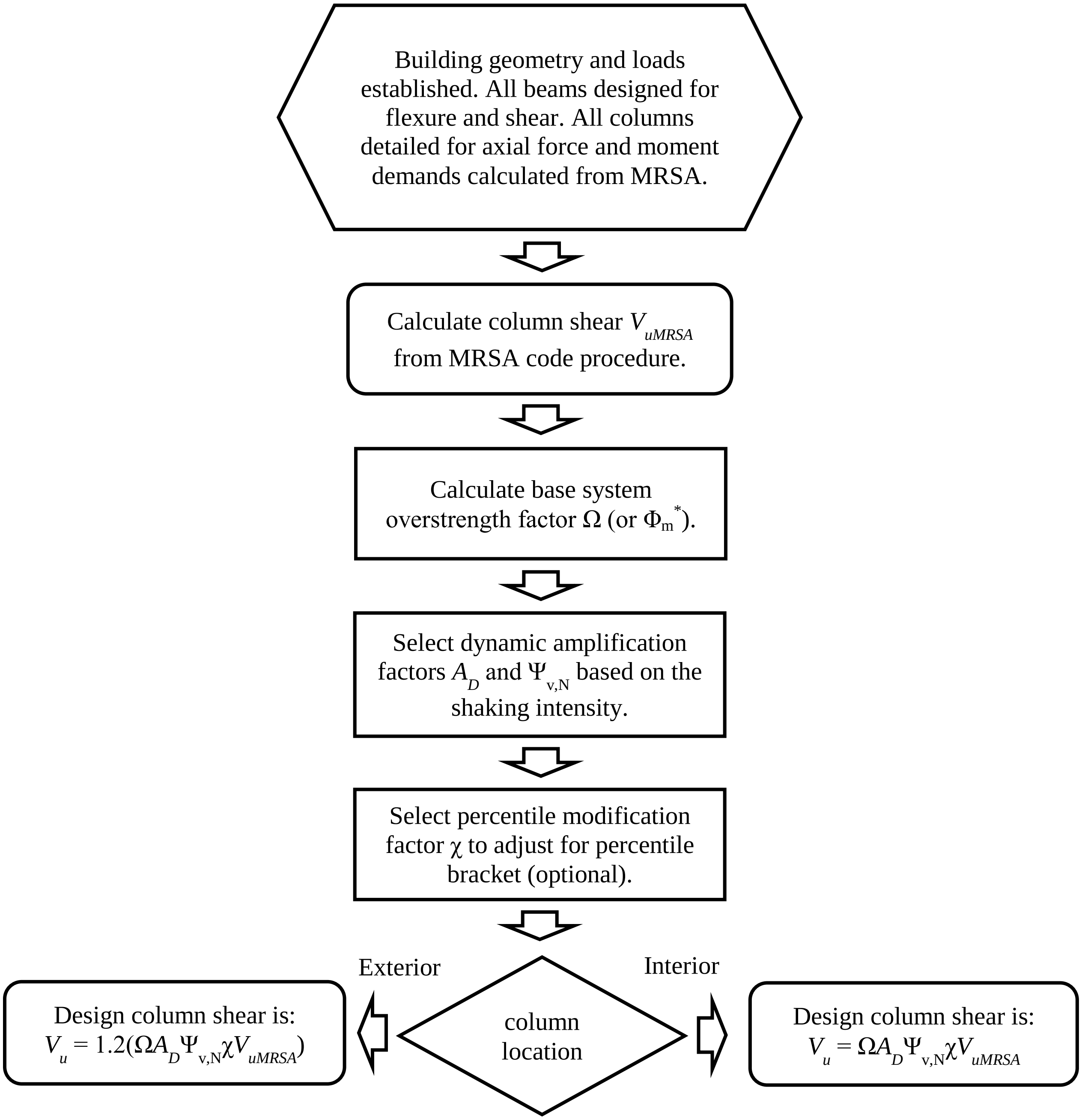

Figure 7.2.4. Flow chart outlining the proposed method for estimating design column shear.

It is important to keep in mind that the discussions and the design recommendations presented in this dissertation are based on results computed using two-dimensional models of regular SMRF buildings with reinforced concrete moment frames located around the perimeter and subjected to unidirectional ground motion components acting in the plane of the SMRFs being analyzed. Recent findings (Reyes and Kalkan 2012, Kalkan and Kwong 2014) indicated that the maximum response of multi-story buildings may occur at the building orientation other than the fault-normal and fault-parallel. The effects of multidirectional ground motion (including the vertical component) and orientation of the building with respect to fault were not considered in the present dissertation but comprise a topic that calls for further investigation.

In addition, the analysis of buildings with irregular elevation and floor plan is strongly recommended. This includes, but is not limited to, the buildings with setbacks, varied bay lengths within a single SMRF, and buildings with torsional eccentricities. A 3-dimensional analysis of SMRF buildings, especially having perimeter frames joined at the corner (i.e., having common corner columns acting as a part of SMRFs in each orthogonal direction) also warrants further examination.

REFERENCES

Alavi, B. and Krawinkler, H., 2004. Behavior of Moment-Resisting Frame Structures Subjected to Near-Fault Ground Motions, *Earthquake Engineering and Structural Dynamics,* 33(6): 687–706.

Akkar, S., U. Yazgan and P. Gülkan, 2005. Drift Estimates in Frame Buildings Subjected to Near-Fault Ground Motions. *ASCE Journal of Structural Engineering,* 131(7): 1014-1024.

American Concrete Institute (ACI), 2008. *BuildingCode Requirements for Structural Concrete, ACI 318*, Farmington Hills, MI.

American Concrete Institute (ACI), 2011. *BuildingCode Requirements for Structural Concrete, ACI 318*, Farmington Hills, MI.

American Concrete Institute (ACI), 2014. *BuildingCode Requirements for Structural Concrete, ACI 318*, Farmington Hills, MI.

ASCE 41, 2006, *Seismic Rehabilitation of Existing Buildings, ASCE/SEI Standard 41-06 including Supplement 1*, American Society of Civil Engineers, Reston, VA.

American Society of Civil Engineers (ASCE), 2010. *Minimum design loads for buildings and other structures, ASCE 7-10*, Reston, VA.

Applied Technology Council (ATC), 2005. *Improvement of nonlinear static seismic analysis procedures,* Rep. No. FEMA-440, Redwood City, CA.

Baker, J. W., 2011. Conditional Mean Spectrum: Tool for Ground-Motion Selection, *ASCE Journal of Structural Engineering*, 137(3), 322-331.

Barbosa, A.R. 2011. Simplified vector-valued probabilistic seismic hazard analysis and probabilistic seismic demand analysis: Application to the 13-story NEHRP reinforced concrete frame-wall building design example, Ph.D. Dissertation, Department of Structural Engineering, University of California, San Diego, CA.

Beckingsale, C. W., 1980. "Post-Elastic Behaviour of Reinforced Concrete Beam-Column Joints," *Report* No. 80-20, Department of Civil and Natural Resources Engineering, University of Canterbury, Christchurch, New Zealand.

Berry, M. P., 2006. "Performance Modeling Strategies for Modern Reinforced Concrete Bridge Columns." Ph.D. Dissertation, Department of Civil and Environmental Engineering, University of Washington, Seattle, WA.

Beyer, K. Dazio, A. and Priestley, N.M.J. 2011. Shear Deformations of Slender Reinforced Concrete Walls under Seismic Loading. ACI Structural Journal, 108(2): 167-177.

Birss, G. R., 1978. "The Elastic Behaviour of Earthquake Resistant Reinforced Concrete Interior Beam-Column Joints." *Report* No. 78-13, Department of Civil and Natural Resources Engineering, University of Canterbury, Christchurch, New Zealand.

Blakeley, R. W. G.; Megget, L. M.; and Priestley, M. J. N., 1975. Seismic Performance of Two Full Size Reinforced Concrete Beam-Column Joint Units. *Bulletin of the New Zealand National Society for Earthquake Engineering*, 8(1): 38-69.

Bournonville, M., Dahnke J., and Darwin, D, 2004. "Statistical Analysis of the Mechanical Properties and Weigth of Reinforcing Bars." SL Report 04-1, Structural Engineering and Materials Laboratory, The University of Kansas.

Calugaru, V. and Panagiotou, M. 2011. Response of Tall Cantilever Wall Buildings to Strong Pulse Type Seismic Excitation, *Earthquake Engineering and Structural Dynamics*, 41(9): 1301-1318.

Chang, G. and Mander, J. 1994. "Seismic Energy Based Fatigue Damage Analysis of Bridge Columns: Part I – Evaluation of Seismic Capacity." NCEER Technical Report 94-0006.

Chang, B. J.; Hutchinson, T. C.; and Englekirk, R. E., 2008. "Experimental Seismic Performance Evaluation of Innovative Beam-Column Subassemblies." *Report* No. SSRP-08/01, Department of Structural Engineering, University of California, San Diego, USA.

Chopra, A. and Goel, R.K.. 2002. A Modal Pushover Analysis Procedure for Estimating Seismic Demands for Buildings, *Earthquake Engineering and Structural* Dynamics, 31(3): 561-582.

Chopra, A., Goel, R.K., and Chintanapakdee, C., 2004. Evaluation of a Modified MPA Procedure Assuming Higher Modes as Elastic to Estimate Seismic Demands, *Earthquake Spectra*, 20(3): 757-778.

Cooper, M., Davidson, B.J., and Ingham J.M., 2005. The influence of axial compression on the elongation of plastic hinges in reinforced concrete beams, in *Proceedings, The New Zealand Concrete Industries Conference*, Auckland, New Zealand.

Corney, S.R., Henry, R.S., and Ingham, J.M. 2013. Performance of precast concrete floor systems during the 2010/2011 Canterbury earthquake series, *Magazine of Concrete Research*, *Paper No*. 1300106, ICE Publishing, London, UK.

Eibl, J. and Keintzel, F. 1988. Seismic Shear Forces in RC Cantilever Shear Walls, in *Proceedings, 9th World Conference on Earthquake Engineering,* Tokyo-Kyoto, Japan.

Eligehausen, R. Bertero, V.V. and Popov, E.P. 1983. "Local Bond Stress-Slip Relationships of Deformed Bars under Generalized Excitations." UCB/EERC Report No. 83/23, Earthquake Engineering Research Center, University of California, Berkeley, CA.

El-Sheikh, M., Sause, R., Pessiki, S., Lu, L.W., and Kurama, Y., 1997. "Seismic Analysis, Behavior, and Design of Unbonded Post-Tensioned Precast Concrete Frames." *Report No*. EQ-97-02, Department of Civil and Environmental Engineering, Lehigh University, Bethlehem, PA.

Elwood, K. J., Pampanin, S., and Kam, W.Y. 2012. NZ 22 February 2011 Christchurch Earthquake and Implications for the Design of Concrete Structures, in *Proceedings, International Symposium on Engineering Lessons Learned from the 2011 Great East Japan Earthquake*, Tokyo, Japan, pp.1157-1158.

Emporis, 2012. Building database. http://www.emporis.com/statistics/.

FEMA 356, 2000. *Prestandard and Commentary for the Seismic Rehabilitation of Buildings*. American Society of Civil Engineers, Reston, VA.

Fenwick, R. C. and Irvine, H. M. 1977. Reinforced Concrete Beam-Column Joints for Seismic Loading – Part II Experimental Results. *Bulletin of the New Zealand National Society for Earthquake Engineering*, 10: 174 -185.

Fenwick, R.C. and Fong A. 1979. "The Behaviour of Reinforced Concrete Beams under Cyclic Loading." University of Auckland Department of Civil Engineering Report No. 176, Auckland, New Zealand.

Fenwick, R.C. and Megget, L. M. 1993. Elongation and Load Deflection Characteristics of Reinforced Concrete Members Containing Plastic Hinges. *New Zealand National Society for Earthquake Engineering*, 26: 28-41.

Fenwick, R. C., Ingham, J. M**.**, and Wuu, P. J. Y. 1996. The Performance of Ductile R/C Frames under Seismic Loading, in *Proceedings*, *NZNSEE Technical Conference and AGM*, New Plymouth, New Zealand.

Filippou, F. C., Popov, E. P., Bertero, V. V. 1983. "Effects of Bond Deterioration on Hysteretic Behavior of Reinforced Concrete Joints." Report No. EERC 83-19, Earthquake Engineering Research Center, University of California, Berkeley, CA.

Ghannoum, W. 2007. "Experimental and Analytical Dynamic Collapse Study of a Reinforced Concrete Frame with Light Transverse Reinforcement." Ph. D. Dissertation, Department of Civil and Environmental Engineering, University of California, Berkeley, CA.

Hall J.F., Heaton, T.H., Halling, M.W., and Wald, D.J. 1995. Near-Source Ground Motion and its Effects on Flexible Buildings, *Earthquake Spectra*, 11(4): 569-605.

Hall, J.F., 1998. Seismic Response of Steel Frame Buildings to Near-Source Ground Motions, *Earthquake Engineering and Structural Dynamics*, 27(12): 1445-1464.

Haselton, C.B., Goulet, C.A., Mitrani-Reiser, J., Beck, J.L., Deierlein, G.G., Porter, K.A., Stewart, J.P., and Taciroglu, E. 2008. An Assessment to Benchmark the Seismic Performance of a Code-Conforming Reinforced Concrete Moment-Frame Building, Tech. Rep. PEER 2007/12 Pacific Earthquake Engineering Research Center, Berkeley, CA.

Haselton, C.B., Liel A.B., Deierlein, G.G., Dean, B.S., and Chou, J.H. 2011. Seismic Collapse Safety of Reinforced Concrete Buildings: I. Assessment of Ductile Moment Frames, *ASCE Journal of Structural Engineering*, 137(4): 481-491.

Hiraishi, H. 1984. Evaluation of Shear and Flexural Deformations of Flexural Type Shear Walls. *Bulletin of the New Zealand Society for Earthquake Engineering*, 17(2): 135-144.

International Council of Building Officials (ICBO) 1994. *Uniform Building Code*, Whittier, CA.

International Council of Building Officials (ICBO) 1997. *Uniform Building Code*, Whittier, CA.

Issa, Mohamed Saad El-Said. 1997. The deformations of reinforced concrete beams containing plastic hinges in the presence of axial compression or tension load. *Ph. D. Thesis*, Department of Civil and Resource Engineering, University of Auckland, New Zealand.

Jirsa, J.O. and Marques, J.L. 1972. A study of Hooked Bar Anchorages in Beam-Column Joints, Reinforced Concrete Research Council Project 33 Report, Department of Civil Engineering, University of Texas, Austin, TX.

Kabeyasawa, T., Sanada, Y., and Maeda, M. 2000. Effect of Beam Axial Deformation on Column Shear in Reinforced Concrete Beams, in *Proceedings, 12 World Conference on Earthquake Engineering*, Auckland, New Zealand.

Kalkan, E. and Kwong, N.S. 2014. Pros and Cons of Rotating Ground Motion Records to Fault-Normal/Parallel Directions for Response History Analysis of Buildings, *Journal of Structural Engineering*, 140(3): 04013062.

Kim, J., Stanton, J., and MacRae, G. 2004. Effect of Beam Growth on Reinforced Concrete Frames, *ASCE Journal of Structural Engineering*, 130(9): 1333-1342.

Krishnan, S. 2007. Case Studies of Damage to 19-storey Irregular Steel Moment-Frame Buildings under Near-Source Ground Motion, *Earthquake Engineering and Structural Dynamics*, 36(7): 861–885.

Kunnath, S., Heo, Y., and Mohle, J. 2009. Nonlinear Uniaxial Material Model for Reinforcing Steel Bars. *Journal of Structural Engineering*, 135(4): 335–343.

Kuntz, G.L. and Browning, J. 2003. Reduction of Column Yielding During Earthquakes for Reinforced Concrete Frames, *ACI Structural Journal*, 100(5): 573-580.

Los Angeles Tall Buildings Structural Design Council (LATBSDC) 2011. *An Alternative Procedure for Seismic Analysis and Design of Tall Buildings Located in the Los Angeles Region*, Los Angeles Tall Buildings Design Council, Los Angeles, CA.

Lau, D.B.N., Davidson, B.J., and Fenwick, R.C. 2003. Seismic performance of r/c perimeter frames with slabs containing prestressed units, in *Proceedings, 7th Pacific Conference on Earthquake Engineering*, Christchurch, New Zealand.

Lee J.Y and Watanabe F. 2003. Predicting the longitudinal axial strain in the plastic hinge regions of reinforced concrete beams subjected to reversed cyclic loading. *Engineering Structures*, 25(7): 927-939.

Lehman, D. E., and Moehle, J. P. 2000. "Seismic Performance of Well-Confined Concrete Bridge Columns," R*eport* No. PEER-1998/01, University of California-Berkeley, Berkeley, CA.

Liao, W., Loh, C., and Wan, S., 2001. Earthquake Responses of RC Moment Frames Subjected to Near-Fault Ground Motions, *The Structural Design of Tall Buildings* 10: 219-229.

MacRae, G. and Gunasekaran 2006. A Concept for Consideration of Slab Effects on Building Seismic Performance, in *Proceedings,2006 NZSEE Conference*, Napier, New Zealand.

Mander, J.B., Priestley, M.J.N., and Park, P. 1988. Theoretical Stress-Strain Model for Confined Concrete, *ASCE Journal of Structural Engineering*, 114(8): 1804-1826.

Marini A. and Spacone E. 2006. Analysis of Reinforced Concrete Elements Including Shear Effects, *ACI Structural Journal*, 103(5): 645-655.

Massone, L. M., and Wallace, J. W. 2004. Load-Deformation Response of Slender Reinforced Concrete Walls, *ACI Structural Journal*, 101(1): 103-113.

Matthews J.G. 2004. *Hollow-Core Floor Slab Performance following a Severe Earthquake*, Ph.D. Thesis, University of Canterbury, Christchurch, New Zealand.

Matti, N. M. 1998. "Effect of axial loads on the behavior of reversing plastic hinges in reinforced concrete beams." *M.S. Thesis*, Department of Civil and Resource Engineering, University of Auckland, New Zealand.

McKenna, F., Fenves, G. L., and Scott, M. H. 2007. Open System for Earthquake Engineering Simulation (OpenSees). Pacific Earthquake Engineering Research Center. http://opensees.berkeley.edu/.

Mergos, P.E. and Kappos, A.J. 2012. A gradual spread inelasticity model for R/C beam – columns, accounting for flexure, shear and anchorage slip. *Engineering Structures*, 44: 94-106.

Moehle, Jack P., Hooper, John D., and Lubke, Chris D. 2008. Seismic Design of Reinforced Concrete Special Moment Frames: A Guide for Practicing Engineers. *NEHRP Seismic Design Technical Brief No.1*, NIST GCR 8-917-1.

Moehle J.P., Bozorgnia,Y., Jayaram, N., Jones, P., Rahnama, M., Shome, M., Tuna, Z., Wallace, J.A., Yang, T.Y., and Zareian, F. 2011. Case Studies of the Seismic Performance of Tall Buildings Designed by Alternative Means. Task 12 Report for the Tall Buildings Initiative. Tech. Rep. PEER 2011/05 Pacific Earthquake Engineering Research Center, Berkeley, CA.

Moehle J.P. 2014. *Seismic Design of Reinforced Concrete Buildings*, McGraw-Hill Professional, New York, NY.

Monti, G., and Nuti, C. 1992. Nonlinear Cyclic Behavior of Reinforcing Bars Including Buckling. *Journal of Structural Engineering*, 118(12): 3268–3284.

Muto, M. and Krishnan, S. 2011. Hope for the Best, Prepare for the Worst: Response of Tall Steel Buildings to the ShakeOut Scenario Earthquake, *Earthquake Spectra*, 27(2): 375-398.

Open System for Earthquake Engineering Simulation (OpenSees) 2012-2014. http://opensees.berkeley.edu/.

Otani S. 1999. RC buildings damage statistics and SDF response with design seismic force. *Earthquake Spectra*, 15(3): 485–501.

Ozcebe G. and Saatcioglu, M. 1989. Hysteretic shear model for reinforced concrete members. *Journal of Structural Engineering*,115(1): 132–48.

Panagiotou, M.; Visnjic, T.; Antonellis, G.; Moehle, J.; and Gallanis, P. 2013. "Effect of Hoop Reinforcement Spacing on the Cyclic Response of Large Reinforced Concrete Special Moment Frame Beams," *Report* No. 2013/16, Pacific Earthquake Engineering Research Center, Berkeley, USA.

Park, R. and Paulay, T. 1975. *Reinforced Concrete Structures*, John Wiley & Sons, Hoboken, NJ.

Paulay, T., and Scarpas, A. 1981. "The Behavior of Exterior Beam-Column Joints," *Bulletin of the New Zealand National Society for Earthquake Engineering*, 14(3): 131-144.

PEER 2014, Gound Moion Database. http://peer.berkeley.edu/peer_ground_motion_database/

Peng, B., Dhakal, R., and Fenwick, R.C. 2006. Causes of Elongation in Reinforced Concrete Beams Subjected to Cyclic Loading, in *Proceedings, Tenth East Asia and Pacific Conference on Structural Engineering and Construction (EASEC10)*, Bangkok, Thailand.

Peng, B., Dhakal, R., and Fenwick, R.C., Carr, A.J., and Bull, D.K. 2013. Multispring Hinge Element for Reinforced Concrete Frame Analysis, *Journal of Structural Engineering*, 139(4): 595-606.

Petrangeli M., Pinto P., and Ciampi V. 1999. Fiber Element for Cyclic Bending and Shear of RC Structures. I: Theory. Journal of Engineering Mechanics, 125(9): 994–1001.

Pettinga, J.D. and Priestley, M.J.N., 2005. Dynamic Behaviour of Reinforced Concrete Frames Designed with Direct Displacement-Based Design, *Journal of Earthquake Engineering*, 9(sup.2): 309-330.

Popov, E. P.; Bertero, V. V.; and Krawinkler, H. 1972. "Cyclic Behavior of Three Reinforced Concrete Flexural Members with High Shear," *Report* No. EERC 72-5, Earthquake Engineering Research Center, University of California, Berkeley, USA.

Qi, X., Pantazopoulou, S. J. 1991. Response of RC Frame under Lateral Loads, *ASCE Journal of Structural Engineering*, 117(4): 1167-1188.

Restrepo, J.I., Park, R., and Buchanan, A. 1990. Seismic Load Tests on Midspan Connections Between Precast Concrete Beams: 3rd Progress Report on the Research Project on the Seismic Performance of Precast Concrete Frames. University of Canterbury Research Rep. ISSN 0110-3326.

Restrepo, J.I.; Park, R.; and Buchanan, A. 1993. "Seismic Behaviour of Connections Between Precast Concrete Elements," *Report* No. 93-3, Department of Civil and Natural Resources Engineering, University of Canterbury, New Zealand.

Reyes, J.C. and Kalkan E. 2012. Relevance of Fault-Normal/Parallel and Maximum Direction Rotated Ground Motions on Nonlinear Behavior of Multi-Story Buildings, in *Proceedings, 15th World Conference on Earthquake Engineering*, Lisbon, Portugal.

Rodriguez, M.; Botero, J.; and Villa, J. 1999. Cyclic Stress-Strain Behavior of Reinforcing Steel Including Effect of Buckling, *Journal of Structural Engineering*, 125(6): 605–612.

Scott, B.D., Park, R., and Priestley, M.J.N. 1982. Stress-Strain Behavior of Concrete Confined by Overlapping Hoops at Low and High Strain Rates, *ACI Journal*, 79(1): 13-27.

Scott, M.H. and Fenves G. 2006. Plastic Hinge Integration Methods for Force-Based Beam-Column Elements, *Journal of Structural Engineering*, 132(2): 244-252.

Sezen H. and Moehle, J.P. 2004. Shear Strength Model for Lightly Reinforced Columns. *ASCE Journal of Structural Engineering*, 130(11): 1692-1703.

Sezen H. and Setzler, E.J. 2008. Reinforcement Slip in Reinforced Concrete Columns. *ACI Structural Journal*, 105(3): 280-289.

Standards New Zealand (SNZ) 2006. Concrete Structures Standard NZS3101, Wellington NZ.

Structural Engineers Association of Northern California (SEAONC) 2007. *Seismic Design and Review of Tall Buildings Using Non-Prescriptive Procedures*, Recommended Administrative Bulletin, SEAONC, San Francisco, CA.

TBI Guidelines Working Group 2010. Guidelines for Performance-Based Seismic Design of Tall Buildings, Tech. Rep. 2010/05 Pacific Earthquake Engineering Research Center, Berkeley CA.

Takiguchi, K. and Ichinose, T. 1977. About change of axial elongation of reinforced concrete beam (in Japanese), Transaction of the Tokai Branch of the Architectural Institute of Japan, pp.251-254.

Taucer, F.T., Spacone, E., and Filippou, F.C. 1991. A Fiber Beam-Column Element For Seismic Response Analysis of Reinforced Concrete Structures, Report No. UCB/EERC-91/17 Earthquake Engineering Research Center College of Engineering University of California, Berkeley.

Tsai, K.C., Hsiao, C.P., and Bruneau M. 2000. Overview of building damages in 921 Chi-Chi earthquake. *Earthquake Engineering and Engineering Seismology*, 2(1): 93–108.

Visnjic, T., Panagiotou, M., and Moehle, J. 2012. Seismic Response of Four 20-story Tall Reinforced Concrete Special Moment Resisting Frames Designed with Current Code Provisions, *UCB/SEMM Report No. 2012/02*, Department of Civil and Environmental Engineering, University of California, Berkeley, CA.

Viwathanatepa, S., Popov, E.P., and Bertero, V.V. 1979. Effects of Generalized Loadings on Bond of Reinforcing Bars Embedded in Confined Concrete Blocks, UCB/EERC Report No. 79-22, Earthquake Engineering Research Center, University of California, Berkeley, CA.

Warcholik, G., and Priestley, M. 1997. “Structural Systems Research Project: High Strength Concrete Joints Tests,” *Report* No. TR-97/10, Department of Structural Engineering, University of California, San Diego, USA.

Warcholik, G., and Priestley, M. 1998a. “Structural Systems Research Project: High Strength Concrete Joints Tests,” *Report* No. TR-98/01, Department of Structural Engineering, University of California, San Diego, USA.

Warcholik, G., and Priestley, M. 1998b. “Structural Systems Research Project: High Strength Concrete Joints Tests,” *Report* No. TR-98/12, Department of Structural Engineering, University of California, San Diego, USA.

Watson-Lamprey, J. and Abrahamson, N. 2006. Selection of Ground Motion Time Series and Limits on Scaling. *Soil Dynamics and Earthquake Engineering*, 26(5): 477-482.

Wiebe, L. and Christopoulos, C. 2010. Characterizing Acceleration Spikes Due to Stiffness Changes in Nonlinear Systems, *Earthquake Engineering and Structural Dynamics*, 39(14): 1653-1670.

Willford, M., Whittaker, A., and Klemencic, R. 2008. *Recommendations for the Seismic Design of High-Rise Buildings*, Council on Tall Buildings and Urban Habitat (CTBUH), Chicago, IL.

Zhao, J., and Sritharan, S. 2007. Modeling of Strain Penetration Effects in Fiber-Based Analysis of Reinforced Concrete Structures, *ACI Structural Journal*, 104(2): 133-141.

APPENDIX A

This appendix contains measurements recorded during the laboratory experiments presented in Chapter 2. The measurements include the individual instrumentation readings from LVDTs and strain gauges, as well as the manually measured crack widths in beam specimens (Tables A1 and A2). Note that the broken instrumentation readings are given a constant zero value and are plotted in red.

BEAM 1 INSTRUMENTATION RECORDINGS: STRAIN GAUGES

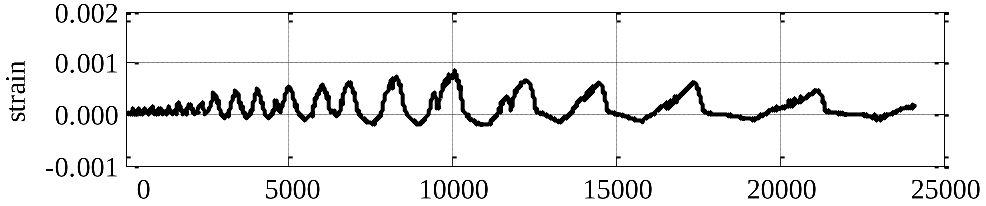
LTI-OUT(-2) (Beam 1)

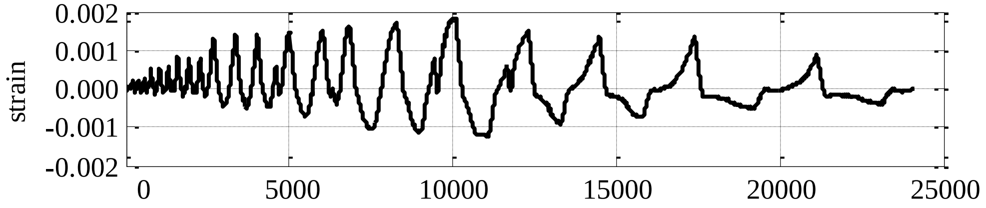
LTI-OUT(-1) (Beam 1)

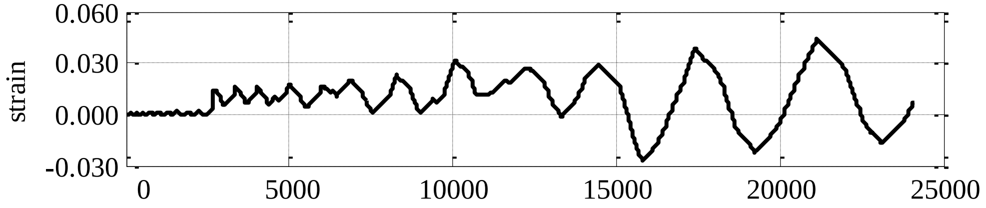
LTI-OUT(1) (Beam 1)

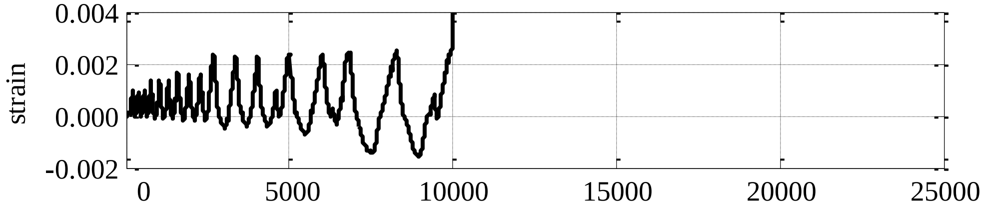
LTI-OUT(2) (Beam 1)

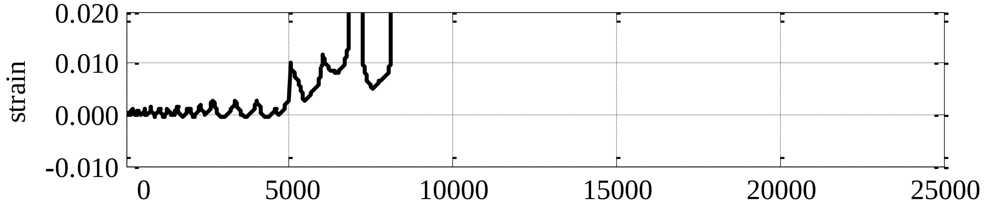
LTI-OUT(3) (Beam 1)

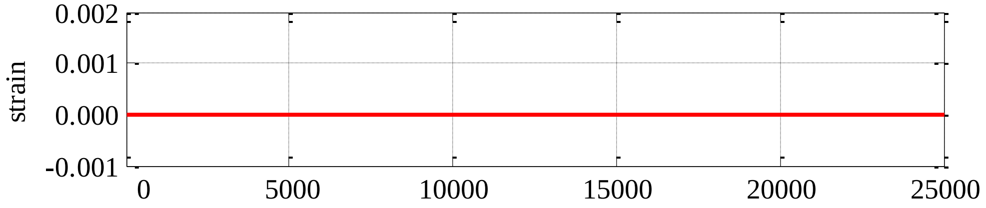
LTI-OUT(4) (Beam 1)

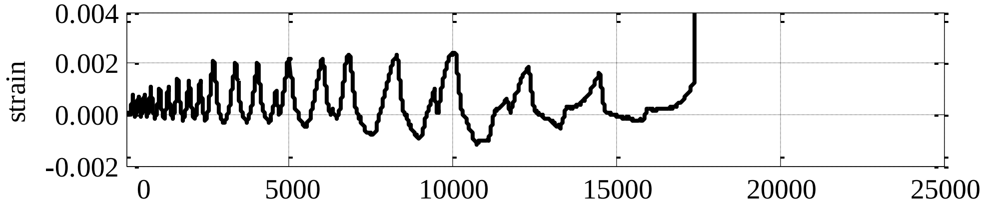
LTI-OUT(5) (Beam 1)

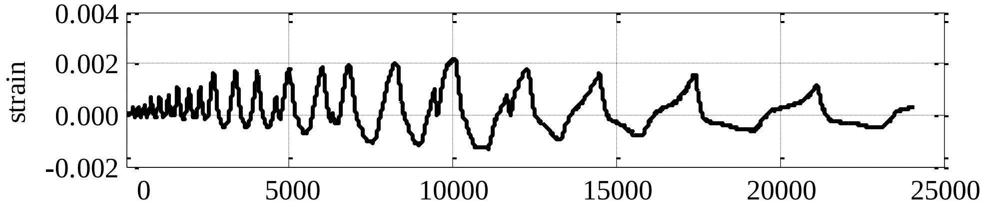
LTI-IN(-1) (Beam 1)

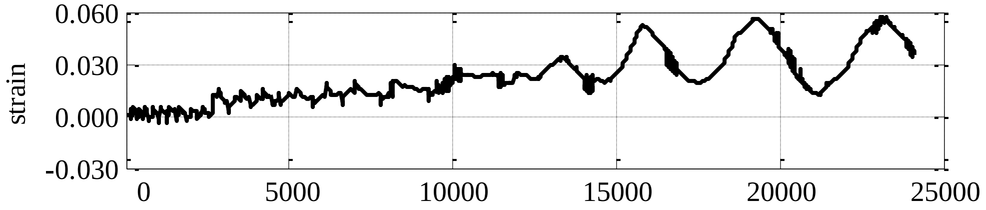
LTI-IN(1) (Beam 1)

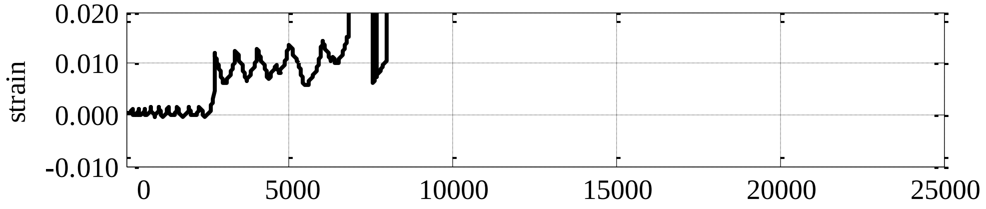
LTI-IN(2) (Beam 1)

LTII-IN(1) (Beam 1)

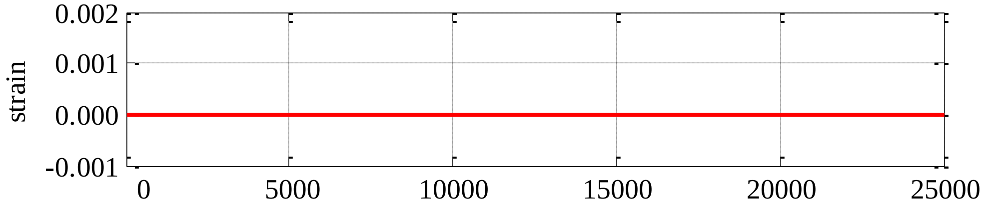

LTII-IN(2) (Beam 1)

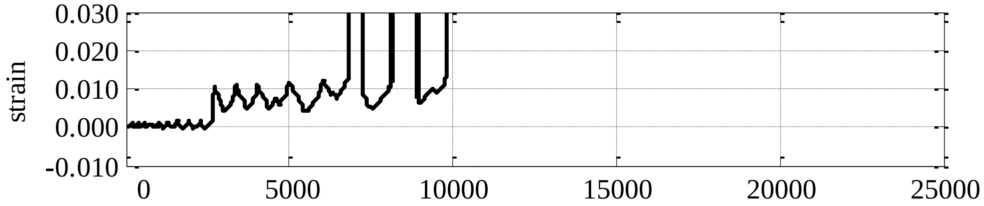

LTII-OUT(1) (Beam 1)

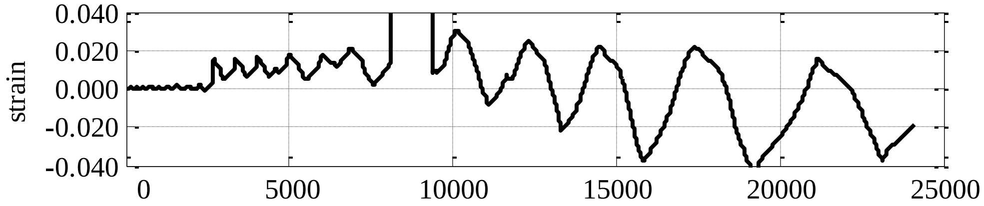

LTII-OUT(2) (Beam 1)

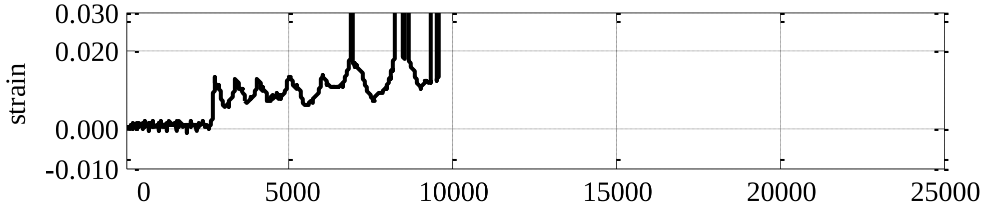

LTII-OUT(3) (Beam 1)

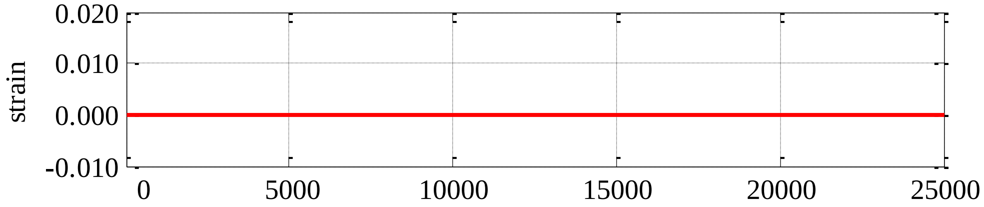

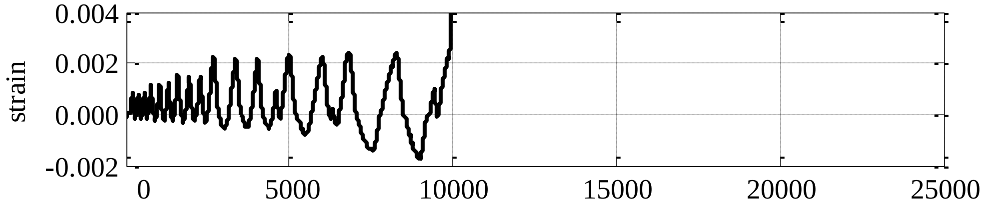

LTII-OUT(4) (Beam 1)

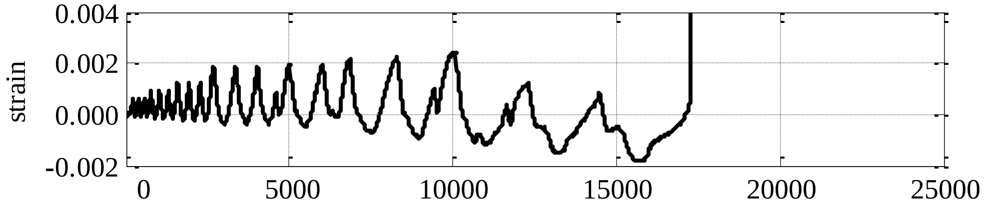

LTII-OUT(5) (Beam 1)

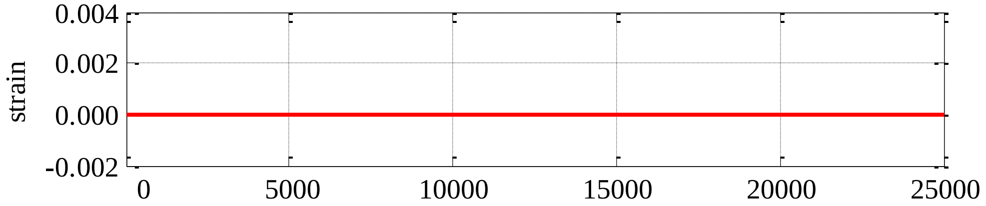

LTII-IN(1) (Beam 1)

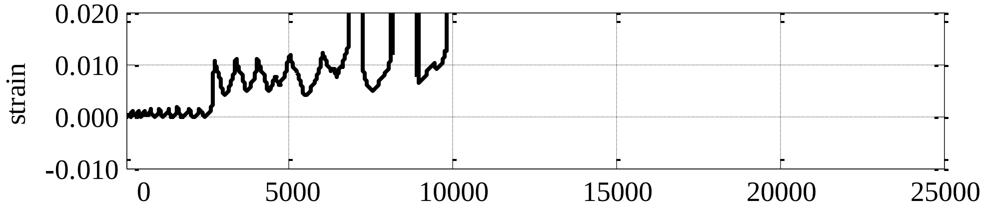

LTII-IN(2) (Beam 1)

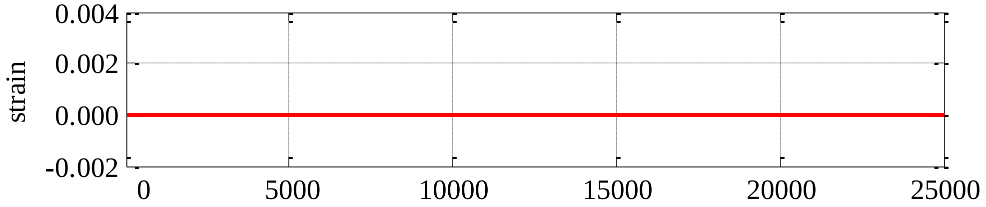

LBI-OUT(-2) (Beam 1)

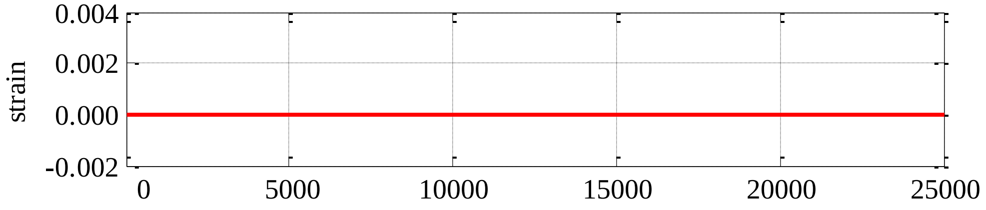
LBI-OUT(-1) (Beam 1)

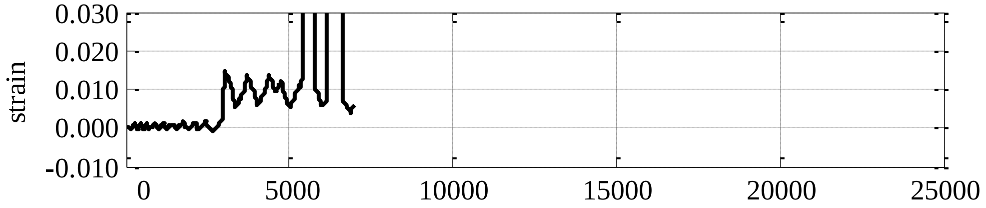
LBI-OUT(1) (Beam 1)

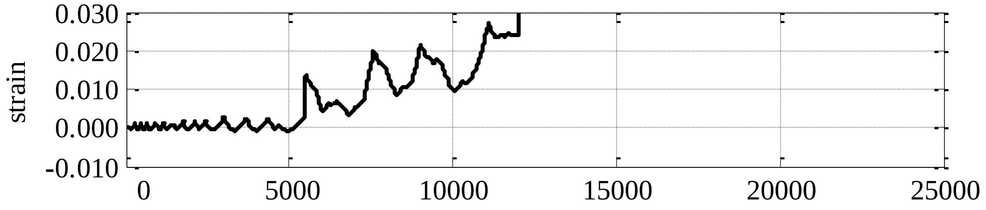
LBI-OUT(2) (Beam 1)

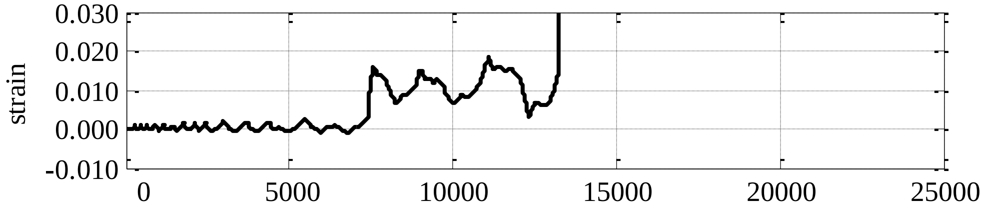
LBI-OUT(3) (Beam 1)

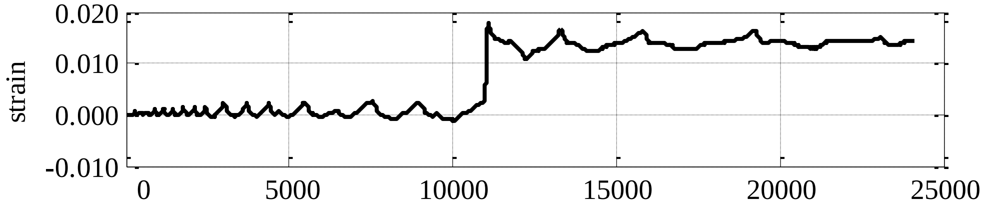
LBI-OUT(4) (Beam 1)

LBI-OUT(5) (Beam 1)

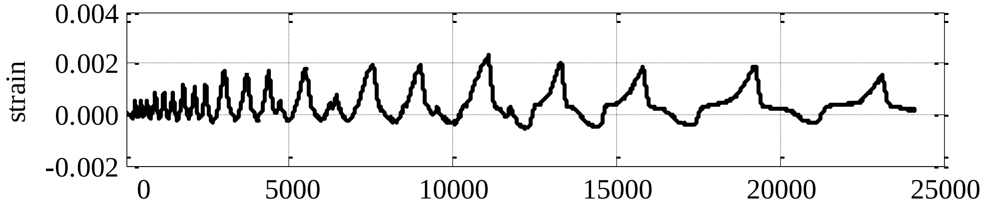

LBI-IN(1) (Beam 1)

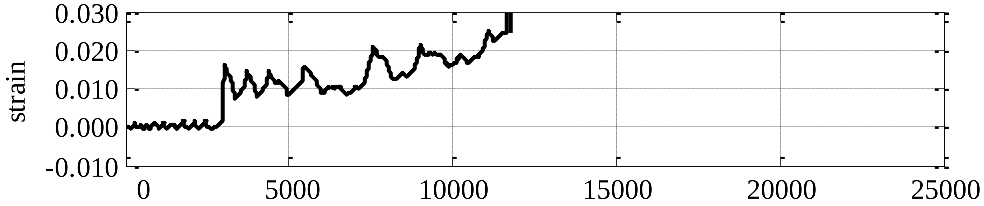

LBI-IN(2) (Beam 1)

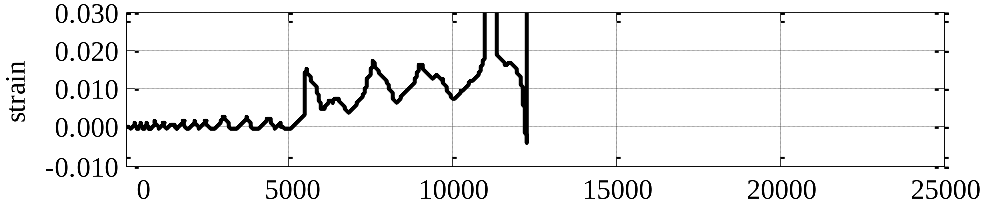

LBI-IN(3) (Beam 1)

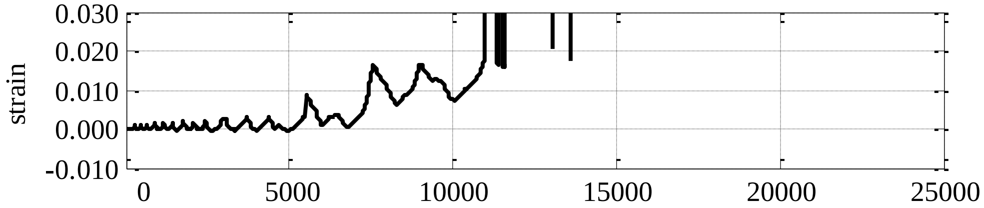

LBII-OUT(1) (Beam 1)

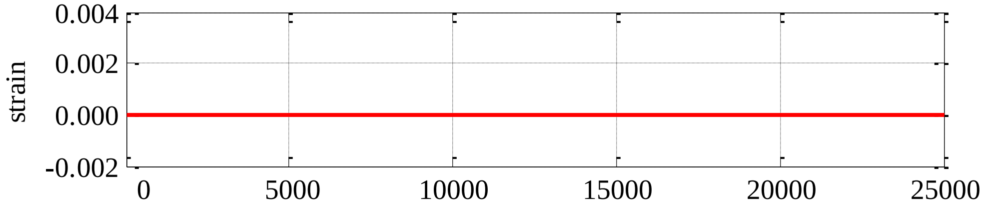

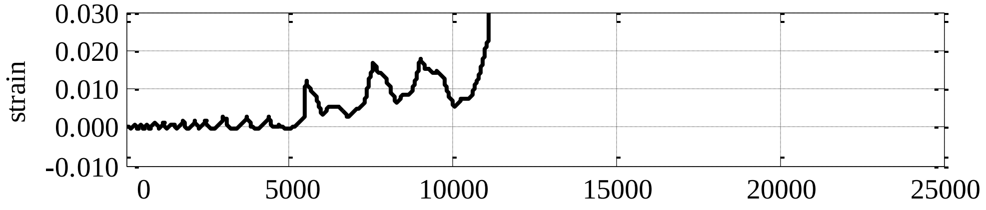
LBII-OUT(2) (Beam 1)

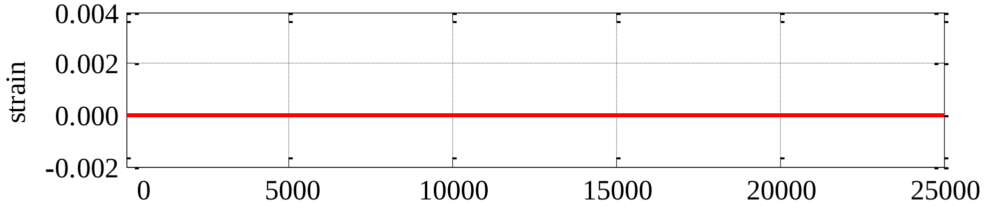
LBII-OUT(3) (Beam 1)

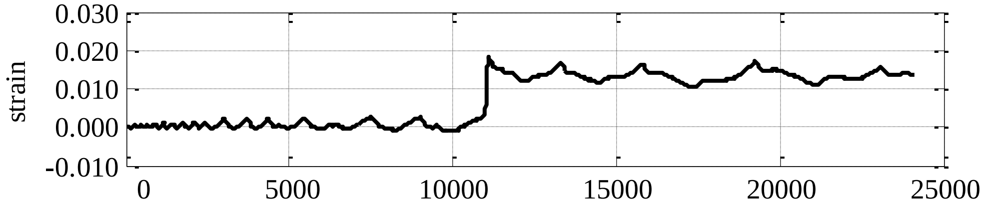
LBII-OUT(4) (Beam 1)

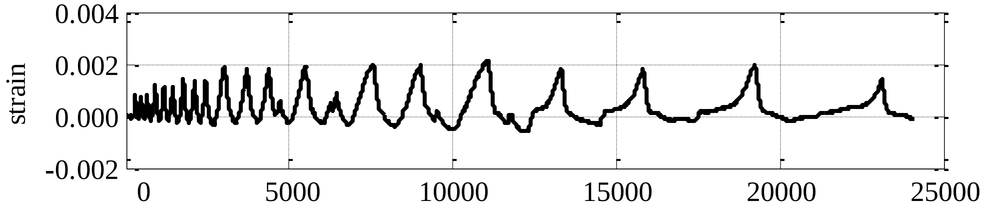
LBII-OUT(5) (Beam 1)

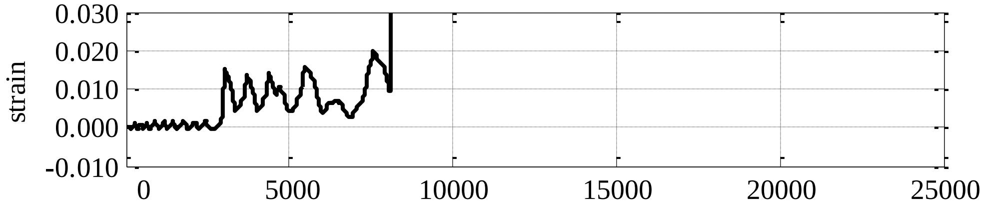
LBII-IN(1) (Beam 1)

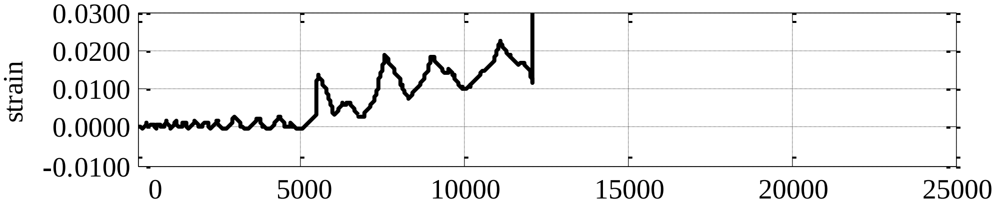

LBII-IN(2) (Beam 1)

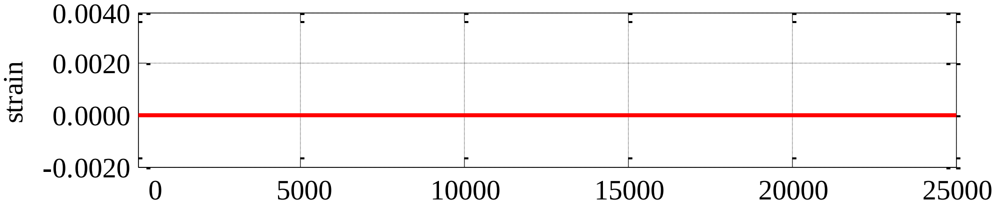

TA1-LEXT (Beam 1)

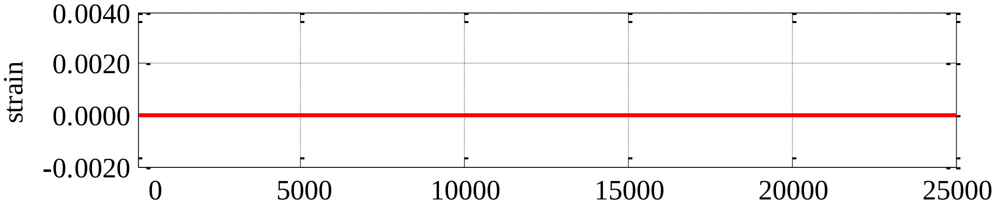

TA1-LINT (Beam 1)

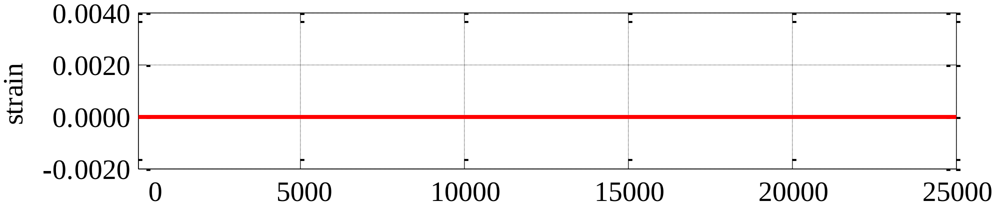

TA1-REXT (Beam 1)

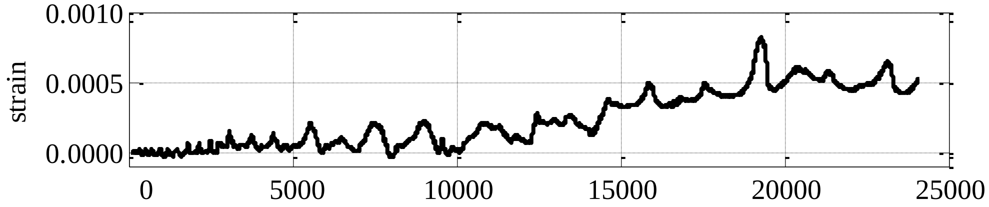

TA1-RINT (Beam 1)

TA2-LEXT (Beam 1)

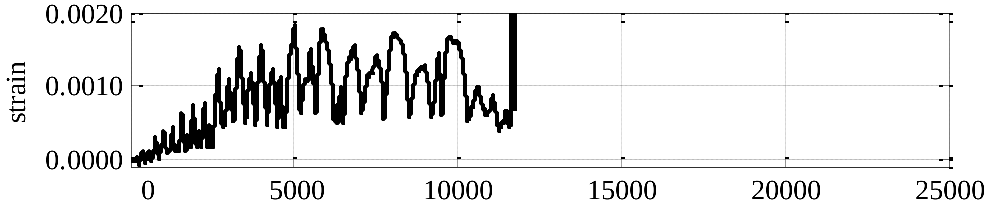

TA2-LINT (Beam 1)

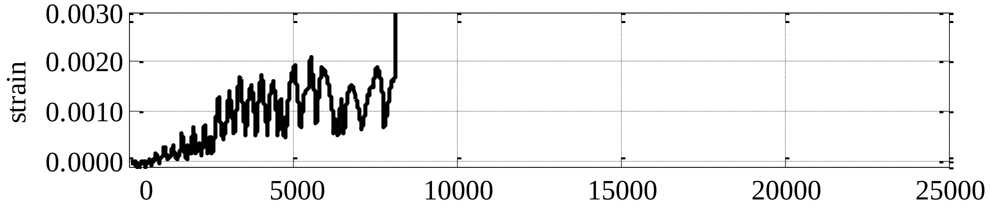

TA2-REXT (Beam 1)

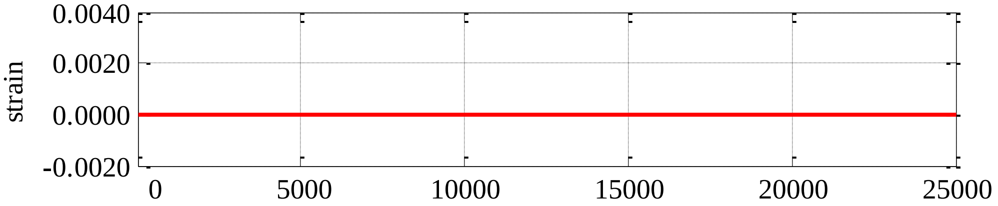

TA2-RINT (Beam 1)

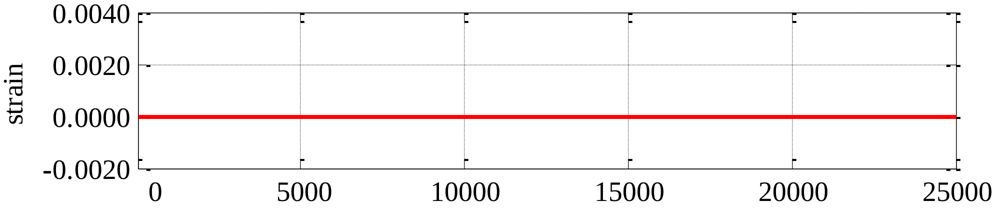

TB1-LEXT (Beam 1)

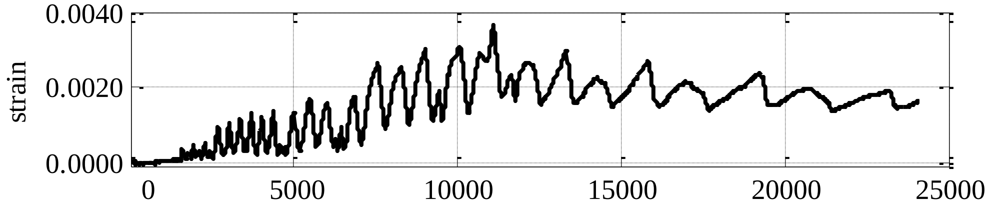

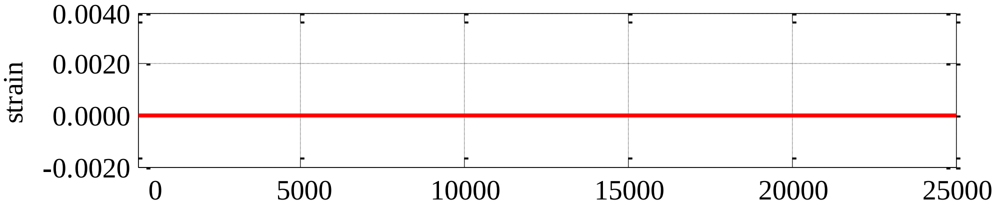

TB1-REXT (Beam 1)

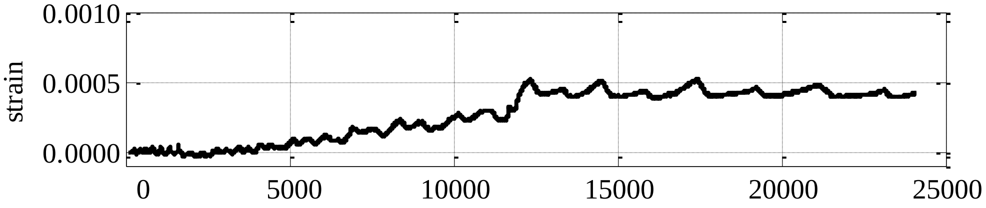

TB2-LEXT (Beam 1)

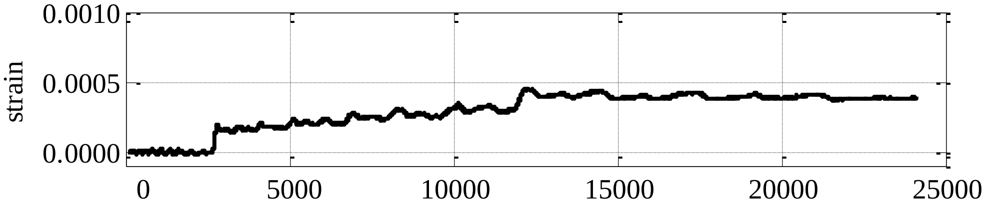

TB2-REXT (Beam 1)

Beam 1 Instrumentation Recordings: LVDTs

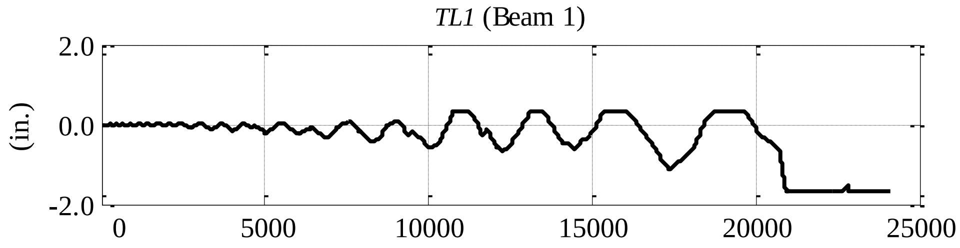

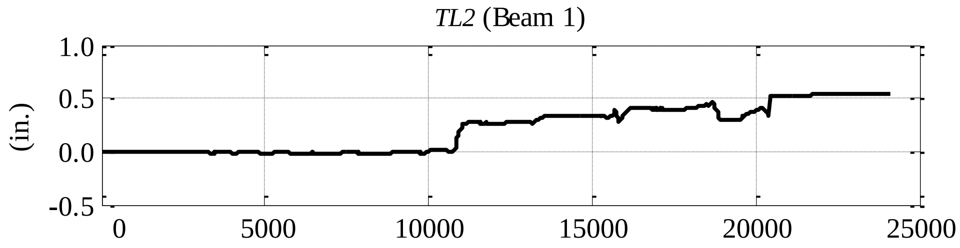

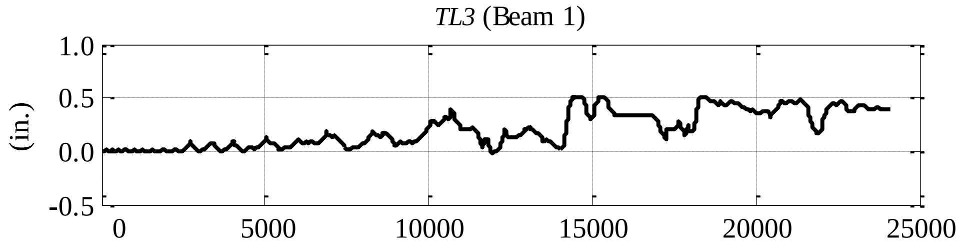

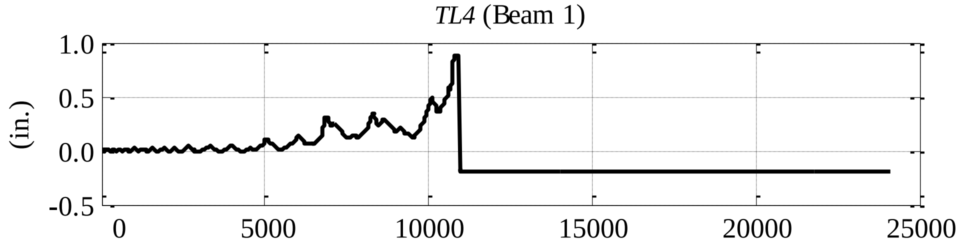

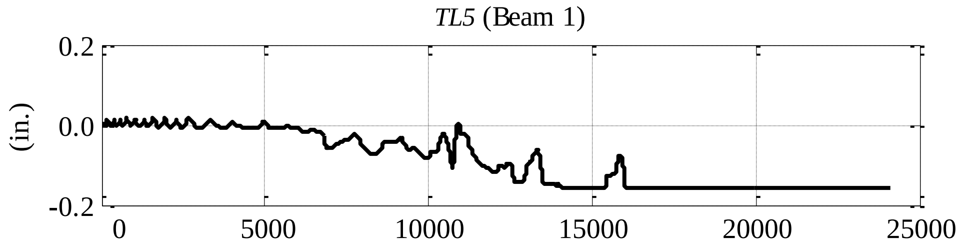

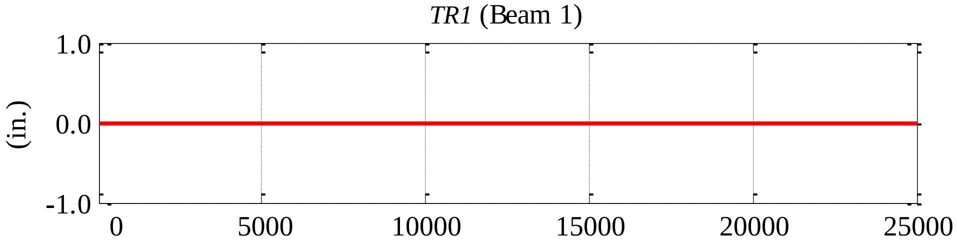
TR1 (Beam 1)

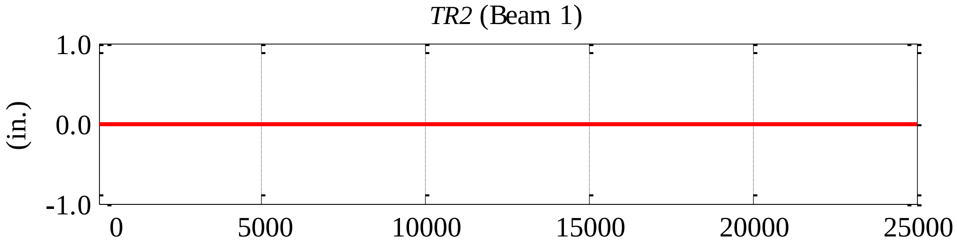
TR2 (Beam 1)

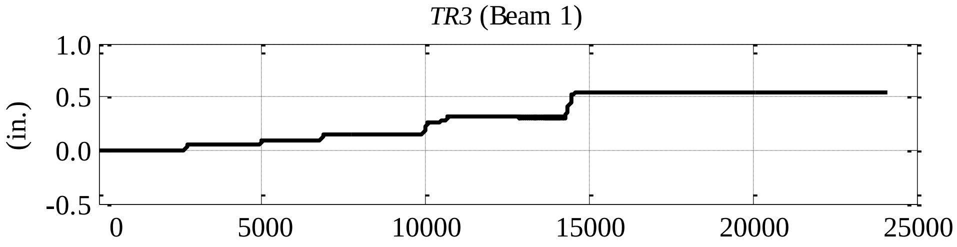
TR3 (Beam 1)

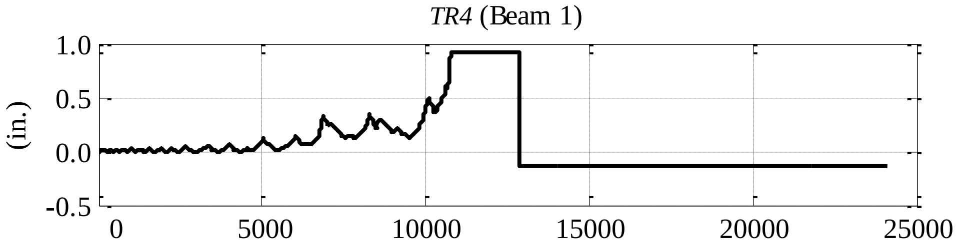
TR4 (Beam 1)

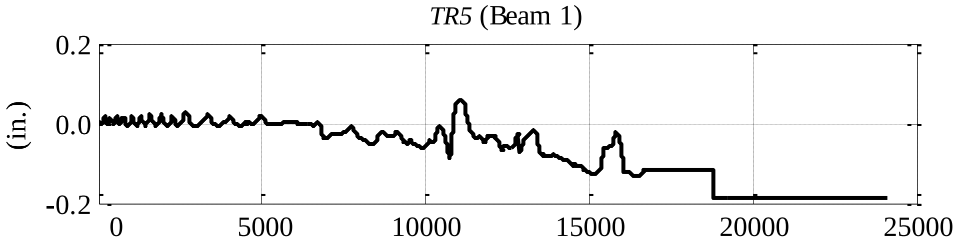
TR5 (Beam 1)

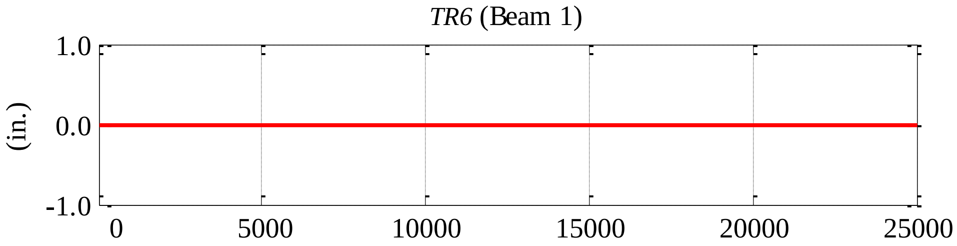
TR6 (Beam 1)

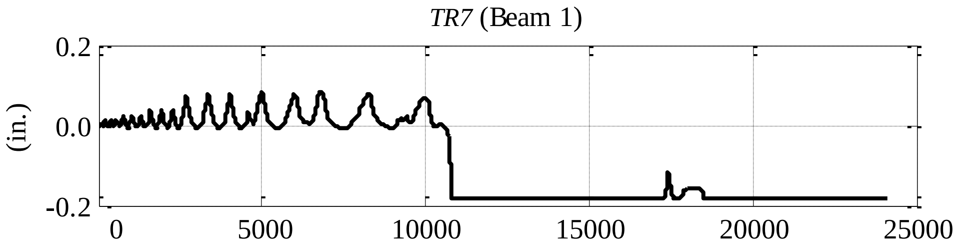
TR7 (Beam 1)

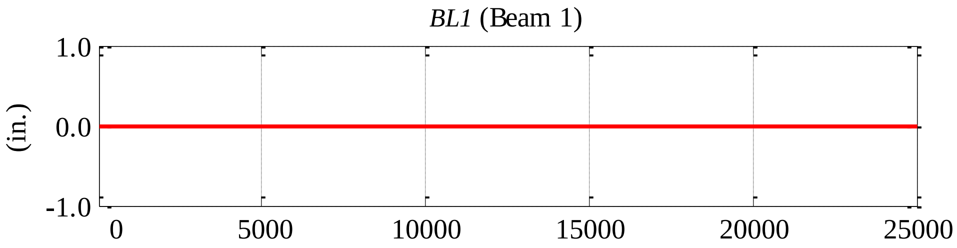
BL1 (Beam 1)

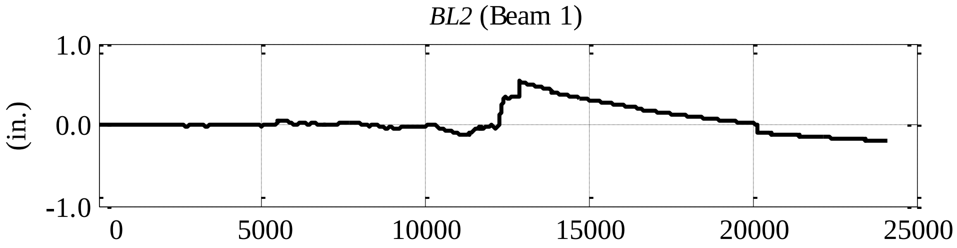
BL2 (Beam 1)

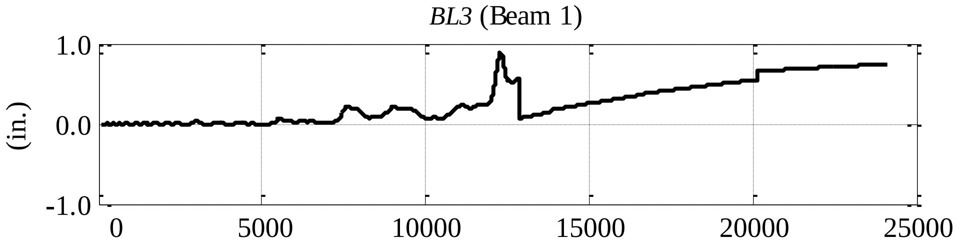
BL3 (Beam 1)

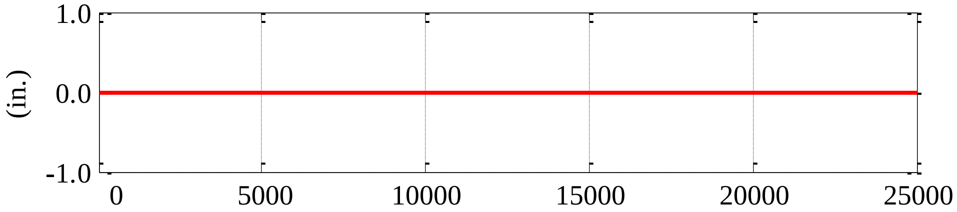

BL4 (Beam 1)

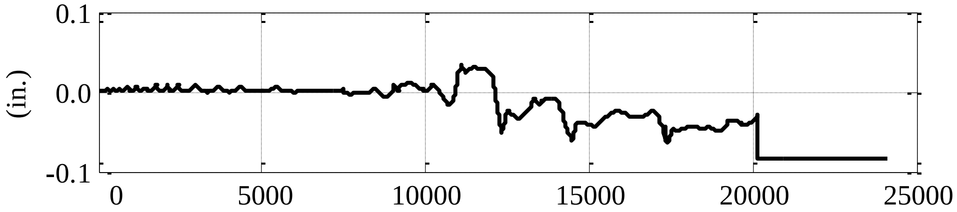

BL5 (Beam 1)

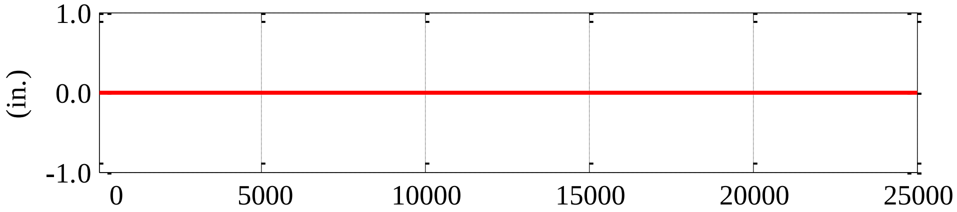

BR1 (Beam 1)

BR2 (Beam 1)

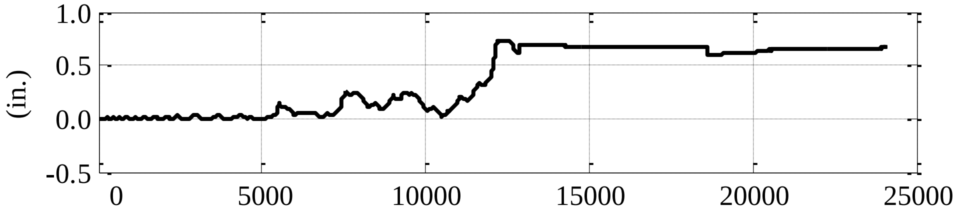

BR3 (Beam 1)

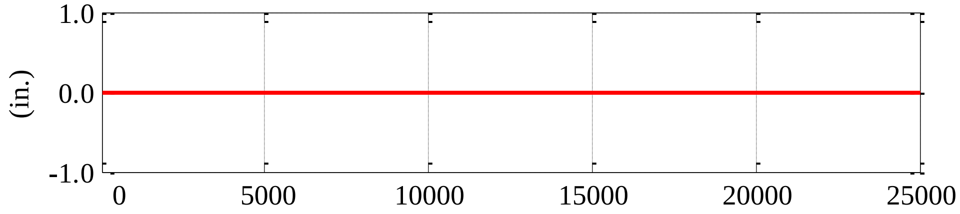

BR4 (Beam 1)

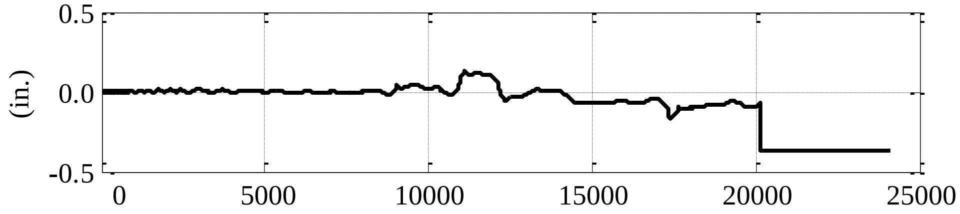

BR5 (Beam 1)

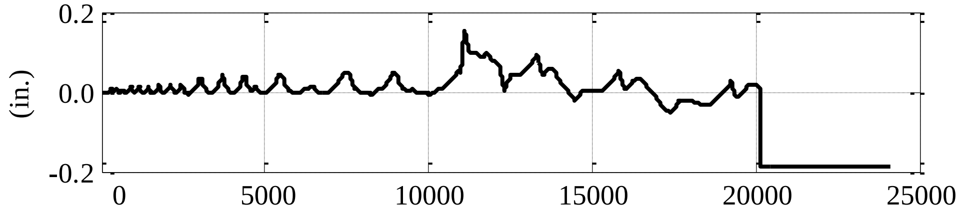

BR6 (Beam 1)

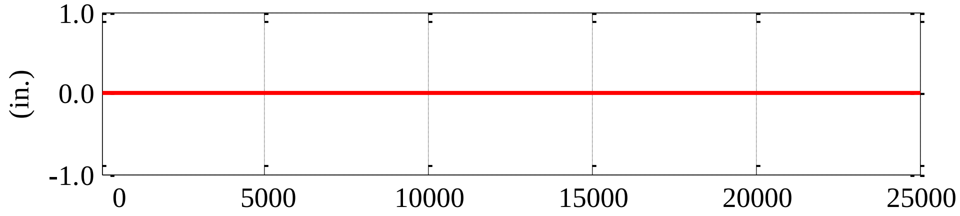

BR7 (Beam 1)

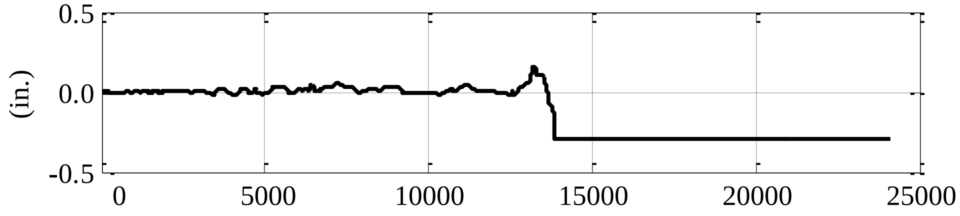

V1 (Beam 1)

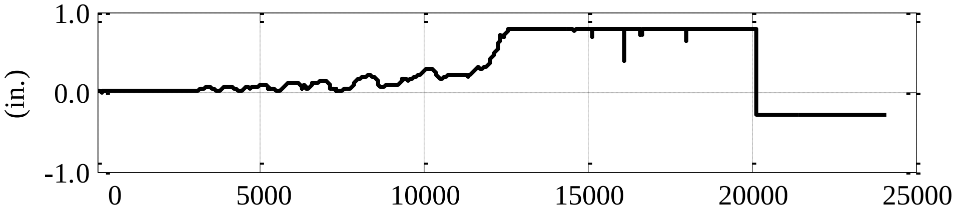

V2 (Beam 1)

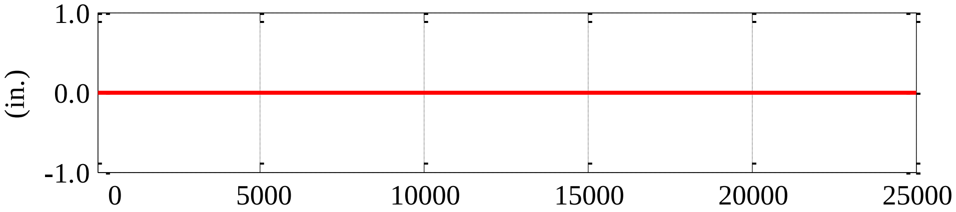

V3 (Beam 1)

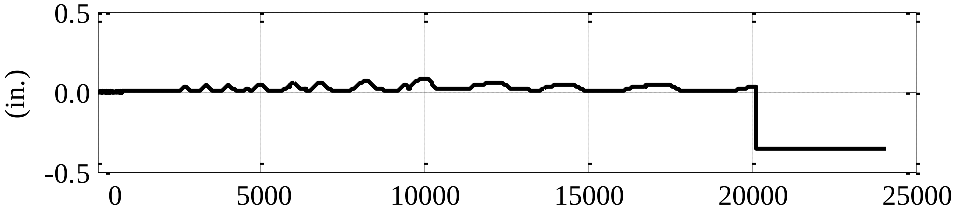

V4 (Beam 1)

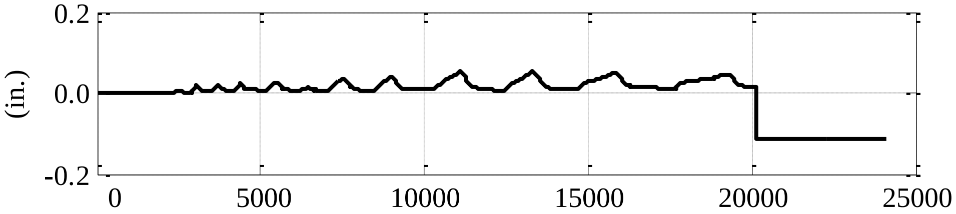

V5 (Beam 1)

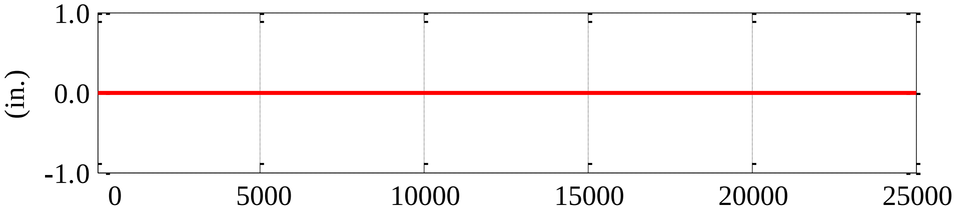

S1 (Beam 1)

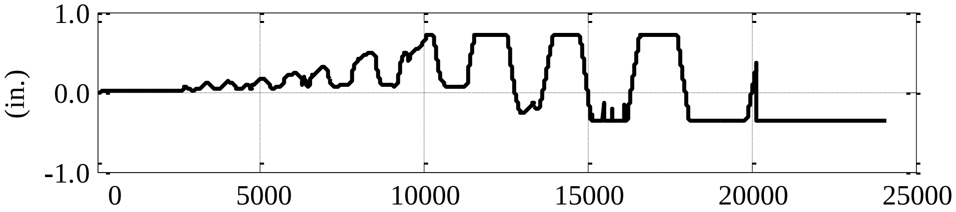

S2 (Beam 1)

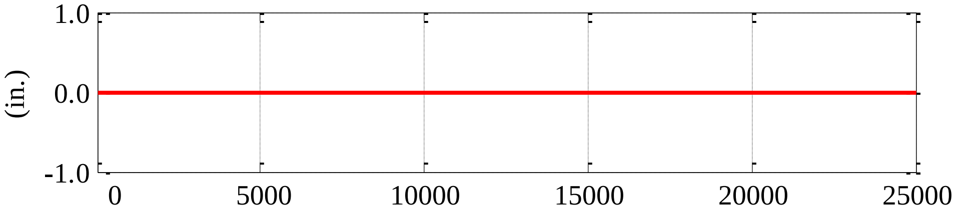

S3 (Beam 1)

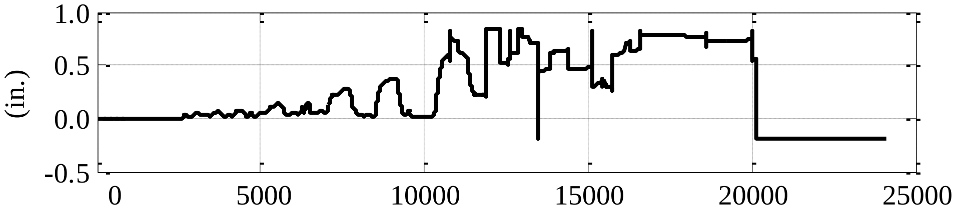

S4 (Beam 1)

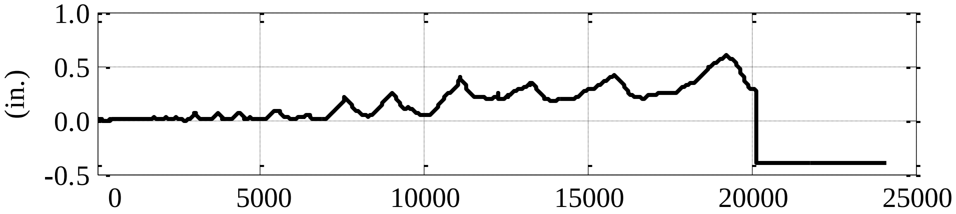

S5 (Beam 1)

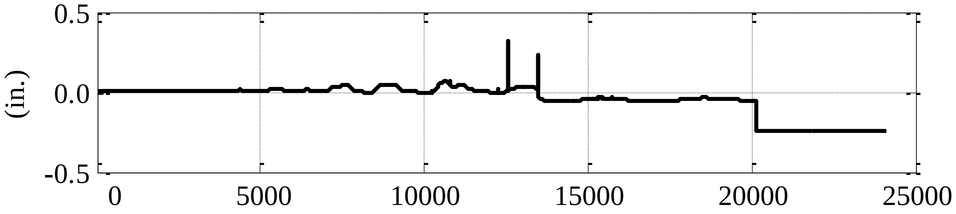

S6 (Beam 1)

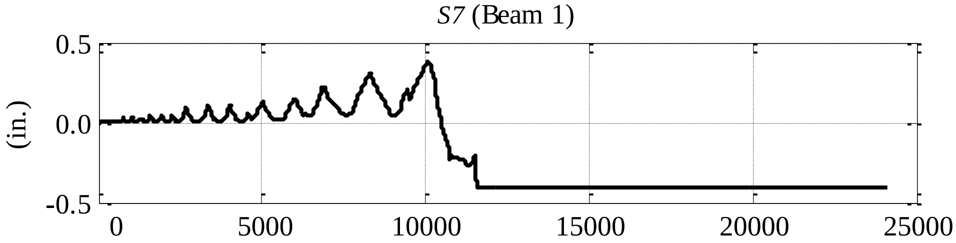

S7 (Beam 1)

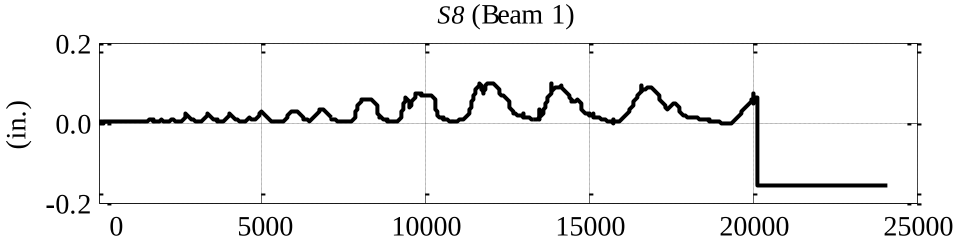

S8 (Beam 1)

<u>BEAM 2 INSTRUMENTATION RECORDINGS: STRAIN GAUGES</u>

LTI-OUT(-2) (Beam 2)

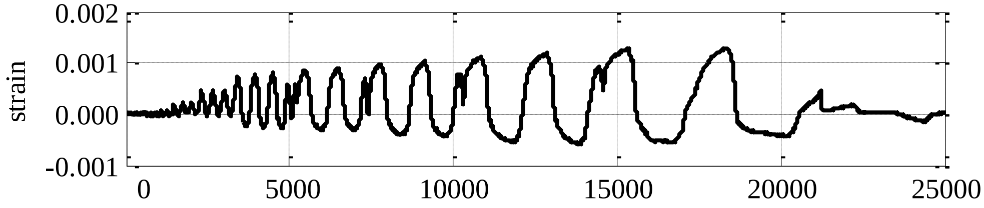

LTI-OUT(-1) (Beam 2)

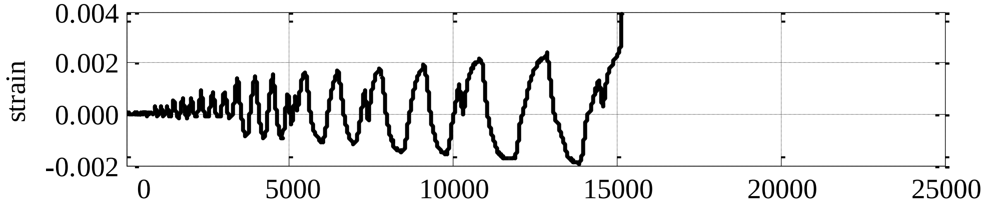

LTI-OUT(1) (Beam 2)

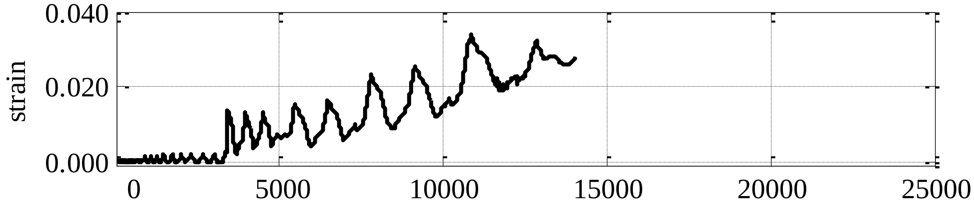

LTI-OUT(2) (Beam 2)

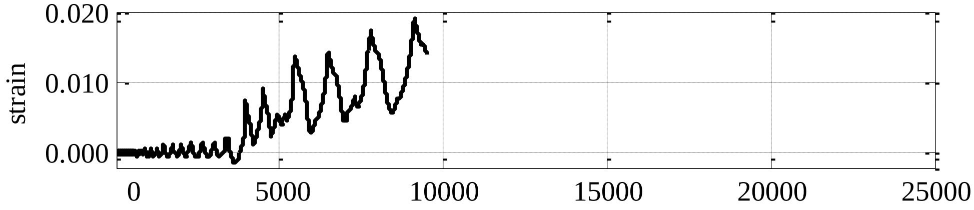

LTI-OUT(3) (Beam 2)

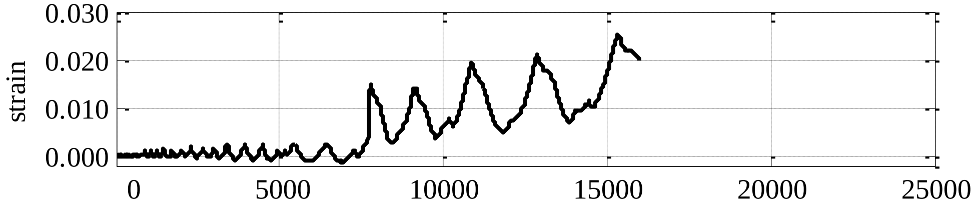

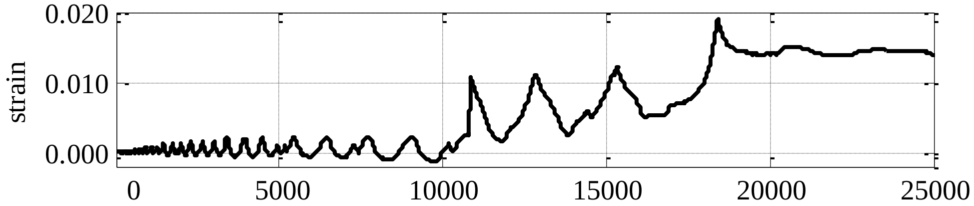

LTI-OUT(4) (Beam 2)

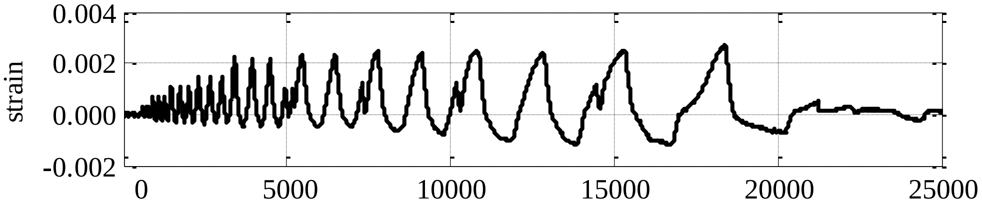

LTI-OUT(5) (Beam 2)

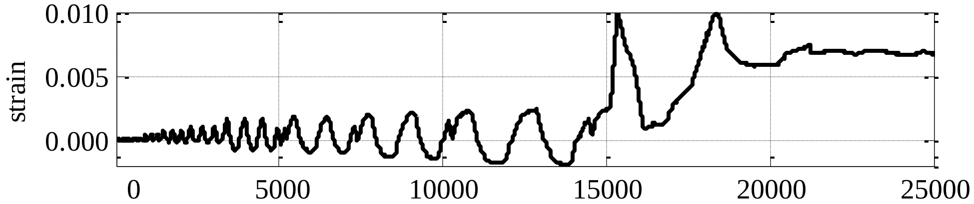

LTI-IN(-1) (Beam 2)

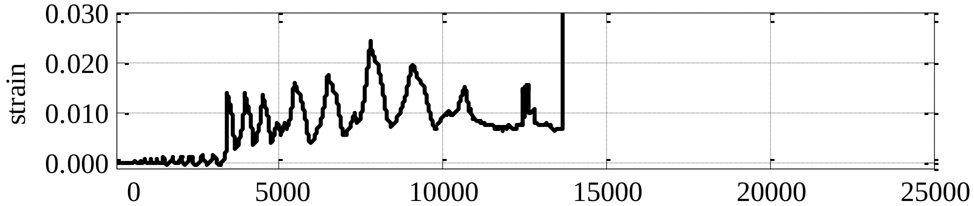

LTI-IN(1) (Beam 2)

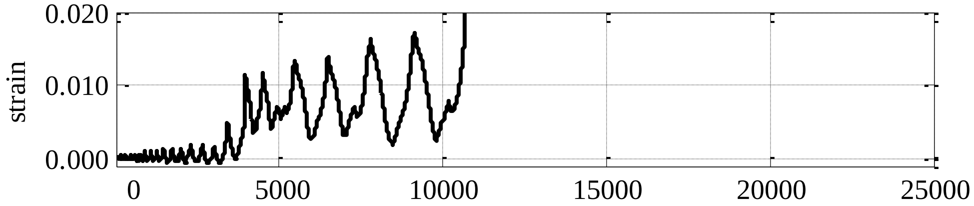

LTI-IN(2) (Beam 2)

LTII-IN(1) (Beam 2)

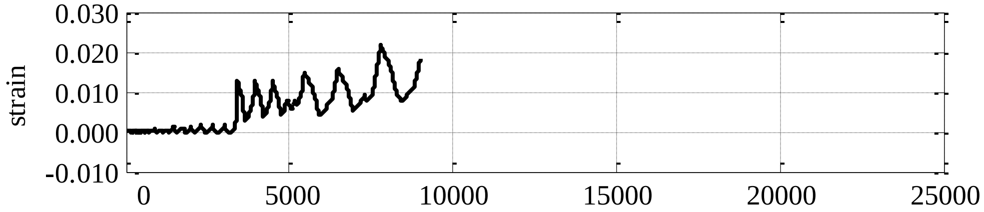

LTII-IN(2) (Beam 2)

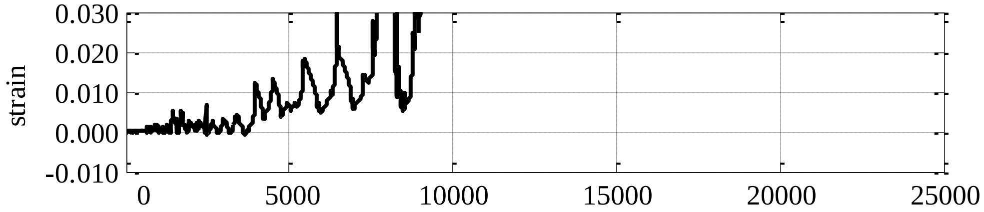

LTII-OUT(1) (Beam 2)

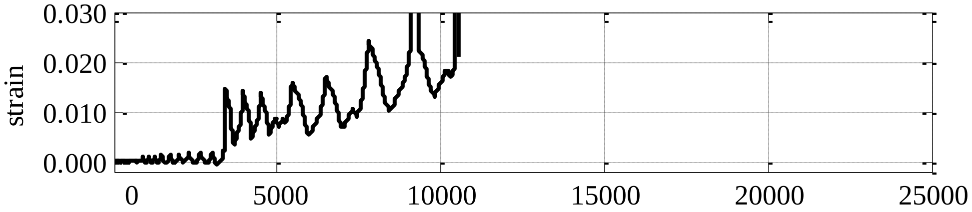

LTII-OUT(2) (Beam 2)

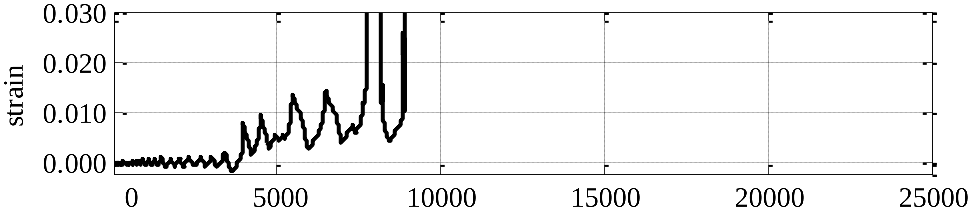

LTII-OUT(3) (Beam 2)

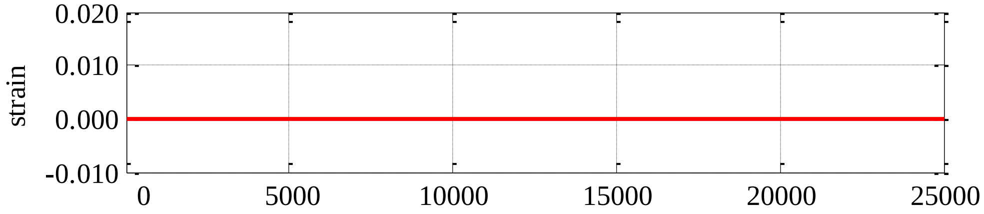

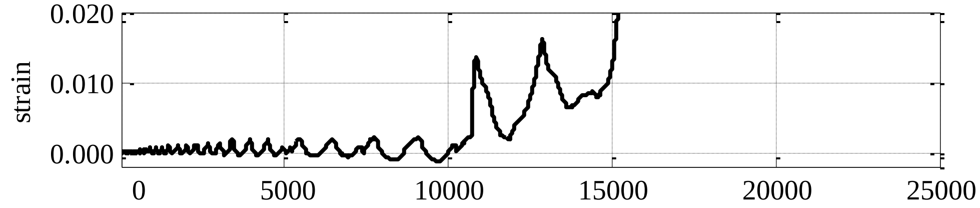
LTII-OUT(4) (Beam 2)

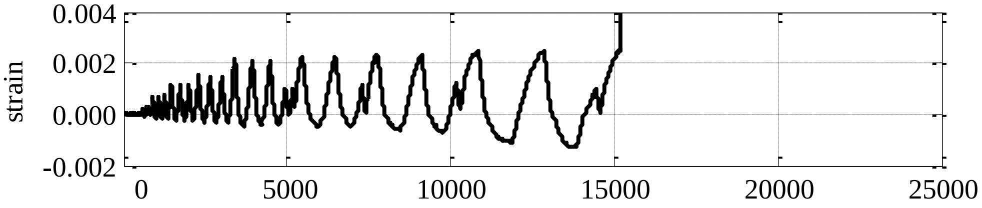
LTII-OUT(5) (Beam 2)

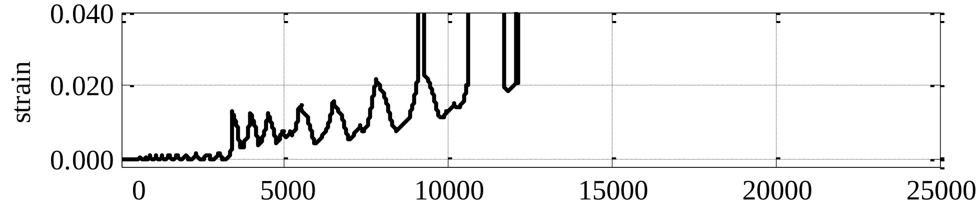
LTII-IN(1) (Beam 2)

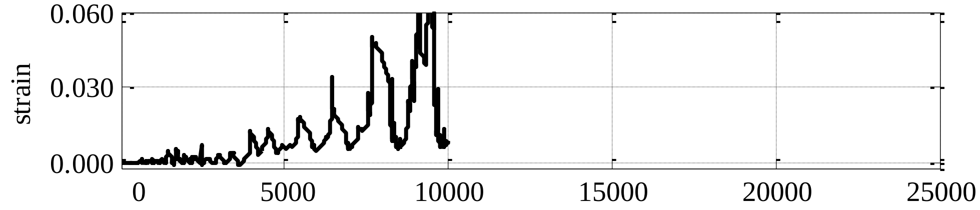
LTII-IN(2) (Beam 2)

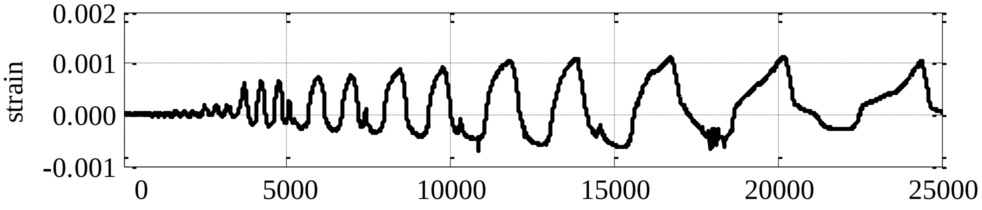
LBI-OUT(-2) (Beam 2)

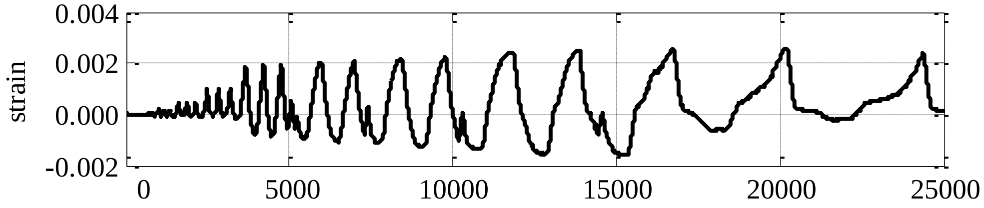
LBI-OUT(-1) (Beam 2)

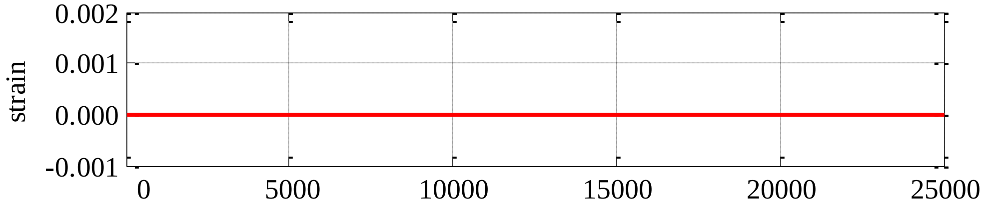
LBI-OUT(1) (Beam 2)

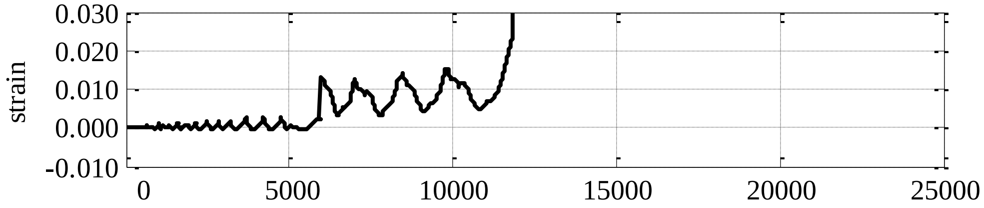
LBI-OUT(2) (Beam 2)

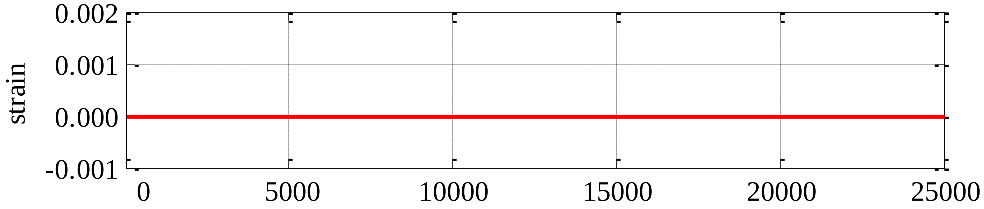
LBI-OUT(3) (Beam 2)

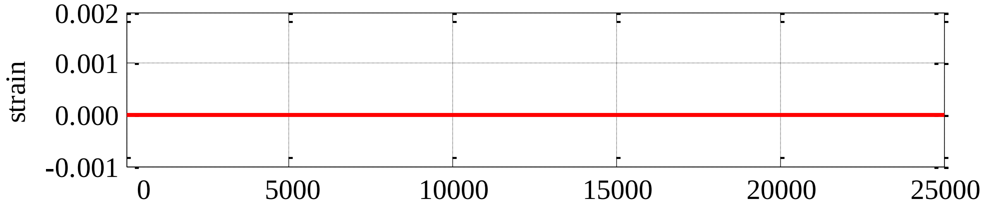
LBI-OUT(4) (Beam 2)

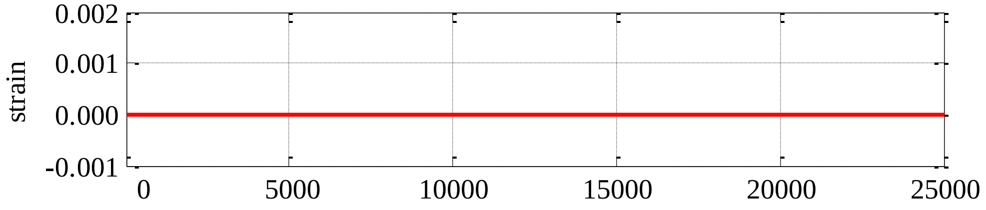
LBI-OUT(5) (Beam 2)

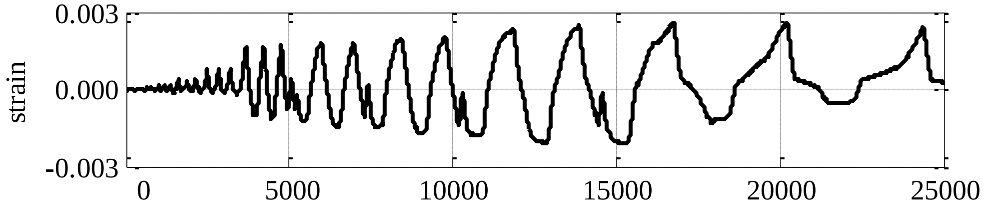
LBI-IN(-1) (Beam 2)

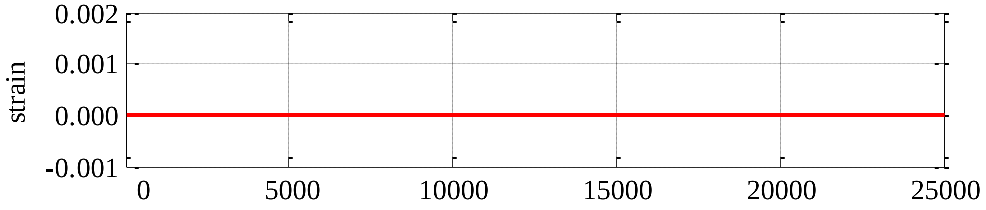
LBI-IN(1) (Beam 2)

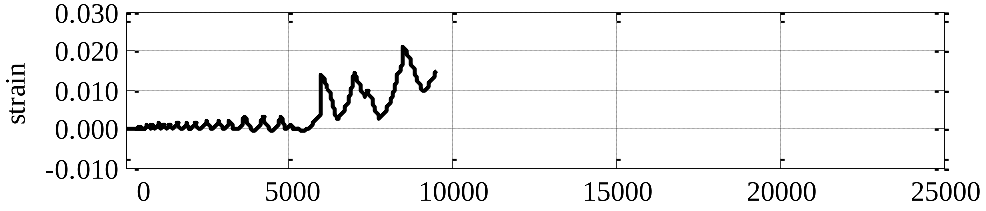
LBI-IN(2) (Beam 2)

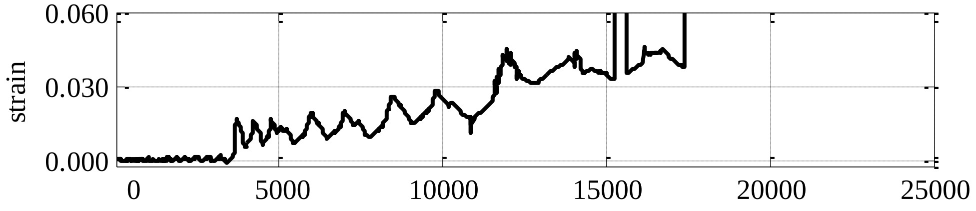
LBII-OUT(1) (Beam 2)

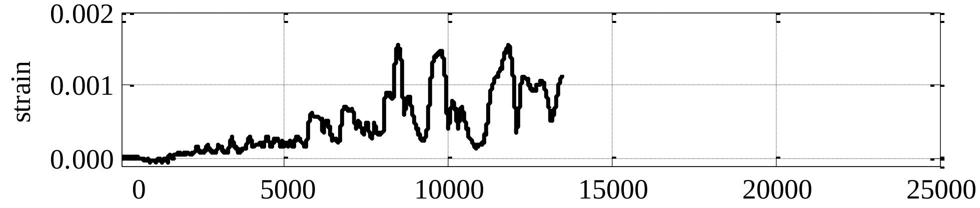

LBII-OUT(2) (Beam 2)

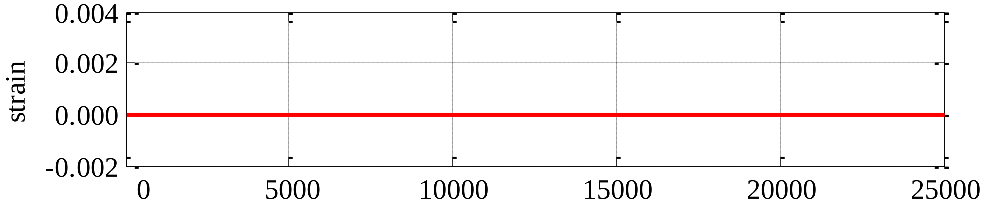

LBII-OUT(3) (Beam 2)

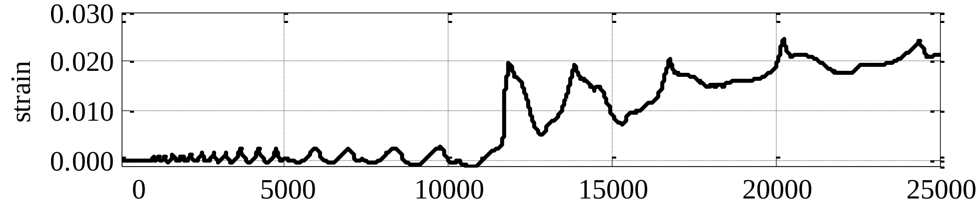

LBII-OUT(4) (Beam 2)

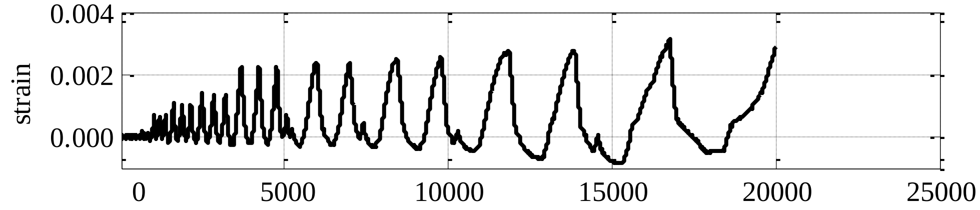

LBII-OUT(5) (Beam 2)

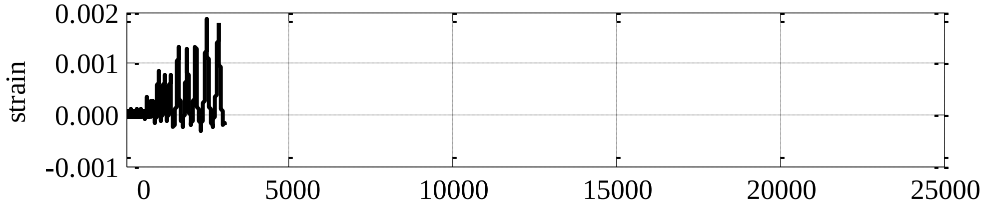

LBII-IN(1) (Beam 2)

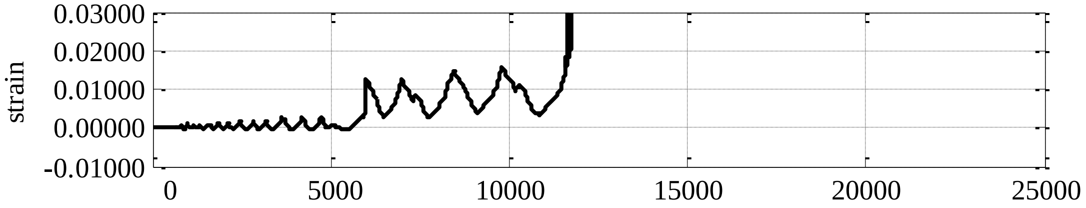
LBII-IN(2) (Beam 2)

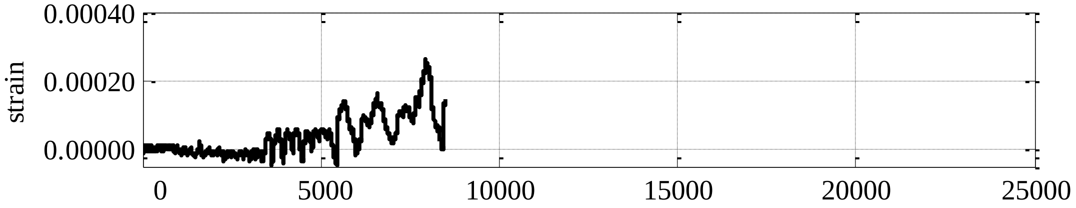
TA1-LEXT (Beam 2)

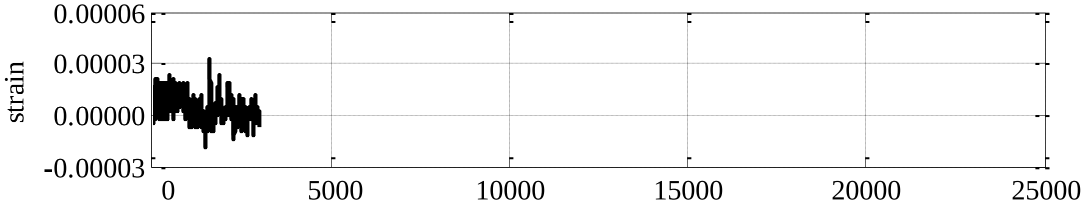
TA1-LINT (Beam 2)

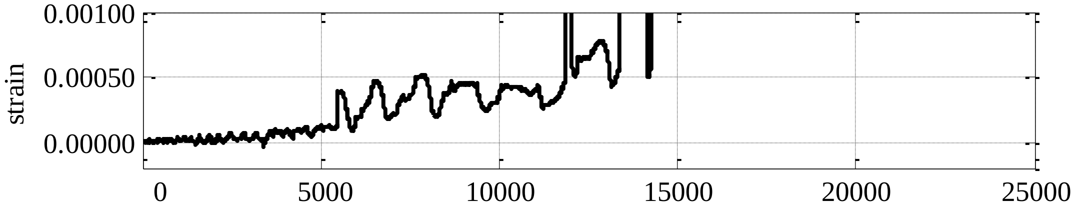
TA1-REXT (Beam 2)

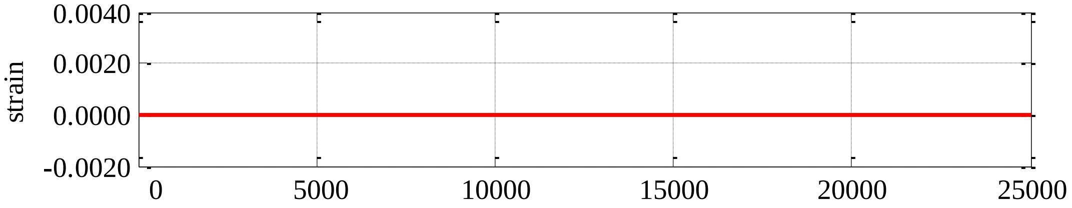
TA1-RINT (Beam 2)

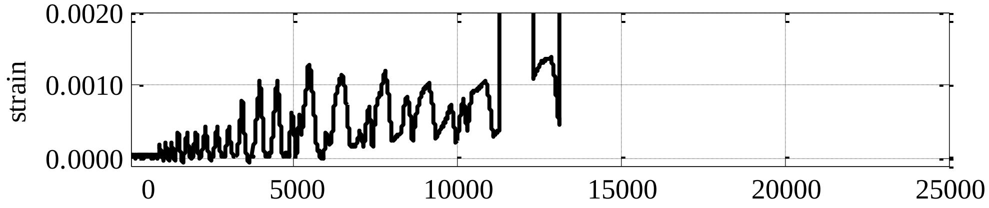
TA2-LEXT (Beam 2)

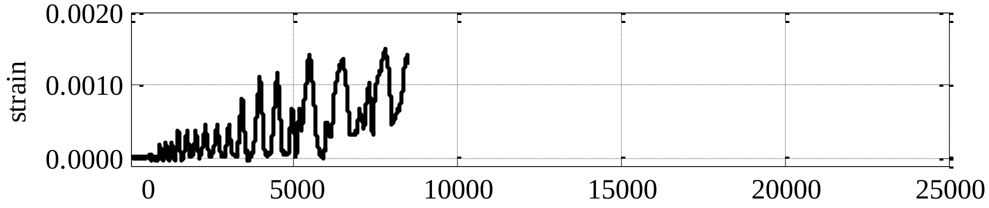
TA2-LINT (Beam 2)

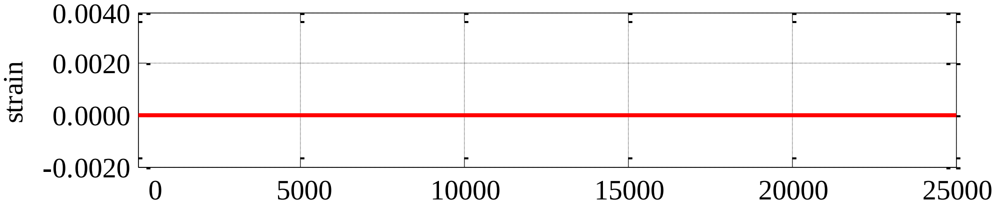
TA2-REXT (Beam 2)

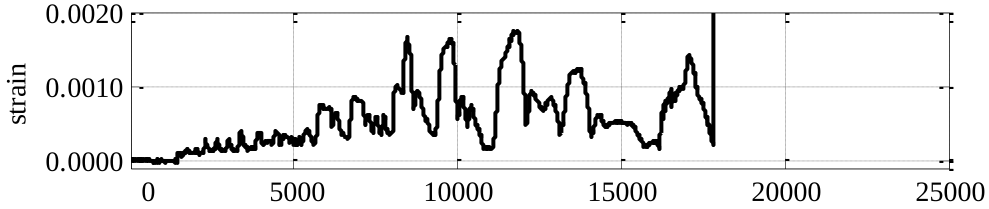
TA2-RINT (Beam 2)

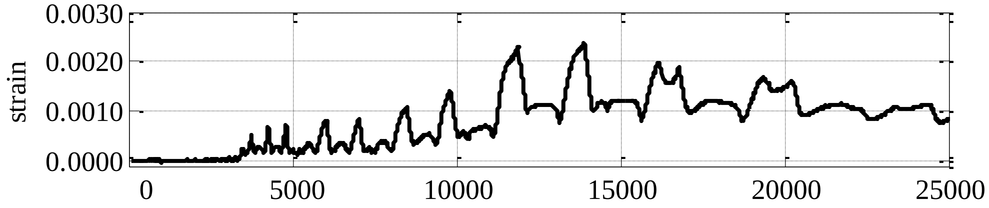
TB1-LEXT (Beam 2)

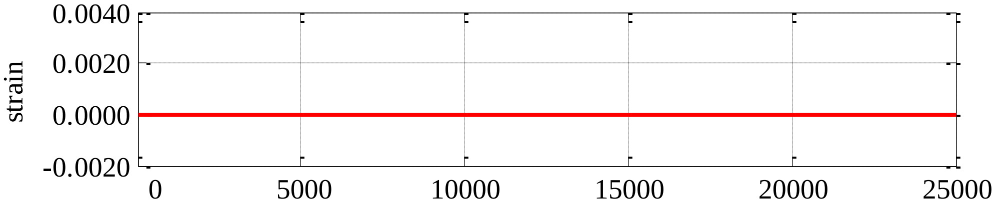

TB1-REXT (Beam 2)

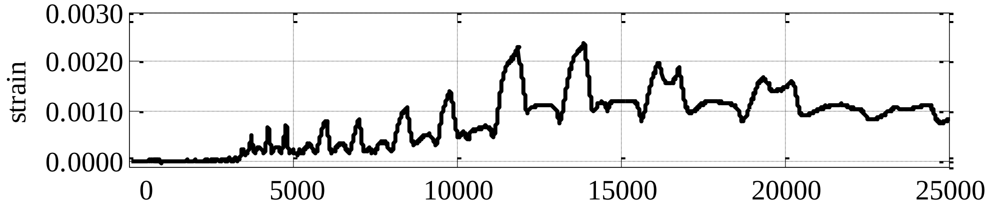

TB2-LEXT (Beam 2)

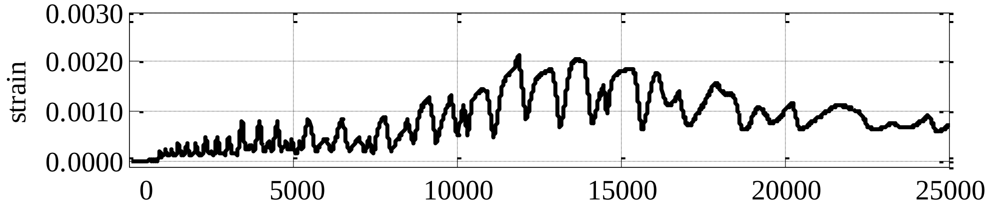

TB2-REXT (Beam 2)

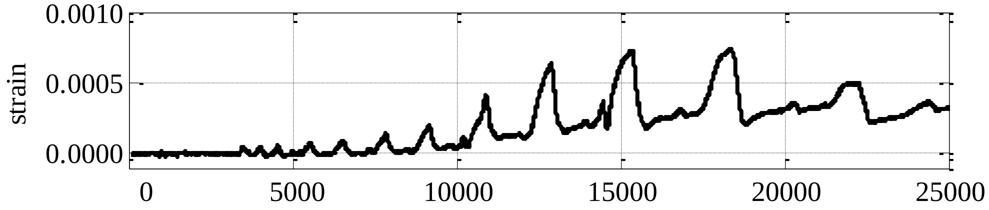

TB3-LEXT (Beam 2)

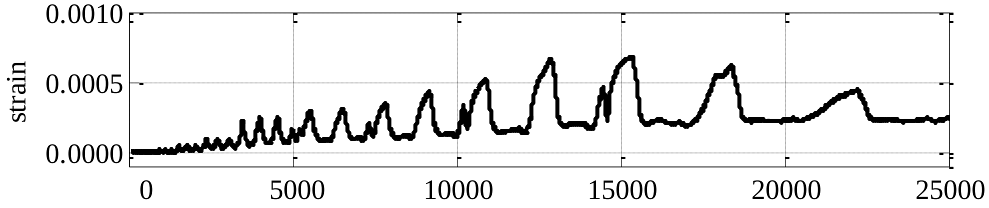

TB3-REXT (Beam 2)

Beam 2 Instrumentation Recordings: LVDTs

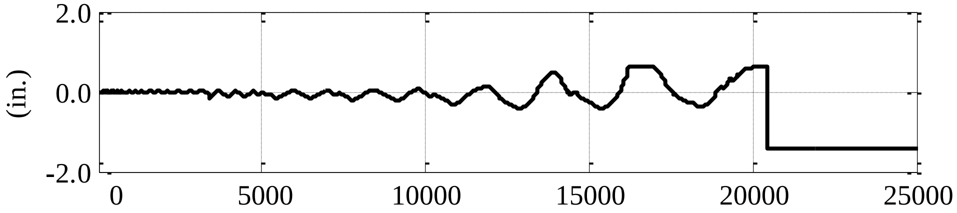
TL1 (Beam 2)

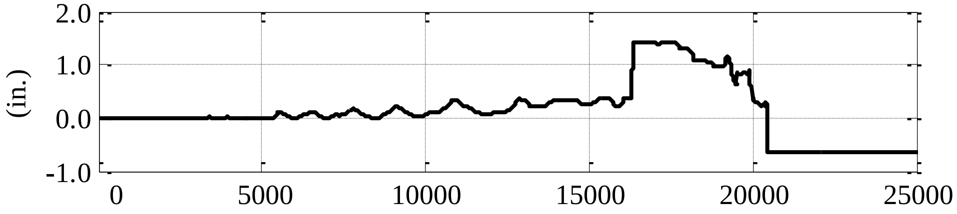
TL2 (Beam 2)

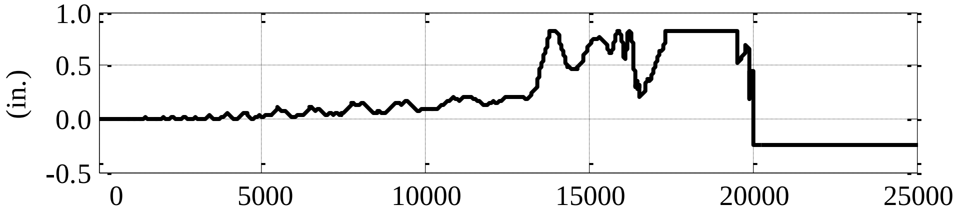
TL3 (Beam 2)

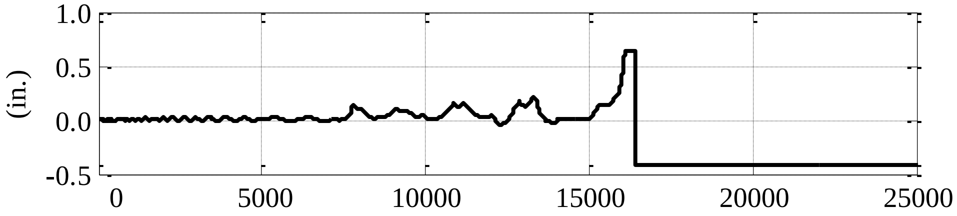
TL4 (Beam 2)

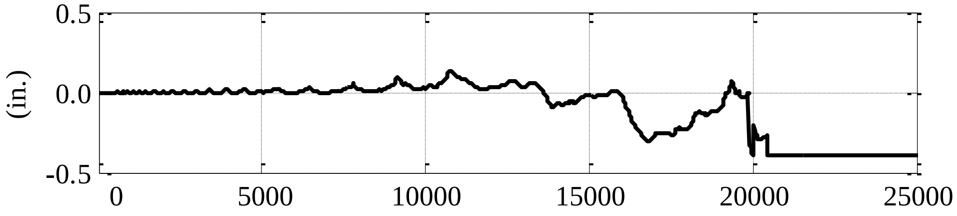
TL5 (Beam 2)

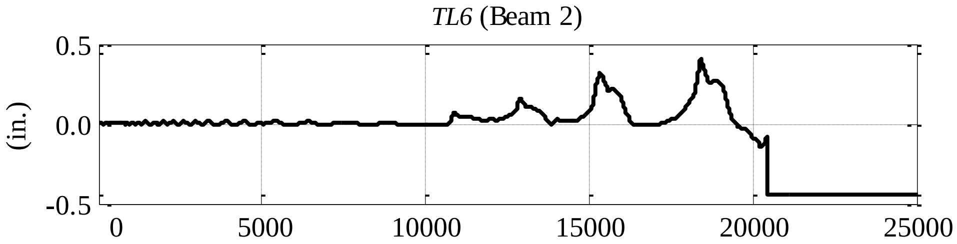
TL6 (Beam 2)
(in.)
0.5
0.0
-0.5
0
5000
10000
15000
20000
25000

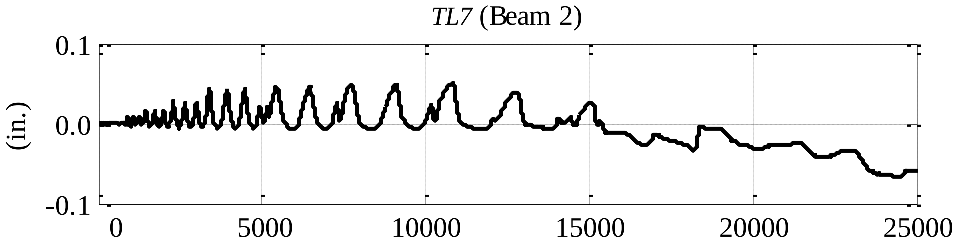
TL7 (Beam 2)
(in.)
0.1
0.0
-0.1
0
5000
10000
15000
20000
25000

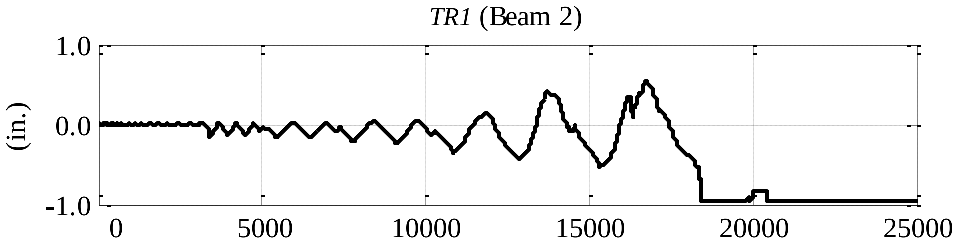
TR1 (Beam 2)
(in.)
1.0
0.0
-1.0
0
5000
10000
15000
20000
25000

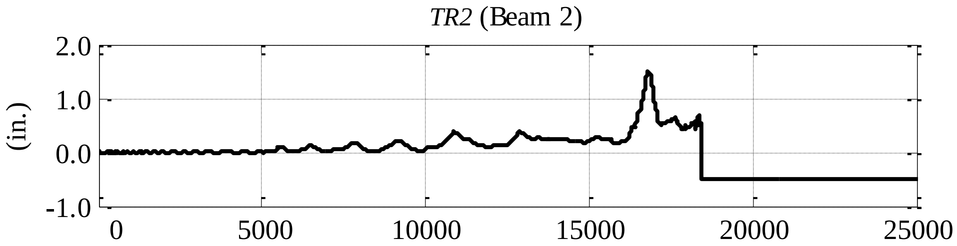
TR2 (Beam 2)
(in.)
2.0
1.0
0.0
-1.0
0
5000
10000
15000
20000
25000

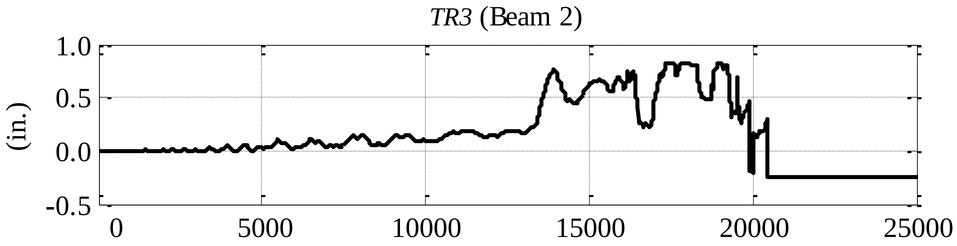
TR3 (Beam 2)
(in.)
1.0
0.5
0.0
-0.5
0
5000
10000
15000
20000
25000

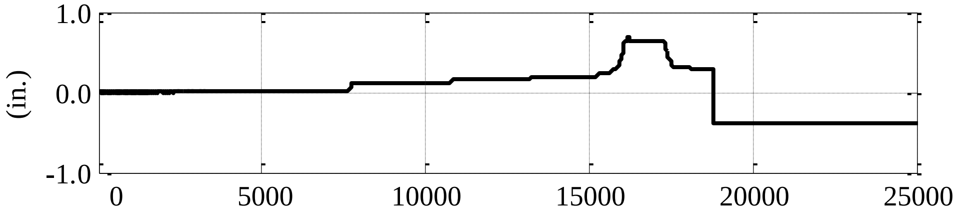

TR4 (Beam 2)

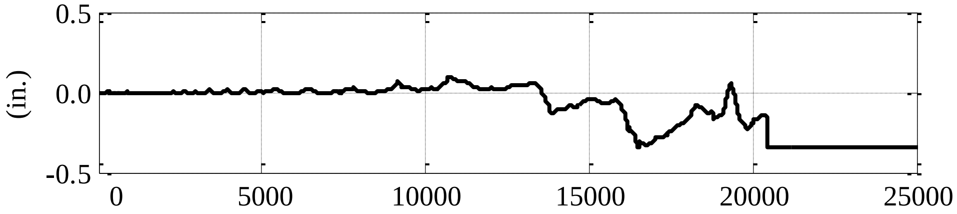

TR5 (Beam 2)

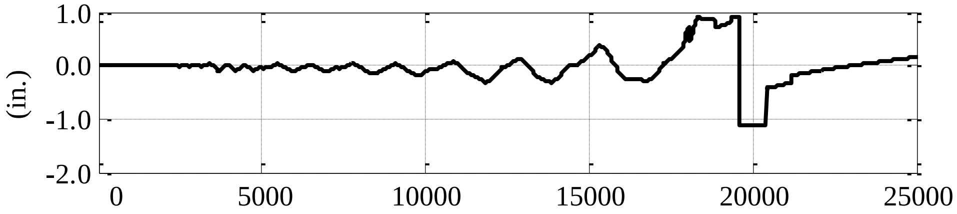

BL1 (Beam 2)

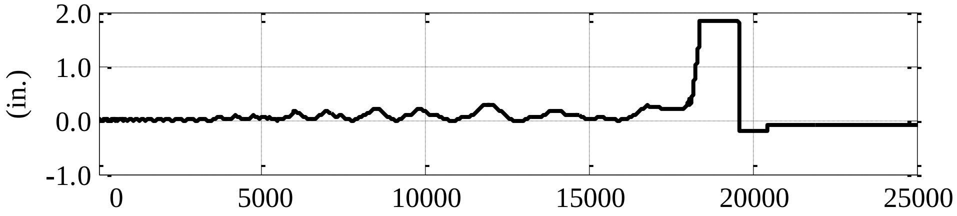

BL2 (Beam 2)

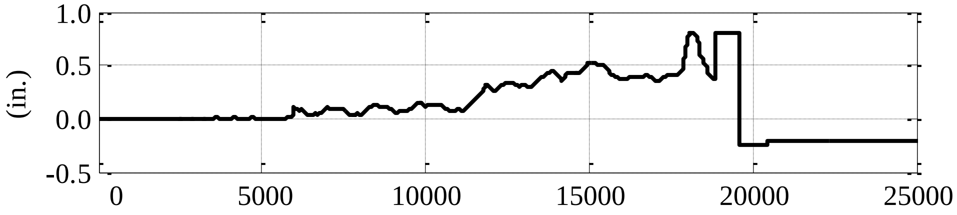

BL3 (Beam 2)

BL4 (Beam 2)

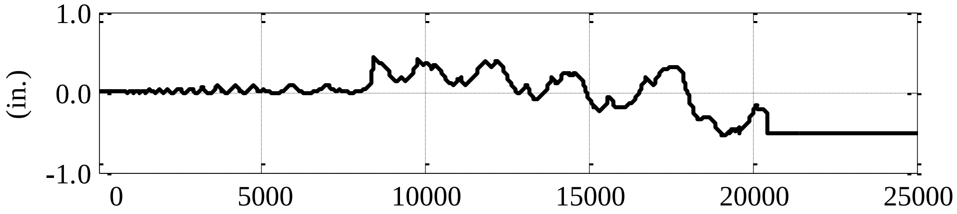

BL5 (Beam 2)

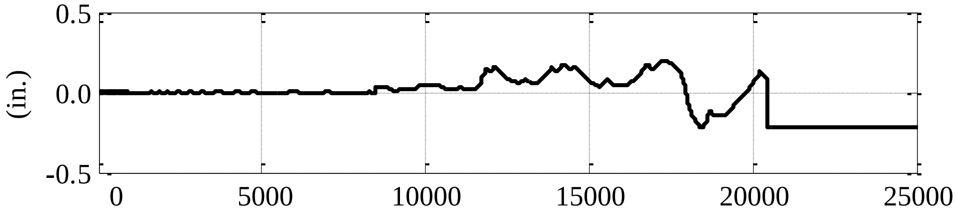

BL6 (Beam 2)

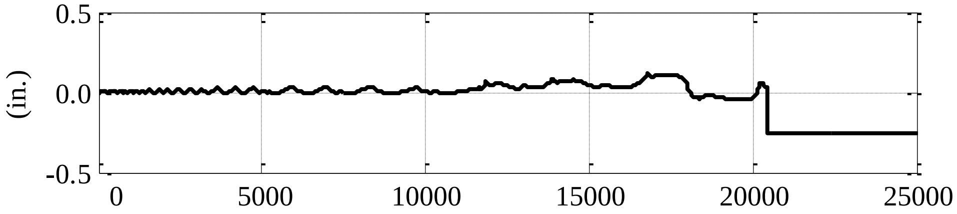

BL7 (Beam 2)

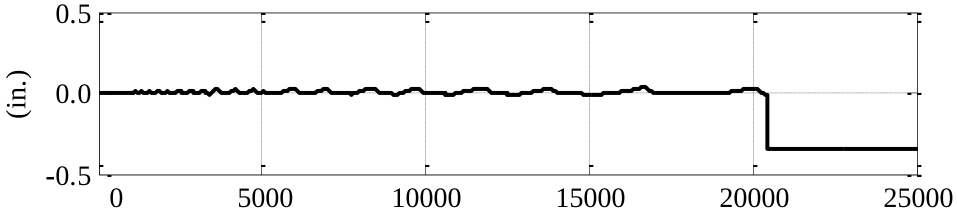

BR1 (Beam 2)

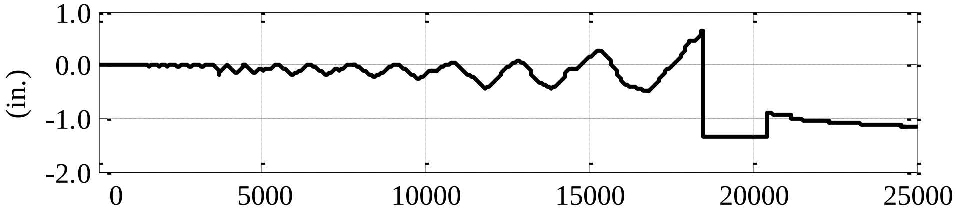

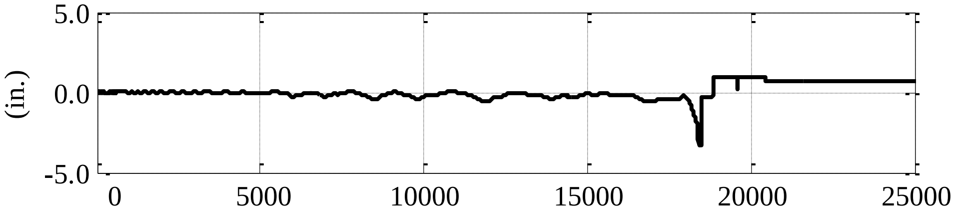
BR2 (Beam 2)

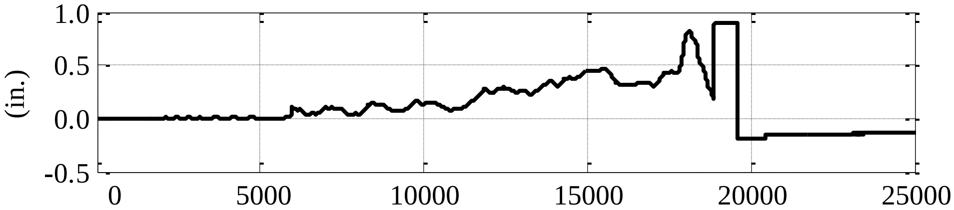
BR3 (Beam 2)

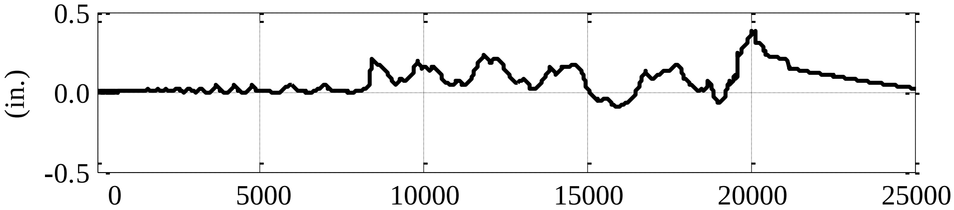
BR4 (Beam 2)

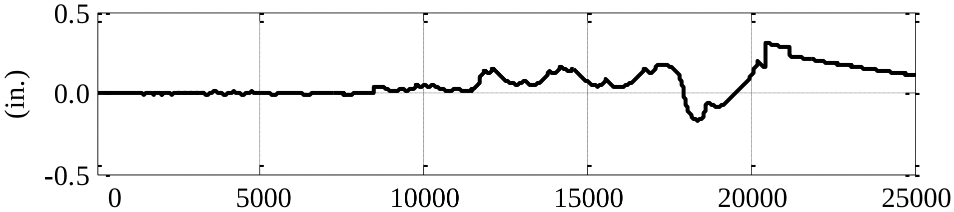
BR5 (Beam 2)

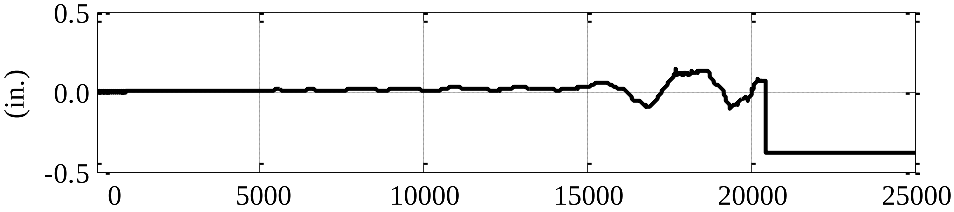
V1 (Beam 2)

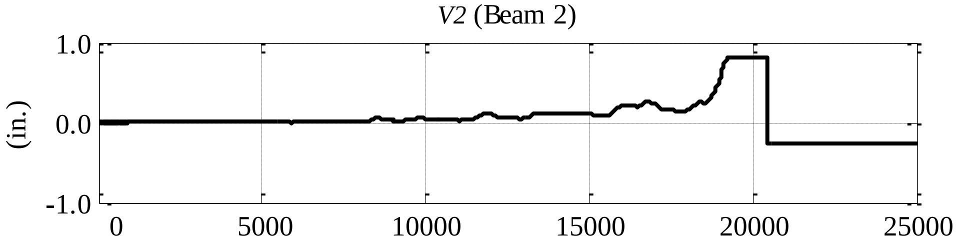
V2 (Beam 2)
(in.)
1.0
0.0
-1.0
0
5000
10000
15000
20000
25000

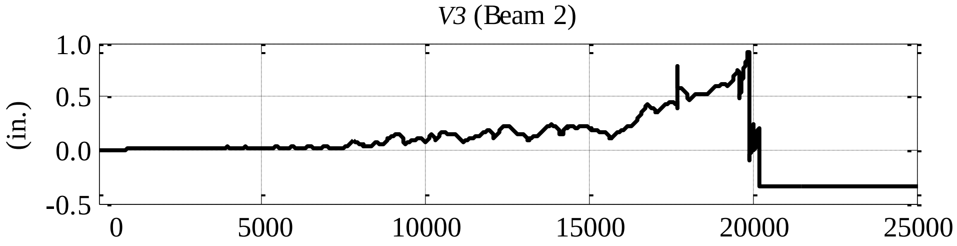
V3 (Beam 2)
(in.)
1.0
0.5
0.0
-0.5
0
5000
10000
15000
20000
25000

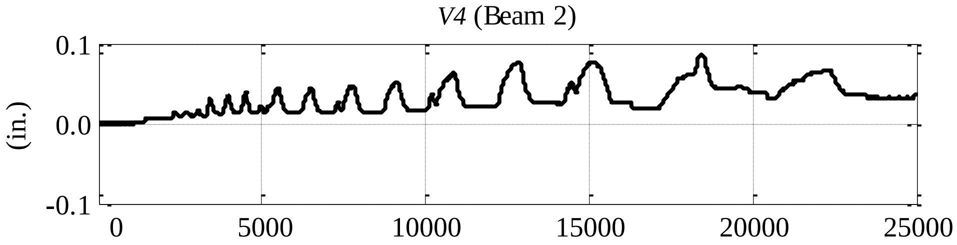
V4 (Beam 2)
(in.)
0.1
0.0
-0.1
0
5000
10000
15000
20000
25000

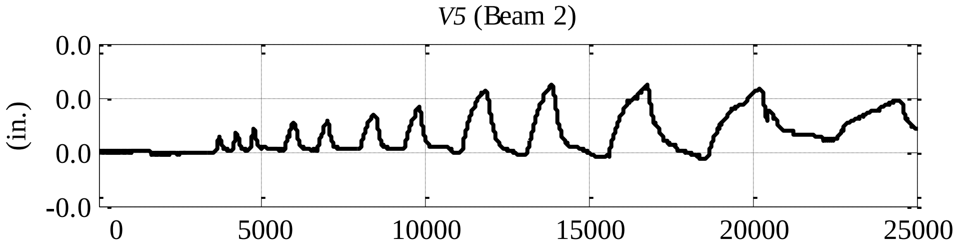
V5 (Beam 2)
(in.)
0.0
0.0
0.0
-0.0
0
5000
10000
15000
20000
25000

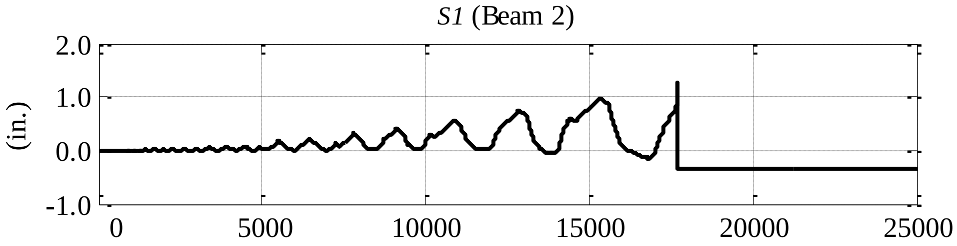
S1 (Beam 2)
(in.)
2.0
1.0
0.0
-1.0
0
5000
10000
15000
20000
25000

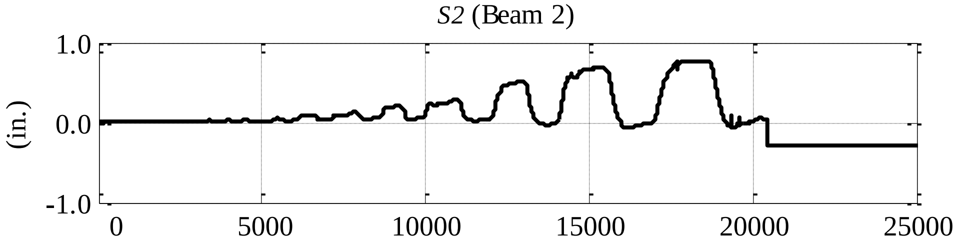
S2 (Beam 2)

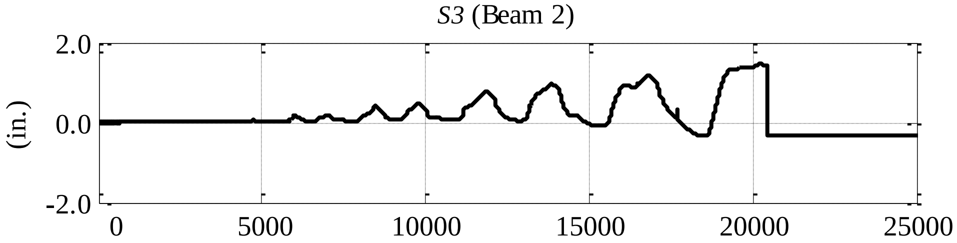
S3 (Beam 2)

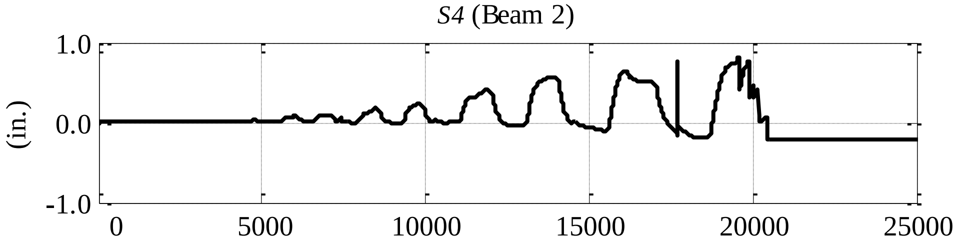
S4 (Beam 2)

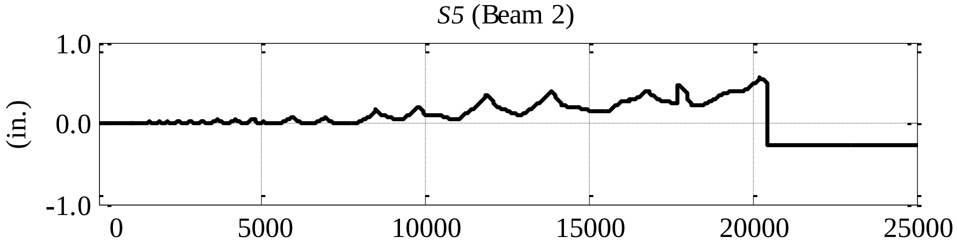
S5 (Beam 2)

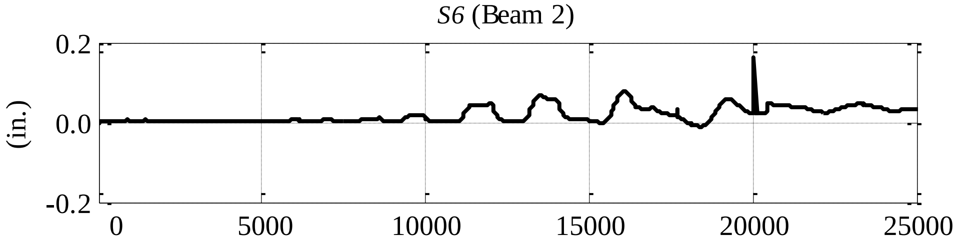
S6 (Beam 2)

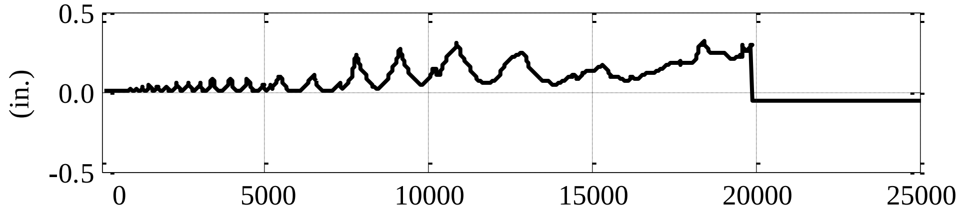

S7 (Beam 2)

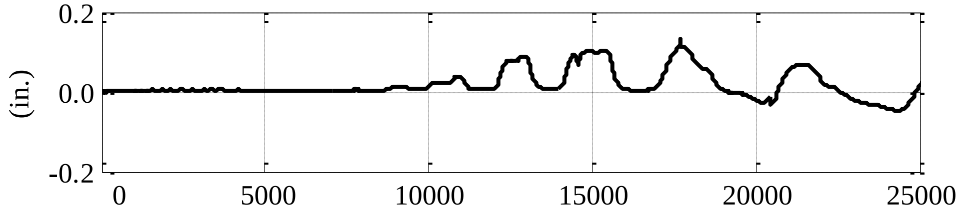

S8 (Beam 2)

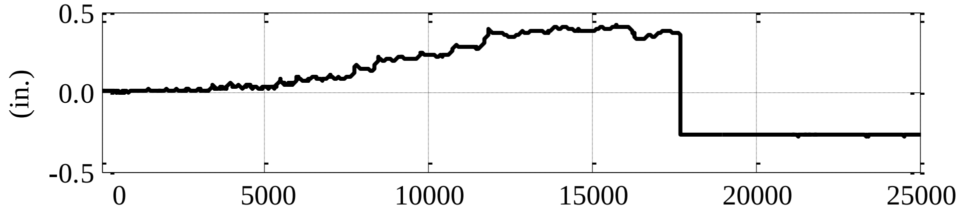

H1 (Beam 2)

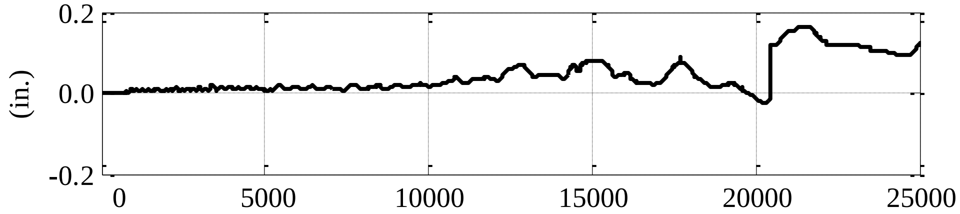

H2 (Beam 2)

MEASURED CRACK WIDTHS FOR BEAMS 1 AND 2

Table A1. Beam 1 Crack Widths

step	# of cycles	tip displ. (mm)	drift ratio	μ_Δ	current cycle #	direction of beam tip displacement	max. diagonal crack width (mm)	max. vertical crack width (mm)	max. interface crack width (mm)
1	3	3	0.07	0.1	1	down			
					1	up			
					1	zero			
2	3	7	0.18	0.3	1	down		0.25	
					2	up		0.2	
					2	zero			
3	3	11	0.28	0.5	1	down		0.33	
					1	up			
					1	zero			
4	3	14	0.38	0.8	1	down		0.6	
					1	up			
					1	zero			
5	3	31	0.81	1.1	1	down		1	0.6
					1	up			
					1	zero			
6	3	46	1.2	2.1	1	down	1.5		3
					1	up			
					1	zero			
7	1	13	0.33	0.7	1	n/a			2
8	2	69	1.8	3.2	1	down	3	2.5	4
					1	up			
					1	zero			
9	1	13	0.33	0.7	1	n/a			
10	2	103	2.7	4.2	1	down	5		5
					1	up	5		
					3	zero		2.5	
11	1	13	0.33	0.7	1	n/a			
12	2	139	3.6	6.4	1	down	25		
					1	up			
					1	zero			
13	1	13	0.33	0.7	1	n/a			
14	1	194	5.1	8.5	1	n/a			
15	1	13	0.33	0.7	1	n/a			
16	1	210	5.5	11.7	1	n/a			

Table A2. Beam 2 Crack Widths

step	# of cycles	tip displ. (mm)	drift ratio	μ_Δ	current cycle #	direction of beam tip displacement	max. diagonal crack width (mm)	max. vertical crack width (mm)	max. interface crack width (mm)
1	3	3	0.07	0.2	1	down		0.08	
						up			
					3	zero			
2	3	6	0.16	0.3	1	down		0.3	
						up			
					3	zero		0.33	
3	3	11	0.28	0.6	1	down	0.2	0.4	
						up	0.2	0.4	
					3	zero	0.1	0.25	
4	3	15	0.4	0.9	1	down	0.3	0.4	
						up	0.2	0.3	
					3	zero	0.15	0.25	
5	3	33	0.87	1.9	1	down	0.5	0.5	
						up	0.3	0.5	
					3	zero	0.15	0.2	
6	3	46	1.2	2.6	1	down	0.6	1	
						up	0.6	1.25	
					3	zero	0.3	0.5	
7	1	13	0.33	0.7	1	n/a	n/a		
8	2	69	1.8	3.9	1	down	1.5	2	
					1	up	0.6	2	
					3	zero	1.5	2	
9	1	13	0.33	0.7	1	n/a	n/a		
10	2	109	2.9	6.2	1	down	3	4	
					1	up	1.5	3	
					3	zero	4	5	
11	1	13	0.33	0.7	1	n/a	n/a		
12	2	147	3.9	8.3	1	down	5	6	11
					1	up	6	8	20
					2	zero	7	15	20
13	1	13	0.33	0.7	1	cycle omitted			
14	1	203	5.3	11.4	1	down	7	9	
15	1	13	0.33	0.7	1	n/a			
16	1	222 (-244)	5.8 (-6.4)	12.5 (-13.7)	1	n/a			

APPENDIX B

Transverse reinforcement volumetric ratios for Chapter 6 archetype buildings are listed below. In the tables provided, ρ_v signifies the volumetric transverse reinforcement ratio required for shear, while ρ_{conf} signifies volumetric transverse reinforcement ratio required for confinement as specified in the ACI 318-11 code. The controlling values are highlighted in the tables.

Table B.1. Building A10-3.

Story	Exterior Column		Interior Column	
	ρ_v	ρ_{conf}	ρ_v	ρ_{conf}
1	0.0115	0.009	0.0108	0.009
2	0.0064	0.009	0.0127	0.009
3	0.0064	0.009	0.0127	0.009
4	0.0064	0.009	0.0127	0.009
5	0.0064	0.009	0.0127	0.009
6	0.0064	0.009	0.0127	0.009
7	0.0064	0.009	0.0127	0.009
8	0.0064	0.009	0.0127	0.009
9	0.0064	0.009	0.0127	0.009
10	0.0064	0.009	0.0127	0.009

Table B.2. Building A10-4.

Story	Exterior Column		Interior Column		Middle Column	
	ρ_v	ρ_{conf}	ρ_v	ρ_{conf}	ρ_v	ρ_{conf}
1	0.0104	0.009	0.0138	0.009	0.0138	0.009
2	0.0066	0.009	0.0132	0.009	0.0132	0.009
3	0.0066	0.009	0.0132	0.009	0.0132	0.009
4	0.0066	0.009	0.0132	0.009	0.0132	0.009
5	0.0066	0.009	0.0132	0.009	0.0132	0.009
6	0.0066	0.009	0.0132	0.009	0.0132	0.009
7	0.0066	0.009	0.0132	0.009	0.0132	0.009
8	0.0066	0.009	0.0132	0.009	0.0132	0.009
9	0.0066	0.009	0.0132	0.009	0.0132	0.009
10	0.0066	0.009	0.0132	0.009	0.0132	0.009

Table B.3. Building A20-3.

Story	Exterior Column		Interior Column	
	ρ_v	ρ_{conf}	ρ_v	ρ_{conf}
1	0.0152	0.009	0.0111	0.009
2	0.0033	0.009	0.0033	0.009
3	0.0033	0.009	0.0034	0.009
4	0.0033	0.009	0.0034	0.009
5	0.0033	0.009	0.0034	0.009
6	0.0033	0.009	0.0035	0.009
7	0.0033	0.009	0.0066	0.009
8	0.0033	0.009	0.0066	0.009
9	0.0033	0.009	0.0066	0.009
10	0.0033	0.009	0.0066	0.009
11	0.0036	0.009	0.0072	0.009
12	0.0036	0.009	0.0072	0.009
13	0.0036	0.009	0.0072	0.009
14	0.0036	0.009	0.0072	0.009
15	0.0036	0.009	0.0072	0.009
16	0.0036	0.009	0.0072	0.009
17	0.0036	0.009	0.0072	0.009
18	0.0036	0.009	0.0072	0.009
19	0.0036	0.009	0.0072	0.009
20	0.0036	0.009	0.0072	0.009

Table B.4. Building A20-4.

Story	Exterior Column		Interior Column		Middle Column	
	ρ_v	ρ_{conf}	ρ_v	ρ_{conf}	ρ_v	ρ_{conf}
1	0.0150	0.009	0.0125	0.009	0.0123	0.009
2	0.0062	0.009	0.0092	0.009	0.0091	0.009
3	0.0062	0.009	0.0124	0.009	0.0091	0.009
4	0.0062	0.009	0.0124	0.009	0.0092	0.009
5	0.0062	0.009	0.0124	0.009	0.0092	0.009
6	0.0062	0.009	0.0124	0.009	0.0124	0.009
7	0.0062	0.009	0.0124	0.009	0.0124	0.009
8	0.0062	0.009	0.0124	0.009	0.0124	0.009
9	0.0062	0.009	0.0124	0.009	0.0124	0.009
10	0.0062	0.009	0.0124	0.009	0.0124	0.009
11	0.0086	0.009	0.0171	0.009	0.0171	0.009
12	0.0086	0.009	0.0171	0.009	0.0171	0.009
13	0.0086	0.009	0.0171	0.009	0.0171	0.009
14	0.0086	0.009	0.0171	0.009	0.0171	0.009
15	0.0086	0.009	0.0171	0.009	0.0171	0.009
16	0.0086	0.009	0.0171	0.009	0.0171	0.009
17	0.0086	0.009	0.0171	0.009	0.0171	0.009
18	0.0086	0.009	0.0171	0.009	0.0171	0.009
19	0.0086	0.009	0.0171	0.009	0.0171	0.009
20	0.0086	0.009	0.0171	0.009	0.0171	0.009

APPENDIX C

Table C.1. Bin 1 ground motion specifics (See Chapter 6).

GM	NGA#	Year	Event	Station	Mag	DE Scale Factor	MCE Scale Factor
1	1119	1995	Kobe- Japan	Takarazuka	6.90	0.6540	0.9810
2	184	1979	Imperial Valley-06	El Centro Diff.Array	6.53	1.1943	1.7915
3	316	1981	Westmorland	Parachute Test Site	5.90	1.9918	2.9877
4	185	1979	Imperial Valley-06	Holtville Post Office	6.53	2.1032	3.1548
5	568	1986	San Salvador	Geotech Investig Center	5.80	0.9732	1.4598
6	159	1979	Imperial Valley-06	Agrarias	6.53	2.0139	3.0209
7	183	1979	Imperial Valley-06	El Centro Array #8	6.53	1.4350	2.1525
8	169	1979	Imperial Valley-06	Delta	6.53	1.5698	2.3547
9	158	1979	Imperial Valley-06	Aeropuerto Mexicali	6.53	2.0269	3.0404
10	1116	1995	Kobe- Japan	Shin-Osaka	6.90	1.7612	2.6418
11	585	1987	Baja California	Cerro Prieto	5.50	1.0520	1.5780
12	178	1979	Imperial Valley-06	El Centro Array #3	6.53	2.2000	3.3000
13	1605	1999	Duzce- Turkey	Duzce	7.14	0.9256	1.3884
14	1634	1990	Manjil- Iran	Abhar	7.37	2.2000	3.3000
15	721	1987	Superstition Hills-02	El Centro Imp. Co. Cent	6.54	1.6199	2.4299
16	180	1979	Imperial Valley-06	El Centro Array #5	6.53	1.2566	1.8849
17	881	1992	Landers	Morongo Valley	7.28	2.1565	3.2348
18	1158	1999	Kocaeli- Turkey	Duzce	7.51	1.2022	1.8033
19	319	1981	Westmorland	Westmorland Fire Sta	5.90	1.2047	1.8071
20	171	1979	Imperial Valley-06	EC Meloland Overpass FF	6.53	1.3093	1.9640
21	879	1992	Landers	Lucerne	7.28	1.6033	2.4050
22	179	1979	Imperial Valley-06	El Centro Array #4	6.53	1.3175	1.9763
23	174	1979	Imperial Valley-06	El Centro Array #11	6.53	1.8730	2.8095
24	165	1979	Imperial Valley-06	Chihuahua	6.53	1.6515	2.4773
25	181	1979	Imperial Valley-06	El Centro Array #6	6.53	1.2397	1.8596
26	170	1979	Imperial Valley-06	EC County Center FF	6.53	1.6856	2.5284
27	2734	1999	Chi-Chi- Taiwan-04	CHY074	6.20	1.3172	1.9758
28	1165	1999	Kocaeli- Turkey	Izmit	7.51	2.2000	3.3000
29	1602	1999	Duzce- Turkey	Bolu	7.14	0.8420	1.2630
30	1176	1999	Kocaeli- Turkey	Yarimca	7.51	1.3547	2.0321

Table C.2. Bin 2 ground motion specifics (See Chapter 6).

GM	NGA#	Year	Event	Station	Mag	DE Scale Factor	MCE Scale Factor
1	184	1979	Imperial Valley-06	El Centro Diff.Array	6.53	1.2419	1.8629
2	169	1979	Imperial Valley-06	Delta	6.53	1.6012	2.4018
3	174	1979	Imperial Valley-06	El Centro Array #11	6.53	1.9822	2.9733
4	182	1979	Imperial Valley-06	El Centro Array #7	6.53	0.8905	1.3358
5	1605	1999	Duzce- Turkey	Duzce	7.14	0.9002	1.3503
6	183	1979	Imperial Valley-06	El Centro Array #8	6.53	1.3904	2.0856
7	725	1987	Superstition Hills-02	Poe Road (temp)	6.54	1.9827	2.9741
8	1158	1999	Kocaeli- Turkey	Duzce	7.51	1.1796	1.7694
9	179	1979	Imperial Valley-06	El Centro Array #4	6.53	1.2101	1.8152
10	879	1992	Landers	Lucerne	7.28	1.4196	2.1294
11	1165	1999	Kocaeli- Turkey	Izmit	7.51	2.1891	3.2837
12	316	1981	Westmorland	Parachute Test Site	5.90	1.7375	2.6063
13	728	1987	Superstition Hills-02	Westmorland Fire Sta	6.54	1.8693	2.8040
14	171	1979	Imperial Valley-06	EC Meloland Overpass FF	6.53	1.1385	1.7078
15	170	1979	Imperial Valley-06	EC County Center FF	6.53	1.4570	2.1855
16	900	1992	Landers	Yermo Fire Station	7.28	1.8146	2.7219
17	721	1987	Superstition Hills-02	El Centro Imp. Co. Cent	6.54	1.6504	2.4756
18	723	1987	Superstition Hills-02	Parachute Test Site	6.54	0.7730	1.1595
19	821	1992	Erzican- Turkey	Erzincan	6.69	0.8867	1.3301
20	1116	1995	Kobe- Japan	Shin-Osaka	6.90	1.9789	2.9684
21	95	1972	Managua- Nicaragua-01	Managua- ESSO	6.24	2.2000	3.3000
22	178	1979	Imperial Valley-06	El Centro Array #3	6.53	2.0716	3.1074
23	159	1979	Imperial Valley-06	Agrarias	6.53	2.2000	3.3000
24	1762	1999	Hector Mine	Amboy	7.13	2.2000	3.3000
25	2734	1999	Chi-Chi- Taiwan-04	CHY074	6.20	1.5936	2.3904
26	729	1987	Superstition Hills-02	Wildlife Liquef. Array	6.54	1.5206	2.2809
27	161	1979	Imperial Valley-06	Brawley Airport	6.53	2.2000	3.3000
28	2114	2002	Denali- Alaska	TAPS Pump Station #10	7.90	0.7485	1.1228
29	185	1979	Imperial Valley-06	Holtville Post Office	6.53	1.7661	2.6492
30	158	1979	Imperial Valley-06	Aeropuerto Mexicali	6.53	2.2000	3.3000